Passage shaping in Axial Flow Turbines

David Andrew Bagshaw

Passage Shaping in Axial Flow Turbines

David Andrew Bagshaw

A Thesis presented for the degree of
Doctor of Philosophy

School of Engineering
University of Durham
England
February 2009

Dedicated to
Amy Herd

Passage Shaping in Axial Flow Turbines

David Andrew Bagshaw

Submitted for the degree of Doctor of Philosophy
February 2009

Abstract

This thesis describes the novel combination of reverse compound lean, leading edge extension and non-axisymmetric endwall profiling in a highly loaded turbine geometry, for the reduction of secondary flow and loss.

The thesis describes each geometrical modification in turn (in addition to their combination) and details their development from concept to experimentally measured performance. The designs are assessed using 3D Navier Stokes modelling. The best performing designs were manufactured and tested experimentally using pneumatic probes, flow visualisation and static pressure tappings.

The key sections of the thesis include:

- A review of previous non-axisymmetric profiled endwalls, with a view to understanding their performance in a full 3D passage design
- The assessment of reverse compound lean in a highly loaded turbine cascade
- The design development and subsequent testing of a 3D turbine passage design for minimising pressure loss associated with and kinetic energy in secondary flows

In summary, Passage Shaping works by using reverse compound lean to draw the secondary flows in to the endwall, where a combination of leading edge extension and non-axisymmetric endwall profiling work on the secondary flows to reduce their intensity. The key changes in the downstream flowfield, as a result of the passage shaping designs, are a reduction in loss (both profile and secondary) and a reduction in secondary flow, resulting in a more uniform exit yaw angle.

Declaration

The work in this thesis is based on research carried out in the School of Engineering at the University of Durham. No part of this thesis has been submitted elsewhere for any other degree or qualification and it is all my own work, unless referenced to the contrary in the text.

Acknowledgements

I would like to thank my supervisor Dr David Gregory-Smith for all his support, advice and without whose considerable experience the research would not have been possible. I would also like to thank Dr Grant Ingram, my unofficial second supervisor and PhD predecessor on this cascade, for his advice on cascade aerodynamics, information on the "intricaces" of the in-house post processing software and more recently for patiently reading drafts of the thesis.

Thanks go to the staff of the mechanical workshop for the construction of various components, including Tony Collinson for the construction of the upgraded cascade and to Gary Parker for every obscure and last minute request that was achieved or obtained.

The experience and support of Dr Mark Stokes, Dr Neil Harvey and Adrian White, of Rolls-Royce Turbine Systems, during my two summer placements is most appreciated. I hope now that they will find use of this work.

Finally, I would like to thank my family for encouraging me to start this and Amy for encouraging me to finish it.

Contents

List of Figures

List of Tables

Nomenclature and Symbols

0.1 Acronyms

CFD Computation Fluid Dynamics

CMM Coordinate Measuring Machine

CV Corner Vortex

ERCOFTAC European Research Community on Flow, Turbulence and Combustion

EWM (Near) Endwall Modification of Aerofoil Section

FAITH Forward And Inverse Three-Dimensional Linear Design System

HSV Horse shoe vortex

IGES Initial Graphics Exchange Specification

LE Leading Edge

NURBS Non Uniform Rational B-Spline

PEW Non-Axisymmetric Profiled Endwall

PIV Particle Image Velocimetry

PS Pressure side/pressure surface

PV Passage Vortex

RCL Reverse Compound Lean

ShV Shed Vortex

SKEH Secondary Kinetic Energy and Helicity

SLS Selective Laser Sintering

SS Suction side/suction surface

STL Stereolithography

TE Trailing Edge

TTL Transistor-Transistor Logic

0.2 Variables

C_{ax} Axial chord

C_{SKE} Secondary kinetic energy coefficient

C_P Specific Heat Capacity at Constant Pressure

C_{p0} Total Pressure Loss Coefficient

C_p Static Pressure Coefficient

C_{SKE} Secondary Kinetic Energy Coefficient

C_V Specific Heat Capacity at Constant Volume

I Streamwise Computational Coordinate

J Tangential/Circumferential Computational Coordinate

K Radial Computational Coordinate

Ma Mach Number

o Throat or Opening

p Static pressure

p_0 Total pressure

r Radial coordinate or Pressure ratio

R Radial coordinate

s Pitch or Entropy

t Tangential coordinate

T Temperature

v Velocity

V Velocity

x Axial coordinate

yaw Yaw angle (from axial)

0.3 Geometries

aggr Aggressive Endwall Profiling of C2 Geometry

C0 Prismatic Blade and planar endwall (reference case)

C1 Reverse compound lean geometry

C2 First generation Passage Shaping

C3 Second generation Passage Shaping

mild Mild Endwall Profiling of C2 Geometry

P0 Planar endwall

P1 First generation endwall

P2 Second generation endwall

P3 Third generation endwall

P4 Fourth generation endwall

0.4 Greek

α Yaw angle

β Pitch angle

γ Ratio of specific heats (C_P/C_V)

ρ Density

ζ Vorticity

η_t Turbine stage efficiency

0.5 Subscript

a Atmospheric

ideal Ideal (Efficiency)

mid Midspan

plot Plotted secondary velocity

r Radial

s Streamwise or Isentropic condition

sec Secondary

t Tangential or Turbine (Efficiency)

ups Upstream

x Axial

Chapter 1

Introduction

The aim of this thesis is to investigate the potential benefit of passage shaping on turbine performance, providing new geometries and design concepts that can be implemented in real aero engine design. The objective of the work is the development of concepts that can reduce the turbine secondary flows.

The work was funded by the Department of Trade and Industry and Rolls-Royce plc under the ATAP-10 project. The aim of this particular work is the development of fully three dimensional turbine design, combining the best of previous secondary flow reduction techniques with new blade shaping geometries.

The thesis is split into a series of design developments that culminate in a passage shaped geometry:

Chapter 5 reviews the current status of non-axisymmetric profiled endwall design within the Durham Cascade. The chapter describes the behaviours and performance of the endwall shapes. Whilst the majority of the experimental work presented in the chapter was performed by previous authors, an additional geometry was investigated and new analysis parameters are used to compare their relative performances.

Chapter 6 investigates (experimentally) the use of reverse compound lean in the high turning, high aspect ratio (1.6:1), high pressure (HP) turbine geometry of the Durham Cascade. The experimental results provide detail of the effect of lean on the secondary flows and the generation of loss.

Chapter 7 details the computational investigations undertaken to develop a first passage shaped geometry for the cascade. The chapter is further split into design stages comprising; axial lean, leading edge extension, and a combination of these geometries with the reverse compound lean described in Chapter 6. The successful design from these stages is combined with non-axisymmetric endwall profiling, with differing shapes at the two endwalls.

Chapter 8 details the experimental investigations of the final design from Chapter 7, at the standard measurement plane at 128% axial chord (C_{ax}). Measurements at planes further upstream, close to the trailing edge, are also presented. The effects of the passage shaping are also observed in surface flow visualisation pictures.

Chapter 9 describes the re-assessment of the profiled endwall designs from Chapter 8. The chapter details the development of a new endwall, with more restrictive design constraints. In addition, a planar endwall is investigated, with a view to understanding the summation of the passage shaping effects. The chapter includes both computational and experimental results.

Chapter 2

Literature Review

THIS chapter contains a review of literature relevant to the understanding of the work in this thesis. It describes the importance of improving efficiency in axial flow turbines. The chapter describes the geometric modifications made by numerous authors, to alter the passage flow field and ultimately improve efficiency.

2.1 The Axial Flow Turbine

The axial flow turbine (in either a steam or gas turbine form) is utilised in the majority of the world's primary energy conversion. Consequently, even minor performance gains have a significant impact on worldwide CO_2 emissions.

Ingram (2003) estimated that a 16% reduction in component total pressure loss (as a result of endwall profiling) would provide a 1.55% improvement in turbine stage efficiency. Nicholson (1981) calculated that a 1% improvement in turbine (stage) efficiency equated to a 0.8% reduction in specific fuel consumption for a Rolls-Royce RB211 engine at cruise condition. Based on the aircraft emissions data of Horton (2004), the 16% component loss reduction, applied across all existing aircraft, would result in a reduction in annual CO_2 of approximately six mega tonnes.

This result clearly indicates the potential benefit of improvements made to the performance of the HP turbine component on aircraft fuel consumption and highlights a significant ongoing need to improve its performance for monetary cost and environmental reasons.

The gas turbine has many uses including: electrical power generation (as in the Alstom GT24 seen in Figure 2.1), shaft power for ship propulsion (or natural gas compression), and aircraft propulsion (as in the Rolls-Royce Trent 1000 engine in Figure 2.2).

The focus of this work is the aeroengine turbine component due, for the most part, to the industrial sponsorship of the work. Despite this focus, the concepts investigated and the results found are equally applicable to other forms of axial flow turbine.

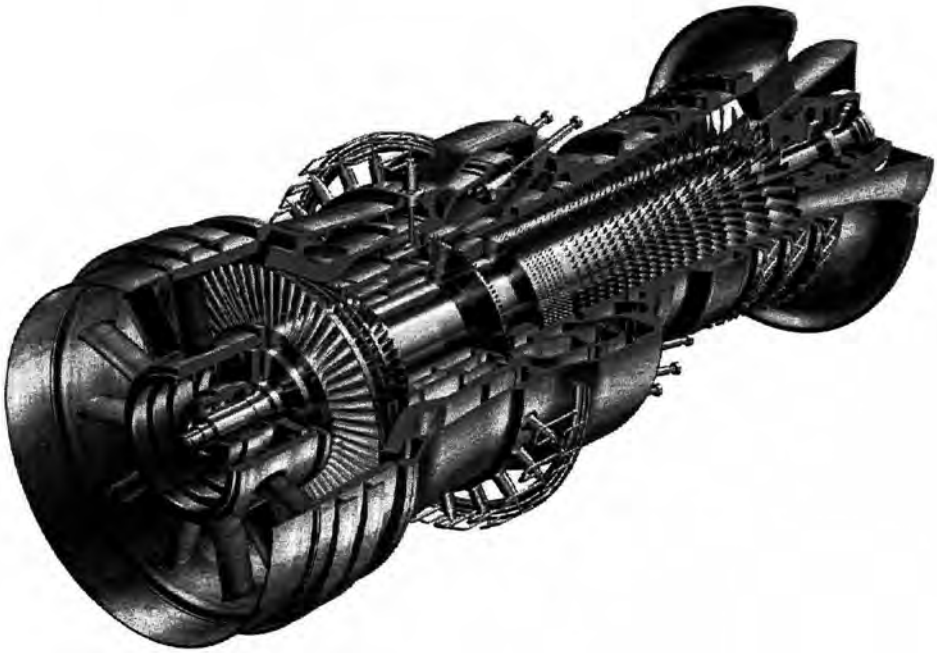

Figure 2.1: Gas Turbine Section - Alstom GT24

Figure 2.2: Aeroengine Section - Rolls-Royce Trent 1000

2.1.1 Thermodynamic cycle

The ideal gas turbine cycle is the Joule (or Brayton) cycle. In this ideal cycle the efficiency (η) depends purely upon the pressure ratio (r) across the turbine and the properties of the working fluid (γ), as presented in Equation 2.1.

$$\eta_{ideal} = 1 - (\frac{1}{r})^{\frac{\gamma-1}{\gamma}} \tag{2.1}$$

The work output is dependent on the pressure ratio but also on the temperature at turbine inlet. This temperature limit is determined by thermomechanical limitations and regulations on the formation of oxides of nitrogen, which are linked to high combustion temperatures.

Actual turbine performance is complicated by entropy generation in all components; compressor, combustor and turbine.

The simplified thermodynamic cycle of a turbojet is a good starting point for a description of the performance of a gas turbine. The temperature-entropy (T-s) diagram in Figure 2.3, taken from Saravanamuttoo et al. (2001), shows the full open cycle as follows:

- $p_a \rightarrow p_{01}$ - compression from atmospheric pressure (p_a) to inlet total pressure (p_{01}), due to the engine air speed
- $p_{01} \rightarrow p_{02}$ - rise in total pressure from the compressor
- $p_{02} \rightarrow p_{03}$ - pressure loss in the combustion chamber
- $p_{03} \rightarrow p_{04}$ - pressure decrease due to work extracted by the turbine
- $p_{04} \rightarrow p_5$ - kinetic energy in the exit flow

With the exception of the compression and expansion to atmospheric conditions this also describes the cycle behaviour of the high pressure core of a turbofan engine. The pressure drop p_{03} to p_{04} typically occurs across multiple blade rows and stages.

The pressure drop across a single HP stage is described by the T-s diagram of Figure 2.4, also taken from Saravanamuttoo et al. (2001). A change of notation is necessary here, and from this point stator inlet conditions use subscript (1), intrarow conditions use subscript (2) and rotor exit conditions use subscript (3).

2.1.2 Turbine performance

The turbine stage isentropic efficiency (η_t) is defined as:

$$\eta_t = \frac{T_{01} - T_{03}}{T_{01} - T_{03S}} \tag{2.2}$$

where T_{01} is the turbine inlet total temperature, T_{03} the outlet total temperature and T_{03S} the isentropic outlet total temperature. Using the isentropic relation for pressure and temperature, this returns the following relationship:

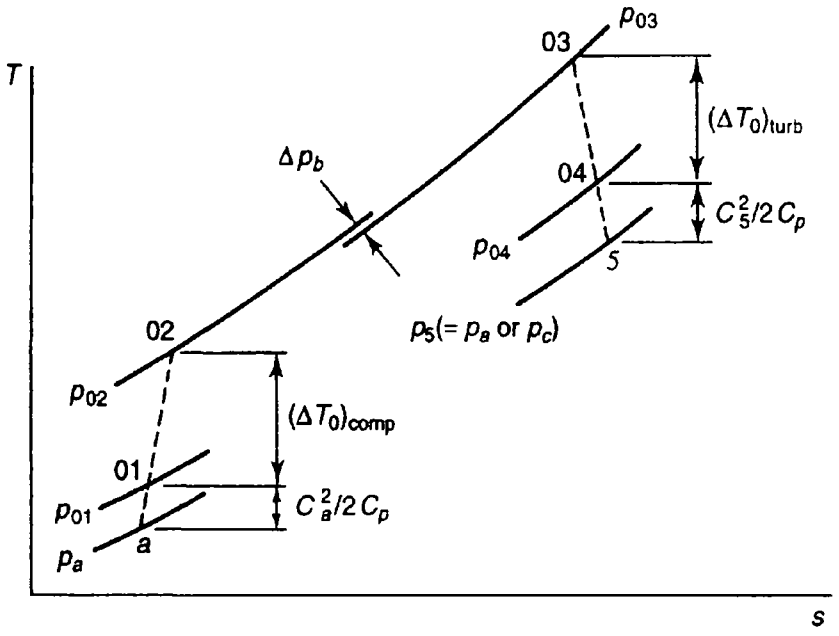

Figure 2.3: Turbojet T-s diagram (Saravanamuttoo et al. (2001))

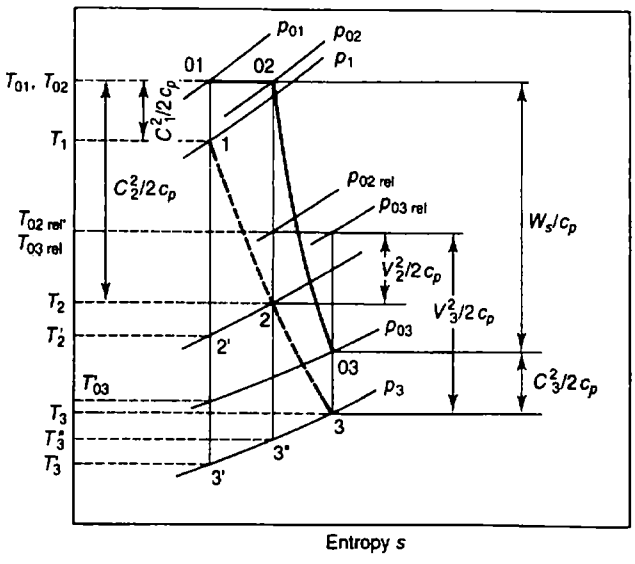

Figure 2.4: Turbine Stage T-s diagram (Saravanamuttoo et al. (2001))

$$\eta_t = \frac{T_{01} - T_{03}}{T_{01}(1 - \frac{1}{\frac{P_{01}}{P_{03}}})^{\frac{\gamma-1}{\gamma}}} \tag{2.3}$$

These assume constant C_P and constant γ. T_{01} is the combustor exit temperature (limited by material developments) and the difference to T_{03} is an indication of the energy extracted from the fluid.

2.1.3 Entropy and engine efficiency

In the diagram in Figure 2.4, the horizontal line between P_{01} and P_{02} and the horizontal component of the line between P_{02} and P_{03} indicate the entropy gained (or drop in total pressure) through the nozzle (stator) and blade (rotor) components respectively. These drops in total pressure are due to a number of different losses. The sources of loss within a typical aeroengine HP turbine stage are as follows:

- profile loss (affected by the geometry, fore or aft loading and component wetted area)
- boundary layer separation (either on the aerofoil and or endwall surfaces)
- leakage (over-tip, disc-cavity)
- cooling flows (film, platform, trailing edge)
- secondary flows (energy lost to the generation of and viscous interaction around vortical motion)

The relative magnitudes of these loss sources are indicated by the chart of Haller (1997) in Figure 2.5. The significance of secondary loss is evident from this chart. The need to reduce this remains an important factor in turbine design.

Losses in turbomachinery are described in depth by the IGTI Scholar lecture of Denton (1993). The paper covers all areas of loss generation and describes methods of approximating these losses based on geometric data. Denton (1993) explains that 90% of the entropy generated in boundary layers occurs in the laminar sub layer and logarithmic regions. This entropy generation dissipates the energy of the fluid and is a loss. The entropy rise (loss of energy) as a result of the viscous dissipation is considered, by Denton (1993), to be proportional to the local velocity cubed.

Entropy and entropy change cannot be measured directly and therefore the change in another fluid property, total pressure, is used to observe the relative performances of components in a linear cascade.

The recovery of energy from vortical flows within the turbine blade passage would be very difficult without the addition of some form of rotating machinery within the passage itself. It is not clear whether the energy in vortical motion can be used to control other loss generating features. As such, vortices are typically considered as lost energy.

The flow within a turbine stage is complex, with leakage flows (Figure 2.6), coolant flows and unsteady effects all impacting performance. By simplifying the

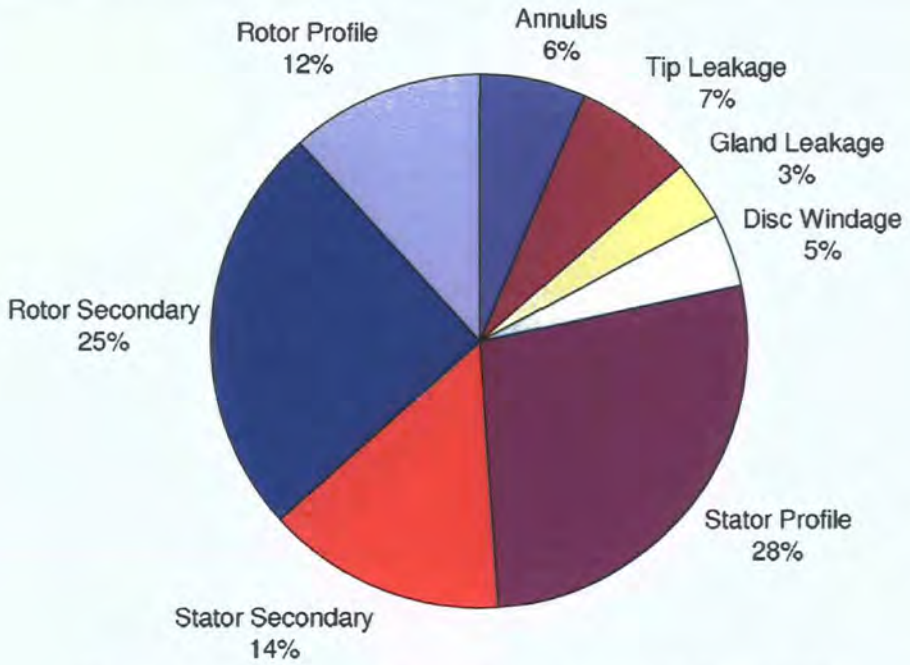

Figure 2.5: Typical HP Stage Losses as per Haller (1997)

study to a single blade row, these complicating effects can be removed and those relating to secondary flows alone may be studied. The flow field can be further simplified by investigation of the normally annular geometry in a linear cascade. In doing so, the strong radial pressure gradients are removed and the impact of any aerofoil changes is more easily observed.

2.2 Secondary Flow

Secondary flows make up a significant proportion of the loss in a turbomachine. For an in-depth discussion of the formation and development of secondary flows, the work of Langston (2001) and the earlier work of Sieverding (1985) provide an excellent starting point.

The classical descriptions of secondary flow provide useful descriptions of the effects and formation of these features.

2.2.1 Classical secondary flow

Classical secondary flow theory can be used to describe the inviscid effects of secondary flows. The theory assumes the existence of an inlet endwall boundary layer of reduced total pressure, which requires viscosity for its formation.

Secondary vorticity

This viscous inlet endwall boundary layer may be modelled, in vortex theory, by the superposition of a normal vorticity component (ζ_n), made of a series of filament vortices, on a uniform velocity field. Perpendicular to the flow direction, as shown

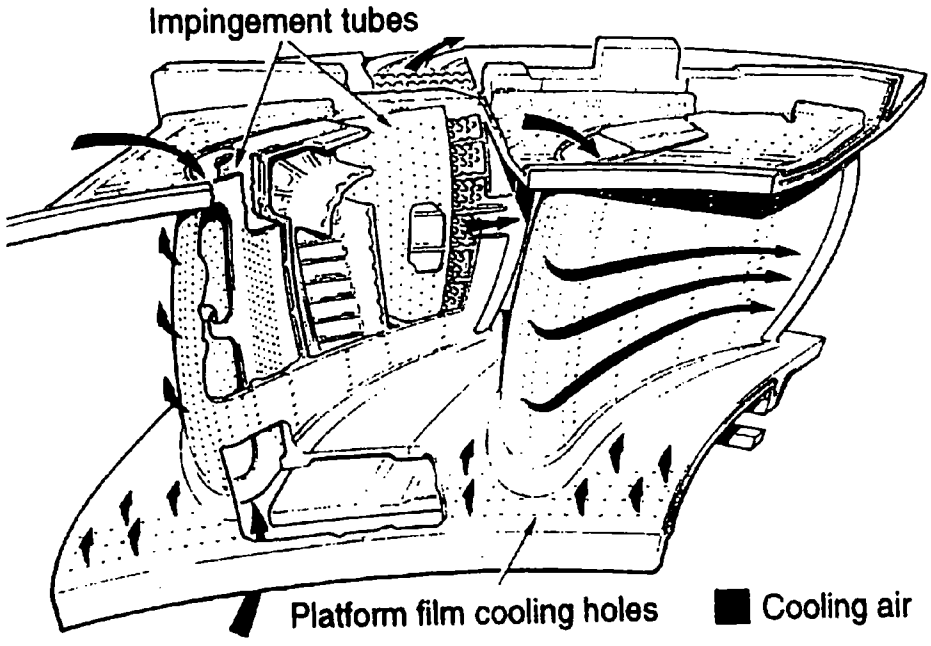

Figure 2.6: Aeroengine HP Nozzle

in Figure 2.7, the vorticity appears as point vortices. The density of the filaments must increase toward the endwall, as the normal velocity gradient ($\frac{dv}{dr}$) increases.

Came and Marsh (1974) produced the following equation for the estimation of downstream streamwise vorticity ζ_{s2}, based on Kelvin's circulation theorem.

$$\zeta_{s2} = \zeta_{s1}\frac{\cos\alpha_1}{\cos\alpha_2} + \frac{\zeta_{n1}}{\cos\alpha_1\cos\alpha_2}\left(\frac{1}{2}(\sin 2\alpha_2 - \sin 2\alpha_1) + (\alpha_2 - \alpha_1)\right) \tag{2.4}$$

Where ζ_{s1} is the inlet streamwise vorticity, ζ_{n1} the inlet normal vorticity, due to the inlet boundary layer and α_1 and α_2 are the inlet and exit yaw angles of the fluid.

Assuming no inlet streamwise vorticity and small angle changes, the Came and Marsh (1974) equation is simplified to Equation 2.5. This is the earlier result presented by Squire and Winter (1951).

The formula indicates a relationship between the strength of the inlet normal vorticity (ζ_{n1}), the overall blade turning ($\alpha_2 - \alpha_1$) and the streamwise component of vorticity (ζ_{s2}) at exit. The formula highlights the important effect of the level of turning on the strength of the secondary flow.

$$\zeta_{s2} = 2\zeta_{n1}(\alpha_2 - \alpha_1) \tag{2.5}$$

Other sources of vorticity within classical secondary flow include: trailing shed vorticity and trailing filament vorticity.

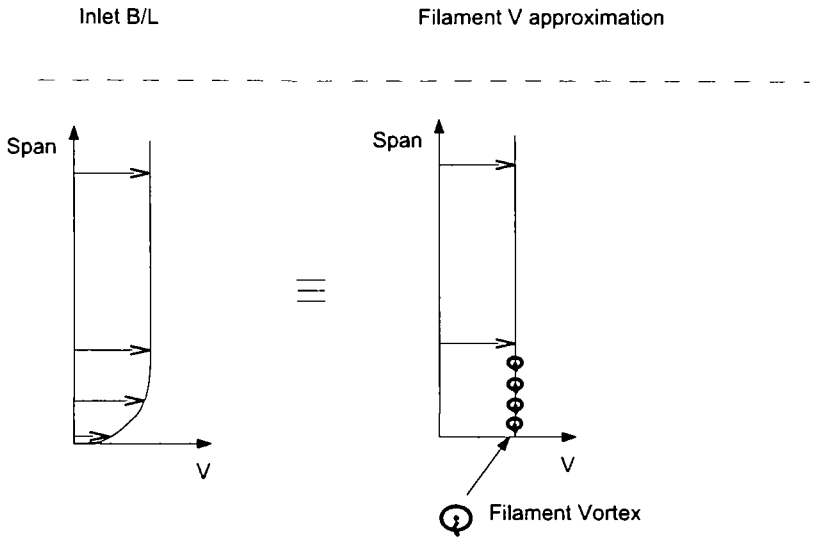

Figure 2.7: Boundary layer as filament vorticity

Shed vorticity

Finite wing theory can be used to describe the effect of aerofoil lift. The lift induced by an aerofoil, can be considered in terms of a bound vortex system which, according to Houghton and Carpenter (2004), is "a hypothetical arrangement of vortices that replace the real physical wing". These are filament vortices which lie along the span.

The magnitude of this bound vorticity follows Helmholtz's 2nd law, which states that "a vortex tube cannot change in strength unless vortex filaments of equivalent strength join or leave the vortex tube".

For an aerofoil in a free stream, the loading changes along its span, and Helmholtz's 2nd law is maintained by the shedding of vortex filaments downstream. For a finite wing, the shed filaments typically roll up to form two counter rotating wing tip vortices and can be observed in Figure 2.8.

For a prismatic aerofoil where there are no designed changes in loading, bound by frictionless endwalls within a cascade, (or by platforms in a shrouded turbine), there would be no change in bound vorticity along the span. However, the endwall boundary layer reduces the local velocity, causing a change in the loading and therefore vorticity is shed. This shedding occurs in the region affected by the inlet boundary layer. Trailing shed vorticity, is an effect of the change in blade loading along the blade span.

Filament vorticity

The stretching of inlet filament vorticity, is described by Came and Marsh (1974). Considering the inlet boundary layer as filament vortices perpendicular to flow direction. These filaments are distorted by a pitchwise velocity gradient as they travel

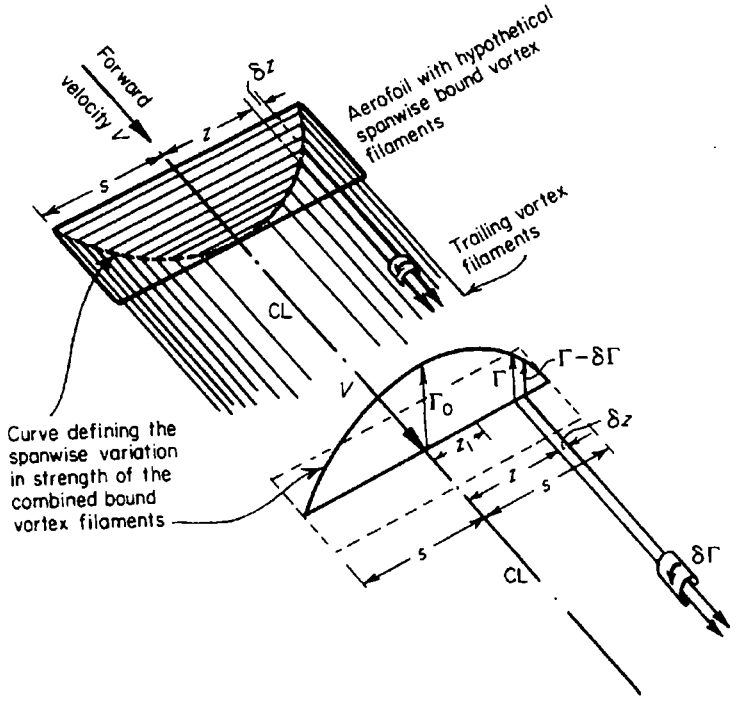

Figure 2.8: Shed vorticity sketch of Houghton and Carpenter (2004)

through the turbine passage. This distortion results in a component of the vortex filament becoming aligned with the flow downstream, as shown in Figure 2.9. Physically, this vorticity component exists in the wake of the aerofoil near to the endwall, up to a span associated with the inlet boundary layer. This vorticity has the same rotational direction as the trailing shed vorticity and is known as trailing filament vorticity. The arrangement of the secondary flow structures downstream is represented by the sketch of Hawthorne and Armstrong (1955), simplified in Figure 2.10. The vertical lines represent blade wakes with trailing vorticity, and the larger recirculations relate to secondary vorticity.

2.2.2 Real secondary flow structures

The following section describes the physically observable vortical structures within the turbine cascade.

Four discrete vortical structures exist within the turbine passage. These are the passage vortex (PV), the two legs of the horseshoe vortex, suction side (SS HSV) and pressure side (PS HSV), and the corner/counter vortex (CV). Downstream of the turbine passage, the PS HSV is combined with the PV and there are only three discrete vortical structures. For unshrouded turbines an additional tip leakage vortex exists, but this structure is not discussed here.

The diagram of Sieverding and Bosche (1983) (Figure 2.11) provides a clear representation of the secondary flows. The model indicates that the PSHSV seeds the PV structure and shows the interaction of the PV and the SSHSV as they are drawn to the SS. These results, along with those of Langston et al. (1977) in Figure

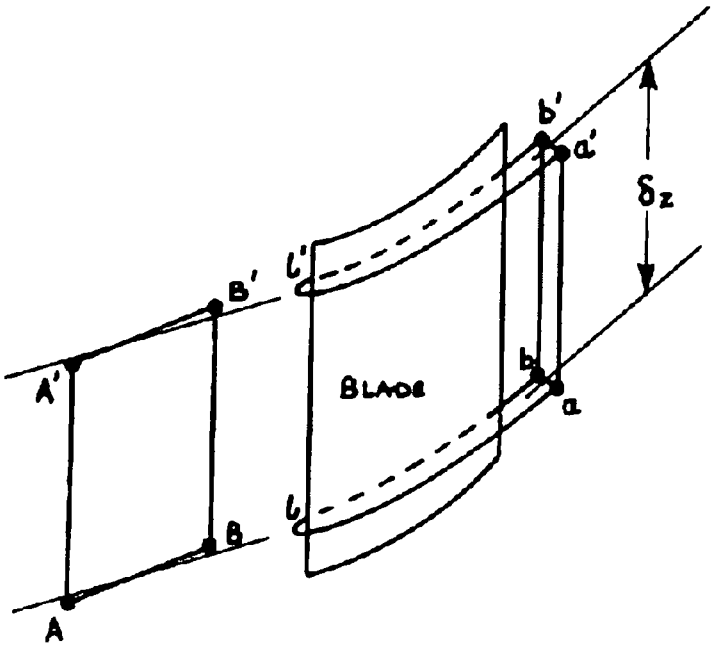

Figure 2.9: Stretching of vortex filaments Came and Marsh (1974)

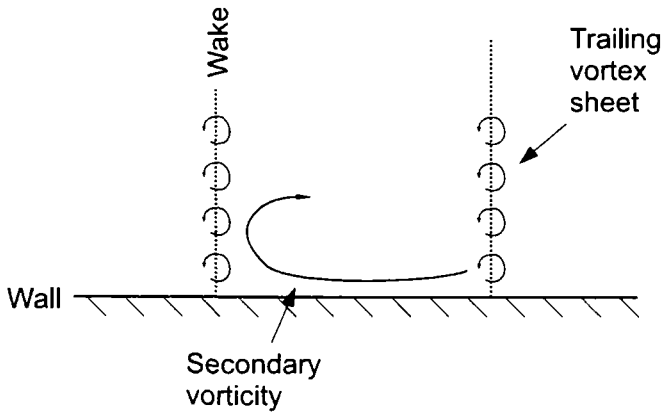

Figure 2.10: Classical Secondary Flow, based on Hawthorne and Armstrong (1955)

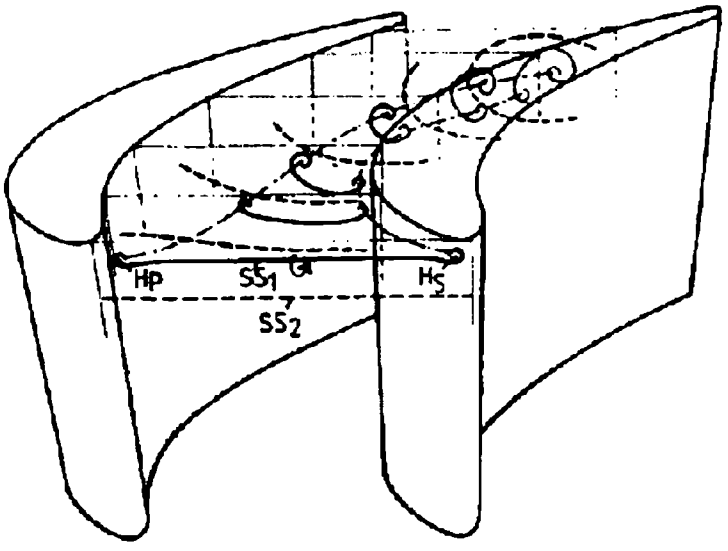

Figure 2.11: Secondary Flow Structures - Sieverding and Bosche (1983)

2.12 indicate something similar to that observed in the Durham Cascade. Both Wang et al. (1997) in Figure 2.14 and Goldstein and Spores (1988) show complex HSV structures that are related to a laminar boundary layer. The complex nature of these structures is not present in the Durham Cascade and is unlikely to exist in the turbulent flow field in a real HP turbine.

Horseshoe Vortex

Eckerle and Langston (1987) (Figure 2.15) show that a vortex forms at the leading edge endwall junction, when the higher momentum fluid at the edge of the boundary layer is slowed by the adverse streamwise pressure gradient in front of the leading edge.

This gradient slows the fluid, the low momentum fluid in the lower part of the boundary layer is also slowed. The stagnation pressure of the low momentum fluid is lower than that of the mainstream, and therefore a radial pressure gradient is set up. The outer boundary layer fluid turns towards the lower fluid. The endwall restricts this movement and the flow turns upstream against the lower boundary layer flow. At some point the pressures balance, and the reversed flow moves tangentially around both sides of the leading edge of the blade.

The shape of the two legs of the vortex stretched around the suction and pressure surfaces give it the title horseshoe vortex (HSV). The direction of rotation of the two legs is opposite. One leg follows the suction surface until it is pushed onto the blade surface by the cross passage flow. The other (PS) leg is drawn across the passage by the cross passage pressure gradient and intersects with the suction surface downstream of the SS leg. According to Wang (1999), the relative locations of intersection of the horseshoe vortex legs with the suction surface depends upon the inlet incidence angle.

The horseshoe vortex is defined differently by different authors. Those investigating cascades with laminar boundary layers note more complex vortex structures

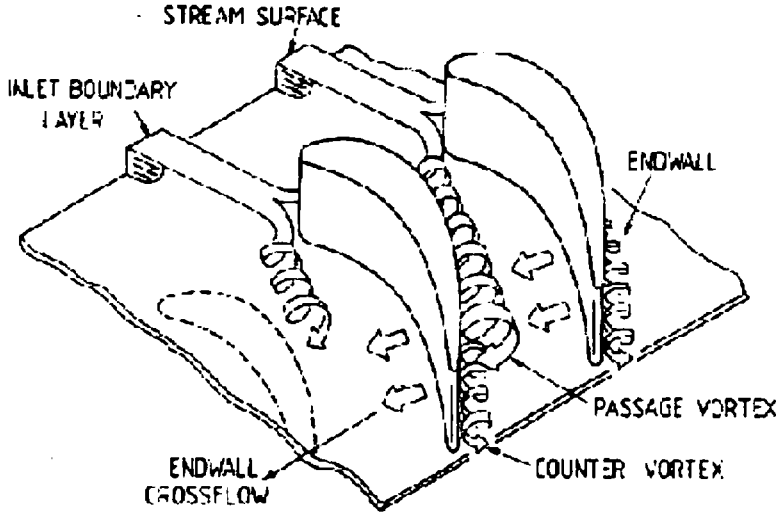

Figure 2.12: Secondary Flow Structures - Langston et al. (1977)

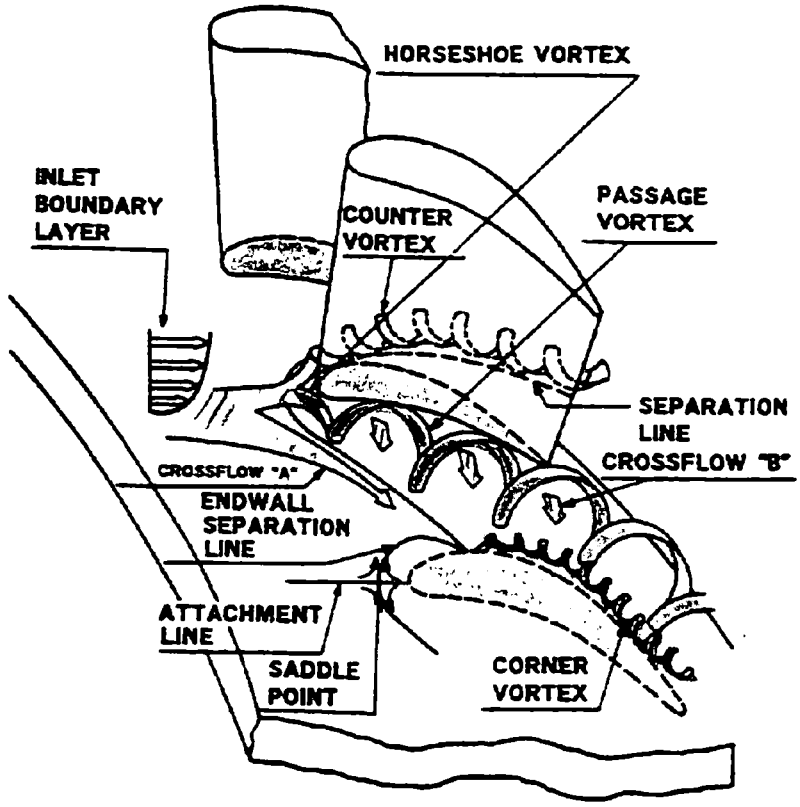

Figure 2.13: Secondary Flow Structures - Takeshi et al. (1989)

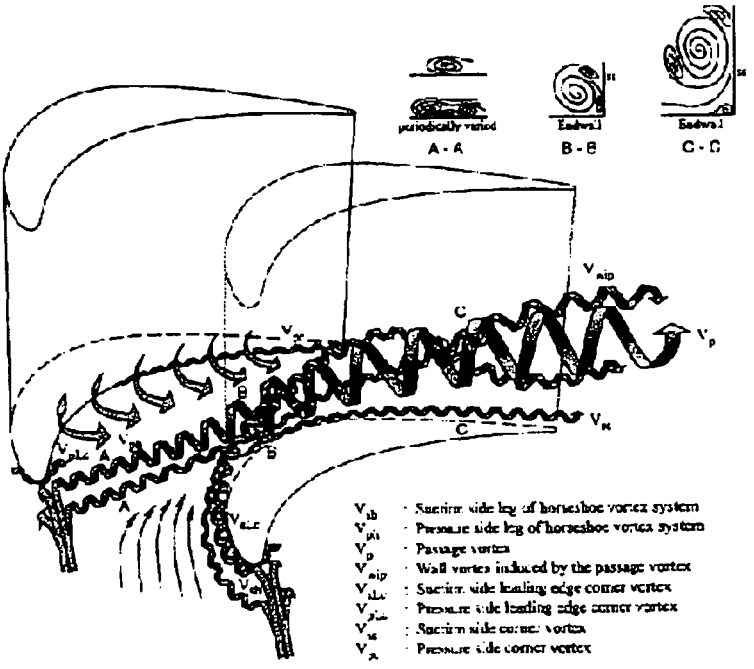

Figure 2.14: Secondary Flow Structures - Wang et al. (1997)

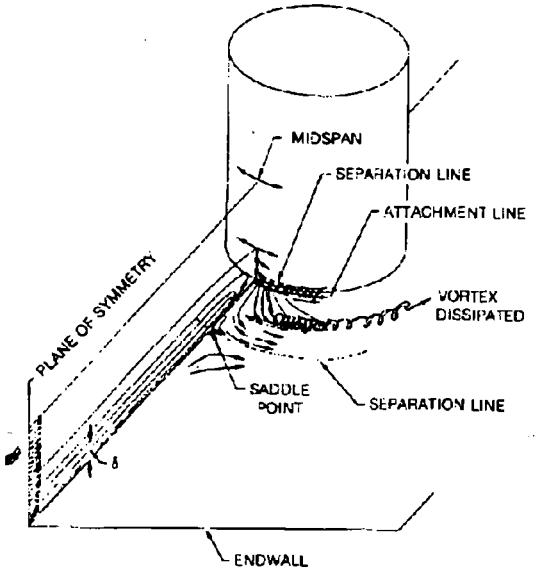

Figure 2.15: Horseshoe Vortex Formation Eckerle and Langston (1987)

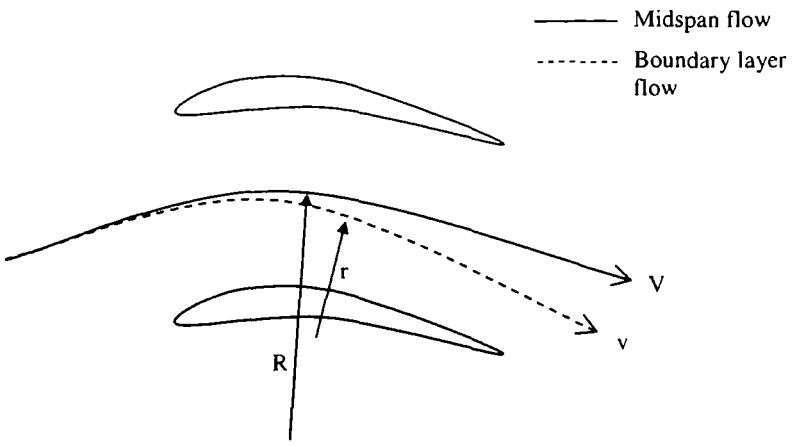

Figure 2.16: Overturned boundary layer flow Gregory-Smith (1997)

formed around the leading edge. In turbulent boundary layers, the structure is simplified and can be defined by one vortex.

Passage Vortex

Gregory-Smith (1997), explained the overturning in the boundary layer in terms of the streamline curvature (see Equation 2.6 and Figure 2.16). The same (cross-passage) pressure gradient ($\frac{\partial p}{\partial R}$) affects both the boundary layer fluid and the midspan flow, but the boundary layer velocities (v) are much lower than those at midspan (V), and thus the radius of curvature of the boundary layer is reduced ($r < R$). This causes overturning of the flow.

$$\frac{\partial p}{\partial R} = \frac{\rho V^2}{R} = \frac{\rho v^2}{r} \tag{2.6}$$

It is considered that, as the horseshoe vortex pressure side leg crosses the passage, it seeds the formation of a vortex. The vorticity in the overturned flow is transferred into this vortex, increasing its intensity. This is the passage vortex (PV). The overturning also causes this vortex to impinge the aerofoil suction surface.

This formation is indicated in the results of Sieverding and Bosche (1983), Langston et al. (1977), Takeshi et al. (1989) and Wang et al. (1997) in Figures 2.2.2 to 2.2.2.

The passage vortex draws the low momentum/high loss fluid of the inlet boundary layer into it. The boundary layer losses that are drawn in and the viscous interaction around the vortex, result in the formation of an associated loss core. A new, overturned, boundary layer is formed in place of the inlet boundary layer.

Counter/Corner Vortex

The viscous action at the outer edge of the PV induces an additional vortex in the endwall suction surface corner. This vortex is known as the corner or counter vortex (CV) and can be observed in Figure 2.2.2 for Langston et al. (1977) and Figure 2.2.2 for Takeshi et al. (1989). The vortex is illustrated in Figure 2.17.

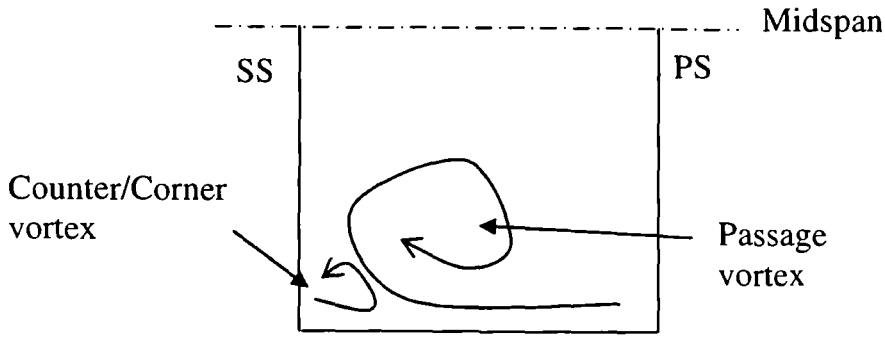

Figure 2.17: Counter/Corner vortex

The inviscid behaviour of the secondary flow features has been described. The significant contribution to total pressure loss that these features make, can only be accounted for when the viscous effects are considered.

2.2.3 Secondary loss

Gregory-Smith (1983) described three key components of the secondary loss, these are:

- The loss in the upstream boundary layer, rolled up into the passage vortex loss core
- The loss associated with the interaction of the passage vortex with the walls
- The loss in the newly formed endwall boundary layer

Part 9 of Denton (1993) (on endwall losses) describes the behaviour of near endwall flows. A brief summary of which can be described as:

1. the inlet endwall boundary layer undergoes a three-dimensional separation. The inlet boundary layer is rolled up in the HSV and later the PV. These vortices are driven to the SS by the cross-passage-pressure-gradient.
2. a new thinner and highly skewed boundary layer forms. The author suggests that this is probably laminar.
3. the $\int u^3 dA$ method on the endwalls predicts a less significant loss than that on the blade SS and it "seems unlikely that entropy generation in the boundary layer within the bladerow can explain the observed magnitude of turbine endwall loss"
4. the author further describes that the size of the inlet boundary layer loss does not affect net loss, i.e. the mixing out of the inlet boundary layer is a small effect.

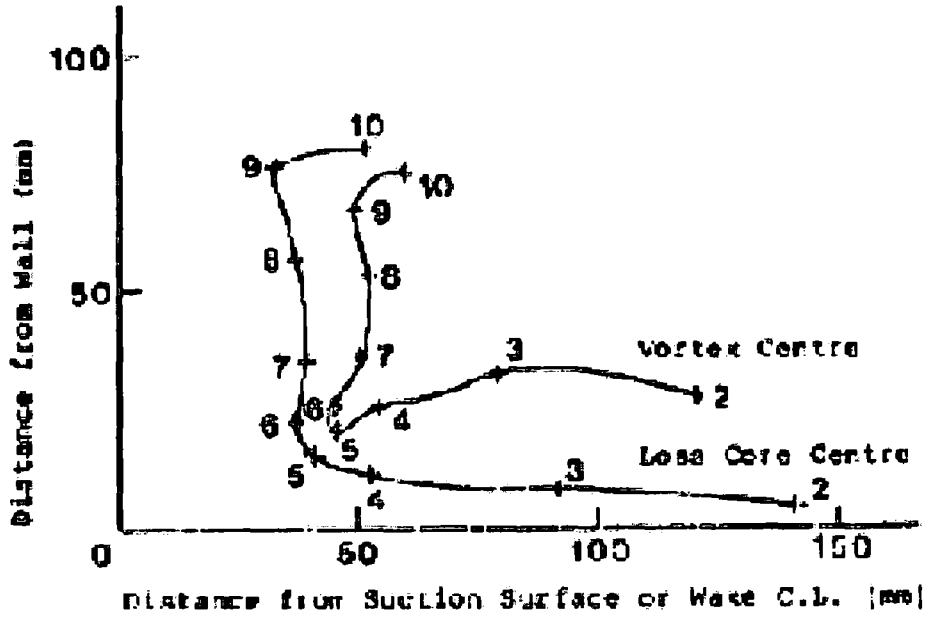

Figure 2.18: Vortex and Loss Cores Gregory-Smith (1997)

5. the author notes that the method of secondary loss calculation of Gregory-Smith (1983) estimates the component of loss associated with secondary kinetic energy

The work of Gregory-Smith and Graves (1983), illustrated in Figure 2.18, indicates that the movement of the vortex is separate from its corresponding loss core.

2.2.4 Secondary loss and secondary kinetic energy in experimental results

Moore (1995) observed a strong link between the dissipation of the secondary kinetic energy within a flow and an increase in total pressure loss.

Ingram (2003) observed a relationship between the reduction in secondary loss (net total loss minus profile loss) and reduction in secondary kinetic energy. This indicated a link between the generation of secondary kinetic energy (mainly within the passage vortex feature) and the viscous dissipation of energy surrounding the secondary flow vortex.

2.3 Aerofoil design

For low pressure (LP) components, aerofoil designs focus on the profile loss. This is because of the relative magnitudes of profile and secondary losses in the LP geometry. The wetted surface area of the LP turbine aerofoil is significant, and any change boundary layer loss has a significant overall effect. Secondary loss components are constant for a given overall turning and inlet boundary layer size. Therefore, for

an LP turbine geometry with high aspect ratio, these losses are small by comparison, and benefits gained by reducing the secondary flows are smaller. LP design is also focussed on the unsteady effects of wake passing and methods to utilise this behaviour to reduce losses for highly loaded blades (see Stieger and Hodson (2004) and other publications by Hodson). For high pressure (HP) components, the aspect ratio is much smaller. The secondary flows dominate the passage and are therefore key to the improvements in HP turbine efficiency.

Typically, vane components have lower amounts of turning than blade components. As shown by Equation 2.5 of Squire and Winter (1951), this results in lower secondary vorticity and therefore less secondary loss to negate. However, vanes have fewer mechanical design restrictions, with respect to the rotational stresses and mass. They therefore have a greater design freedom.

Duden et al. (1999) used a highly loaded LP turbine cascade as a base for aerodynamic design changes. In their paper, the authors note the following methods for the reduction of loss in turbines:

1. lower endwall (cross passage) pressure gradient cuts the passage vortex potential

2. negative gradient to the endwall (higher pressure at midspan) on the suction surface reduces radial migration

3. lowering the pressure surface pressure to even out cross passage gradient caused by (2). This increases pressure surface outward flow, but the loss here is comparatively low

4. suppressing the suction surface deceleration to reduce the growth of the blade surface boundary layer

The pressure gradients mentioned above, control the movement and accumulation of the boundary layers, on both the blade and endwall surfaces, to restrict the build up of loss. The modification of the various boundary layers cannot be achieved independently. The reduction of a cross passage gradient is typically achieved by reducing the suction surface loading at the endwall. This increased pressure at the endwall intensifies the radial pressure gradient and also the loss core radial movement.

The cross passage pressure gradient can also be controlled by adjustment of the pressure surface loading. This method also alters the radial pressure gradient but, as mentioned by Duden et al. (1999) the boundary layer thickness here is much smaller, and therefore the increased loss is relatively small.

2.3.1 Blade loading distributions

Weiss and Fottner (1993) investigated the effect of the distribution of loading on the flow field. They undertook experimental investigations in linear cascades on two LP turbine geometries with the same overall loading but different axial distributions of load. Principally, they noted that the "front loaded cascade exhibits the stronger passage vortex" and the associated "dissipation of the kinetic energy is responsible

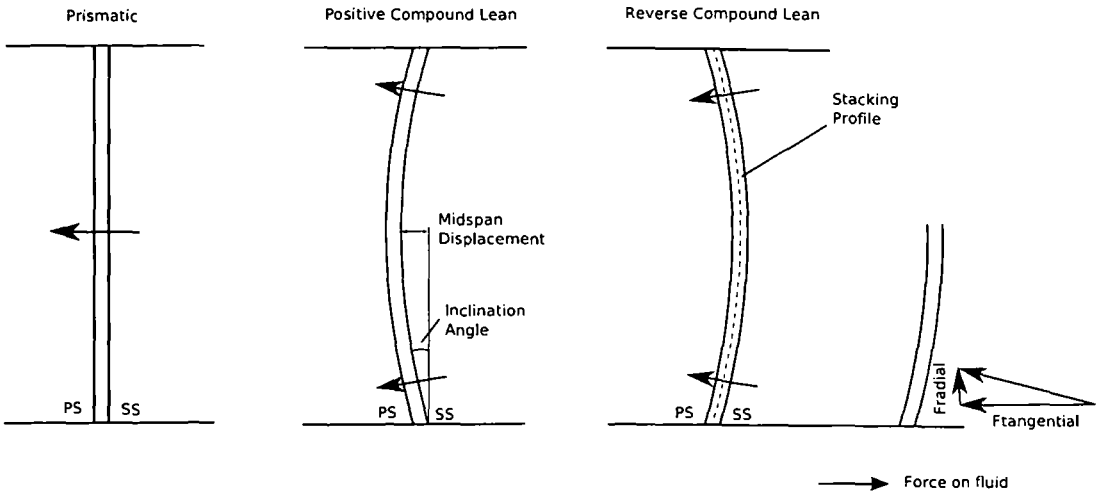

Figure 2.19: Tangential Lean

for the higher magnitude of secondary loss". The authors also presented surface flow visualisation results. These results indicated earlier separation of the endwall boundary layer for the forward loaded geometry and the increased depth of penetration (radial migration) of the secondary flows for this same geometry. The authors note that, the aft-loaded blade is doing most work in a region of the passage where a thinner endwall boundary layer exists. Corriveau and Sjolander (2004) investigated loading distributions for transonic HP turbine blades and found similar effects.

2.4 Aerofoil lean

A number of researchers have investigated the effect of lean on the flow field of axial flow turbines. Investigations of note are that of Sharma et al. (2003), Harrison (1990) and Walker and Hesketh (1999). A review of the three dimensional design of aerofoils, which includes blade lean was undertaken by Denton and Xu (1999). Figure 2.19 illustrates the differences between the leaned shapes.

The work of Sharma et al. (2003) is both experimental (linear cascade) and computational. In the first section of the paper, a blade is investigated with circular arc positive compound lean with 20^o inclination at the endwall. The benefits of the new stacking were not seen as a loss reduction, but instead in a redistribution of loss in the spanwise direction. The midspan region saw a reduction in efficiency and the endwalls an increase. In the second section of the paper, results are presented for linear cascade investigations of a 40^o inclination compound leaned blade and a 25^o reverse compound leaned blade. The compound leaned blade reduces the endwall losses at the expense of large midspan loss, this midspan loss is more than double the previous value for the prismatic blade.

The exit angle distribution has also changed considerably, with much greater turning at midspan and less at the endwall. The reverse compound leaned blade has a reduced loss at midspan but increased at the endwall.

In the work of Sharma et al. (2003), all the significant changes in static pressures occur on the suction surface. The reduction in loading for the endwall (7mm from

the endwall) occurs in the front to mid chord section of the passage.

The work of Harrison (1990) is a study of tangential blade lean, based on experimental results undertaken on a linear cascade. Harrison investigates three blade stacking arrangements: a prismatic reference case, a straight leaned case and a compound leaned case. All the blades have approximately 107^o of turning and a similar pitch to chord ratio as the Durham Cascade. Other conditions include a Reynolds number double that of the Durham Cascade, a similar exit Mach number, but much lower inlet turbulence level. The prismatic blade surface static pressures indicate a flat topped profile similar to the Durham Cascade. The surface static pressures for the compound leaned blade show a behaviour similar to that of Sharma et al. (2003).

The effect of blade lean on the loss cores diminishes as the lean induced pressure difference disappears. After the trailing edge (at 123% axial chord), the loss cores for the simple leaned blade appear almost symmetric about midspan.

The simple leaned blade has linear loading variation across span. The compound leaned blade keeps a similar distribution of loading as straight blade, but with off loaded endwalls and more turning at midspan. The exit angle variation is reduced by 30% compared with a straight blade. Higher loading at midspan leads to higher profile losses, thus a thicker wake. The spanwise pressure variation shifts endwall fluid towards the midspan, further increasing the measured midspan loss.

Changes in boundary layer incidence, because of boundary layer acceleration, can be seen in the results of the flow visualisation, where the saddle point of the horseshoe vortex has moved closer to the leading edge.

The main points of Harrison's work are that compound lean:

- Creates a thicker midspan wake due to increased loading over this section
- Reduces the endwall loss - this is attributed to local velocity reductions
- Reduces the exit angle deviations, which in turn reduces downstream mixing losses

The work of Denton and Xu (1999) includes tangential lean. The paper derives (from the radial equilibrium equation) a qualitative relationship between the lean induced blade forces, the radial pressure gradient and the streamline curvature acceleration. It notes that for low aspect ratio blades the radial pressure term dominates and hence "the radial blade force will be opposed mainly by the increased radial pressure gradient". The authors also note that the effect is limited to within the blade row itself.

Denton and Xu discuss the design of the compound leaned blade of Harrison and report that:

- More work is done by the most efficient part of the blade
- The redistribution of low energy fluid prevents the accumulation of loss at the endwall, giving a more uniform exit flow
- The entropy generation is proportional to the local relative velocity cubed and a good design would be to reduce the velocity over the majority of the surface area and increase it over the smaller surface areas

Wang (1999), in his VKI lecture, reviews a significant proportion of the existing work on tangential lean in steam and gas turbines. He discusses the radial equilibrium equation and suggests an additional term be added for non-prismatic blades. The term includes the radial blade force. The radial blade force for prismatic/unleaned blades will be very small, here "the dominating term is the inertial-centrifugal, due to tangential velocity in a circumferential surface". For leaned bladerows the radial force term exceeds the other three terms.

Wang's own work includes investigations into the effect of varying incidence angle on the loss benefits, where he found that the compound leaned design is beneficial at all reasonable levels of incidence. Wang investigated a series of blade profiles/aerodynamic conditions and established an optimal lean angle for each design. He suggests this is "a balance between a reduction in loss associated with secondary flows and the increase in loss associated with friction on the (increasing) surface area".

Positive compound lean reduces the over and under turning magnitudes, thereby reducing incidence and its associated loss in the downstream row. Wang notes, (as mentioned previously) that the "saddle point in the endwall region... moves toward the middle of the blade pitch" because of a "local increase in effective flow incidence".

Vand and Songtao (2005) present a numerical study on the effect of positive compound lean on the stator of a single stage turbine. The authors observed similar effects to those seen by Harrison (1990). D'Ippolito et al. (2007) investigated similar lean arrangements to Harrison (1990), but extended the investigation and showed the impact of the lean on the streamwise vorticity.

The following authors have investigated the use of lean in the redesign of steam and gas turbine blade rows. Hourmouziadis and Huebner (1985) found that straight lean "reduced losses at the hub and increased losses at the casing" for an acute PS hub angle. Kawagishi and Kawasaki (1991) discuss the refurbishment of a steam turbine using leaned geometries. They investigate no lean, straight lean and compound lean. Overall the authors note a one percent improvement in stage efficiency when using compound lean and a 0.5% improvement for straight lean. Wallis et al. (2000) report on the redesign of an HP steam turbine blade with low aspect ratio. They suggest that destroying the streamwise vorticity reduces secondary velocities and losses, as they are amplified by the acceleration of the flow in the downstream row. Granovskiy et al. (2007) observed secondary loss reductions with positive compound lean in a two stage turbine redesign. The authors used 8 - 10° of bow in the vane.

An alternative use of blade lean is reported in the paper of Fischer et al. (2004). The authors investigated the compound lean (approximately 30°) of stators in a high speed compressor. Here the lean lessens the probability of the hub separation by increasing the hub pressure upstream and thereby reducing the local adverse pressure gradient at the hub. The authors also note that the blade surface area was increased by 7.5% which lead to increased profile losses.

In general, all of the researchers obtain similar flow behaviours, but the benefits of the leaning i.e. loss reduction and exit yaw angle distribution seem to vary depending on the initial flow regime. Wang (1999) warned that "sometimes the energy loss in a cascade of positively leaned blades is higher than in a cascade of

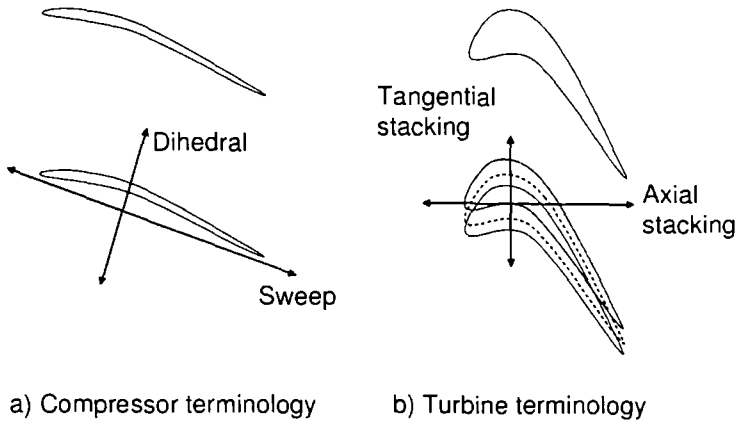

Figure 2.20: Lean and Sweep Terminology

straight conventional blades". It is important to consider the split of secondary and profile loss existing in the aerofoil geometry prior to any lean modification, as this split will determine the potential benefit of lean. For example, an aerofoil with low profile loss and short span may not benefit from the offloading effect of reverse compound lean.

As Walker and Hesketh (1999) highlight, inadequacies in the two-dimensional design can be alleviated or exacerbated by the three-dimensional shaping.

2.5 Aerofoil Sweep

2.5.1 Definition

Sweep is where the blade is leant in a chord-wise direction. For blade rows with low turning (in compressors), sweep is defined as being in the chord-wise direction. For compressors, where the overall level of turning is low, the definitions of sweep and dihedral correlate to the streamwise and cross-stream directions. They are useful definitions, as they enable the designer to modify the design with clear impact on the flow field. In turbine components, the level of turning is considerably greater and translation in the camber line direction would not provide a similar effect to sweep in compressors. For turbine components sweep may be defined in the axial direction. Figure 2.20 illustrates the differences between these two definitions.

Forward sweep is where the section of the blade close to the endwall is upstream of that at midspan. Straight sweep is defined as a simple linear variation in axial position of the sections. This geometry causes one end of the blade to be forward of the midspan and one end to be rearwards of it. This form of sweep gives different effects on the near endwall flow for either end. This is illustrated in Figure 2.21.

The theory behind the effects of axial lean stacking lines on flows in turbomachinery originates from linear cascade studies by Smith and Yeh (1963) and was further developed by Lewis and Hill (1971). Smith and Yeh consider the flow on swept blades in terms of "an infinite cascade of infinite span" and translate the geometry of an aerofoil in a known velocity field. They note that the flow over the aerofoil can be considered as that without sweep "but with a uniform spanwise

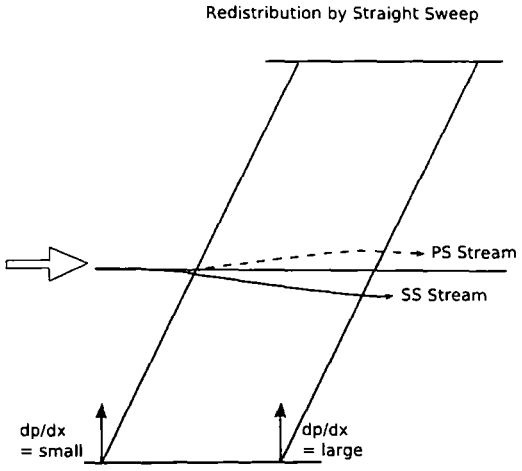

Figure 2.21: Sweep

velocity.. added". The authors suggest that the effect of sweep on the streamline paths either side of the blade, is such that "the flow will not remain on axisymmetric stream surfaces". Significantly, the suction surface streamline is deflected towards the normal to the leading edge and the pressure surface streamline is deflected away from the normal. Lewis and Hill (1971) expand the theory and suggest that the exit angle of the flow is determined by the exit metal angle *and* the sweep angle, and that the exit angle reduces as the sweep angle increases.

In a later paper by Hill and Lewis (1974), blade sweep is investigated experimentally for a linear cascade of LP steam turbine blades with 0^o, 20^o and 40^o of sweep. Their midspan pressure distributions indicate a reduction in aft suction surface loading with an increase in sweep angle. The authors find an exit angle reduction as theorised in their earlier paper. They note disturbances (spanwise axial velocity variation) to 2.7 axial chord distances downstream for their geometry with 20^o sweep.

Denton and Xu (1999) discuss the effects of blade sweep. They add that the effects of sweep can be considered in terms of the pressure gradients in the near endwall regions. The authors note that for any swept blade section, the loading levels at the wall are determined by the pressure field a short radial distance away. The forward swept leading edge section is unloaded because of the even pressure field above it, and the trailing edge section is highly loaded due to the strong pressure field above it. The use of forward sweep (as seen on the lower endwall in Figure 2.21), significantly offloads the front of the blade, whilst increasing the loading on the rear section.

Additionally, the authors illustrate a blade with forward swept endwall sections and a straight trailing edge, as shown in Figure 2.22. This extension of the chord in the near-endwall sections tends to offload the front of the aerofoil as per simple forward sweep, whilst maintaining the same rear section pressure distribution and therefore exit angle. The forward sweep at the endwall has the effect of drawing massflow in toward the endwall. This effect is similar to the behaviour of reverse compound lean.

Recently, Pullan and Harvey (2006) investigated the impact of lean on midspan

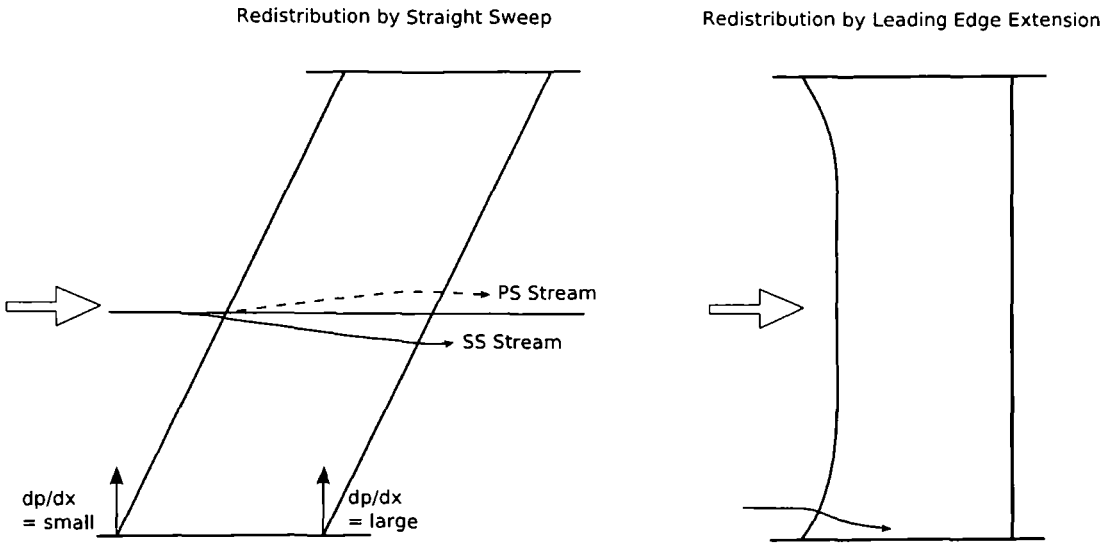

Figure 2.22: Axial chord extension

aerodynamics, using an interesting twisted wind tunnel arrangement. The authors observed increases in profile loss with sweep angle, due to increased surface area and higher surface velocities. The decrease in blade loading, due to unused radial velocity components, was defined by a spanwise dynamic head component. Pullan and Harvey (2007) investigated the effect of lean at the endwalls and observed a significant reduction in over and underturning due to the backward sweep, i.e. a clear reduction in the level of secondary flow. The loss peaks were pushed further out at this end. The forward swept endwall had reduced underturning, an indication of the secondary flow magnitude, and the loss peak was shifted inward toward the wall.

As indicated, forward sweep encourages suction surface flow to move towards the end wall, helping to restrict the radial migration of the secondary flow in much the same way as reverse compound lean.

2.6 Thickened end wall section

Thickening of the pressure side, or "in-filling", in the end wall region adds blockage which raises the local flow velocities, reduces the diffusion and may prevent flow separation. This will prevent loss being generated in the separation and this being fed into the secondary flow.

A recent example is the work of Gier et al. (2002), who investigated aerofoil thickening combined with axisymmetric endwall profiling in a multi-stage LP turbine rig. The authors found that thickening the aerofoil in the end wall region achieved a similar effect to positive compound lean (which they refer to as bowing). Figure 14 from their paper shows the majority of the thickening is applied to the suction side of the blade.

Although Gier et al. (2002) did measure an overall reduction in loss for their geometry, they showed that locally some losses increased (at about 20% span) due

to the modified hub geometry. They conclude that producing a concave radial stack on the suction surface, by thickening the aerofoil section on that surface, had resulted in additional loss.

2.7 Leading edge modifications

2.7.1 Types

There are two types of leading edge modification, made at the intersection between the blade leading edge and the endwall. These are indicated in Figure 2.23.

1. Bulb type geometries (coloured pink in Figure 2.23) are blunt structures that are thicker than the leading edge at midspan, extend upstream and are perpendicular to the endwall. The bulb geometry is smoothed into the aerofoil around the suction and pressure surfaces and up the leading edge. Examples of bulb geometries are given in Sauer and Wolf (1997) and Becz and Majewski (2003).

2. Fillet type geometries (coloured red in Figure 2.23) smooth the intersection between blade and endwall, using a radiussed or linear geometry. The fillet height does not typically extend beyond the boundary layer, but its length may extend several boundary layer thicknesses upstream. This gives a low aspect ratio and shallow angles between the endwall and the fillet geometry. Examples of fillet geometries are given in Zess and Thole (2002), Mahmood et al. (2005) and Saha et al. (2006).

Bulb geometries are used to enhance the horseshoe vortex, by virtue of their larger frontal area. The intensified suction side HSV interacts with the passage vortex during its early formation, and is thought to cancel some of its vorticity. However, this viscous interaction may locally increase loss, Hoeger et al. (2002).

Fillet geometries are designed to reduce the horseshoe vortex intensity. Fillets are thought to work by reducing the impact of the static pressure field around the leading edge of the blade. This may be achieved by 1) accelerating the local boundary layer flow, decreasing the adverse pressure gradient in the axial direction and reducing the tendency of the flow to reverse and by 2) allowing the boundary layer fluid to split around the leading edge in a controlled manner.

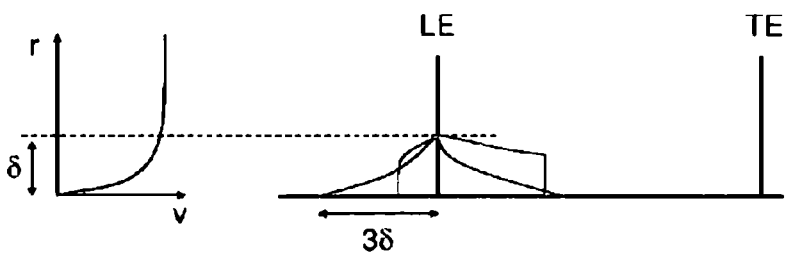

Figure 2.23: Sketch of leading edge modifications

Sauer and Wolf (1997) used leading edge bulbs and found that the HSV pushed the passage vortex away from the suction side and decreased the secondary losses. Becz and Majewski (2003) used three different bulb and fillet geometries in an attempt to reduce loss, but do not discuss the mechanisms involved. They claim an 8% reduction in total pressure loss over a geometry with no leading edge modifications. However, they also have some failed designs and note that the leading edge geometry was not optimal. Zess and Thole (2002) aimed to reduce the horseshoe vortex for an HP vane. The authors investigated a number of fillet geometries, including shapes defined by power law (1/7 and 1/4 exponents) and elliptical profiles. The fillets were all the same height, equalling the inlet boundary layer height, but the lengths varied. The authors claim to have eliminated the horseshoe vortex using a fillet one boundary layer high and two boundary layers in length.

Mahmood et al. (2005) investigated the heat transfer effects of a number of fillet geometries. The majority of fillets tested indicated increased total pressure loss values. Pieringer and Sanz (2000) applied fillet radii to stop or delay the boundary layer separation near the endwall. The geometries caused blockage, but increased the "specific angular momentum" (turning).

The literature indicates that it is possible to improve aerodynamic efficiency by reducing secondary flow and loss, by modifying the leading edge geometry at the endwall. However, some researchers have managed to increase losses.

2.8 Endwall profiling

2.8.1 Types

Axisymmetric endwall profiling alters the endwall height by the same extent across the pitch. Axisymmetric geometries can affect the flowfield by causing local diffusion and accelerations independent of the aerofoil shape. These changes occur along the axial direction.

Non-axisymmetric endwall profiling independently alters the height over the entire endwall and can control static pressure in the tangential direction.

Rose (1994) demonstrated the effects of non-axisymmetric endwall profiling on the circumferential static pressure distribution at blade exit. The author used profiling to reduce rim-seal leakage flows caused by non-uniform static pressures. Considerable research on the subject of non-axisymmetric endwall profiling has subsequently been undertaken both at the University of Durham and within Rolls-Royce. Some examples of this work are Hartland et al. (1998), Harvey et al. (2000) and Hartland et al. (1999). Ingram et al. (2002) provide a review of the earlier (successful) work on the Durham Cascade and explain that "non-axisymmetric endwall profiling works by reducing the cross passage pressure gradient at the endwall by means of streamline curvature". The authors also note that the aim of the designs was to reduce this cross passage gradient which "results in less secondary flow and therefore loss".

Alternative endwall profiling concepts include that of Torre et al. (2006), who investigated the effect of a large singular hump on the endwall around the suction side of the leading edge of an LPT. The design had no corresponding dip. The

design is thought to work by enhancing the SS HSV and delaying the interaction of the cross passage flow with the SS. In doing so, the PV formation is delayed and secondary losses reduced. The deceleration off the back of the hump also acts to decrease the local cross passage pressure gradient.

Corral and Gisbert (2006) investigated the automated and manual optimisation of non-axisymmetric endwall profiling. The authors focussed on an LPT blade geometry and generated complex endwall geometries with multiple harmonics (multiple hump and dips across the pitch). The computations indicated reductions in the secondary flow parameter (SKE.H) and reductions in the yaw angle variation at exit. Saha and Acharya (2006) investigated non-axisymmetric profiled endwalls similar in shape to those of Ingram et al. (2002). The authors noted reductions in endwall heat transfer around the leading edge, related to changes in the formation of the HSV.

Non-axisymmetric end wall profiling is now a well established aerodynamic design tool within Rolls-Royce, see Harvey et al. (2000) and Shahpar and Lapworth (1998).

Not all profiled endwall designs have been successful. Feiler et al. (2005) used them and noted a 13 - 19% increase in total pressure loss, along with a 2.5^o reduction in exit yaw angle. Note should be taken of the limits of endwall profiling in terms of maximum values of perturbation magnitudes and endwall curvatures. This is highlighted in the work of Ingram et al. (2005) and the PhD thesis of Ingram (2003). Ingram (2003) wrote that; if the profiling is too extreme, local separation of the end wall boundary layer will occur increasing the overall loss - rather than reducing it.

2.9 Vortex stretching

Vortex structures that are convected into the next blade row are accelerated through it. This acceleration of the vortex tube stretches it and therefore intensifies it, Denton (1993). The use of blade section design, to combine the counter rotating flows (PV and SSHSV) to destroy vorticity before the next row (by mixing), is thought to improve the downstream row efficiency, Denton and Xu (1999).

2.10 Stage Efficiency

The stage efficiency can be improved by considering the impact of geometrical changes on the exit flowfield. By balancing the improvements between the vanes and the blades, overall stage efficiency gains can be made. An example of this might be the exit angle variation and its effect on the incidence angle (and loss) on the downstream blade.

2.11 Complex flow field

The flow field within a turbomachine is complicated by leakage and cooling flows. The flow through the discourager seal (from the rotor-stator cavity) into the passage has a considerable impact on the secondary flow structure. Reid et al. (2006a) investigated this experimentally using a variety of leakage conditions. The authors

noted that by pre-swirling this leakage, its impact may be reduced considerably. Rehder and Dannhauer (2006) used PIV techniques to observe the impact of these leakage flows on the secondary flow field. They observed the removal of the HSV by leakage ejection.

Similarly the existence of the inter-platform gap between individual rotor blade castings impacts the near endwall flow. Reid et al. (2006b) investigated leakage through this gap, and with a number of design iterations, were able to improve the efficiency of the model investigated. The optimum slot arrangement being that which was aligned with the endwall pressure contours.

The tip leakage of unshrouded rotor blades provides the largest impact on the flow field and its effect has been well researched. Palafox et al. (2005) used an enlarged Durham Cascade geometry, in a linear cascade arrangement, to investigate tip leakage flows in detail. The authors used pressure probe and surface flow visualisation, as per most research on this geometry. The authors also used particle image velocimetry (PIV), from within the aerofoil itself, to detail the velocity field at the tip without interference. The authors observed significant changes in the secondary flow field due to the leakage, and the further impact of a moving endwall (belt) on these flow structures.

The impact of inlet turbulence intensity on the loss cores, vorticity, and secondary vectors was researched by Barrigozzi et al. (2007). The increased turbulence resulted in faster mixing and reduced vorticity peaks, but mass averaged loss coefficients remained the same. The different inlet boundary layers for the different cases makes direct comparison difficult.

2.12 Durham Cascade

Numerous researchers have used the Durham Cascade for their PhD investigations. These include; Walsh (1987), who investigated the effect of inlet skew by use of a moving belt upstream of the blade leading edge.

Cleak (1989), who used the cascade to compare three CFD codes and numerous combinations of turbulent and laminar flow specification and provided the hot wire anemometry measurements required for the inlet turbulence specification of this thesis. Biesinger (1993) investigated the impact of upstream slot injection on the secondary flow structures and showed that reductions can be made by energising the inlet boundary layer. Moore (1995) used hot wire anemometry to investigate the cascade, providing information for the validation of turbulence models. Hartland (2001) investigated the first non-axisymmetric profiled endwall geometry.

Ingram (2003) investigated all the Durham cascade endwalls to date with analysis focussing on the secondary loss reduction. As a result of this, the ranking of the best performing endwall designs has altered and a greater understanding of the behaviour of the endwalls exists. The author also investigated a new endwall design which presented an increased loss and greater understanding of the limitations of endwall profiling.

The Durham Cascade geometry has also been extensively computationally investigated through the ERCOFTAC programme, see Gregory-Smith (1993), Gregory-Smith (1995a) and Gregory-Smith (1995b).

2.13 Experimental Technique

The techniques used in this work are based on previous research. Biesinger (1993) developed the automated measurement system, Ingram (2003) improved upon it and Ingram and Gregory-Smith (2006) describe it. Barlow et al. (1999) provide a good background on wind tunnel testing. Treaster and Yocum (1979) and Dominy and Hodson (1992) are a good source of data for the calibration and use of pneumatic probes.

Flow visualisation in turbomachinery cascades is described by Wang et al. (1997) and Merzkirch (1974) provides a more general overview on flow visualisation.

2.14 Aims and Objectives of Work

The aim of this thesis is to investigate the potential benefit of passage shaping on turbine performance. It has been shown that aerofoil geometric modifications provide a means to improve performance, but that the choice of modification is dependant on the pre-exisiting flow regime. The combination of modifications has been investigated to a limited extent but the combination of endwall profiling with aerofoil modifications has not had significant investigation. The passage shaping investigated within this work aims to further the knowledge of 3D turbine design.

Chapter 3

Experimental Setup

THE experimental measurement techniques that are used throughout this thesis, are descibed in this chapter. The refurbishment of the cascade equipment is described - including an upgrade to the aerofoil mounting method and a description of the two different measurement systems.

3.1 Introduction

The low speed linear cascade relies upon total pressure measurement and its relation to turbine component efficiencies for its relevance. The continued use of cascade testing in turbine design development is because of its relatively low cost and simplified flow field.

Aerodynamic concepts continue to be developed in the linear cascade environment. Examples include: profiled endwalls (Ingram (2003)), sweep (Pullan and Harvey (2006)), lean (Harrison (1990)) and tip leakage (Palafox et al. (2005)). These few examples imply a limitation of computational modelling for new concepts and reiterate the need for continued experimental research.

This section describes the experimental techniques and apparatus used in the assessment of a linear cascade of highly loaded turbine blades. The first section of the chapter describes the use of pressure probes. The probe traversing systems are described, including both the new and old traversing techniques. The cascade was redesigned to provide symmetrical inlet conditions and enable full 3D geometries to be investigated. The re-development of the cascade is discussed and compares the old and new geometrical definitions and their impact on measurements and design loop flexibility. The inlet flow conditioning techniques and the differences in inlet conditions are then detailed. Other measurement techniques that are used in the thesis are described, including surface flow visualisation and static pressure measurement. Finally, the new aerofoil geometries and manufacturing techniques are discussed.

3.2 Performance Parameters

The performance is measured through a combination of parameters. The first, C_{p0}, presents information on the energy lost in the form of total pressure. The second C_p

helps detail the surface-local flow behaviours. The third, C_{SKE}, and fourth, SKEH, provide an indication of the level of kinetic energy in the secondary flows. The final parameter, vorticity, is not used as a global performance indicator, but is of interest when observing the development of flow features.

3.2.1 Total Pressure Loss Coefficient

The total pressure loss coefficient (C_{p0}) for a pressure of interest (p_{02}) is calculated as shown in Equation 3.1. The coefficient shows the change in total pressure relative to an upstream value, taken from a reference pitot probe and normalised by the upstream dynamic head (the difference between p_{01} and p_1) measured on the same pitot probe. This definition differs from conventional turbine cascade practice, where a downstream reference pressure is used.

The total pressure loss is the key parameter of linear cascade performance and is used to rank all competing geometries experimentally.

$$C_{p0} = \frac{p_{01} - p_{02}}{p_{01} - p_1} \tag{3.1}$$

The accuracy of loss measurements used in this thesis was observed by Ingram (2003) (using the same equipment) to be ± 0.005 in loss coefficient, and compared with a typical mass averaged loss C_{p0} of 0.17 is less than $\pm 3\%$ of gross loss at the key measurement plane.

Detailed experimental data comparisons are typically made using loss contour plots. An example of this is annotated in Figure 3.1. The key features observed in the plot are as follows:

- The aerofoil wake (A) observable in the middle of the plot
- The passage vortex loss core (B), typically the largest loss core seen in the Durham Cascade. This loss is tangentially displaced, away from the wake
- The suction-surface-horseshoe-vortex loss core (C), at a greater radial extent than the passage vortex loss core and typically more aligned with the wake
- The corner vortex loss core (D), which remains close to the endwall

3.2.2 Static Pressure Coefficient

The static pressure coefficient (C_p) is calculated as shown in Equation 3.2, where p_{01} is the upstream total pressure and p_1 is the upstream static pressure, both taken from a reference pitot probe. The local pressures, p_{local}, are obtained from the surface tappings of the blade or endwall. The static pressure coefficient is used to identify changes in loading and separations.

$$C_p = \frac{p_1 - p_{local}}{p_{01} - p_1} \tag{3.2}$$

3.2.3 Secondary Velocity

Secondary velocity (V_{sec}) is dependent on the sine of the yaw angle difference, between the local and the midspan flows (Equation 3.3). This velocity is used to highlight the extent of the secondary flows and is typically presented as a vector combined with the radial velocity (V_r) component (Equation 3.4).

When plotted as a vector, the secondary velocity is projected in the direction of the midspan velocity onto the axial viewing plane, as shown in Figure 3.2.

$$V_{sec} = V \sin(yaw - yaw_{mid}) \tag{3.3}$$

$$V_r = V \sin(pitch) \tag{3.4}$$

An example plot of the secondary velocity vectors observed in the Durham Cascade, is annotated in Figure 3.1. The key features observed in the plot are as follows:

- The passage vortex (A), the most significant secondary flow feature
- The suction surface horseshoe vortex (B), a weaker vortex which lies above the passage vortex, rotates counter to it and interacts with it
- The corner vortex (C), a small vortex rotating counter to the passage vortex located close to the endwall
- The endwall overturning (D), which can mask the corner vortex

3.2.4 Kinetic Energy In Vortical Flows

The following two performance parameters are used in the course of investigations to highlight the secondary flow structures. The first, Secondary Kinetic Energy Coefficient or C_{SKE}, has been used by numerous researchers and provides an indication of the kinetic energy in the vortical flows. The second, SKEH, is a modification of the first parameter using helicity and was first considered by Brennan et al. (2001). SKEH provides additional insight into the flow structures.

Both C_{SKE} and SKEH are very sensitive to changes in secondary flow strength as they are a function of the square of the velocity.

C_{SKE}

The classic definition of C_{SKE} uses both the radial component of velocity V_r and the secondary velocity V_{sec}. C_{SKE} is defined as the sum of the squares of these two velocities, normalised by the square of the upstream velocity (see Equation 3.5).

$$C_{SKE} = \frac{V_{sec}^2 + V_r^2}{V_{ups}^2} \tag{3.5}$$

Vorticity

Vorticity is defined as the curl of the velocity vector (Equation 3.6). It is thus a vector itself. The vorticity values presented within this work are the streamwise component calculated at the experimental measurement planes. Streamwise vorticity is obtained from the method of Gregory-Smith et al. (1987).

$$\zeta = \nabla \times u \tag{3.6}$$

SKEH

SKEH is calculated as the product of secondary kinetic energy and helicity. The SKE is similar to the C_SKE described above, but takes the mean velocity at each radial (traverse/computational) plane to provide the mean yaw component of Equation 3.3). The definition (Equation 3.8) was originally published by Brennan et al. (2001). By including helicity in the equation, areas such as the midspan flow, where no secondary activity is expected, have a zero value.

Helicity is defined as the dot product of vorticity and velocity, defined in Equation 3.7 and is thus a scalar quantity. By using the dot product, the vorticity is scaled by the angle to the streamwise direction and thus the streamwise components can be focussed on.

$$H = u \cdot (\nabla \times u) \tag{3.7}$$

$$SKEH = SKE.H \tag{3.8}$$

SKEH is presented in this work as a useful indicator of performance. The parameter is used to indicate performance gains related to the reduction in secondary flows, see Corral and Gisbert (2006) and Brennan et al. (2001).

The use of SKEH in isolation will not provide enough information on the comparative performances of turbine blade designs. Because of this, the effect on total pressure loss is also taken into account.

3.2.5 Averaging

The calculation of pitch averaged quantities utilises Equation 3.9 (for variable of interest 'a'), the area mass averaged quantities (referred to in the text as mass averaged) utilise the pitch averaged data ($\overline{a}$) and Equation 3.10. Both pitch and mass averaged data are calculated using the trapezium rule. A more in-depth discussion of the data processing is given in Ingram (2003)

$$\overline{a} = \frac{\int_0^s a V_x \Delta r \, dt}{\int_0^s V_x \Delta r \, dt} \tag{3.9}$$

$$\overline{\overline{a}} = \frac{\int_0^h \overline{a} \overline{V_x} \, dr}{\int_0^h \overline{V_x} \, dr} \tag{3.10}$$

It should be noted that the averaged loss values presented in this thesis are representative of the behaviour of the flow at the traverse plane of interest and are not to be confused with mixed out loss.

3.3 Pressure Measurement

In this section, the experimental apparatus used for taking pressure measurements is described. The typical experimental setup consists of a pneumatic probe connected to a series of differential pressure transducers. These transducers measure the pressures on the individual holes of the probe head relative to an upstream reference total pressure, determined by a pitot-static probe. Five hole and three hole type probes are both used in cascade measurement.

A schematic of the pressure measurement equipment used in the work is given in Figure 3.4.

The five hole probe is suitable for the majority of the measurement region, but its use is limited in the region close to the endwall and aerofoil surfaces, due to its relatively large size. For these areas, a three hole probe is used, capable of determining only the local yaw angle and total pressure loss.

3.3.1 Transducers

The pressure transducers used in this work are the CMR P-Sensor. The transducers were calibrated at the start of the project using an inclined tube manometer. The response curve of the transducer (pressure vs. output voltage) was then included in the post processing software, for each device, as hard coded data.

Transducers are more commonly affected by drift of the output voltage. To ensure that the effect of drift was kept to a minimum, a zero pressure (differential) reading was taken on each transducer before the fan was started. This value is used to correct the raw data taken from the experimental measurements. By observing these drift correction values, from a sequence of traverses taken over a ten day period, the transducer output was not found to vary significantly. The standard deviation of the drift correction was found to be 0.12% of full transducer range. Comparing this with the absolute value of the drift correction (around 1.86% of full transducer range), confirms the suitability of the current correction method.

Both the three and five hole probes are connected to a series of differential pressure transducers. The central hole of the probes is connected to two transducers of ranges $\pm$200 Pa , 0-500 Pa, with sensitivities 0.02 V/Pa and 0.025 V/Pa respectively. The central hole is key to the measurement of total pressure loss in the cascade and as such requires both the measurement sensitivity of the $\pm$200 Pa device and the range of the 0-500 Pa device. The remaining holes are connected to 0-2000 Pa transducers (sensitivity is 0.0025 V/Pa).

The static pressure hole on the upstream reference pitot probe is connected to a separate transducer measuring the inlet velocity. The resulting inlet dynamic head is used to normalise all the pressures and provide a total pressure coefficient C_{p0}.

A more in depth description of probe measurement is given by Treaster and Yocum (1979) and Dominy and Hodson (1992). In addition, the specific details of

Parameter	Value
Inlet Dynamic Head (p_{dyn})	215 Pa
Inlet Velocity (v_{ups})	19.1 m/s
Air Density (ρ)	$1.179 kg/m^3$
Air Viscosity (μ)	$1.814 * 10^5 kg/m^3$

Table 3.1: Standard Day Conditions

the probe measurement system on the Durham Cascade are described by Ingram (2003). This system is virtually unchanged, so details are not repeated here.

3.3.2 Standard day conditions

Through all previous research projects using the Durham Cascade, a standard running condition has been used. This running condition is defined by a Reynolds number of 4x10^5, based on axial chord and inlet velocity. For all traverses during this work, the atmospheric conditions (P_a and T_a) have been measured and the inlet dynamic head set to maintain the Reynolds number at this 'Standard Day' condition. Table 3.1 contains the standard day operating conditions of the Durham Cascade.

3.3.3 Measurement Grid

The probes are traversed over a grid of points, to achieve coverage of all the flow features in the region of interest. This traversing may include a finer grid spacing in regions of large pressure gradients. The grid shape and density are determined prior to measurement, using existing knowledge of the flow structures. An example of a measurement grid is presented in Figure 3.5, showing the higher density regions covering the blade wake and near the endwall.

The blade wake is an important region due to the rapid changes in total pressure occurring here. The near-endwall regions are refined to enable resolution of both the large pressure gradients associated with the low total pressure regions (loss cores) and the large velocity gradients associated with the vortex structures.

3.4 Two cascades

Two different cascade designs are utilised in this work. One is the pre-existing endwall-focussed design, the other a new passage-focussed design. The cascade geometry is defined by Gregory-Smith (1993), key parameters from which are contained within Table 3.2.

3.4.1 Pre-existing cascade (geometries P4, C0 and C1)

The pre-existing cascade consisted of six blades in a linear arrangement, cantilevered at one end by a nut and bolt and supported and aligned at the other end by a removable endwall piece.

Parameter	Value
Inlet Yaw Angle (α_1)	42.75^o
Exit Yaw Angle (α_2)	-68.7^o
Axial Chord (C_{ax})	181 mm
Pitch (s)	191 mm
Span (h)	400 or 375 mm
Reynolds Number (Re)	400,000

Table 3.2: Durham Cascade Geometry

Endwall geometries were applied to this removable endwall piece, as detailed by Hartland (2001) and Ingram (2003). Measurements were taken using the slot-based traverse, typically over half of the cascade, where the flowfield was known to be undisturbed.

A bi-directional turbulence grid, built from 25mm bars, was installed downstream of the tunnel inlet contraction, at a known distance upstream of the leading edge of the blades. The spacing and bar diameter were installed by Cleak (1989), who determined the necessary sizes using the equations of Roach (1987). This grid of bars gives a streamwise turbulence intensity (Tu) of 4%. The grid is inclined to the inlet flow by the same angle as the cascade to ensure that the distance to the leading edge of each blade remains equal. The turbulence intensity was verified by the experimental work of Moore (1995).

A proportion of the fluid is bled off from one side of the cascade, which in combination with a false wall provides a new boundary layer of known size. The proportion of bleed was controlled by a flap, until the static pressure either side of the false wall equalises.

The single boundary layer bleed leads to a non symmetrical inlet flow. This was not previously a problem, as investigations involved only half of the blade/passage span. The flow at midspan remained unaltered throughout these investigations, thereby proving the independence of the half passage result.

Inlet boundary layer

The pre-existing inlet loss profile, taken from three hole probe traverses at -100% C_{ax}, is given as "P0" in Figure 3.6. This boundary layer is the same as that of Ingram (2003) and was present during the analysis of geometry P4 of this work.

Later, modifications were made to the inlet conditions in order to improve the symmetry of the upper and lower boundary layers. This was achieved to some extent and the modified inlet boundary layer profile is shown as "C0" in Figure 3.6. The key differences being the removal of the negative loss region and an improved symmetry of the two endwalls.

The impact of the modified boundary layer is significant, and thus comparisons betwen cases using the differing inlet conditions should consider the effect of the changes in boundary layer shapes and magnitudes.

The boundary layer is defined using a free stream velocity. This would typically be the mid passage velocity, but because of the velocity variation in the mid passage, the flow 50mm from the wall was taken to be the free stream condition. The new

Item	P0 Lower wall	C0 Lower wall	C0 Upper wall	C0a Both endwalls
99% thickness	30mm	38mm	28mm	20mm
Displacement thickness	2.13mm	3.44mm	2.53mm	3.80mm
Momentum thickness	1.76mm	2.99mm	2.12mm	3.30mm
Shape factor	1.21	1.15	1.19	1.14

Table 3.3: Boundary Layer Definitions

inlet conditions based on this definition are specified in Table 3.3. The table refers to upper and lower passages. The lower passage is defined as the half of the passage closest to the removable endwalls, i.e. the 0-200mm region. The upper passage is defined as the half of the passage closest to the instrumentation and traversing slots, i.e. the 200-400mm region. These upper and lower definitions are used throughout the work.

It can be observed that the shape factor of the inlet boundary layer, at both upper and lower endwalls, is low. It is not clear why the boundary layer is so formed, however the interaction of the turbulence grid with the upstream (pre-bleed) boundary layer and other inlet flow conditioning measures are likely to affect this. The shape factor results for the previous and new cascade designs indicate similarly low values.

The inlet boundary layer loss value is obtained from the integration of the pitch-wise averaged total pressure loss (Figure 3.6) at the inlet traverse location. This value, presented in Figure 3.7, is used to calculate net loss values downstream.

3.4.2 New cascade (for geometries C0a C2 C3)

A new cascade was designed, which removed the inlet asymmetry and enabled the testing of more complex aerofoil geometries. The new cascade retains the same arrangement of blades, including the number, pitch and inlet angle, but with key alterations. The span has been reduced by 25mm (6%) to accommodate a second boundary layer bleed at the other endwall. This is to ensure a symmetrical inflow to the cascade. The bleed slots are based on the previous cascade and were similarly controlled and balanced.

Reducing the span whilst retaining the same blade pitch alters the aspect ratio; this will alter the balance of loss features, i.e. the ratio of profile loss to secondary loss, this should be noted in any comparison with previous data. Additionally, the reduction in span will bring the secondary flow vortical structures closer together. However, the 25mm reduction on 400mm span is not large enough to cause the passage vortices to interfere.

Downstream of the bleed slot, the false wall develops a new inlet boundary layer, the thickness of which is determined by its length to the cascade inlet. This length has been kept the same compared to the old cascade, but the inlet conditions have not been made identical to the old cascade.

Inlet flow

The old cascade inlet conditions were measured as a simple line traverse, giving basic boundary layer information for a particular tangential location. For the new cascade a large slot was cut to permit a full 2D planar investigation. A traverse plane 100% C_{ax} upstream of the blade leading edge was used, as shown in Figure 3.13. The traverse covers an area 5mm to 350mm radial, -125 to -325mm tangential.

Figure 3.8 shows the results of a traverse at -100% C_{ax}. The initial results indicate two non uniformities in the total pressure, one in the tangential and one in the radial direction. The radial total pressure gradient is most significant in the near wall region, i.e. in the developing boundary layer.

The effect of the bleed/false wall on total pressure distribution, is seen as a negative loss region close to both false walls. Pankhurst and Holder (1968) suggest that spatial non-uniformity may be overcome by dissipating the excess total pressure using gauze or honeycomb structures. Cleak (1989) used an additional 8mm bar, inclined like the turbulence grid, to increase the loss in near wall region. This method has been used again to even out the total pressure distribution. The bar can be identified as 'B' in Figure 3.9.

A number of positions were trialled and the most suitable used. Figure 3.10 shows the impact of bar B. The negative loss region is clearly eliminated by this modification.

The traversing region was extended tangentially (+25mm to -410mm) and a repeat traverse taken. The tangential variation is clearly observed in Figure 3.11.

The tangential variation was subsequently reduced by the introduction of small (4mm) horizontal bars (A in Figure 3.9), placed with non-linear vertical spacing upstream of the turbulence grid. The final inlet total pressure distribution is shown in Figure 3.12. The reference Pitot probe was moved for this final inlet measurement, to better illustrate the improved spatial uniformity.

The small diameter of the horizontal bars ensures that they do not affect the level of streamwise turbulence, whilst their spacing is determined to decrease the total pressure in the upper half of the tunnel.

The resulting inlet boundary layer is presented in Figure 3.6, alongside the earlier boundary layers of the P-Series work and C0/C1 investigation. The new boundary layer is named C0a in this Figure and relates to the cartridge based, downstream access traverse system. The boundary layer is much smoother with smaller variations of total pressure.

The total pressure loss of the three individual boundary layers is presented in Figure 3.7. The figure indicates an increased and more uniform boundary layer loss. These inlet loss values are subtracted from downstream measurements to provide net losses for comparison. The inlet conditions have also been used to define the boundary conditions for the computational work.

Two Part Construction

The new tunnel has been constructed such that additional inlet flow modifications can be included without significant alteration. The tunnel consists of two parts, an upstream tunnel with honeycomb flow straightener and turbulence grid, allowing

consistent inlet condition setting and a blade containment box which fixes the position of the blade cartridges tangentially and radially and also provides location for the traverse slides.

Figure 3.13 is an overview of the entire wind tunnel. It locates the inlet measurement slot, upstream of the aerofoils, where the boundary layer measurements are taken, the cartridge box which constrains the individual units being tested, and all of the upstream flow conditioning modifications.

In Figure 3.14, the cartridge box is detailed. The cartridge insertion method is shown and the access holes are also highlighted. These holes enable the tubes of the pressure tapped aerofoil to route to the manometer.

3.5 Traversing systems

The following section describes the apparatus used to traverse the probes over the desired measurement plane. During this work, two different probe traversing systems have been used. A slot based system was used, which focused on planar measurement regions at discrete axial locations. A more recent downstream access system has been used, where the measurement region was accessed from downstream using long stem probes.

3.5.1 Slot traversing

For the slot based system, the probe was traversed over an axial plane, moving in the tangential and radial directions within this plane. The advantage of this method is the ability to traverse within the blade passage itself, at any axial plane.

To enable the probe to access the flow, slots were cut into one side (one endwall) of the cascade. The image in Figure 3.15 shows the position of the axial planes at which the slots were cut, covering the whole passage. These slots have allowed the investigation of secondary flow axial development in some detail, see Ingram (2003).

For the majority of investigations, the key measurement is taken a distance downstream of the passage, representative of inlet conditions to the next blade row. For the Durham Cascade this is 128% C_{ax} or 28% C_{ax} (51 mm) downstream of the trailing edge. In Figure 3.15 this relates to slot 10. Some work has also been undertaken at a location equivalent to slot 8 and as indicated by the dashed line; either side of the trailing edge. A limitation of the slot based traversing system is only one endwall is measured well.

3.5.2 Downstream traversing

For the new cascade the probes were designed to access from downstream. To minimise interference the probe stem was designed to enter at the same angle as the exit flow. For this a long stem was required. The stem was supported on a large diameter bar, held at both ends, and traversed in tandem. An example of such a probe-stem is presented in Figure 3.16. The figure shows a stem with a large upstream reach, capable of reaching to the same axial position as Slot 4.

The downstream access probe can be used for measurement close to both endwalls and, with a suitably designed probe-head, will access close to all wetted surfaces.

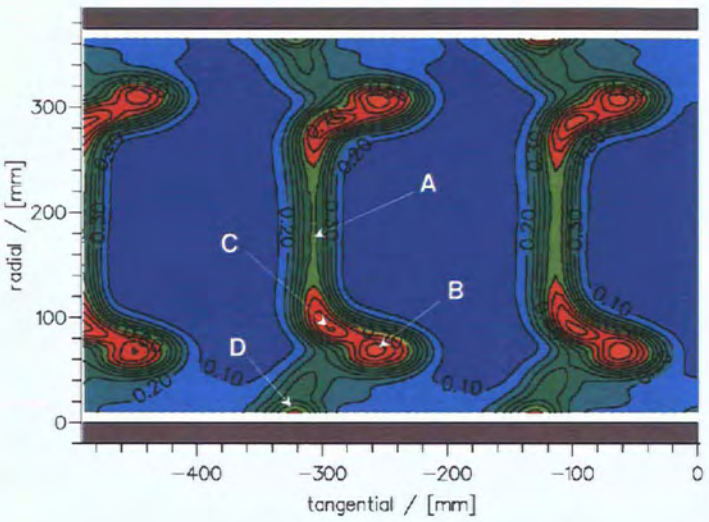

Figure 3.1: Typical total pressure loss contours

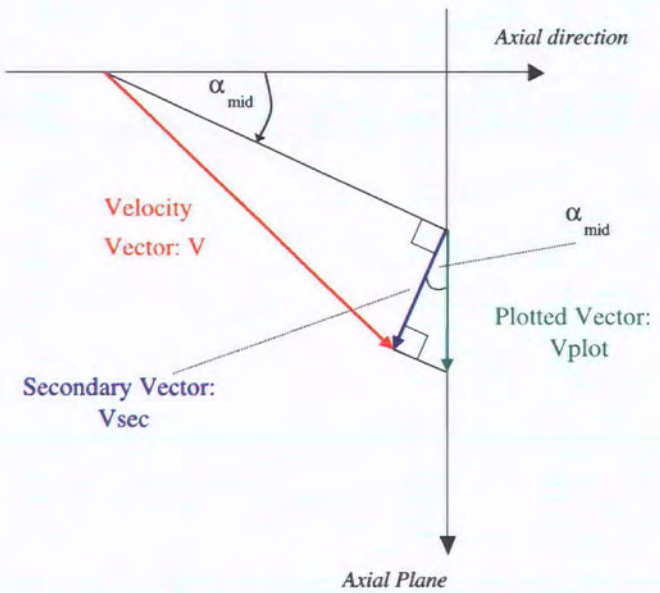

Figure 3.2: Definition of secondary velocity

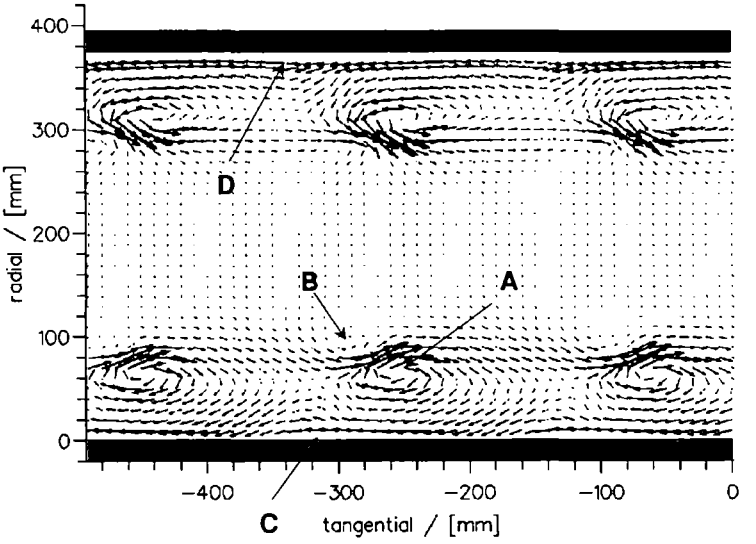

Figure 3.3: Typical secondary velocity vectors

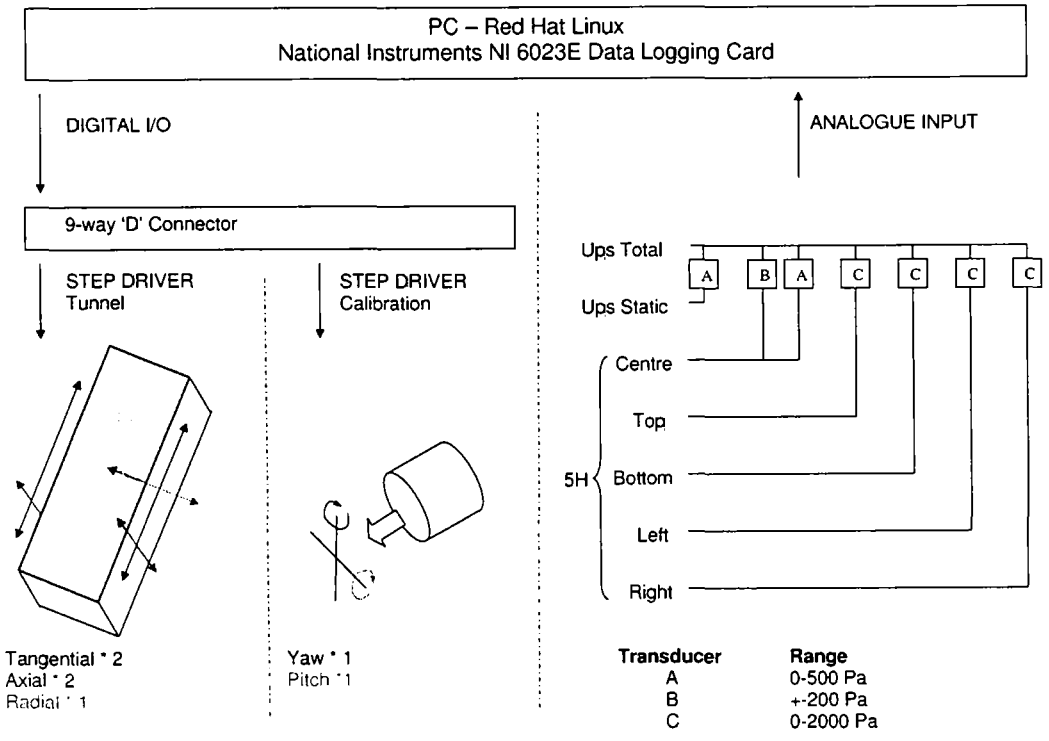

Figure 3.4: Pressure measurement instrumentation

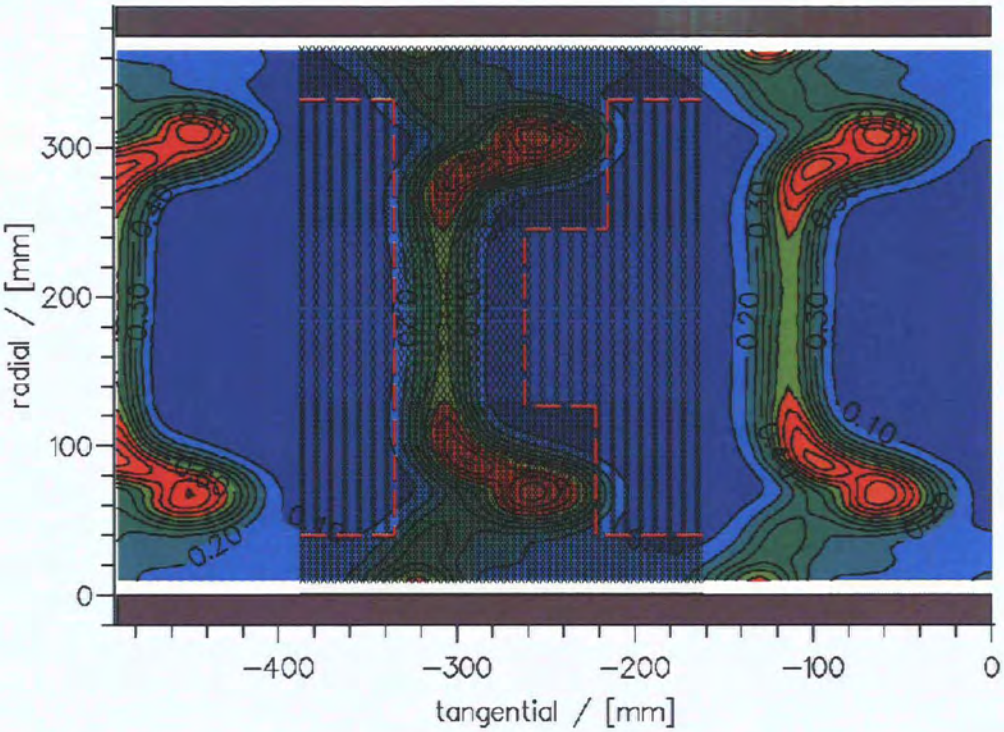

Figure 3.5: Example Mesh Resolution

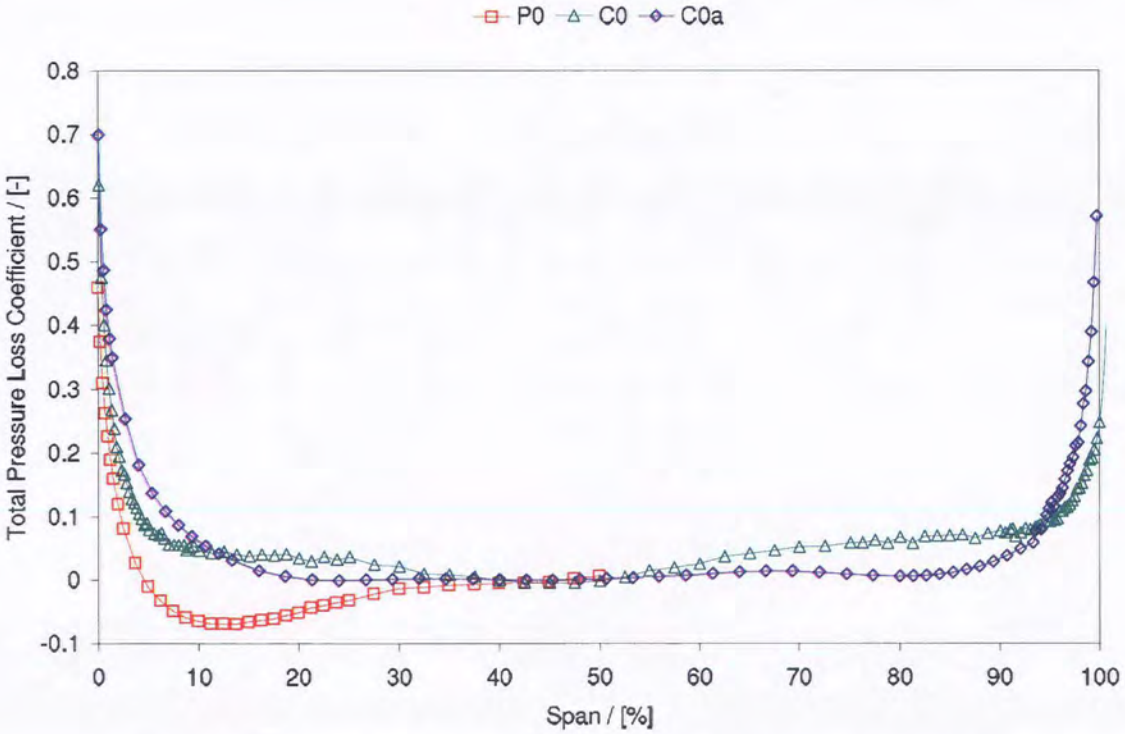

Figure 3.6: Boundary Layer Profile - All Cascade Arrangements

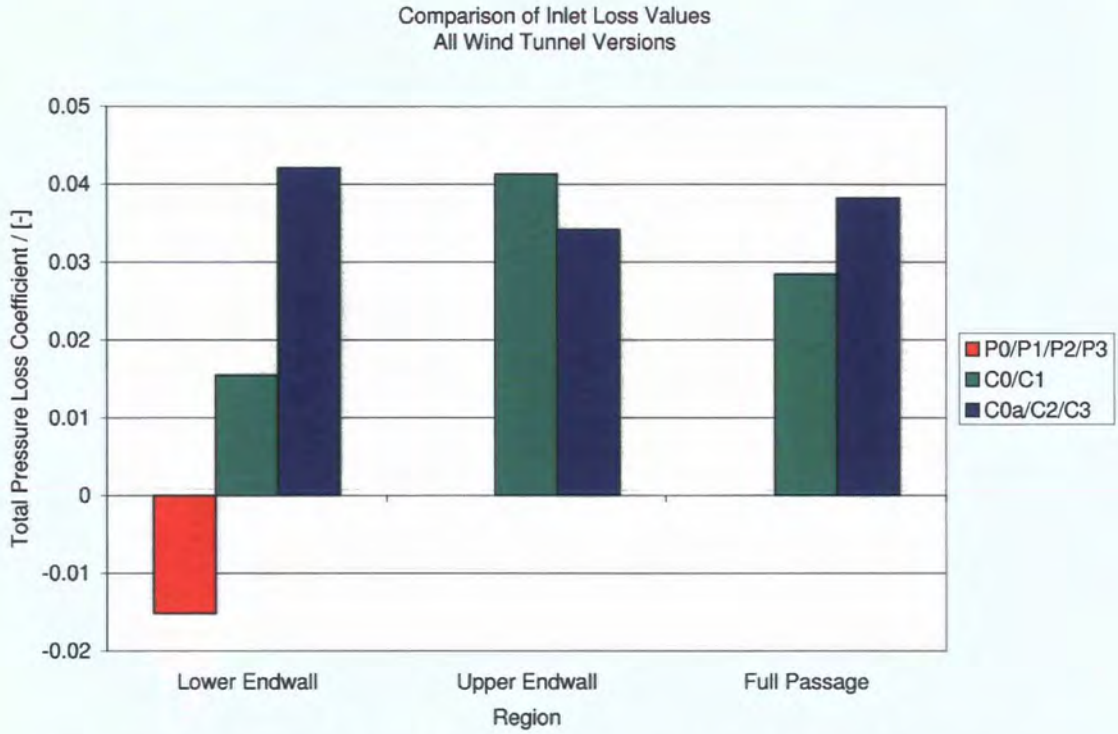

Figure 3.7: Boundary Layer Loss Measurements - All Cascade Arrangements

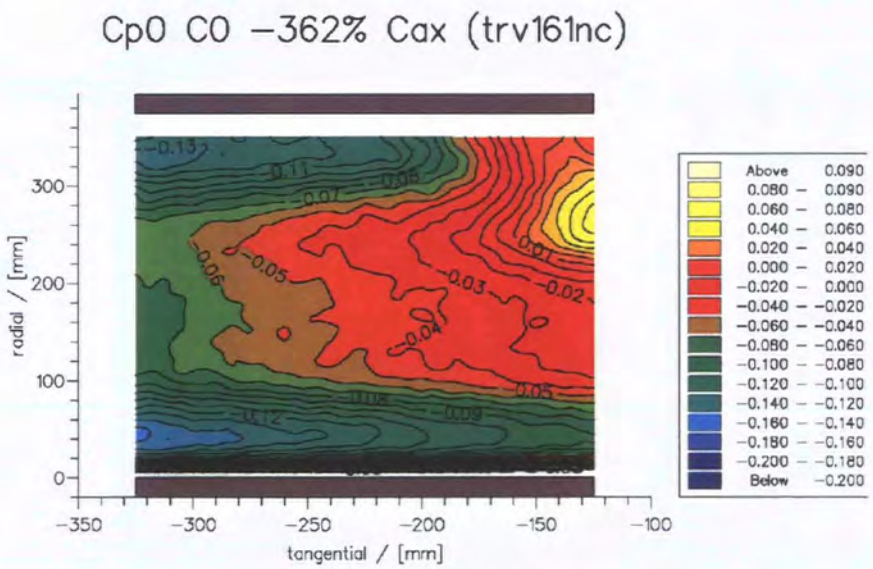

Figure 3.8: Inlet C_{p0} Distribution - No Bars

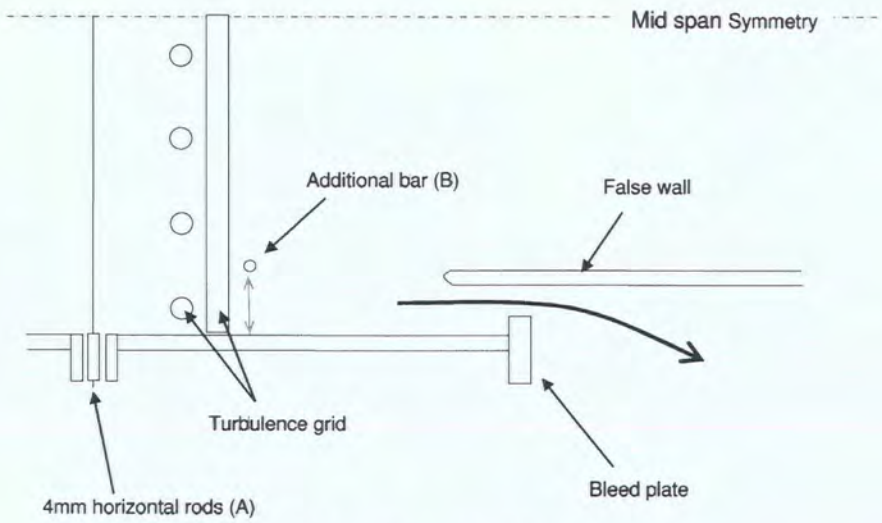

Figure 3.9: Inlet Flow Modification Features

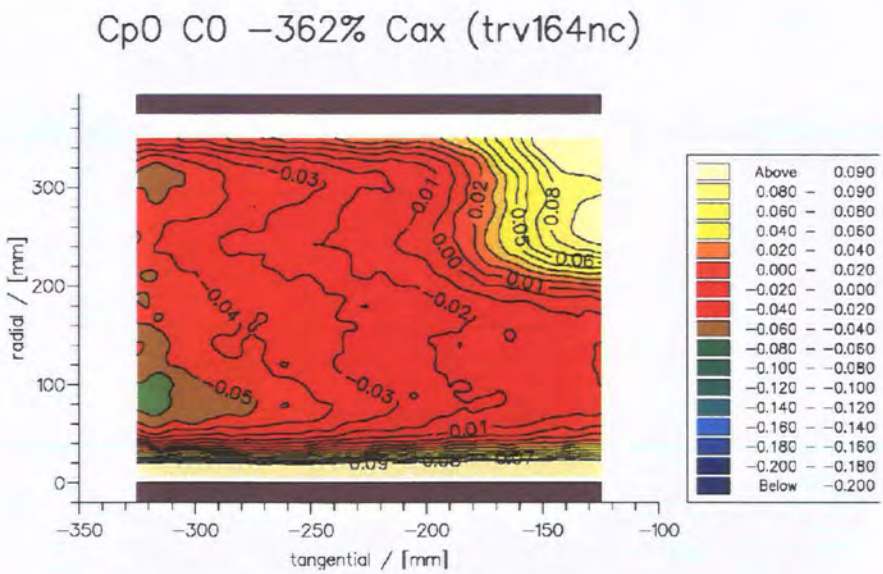

Figure 3.10: Inlet C_{p0} Distribution - Bar at 35mm offset

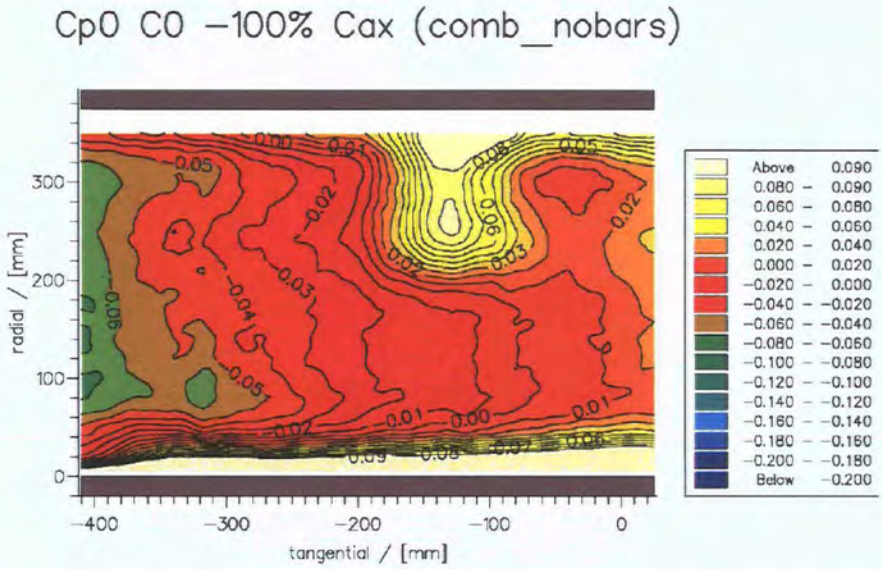

Figure 3.11: Inlet C_{p0} Distribution - No bars

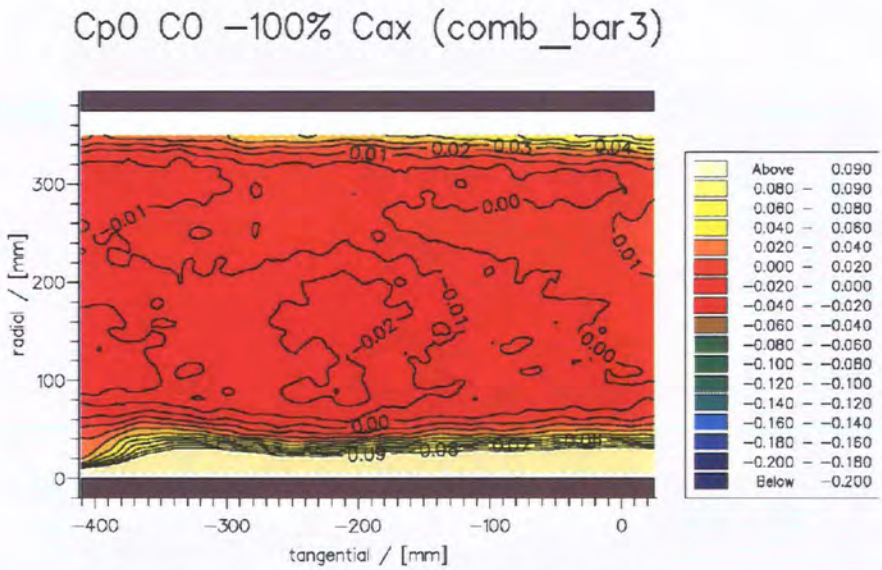

Figure 3.12: Inlet C_{p0} Distribution - Final Arrangement

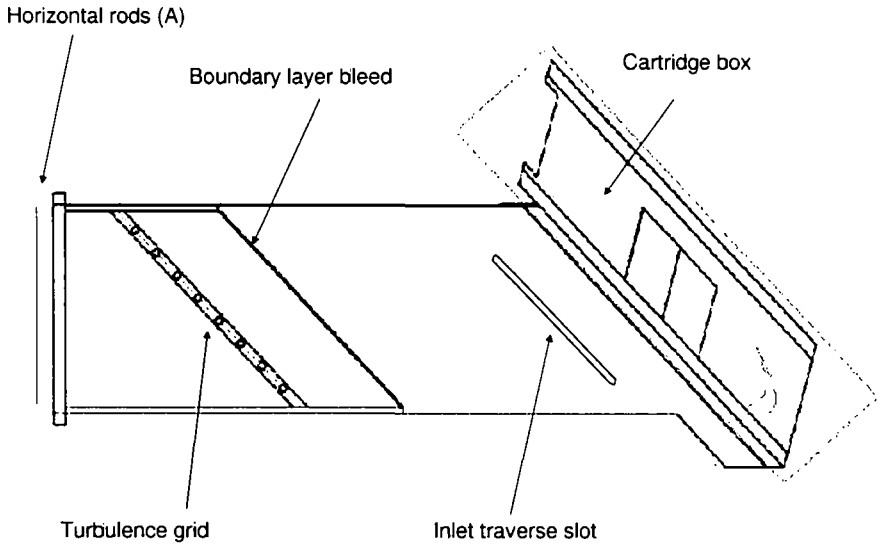

Figure 3.13: Durham Cascade Wind Tunnel

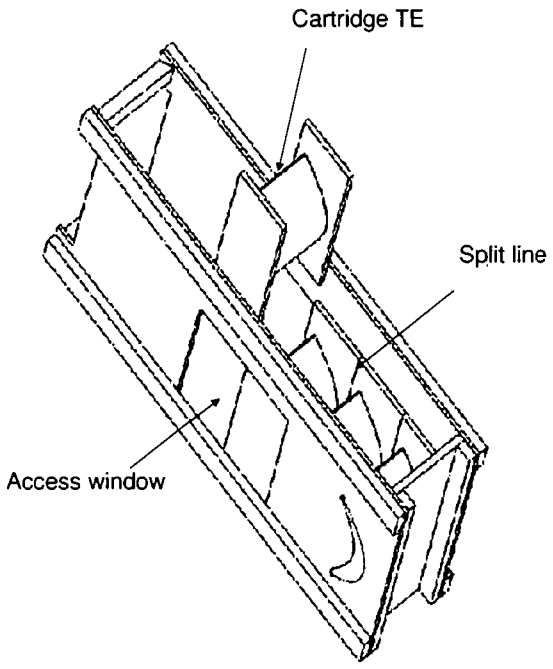

Figure 3.14: Cascade Endbox Arrangement

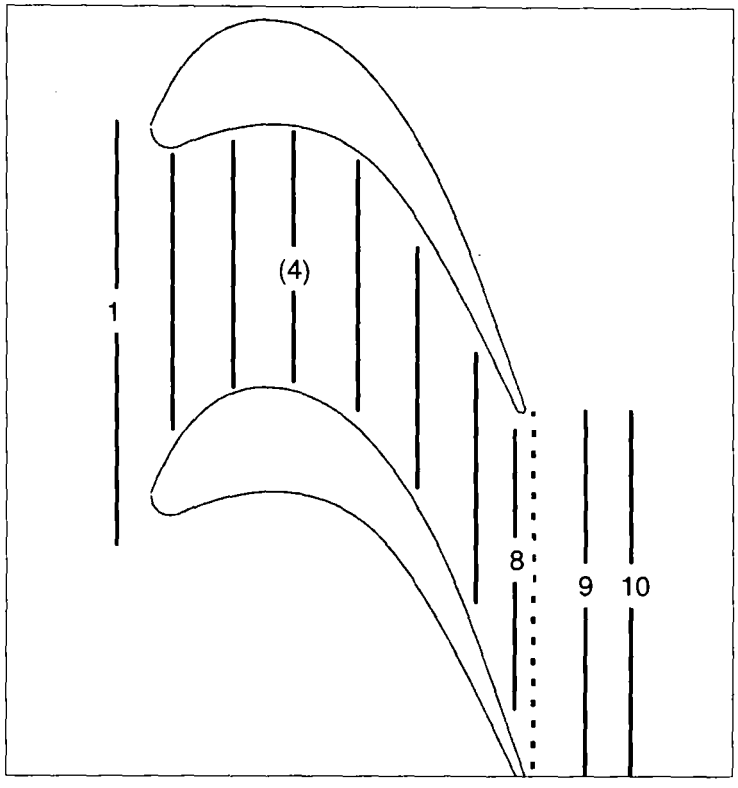

Figure 3.15: Slot traversing locations

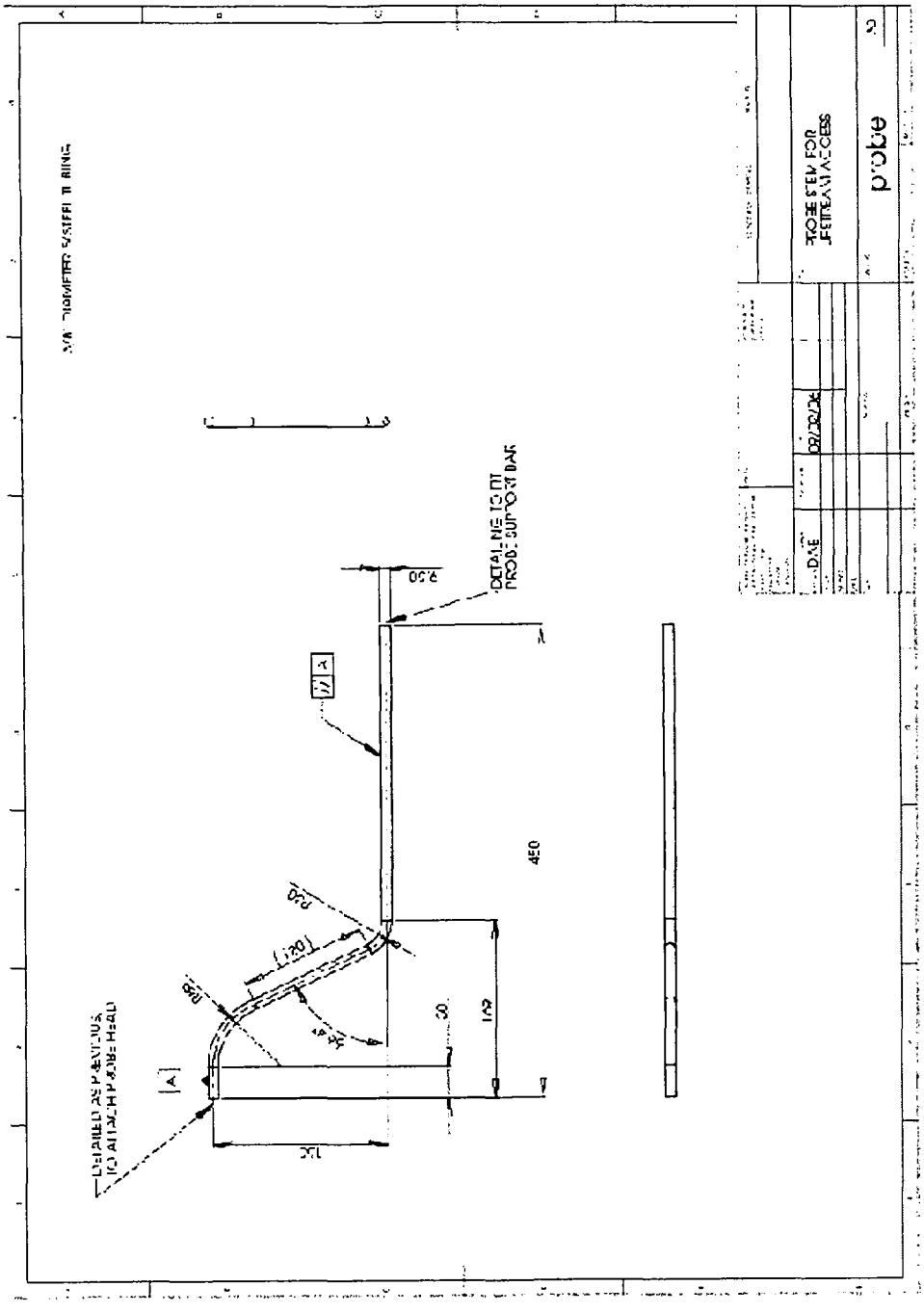

Figure 3.16: Stem extension

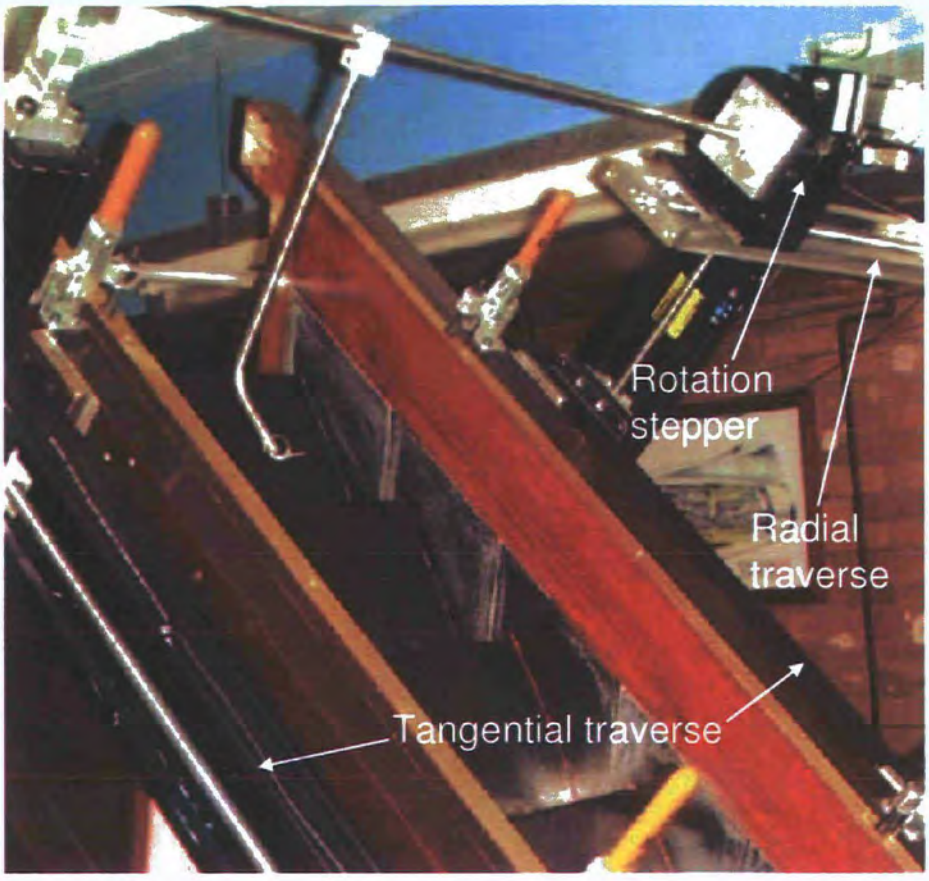

Figure 3.17: Photograph of traverse

3.5.3 Equipment

The traversing equipment for the downstream access was upgraded to enable a tandem arrangement of slides. Photographs of this traversing equipment are given in Figures 3.17 and 3.18. Figure 3.17 shows the right hand side of the system; incorporating a radial slide and probe rotation device, in addition to the tangential and axial slides. Figure 3.18 shows the left side of the cascade with the 250 mm axial and 500 mm tangential slides. These slides are a mirror of the traverse equipment on the right hand side of the cascade. The figure shows a linear bearing mounted on top of the axial slide, used to support one end of the probe bar. This bearing constrains the probe both tangentially and axially, but allows it to move radially and rotationally.

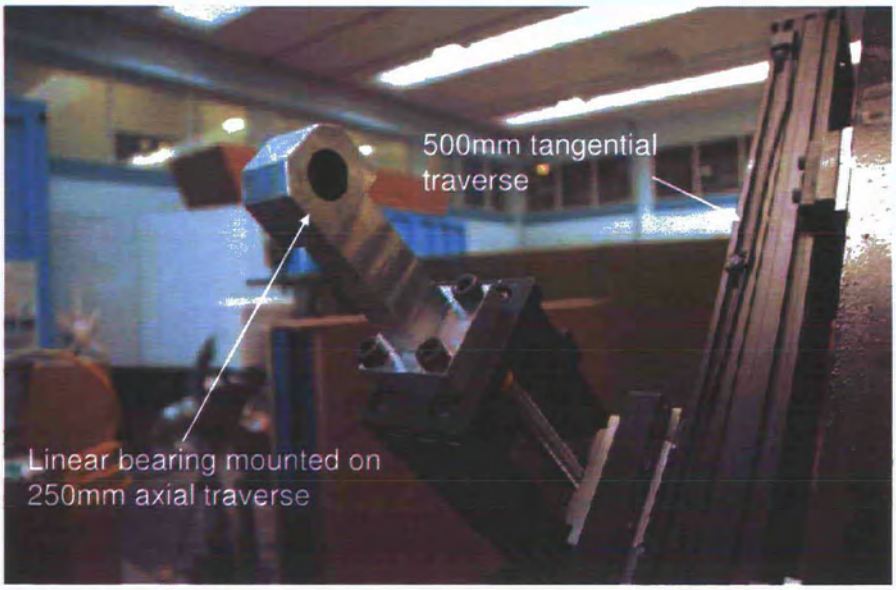

Figure 3.18: Photograph of traverse

The control (step drive input) signals are wired in parallel for the two tangential and two axial slides, thereby synchronising their movement at both ends. The positional accuracy of the new system is 0.0025 mm in axial, tangential and radial directions. The angular rotation is accurate to 0.01°. This level of accuracy is more than adequate for a large scale (375 mm span) cascade. The advantages of the new traversing system are:

- there is no leakage through endwall slots
- there is very little disturbance due to the probe stem
- a 3D volume rather than a 2D plane can be measured
- the new traverse can cover a much larger area than the old one
- the new traverse is supported at both ends rather than being cantilevered, thus increasing probe rigidity

The primary disadvantage of the new system, is that access to the upstream portion of the blade passage is restricted. The amount of access to the upstream blade passage depends upon the geometry of the blade passage.

3.6 Cartridge

The construction of a new cascade allowed consideration of alternative concepts for blade fixing. The key requirements were the rapid, simple and accurate exchange of a complete integrated set of wetted surfaces. The resultant geometry is a combination of blade and both endwalls, upper and lower, integrated into a single cartridge unit with platform extents similar to a generic HP turbine. The cartridge design necessitates splits in the middle of the passage, similar to a real engine. This is in contrast to the previous cascade with endwalls, where the split line lay along the blade camber line.

The streamwise split line angle and position, and upstream and downstream axial extents were also chosen based on generic HP platform information, as shown in Figure 3.19. This pseudo HP turbine geometry was considered useful for future research into a variety of areas including, disc leakage/cooling effects and split line leakage effects.

The integration of the cartridge into the new tunnel is shown in Figure 3.14. The cartridge slots in from downstream, between two containment walls and is retained by quick release toggle clamps.

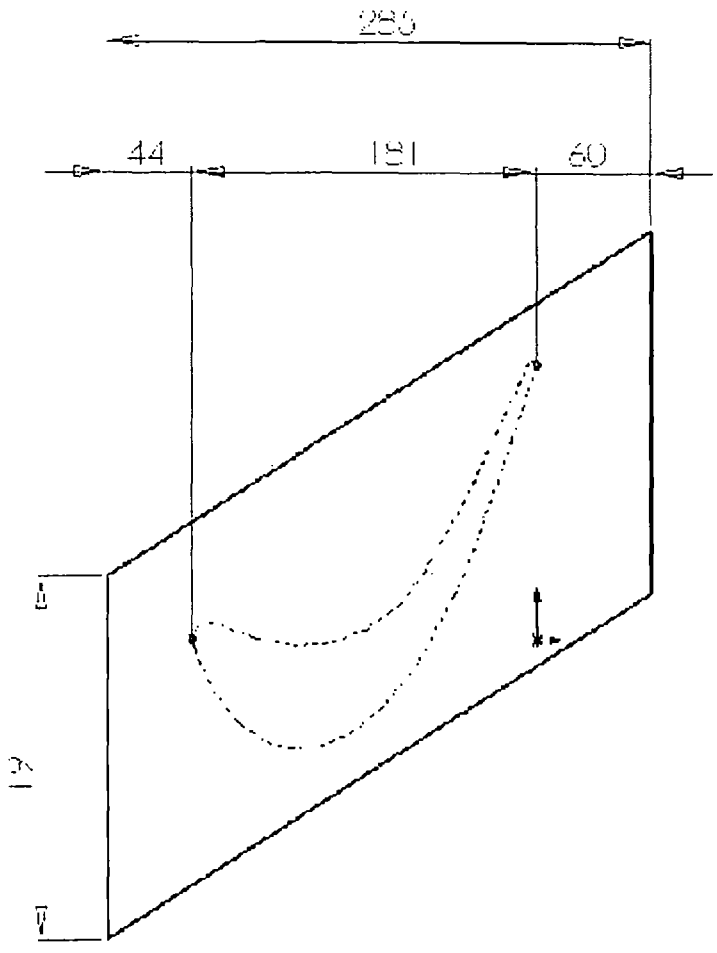

Figure 3.19: Cartridge Platform Extents

A drawing of the prismatic cartridge is in Figure 3.20. A drawing of one of the passage shaped cartridges is detailed in Figure 3.21. The figure illustrates how the aerofoil splits and includes detail of the location lug on the aerofoil.

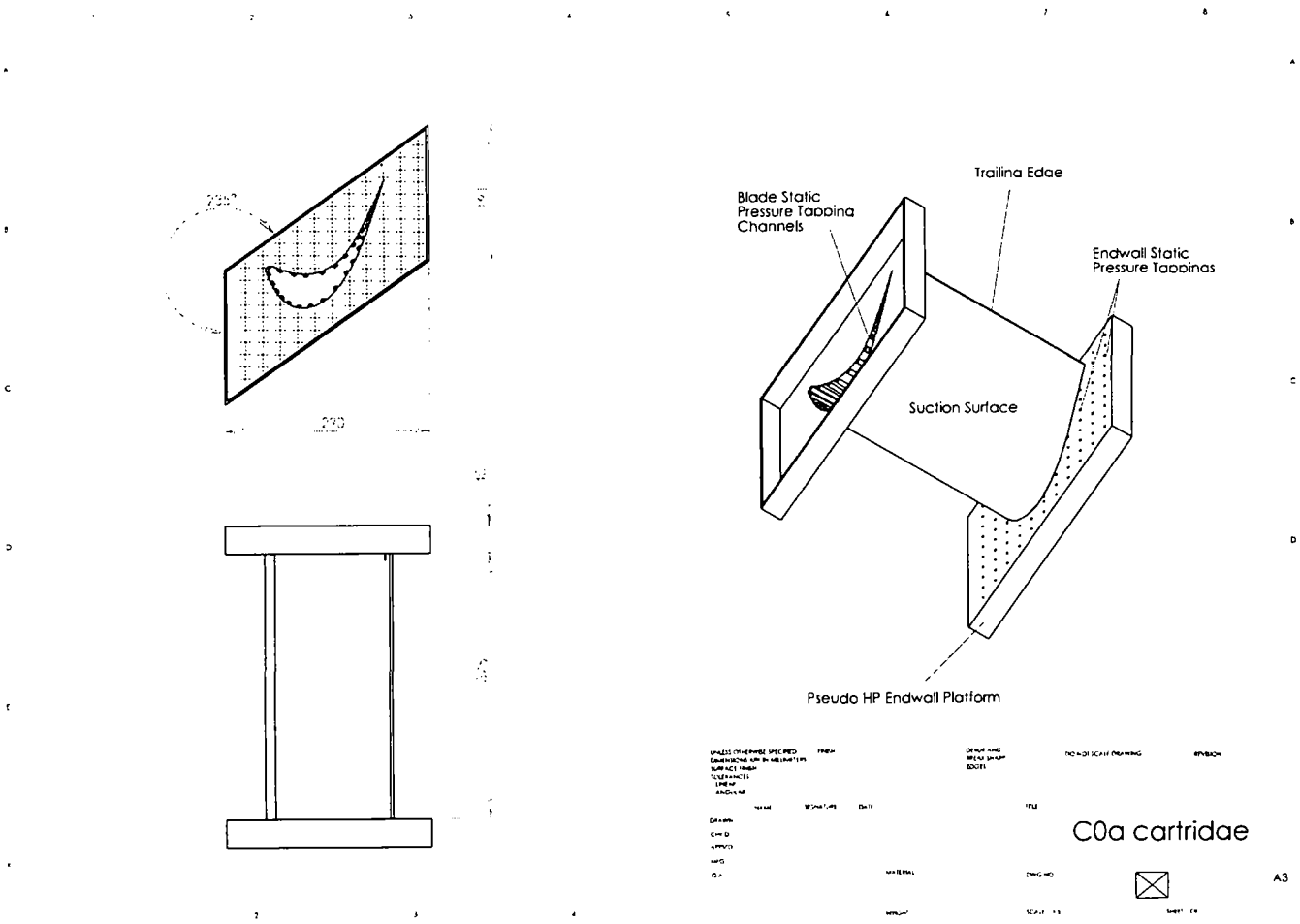

Figure 3.20: Datum aerofoil cartridge geometry

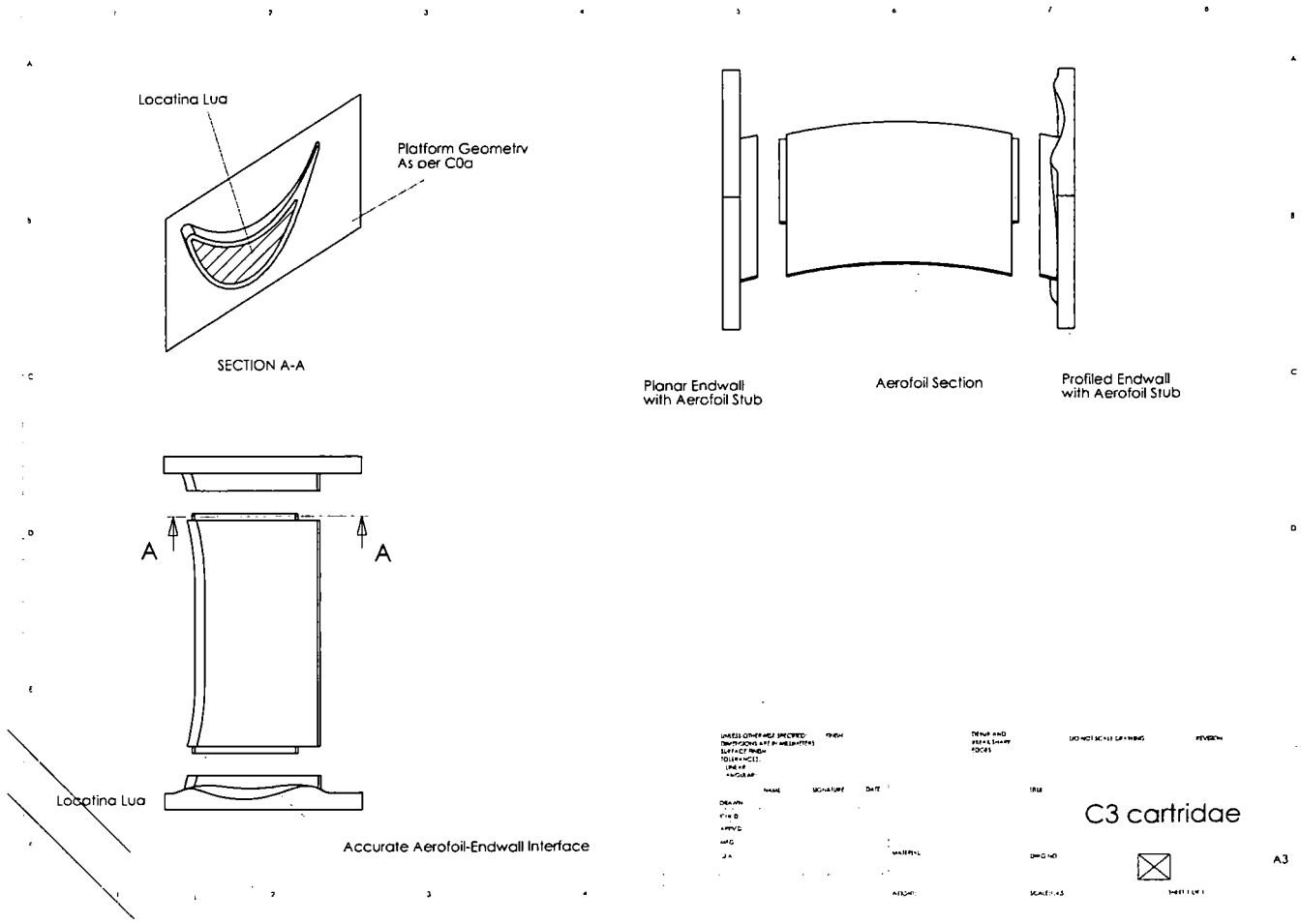

Figure 3.21: Passage shaped aerofoil cartridge geometry

3.7 Probes

As described earlier, the pressure measurements are taken using three and five hole probes. To ensure the repeatability of the probe location, the following alignment routine is undertaken.

3.7.1 Alignment

The probe head is inserted into the appropriate stem. The position of the head is set in the following order:

- The turret angle is altered by driving the rotary table. The angle is set by aligning the head with a plumb line. This was found to be the most accurate setting method
- The radial location is found by driving the probe tip to a known distance from the lower endwall, at a location where it is planar
- The axial position is measured relative to the point where the trailing edge circle meets the suction surface
- The tangential position is also set relative to the trailing edge.

Typically, the probe is driven in the tangential and radial directions. The axial and turret angle settings do not alter within an individual traverse, thereby simplifying the probe positioning.

3.7.2 Modular design

Prior to the redesign, each individual probe was built as a single unit, with head and stem fixed together. The size of the new downstream access probes means that they are better suited to a modular arrangement. This reduces the manufacturing time and material costs of each new probe head, and also allows a rapid exchange of head type during experimental work.

The head is connected to the differential pressure transducers via 1mm flexible silicon tubing. The stem and support bar are constructed from tubular stainless steel. This allows access for the flexible tubing and protects it from aerodynamic loading inside of the cascade.

The measurement probes for the new cascade are designed to be modular, with different stems and detachable heads. The new probe consists of a support bar onto which a suitable stem is attached depending on the required reach. A probe head, such as those in Figure 3.22 is fitted to the stem end.

Both the stem and the head locate by pin and slot, ensuring good repeatability of probe head alignment. This modular system could also be used to position hot wire type probes.

The probe heads are of 'forward facing pyramid' design, as described by Dominy and Hodson (1992). The probe uses 1 mm outer diameter stainless steel hypodermic tube, the tubes are placed in a jig, cleaned and glued. The 5-hole probe is 3 mm

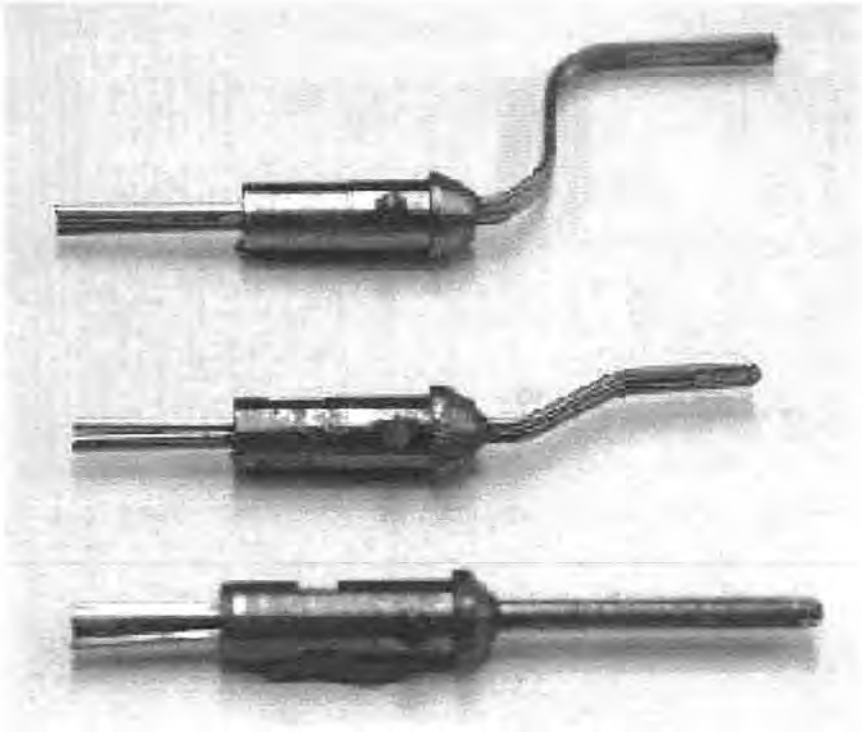

Figure 3.22: Three probe heads

in diameter, this diameter continues for 30 mm length at which point the head is mounted on 8 mm diameter stainless steel tube. The 3-hole probes are 3 mm width x 1 mm thick and between 25 and 30 mm in length.

The probe head size compares favourably with the throat area of the cascade. (7 mm^2 compared to 26,400 mm^2) and thus does not add to the blockage.

3.7.3 Calibration

The probe must be calibrated in a known flow condition. Here a jet is used with uniform total pressure profile and velocity close to the maximum observed in the cascade. The probe is aligned with the axis of the jet, supported on a two axis traverse system. The rig is designed to rotate the probe about its tip, moving it through a pitch-yaw grid of approximately 1400 points. At each point the pressures at each hole are logged.

An example of the calibration map output from this process is shown in Figure 3.23 for $\pm 25^o$ in yaw and pitch. Whilst slightly skewed, the grid is rectangular and therefore of high accuracy. At the combined extremes of pitch and yaw, the calibration map can become skewed. In these conditions the probe becomes less accurate. For the majority of the cascade measurement this is not a problem.

3.7.4 Hand test

In order to check the calibration, a manual test is performed. A reduced measurement grid in pitch and yaw is traversed by hand. This is logged with the cascade

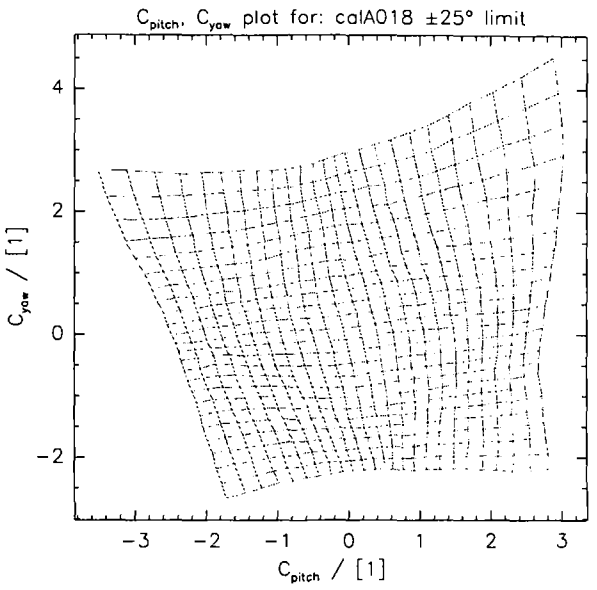

Figure 3.23: Pitch-Yaw Calibration Map $\pm 25^o$

standard logging program, to obtain total pressure coefficients, and pitch and yaw angles. These are compared with the actual yaw and pitch positions and the total pressures measured on the pitot probe.

Contour plots are generated to visualise any differences between measured and actual results. Typical contour plots in Figures 3.24 to 3.26 show the error in total pressure (as a coefficient), and the error in yaw and pitch angles as an angle. The test may be repeated after a series of cascade measurements to check whether the head has been damaged during running.

3.7.5 Measurement Correction

Corrections were applied to the section of the work using the 'old' cascade, Ingram (2003) details the process. The corrections are applied, because of a known variation of loss in the inlet, covering the region where the reference total pressure probe (pitot probe) is located. Variations in the inlet total pressure, as a result of small location changes of the reference pitot probe, result in changes to the performance prediction (C_p0 values) of the measured data.

To ensure that this variation does not impact the experimentally measured results a correction is applied to each dataset. The correction relies on the existence of an undisturbed (zero loss) region at the measurement plane.

A region of the plane of interest (e.g. at 128% Cax), where there is no expected impact of the aerofoil wakes nor endwall and secondary flows, is manually checked to ensure that it the region is suitably small enough and sufficiently distant from the losses associated with the aerofoil wakes and secondary flows. The total pressure values, for the entire measurement plane, are corrected to obtain zero loss in this region.

This correction procedure was found to be unnecessary for the new cascade setup, due to the improved inlet flow conditions.

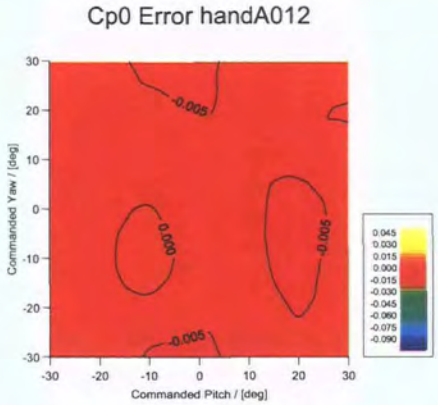

Figure 3.24: Hand Test Result - C_p0

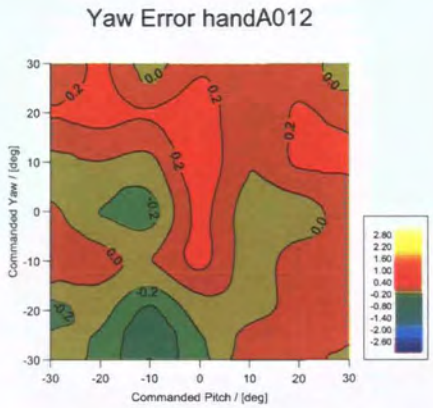

Figure 3.25: Hand Test Result - Yaw

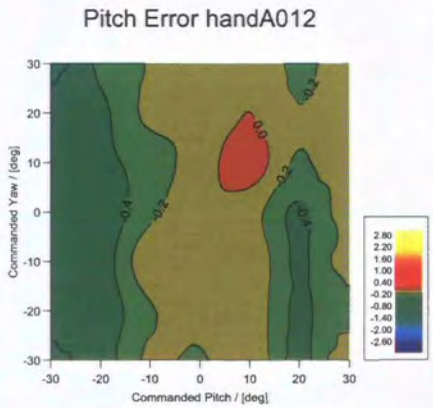

Figure 3.26: Hand Test Result - Pitch

3.8 Flow visualisation

Different surface visualisation techniques can be used, depending on the expected shear level. The oil and dye technique is a flexible surface visualisation method, as the viscosity of the mixture can be changed by altering the ratio of oil to dye. The oil and dye technique works well for the Durham Cascade for all surfaces except the aerofoil pressure surface, here the velocities are too low - even for low viscosity mixtures.

More recently, quantitative surface flow visualisation techniques have been used to determine the local flow patterns and boundary layer state. An example of which is Holley and Langston (2006), who used the oil shear inferometery patterns of a spacial array of oil droplets to observe and quantify the endwall shear. This technique is time consuming and not practical for the time scales involved in this study.

3.8.1 Surface flow visualisation

After pressure probe measurement results have been analysed, further information is typically required to determine the state of the boundary layer flow at, or very close to, the wetted surfaces, i.e. on blade suction and pressure surfaces, and endwall surfaces.

Oil and dye surface flow visualisations are used to give qualitative information on the boundary layer behaviour. The technique is also used to detect any interaction of secondary flow structures with the blade and endwall wetted surfaces.

Prior to flow visualisation, the wetted surfaces are coloured and protected using a permanent melamine lacquer. To generate a surface flow visualisation, the areas of interest are painted with a mixture of oil (typically paraffin) and a polymer based dye powder. The components are placed in the cascade and it is run at the desired Reynolds number until the paraffin has fully evaporated. The resulting patterns may be photographed and the dry dye is easy to remove. Different colour dyes may be used for the blade and endwall surfaces. This technique helps locate the endwall fluid that is drawn onto the suction surface.

A typical result from surface flow visualisation is shown in the photographs in Figures 3.27 and 3.28. The image in Figure 3.27 indicates a number of key features that are due to the secondary flow structures:

A points to the stagnation of the inlet boundary layer upstream of the blade leading edge. A separation line can be seen, indicating the interaction of the horseshoe vortex and endwall.

B points to the trace of the pressure side leg of the horseshoe vortex, which typically runs across the passage to the suction surface of the adjacent blade.

C points to the newly formed endwall boundary layer, downstream of the aforementioned separation line. This new boundary layer is much thinner and is of laminar type.

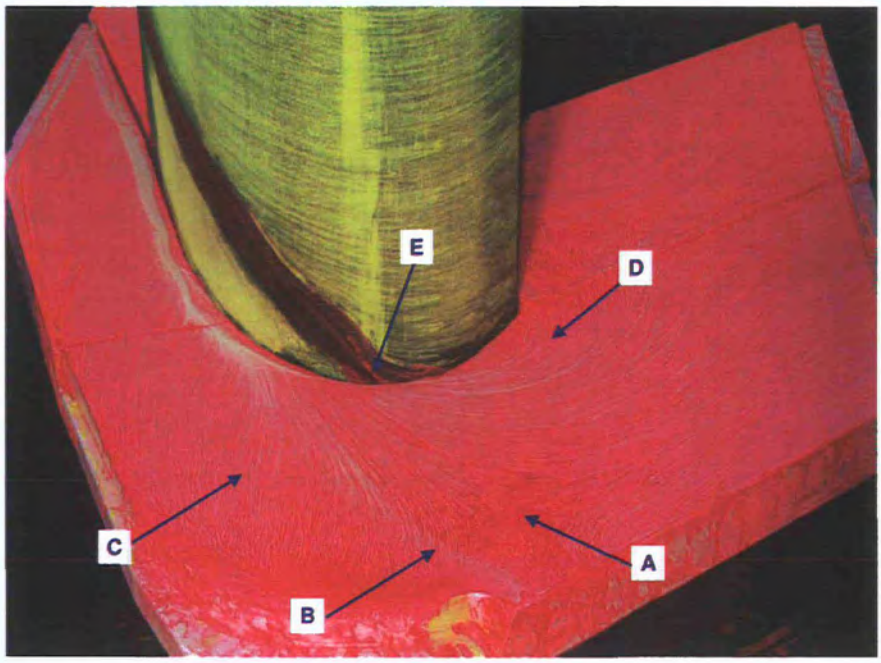

Figure 3.27: Typical Flow Visualisation

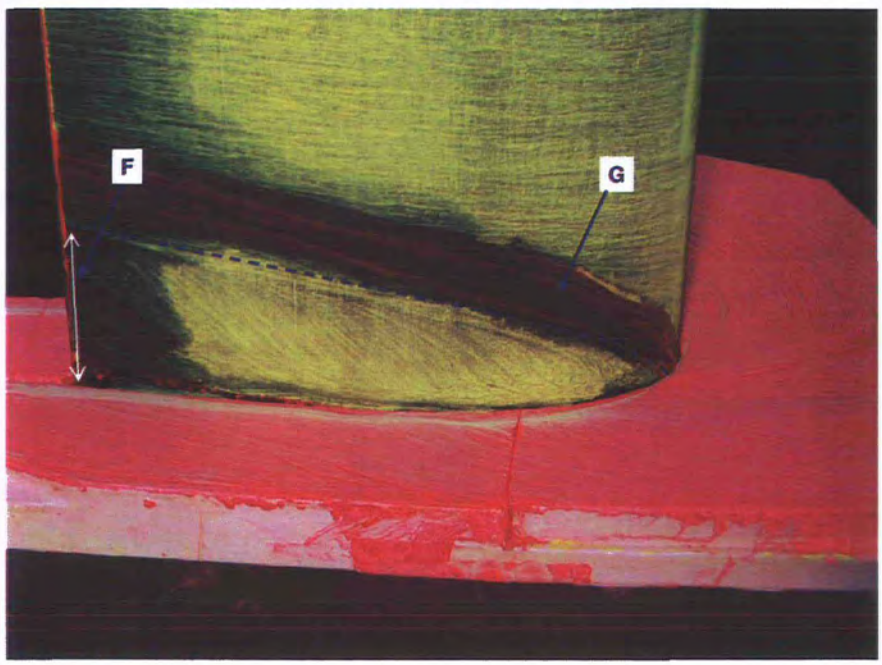

Figure 3.28: Typical Flow Visualisation

D points to the suction side leg of the horseshoe vortex. This leg is also drawn toward the suction surface by the cross passage pressure gradient. At point 'E' the SS leg interacts with the suction surface itself.

The progression of the secondary flow features on the suction surface is shown in Figure 3.28. The passage vortex interacts with the suction surface, the radial extent of this interaction can be approximated by the height at the trailing edge, here shown as measurement 'F'. Fluid drawn onto the suction surface by the SS leg of HSV can be seen above the PV at point 'G'.

3.9 Static pressures

Surface static pressure measurements are used in this work to determine the loading distribution on the different blade shapes and also the impact of the various endwall designs.

The aerofoil surfaces are built with pneumatically sealed channels below the surface, running from endwall to endwall and maintaining a constant percentage of axial chord. Surface tappings are drilled into the sub-surface channels at the necessary radial heights. The endwall surfaces are typically tapped with small diameter stainless steel tubing over a uniform grid.

The pressures are measured by connection to a multitube manometer. The manometer height readings are normalised by readings from the pitot probe and provide static pressure coefficients (C_p), as defined in Equation 3.2.

To measure the aerofoil surface pressure distribution at a specific radial height, all other radial tappings must be covered. This is achieved with good quality sticky tape pressed firmly on a clean and oil-free aerofoil.

3.10 New cascade performance

The asymmetry in the cascade flows has already been detailed. The plot of total pressure loss for the old cascade (Figure 3.29), illustrates the asymmetry in the magnitude of the passage vortex cores. For the new cascade this difference has been eliminated by the inlet flow conditioning and the new method of downstream probe access. The good periodicity in Figure 3.30 shows this.

The change in aspect ratio of the blades from 1.79 for the old cascade, to 1.67 for the new cascade, pushes the vortical structures closer together. The vortices and loss cores nevertheless remain separate and the two dimensional nature of the midspan flow is maintained.

3.11 Aerofoil manufacturing

This section covers the various manufacturing methods and resulting component quality of the different stages of the aerofoil design.

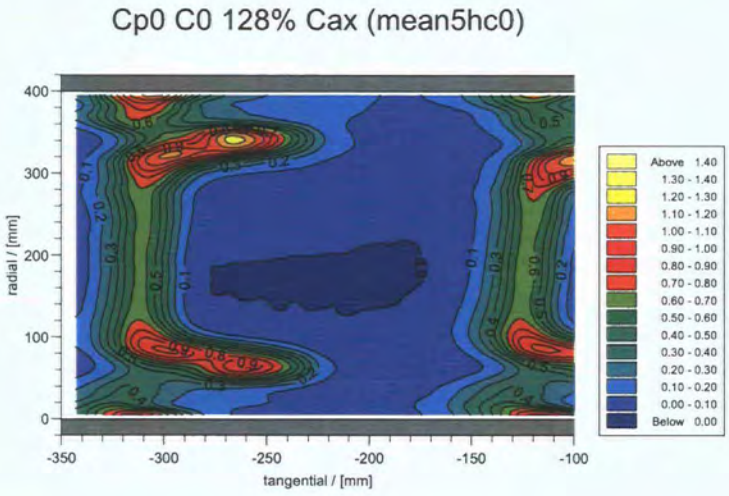

Figure 3.29: Typical Total Pressure Loss - Old Cascade

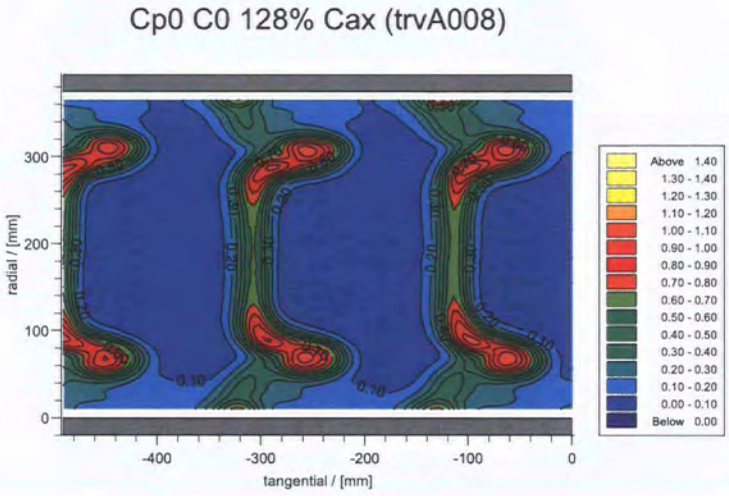

Figure 3.30: Typical Total Pressure Loss - New Cascade

Machine	Mitutoyo Euro-C-A544
Head	Renishaw PH10T
Probe	Ruby Stylus (0.1 N)
Software	WinCMM

Table 3.4: Coordinate Measuring Machine

The definition of the wetted-surfaces was typically exported from the turbine design system as a series of IGES surfaces. To obtain the necessary computer-aided-design (CAD) models for manufacture, the aerofoil and endwall surfaces were imported into the CAD software package Solidworks. The surfaces were converted into solids and the endwall extents and split line specified. The definition of complex internal pressure tapping channels was simplified by the use of these solid models. The models were provided for the geometrical specification of manufacture to external suppliers.

3.11.1 Techniques Used

The component manufacturing techniques changed for each aerofoil design. For cost reasons, where possible, components were manufactured using cast polycarbonate. For more complex manufacture, including pressure tapped geometries, rapid prototyping techniques, including stereolithography (STL) and selective laser sintering (SLS) were utilised.

The majority of the manufacturing was undertaken outside of the University, due to the techniques involved. The details of the manufacturing techniques used for the C-series geometries are contained within Appendix A.

The C1 geometry used STL and polcarbonate casting. C0a and C2 were constructed from CNC machined model board and the C3 geometry used the SLS technique.

3.11.2 Manufacturing Errors

A visual inspection of some of the incoming components, indicated distortion at the trailing edge. To alleviate concerns about the level of these distortions, the blade dimensions were checked against the given geometry using a coordinate measuring machine.

Surface Coordinate Measurement - C0a

The coordinate measuring machine (CMM), described in Table 3.4, was used to determine the extent of the distortions in the blade castings. To do this, each individual blade was located on a steel bed with the suction surface facing upwards. The cartridge was aligned with two stops and clamped down by its endwall edges. The suction surface of each blade was measured in two halves (upper and lower) at a total of 30 radial locations. The measurement path that the CMM takes is indicated in Figure 3.31. The measurement results of the C0a geometry are presented in Figure 3.32 with the distortion at the trailing edge enlarged in Figure 3.33.

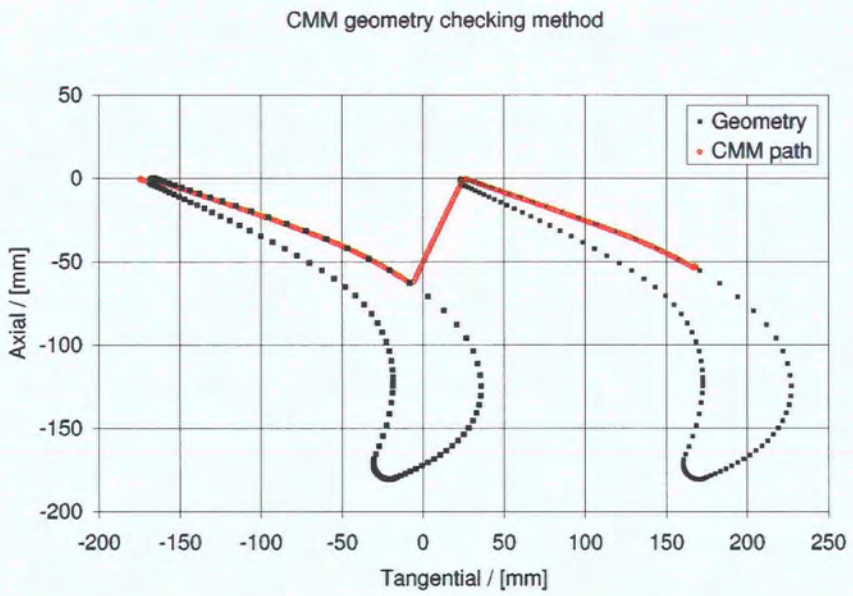

Figure 3.31: CMM Surface Measurement Path

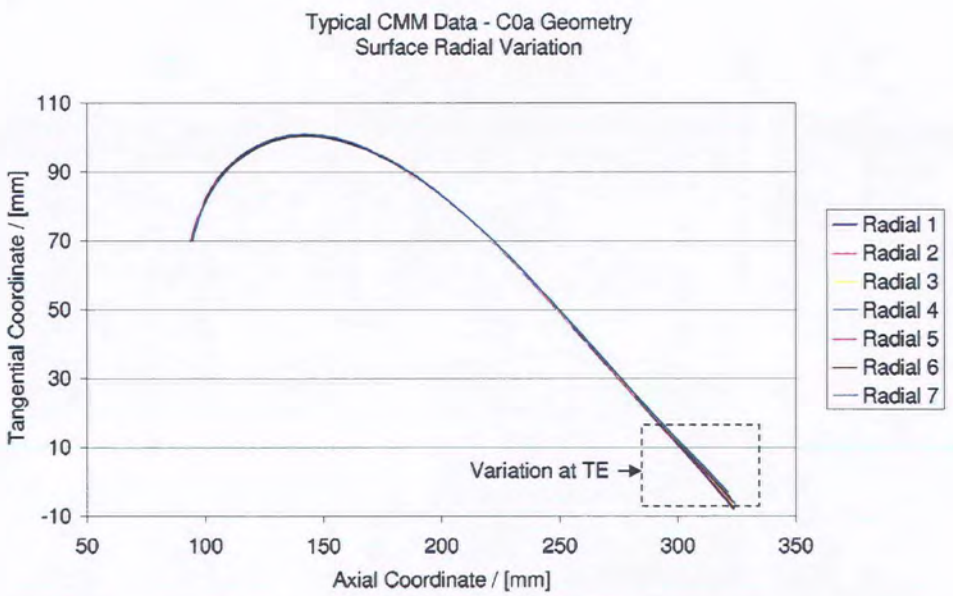

Figure 3.32: Typical CMM - Full SS Measurement

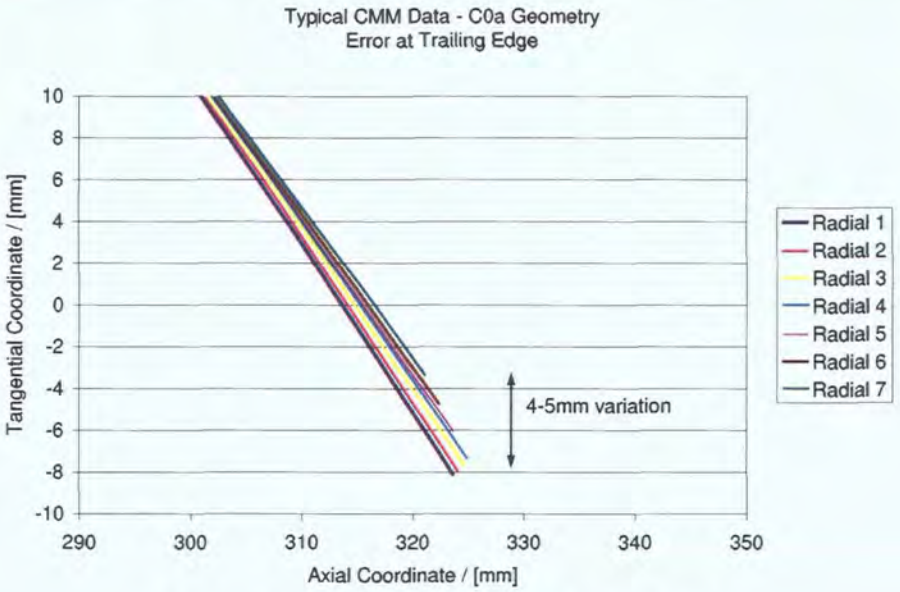

Figure 3.33: Typical CMM - Error at TE

Blade	LH Deviation / [deg]	RH Deviation / [deg]
1	0.02	0.59
2	0.53	0.56
3	0.64	0.33
4	0.90	0.30
5	0.40	0.11
6	0.47	0.63
Tapped	0.02	0.11

Table 3.5: Exit Angle Deviation - CMM results

These results were used to calculate the level of casting distortion as an exit flow angle. The exit angle (α) was determined using a known pitch (s) value and calculating the throat (o) value from the CMM data, where $\alpha = \arccos \frac{o}{s}$.

Deviations in the angle were calculated as a difference to the midspan value. These deviations are shown in Table 3.5 for the physical limits of measurement of the aerofoil surface. The deviation from midspan at the left hand end is labelled LH and at the right hand end is labelled RH. Where an aerofoil exceeded a reasonable level of deviation (greater than 0.6^o) it was returned to the supplier. The remaining aerofoils were ordered in the cascade to ensure those with the greatest geometric accuracy were placed at the centre (the region to be traversed).

The problems encountered with the C0a geometry, were limited to those parts created in a casting process. The endwalls were machined using CNC processes and had no observable errors. In addition, the tapped geometry made by STL process has no observable distortion.

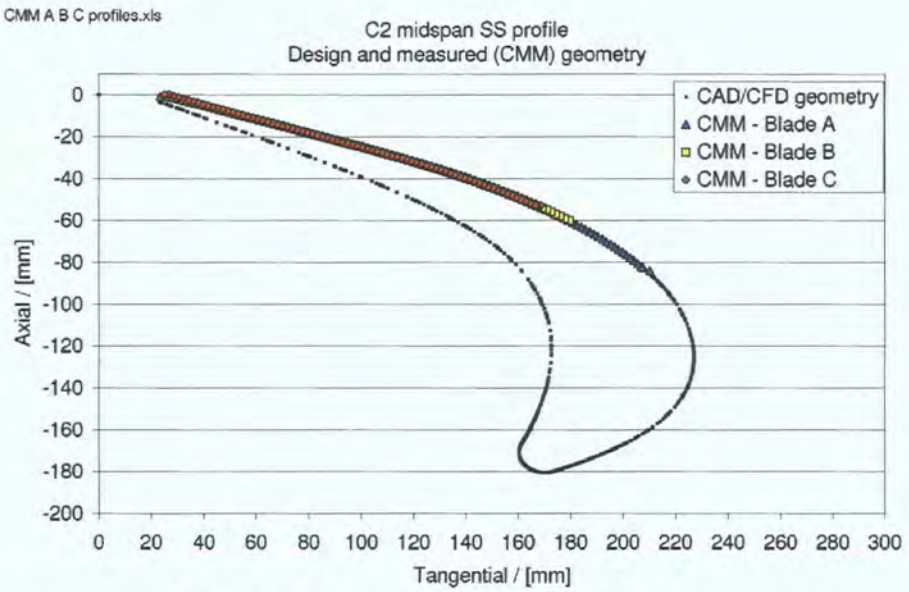

Figure 3.34: CMM Suction Surface Measurement Results

Surface Coordinate Measurement - C2

For the C2 geometry, there was no observable trailing edge distortion. Here the use of CMM was purely to ensure that the camber angle of the aerofoils was set correctly during manufacture. The results of the C2 suction surface measurement, are presented in Figure 3.34. The trailing edge region is shown at a large scale in Figure 3.35, where a ± 0.5mm error can be seen. In general, the results show the CMM data overlaying the CAD data, providing confidence in the manufactured geometry. The minor differences in trailing edge location were not considered to be significant.

3.12 Software

A comprehensive description of the logging and post-processing software was given by Ingram (2003) and is summarised by Ingram and Gregory-Smith (2006). No significant developments have taken place since this and thus only a brief description of each component will be given here.

3.12.1 Traversing software

The traversing software is used to control a pulse stream (TTL) output from the digital I/O portion of the PC logging card. This pulse stream is used to drive the stepper motors and alter the traverse slide location. The program contains ramped acceleration and deceleration curves to avoid stepper motor slip. The probe locations are read from a grid file, and measurements are taken at each predefined position.

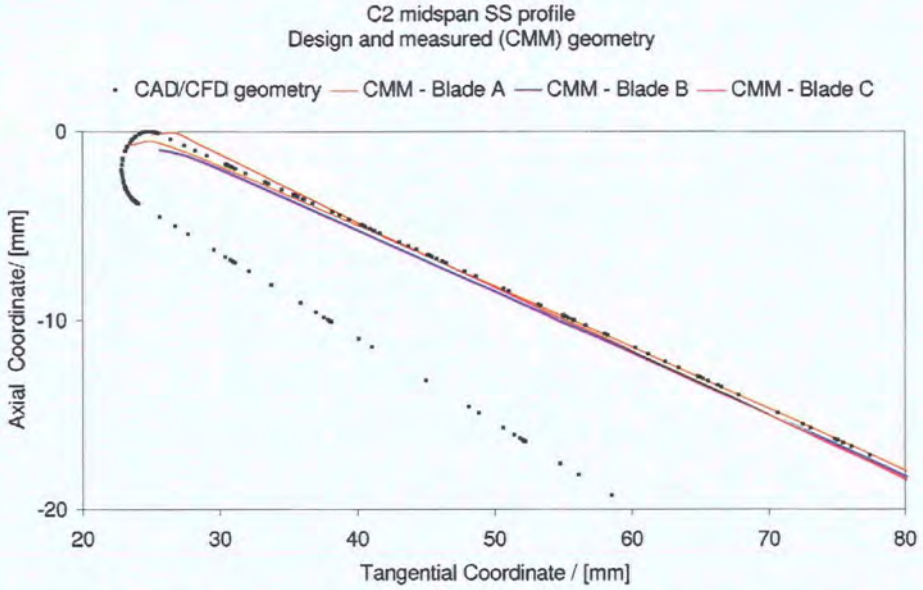

Figure 3.35: CMM Suction Surface Measurement Results - Large Scale

3.12.2 Measurement software

The measurement software reads the voltage outputs from the pressure transducers. Time averaged values of the raw data are checked using a confidence test defined by Biesinger (1993). If the confidence test fails the process is repeated, until the spread of data is within bounds. This data is stored as voltages for post-processing.

3.12.3 Post-processing software

The post-processing software is used after a complete traverse has been taken. For each measurement point the voltages are converted into pressures. These probe head pressures provide coefficients at the probe head, which are checked against the calibration map and combined with turret yaw angle, to provide real flow data (pitch angle, yaw angle, total and static pressure). The secondary kinetic energy, vorticity and loss are determined from these values.

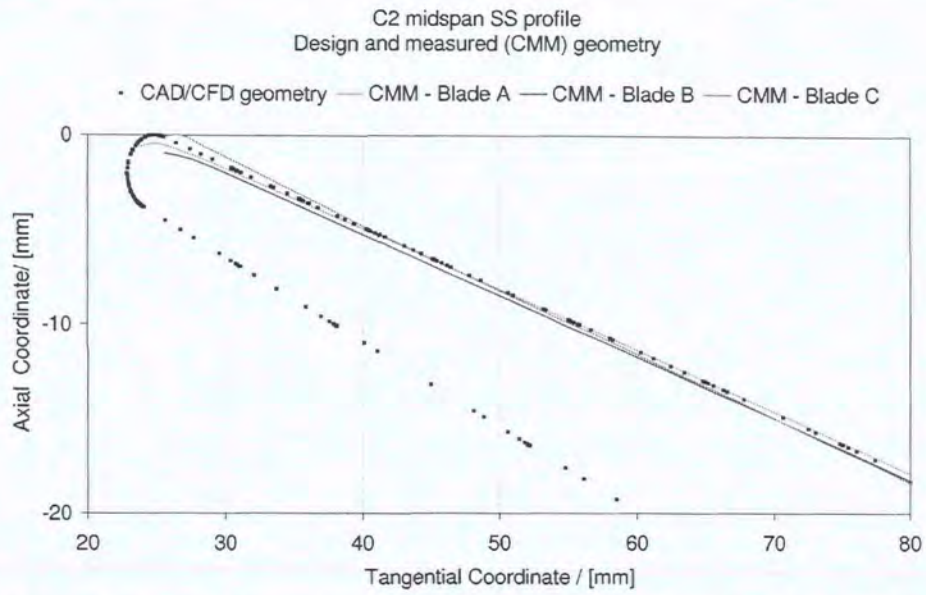

Figure 3.35: CMM Suction Surface Measurement Results - Large Scale

3.12.2 Measurement software

The measurement software reads the voltage outputs from the pressure transducers. Time averaged values of the raw data are checked using a confidence test defined by Biesinger (1993). If the confidence test fails the process is repeated, until the spread of data is within bounds. This data is stored as voltages for post-processing.

3.12.3 Post-processing software

The post-processing software is used after a complete traverse has been taken. For each measurement point the voltages are converted into pressures. These probe head pressures provide coefficients at the probe head, which are checked against the calibration map and combined with turret yaw angle, to provide real flow data (pitch angle, yaw angle, total and static pressure). The secondary kinetic energy, vorticity and loss are determined from these values.

Chapter 4

Computational Setup

THIS chapter briefly describes the design processes involved in reaching a passage shaped geometry, including the use of throughflow calculations and aerofoil section stacking software. The descriptions are brief, with the aim of alerting the reader to the range of processes involved. The design processes seem (to the author) to be consistent across turbomachinery industries.

The chapter also describes the setup of the computational models used in the work. It includes a description of the Navier-Stokes solver used, the boundary conditions that were set, the turbulence modelling parameters and convergence criteria.

4.1 Design processes

The flow of data and the design steps involved in the development of the C-series aerofoils, are highlighted by the flow chart in Figure 4.1.

The design process may be split into a manual aerofoil design section and an automated endwall design section. The manual process takes the design from initial concept, including massflow and turning required, through individual radial section design and section stacking, to a complete aerofoil. The endwall design process is automated, but relies upon a designer's choice of constraint and perturbation location.

The choice of passage massflow, overall turning and inlet angle are specified. For the Durham Cascade this matches previous definitions, enabling some comparison and continuity of the design concepts.

4.1.1 Throughflow

A two dimensional specification of the channel (the S2 plane) is fed into the throughflow calculation. For the cascade this is a constant annular geometry with no change in radius. Modifications are made to the inlet and exit conditions, using data taken from recent experimental measurements at -100% C_{ax} (one axial chord upstream) and at 128% C_{ax} (downstream).

The throughflow calculation works on a series of streamlines and performs a streamline curvature calculation. The geometry of the resulting streamlines (axial - radial planes) is used to intersect the existing datum aerofoil geometry and provide

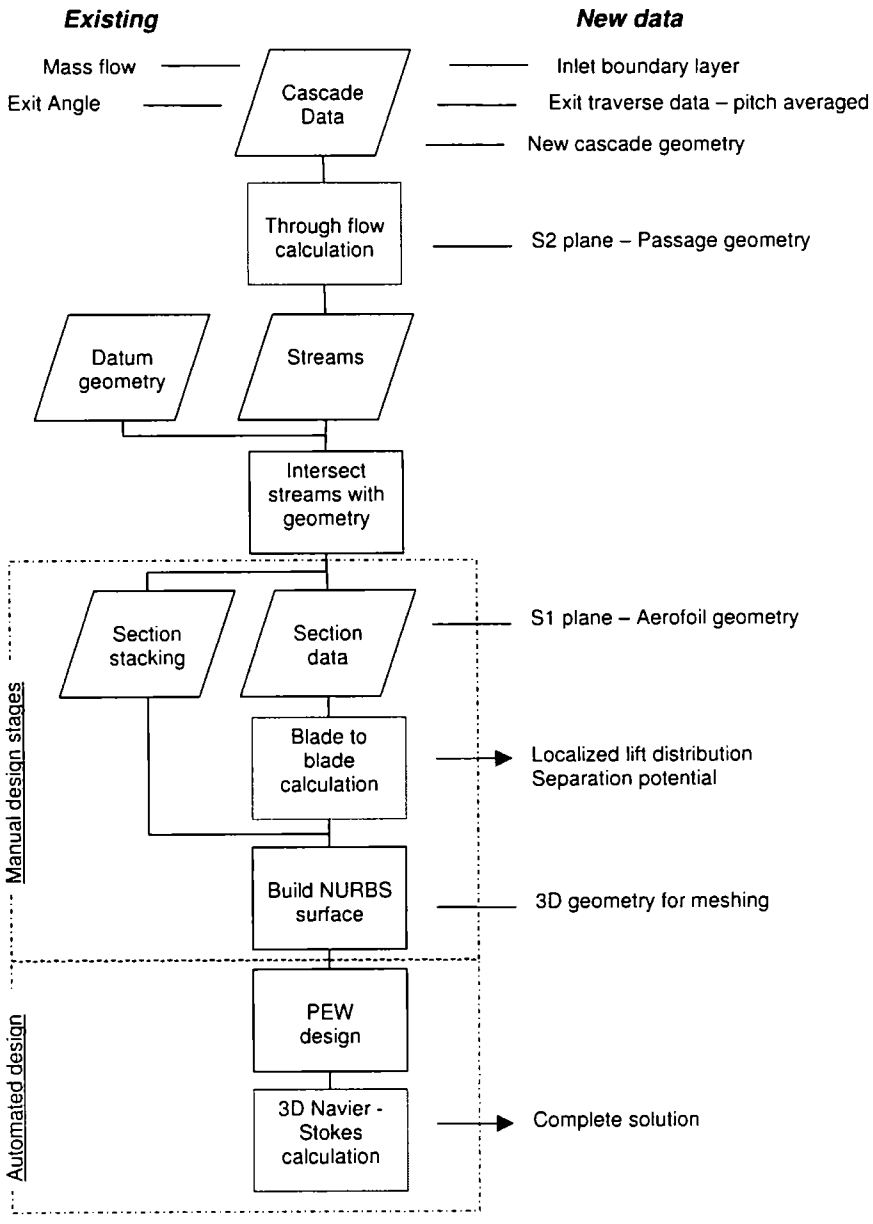

Figure 4.1: Passage design processes and flow of data

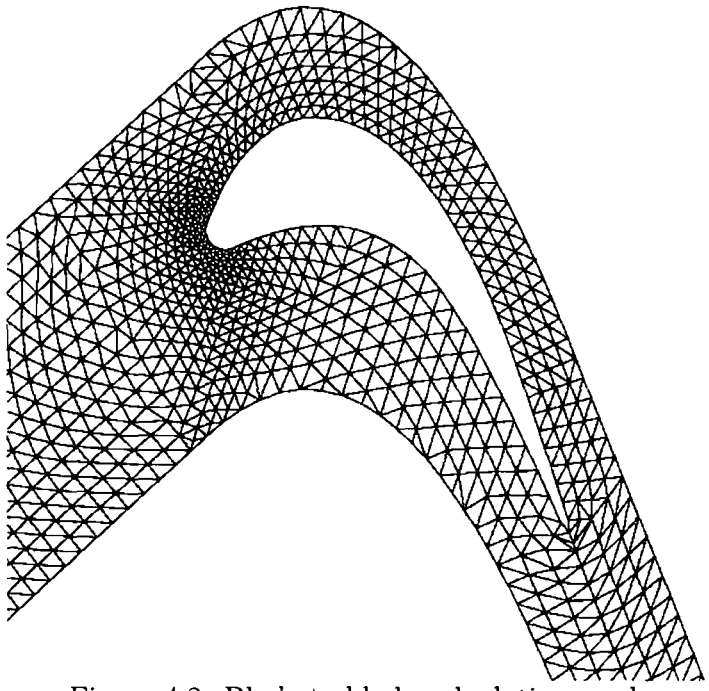

Figure 4.2: Blade to blade calculation mesh

a two dimensional (S1 plane) aerofoil definition. This 2D section is analysed using the blade-to-blade solver and forms the basis for geometric changes to the aerofoil.

The solver uses empirical representations of loss and existing geometrical information to provide basic detail of the expected aerofoil performance. The inlet and exit conditions of the throughflow provide the boundary condition specifications for the Navier-Stokes solver.

4.1.2 Blade-to-Blade

From the intersected streamline sections an aerofoil is defined. These sections may be manually modified to alter the loading distribution, depending on the design intent.

For each defined section, a blade-to-blade calculation is performed, using an Euler based solver. A typical mesh for this calculation is provided in Figure 4.2. Calculations on the S1 plane provide the local loading distribution, which is important when checking for potential boundary layer separation from the aerofoil.

4.1.3 Section stacking

The S1 plane sections are stacked on lines defined along the trailing edge, leading edge, or blade centroid. The stacking of the profiles provides a simple method of displacing the individual sections, axially and tangentially, to create straight or compound leaned geometries.

Stacking line shapes are typically mathematically based curves which avoid sudden changes in curvature and can be elliptical, circular-arc or power-law based.

A B-Spline (NURBS) surface is fitted to the stacked 2D sections, thereby defining the entire wetted area. The final 3D surface is then checked for interpolation anomalies caused by the B-Spline fitting. If problems are found they are typically resolved by the addition of intermediate 2D sections to give greater shape control.

During stacking of the sections, the static pressures from the blade-to-blade calculation are used to ensure a smooth transition of load. Additional radial sections at may be defined and altered to improve this radial distribution.

4.1.4 PEW design process

The non-axisymmetric profiled endwall is designed using a process similar to that described by Harvey et al. (1999). The FAITH design system described by Shahpar and Lapworth (1998) was used in the setup of the automated optimisation. The system enables the definition of perturbation stations, design constraints and optimisation targets. More detail on the design of profiled endwalls is presented in Chapter 7

4.2 Navier-Stokes Solver

The 3D Navier Stokes computations used a steady flow code based on the Moore Elliptical Flow Program (MEFP). The structured grid solver is described by its authors in Northall et al. (1987). The continued updating and relevance of the solver is evident in the papers of Northall (2006) and Shahpar (2001).

The solver uses the pressure correction method of Moore (1985). Harvey and Ramsden (2000) state that the code is good at estimating aerodynamic losses, because of the low level of numerical mixing. However, the key reason for the use of this solver in this work is because it was the only available solver that could handle the non-axisymmetric profiled endwalls.

The VKI lectures of Gregory-Smith (1997) describe in considerable detail the impact of the differences in computational modelling (turbulence model, wall functions), on the accuracy in the prediction of secondary flows and loss. The work originated in the ERCOFTAC seminar series and was organised by the same author. The test case for this computational work is the Durham Cascade prismatic geometry. The key outcomes are of clear interest for this work. These were:

- The numerous modelling techniques provided significant variation in the prediction of secondary flows and losses
- The position (tangential, radial) of the passage vortex was affected by the choice of turbulence model
- The MEFP based solver using the mixing length model provided the closest experimental match, in terms of PV position, C_{SKE}, and loss magnitudes
- The tuning of this model, by forcing transition close to the experimentally measured value provided even closer midspan loss prediction.

Region	Resolution
I	105
I-LE	25
I-TE	77
J	45
J-BladeSurface	16
J-BladeSurface	30
K	80

Table 4.1: Navier-Stokes Solver Mesh Statistics

- The position of the PV is linked to its strength, which is underpredicted by most modelling techniques

The results of the ERCOFTAC studies confirm MEFP as the most appropriate solver. For the computational modelling presented in this thesis the solver was used in a simple manner. The investigations focussed on one or two key measurement planes, at the exit of the computational domain and at 128% C_{ax}.

The computational domain starts one (midspan) axial chord upstream of the leading edge and ends approximately 78% C_{ax} downstream of the trailing edge. The passage geometry was modelled using an H-grid topology. Examples of the mesh resolution of the leading and trailing edges can be found in Figures 4.3 to 4.6. The mesh contained approximately 378,000 cells - considered low by most modern standards - but was retained because of the need to calculate a considerable number of endwall perturbations. The mesh was generated using the turbine design system within Rolls-Royce. The mesh control parameters were selected on advice by the turbine design team within Rolls-Royce. The detail of the mesh resolution is given in Table 4.1. For each design perturbation the same grid variables were used, with the meshes fitting to the leaned and stretched geometries.

The calculations were initially run on a network of Sun Blade machines, but later migrated to a new Linux compute cluster.

4.2.1 Convergence check

The plot in Figure 4.7 shows a typical convergence behaviour for the MEFP based solver. The figure indicates that the domain reaches convergence after 100 to 120 iterations. This typical time was used in the automated PEW design process, as a minimum solution time for each endwall perturbation. Confidence in this convergence time is given by Harvey et al. (1999), where typically 150 iterations were required for convergence using the same solver.

4.2.2 Boundary conditions

The computational models are run at the standard day operating condition, as described in Table 3.1 in Chapter 3. An initial throughflow computation was run to provide the inlet and exit conditions of the full three dimensional calculation. The calculation uses experimental inlet boundary layer (total pressure and yaw

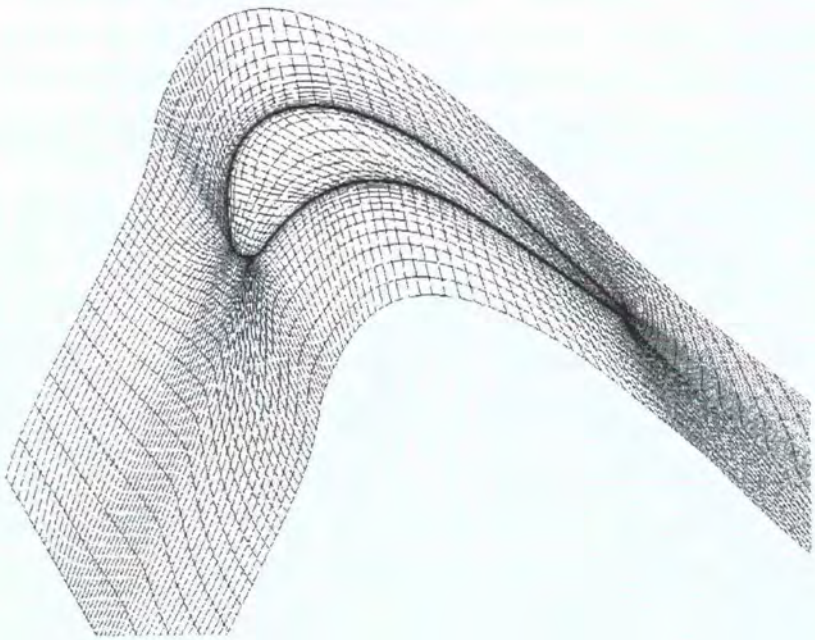

Figure 4.3: Mesh Pitchwise Resolution

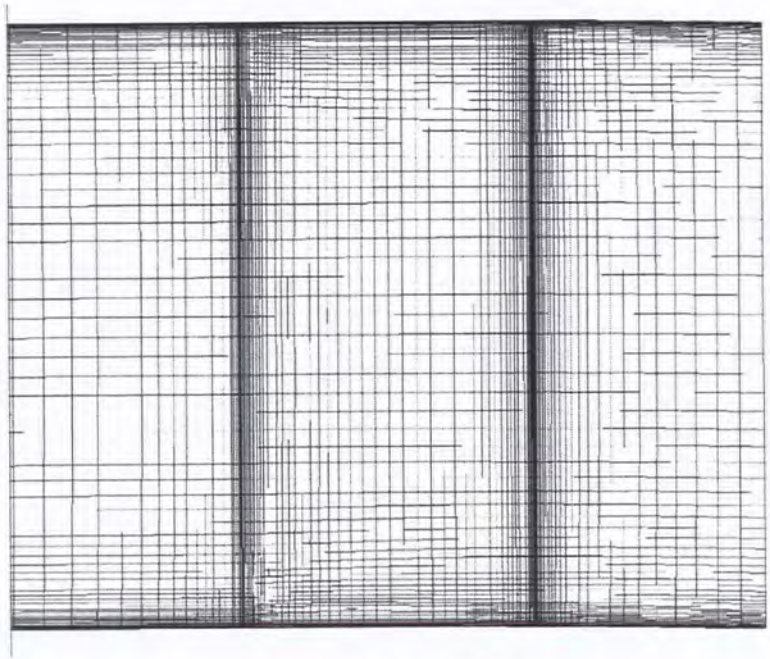

Figure 4.4: Mesh Radial Resolution

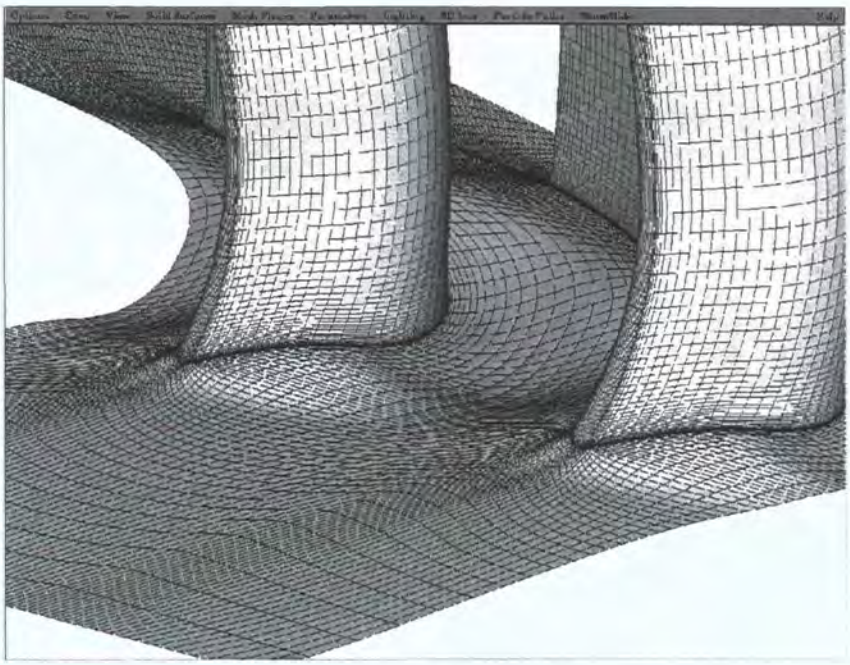

Figure 4.5: Isometric View - C2 Lower Endwall

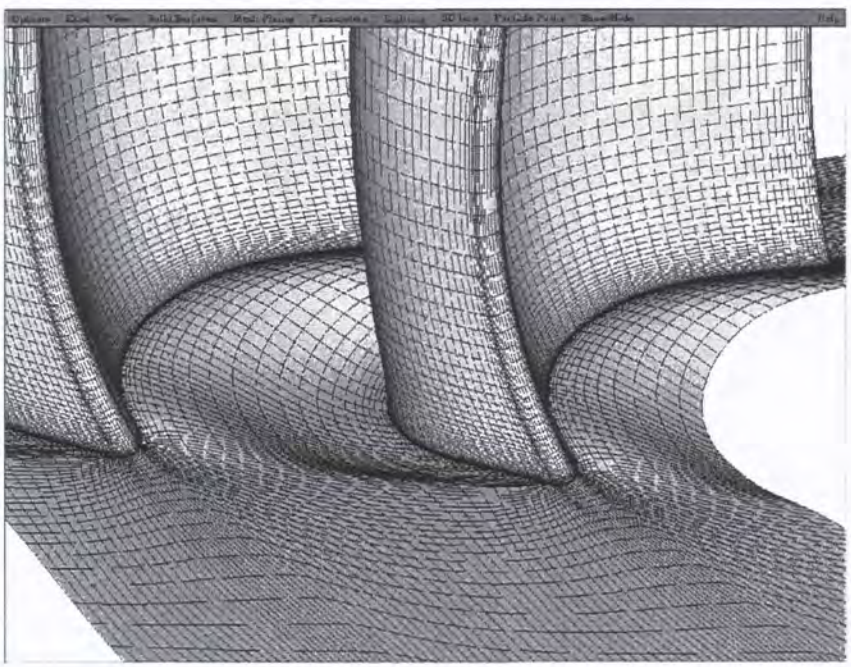

Figure 4.6: Isometric View - C2 Upper Endwall

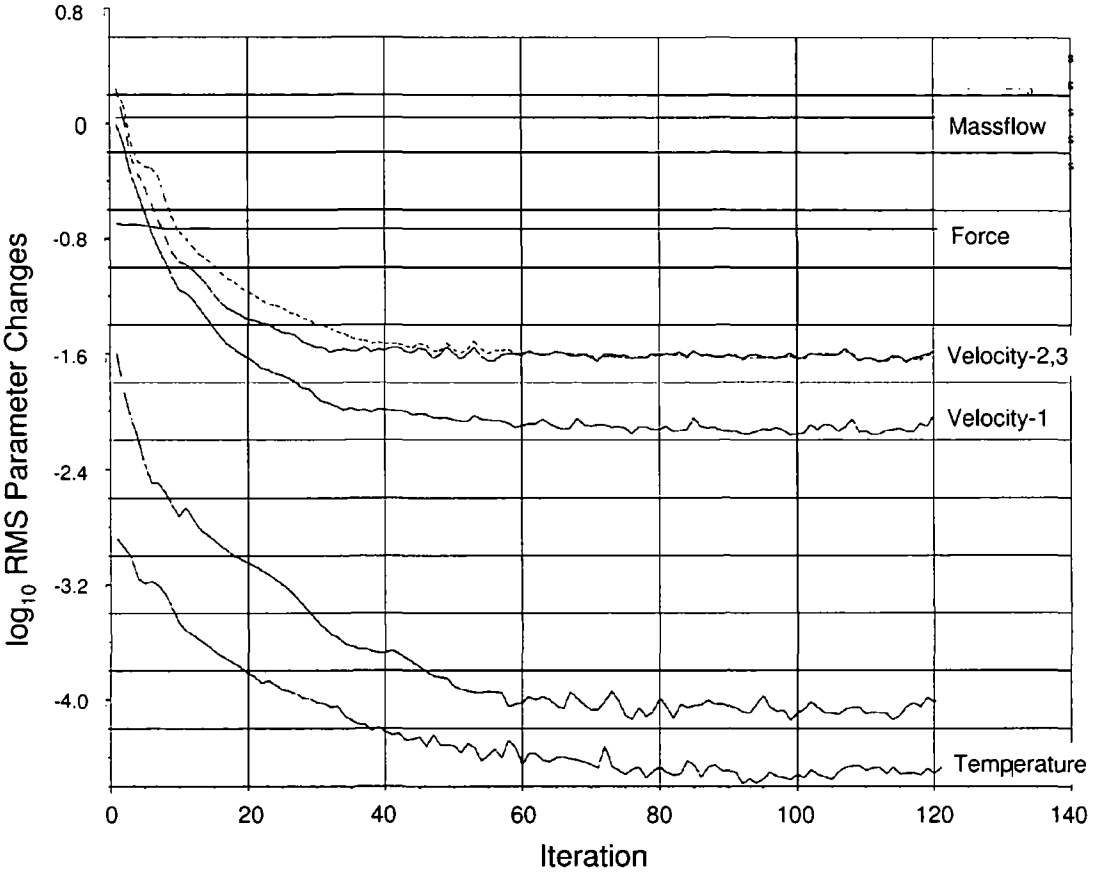

Figure 4.7: Typical Convergence of MEFP based solver

angle) distributions to define the inlet flow field. These values are based on results taken with a 3-hole pressure probe, 100% C_{ax} upstream of the leading edge of the cascade geometry (see Figure 3.6 from Chapter 3). The exit static pressure was taken from the mean value of a previous 5-hole probe traverse on the cascade itself and is pitchwise varying. The inlet total temperature was set to the standard day condition described in the previous chapter. The endwalls and aerofoil surfaces were defined as no-slip.

4.2.3 Turbulence modelling

An algebraic mixing length model is used throughout the work, this is based on Prandtls. Wall functions are used to avoid the need to resolve the boundary layer and according to Harvey et al. (1999) are "valid for y+ values up to 100 and above". An inlet turbulence intensity (Tu) of 1% was specified. Because of an oversight, the computational level of turbulence does not reflect the conditions of the cascade, where the turbulence level is 4%. It was decided however, that for a purely computational study, the absolute level of turbulence will not affect the design outcome. This reduction in the freestream turbulence may decrease the rate of mixing of loss and increase the strength of the vortex cores.

By keeping the boundary layers fully turbulent, the benefits gained in the study are more applicable to the engine environment. The suction surface boundary layer of the Durham Cascade geometry is known to be transitional. Previous authors have investigated the tuning of the Navier-Stokes solver to more accurately model the real cascade transitional behaviour. The tuning forces the boundary layer state to be either fully turbulent or laminar on sections of the endwall and suction surface. This tuning would necessarily be a result of experimental measurement of the boundary layer state for a particular geometry.

This tuning was not undertaken for the current series of results because the changes in blade loading, brought about by the tangential lean, cannot be predicted without prior knowledge of the experimental flow field. This tuning could force the transition unrealistically and ultimately alter the choice of geometry.

4.3 Processing CFD results

To enable direct comparisons between the computational and the experimental results, the same processing techniques were applied to both types of data and the same programs were used to produce the majority of the plots in this thesis.

The process is as follows:

- The computational solution is read into a commercial CFD post processing tool (Fieldview)
- Point probe data is extracted, using this tool, for the measurement planes of interest. The probe point locations are exactly the same as the traverse measurement points

- The point probe data is saved in an experimental data format and processed using the same software as mentioned in Chapter 3 and described by Ingram and Gregory-Smith (2006)

As a result of this technique the pitch and mass averaged computational results can be directly compared with the experimental data. Where possible the contour plots and velocity vectors use the same scales and range to simplify the comparison.

Where multiple computational datasets (design concepts) are compared as part of the design process, the results were not processed using the experimental post-processing tools as described above. Instead, the in-built post-processing capabilities of the (Rolls-Royce) proprietary software were utilised. Here the mass averaging and pitch averaging is done at a specific grid (I) plane. All grid points on the chosen I-plane are used in the averaging.

At the I-plane relating to the exit of the computational domain (178% C_{ax}), the points are all at the same axial location. At the plane relating to 128% C_{ax}, some distortion of the grid is present and not all points are at the same axial location.

4.4 Conclusions

Overall, the computations presented in this work were undertaken on relatively coarse grids with approximately 400,000 cells. These resolutions compare poorly with research based CFD. However, the desire to use a realistic component design process and the considerable number of endwall design perturbations calculated, means that large mesh sizes would not be feasible.

The work of Gregory-Smith (1997) indicated that, the MEFP based solver with mixing length model and wall functions provided a reasonable match with the experiment. For this reason and other practical considerations this solver was chosen.

Chapter 5

PEW review

THIS chapter reviews the current status of non-axisymmetric profiled endwall (PEW) design within the Durham Cascade. The chapter describes the behaviours and performance of the endwall shapes. Pitchwise averaged loss, yaw angle and SKEH results are compared for three pre-existing endwall designs and one new design.

5.1 Disclaimer

It should be noted that the experimental results presented here are the work of a number of authors. The work on geometries P1 to P3 was not undertaken by this author, but is presented here to show the development of PEW design and put the P4 geometry (this author's work) in context. A thorough reassessment of geometries P1 to P3 was undertaken by Ingram (2003) and the reader is strongly recommended to review this work for a more in depth analysis of the behaviour of PEWs.

Whilst the majority of the results have already been published, the parameter SKEH was not previously included and is shown here for the first time. Again, the traverse data of Ingram (2003) is the basis for this additional analysis.

5.2 Design philosophy

The original investigations of non-axisymmetric profiled endwalls were undertaken by Rose (1994). Rose designed the PEWs for the reduction of the static pressure variation at the blade platform edge, in order to control the rim seal leakage. This design was successful in controlling the local static pressures, but resulted in an overall increase in total pressure loss.

Endwall profiling was subsequently used for the control of static pressure within the blade passage itself. To this end a series of endwall designs (P1 to P3) were modelled computationally and experimentally tested. The designs reduce the cross passage pressure gradient at the endwall, with the aim of reducing the magnitude of the passage vortex and its associated losses.

Hartland (2001) and Jayaraman (2000) experimentally investigated the P1 and P2 geometries in the Durham cascade. Ingram (2003) reassessed the P1 to P2 ge-

ometries and analysed a new geometry, P3. In this work, a further endwall geometry (P4) is investigated.

In all of these P-series endwalls, the static pressure is raised close to the suction surface by decelerating and diffusing the flow into a dipped region. The pressure is dropped close to the pressure surface by a hump, which accelerates the flow.

For the P1 geometry a secondary hump/dip arrangement existed downstream with the key aim of reducing the overturning in the yaw angle. This secondary hump and dip were the opposite orientation of the primary profiling.

5.3 Geometries

The height contours for endwalls P1 to P4 are detailed in Figures 5.3 to 5.6. The plots show the heights using 1mm contour spacing. The hump and dip regions are indicated by the arrows on the plots; the minima and maxima are also labelled.

Figure 5.3 shows the height contours for design P1. The profiling, in the early part of the passage, consists of a hump (positive profiling) close to the pressure surface and a dip close to the suction surface. In the later part of the passage (from 70% C_{ax}) there is an opposite arrangement of features, with a dip close to the PS and hump close to SS. The shapes extend to -50% C_{ax} upstream and return to a zero height (planar) position by 70% C_{ax}, (i.e. within the passage). The downstream shapes run from this position to 170% C_{ax}. The upstream profiling was primarily used for the reduction in cross passage pressure gradient and passage vortex strength. The downstream profiling was used to reduce the overturning on the endwall, with the design requirements at the time focussing on a minimum of exit angle deviation. The result of this secondary profiling can be seen in the exit yaw angle in Figure 5.12. The large extent of the profiling was due to a limitation of the endwall design system, which required the perturbation to exist over the entire computational domain. The large axial extent means that it is not practical for an engine. A modification of this design led to the P2 design.

Figure 5.4 shows the height contours for design P2. The profiling here is different to P1 in two respects. Firstly, it is restricted to within the blade extent, i.e. between the leading edge (LE) and trailing edge (TE). Secondly, there is a single feature - the profiling is not split into two components. The profiling extends from the leading edge (0% C_{ax}) to 70% C_{ax}. The P2 design was considered a success but further benefit was sought in the next iteration, thus the next design (P3) had greater first harmonic amplitude.

Figure 5.5 shows the height contours for design P3. Here the profiling is more complex. The same hump/dip arrangement in the early part of the passage remains, but there is also a secondary profiling downstream. The downstream profiling is different to the P1 design, as it follows the same alignment as the upstream one. The two humps combine at 70% C_{ax} to form a double peaked ridge that runs beyond the trailing edge to 150% C_{ax}. Similarly, the two dips combine to form an extended trough.

Figure 5.6 shows the height contours for design P4. The P4 design is identical to P3 everywhere except for the tangential position of the upstream hump and dip. The sinusoid associated with these features has a phase shift. This was done to

bring the dip minimum further away from the suction surface.

The details of the endwall height maxima and minima are contained within Table 5.1, the values indicate another difference between the P1/P2 and P3/P4 designs. The P1 and P2 designs contain a positive zero order harmonic (axisymmetric hump) in addition to the intended first order harmonic. This has resulted in the hump of the sinusoid being larger than the dip. The P3 and P4 designs do not have this zero order component, and the dip is the same size as the hump. The P3 and P4 designs can be considered as more aggressive in their dip magnitude, whilst their hump magnitudes have remained approximately the same. The P1 design had its upstream peaks at 10% to 20% C_{ax}, the P2 design was restricted and its peaks were at 30% to 40% C_{ax}, the peaks for the P3/P4 designs were shifted further within the passage to 50% C_{ax}.

The use of the discrete features in the early endwall designs, reflects the state of the endwall design system used at that time.

Observation of the P-series geometries highlights some common themes in their design: The hump and the dip are aligned such that they both occur at the same axial location. The limitations of using a first-harmonic design are apparent in the P3 and P4 endwalls, where the hump and dip are always the same magnitude. This was not so in the P1 and P2 geometries however.

5.4 Results and Analysis

A short analysis of the effects of the endwall designs (P1 to P3) is provided through a review of the pressure probe traverses taken by Ingram (2003). An additional comparison with latest endwall design P4 is also provided.

The majority of the results have been presented by Ingram (2003) already. However, some additional analysis has been made using the parameter SKE.H, since its publication by Brennan et al. (2001). Area contour and velocity vector plots for the traverse data were previously published and will not be covered here.

5.4.1 Endwall static pressure

Figures 5.7 to 5.10 detail the experimental static pressure distribution on the endwall, taken through an array of tappings covering the endwall surface and represented as a coefficient (C_p). The measurements are shown as area plots covering two blade pitches. The measurements for geometries P0 to P2 were taken by Hartland

	Primary	Primary	Secondary	Secondary
Geometry	Hump	Dip	Hump	Dip
P1	23	-11	11	-5
P2	21	-10		
P3	19	-19	19	-19
P4	19	-19	19	-19

Table 5.1: Endwall Height Extremes [mm]

(2001) and Jayaraman (2000), the measurements for geometry P3 were taken by this author.

The static pressures on the endwall are dominated by the blade loading distribution. Any effects due to the PEW are small when compared with these large magnitudes. However, it is still possible to observe the effects of PEWs on the cross passage pressure gradient and localised diffusion.

In general, the endwall geometries can be seen to reduce the pressures near the PS. The pressure minima on the SS (loading peaks) can be seen to move forward, toward the leading edge. In the case of P3, two peaks can be seen on the SS. This is an early SS acceleration, diffusion and second reacceleration.

5.4.2 Flow visualisation

Oil and dye surface flow visualisation was undertaken for the P4 geometry and its datum P0. The photographs in Figures 5.1 and 5.2 show the aerofoil suction and endwall surfaces. Red dye was applied to the endwall surfaces, yellow dye was applied to the aerofoil surfaces. The use of two colours aids the analysis of the photographs.

Figure 5.1 shows the typical features of the P0 geometry, as discussed in Chapter 3. The P4 geometry in Figure 5.2, shows an additional feature on the endwall, close to the suction surface, indicating a sudden change in direction. The feature appears to impinge the suction surface and move radially outward, up the suction surface. The red dye, drawn onto the SS by the feature, gives a clear indication of the radial extent. This feature is similar to that observed by Ingram et al. (2005) for the geometry P3. It is thought that this feature is the result of a comparable three dimensional separation. .

Additionally, the pressure surface leg of the HSV appears to have been enhanced for the P4 geometry.

5.4.3 Pressure probe results

Pitch mass averaged results are presented in Figures 5.11 to 5.14. Total pressure loss is presented in Figure 5.11, yaw angle in Figure 5.12, secondary kinetic energy (C_{SKE}) in Figure 5.13 and SKE.H in Figure 5.14.

Pitchwise Averaged Loss

The pitchwise averaged loss results in Figure 5.11 highlight the significant variation in the effect of PEW application. The endwall profiling appears to affect the loss from 35% span and inwards to the endwall itself. The radial extent of these changes is due to the impact on the passage vortex and not the radial extent of the endwall pressure field. The following key effects can be seen in the total pressure loss plot:

- The P1 and P2 geometries reduce the passage vortex core from a peak of 0.35 to below 0.3
- The P3 and P4 geometries increase the loss in the core to a value above 0.4

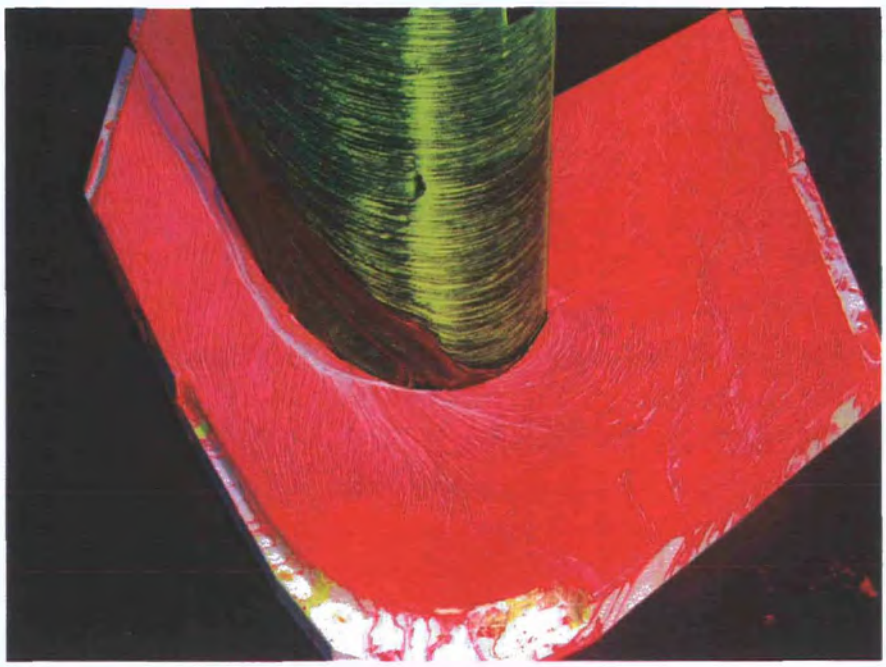

Figure 5.1: Flow Visualisation - P0 Geometry

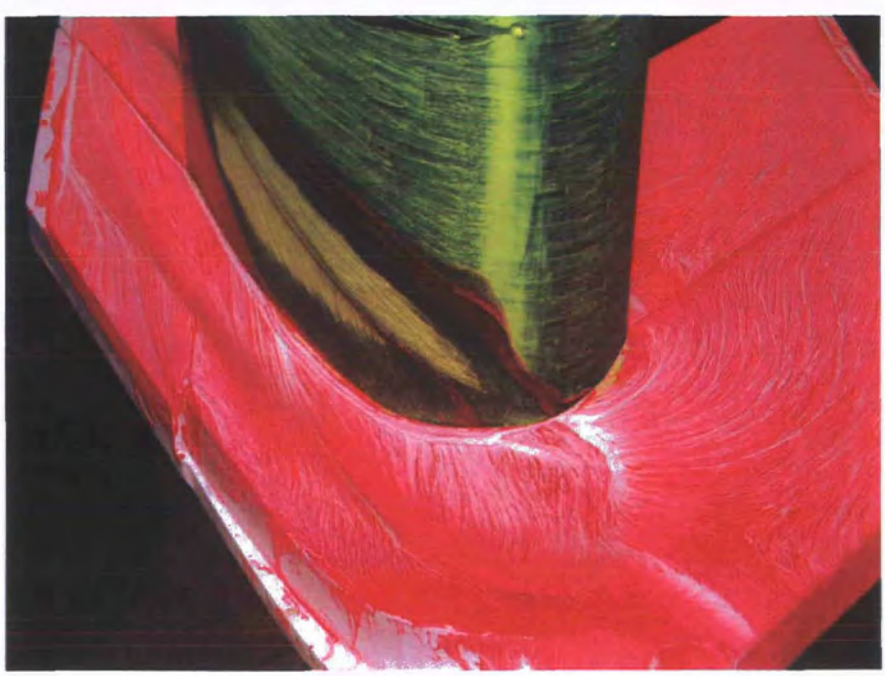

Figure 5.2: Flow Visualisation - P4 Geometry

- All endwall geometries increase the loss between the endwall and the passage vortex core, relating to the range 3% to 10% span
- The P1 geometry has an additional loss region close to the endwall which is not observed in the other results

For all geometries, as the peak loss in the passage vortex is reduced, the position of the peak is shifted radially inwards. The additional loss core in P1 (close to the endwall) reduces its performance and overall the P2 geometry has the most significant loss reduction.

Pitchwise averaged Yaw Angle

In Figure 5.12 the pitchwise averaged yaw angle is seen to vary from 30% span inwards. In general, the endwall profiling reduces the peak underturning and shifts it inwards. The endwall also reduces the level of overturning at 10% to 12% span. Both of these effects are associated with a reduction in the strength of the passage vortex. The key detrimental effect of the profiling is the increased turning close to the endwall.

The Figure illustrates the following effects:

- The P1 and P2 reduce the peak underturning by 2 - 2.5^o and the overturning by 3^o
- P3 and P4 are less effective and reduce underturning by 1.8 - 2^o and overturning by 1^o
- Between 0% and 5% span P2, P3 and P4 all increase overturning by 2^o, 2.5^o and 3^o respectively
- P1 shows no increase in overturning at the wall. This is the effect of the secondary (downstream) profiling region

Pitchwise averaged C_{SKE}

The pitchwise averaged C_{SKE}, shown in Figure 5.13, also varies from 30% span inwards. All endwall designs can be seen to reduce the peak C_{SKE} and, as other parameters have shown, shift the peak radially inwards. The profiling also acts to increase C_{SKE} close to the wall. This apparent increase in secondary flow near the endwall is a result of the accelerated endwall boundary layer. The P1 geometry has high magnitudes here because of the energy in the enlarged corner vortex.

Pitchwise averaged SKE.H

The pitchwise averaged SKE.H, in Figure 5.14, is decreased with the application of PEWs. The extent of the decrease is dependent on the effectiveness of the geometry. SKE.H behaves similarly to C_{SKE}, with the benefit ranking being the same as it. The SKE.H profile consists of a single peak at 15% span and an increase at the endwall. Endwall designs P1 and P2 have similar behaviour for all areas except close to the wall, where for P1 the corner vortex feature is evident. P4 has a similar

secondary flow strength to P0 - indicating that the endwall design has not worked experimentally. P3 is less successful than P1 and P2, but better than the P4 design.

Mass Averaged Loss and SKE.H

The mass averaged total pressure loss and SKE.H are plotted in Figure 5.15 as a percentage change from the datum (P0) result. Here the effect of the four PEW designs is most striking. The image shows a linear relationship between the SKE.H and loss reductions for the P1 and P2 geometries. This relationship has been discussed by previous authors (Ingram (2003)) and indicates a link between the energy within the secondary flow and the magnitude of the associated loss.

The plot also contains the P3 and P4 geometries. These geometries do not follow the same trend and instead indicate an increase in loss, linked to the observed endwall separation. This separation feature, identified in the flow visualisation results, is turbulent and highly dissipative in nature, causing a loss of total pressure. This low momentum fluid is drawn into the passage vortex, giving the large PV loss peak seen in the pitchwise averaged data. Both the P3 and P4 also show lessened SKE.H benefit, as the endwall is not able to operate correctly.

The loss reductions presented in Figure 5.15 relate to changes in total (net) loss and therefore include the profile loss component. The profile loss is largely unaffected by changes to the endwall shape and its significant contribution to the total loss value, results in the link between SKEH and secondary loss appearing smaller in this diagram.

5.5 Conclusions

The overall behaviour of PEWs in successful operation is characterised by a drop in the strength of the passage vortex, controlled by a primary hump/dip arrangement. The strength of the passage vortex is evident in yaw angles, C_{SKE} and SKE.H. This drop in the PV strength impacts on the associated loss core and works in two ways:

1. The smaller PV draws less low momentum fluid from the endwall boundary layer

2. The reduced kinetic energy in the PV results in less viscous loss generation by the sheared flow around and within the vortex structure

The P3 and P4 designs indicate a limit to the PEW magnitudes. In these cases the dipped region close to the SS has resulted in a large diffusion and subsequent separation. The two successful PEW designs have an asymmetry in the size of the hump and dip. This asymmetry has produced a larger hump and smaller dip. The removal of the asymmetry in designs P3 and P4 has (indirectly) caused the separation by allowing a larger dip size.

The P1 design effectively reduced the overturning at the wall, but to the detriment of loss in the corner vortex. The success of the P2 design shows that a working design can be achieved within the tight axial restrictions of a turbine blade component.

5.6 Figures

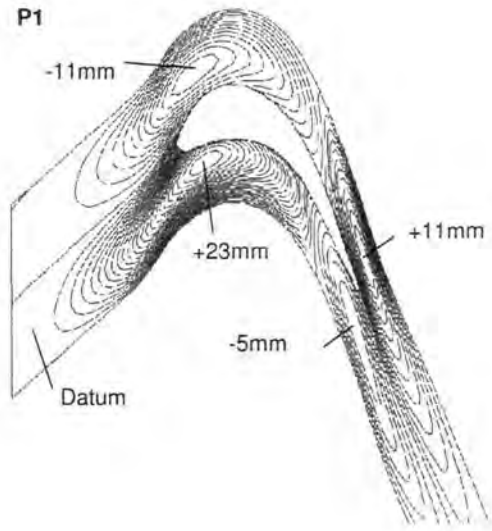

Figure 5.3: Endwall height contours - P1

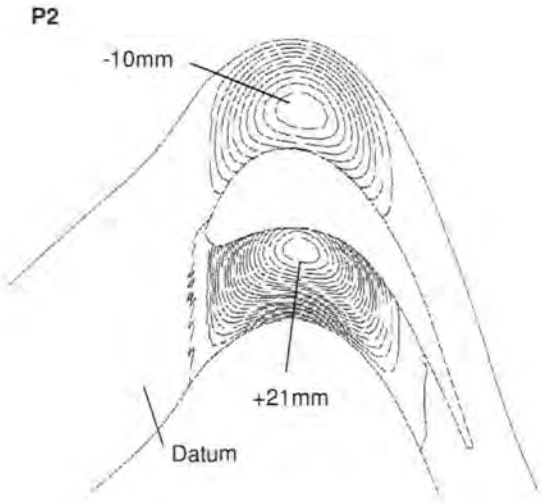

Figure 5.4: Endwall height contours - P2

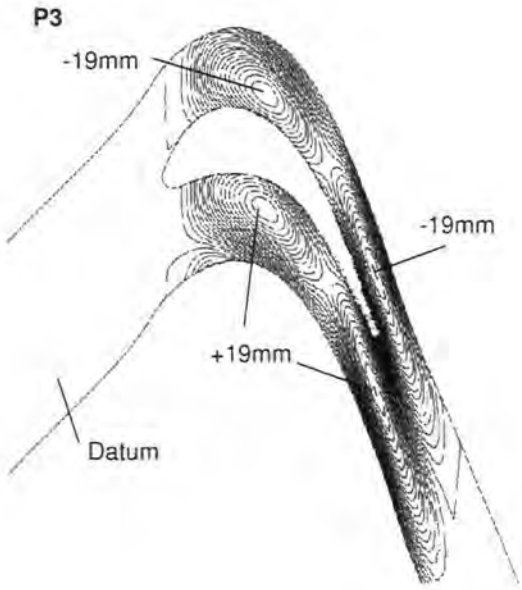

Figure 5.5: Endwall height contours - P3

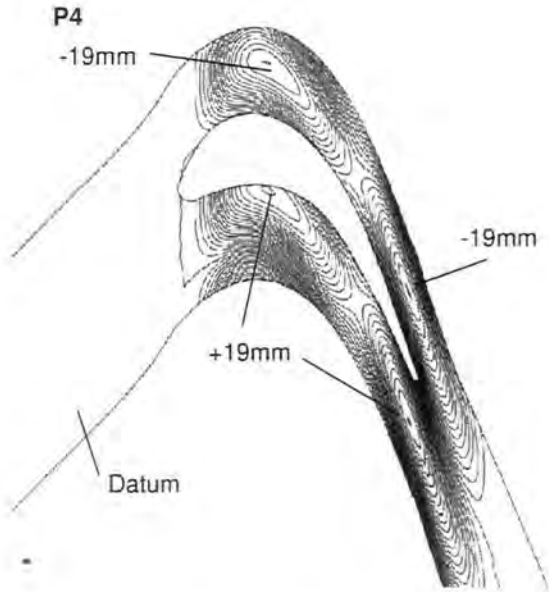

Figure 5.6: Endwall height contours - P4

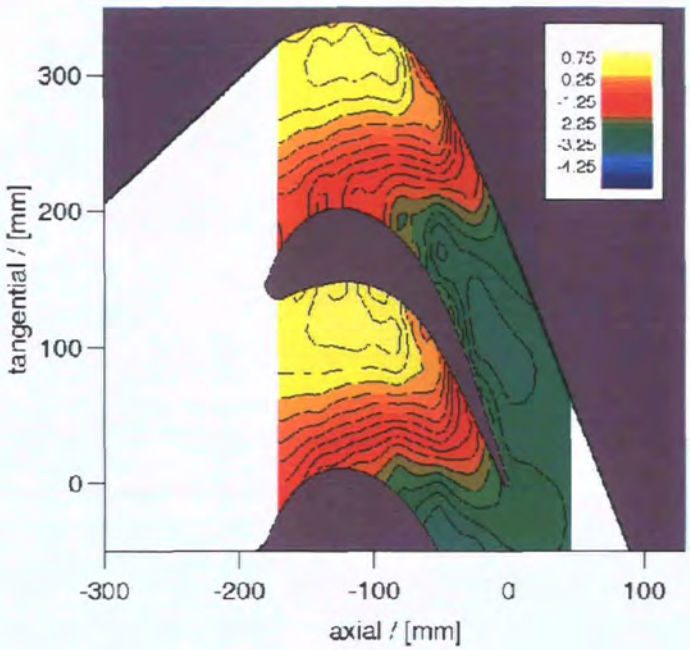

Figure 5.7: Endwall C_p contours - P0

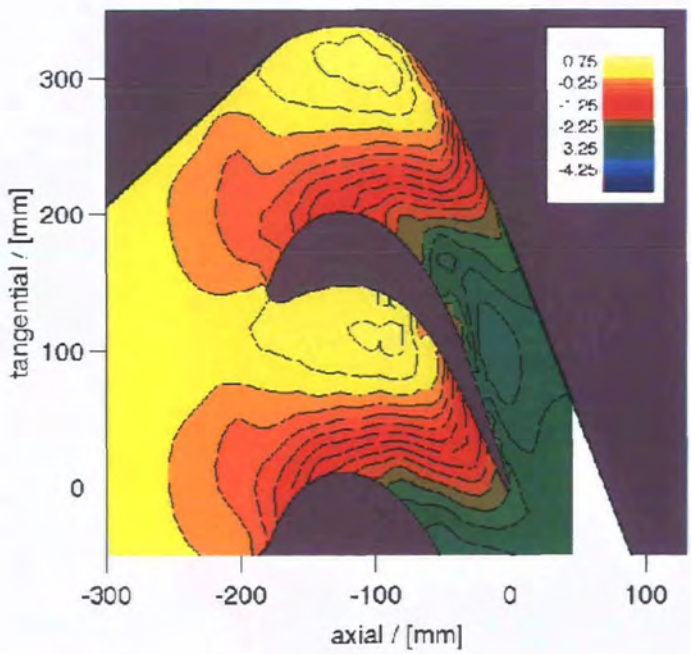

Figure 5.8: Endwall C_p contours - P1

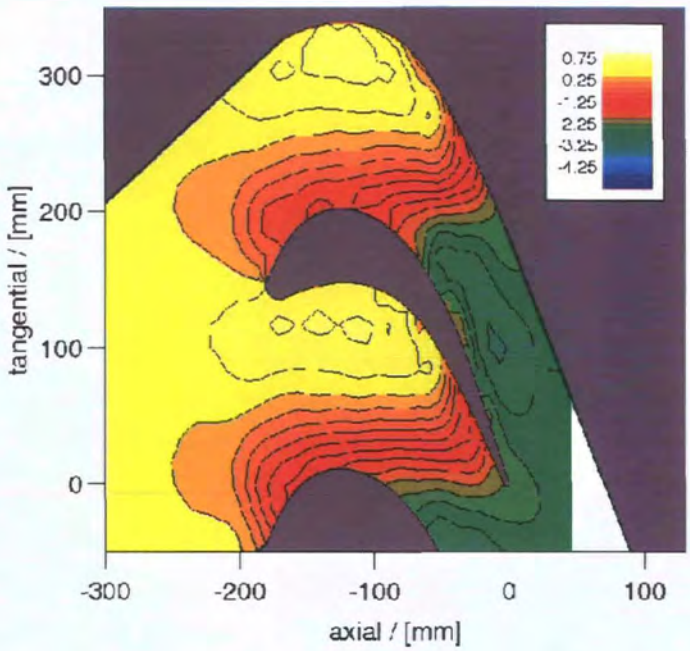

Figure 5.9: Endwall C_p contours - P2

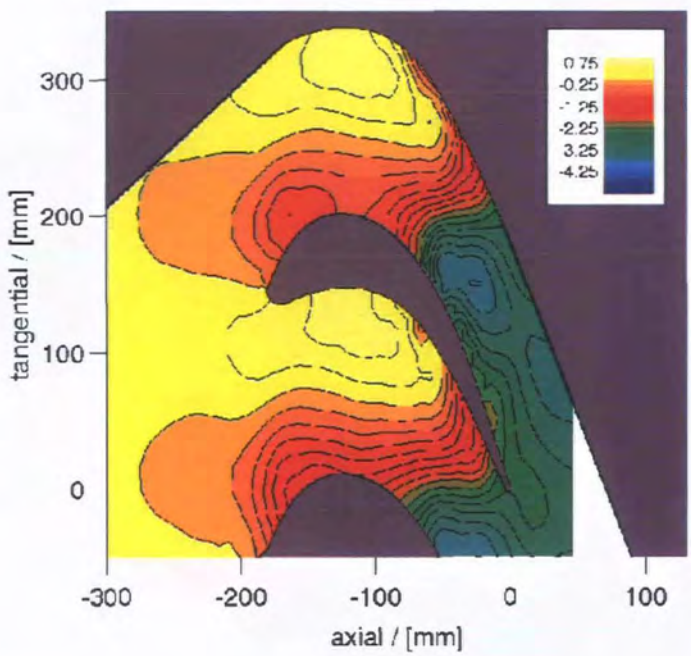

Figure 5.10: Endwall C_p contours - P3

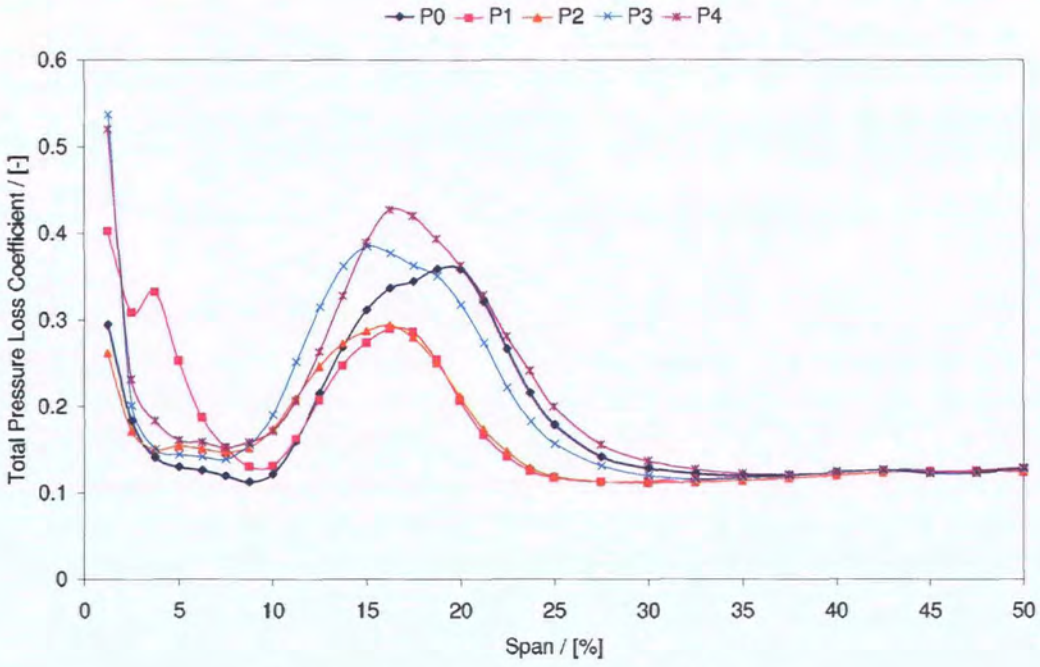

Figure 5.11: Pitchwise averaged Loss

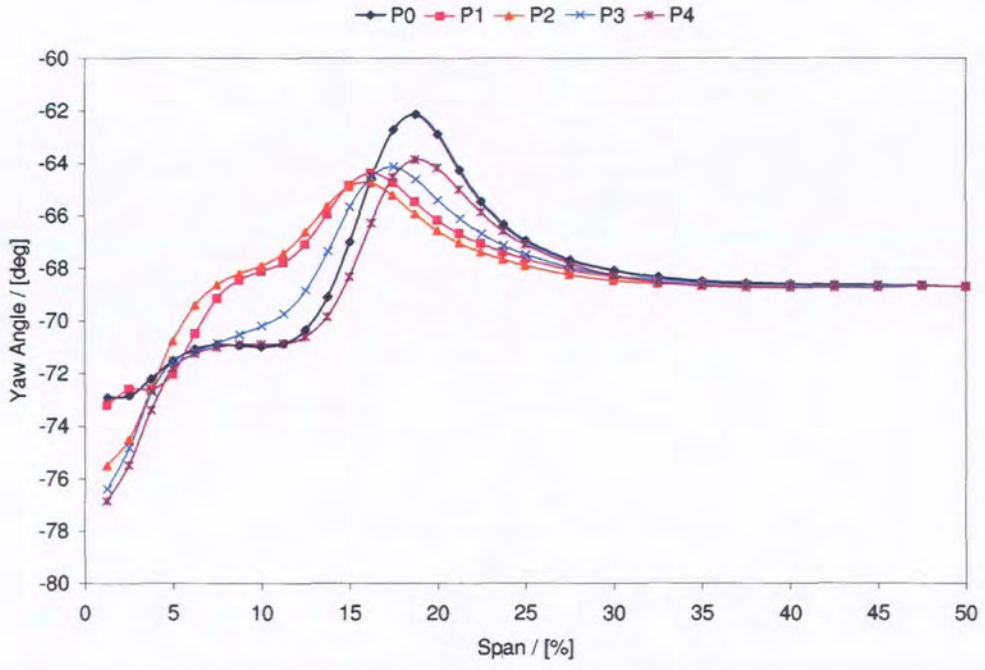

Figure 5.12: Pitchwise averaged Yaw

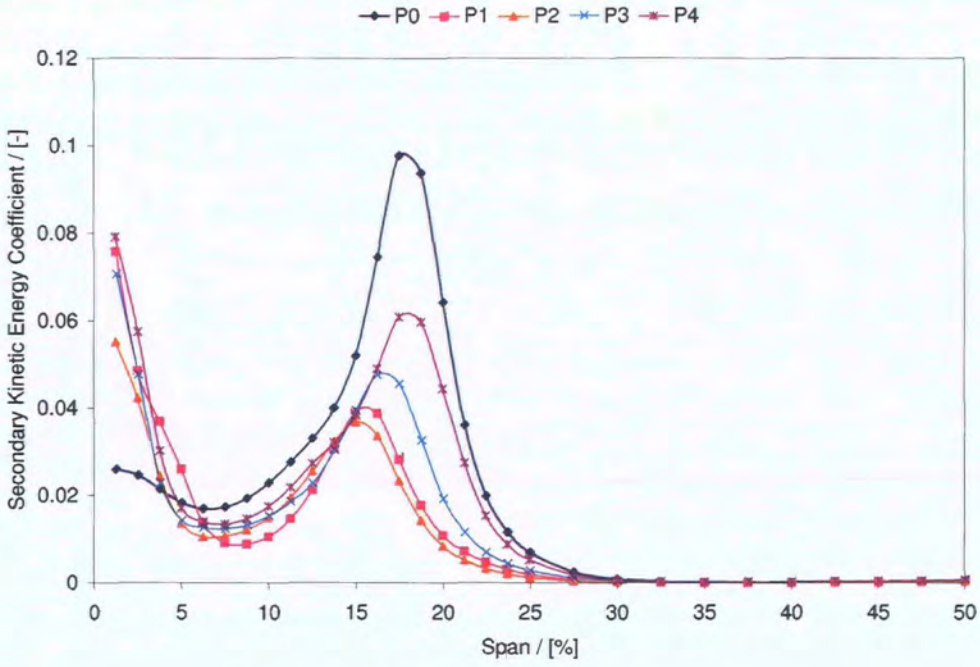

Figure 5.13: Pitchwise averaged C_{SKE}

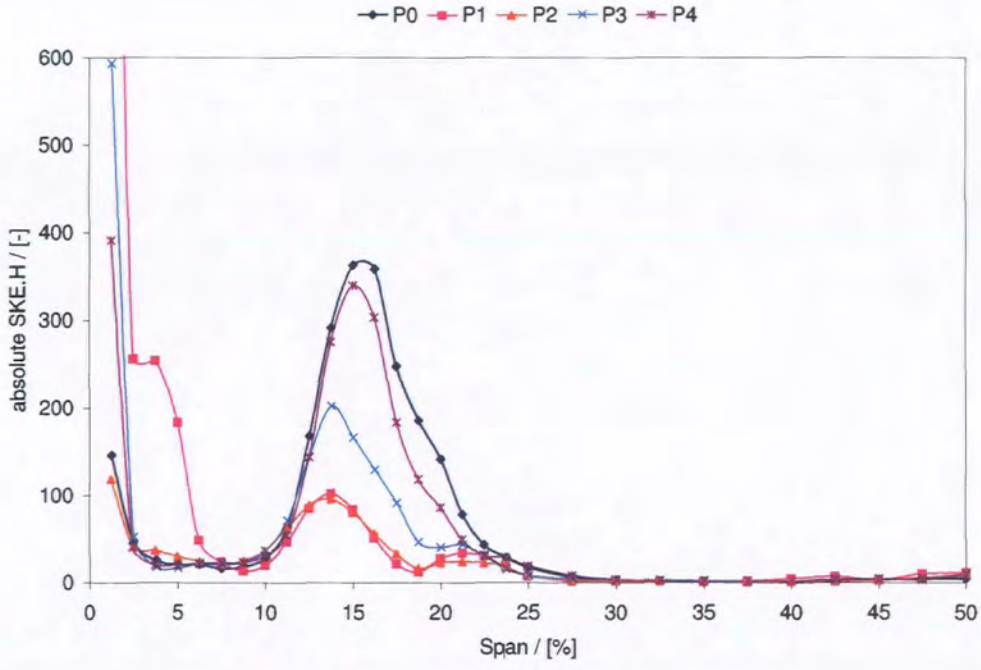

Figure 5.14: Pitchwise averaged SKE.H

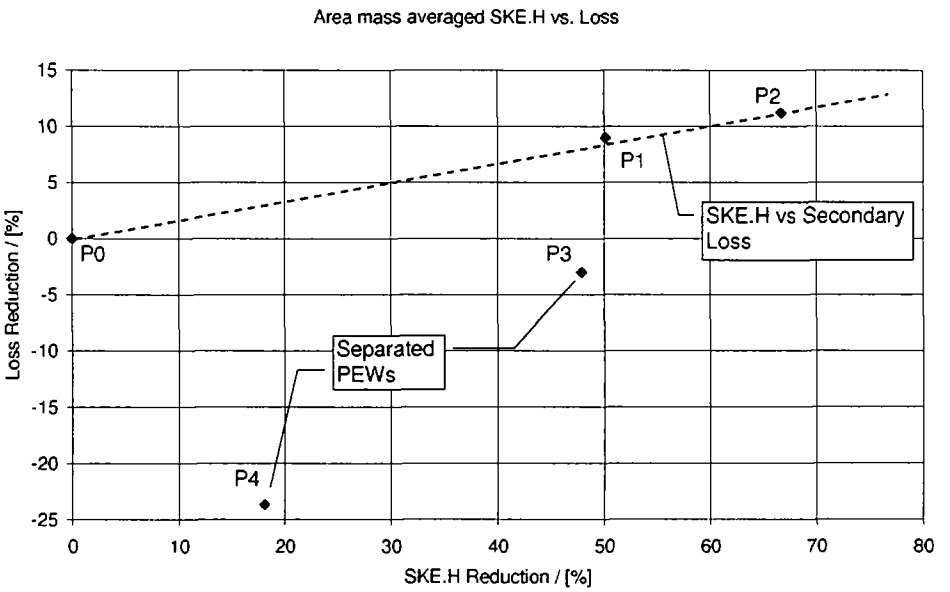

Figure 5.15: Mass Averaged SKE.H vs. Loss

Chapter 6

Reverse Compound Lean - C1

In this chapter, the experimental investigation of reverse compound lean in the Durham Cascade is presented. The experimental results are compared with a pre-existing computational result provided by Rolls-Royce. The results include pressure probe traverses, surface static pressure measurements and surface flow visualisation images.

The three dimensional nature of the effects of compound lean, required the measurement of the entire span of the existing cascade. As such, modifications were made to the inlet conditions, providing similar boundary layers at the two endwalls.

6.1 The C1 blade

A preliminary investigation was undertaken at Rolls-Royce Derby (Stokes (2003)) to decide on a suitable reverse compound leaned geometry for investigation. A series of profiles were examined, with varying angles of inclination to the endwall. Elliptical, power law, parabolic and circular arc profiles were investigated. The profiles were all leaned in a purely tangential direction. For each geometry a CFD solution was generated. The results from the computations indicated that the benefits of the lean were strongly related to the displacement of the blade section at midspan. The comparison criteria included; the strength of the secondary kinetic energy (SKEH) and the level of diffusion on the aerofoil surface. The geometry chosen for investigation is an elliptical profile with 15^o inclination at the endwall. This particular design was not one which gave the maximum reduction in SKEH, but was a compromise between this and the level of diffusion.

To enable direct comparison with the existing prismatic geometry, the reverse compound leaned aerofoil was chosen to have the same blade profile (2D section) and same overall turning. The final blade design is shown in Figures 6.5 and 6.6.

6.2 Blade Lean

Blade lean is defined as the tangential displacement of the profile over the radius. This is not the same as dihedral, which is a displacement perpendicular to the chord line.

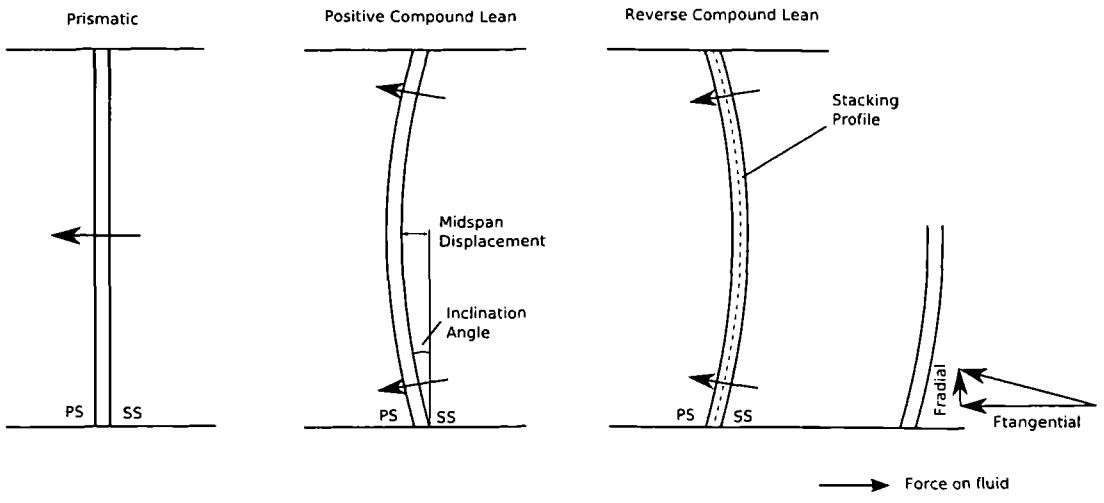

Figure 6.1: Tangential Lean

Straight lean is achieved by the linear increase in tangential displacement with radius, resulting in opposing effects at either end. Compound lean is achieved through the use of a non linear displacement profile, this profile can be a hyperbola, ellipse, or power law function. Defining the lean by mathematical profile ensures a smooth variation of curvature of the suction and pressure surfaces radially. For compound lean the alignment of the upper and lower (endwall) aerofoil sections is the kept the same. The intermediate aerofoil sections are displaced tangentially to generate the required profile.

In positive compound lean the pressure surface makes an acute angle with the endwall and its shape, when viewed axially, is convex on the pressure surface. Reverse compound lean is the reverse of this and gives a concave pressure surface.

Figure 6.1 shows the parameters used to define the tangential lean. This figure shows an axial cross-section through an aerofoil and indicates two key parameters: the midspan deflection, and the inclination angle, made at the end wall between the aerofoil and a (radial) line normal to the wall.

6.2.1 Effects

Lean can be explained by one of the following two descriptions:

1. The static pressure contours within the blade passage are a result of the streamline curvature of the main flow direction. The contours of static pressure run radially in the case of a straight prismatic blade as the largest change of flow direction is perpendicular to this. The leant stacking line cuts through the contours and the suction surface experiences different local static pressures along the span. (At one end the suction surface loading is greater as the blade has moved into an area of lower static pressure, at the opposite end the loading of the local surface is reduced as the static pressure increases). The pressure gradient moves fluid in to the endwall, increasing the momentum of the boundary layer. By reverse compound leaning the profile, both hub and casing ends are shifted into a region of lower static pressure, as shown in Figure 6.2, causing a

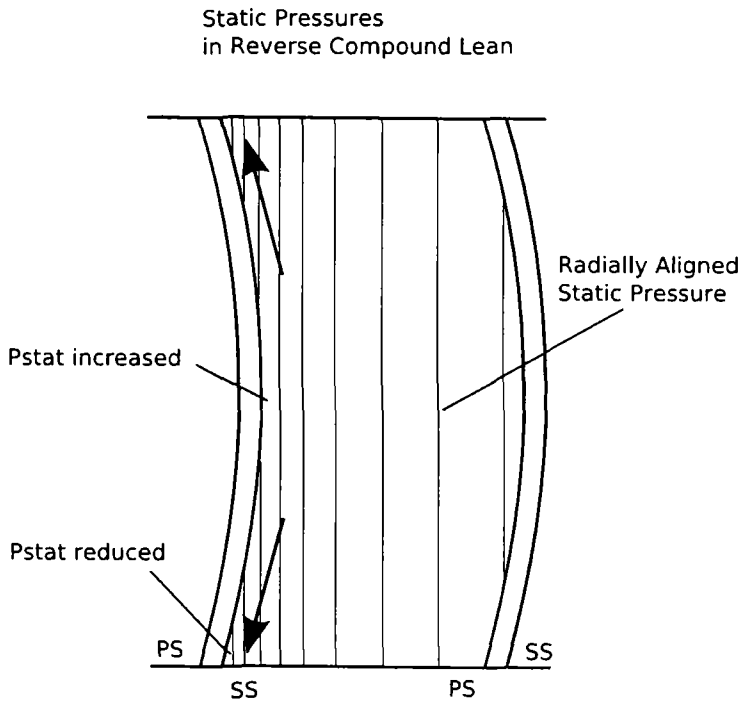

Figure 6.2: Lean - Pressure Contours

radial flow from midspan to both ends. This radial flow shifts the streamline whilst it is within the passage. Outside of the passage the flow redistributes to even out the mass flow distribution

2. The blade exerts a force on the fluid perpendicular to the wetted surface. For prismatic blades, with no lean or sweep, the force vector (at a point along the chord) is purely tangential (circumferential). As the blade is leant, the force vector is leant and a component of the force exists in the radial direction. Reverse compound lean gives a force vector on the fluid toward the midspan, this raises the pressure at midspan. The relative reduction in pressure at the endwall draws fluid in toward the endwalls, see Figure 6.1.

For the Durham Cascade geometry, the peak loading (the greatest force vector) is at a point where the suction surface is normal to the tangential direction. By leaning tangentially, the radial force component is maximised for a given blade loading.

6.3 Reverse Compound Lean

For reverse compound leaned blades, the suction surface endwall corner sees a lower pressure and the midspan suction surface sees a slightly higher pressure. Near the PS the effect is opposite. The tangential pressure contours here are further apart and thus the effects are reduced at this side of the passage. This increases the cross passage pressure gradient at the endwall and the strength of the secondary flows.

The suction surface (radial) pressure gradient draws massflow in toward the endwall. This results in a reduction in the radial migration of flows, such as the PV.

By forcing the fluid to the endwalls the reverse compound lean reduces the mass flow in the middle of the passage. This in turn reduces the local loss, due to the decrease in local boundary layer friction. The radial flow towards the endwalls restrains the secondary flow structures whilst they are within the passage. This radial restraint reduces the mixing with the 'clean' two dimensional 'primary' flow and maximises the region of two dimensional flow.

There are two competing effects on the secondary flow. The increased momentum of the accelerated near-endwall flow may help reduce secondary flows. However, the increased loading will increase the cross-passage pressure gradient, which may exacerbate the secondary flows.

Reverse compound lean reduces loss in the midspan region due to reduced loading, but increases the end wall loss - due to the higher velocity here.It increases the exit angle deviations up the span. However, the radial extent of the deviations is decreased.

6.3.1 HSV effect

The reverse compound leaned shape produces an acute angle at the suction surface endwall corner. At the leading edge, the acute angle offsets the effect that the boundary layer stagnation has on the formation of the horseshoe vortex. The higher momentum fluid at the edge of the inlet boundary layer, that normally rolls up at the leading edge, is instead diverted to the suction surface and also down towards the endwall. This effect, as noted by Harrison (1990), accelerates the boundary layer fluid and thins the boundary layer itself.

6.4 Pressure Probe Results

The pressure probe results at a traverse location 28% C_{ax} downstream of the trailing edge (128% C_{ax}), are presented in the following section.

To aid in the comparison of CFD and experimental data, the results of the CFD solution are interpolated onto the measurement grid of the experimental data. This grid is much coarser than that of the CFD and therefore some detail from the CFD solution will be lost. However, the use of the same grid for both datasets enables direct comparison, as the data sampling is the same. A correction is applied to the experimental data, to obtain a zero loss value at the midspan - mid pitch position. No correction is made for the yaw angle, in contrast to Ingram (2003), as the midspan yaw angle is no longer expected to remain constant.

The computational and experimental results are compared simultaneously. Unless explicitly described, the effects detailed are describing the behaviour of both computational and experimental results.

6.4.1 128% C_{ax} - Area plots

The following results are the mean of three traverses, each taken back-to-back, but with a reset of the probe positioning system each time. The reset of the probe allows

the variability of the probe setup to be accounted for in the data. This gives more confidence in the conclusions drawn.

6.4.2 5 hole probe data

The results for 128% C_{ax} are presented in Figures 6.7 to 6.22, with loss contours in Figures 6.7 to 6.10, secondary velocity vectors in Figures 6.11 to 6.14, secondary kinetic energy in Figures 6.15 to 6.18 and vorticity in Figures 6.19 to 6.22. For each quantity the reverse compound leaned blade, C1 (found on the right of the page) is compared with the prismatic blade, C0 (on the left of the page). Experimental results are positioned at the top of the page and computational ones are placed at the bottom.

Loss contours

The effects seen in the loss contour plots of Figures 6.7 to 6.10 are as follows:

- The reverse compound leaned blades produce a noticeably bowed wake. The midspan of this wake has a slightly lower peak loss than that of the prismatic blades. For the experimental result this relates to a C_{p0} of 0.4 for C1, compared with 0.5 for C0. The reduction in midspan loss is of the same magnitude for the experimental and CFD results. However, the CFD overpredicts the absolute midspan loss because of the specification of a fully turbulent blade boundary layer, which is transitional in reality

- The experimental corner vortex loss core (seen in Figure 6.7 at -320mm tang, 5mm rad for C0) is shifted tangentially relative to the wake position in C1. This is due to increased overturning at the wall. The corner vortex in the CFD solution is translated further, due to increased overturning in the computational result

- The experimental shed vorticity/suction-surface-horseshoe-vortex (ShV/SSHSV) loss core is much weaker in the C1 blades. In C0 this loss was clearly defined and separate. For C1 the region appears to have merged with the passage vortex core (located at -250mm tang, 60mm rad)

- In the computational solution of C1, the mixing of the passage and SSHSV cores is weak, thus the single peak observed in the experimental work is not predicted. This weak mixing can be seen in both C0 and C1

- The passage vortex loss core has itself increased in strength for the C1 blades. Some of this loss can be associated with the reduction seen in the ShV/SSHSV core. However, the higher near-wall velocities will also increase this loss

- The radial movement of the secondary losses, toward the endwall, is minor. The passage vortex loss feature is in a similar position in both C0 and C1. Only the decrease in strength of the trailing vorticity/SSHSV loss core has brought about any apparent shift in loss

Secondary velocity vectors

The effects seen in the secondary velocity vector plots of Figures 6.11 to 6.14 are as follows:

- The SSHSV vectors are weaker in C1 than C0 - this leads to a weaker interaction with the passage vortex
- The passage vortex is similar in size and strength for C0 and C1, but has shifted slightly radially toward the endwall
- Strong overturning is observed near the endwall for C1
- The corner vortex is more difficult to discern in C1 due to this strong overturning
- The CFD over predicts the secondary flow magnitudes (see pitchwise averaged yaw in Figure 6.34), but the correct behaviour and changes between C0 and C1 can be observed

C_{SKE} contours

The effects seen in the C_{SKE} contour plots in Figures 6.15 to 6.18 are as follows:

- For the C1 and C0 experimental results, the increased overturning is seen as a higher secondary kinetic energy (SKE) in the 0-20mm span region. The close wall SKE for the CFD solution is also higher in C1 than in C0 due to overturning
- For C1, the SKE strength is reduced in the 60-70mm span region. This indicates a reduced interaction of the passage vortex and SSHSV. This confirms the vector plot result which indicates the SKE from the SSHSV has been reduced from C0 to C1
- The computational SKE values are more significant for both C0 and C1. The over prediction of the CFD is more noticeable here because the secondary kinetic energy is a function of the velocity squared. The reduction in SKE due to a weaker SSHSV is evident in the CFD too, with a smaller peak SKE in the 60-70mm region for C1.

Vorticity contours

The effects seen in the vorticity contours presented in Figures 6.19 to 6.22, are as follows:

- The size and shape of vortical structures in the experimental results are the same between C0 and C1
- There is a slight shift of the vorticity peaks towards the wall on between C0 and C1 experimental

- The vorticity plot of the computational result is more complex than the experiment. The vorticity associated with the wake (trailing shed and filament vorticity) is discernible here as a diagonal region that connects the SSHSV with the CV at the endwall.
- Despite the additional complication, the passage vortex has a similar pattern between experiment and CFD. The computational result again has greater magnitude.
- The near wall vorticity is higher in the CFD solution.

6.4.3 3 hole probe (near-wall) data

The near wall region was investigated using a three hole probe, providing data for loss and yaw angles only. The following results are the mean of three back-to-back traverses, as per the five hole method. The vectors in the secondary velocity plots are pseudo-secondary vectors, based on three hole probe data, and do not contain a radial component of the velocity vector. The vectors do however give an indication of the overturning at the endwall. The loss from the three hole probe readings is shown in Figures 6.23 and 6.24 and the pseudo secondary velocity vectors are shown in Figures 6.25 and 6.26. The results show that:

- There is little difference between the shape of the C0 and C1 results. The magnitude of the corner vortex loss core is slightly larger for C1 and it has shifted slightly tangentially
- The pseudo-secondary vectors show an increase in overturning in the near wall region for the C1 blade
- The overall pattern of the velocity vectors in this region does not differ between C0 and C1

6.4.4 Combined data set

The mean data sets for the five and three hole probes are combined to give a complete passage loss distribution. The combined dataset is limited to loss as the three hole probe data cannot give pitch angles and therefore neither secondary velocities nor secondary kinetic energy. The combined loss contour plots for C0 and C1 at 128% C_{ax} are found in Figures 6.27 and 6.28. This combined dataset successfully illustrates the effect that the overturning has on the corner vortex loss core, it also gives a more complete picture of the loss distribution.

6.5 Pitchwise averaged plots - 128% C_{ax}

6.5.1 Repeatability - 5 hole

The pitch averages of the six traverses that make up the 5h probe repeatability data, are presented for total pressure loss in Figure 6.29 and for yaw angle in Figure 6.30.

The variability of the loss distribution in Figure 6.29 can be seen to be much smaller than the difference between the two blade types. The three traverses lie on top of one another, giving confidence in the repeatability of both the measurement and traversing systems.

The yaw angle is more susceptible to the resetting of the probe positioning system. The variability in Figure 6.30 indicates a 0.4^o variation for the C1 blades at midspan. The C0 blades have a comparatively smaller variation, of less than 0.2^o at midspan.

6.5.2 Repeatability - 3 hole

The three hole probe traverse was also repeated three times using the back-to-back method. The repeatability of these results is illustrated in the pitchwise averaged loss and yaw angle in the figures 6.31 and 6.32. For this near wall region the changes in loss are small, making the variability of the dataset seem large. The variability of the yaw angle, Figure 6.32, appears to be poor; this reflects the difficulty in precisely setting the probe head for the three hole measurements. It should be noted that for each three hole probe traverse, a midspan reading is taken. This midspan reading is used to match the data of the five hole probe, thus eliminating some of the error.

6.5.3 Pitchwise averaged - Experimental and Computational

The pitchwise averaged values of both the experimental and computational results at 128 % C_{ax} are presented in Figures 6.33 to 6.36. The figures provide a quantitative comparison of the computational and experimental results. As described earlier, the pitchwise averaged loss is corrected to zero at midspan-midpitch.

Asymmetry

The pitchwise averaged data show more clearly that there is a poor symmetry in both the C0 and the C1 experimental results. The loss cores at either endwall are of different size, there is more underturning at the lower endwall (0-200mm) of the experimental result for both C0 and C1.

These effects are thought to be due to:

- An aerofoil extension, used at the upper endwall to extend the span, which is generating additional loss
- The inlet loss profile being slightly asymmetric. This asymmetry will convect through the cascade and impact on the downstream result
- The traversing slot, in the end-wall, introduces an imperfect near wall flow

These effects were not considered in the earlier cascade work, as the analysis focussed on the lower endwall only.

Total Pressure Loss

The pitchwise averaged total pressure loss is presented in Figure 6.33, where a number of key features of the experimental results can observed:

- The reverse compound lean offloads the midspan region of the blade, this reduces the profile loss which appears as a uniform reduction in the total pressure loss (0.35 C_{p0}) for the middle 50% span.
- The loading is redistributed to the endwall regions, increasing the total pressure loss in the passage vortex core.
- The passage vortex loss core is also shifted radially in toward the endwall, by the reverse compound lean.
- The endwall boundary layer loss magnitudes also increase with the introduction of reverse compound lean.

The computational result indicates a similar behaviour of the reverse compound lean, but with a number of key differences:

- The computation predicts two separate loss peaks for the passage vortex and SSHSV cores. This was also observed in the contour plots (Figures 6.7 to 6.10) and is thought to be a result of the lower mixing rate of the computation.
- The radial shift of the loss core, associated with the passage vortex, is not observed in the computational result. The radial movement observed here is limited to the squeezing of the SSHSV. However, the increased loss peak in the PV core is also observed for the computational result.
- The computation over predicts the midspan loss for both cases, due to the definition of fully turbulent boundary layers. The benefit seen in profile loss for the C1 geometry, is approximately 50% less in the CFD solution.

Yaw

The pitchwise averaged yaw angle is presented in Figure 6.34 for both the computational and experimental results. The key effects of reverse compound lean are; a reduction in turning at midspan (1.5^o), an increase in the overturning at the wall (2.5^o), and a similar level of underturning.

The computational result follows this behaviour, with an identical change in and absolute level of yaw angle at midspan. The computational result over predicts the under and over turning by 3^o and 4^o respectively. The over prediction of secondary flows occurs for both prismatic and reverse compound leaned geometries. In general, the vortical structure is modelled correctly, seen in the vector plots in Figures 6.11 to 6.14.

Pitch

The pitch angle, presented in Figure 6.35, describes the flow in a radial direction. A negative pitch angle relates to flow from the lower endwall toward the upper.

Downstream of a prismatic blade, radial flow is typically limited to the endwall regions, where the secondary flow vortices have radial components. The region of interest in pitch angle is that from 100mm to 300mm span, i.e. the region largely unaffected by secondary flows at this particular axial location.

The reverse compound leaned results at 128% C_{ax} are influenced by the streamline curvature due to the downstream redistribution of flow, as shown in Figure 6.4. Within the passage, the radial pressure gradient of the reverse compound lean encourages outward (toward the endwalls) radial flow. Outside of this influence a streamline redistribution occurs (Figure 6.4b) , this can be seen at 128% C_{ax} as a pitch angle component toward the midspan.

Both the experimental and computational results show this effect. The computational result has higher pitch angles throughout, indicating a greater level of redistribution at this plane.

The experimental result for C0 has a flat midspan indicating no radial flow. The computational result for C0 shows a significant radial flow. This radial flow may be caused by blockage from the endwall boundary layer or secondary flows. This blockage can cause a redistribution and radial velocity component as illustrated in Figure 6.4a.

C_{SKE}

The pitchwise averaged C_{SKE} results in Figure 6.36 show the following behaviours:

- The C_{SKE} is a highly sensitive variable and as such the small differences observed in the secondary vectors, are magnified in the C_{SKE} result.
- The new C1 blades have reduced secondary kinetic energy in the passage vortex and SSHSV interaction, but have increased SKE in the overturning region at the wall.
- The behaviour of SKE in the upper half of the passage is similar to the lower half but with reduced intensity.

SKEH

The pitchwise averaged SKEH is presented in Figure 6.37. The SKEH indicates:

- With the application of RCL the SKEH magnitude is reduced in the region associated with the passage vortex
- There is no discernable difference between C0 and C1 at the endwall

Item	C0	C1	C0 CFD	C1 CFD
Total	100	85.6	100	101.2
Midspan	100	57.9	100	92.4

Table 6.1: Net Loss at 128% C_{ax}, 5h probe, CFD comparison

6.6 128% C_{ax} - Mass averaged Results

6.6.1 Mass averaged loss

The mass averaged data for the C0 and C1 geometries, are presented here for the lower half of the passage. The conclusions are similar for the upper endwall. All losses in Table 6.1 are net of the inlet boundary loss value given in Figure 3.7 in Chapter 3.

The experimental result of the five hole probe, gives an overall loss for C1 14.4% lower than C0 and a 42.1% lower midspan loss. The CFD gives a 1.2% increase in overall loss for C1 relative to C0 with a 7.6% lower midspan loss. Both computational and experimental results show that the midspan offloading reduces the midspan losses.

Boundary Layer Modelling

The differences in midspan loss between the computation and experiment, are due to the computational boundary layer definition. By defining the entire suction surface as fully turbulent, when it is reality transitional, any changes in transition point relating to off-loading will not be fully accounted for in the computation.

Probe traverse overlap

Table 6.2 details the mass averaged losses for the different probe types. The results for the three and five hole probes are shown as a combined loss value and also in their component parts. Again the values in Table 6.2 are net of inlet loss. The three hole probe is traversed 0-15mm radially, the five hole probe is traversed 5-395mm radially, this provides an overlap of the data. For the combined dataset the two datasets were joined at 10mm radius. This particular radius was chosen to ensure the maximum use of the five hole probe, whilst avoiding five hole probe errors in close proximity with the wall.

From the results of Table 6.2, it can be seen that the loss measured by the three hole probe for the 0-15mm region for C1 is 29.2% greater than C0. The mass averaged loss measured by the traverse of the five hole probe for C1 shows a reduction of 14.4% of the C0 value. The combined mass averaged loss is reduced from C0 to C1 by 10.7%. The addition of the three hole data reduces the benefit of the reverse compound leaned blade by 3.7%.

6.6.2 Mass averaged Yaw

The mass averaged yaw angle for C0 and C1, both experimental and computational, is presented in Table 6.3.

Item	Area	C0	C1
5hole	5-200mm	100	85.6
3hole	0-15mm	100	129.2
Combined	0-200mm	100	89.3

Table 6.2: Net loss at 128% C_{ax} for 5h and 3h probes

Item	C0	C1	C0 CFD	C1 CFD
Yaw Angle	64.50°	64.09°	67.95°	67.82°

Table 6.3: Yaw Angle at 128% C_{ax}, 5h probe, CFD comparison

The table shows that overall differences in mass averaged yaw angle are small. The difference between the experimental results is 0.4°. This is within the accuracy of the experimental measurement system, see Ingram (2003). The difference between the computational results is less, at 0.1°. These results show that the overall turning has not changed significantly. The changes in loss cannot, therefore, be attributed to changes in overall blade loading.

6.6.3 Mass averaged C_{SKE} and SKEH

The mass averaged C_{SKE} and SKEH values for the same four cases can be found in Table 6.4. The experimental results show C_{SKE} increases by 2.3% for C1, whereas the SKEH decreases by 7%. The computational result indicates a C_{SKE} reduction of 3.7% and a 14% reduction in SKEH. The benefit observed in SKEH is greater than the C_{SKE}, as the endwall overturned region (which has increased in C1) is not resolved by the parameter.

6.7 Blade surface static pressure

The static pressure distributions for the aerofoil surfaces are presented as coefficients, C_p, defined in Equation 3.2 in Chapter 3. The coefficients are presented for six different blade heights between 1% and 50% span for the CFD solution in Figures 6.38 to 6.44. The image in Figure 6.41 provides a visual indication of the relative blade spans where the CFD pressure readings were taken.

The C_p values for six different heights between 50% and 5% span from experimental work are given in Figures 6.45 to 6.48. The experimental results are expressed as approximate span values, as the radial locations of the tappings (for the two geometries) differ slightly.

Item	C0	C1	C0 CFD	C1 CFD
C_{SKE}	100	102.3	100	86.3
SKEH	100	93.0	100	86.9

Table 6.4: C_{SKE} and SKEH at 128% C_{ax}, 5h probe, CFD comparison

Computational

The results in Figure 6.38 show a typical flat topped loading distribution at midspan for both C0 and C1. The offloading due to the reverse compound lean is shown in the reduced suction surface loading (lower C_p value in the upper half of the chart).

At a point between 25% span and 12% span the suction side loading is the same for C0 and C1 . From 12% span inwards C1 has a higher loading than C0. At 4% span the reduction in loading in the front part of the passage is clear for the prismatic blade. At 1% span the reverse compound leaned blade sees a large increase in loading for the front suction surface.

Experimental

The experimental C_p plots show the same trends in loading as the computational result. As with the CFD result, all of the changes due to the reverse compound lean are seen in the suction surface only. This ties in with Sharma et al. (2003). The strong early suction surface lift on the C1 blade for CFD (seen in Figure 6.44), is not seen in the experimental result because the closest spanwise measurement is at 5%. The offloading of the front section of the suction surface of the C0 blade is seen clearly here in Figures 6.47 and 6.48. The higher midspan loading of the C0 blade can be seen in Figure 6.45.

6.8 Flow visualisation

The conventional oil and dye visualisation technique was used to obtain the following images. As per previous work, a yellow dye was used on the blades and a red dye on the endwall, making interpretation of the flow patterns slightly easier. The flow visualisation images are split into three views, each one comparing C0 and C1 geometries.

Figures 6.49 and 6.50 show the growth of the passage vortex along the blade surface close to the endwall. Note that the red streak on the SS is not the extent of the passage vortex, but is probably caused by the suction side horseshoe vortex (SSHSV) drawing flow (and dye) from the endwall onto the blade. The maximum extent of the passage vortex is visible on closer inspection and is just below the red streak. The reverse compound leaned blades have a reduced height of the passage vortex at the trailing edge on the suction surface, indicating a smaller spanwise influence of the losses for C1. This is the "penetration height" defined by Sharma et al. (2003).

Figures 6.51 and 6.52 show the rearward shift of the SSHSV blade attachment point on C1. The pressure side horseshoe vortex, seen close to the bottom of the image in Figure 6.51 for C0, is not visible on C1.

The vertical yellow line on the blade suction surface in the same figure is not a flow feature. This is most likely the settling of the oil and dye mixture due to gravity. This is the lowest point on the blade when positioned in the cascade. The dark horizontal line, on the left hand portion of endwall flow visualisation in Figure 6.51, is a split in the endwall surface that was repaired. This is not a flow feature.

Figures 6.53 and 6.54 show the leading edge region of the blades. The figures indicate the absence of the pressure side leg of the horseshoe vortex for C1.

6.9 Conclusions

This chapter has described the experimental testing of a reverse compound leaned geometry and reference prismatic blade, in order to examine the fundamental flow effects of lean in highly loaded turbine components. The chapter has presented; pressure probe results, which have enabled the performance ranking of the geometry; surface static pressures for a greater understanding of the impact on the redistribution of loading; and flow visualisation for the impact of the lean on the secondary flow structures.

With reference to Figure 6.3, the fundamental effects of the reverse compound lean are:

- The lean offloads the midspan section, reducing the profile loss
- The loading is increased toward the endwalls. This causes an increase in the secondary flow strength, seen in the PV vorticity
- The lean induces a radial pressure gradient, which constrains the enhanced secondary flows, keeping them closer to the endwall, thereby maintaining a cleaner mid passage flow

A number of conclusions can be drawn from the various experimental and computational results, these are:

- The exit yaw angle has become more non-uniform and this may result in increased downstream mixing loss. The loss peaks have been moved toward the endwall and the midspan value has dropped. The secondary kinetic energy coefficients show a reduction of energy in the underturned region (PV and SSHSV interaction), but a rise in the overturned region near the wall. The pitch angle results show that the flow downstream of the blade row redistributes radially, when no longer influenced by the radial pressure gradient
- The reverse compound leaned blade reduces the loss through a combination of increased endwall loss and significantly reduced midspan loss. The mass averaged yaw angle remains the same for both cases, confirming a loss reducing design and not just a reduced blade loading
- The blade loading values appear to follow the behaviour of the linear cascade results of Sharma et al. (2003). The reverse compound lean, offloads the profile for the mid section and increases it near the endwall, particularly at the front of the passage. The experimental static pressure results follow those of the CFD.
- The flow visualisation images confirm the result of the pneumatic pressure probes. The shift of the endwall saddle point, between Figures 6.53 and 6.54, follows the description of Harrison (1990) for his "low pressure" end of the straight leaned cascade.

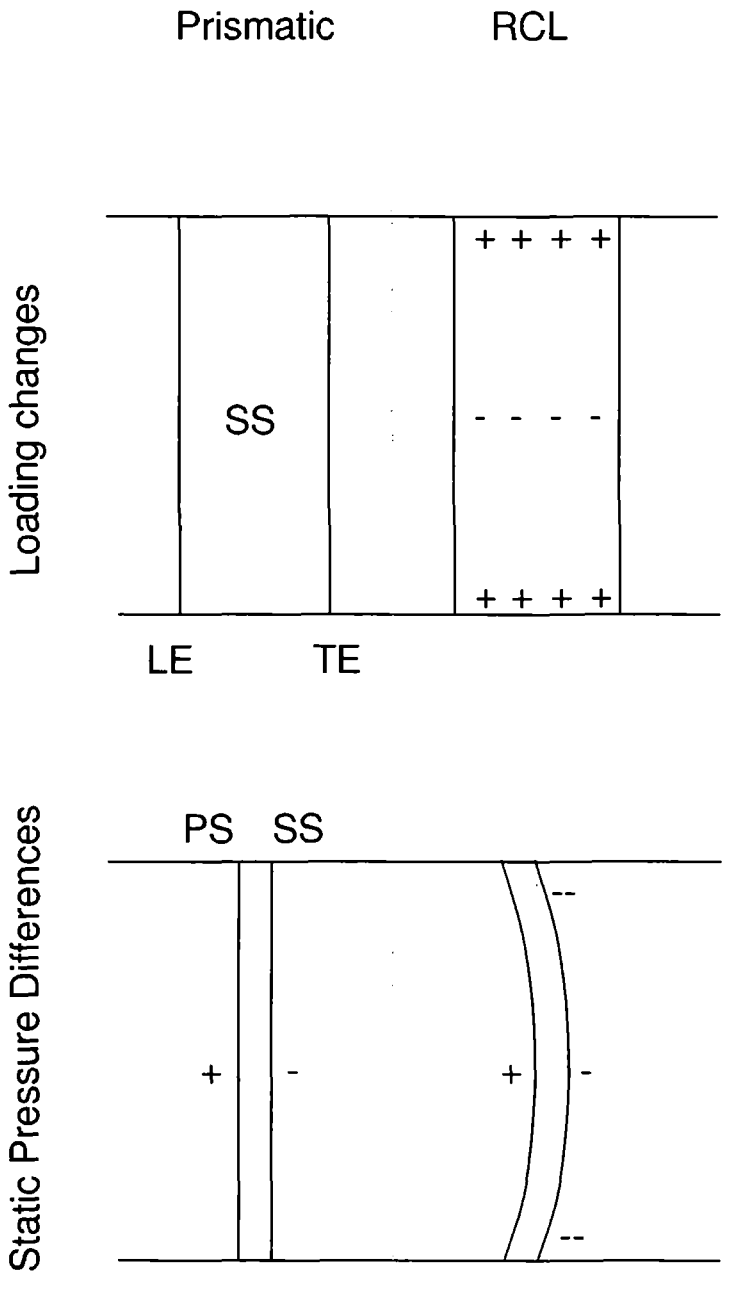

Figure 6.3: Effects of Reverse Compound Lean

The overall loss is reduced by approximately 11% for the reverse compound leaned blade. This is composed of an increase in secondary losses and a large decrease in midspan losses. The mass averaged exit yaw angle remains the same, but the radial variation in yaw angle has increased. The blade was designed to reduce exit secondary kinetic energy. The SKEH parameter indicates its success, but conflicts with the C_{SKE} parameter which indicates high secondary kinetic energy due to the resolution of the endwall boundary layer. The distribution of secondary kinetic energy has altered.

For reverse compound lean, there is no link between the observed change in total pressure loss and the secondary kinetic energy. The majority of the loss reduction is due to two dimensional loss effects in the aerofoil boundary layer. This differs from the profiled endwall results which indicated a linear relationship between SKE and loss for non-separating profiled endwall designs.

6.10 Figures

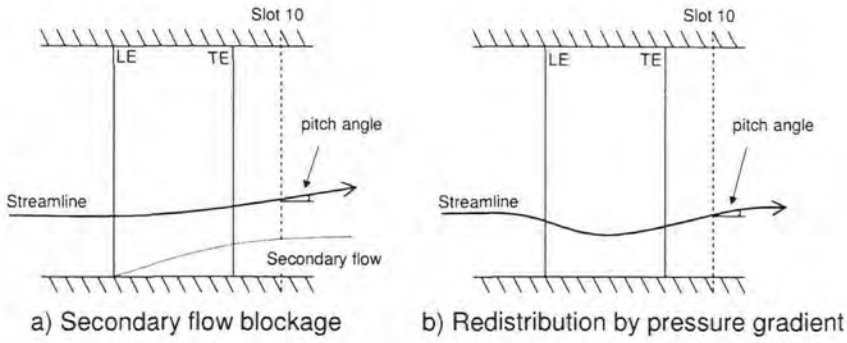

Figure 6.4: Streamline redistribution - two effects

Figure 6.5: C1 blade geometry - suction surface isometric

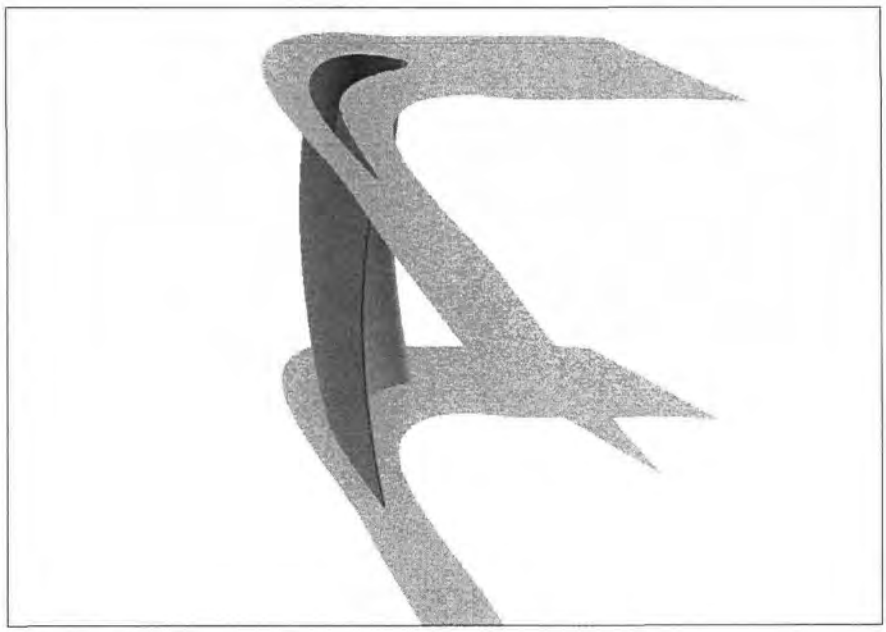

Figure 6.6: C1 blade geometry - trailing edge isometric

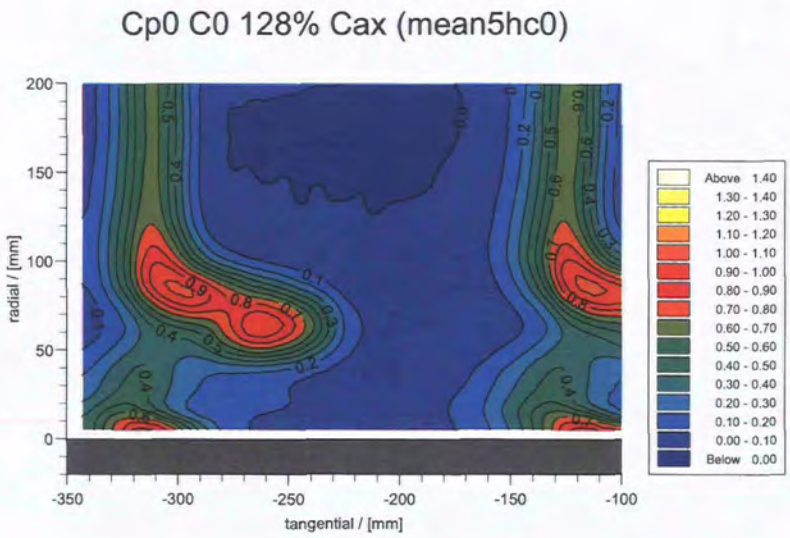

Figure 6.7: Expt. Prismatic - Area loss at 128% C_{ax}.

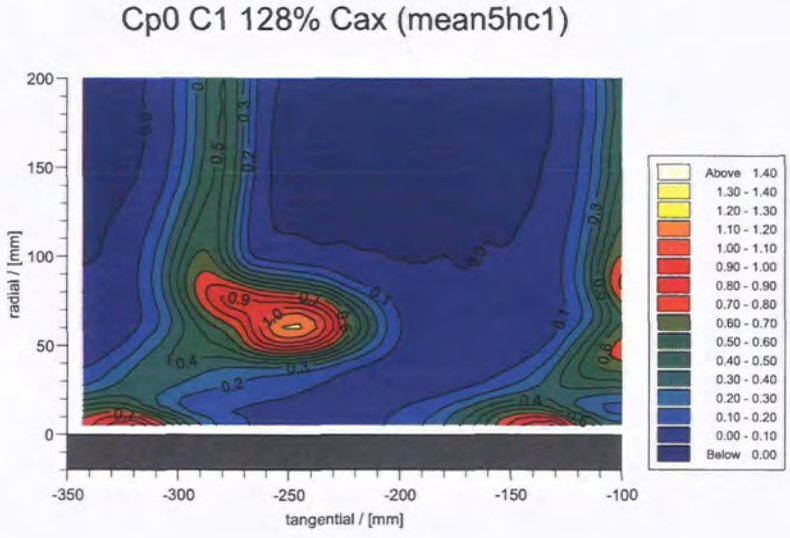

Figure 6.8: Expt. Reverse Compound Leaned - Area loss at 128% C_{ax}.

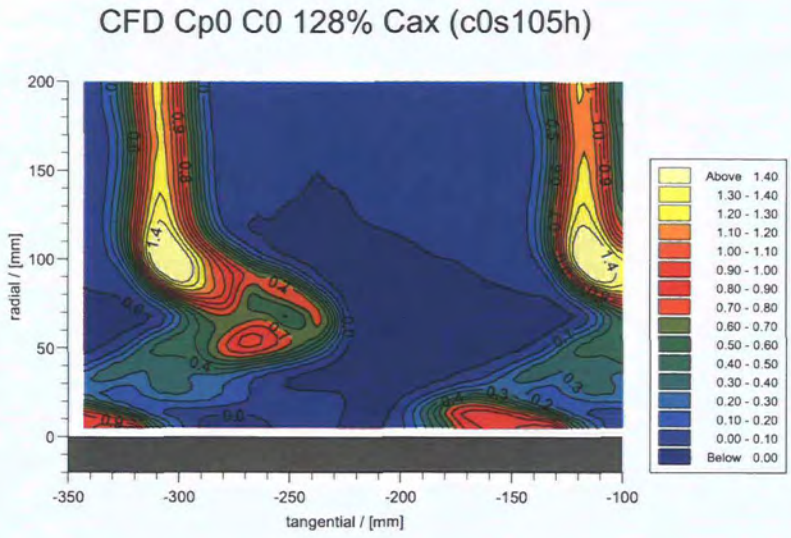

Figure 6.9: CFD Prismatic - Area loss at 128% C_{ax}.

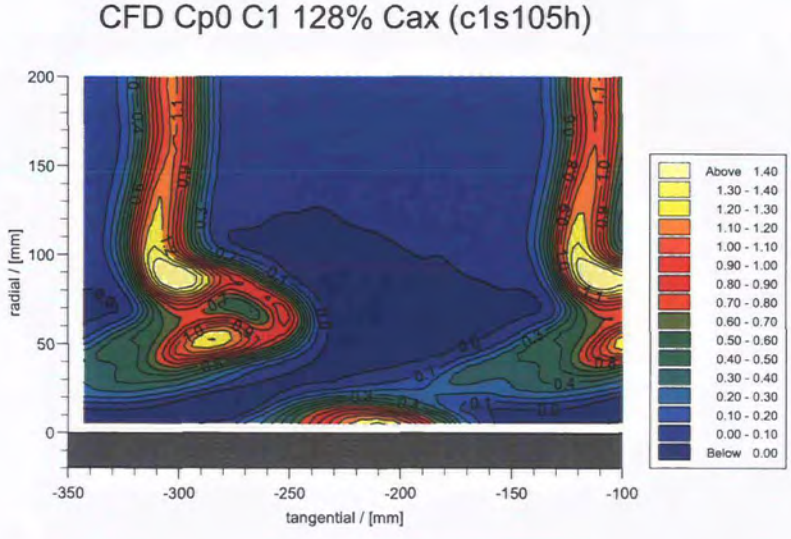

Figure 6.10: CFD Reverse Compound Leaned - Area loss at 128% C_{ax}.

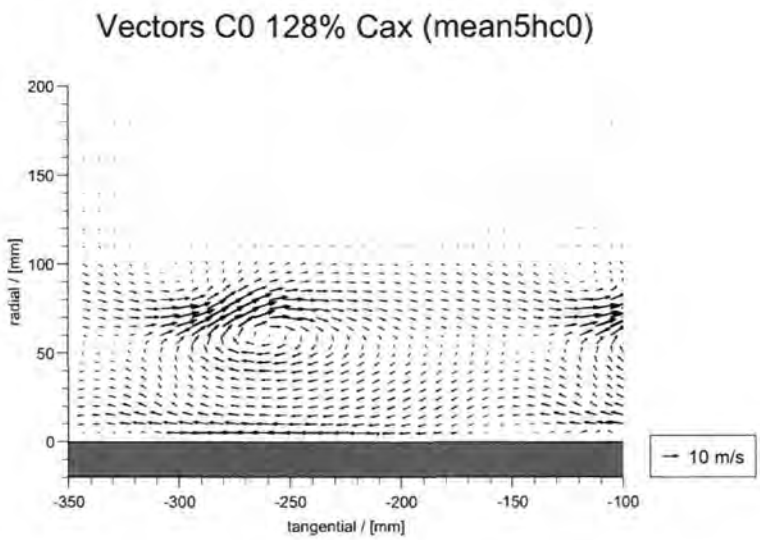

Figure 6.11: Expt. Prismatic - Vector plot at 128% C_{ax}.

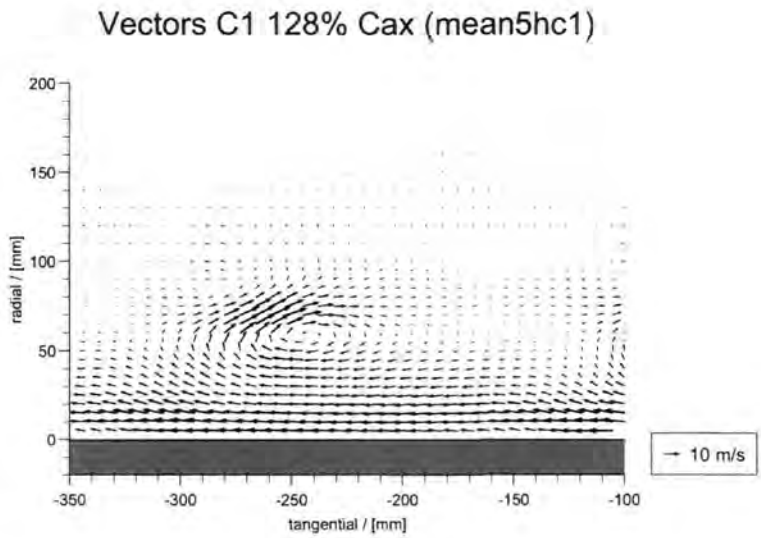

Figure 6.12: Expt. Reverse Compound Leaned - Vector plot at 128% C_{ax}.

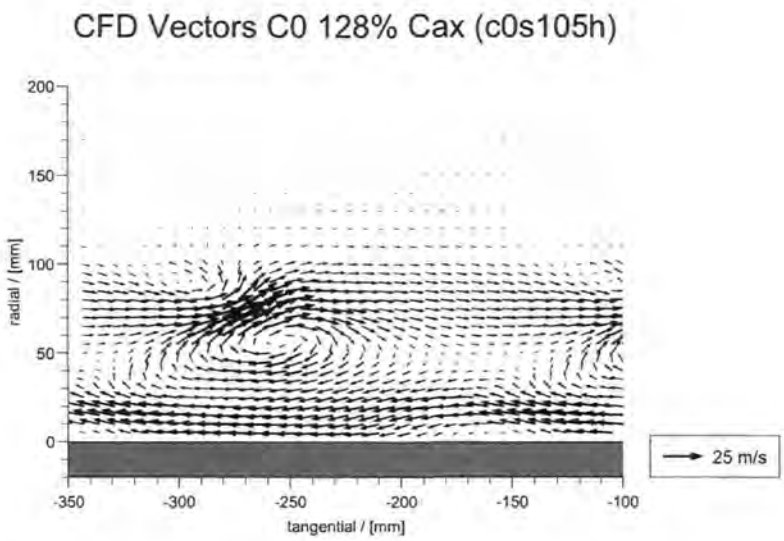

Figure 6.13: CFD Prismatic - Vector plot at 128% C_{ax}.

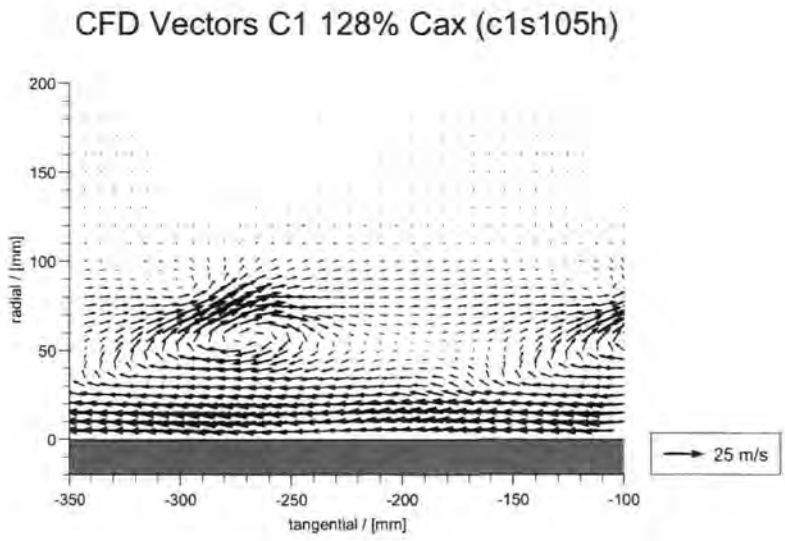

Figure 6.14: CFD Reverse Compound Leaned - Vector plot at 128% C_{ax}.

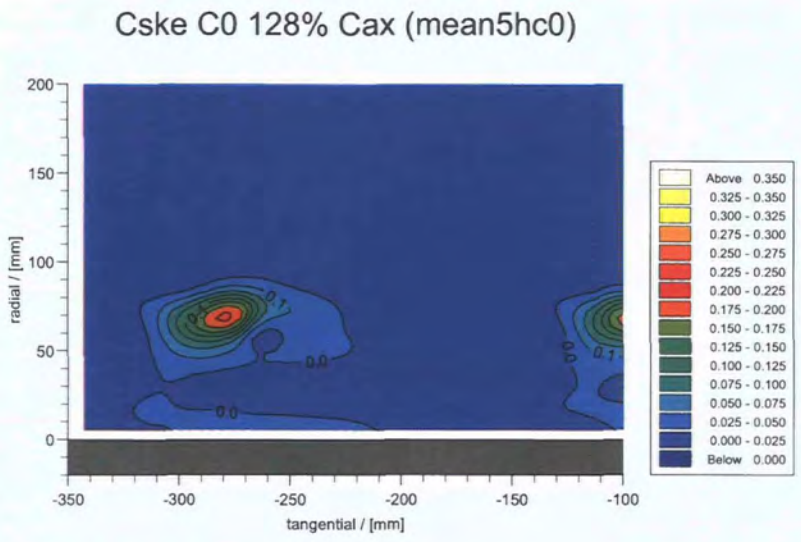

Figure 6.15: Expt. Prismatic - C_{SKE} at 128% C_{ax}.

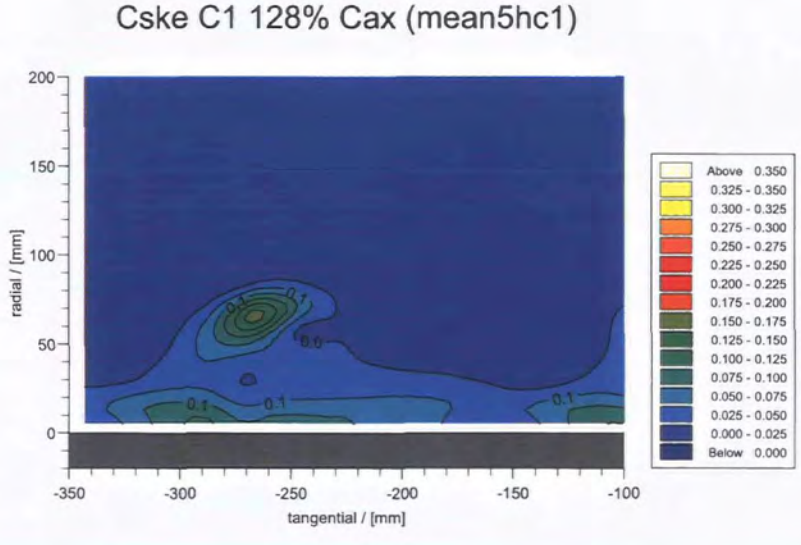

Figure 6.16: Expt. Reverse Compound Leaned - C_{SKE} at 128% C_{ax}.

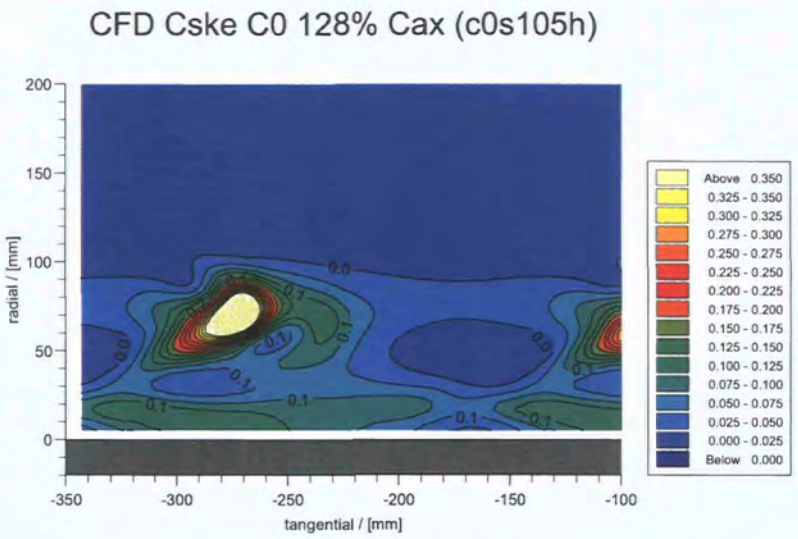

Figure 6.17: CFD Prismatic - C_{SKE} at 128% C_{ax}.

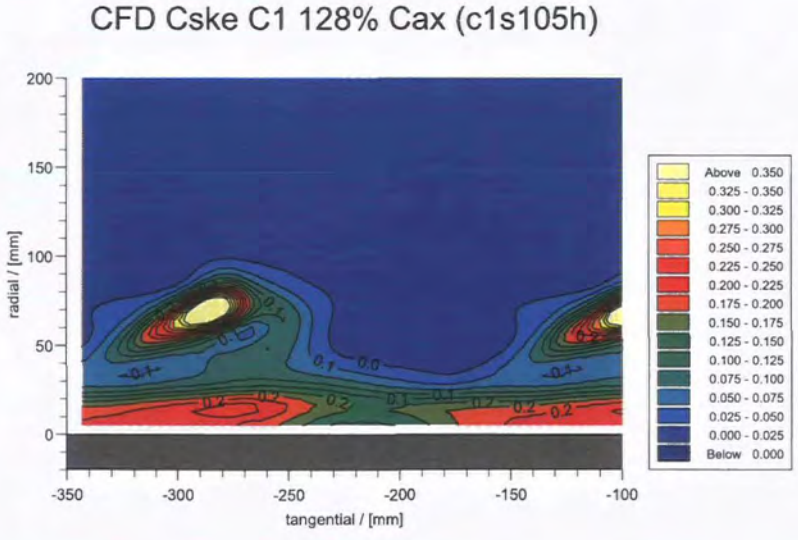

Figure 6.18: CFD Reverse Compound Leaned - C_{SKE} at 128% C_{ax}.

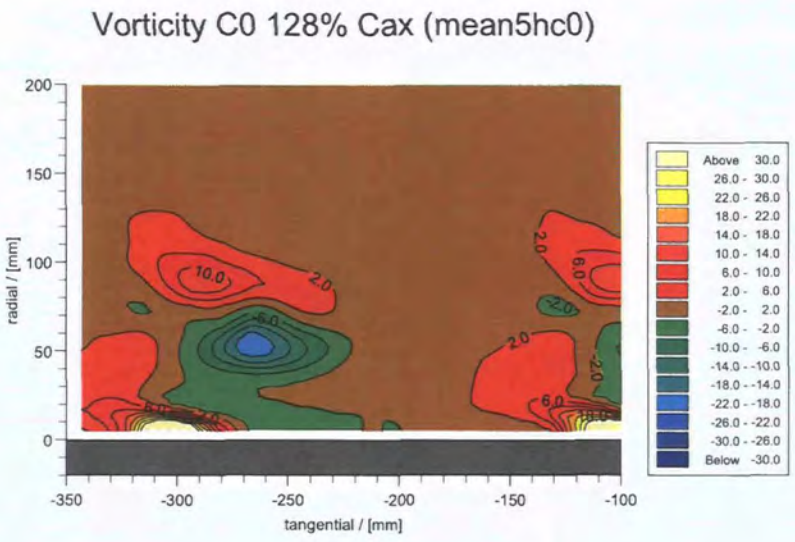

Figure 6.19: Expt. Prismatic - Vorticty plot at 128% C_{ax}.

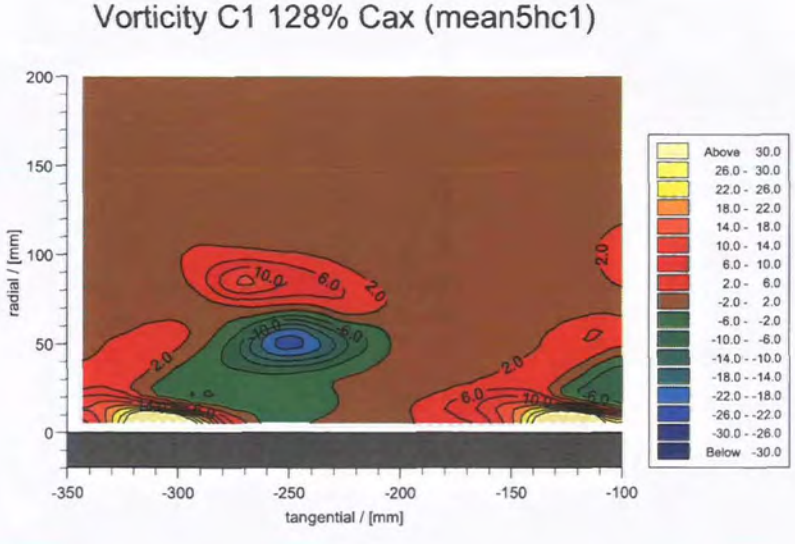

Figure 6.20: Expt. Reverse Compound Leaned - Vorticty plot at 128% C_{ax}.

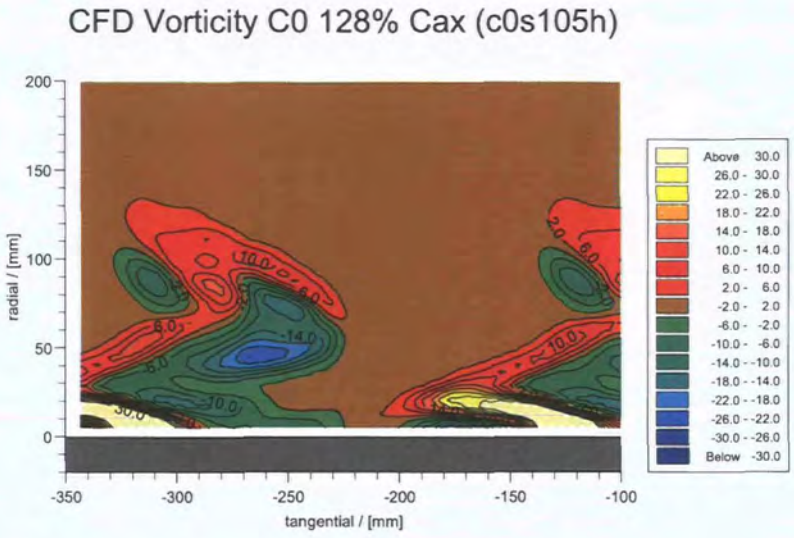

Figure 6.21: CFD Prismatic - Vorticty plot at 128% C_{ax}.

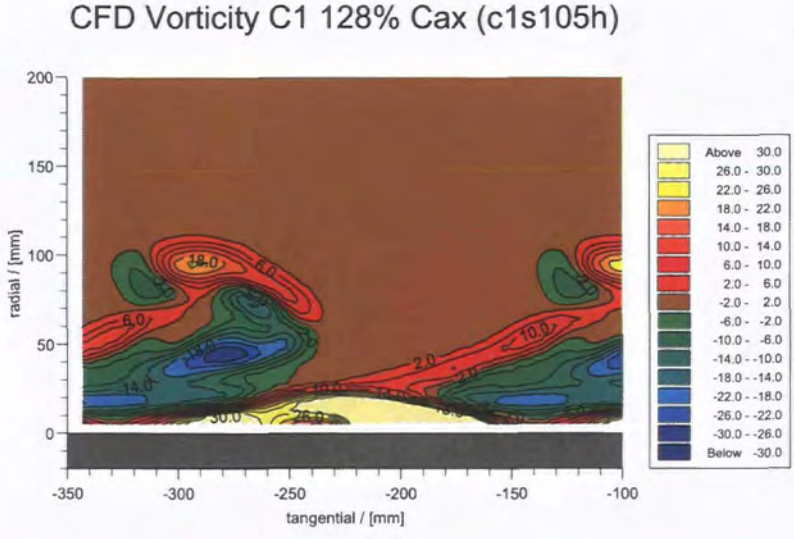

Figure 6.22: CFD Reverse Compound Leaned - Vorticty plot at 128% C_{ax}.

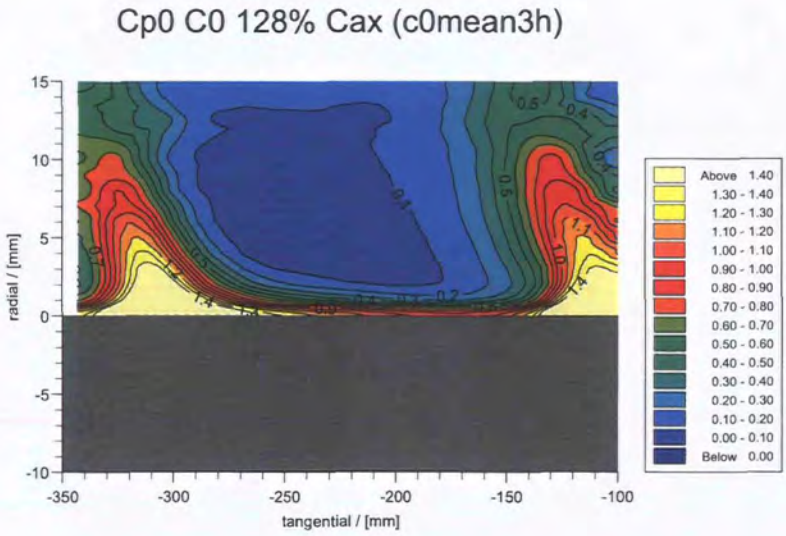

Figure 6.23: Expt. Prismatic - Area loss at 128% C_{ax}.

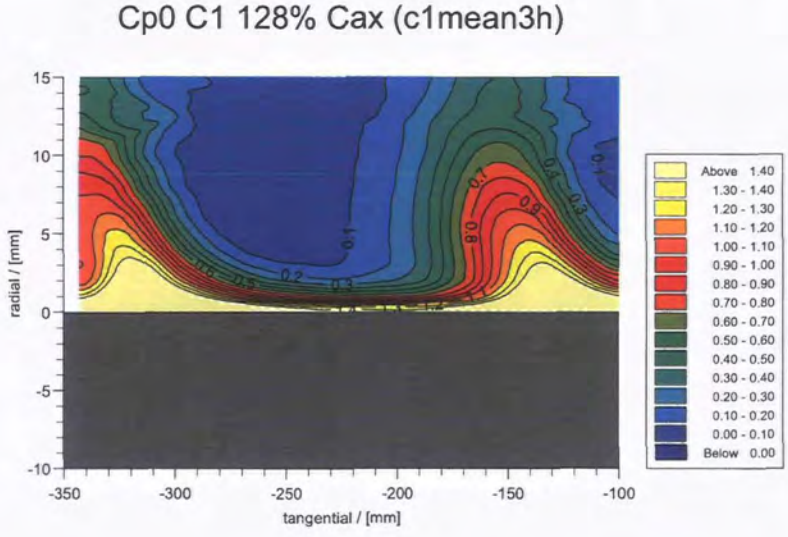

Figure 6.24: Expt. Reverse Compound Leaned - Area loss at 128% C_{ax}.

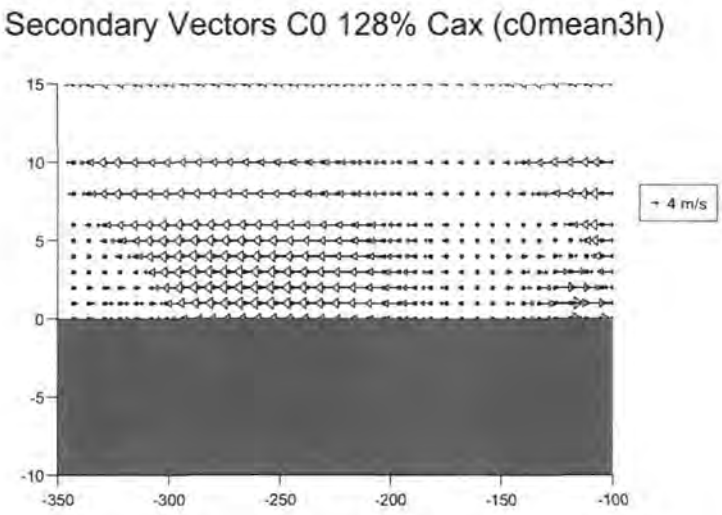

Figure 6.25: CFD Prismatic - Area loss at 128% C_{ax}.

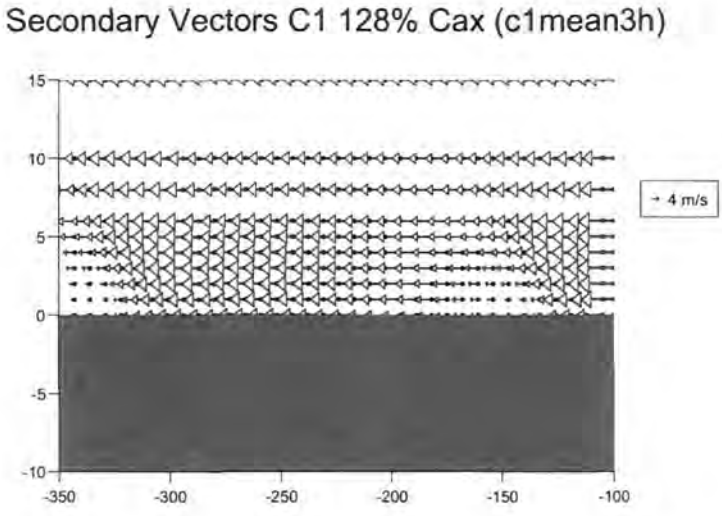

Figure 6.26: CFD Reverse Compound Leaned - Area loss at 128% C_{ax}.

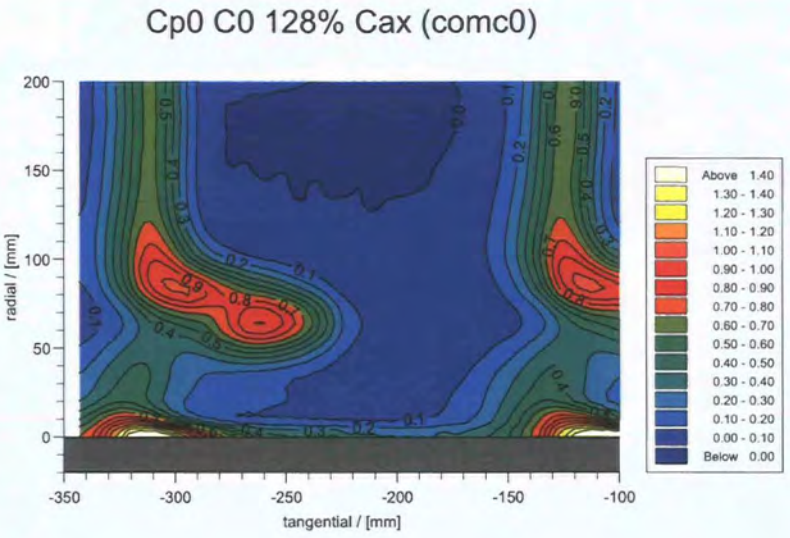

Figure 6.27: Combined 3h/5h dataset - Loss at 128% C_{ax} - C0

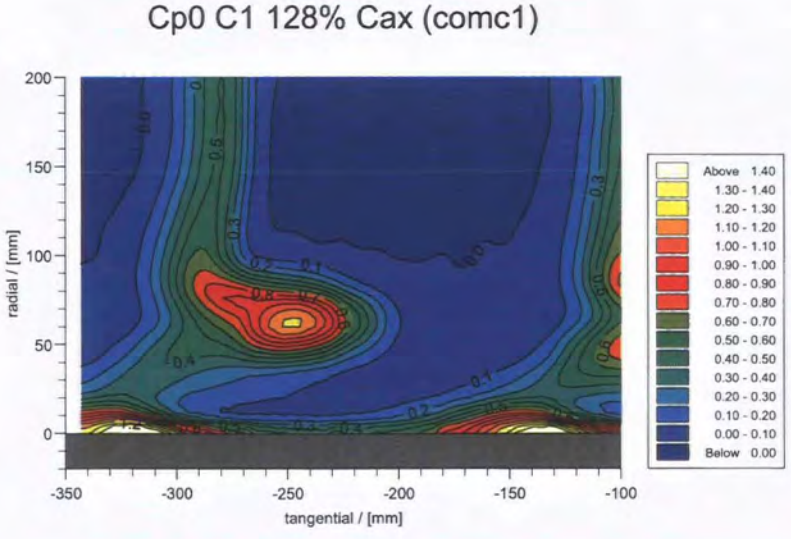

Figure 6.28: Combined 3h/5h dataset - Loss at 128% C_{ax} - C1

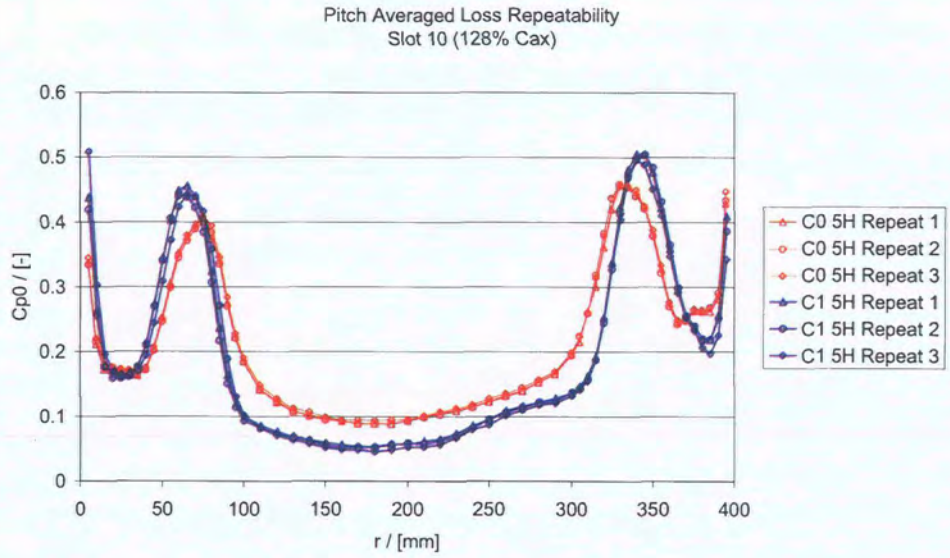

Figure 6.29: Repeatability of loss

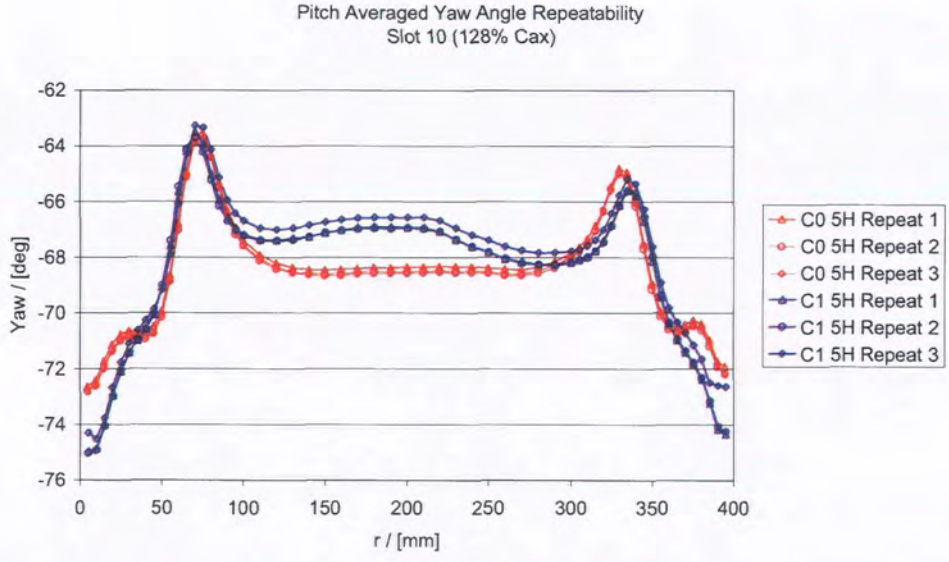

Figure 6.30: Repeatability of yaw angle

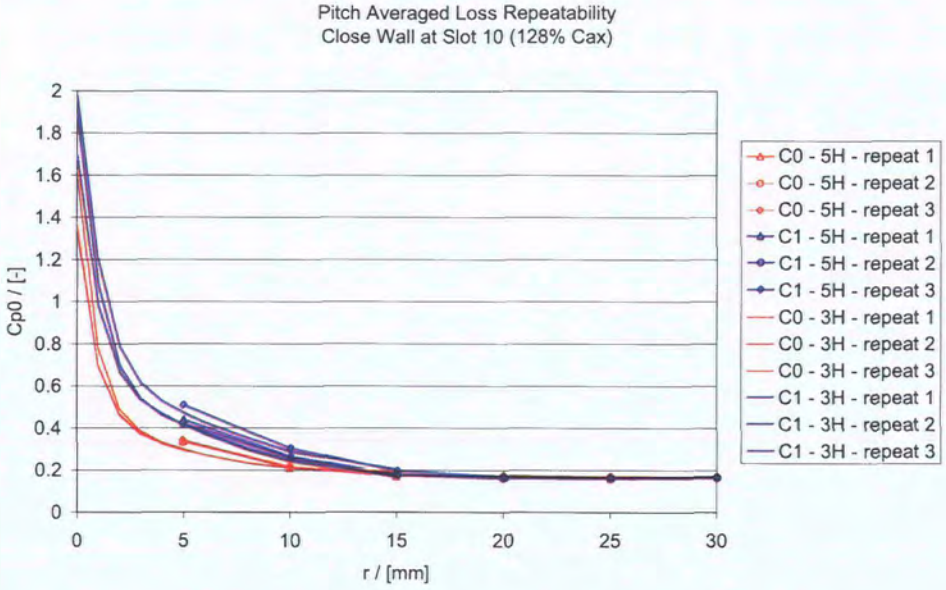

Figure 6.31: Repeatability of 3 hole loss

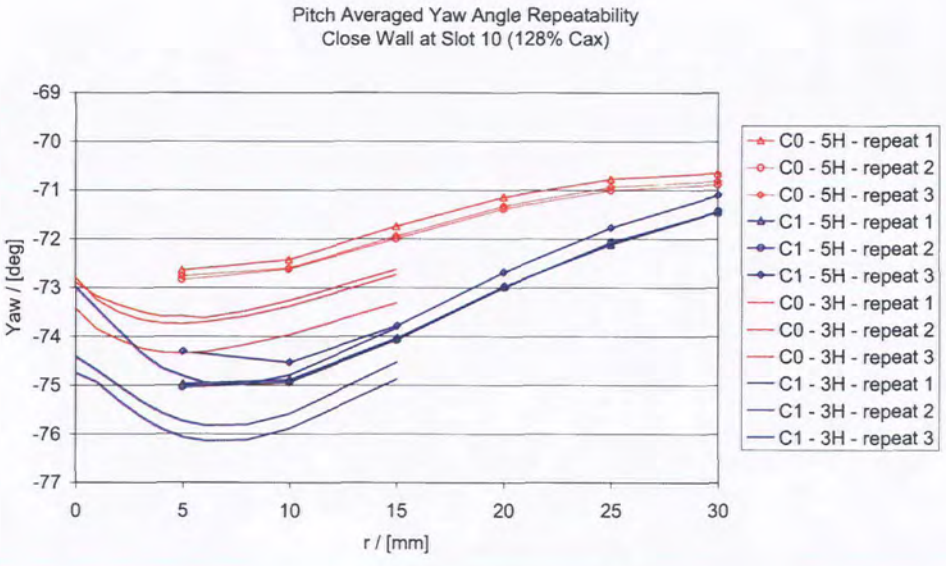

Figure 6.32: Repeatability of 3 hole yaw

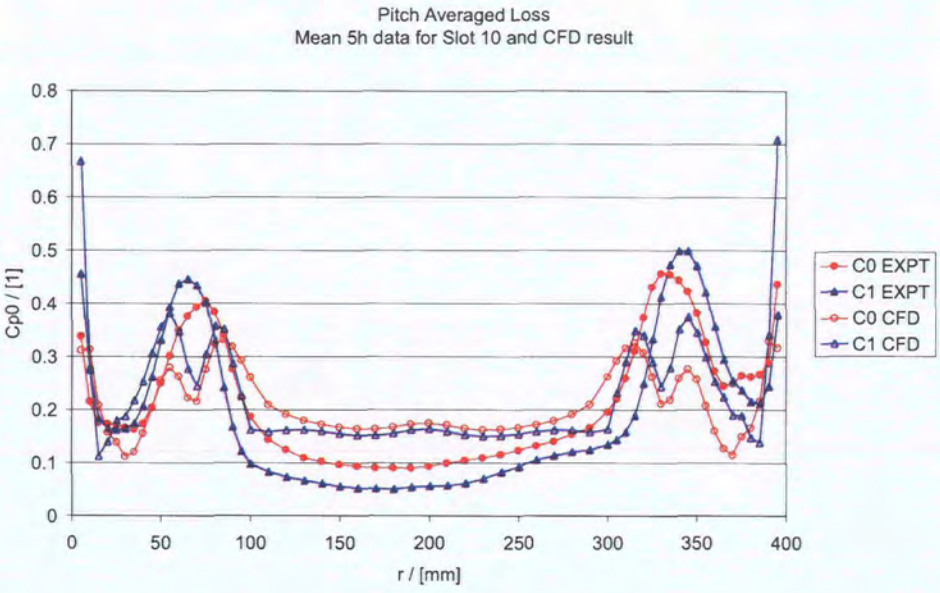

Figure 6.33: Pitchwise averaged loss

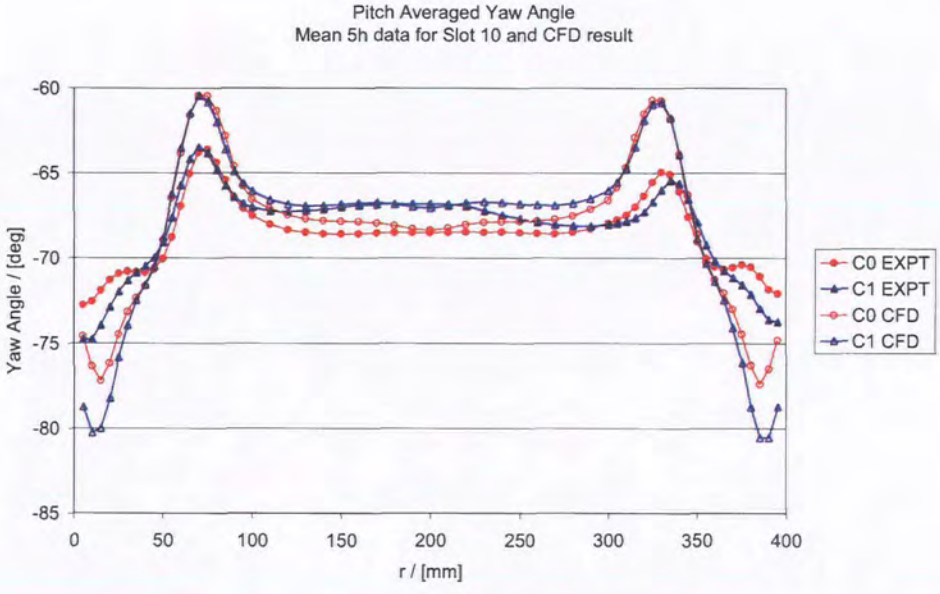

Figure 6.34: Pitchwise averaged yaw

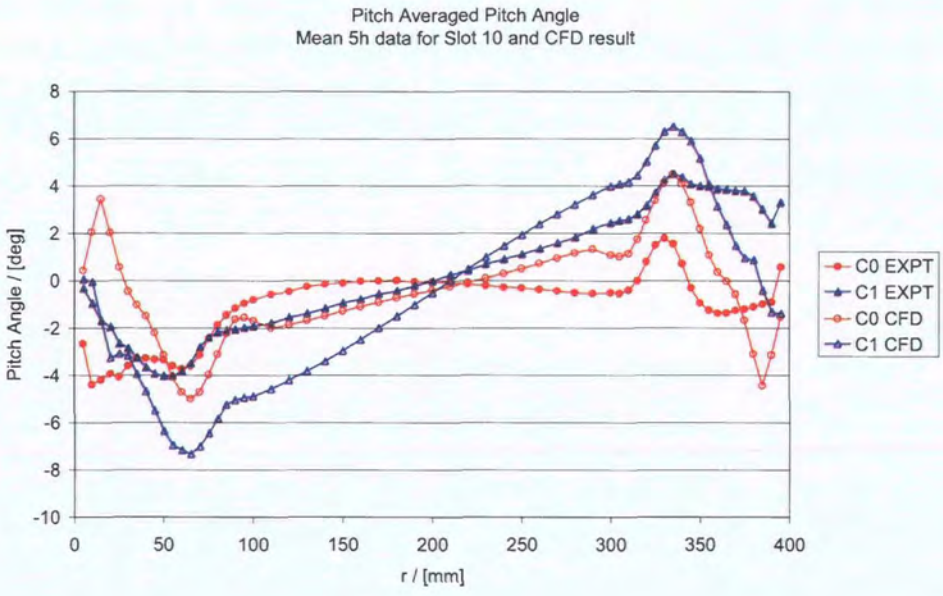

Figure 6.35: Pitchwise averaged pitch angle

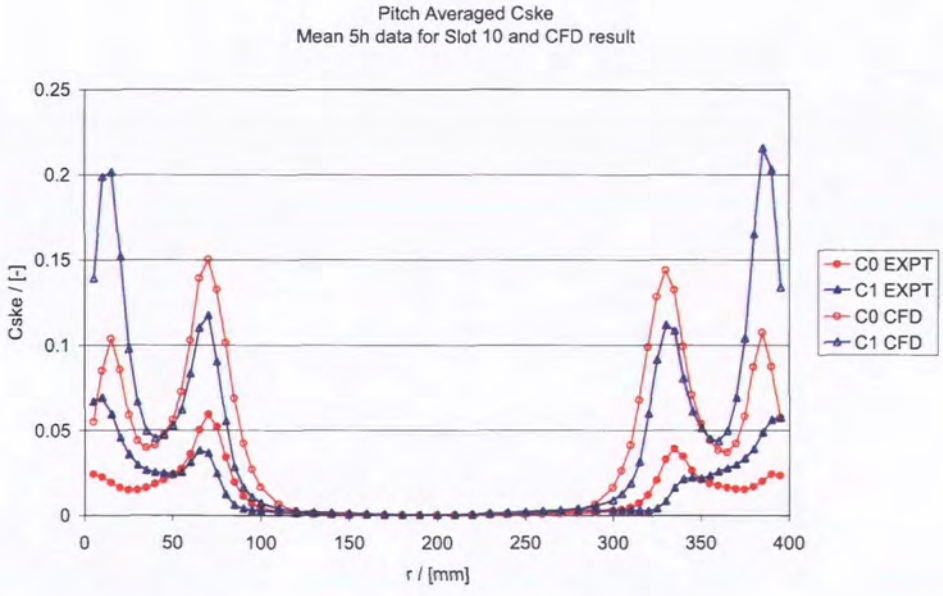

Figure 6.36: Pitchwise averaged C_{SKE}

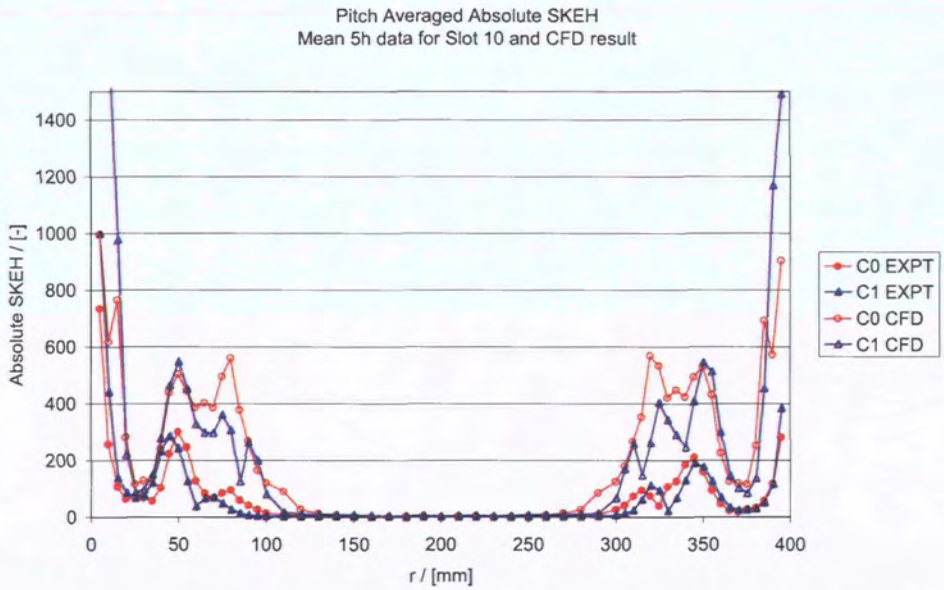

Figure 6.37: Pitchwise averaged SKEH

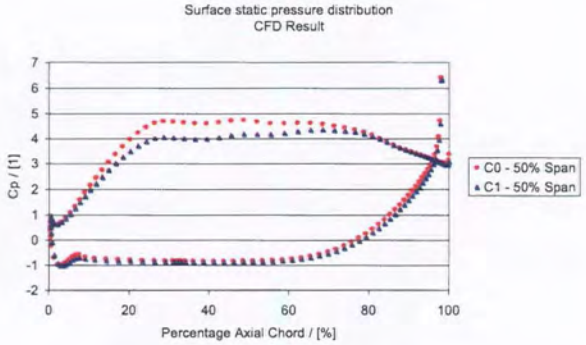

Figure 6.38: Surface static pressure distribution - 50% Span.

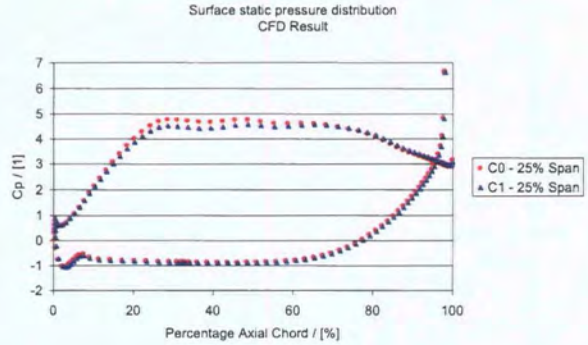

Figure 6.39: Surface static pressure distribution - 25% Span.

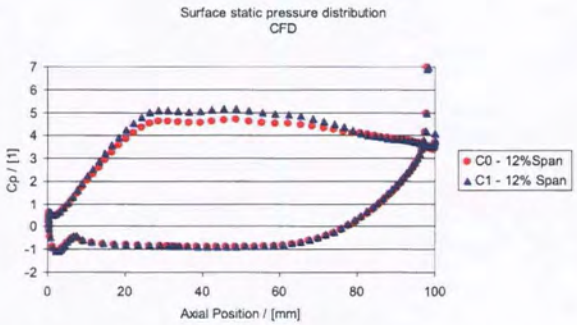

Figure 6.40: Surface static pressure distribution - 12% Span.

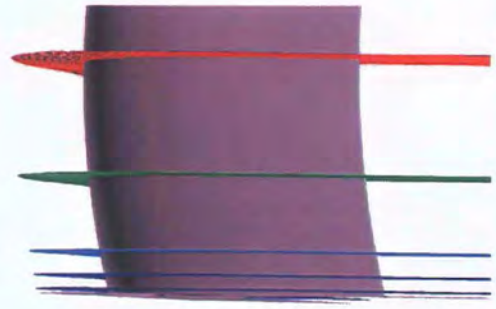

Figure 6.41: Pressure reading positions.

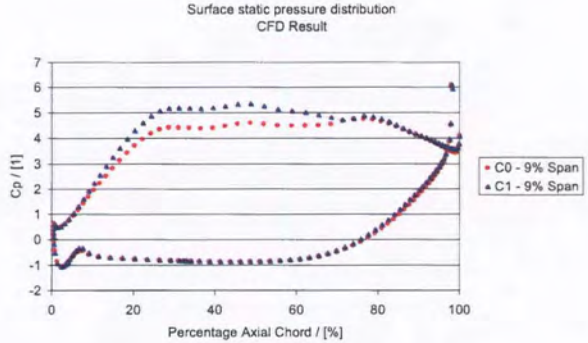

Figure 6.42: Surface static pressure distribution - 9% Span.

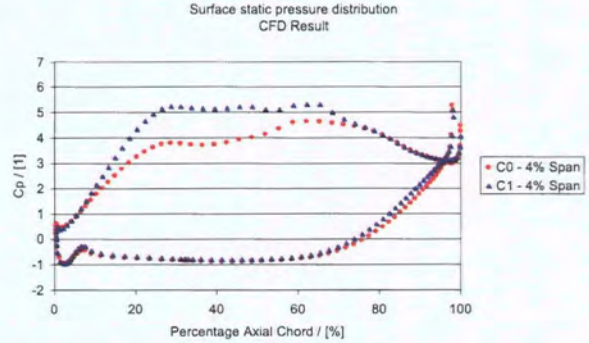

Figure 6.43: Surface static pressure distribution - 4% Span.

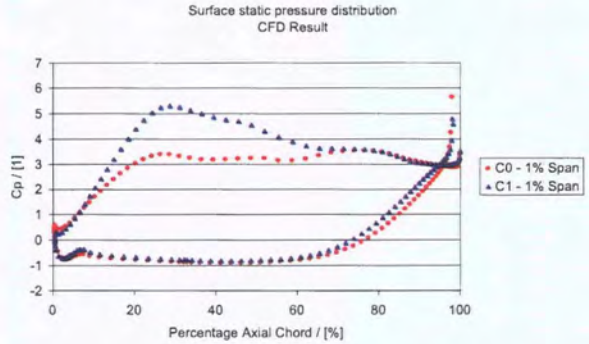

Figure 6.44: Surface static pressure distribution - 1% Span.

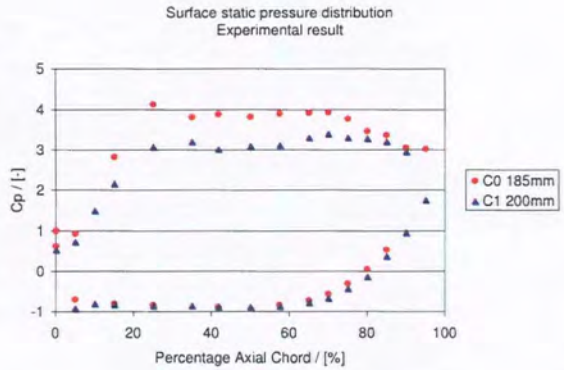

Figure 6.45: Surface static pressure distribution - approx. 50% Span

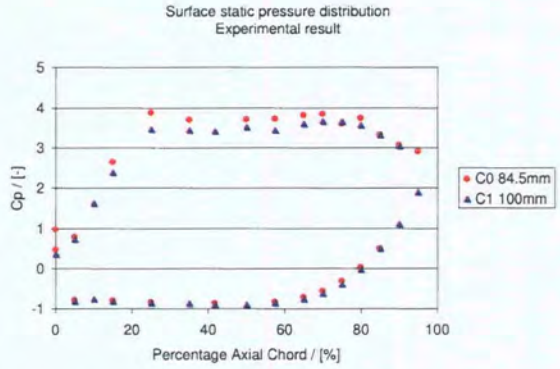

Figure 6.46: Surface static pressure distribution - approx. 25% Span

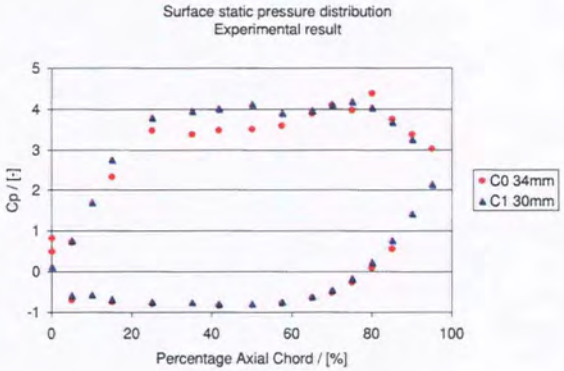

Figure 6.47: Surface static pressure distribution - approx. 7.5% Span

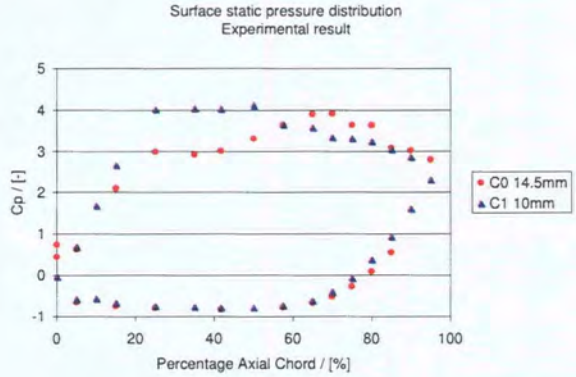

Figure 6.48: Surface static pressure distribution - approx. 5% Span

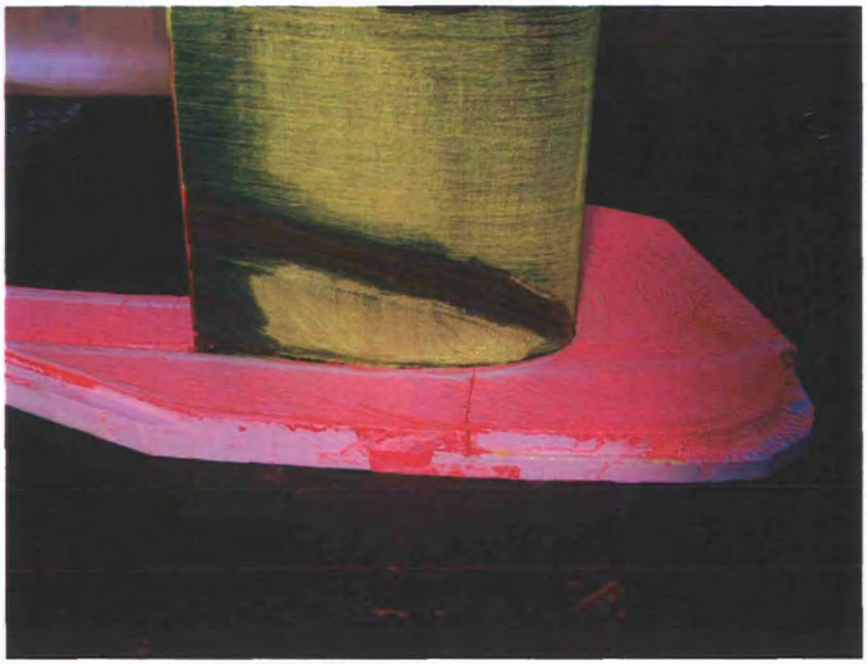

Figure 6.49: Flow visualisation - C0 Passage vortex growth

Figure 6.50: Flow visualisation - C1 Passage vortex growth

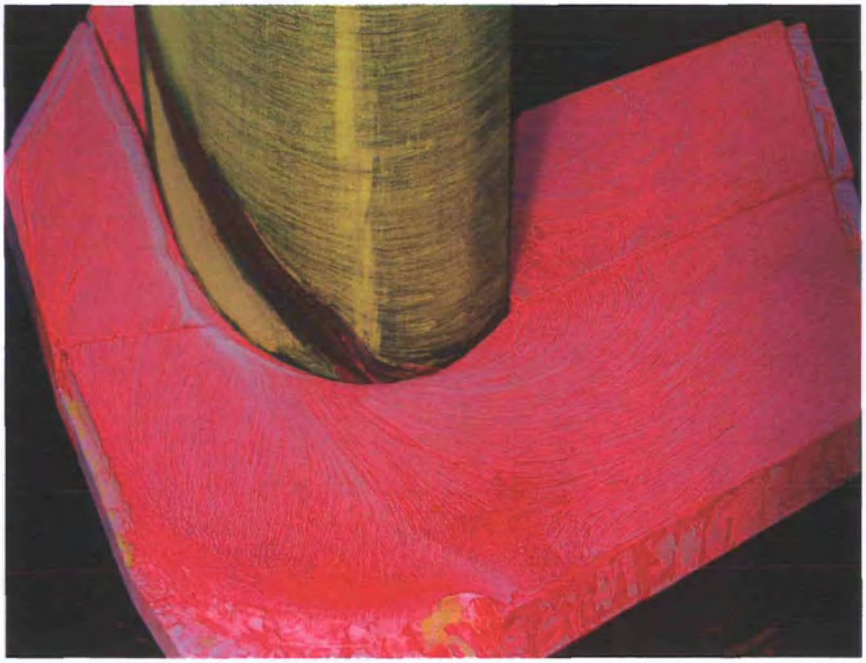

Figure 6.51: Flow visualisation - C0 Maximum curvature

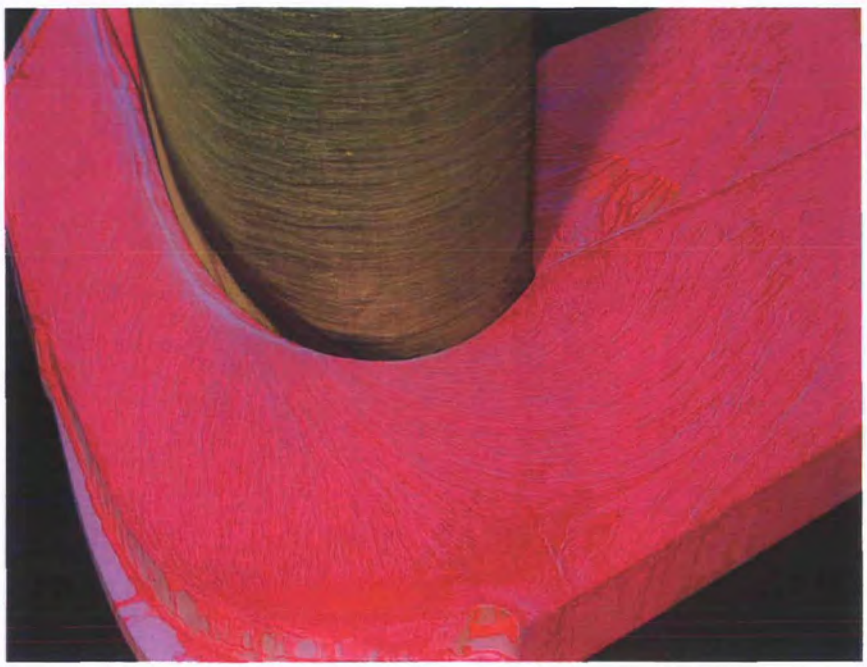

Figure 6.52: Flow visualisation - C1 Maximum curvature

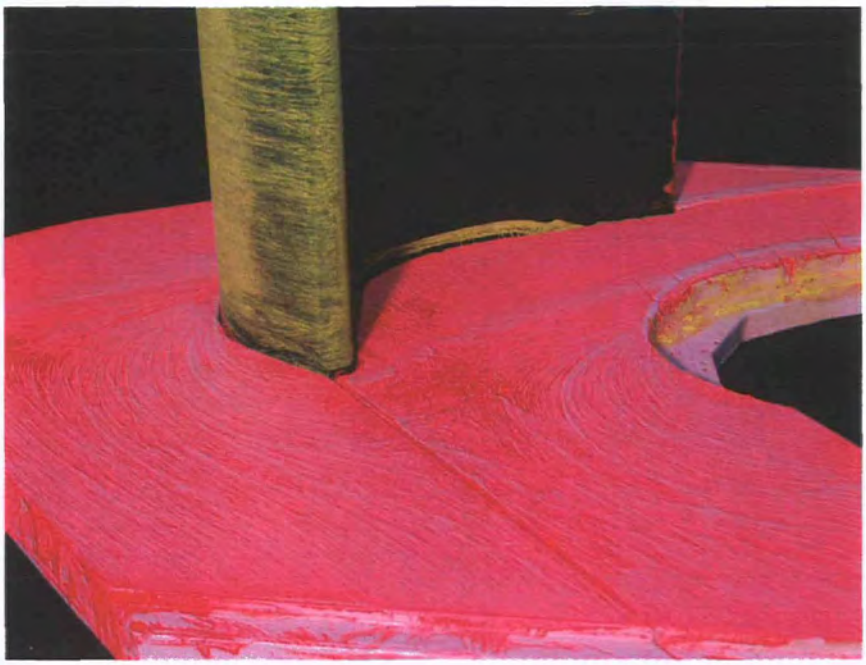

Figure 6.53: Flow visualisation - C0 Leading edge

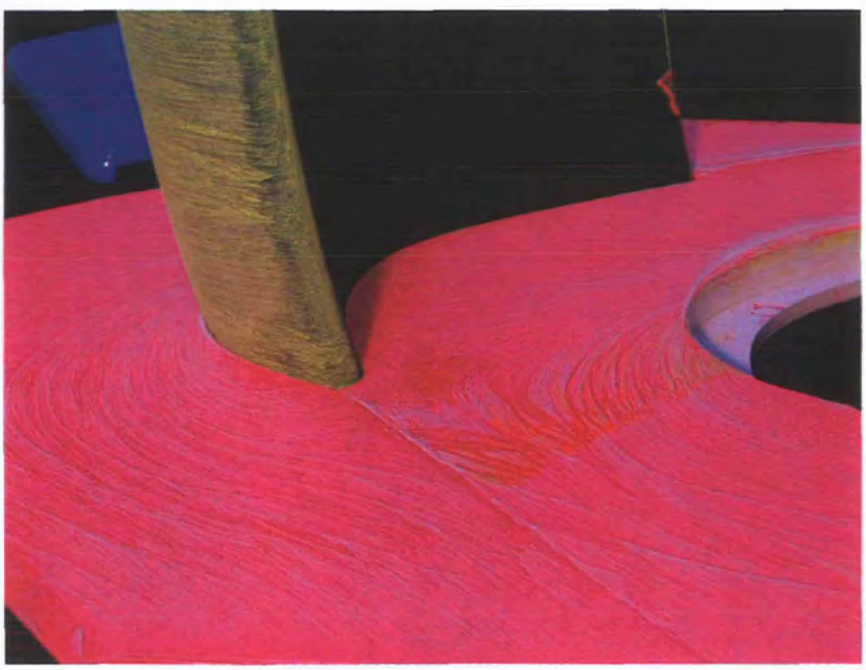

Figure 6.54: Flow visualisation - C1 Leading edge

Chapter 7

Passage Shaped C2 - Design

THIS chapter details the design development and accompanying computational investigations, of the first passage shaped turbine geometry for the cascade. The chapter examines simple axial lean, leading edge extension, and a combination of these geometries with the reverse compound lean. The final aerofoil design is combined with non-axisymmetric endwall profiling, similar to that described in Chapter 5.

7.1 Introduction

A limiting factor in endwall profiling design is the resulting acceleration and diffusion in the leading-edge/suction-surface region. High levels of diffusion caused by the convex-concave endwall geometry, lead to separations in the most extreme designs, as found by Ingram et al. (2005). Such boundary layer separations generate losses that negate the benefit of PEWs.

The use of reverse compound lean, as per geometry C1 in Chapter 6, significantly increases the endwall loading, particularly in the front of the suction surface. Thus any combination of reverse compound lean with profiled endwalls is restrictive. As described in the literature review, local axial lean or forward sweep can be used to offload the forward region of the aerofoil near the endwall. This offloading can prepare a blade section for combination with endwall profiling.

The following computational design studies investigate the potential of these theoretical arguments, in a highly loaded turbine component.

The design work, the results of which are presented herein, was undertaken on the Rolls-Royce in-house design system. Where possible the design processes follow those of an engine component. Due to the nature of designing a linear cascade within an annulus based design system, some modifications have been made. This includes the specification of the aerofoil at a very high radius to approximate the rectilinear cascade arrangement.

7.2 Definitions

The terminology of blade sweep and dihedral originates in compressor and fan technology. True sweep is defined as the translation of blade sections in the direction of

the chord line. For reference, true dihedral is defined as movement perpendicular to the chord line. A comparison of the terminology for compressor and turbine profile stacking is given in Figure 7.10. In the following studies, the blade sections are altered purely in the axial direction, these geometrical changes are referred to as axial stacking.

7.3 Computations

The following studies were all undertaken using the Navier-Stokes Solver, MEFP . Details of the solver were given in Chapter 3, including typical mesh sizes, turbulence modelling and boundary conditions.

7.3.1 Analysis

Due to the large number of design permutations involved, the analysis of the results was initially kept simple. The analysis was based on mass averaged values of total pressure loss, SKE.H and yaw angle at the exit of the computational domain. The computational total pressure loss values are normalised by the exit dynamic head, as opposed to the experimental loss values where the inlet dynamic head is used.

Later studies include additional analyses of pitchwise averaged distributions and surface static pressure distributions. In these cases the mass averaged exit values remain the key design criteria.

7.3.2 Design Stages

The design is split into a series of studies, over which the concepts were refined. Initially, pure axial stacking (axial displacement of existing 2D S1-plane sections) was investigated, the results from this are in Section 7.4.

In Section 7.5 chord extension by near-endwall modification was considered and a number of designs were investigated. The designs involved modification of the existing blade profile and a number of rules were set out, to limit the impact of these changes on the original intent.

A third study, in Section 7.6 used the successful near-endwall modifications in various combinations with a reverse compound lean to investigate the compatibility. From this study the final geometry was chosen.

Section 7.7 describes the semi automated endwall design process. The resulting endwall shapes and impact on the performance are described here.

7.4 Study 1 - Axial stacking line investigations

The work contained within this section involves axial lean. The geometries use mathematical stacking line definitions to generate a compound axial lean where the leading edge is forward of the midspan. The designs are symmetrical about the midspan and only the lower half of the computational model is presented. The axial lean geometries are generated by displacing the 2D sections axially.

7.4.1 Stacking geometries

Two stacking line styles were investigated; these are based on elliptical and power law equations. Three variants were studied for each stacking style with an axial displacement at midspan of 10, 20 and 30% C_{ax}. The elliptical profiles are based on Equations 7.1 and 7.3, the power law profiles are based on equations 7.2 and 7.3. All stacking lines produce a blade with the endwall sections forward of the midspan section.

$$x_{elliptical} = \sqrt{a^2 - \frac{a^2(r_{midspan} - r)^2}{b^2}} \tag{7.1}$$

$$x_{power} = \frac{|r_(midspan) - r^a}{b} \tag{7.2}$$

$$\theta = \arctan \frac{\delta x}{\delta r} \tag{7.3}$$

The angle θ, at radial position $r = 0$, (calculated in Equation 7.3) defines the tangent to the stacking line at the endwall (where r is 0). $\frac{\delta x}{\delta r}$ is the local gradient of the axial displacement (x) of the aerofoil stacking line. A series of angles, one for each radial coordinate, defines the curvature of the axial displacement stacking line and is used for input into the blade stacking program.

The three elliptical and three power-law stacking line shapes are illustrated in Figure 7.11. It is clear from the figure, that the power law geometries have very large inclination angles (relative to radial) at the endwall, and that these shapes are possibly too severe to be suitable for blade manufacture. Also of note from the figure, are the displacement distances of the midspan section of the stacking line, i.e. the maximum displacement. The elliptical and power law profiles are stacked to the same axial displacement, to allow direct comparisons to be made. The wall inclination angles (θ) for the 10% power law and the 30% elliptical stacks are quite similar too, and as such another comparison can be made here.

The elliptical stacking lines are gradual and modifications to the profile are observable up to 40% span. The power law stacking lines are more severe at the endwall, with the profile shape returning to the datum at a relatively low radius.

The geometries are defined by constants 'a' and 'b', but are compared using the endwall inclination angle and the midspan deflection as a percentage of the axial chord. The inclination angle and midspan deflection values are documented in Table 7.1 for each stacking line examined.

Type	Eqn used	Inclination angle [deg]	Midspan Defln [% C_{ax}]
Elliptical	1+3	11	10
Elliptical	1+3	21.3	20
Elliptical	1+3	30.3	30
Power Law	2+3	34	10
Power Law	2+3	53.5	20
Power Law	2+3	63.75	30

Table 7.1: Elliptical and power law stacking geometries

7.4.2 Mass Averaged Results

For each case the same computational mesh and inlet conditions were used, and the solution was run to convergence. The results were mass averaged from the exit of the computational domain, at 178% C_{ax}. The geometries are compared using loss, SKE.H and yaw angle. All results, except yaw angles, are presented as a percentage of the prismatic geometry.

The results are labelled 10% - 30% Ellip and 10% - 30% Power for the six cases.

Massflow and Yaw Angle

The small changes in mass averaged massflow (±0.5%) in Figure 7.13 and the small variation in exit yaw angle in Figure 7.14 indicate that the designs maintain performance.

Loss

The result in Figure 7.15 shows the total pressure losses of both stacking styles. The loss increases for all shapes up to a displacement of 20% C_{ax} but drops back again at 30% C_{ax} displacement, resulting in a slight reduction of loss for the 30% power law. The values indicate a generally reduced performance for lean on this geometry. Whilst this is not a good result, it is not immediately discounted due to the positive SKEH result.

SKE.H

The result in Figure 7.16 shows a clear reduction in SKEH with increasing axial lean extent. Both the elliptical and power law geometries behave similarly. The magnitudes of the SKEH reduction are similar for the two geometric styles (for both 20% and 30% displacements). This similarity indicates that the key parameter is the displacement, and the local angle is less significant in the SKEH reduction.

The SKE.H result in Figure 7.16 indicates a reduction of 45% for both stacking styles with 30% C_{ax} displacement. The differences noted between elliptical and power law axial stacking lines, are thought to be an effect of the local inclination angle at the endwalls.

7.4.3 Pitchwise averaged Results

The results discussed below are the pitchwise averaged distributions at 128% axial chord. The results discussed are primarily those of the elliptical axial stacking line, additional comments are made for power law stacking profiles where differences exist. The data for the pitchwise averaged analysis described here were overlaid and printed in hardcopy during secondment to Rolls-Royce. The assessment of the results presented here was recorded, but both the electronic data and the original print-outs have been lost. The assessment of results is included here to provide some additional insight.

Loss

The use of axial stacking shifts the loss cores towards the endwalls and reduces the strength of the loss core at 20% span. This is the region associated with the suction surface horseshoe vortex. The stacking increases the strength of the loss core at 10-15% span, associated with the passage vortex and increases the loss in the near wall overturned region.

SKE.H

The stacking reduces the magnitude of SKEH peaks for the designs with 10% and 20% axial chord extension, but increases them again for 30% axial chord. This is the reverse effect to total pressure loss. The stacking increases the SKEH values in the near wall region, but the increases are comparatively small. It also shifts the main SKEH peaks towards the wall.

Massflow

The massflow downstream is affected by a redistribution. The massflow in the 0-10% region is reduced as the flow moves radially outward. The massflow in the midspan region increases for the same reason. The forward leaned leading edge causes the massflow to shift radially inward. This effect is seen in swept blade profiles and exists until the trailing edge where a redistribution occurs. Axial stacking reduces the massflow in 0-10% region, this effect is associated with a redistribution of flow downstream at the trailing edge. The power law profile shows a greater strength of these effects

Yaw angle

The midspan turning is reduced by 1^o and the overturning increases by 5^o for 30% C_{ax} deflection. The reduction in turning is related to the redistribution outside of the influence of the leaned aerofoil as observed downstream of the C1 geometry in Chapter 6. The underturning levels are not affected, but the under turned area is moved radially inwards. The power law profiles behave as per the elliptical profiles, but with up to 8^o overturning at the endwall and increased underturning.

Surface static pressure

Blade loading distributions are investigated using surface static pressure values at a series of radial positions (computational K planes).

At the endwall and 3% span (K planes 2,10) the results show a weakening of the double peak loading distribution in near wall region, an offloading of front section on the suction surface in line with expectations, but no real change to aft section (last 50mm of axial chord). There is also increased loading of the mid chord suction surface, as a consequence of the offloading. There is no change to the loading levels or their distribution at midspan.

7.4.4 Summary

The use of axially leaned geometries has reduced the mass averaged SKEH by up to 45%, this compares with a 50% reduction for reverse compound lean. In general the axial lean geometries affect the flow by offloading the front of the blade at the endwall section, thereby reducing the cross passage pressure gradient, reducing the potential for secondary flows.

The power-law geometries have a similar effect to elliptical geometries indicating that the major influence is the overall displacement and not the angle of inclination.

These results highlight the potential of axial sweep in preparing an aerofoil for the application of PEWs.

7.4.5 Combining with reverse compound lean

Attempts to combine axial profile stacking with existing tangential lean proved unsuccessful. The design resulted in high loss and high SKEH values. The combination of axial and tangential stacking causes unconventional blade surface curvatures, which increase diffusion and the possibility of separation. The resulting suction surface concave geometry, seen in Figure 7.17, is thought to encourage the low momentum endwall flows to migrate radially outwards, thereby advancing the mixing of secondary flow structures with the primary flow. The exact details of the effect were not investigated, as the reduced performance was sufficient to dissuade further investigation.

7.5 Study 2 Near endwall modifications

7.5.1 Motivation

Denton and Xu (1999) suggest that axial lean by chord extension in the near endwall region can be used to create a similar geometric shape and flow structure modifications as simple axial stacking. Chord extension enables the trailing edge region to remain unaffected. The computational result in Figure 7.18, by Denton and Xu (1999), demonstrates chord extension in a compressor blade geometry. The figure indicates a clear offloading of the extended section of the aerofoil.

To enable a specific sweep at both endwalls the blade can be modified by a mathematical profile that is symmetrical about the midspan.

For an aerofoil with even a moderate inlet angle, the extension of the blade in a purely axial sense may cause strong local curvature. To alleviate this, the modifications may be made in the direction of the camber line.

7.5.2 Axial Chord Extension

This study examined the modification of the blade profiles in the near endwall section, to obtain geometries similar to axial stacking, whilst maintaining a straight trailing edge.

Initially a simple change was made to the length of the near endwall section. The section was extended purely axially upstream, to give 110% of the original chord length. This blade section was not redesigned aerodynamically after stretching. The section was merged with the original geometry at 30% span. The resultant geometry had a strong localised positive compound lean close to the endwall. This leaned shape appeared to draw the secondary flows away from the endwall and increased the secondary kinetic energy and the loss generation within the bladerow. The geometry produced:

- Higher SKEH peaks that were situated further radially outward toward the midspan
- Similarly shifted and increased magnitude loss peaks
- Reduced overturning at the endwalls. Similar underturning but shifted radially inwards

The surface static pressures indicate:

- Considerable off loading in the front section of the suction surface at near wall spans, whilst the remainder of the aerofoil had the same level of loading.

7.5.3 Two Dimensional Section Design Criteria

From this it is clear that simple axial extension does not reduce loss or SKEH and more detailed design work is required. A second iteration of the axial chord extension was considered. The aerofoil geometry was controlled in order to avoid the

poor performances observed earlier. The key requirement of this upgraded design, was the avoidadnce of SS concavity.

With this in mind, a series of aerofoil section designs were analysed; each with the same level of chord extension. For each of the geometries investigated, the same midspan shape was maintained and a radial stacking line was used, there was no lean or sweep component. The following guidelines, highlighted in Figure 7.19, were drawn up for 2D section design purposes.

Geometric

- Maintain the trailing edge wedge angle, thickness and exit metal angle. These were considered critical, as they ensure the same overall turning and therefore duty of the design
- Maintain the original suction surface geometry as far as possible. This criterion avoids the creation of strong suction surface radial curvatures. It also ensures that the modifications are limited to the region local to the extension
- Modify the position of leading edge to give the required axial chord extension. This was controlled through the axial shift of leading edge circle centre
- Shift the leading edge circle centre tangentially to coincide with line of original inlet metal angle. Where the overall loading of the aerofoil is maintained (circulation remains unaltered), this will maintain similar incidence angles up the leading edge
- Allow the pressure surface to spline fit to the new geometry. This was included to improve the pressure surface curvature and reduce the possibility of a pressure surface separation

Aerodynamic

- Where possible maintain the existing flat topped lift distribution, similar to the midspan design. This constraint is secondary to the geometric design constraints
- Avoid large diffusions

7.5.4 Generation of 3D geometries

The generation of a three dimensional geometry was undertaken as follows.

1. Decide on a suitable near wall profile design based on the criteria above. Designs were assessed in an Euler based S1-plane (blade-to-blade) solver. This provided information on the local blade loadings and diffusion levels.
2. Choose the radial extent over which the merging takes place and number of stream surfaces required in the midspan section to control this.
3. Use the profile stacking program to generate a stacking line and thus a NURBS surface definition.

4. Intersect the streamlines from the throughflow calculation with the new geometry to create profiles at 21 separate heights.

5. Check the generated profiles for diffusion and check the NURBS surface for anomalies.

Radial merging extent

The radial extent of the thickened near wall profiles was limited by the number of midspan sections used. The NURBS surface geometry is controlled by the blade profile sections given to the stacking software. If a radially restricted design is required, the midspan geometry is copied to stream sections closer to the endwall.

Axial extension limits

The limits of possible axial extension of the profile were set at 10% axial chord. This value was decided upon due to the design restrictions in a real machine, caused by the blade platform geometry.

Geometries

The following are the geometrical differences in the EWM designs. All geometries have the same 10% axial chord extension of the aerofoil at the endwall, but differing radial extent and section thickness. The sections are also presented in Figure 7.1. The EWM designs are wholly aerofoil based modifications and are not to be confused with endwall profiling (PEW) designs.

- EWM1 - extended profile design, filled-in pressure surface, smoothed to 30% span
- EWM2 - the same as EWM1 but smoothed to 20% span
- EWM3 - modified EWM1 profile, also to 30% span
- EWM4 - cut back pressure surface design to 30% span
- EWM5 - partial cut back pressure surface design to 30% span

EWM6 has a reduced chord (90% of the midspan value) at the endwall. The modified section was designed using the same constraints as far as possible.

Designs EWM3, EWM4 and EWM5 are not covered in the following discussions for brevity. The results were not significantly different from those of designs EWM1 and EWM2.

7.5.5 Mass Averaged

The following section details the mass-averaged data taken at the exit of the computational domain, equivalent to 178% C_{ax}.

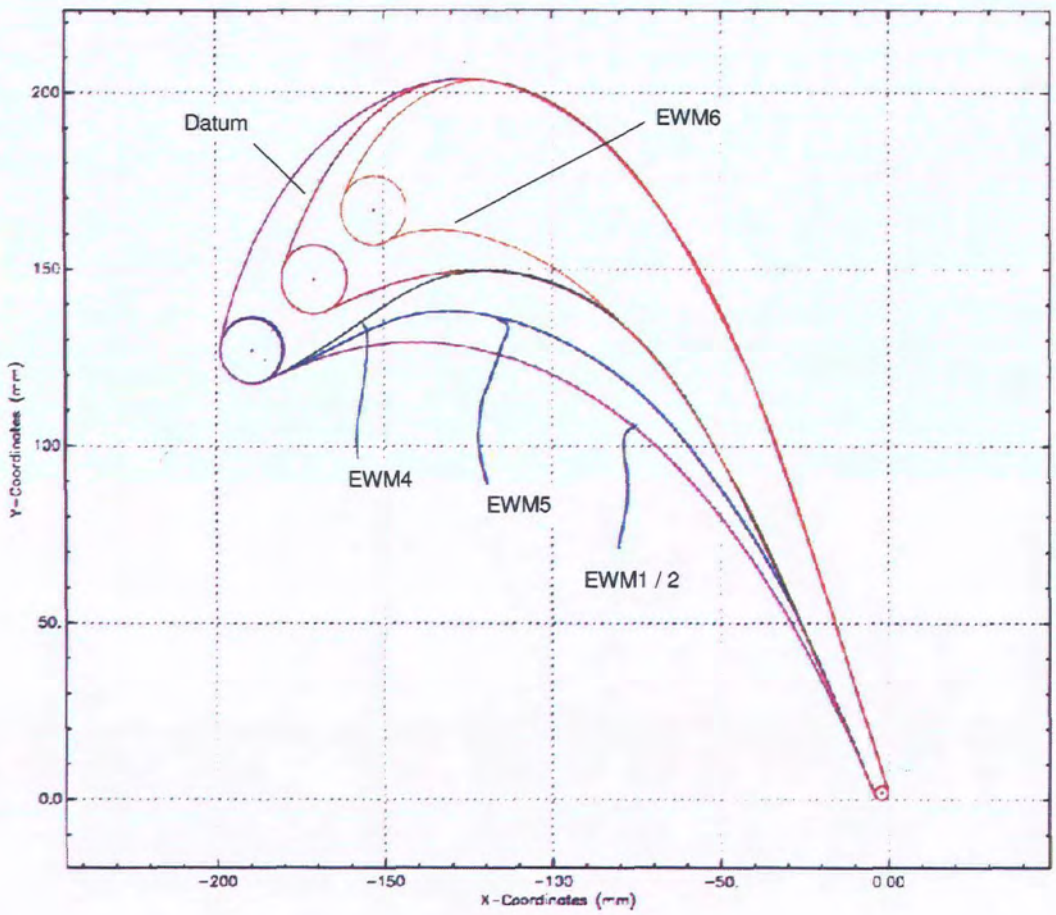

Figure 7.1: Aerofoil section designs

Massflow

The results in Figure 7.13 indicate a massflow reduction up to 0.4% for the two geometries under investigation. This was considered an acceptable variation for the purposes of initial design.

Loss

The mass averaged total pressure loss coefficient in Figure 7.15 shows EWM 1 and EWM 2 with loss reductions of 2.1% and 2.5% respectively. EWM6, with the decrease in axial chord, has a loss value higher than the base C0 design. However, the loss rankings for the different designs changed as the measurement plane moved downstream. This gave little confidence in the final ranking and the absolute values of loss from the CFD.

Yaw angle

The exit yaw angle (Figure 7.14) has a variability of +0.3/-0.2 degrees; positive being increased overall turning. Both EWM1 and EWM2 show increased overall turning relative to the base (C0) design. This is encouraging, as any benefits seen by the redesign cannot be associated with reduced turning.

The two charts in Figures 7.13 and 7.14 indicate that the designs are all performing the same level of duty.

SKEH

The mass averaged SKEH values in Figure 7.16 have similar ranking of results as the loss values. The two best designs are EWM1 and EWM2, the worst is EWM6 with a higher-than-base value and the other designs are in between. EWM2 gives a 37% reduction in SKEH over the base design, EWM1 gives a 29% reduction, whereas EWM6 gives a 29% increase over the base design.

7.5.6 Surface Static Pressure Results

Blade loading distributions and diffusions (leading to separation) are investigated using surface static pressures, at a series of radial positions. Since the blade geometry is symmetrical and the inlet conditions are almost identical, the surface static pressures were compared to the midspan position only.

0% span (K plane 1)

The static pressure plots in Figure 7.20 clearly show the extent of the axial chord alterations. The base design (C0) presents a typical suction surface loading distribution for the Durham Cascade, with a double loading peak. The second peak is an effect of the roll up of the passage vortex, the additional velocity comes from the radial velocity component in the passage vortex.

The extended designs (EWM1 and EWM2) reduce the magnitude of the peak at the front of the passage on the suction surface. This peak is associated with an over

speed, which is reduced due to the smoother geometric transition from the leading edge in these geometries. All of the extended geometry designs reduce the curvature in this short section of the suction surface. It is clear that the extended chord gives a greater area over which the load can be distributed, thereby reducing the local loading coefficient.

For the EWM1 and EWM2 designs, the pressure surface geometrical changes bring about a reduction in pressure over the region -125mm to -25mm axial (30% C_{ax} to 86% C_{ax}), but an increase from -25mm (86% C_{ax}) to the trailing edge. This increase in pressure on the pressure surface will tend to increase the overturning at the wall.

EWM6 does not have this behaviour. It has a sub-optimal (with regard to inlet angle) leading edge design and a strong pressure gradient across the early part of the passage. The higher pressure gradient is a consequence of the pressures on the aerofoil a short distance away from the endwall. The creation of this shorter axial chord, whilst maintaining the geometry in the later passage, increases the curvature of the suction surface. This increased curvature is seen in the large acceleration and diffusion in the early passage.

10% span (K plane 20)

Figure 7.22 shows the static pressure distribution at 10% span. At this radial distance the geometrical differences are greatly reduced. The acceleration at the rear of the passage due to the secondary flows is approximately equal for all designs. The differences in acceleration at the front on the suction surface are still noticeable and differences remain in pressure surface loading.

50% span (K plane 40)

Figure 7.23 shows the midspan static pressure distribution. At midspan all loading distributions are equal. The distribution around the leading edge indicates a slight off design inlet angle. The inlet angle specified for the designs under investigation was taken from the best experimental data available and may not correspond to that of the original profile design. The flat topped distribution of the original blade is still maintained for the new EWM designs. Importantly the midspan flow is not affected by the changes near the endwalls.

7.5.7 Pitchwise averaged data

The pitchwise averaged data was taken at a computational I-plane relating to 128% C_{ax}.

Massflow

In Figure 7.24 the pitchwise averaged massflow shows a slight redistribution; with successful designs (i.e. those reducing mass averaged SKE.H) increasing the massflow in the 10% span region and reducing it at 20% span. The midspan massflows for all geometries are equal.

Total pressure

In Figure 7.25 the total pressure distribution indicates that the extended endwall designs have reduced the loss in the region from mid span to 20% span. This is countered by increased loss in the region 15% to 5% span. This behaviour, with respect to loss redistribution, is similar to that of a reverse compound leaned blade. The EWM6 geometry indicates the reverse of this.

Yaw angle

In Figure 7.26 the pitchwise averaged yaw angle shows variation at all radii. The variation in midspan yaw angle (an increase in turning for the designs EWM1-2) is possibly an effect of flow redistribution at exit of the passage. The successful designs show reduced underturning (approximately 1.5°) in the 20% span region and reduced overturning (approximately 2°) in the 10% span region. This suggests a reduction in the strength of the passage vortex for the extended chord geometries. The overturning at the wall has however increased, by up to 1° relative to the base design.

SKEH

Figure 7.27 shows the pitchwise averaged SKE.H results. The design EWM6 has higher peak SKEH values and ties in with the mass averaged result. EWM2 has a lower SKEH value than EWM1. As the magnitude of the peak is reduced, it is also shifted radially towards the endwalls, this reduces the area of passage affected by secondary flows, leaving a larger region of primary flow.

7.5.8 Comments on the blade section design

A requirement of the improved design, was the retention of the original loading distribution, over the majority of the span. This has not been entirely possible and some of the performance changes seen may be due to the aft loading effect of the sections.

The original concept was to increase the axial chord, in order to replicate an axial compound lean stacking line. The chord extension has achieved this, but with additional modifications to the geometry, specifically a filled in pressure surface.

The reduction of axial chord for design EWM6 has increased suction surface curvatures too much. Ideally the thickness for this design would have been adjusted to compensate, however a blade design with greater thickness in the mid passage than the endwall is likely to give mechanical design problems.

Any concavity in suction surface 3D curvatures is to be avoided. This rules out the use of certain blade section designs. Specifically, when generating the axially extended profiles the suction surface shape should be maintained.

7.5.9 Summary

The use of axial extension in the near endwall profile design creates geometries similar to axial stacking. They differ however, in that the pressure surface geometry

has been altered and the effect that this has on secondary flow structures should be considered.

The effect on SKEH values is comparable with that of power law axial stacking with the same midspan displacement. However, the inclination angles involved in axial extension are much smaller and thus the designs are less extreme for an equivalent benefit.

The mass averaged loss values at the exit are lower than those for simple axial stacking and the overall turning is higher.

Similarly to axial stacking, the geometries affect the flow by offloading the front of the blade at the endwall section, reducing the cross passage pressure gradient and the potential for secondary flows. Additionally, the thickened near endwall section, caused by a filled in pressure surface, further reduces the cross passage pressure gradient. This is illustrated in Figure 7.2.

Designs EWM1 and EWM2 were both taken forward into Study 3. They have the same aerofoil profile, but different radial extent for smoothing (30% and 20% span respectively). The two designs gave similar behaviour and overall improvement, but are suitably different shapes to use in the next stage.

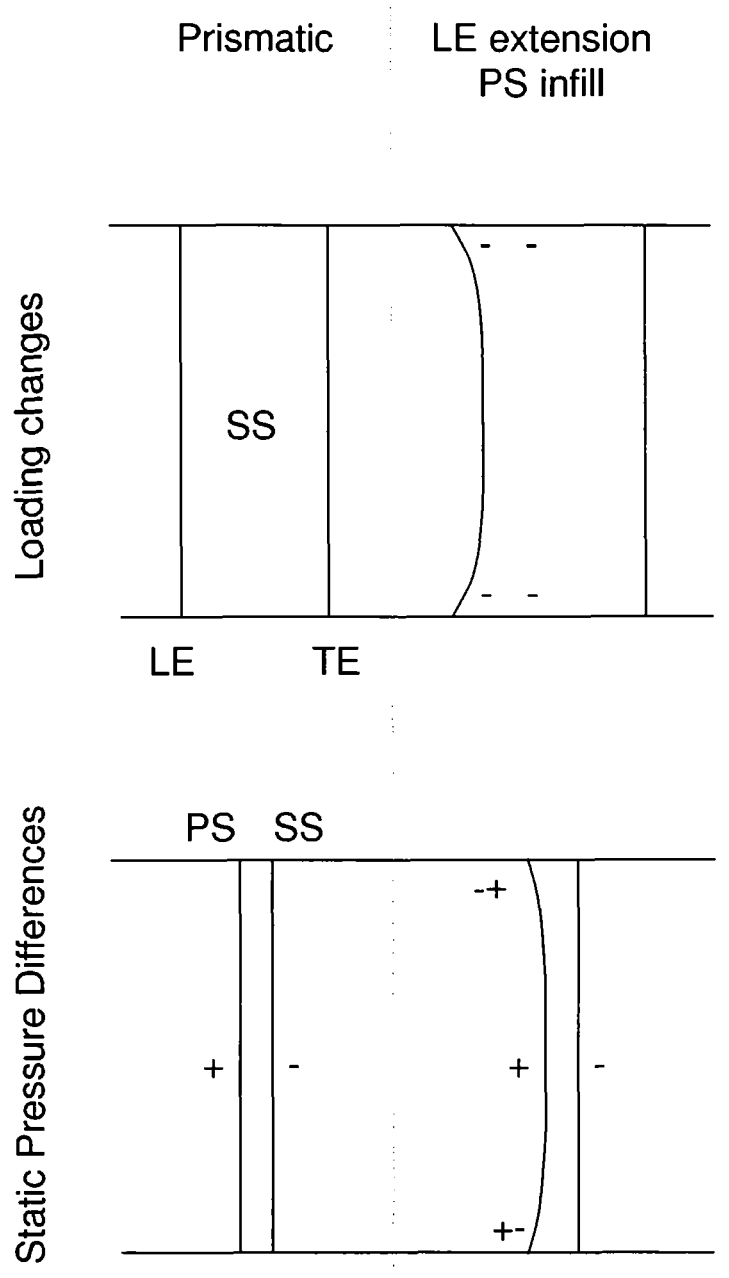

Figure 7.2: Effects of Axial Chord Extension

7.6 Study 3 - Combining with RCL

The following section investigates the performance of the new aerofoil designs, as they are combined with reverse compound lean stacking. At this stage in the design, the new cascade geometry was finalised and to ensure comparable analysis the span of the computational domain was reduced to 375mm (from 400mm). This reduction in span will not affect the structure of the secondary flows, which are driven by inlet boundary layer and overall turning. However, the change in span does impact the use of reverse compound lean.

The reverse compound lean has an elliptical profile, defined by Equations 7.1 and 7.3 of Section 7.4, with 15° inclination at the endwall, resulting in 24 mm displacement (12% pitch) at midspan. The values of 'a' and 'b' are 1313 and 968 respectively. Note here that the displacement 'x' (in the equations) becomes 't' for the tangential lean.

By reducing the span and retaining the same RCL definition (based on the stacking angle (θ) distribution), the midspan displacement due to the RCL decreases. This geometric change reduces the capacity of the RCL to redistribute the massflow and the potential to constrain the secondary flows at the endwall.

An additional effect of the change in midspan displacement, is the reduction in profile loss benefit, due to a reduction in the area dominated by 2D losses. The relates to the work of Walker and Hesketh (1999), who commented on the benefits of lean with respect to aspect ratio.

The aerofoil designs of EWM1 and EWM2 were both considered for combining with reverse compound lean. A limited result set is discussed below, which compares the relative effects of a reverse compound lean on the new designs EWM1 and EWM2.

7.6.1 Results

7.6.2 Mass averaged data

The mass averaged results for these latest designs are included in the earlier bar charts, Figures 7.13 to 7.16.

Massflow

Figure 7.13 shows the changes in massflow between radial stacking and reverse compound lean stacking. The plot indicates a 0.1% reduction due to the application of RCL for geometry EWM1. Geometry EWM2 is not affected by the application of RCL.

Total pressure loss

Figure 7.15 shows the total pressure loss coefficient. As noted earlier, the designs EWM1 and EWM2 reduce the loss relative to the datum. The addition of reverse compound lean tends to increase the loss for both designs, bringing them above the datum value.

Yaw angle

Figure 7.14 shows that the turning for both EWM1 RCL and EWM2 RCL is 0.6 degrees lower than their prismatic equivalent. Relative to the Base design the angle changes are much lower and therefore less important (of the order 0.3-0.4 degrees). These compare to an approximate 0.25 degree reduction in turning for reverse compound lean alone, as seen between C0 and C1.

SKEH

Figure 7.16 shows the SKE.H comparison. The values indicate that the use of reverse compound lean significantly reduces the SKEH, when combined with a near endwall modification. EWM1+RCL gives the greatest reduction in SKEH.

It is clear at this stage that the geometry EWM2+RCL indicates a reduced benefit. The remainder of the analysis will focus on the impact of RCL on the EWM1 geometry, thus simplifying the analysis and focussing on the RCL effect.

7.6.3 Surface static pressure

0% span (K plane 1)

Figure 7.28 shows the static pressure distributions at the lower endwall. The blade surface static pressures at the endwall show a significant increase in loading due to the reverse compound lean and offloading to the rear of the pressure surface. The acceleration around the early suction surface is followed by a gentle deceleration and diffusion with no second acceleration typically associated with the passage vortex. The smooth deceleration negates a separation and permits the potential use of stronger endwall profiling. The higher cross passage pressure gradient to the leading edge would indicate stronger secondary flows.

3% span (K plane 10)

Figure 7.29 shows the static pressure distributions at 3% span. At this span the high loading levels remain on the suction surface to a greater distance along the chord. The pressure surface appears to be unaffected, this is expected as the effect of RCL is concentrated on the SS.

10% span (K plane 20)

Figure 7.30 shows the static pressure distributions at 10% span. At this location, the reverse compound lean gives higher loading over the entire suction surface. The differences between the datum design and EWM1 are relatively minor, indicating that the influence of the extended geometry is limited to the region close to the endwall, despite its 30% span extent. This is in contrast to the effects of reverse compound lean, which alters the blade loading over the entire span.

50% span (K plane 40)

Figure 7.31 shows the static pressure distributions at midspan. At this location the datum design and EWM1 have the same pressure distributions. The differences between the EWM1 and EWM1+RCL can be wholly attributed to the effects of reverse compound lean.

7.6.4 Pitchwise averaged data

Massflow

Figure 7.32 shows the differences in pitchwise averaged massflow at midspan and the endwalls. The massflow at this plane is influenced by the downstream redistribution effect, described for RCL in Chapter 6.

Total pressure

Figure 7.33 shows the pitchwise averaged total pressure at 128% C_{ax}. The plot indicates increased loss, associated with the PV, for the application of RCL. The loss at midspan also appears greater for RCL, this behaviour does not follow that of the previous reverse compound lean design, (C1) but does confirm the increase in mass averaged loss.

Yaw angle

Figure 7.34 shows the pitchwise averaged exit yaw angle at 128% C_{ax}. The RCL shows a significant increase in overturning at the wall and a minor reduction in the underturning of the PV. The maximum overturning has jumped from 75° to 78°, whilst the underturning has reduced by less than half a degree. The reduced turning at midspan is a redistribution effect, due to a change in stream tube thickness at the blade exit as detailed in Chapter 6.

SKEH

Figure 7.35 shows the pitchwise averaged SKEH at 128% C_{ax}. The reverse compound lean can be seen to shift the SKEH peak radially in towards the endwall, providing a larger area of clean undisturbed flow. Importantly, the magnitude of the peak, associated with the PV is also reducing. Overall, the SKEH value for the design EWM1 RCL is significantly lower than EWM1.

7.6.5 Summary

This study has highlighted the difficulty of combining axial chord extension with tangential stacking. The favoured design of Study 2 (EWM2) has performed less favourably than the EWM1, when combined with the reverse compound lean. The only difference between EWM1 and EWM2, is the radial extent of the merging of the aerofoil section. Considering this, the suction surface curvatures are again likely to be a significant factor.

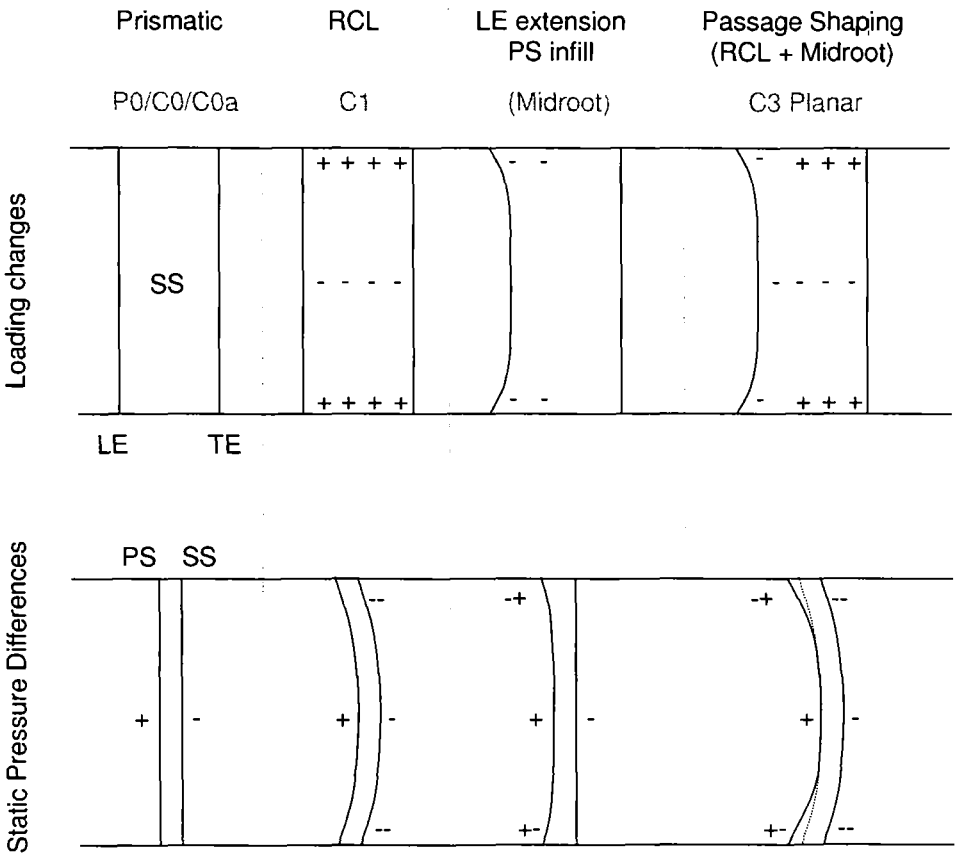

Figure 7.3: Effects of Combining RCL with Axial Chord Extension

The key effects of combining axial chord extension with tangential stacking are presented, alongside earlier modifications, in Figure 7.3. Here the changes in static pressure and localised loading effects can be seen.

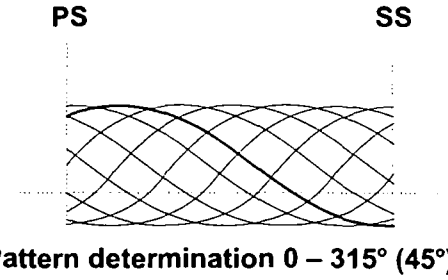

Figure 7.4: Pattern Determination in Optimiser

7.7 Study 4 - Endwall profiling

The final stage in the design process for the C2 geometry is the endwall profiling. This must be undertaken after the blade design because it modifies an existing computational mesh. The process of endwall design is sufficiently developed to be integrated into an automated system. The endwall profiling method used in this work is based on that of Harvey et al. (1999). A brief description of the operation of this system is given below.

It should be noted that the automated optimisation of the endwall profiling design system is a development of Dr. Stokes of Rolls-Royce. The system is currently undocumented and as such a limited description of the process is given here.

7.7.1 Phase optimisation process

The optimisation process comprises two stages for each perturbation station. A first stage in which the endwall pattern is set and a second stage in which this pattern is mapped to find the optimum magnitude of the harmonics; zero order (or axisymmetric) and first order comprising sine and cosine components. The perturbations defined are used to control a continuous b-spline surface.

Pattern determination

A series of ten patterns, as seen in Figure 7.4, are used as control splines for a b-spline (NURBS) surface which defines the entire endwall shape. The ten seperate NURBS surfaces are used to morph the pre-existing computational mesh into ten seperate mesh shapes. These include eight sine wave patterns with phase angle shifts between 0^o and 315^o in 45^o increments. Two additional patterns, with zero order displacements in the positive and negative radial directions, make up the remaining calculations. Each of the patterns has a lower magnitude than the maximum permissable endwall height (set by the user). This pattern determination process is split over 10 processors.

Mapping

The best (in terms of the optimisation criteria) first and zero order patterns are combined in a 4x4 matrix. The matrix includes a 0/0 option where no changes are

made. This map generates 16 permutations.

Perturbation Stations

The above described two stage optimisation process is repeated for each of the user defined perturbation stations in series, see Figure 7.5. The optimisation begins at the most upstream station on the lower endwall (number 1), it completes the pattern determination and combination (first and zeroth order perturbation) mapping for this station and steps downstream until all the stations on the endwall are complete, see Figure 7.6. After the lower endwall is complete, the process continues on the first station of the upper endwall (number 7). Using this method the convective nature of the effect of the modifications can be taken into account.

The design of the endwalls as two separate consecutive components is a result of the process built into the turbine design system, where the hub and shroud endwalls are currently designed in sequence. This order of station optimisation could however be altered within the optimisation software.

Determination of the 'best' sequence in which to optimise the perturbation stations will depend on; the location of the stations in relation to the aerofoil loading distribution, the relative independence of the two endwalls from one another (linked to the aspect ratio) and the pre-existing level of secondary flow, i.e. the potential benefit to be gained. For the optimisation of this high aspect ratio aerofoil, with similar magnitude secondary flows (upper and lower), it was considered that the endwall designs would be independent and thus could be optimised independently.

In the following design, the perturbation stations are spaced evenly between the upper and lower limits (control stations where the control curve is linear) of the endwall.

Optimisation criteria

The criteria used in the optimisation include:

- performance - measured through exit yaw angle and massflow
- efficiency - measured through total pressure loss and SKE.H
- separation - checked by measuring diffusion at a number of radial locations on the aerofoil

7.7.2 Diffusion limits

The level of diffusion has been of concern with previous endwall designs used in the Durham cascade. As such the diffusion levels on the blade surface are now automatically checked at a series of user-specified radial positions during the optimisation process. The maximum diffusion level was set at 0.4, and can be calculated as follows:

$$D = \frac{\left(\frac{p}{p_0}\right)_B - \left(\frac{p}{p_0}\right)_A}{1 - \left(\frac{p}{p_0}\right)_A} \tag{7.4}$$

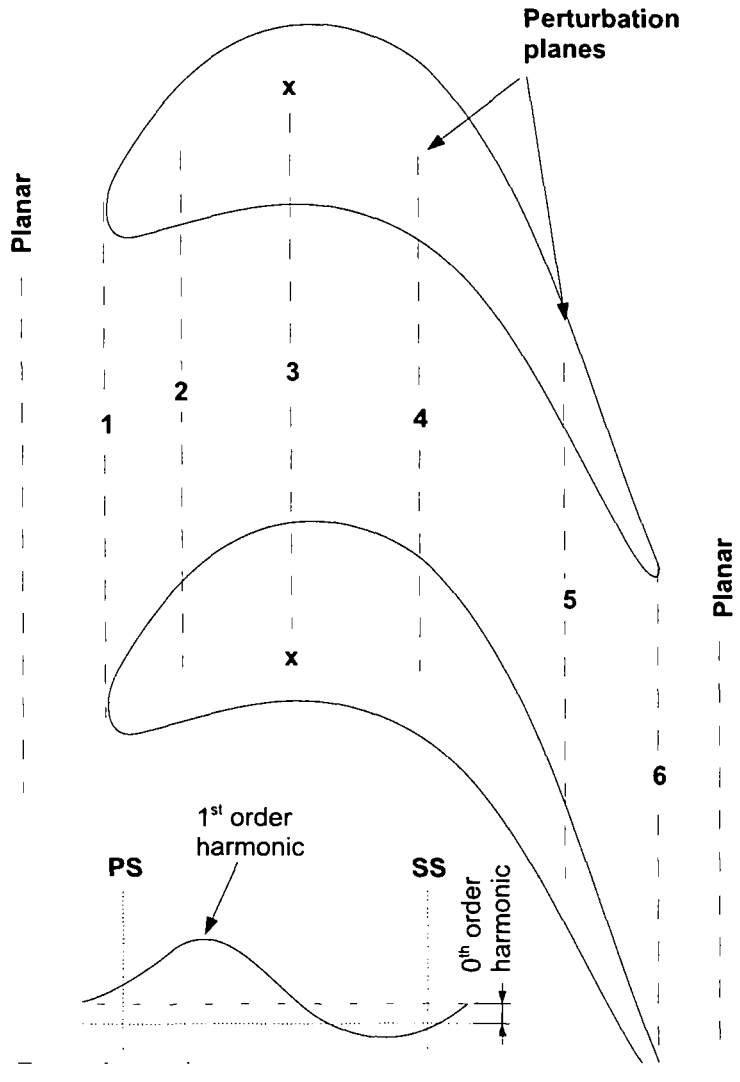

Figure 7.5: Perturbation Stations

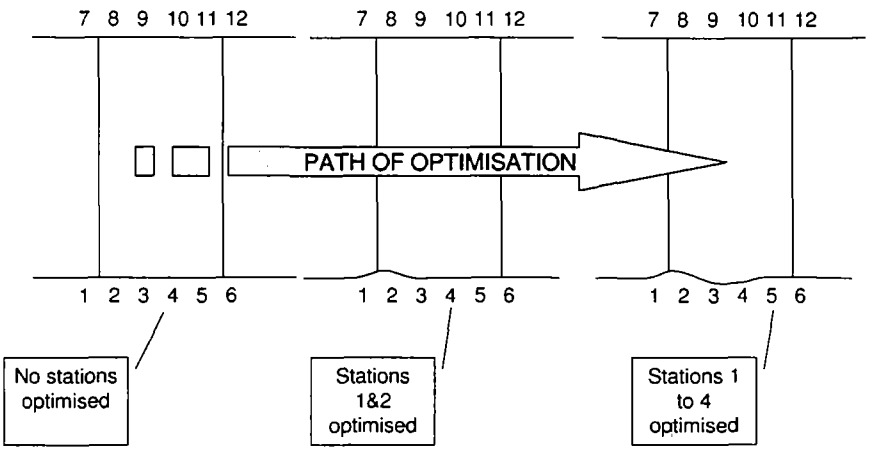

Figure 7.6: Endwall Optimisation Route

$$\frac{p}{p_0} = \left(1 + \left(\frac{\gamma - 1}{2}\right) Ma^2\right)^{\frac{-\gamma}{\gamma - 1}} \tag{7.5}$$

where A is the point of local minimum pressure and B is the point of local maximum pressure across the diffusion as illustrated in Figure 7.36.

This diffusion checking is not undertaken for the endwalls themselves. An equivalent manual process using the same criteria is followed for a number of pathlines of interest. This process is relatively labour intensive and as such only a few streamlines can be checked, typically for the final design.

7.7.3 Progression of the phase optimisation script

Figure 7.12 shows the development of selected parameters evaluated at a specific axial location downstream of the blade row. The results illustrate the construction of a non-axisymmetric profiled endwall by the script on a station by station basis.

The plot is a summary of the changes to parameters SKE.H, diffusion and capacity. As the solution is low speed and incompressible, the capacity is simply the massflow. The SKE.H value is given as a percentage of the planar endwall case and is calculated at 128% C_{ax}. The diffusion value is a percentage of the diffusion limit, measured on a number of discrete radial planes chosen by the designer. The optimiser will restrict the design if any of the radial planes reach the diffusion limit. The capacity values presented, are the change relative to the planar endwall case, magnified in the plot for clarity.

The plot also illustrates the amplitude of perturbations that were chosen in the first and zero order harmonics.

The profiling is designed one endwall at a time, from Station 1 to 6 for the lower

endwall and then Station 7 to 12 for the upper endwall. For this geometry, Station 1 is at the same axial location as Station 7 and so on.

Results

The plot in Figure 7.12 indicates a decrease in SKE.H value as each station is defined. Between Stations 5, 6 and 7 there is no change in SKE.H. These stations relate to the back of the lower endwall and the front of the upper endwall. It is believed that the level of diffusion already existing on the lower endwall is already high and further perturbations have impacted the diffusion constraint and limited the design. The effect of profiling at Stations 1 to 5 is a reduction of 37.7% of the datum SKE.H value. Stations 8 to 11 give a further reduction of 18.8%, resulting in an overall reduction of 56.5% for the dataset in question.

The diffusion limit on the lower endwall is reached at an early stage of the design (Station 4) and remains against this limit for the rest of the process. The limit appears to be controlling the design for the subsequent 3 stations. This suggests that the optimiser is given too much freedom too soon in the process and restriction of this could benefit the final design.

The capacity value is slightly above the planar, indicating higher mass flows for the majority of the design process. At Station 11, Tip 5 the capacity change flips from being positive to being negative, this relates to a large negative amplitude (hump) on the zero harmonic.

7.7.4 Results

The resultant endwall designs are presented in Figures 7.37 and 7.38. The endwall design is assessed in more detail in this section.

The mass averaged massflow and yaw angle results indicate no change. This is to be expected, due to the performance controls placed on the optimisation routine. There is, however, a reduction in the total pressure loss.

7.7.5 Endwall Heights

The profiled endwall shapes are shown in Figures 7.37 and 7.38 and are referred to as the mild design and the aggressive design (aggr). The aggressive endwall corresponds to the lower endwall boundary and has much larger perturbations from the planar case than the mild endwall at the upper boundary. The figures show a difference relative to the mean endwall height. The contours are set at 1mm height difference. The colours red and yellow indicate a hump or ridge, the colours blue and green indicate a dip or trough. The figures show the following:

- The mild endwall has a fairly conventional appearance. There is a hump on the pressure side of the endwall and a dip on the suction side of the endwall.
- The aggressive endwall shows a more unusual design, with a complex hump that surrounds the leading edge and wraps around both suction and pressure surfaces. There is a dip that runs from mid-passage to the suction surface,

which in combination with the hump gives a strong concave shape along the suction side of the endwall.

Further discussion of the possible reasons for the differences between the endwall designs is given in Section 7.7.7.

7.7.6 Surface static pressures

The surface static pressures indicate the changes in blade loading caused by the addition of profiling. The figures are arranged to combine both the mild (upper) and aggressive (lower) endwall results into a single chart for ease of comparison. There are four plots in Figures 7.39 to 7.42 with measurements at 0% 3% 10% and 50% respectively.

0% span

Figure 7.39 is taken at K-planes 1 and 80 and shows the impact of the profiling at the endwall itself.

At the lower passage endwall the pressure distribution is characterised by a double hump. The first is caused by the large convex curvature near the leading edge which accelerates the endwall flow, see Figure 7.37. The second is the acceleration of the fluid out of the downstream concave section, back to the exit endwall height. The profiling on the lower passage endwall does not affect the pressure surface distribution.

The levels of acceleration and subsequent diffusion appear to be high, but the diffusion levels were checked and were within the specified limit. The overall effect of endwall profiling on the lower passage endwall is to off load the mid section and increase the loading to the front and rear. The increase in suction surface pressure in the mid chord reduces the cross passage pressure gradient here, thereby reducing the passage vortex potential.

The endwall profiling at the upper passage endwall does not behave as previous designs. The leading edge suction surface region shows no increase in acceleration and no rapid deceleration. This relates to Figure 7.38, where the profiling can be seen to be mild, close to the front of the suction surface. The most significant changes to the pressure distribution on the upper passage endwall, are to the rear of the aerofoil. Both the suction and pressure surfaces see increased loading in the later part of the passage. These relate to the reacceleration on the suction surface and the decrease in height and diffusion on the pressure surface.

3% span

Figure 7.40 is taken at 3% span (K-planes 10 and 70) and shows the radial extent of the effects. The effect is marked at the lower endwall, with the double hump still very clear. However, the strong diffusion levels noted at 0% span have been depressed. The diffusion limit appears to have been reached first at the endwall. The effects at the upper endwall are relatively minor.

10% span

Figure 7.41 is taken at 10% span (K-planes 20 and 60) where the effects of both PEWs are still evident. The profiling used on the lower endwall has a minor effect at 10% span, with a slight off loading of the mid chord section only.

The effects of the upper passage endwall design, are noticeable here as an offloading toward the rear of the midchord.

50% span

Figure 7.42 shows that there is no impact on the midspan flow with the addition of PEWs.

Pitchwise averaged data

The following describes the pitchwise averaged values taken at 128% C_{ax}.

Massflow

Figure 7.43 details the pitchwise averaged massflow at 128% C_{ax}. The massflow indicates a shift in streamlines when the profiling is applied. The lower half has reduced massflow from 15% to 40% span. The upper half sees increased massflow from 100% to 55% span.

Total pressure

Figure 7.44 shows the total pressure distribution at 128% C_{ax}. The total pressure distribution indicates an increase in the area of clean flow in the middle of the passage. Alternatively, it may be considered that the loss cores have been shifted radially inwards to the endwalls. The strength of the lower passage loss core appears the same, the upper passage core has a clearly higher loss value associated with it.

Yaw angle

Figure 7.45 details the pitchwise averaged yaw angle at 128% C_{ax}. The yaw angle shows two separate behaviours for the two endwall designs. The lower passage endwall behaves as previous endwall profiling designs have. The overturning at the wall increases by approximately 1.3^o, the magnitude of the underturning reduces and the underturned region has shifted toward the endwall.

The upper passage has actually reduced the overturning (by less than 0.5 degrees) and slightly reduced the underturning. The reduction of underturning is a good indicator for a reduction in the strength of the passage vortex.

SKEH

Figure 7.46 shows the pitchwise averaged SKEH at 128% C_{ax}. The SKEH for the EWM1+RCL design was already noted as being very low. The addition of profiled endwalls reduces the peaks further and shifts them to radial positions nearer the endwalls.

7.7.7 Discussion

The two endwall designs have significantly different shapes. The lower passage endwall has strong profiling around the leading edge. This causes the strong acceleration-deceleration seen in the pressure distribution at 0% span in Figure 7.39. On the rear of the suction surface, the profiling gently returns to the axisymmetric condition. Near the pressure surface the profiling fills in the front and middle sections of the passage and is comparable with the previous endwall profiling designs.

In contrast, the upper passage endwall has minor geometric changes from the front to the middle section of the suction surface. The rear is strongly contoured, but with concave curvature which causes a diffusion and late acceleration as seen in Figure 7.39. Again the pressure side is filled in.

The double hump geometry of previous endwall profiling designs (P3/P4) is not seen at either endwall.

The optimisation of endwall profiles might be expected to produce two similar geometrical shapes. Two possible reasons for the observed differences are; different inlet boundary layers, and sensitivity in the optimisation weightings.

Looking at the inlet boundary layer profiles in Chapter 3, the differences specified for the two endwalls appear minor and are unlikely to be the cause of the design differences. Additionally, the inlet boundary layer profiles are smoothed onto a coarse throughflow grid, prior to being input into the Navier-Stokes solver, further reducing these differences.

Initial investigation of the CFD result files indicated a small but significant cross span influence of the endwall design. Further analysis of the optimisation log file, shows that the diffusion criterion of a lower endwall section was influenced by this small amount of cross span talk. This oversensitivity of the diffusion criterion, combined with the small amounts of cross span influence, have limited the extent of profiling in the rear section of the lower passage endwall, and in the front section of the upper passage endwall.

7.7.8 Summary - Endwall profiling

It was considered that the two different endwall profiling designs would be of considerable interest, potentially providing two separate investigations from one cascade geometry. The upper endwall would test the feasibility of rear passage profiling as an alternative design, whilst the lower endwall would check the suitability of the specified diffusion limit. Importantly, the profiling of the upper passage, which is mostly to the rear, is capable of a 20% SKEH reduction (compared to a 30% reduction in the lower passage), without any real diffusion effects.

7.8 Conclusions

7.8.1 Geometry

The design process has produced a passage with several geometric alterations. The blade combines the previously successful reverse compound lean stacking with an axially extended near endwall section (shown in Figure 7.47). The near endwall

section maintains the trailing edge geometry whilst extending the leading edge. The section is also thickened by a pressure surface infill. The extended geometry is merged with the original section at a distance of 30% span from the endwall; this gradual merging brings about a local axial stacking equivalent to axial sweep. The lower endwall profiling is strong in the early passage, the upper endwall profiling is strong to the rear of the passage.

The geometry of a leading edge fillet, shown in red in Figure 7.7, typically extends to the boundary layer radially and up to three boundary layer thicknesses upstream. The geometry of a leading edge bulb, shown in magenta in Figure 7.7, typically enhances the HSV by imposing a larger leading edge in the region of the boundary layer. The leading edge extension resulting from the passage shaped design, shown in blue in Figure 7.7, is not a classical leading edge modification. The aspect ratio of the leading edge geometry (radial extent / axial extent) is 6.2:1, compared to 1:3 for leading edge fillets and 1:1 for leading edge bulbs. The extension is merged at 30% span (112.5 mm) around two times the height of the inlet boundary layer. Whilst the modification may impact the HSV, it is not its primary purpose.

7.8.2 Effects

Figure 7.8 indicates the combination of geometric modifications and their effect on the loading and static pressure distributions. The axial stacking of the leading edge of the blade has reduced the local loading coefficient and the cross passage pressure gradient. The pressure surface infill has further reduced the cross passage pressure gradient. The reverse compound lean stacking has offloaded the mid span section of the blade whilst increasing it toward the endwall, thereby cancelling some of the benefit of the other modifications. The lower endwall profiling has reduced the cross passage pressure gradient in the early section of the passage at the expense of an increased endwall diffusion. The upper endwall profiling has not introduced significant diffusion, but has shifted the loading toward the rear of the blade at the endwall.

7.8.3 Endwall Static Pressure

Endwall static pressure predictions for the C2 geometry, with planar, mild and aggressive endwall geometries, are presented in Figures 7.48 to 7.51. The endwall static pressures show similar behaviour to the loading distributions in Figure 7.39 for the application of PEWs. Pressure surface offloading and an increase in suction surface loading can be seen in the C2 planar endwall geometry. The C2 aggressive shows the reduction in forward SS loading and the region of diffusion on the endwall associated with the dip in the endwall height. An increase in aft loading is also visible for the C2 aggressive geometry.

The C2 mild geometry has no observable change in the forward SS loading, unlike the C2 aggressive geometry, but the aft section has increased loading as observed in Figure 7.39.

7.8.4 Blade Static Pressure

Blade suction surface static pressure distributions for the C0a, C2 planar and C2 PEW geometries are presented in Figures 7.52 to 7.54. The plots show the three geometries with the leading edge on the left hand side.

The key C0a effects are; a flat topped distribution, with peaks observed near the endwall associated with the radial velocity component in the passage vortex.

The C2 planar geometry appears to offload the midspan, it loads up the endwalls and the passage vortex traces dissappear. The extended leading edge regions indicate a localised offloading.

The C2 PEW geometry has the same overall effects to the C2 planar geometry. The aggressive (lower) endwall causes a local decelration and static pressure rise to the front of the aerofoil. The mild (upper) endwall has no significant diffusion. The loading near the endwall, appears to have shifted forwards.

7.8.5 Artificial Flow Visualisation

Blade suction surface

The images in Figure 7.55 show an artificial flow visualisation. The CFD equivalent of oil and dye flow visualisation. The streaklines are seeded and run on a constant 'j' surface corresponding to the suction surface.

The C2 planar geometry indicates a radially inward movement on the front of the SS, this is due to the RCL. The height of the PV trace at the trailing edge is reduced for C2 planar. The C2 PEW aggressive endwall (lower end) indicates forward movement of the start of the PV trace, but a slightly lower height of the trace at the trailing edge. The C2 PEW mild endwall (upper end) has similar results to C2 planar.

Endwall surface

Figure 7.56 details the K-plane streak lines, defined one cell away from the endwall (k2 and k79). The aim of the flow visualisation at this location, is to resolve the HSV structures, observe the point at which the SSHSV interacts with the SS and obtain an indication of the level of overturning on the endwall boundary layer. The Figure compares the C0a, C2 planar and C2 PEW designs. Figure 7.9 describes the key features including:

- Saddle point (red dot)
- Separation line (red line)
- Suction surface attachment of HSV
- New boundary layer overturning magnitude (blue line)
- Overturning magnitude near passage exit

Between C0a and C2 planar the saddle point shifts to the SS side of the leading edge. The SS attachment point of HSV is shifted aft, this is mostly the appearance of a shift due to the new SS length of the extended geometry.

Between C2 planar and C2 aggr there is a slight increase in overturning at exit. Within the passage the new boundary layer overturning is further decreased. There is no difference in rear suction surface. The saddle point is in the same location. The HSV and associated separation lines have shifted. The SS leg moves away from suction surface around the convex curvature of endwall profiling, but attachment point is brought forward. The PS leg attachment is also brought forward contrary to the decrease in boundary layer overturning.

Between C2 planar and C2 mild there is a large change in rear section overturning relating to the aft blade loading seen in C_p plots. There is a notable increase in the overturning at the exit. The overturning of the new boundary layer has decreased with the application of the endwall. The saddle point is now in line with LE. The HSV and associated separation lines have shifted. The SS leg attachment point is brought forward and the PS leg attachment is pushed back.

7.9 Axial development of parameters

The axial development of SKE.H downstream of the trailing edge is important when considering its use in endwall design optimisation routines. The choice of axial plane (or grid I-plane) at which the parameter is measured can affect the quoted benefits (SKE.H reduction). This section looks at the effect of the passage shaped geometry with and without PEWs on a couple of parameters. The mass averaged SKEH through the entire domain is presented in Figure 7.57. The area of interest is within the dashed box and relates to the region at and downstream of the trailing edge.

Two I-planes are analysed; I83 is approximately 2% C_{ax} downstream of the trailing edge, I97 approximately 28% downstream and corresponds to the experimental measurement plane.

7.9.1 SKEH Reduction

Figure 7.58 contains the raw SKE.H values for geometries Datum (C0a), passage shaped geometry without PEWs (C2 planar) and with PEWs (C2 PEW). The general shape of the three curves is the same, with the previously observed reductions due to the redesign noted.

Figure 7.59 plots the reduction of SKE.H and total pressure loss for geometries C2 and C2 PEW, as a percentage of reference prismatic geometry C0a.

A small reduction in SKE.H (30%) is seen at the trailing edge, this benefit increases rapidly to 60-70% by 105% C_{ax} from the trailing edge, where the gradient eases. The SKE.H benefit is improved further from 105% C_{ax} to the exit of the computational domain. The gradients for both C2 and C2PEW appear to be the same in general.

The sudden jump in SKE.H benefit (100-105% C_{ax}) may be an effect of the redistribution or wake mixing downstream of the trailing edge. The key difference

between the two geometries and the datum, is the application of reverse compound lean.

7.9.2 Loss Reduction

The total pressure loss coefficient does not appear to be affected in the region 100-105% C_{ax}. The benefit of the C2 PEW geometry over prismatic C0 follows that of C2, with about 1% difference for the majority of the downstream section of the domain. It could be considered that the benefit of C2 over C0 begins at the bend point in the SKE.H plot, around 105% C_{ax}.

Figure 7.60 details the SKE.H reduction due to the PEWs alone. This plot highlights the similarity of the SKEH reduction for the two cases from 115% C_{ax} onwards.

7.9.3 Problems with SKE.H

There are two concerns over the use of SKE.H for design assessment.

1. The parameter is highly sensitive to secondary flow structure and therefore sensitive to the grid resolution used, making any comparison between grids impossible

2. The parameter exhibits an unusual behaviour downstream of the trailing edge. As such additional parameters and analysis locations should be considered

7.9.4 Conclusion

The rapid changes in SKE.H benefit close to the trailing edge, suggest that a change of approach is necessary. It appears that the full benefit of PEWs is not seen until 15 - 20% C_{ax} downstream of the trailing edge.

When assessing geometries using the phase optimization script, for this specific geometry, the SKE.H should be assessed at least 5% C_{ax} and preferably 20% C_{ax} downstream, for changes related to endwall profiling. These results are likely to be geometry specific, but a minimum distance between the trailing edge and the SKE.H measurement plane should be determined.

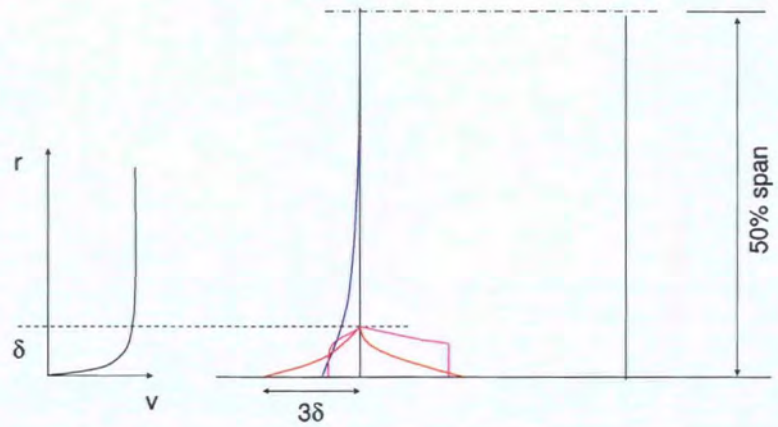

Figure 7.7: Sketch of leading edge modifications

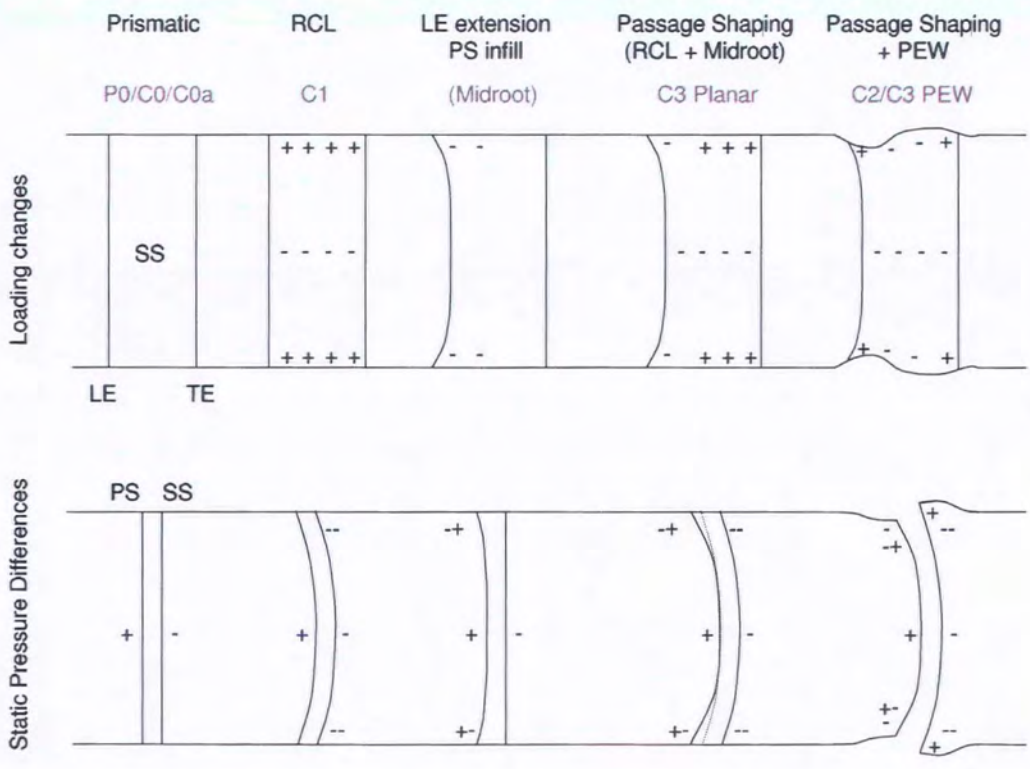

Figure 7.8: Effects of combining aerofoil with endwall profiling

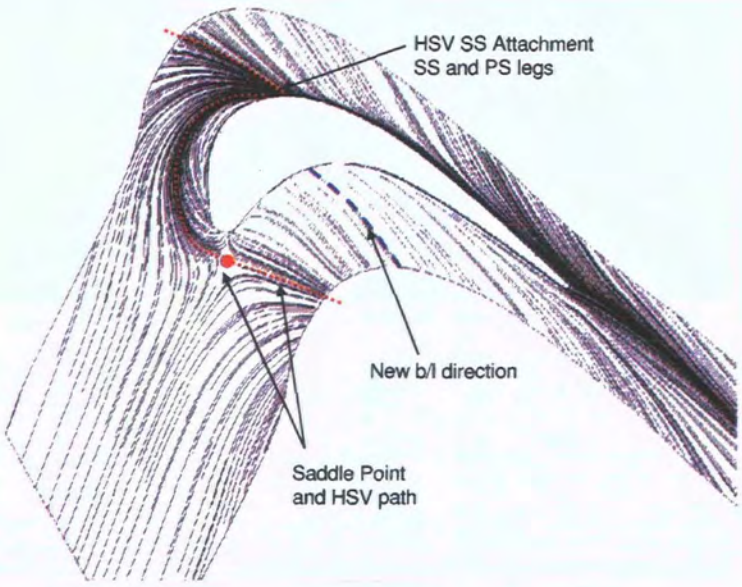

Figure 7.9: Endwall Surface Flow Visualisation

7.10 Figures

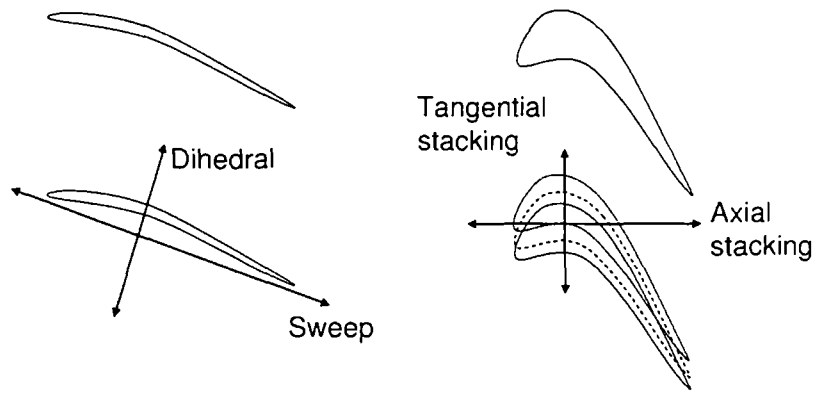

a) Compressor terminology b) Turbine terminology

Figure 7.10: Lean and Sweep Terminology

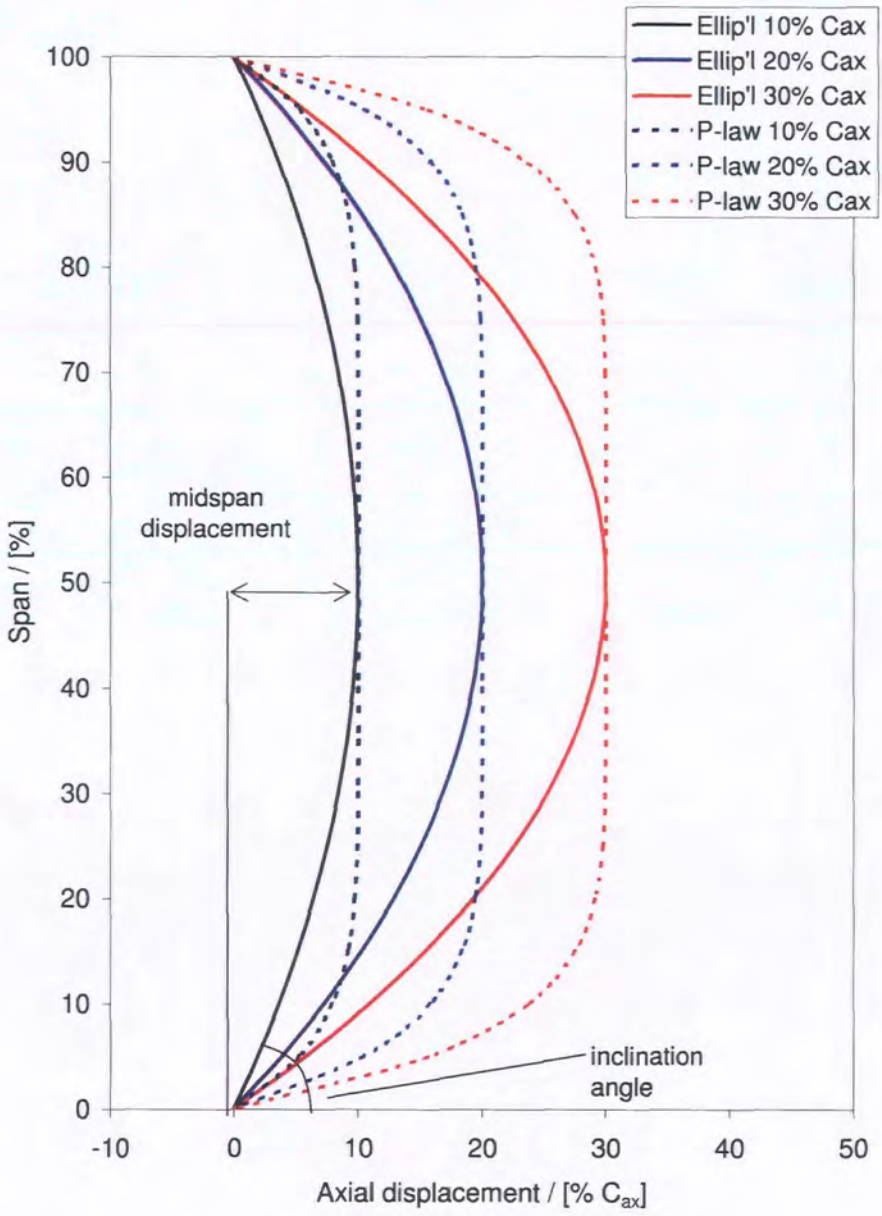

Figure 7.11: Axial Sweep Stacking Lines

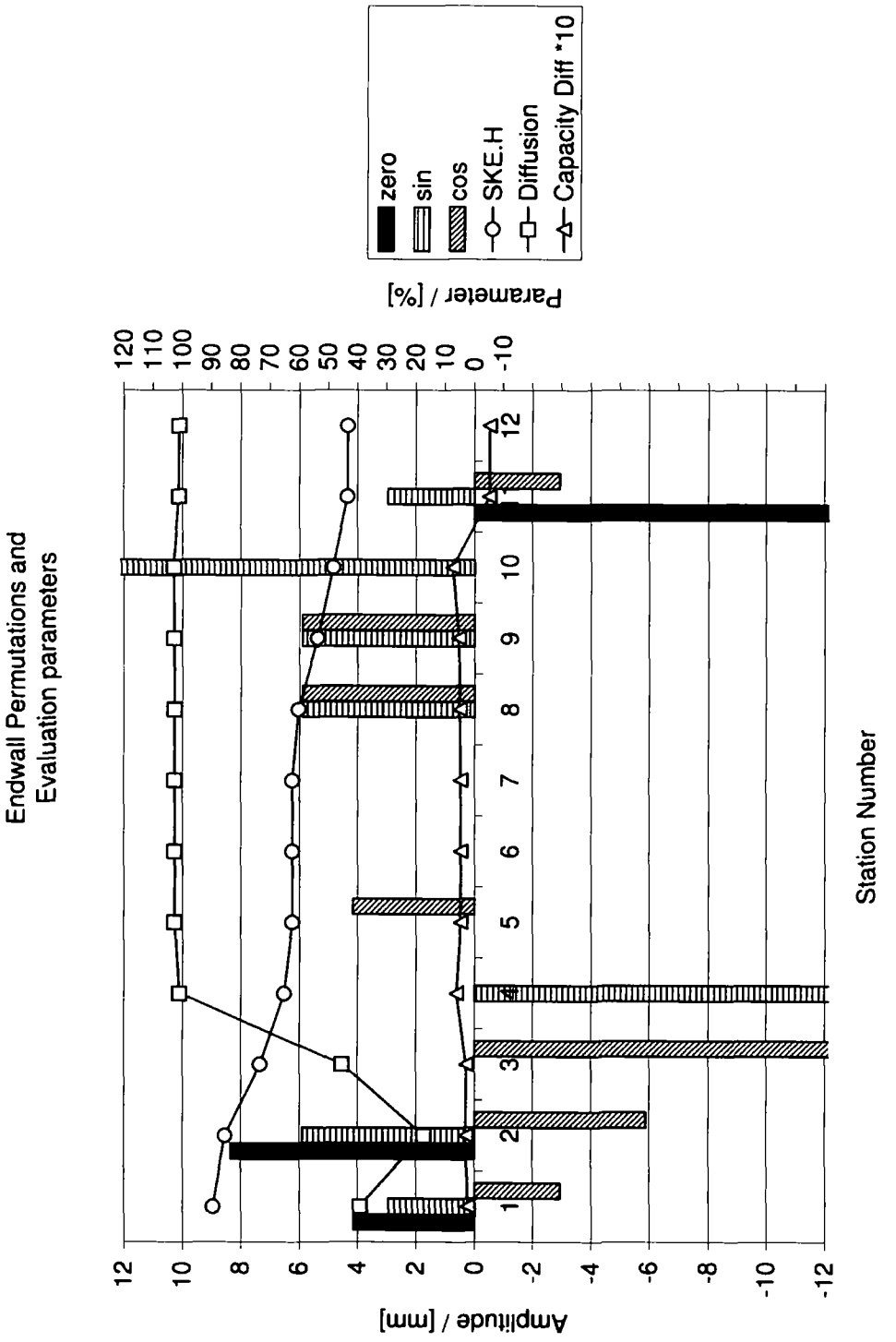

Figure 7.12: Progression of PhaseOpt design process

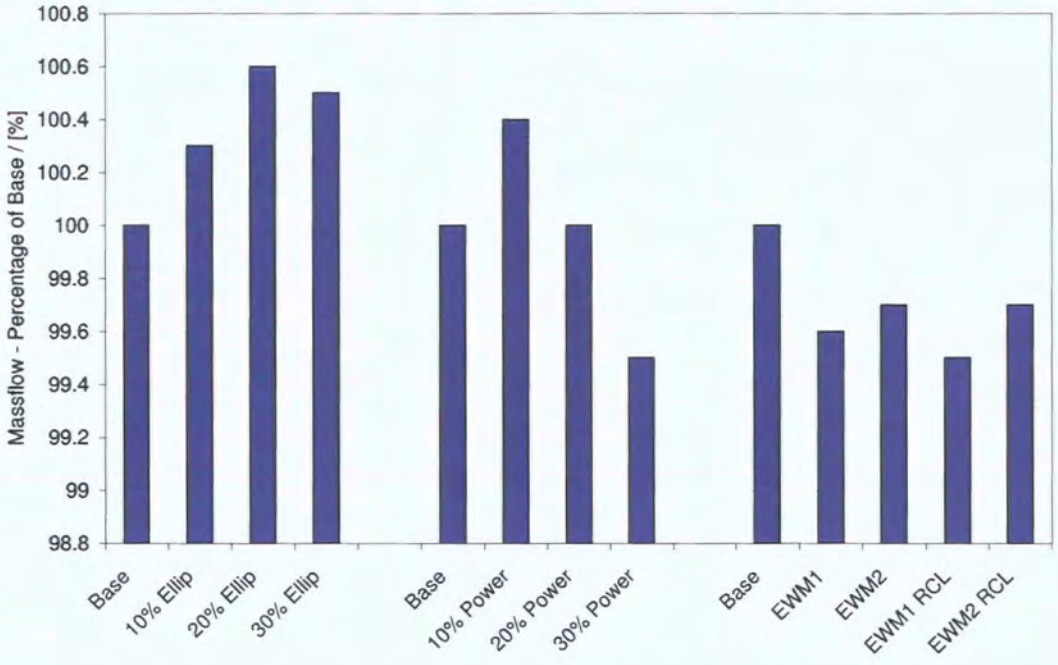

Figure 7.13: C2 Design Iterations - Mass Averaged MassFlow

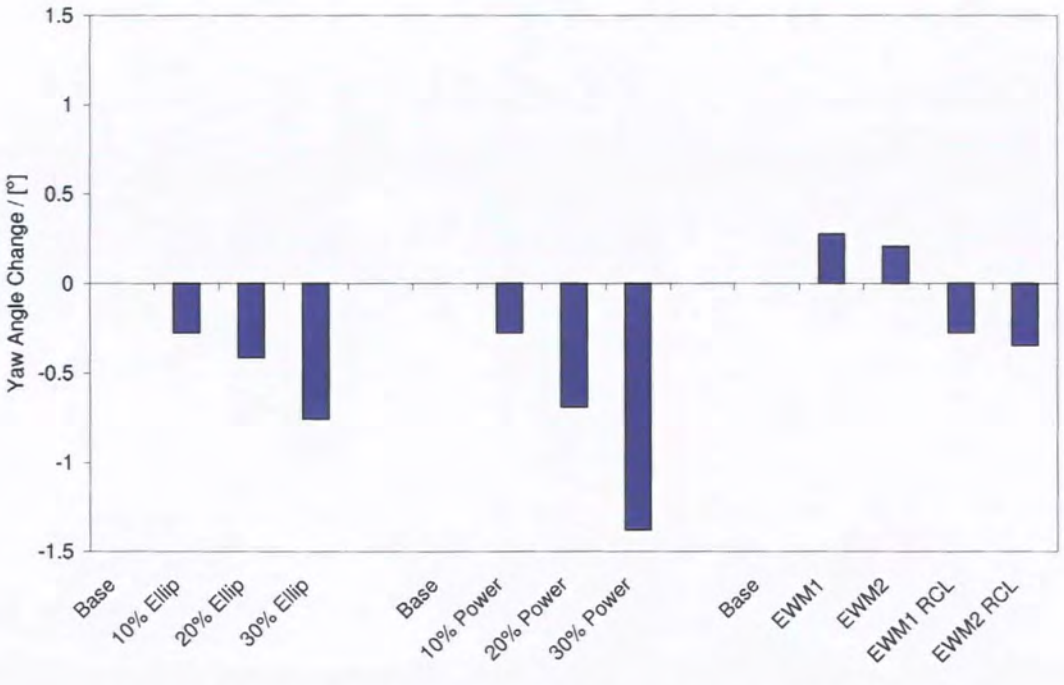

Figure 7.14: C2 Design Iterations - Mass Averaged Yaw Angle

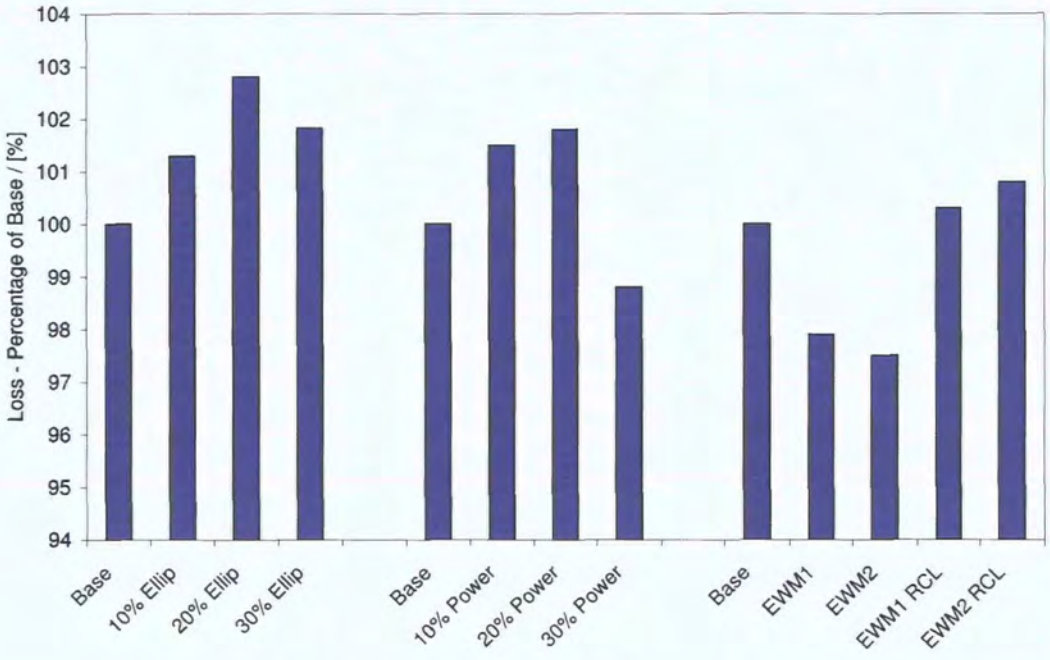

Figure 7.15: C2 Design Iterations - Mass Averaged Total Pressure Loss

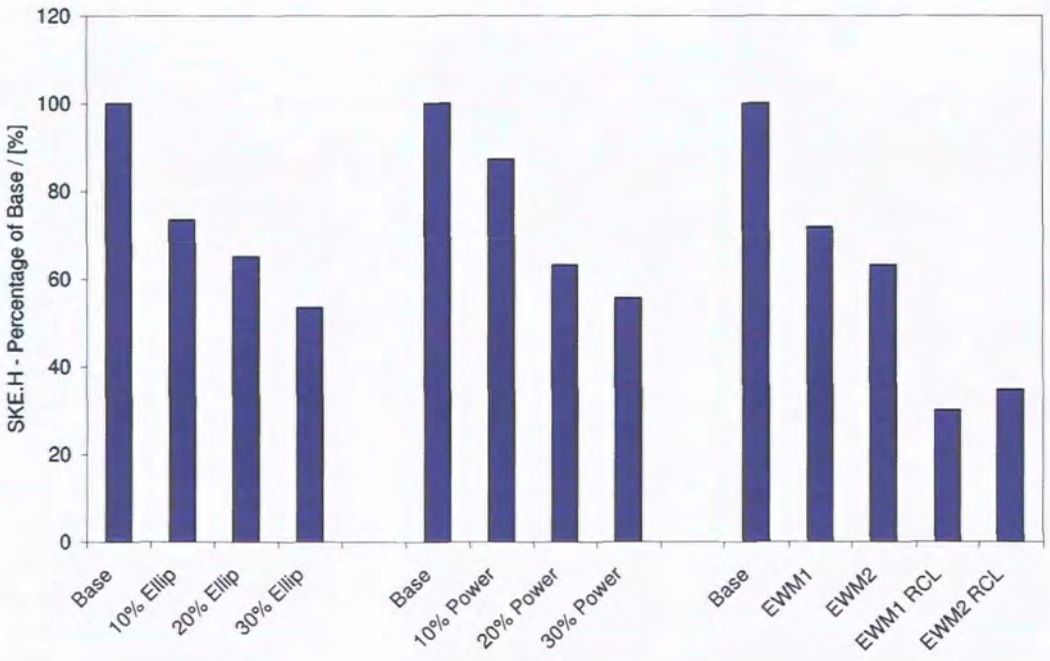

Figure 7.16: C2 Design Iterations - Mass Averaged SKE.H

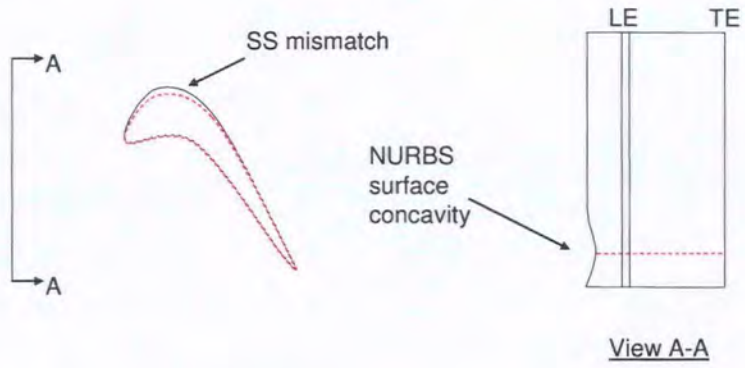

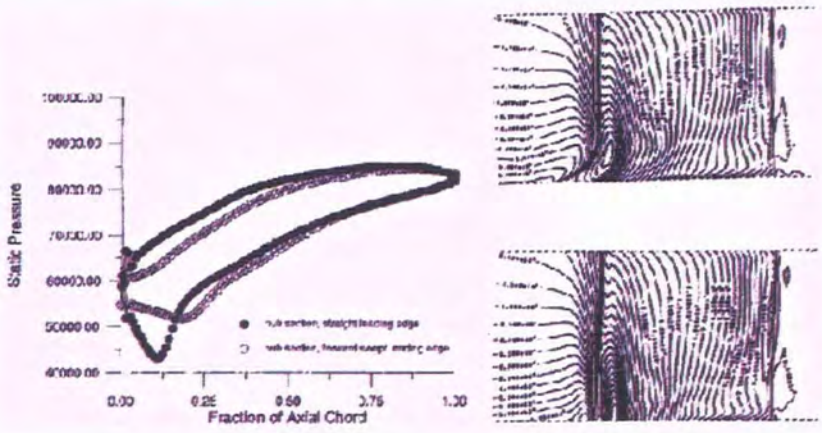

Figure 7.18: Sweep Effect as detailed by Denton and Xu (1999)

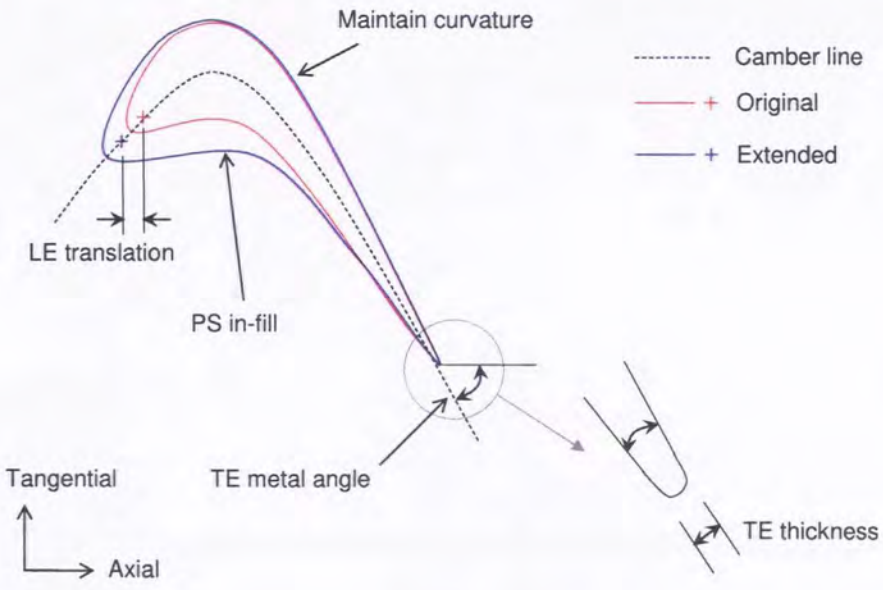

Figure 7.19: Blade Section Changes

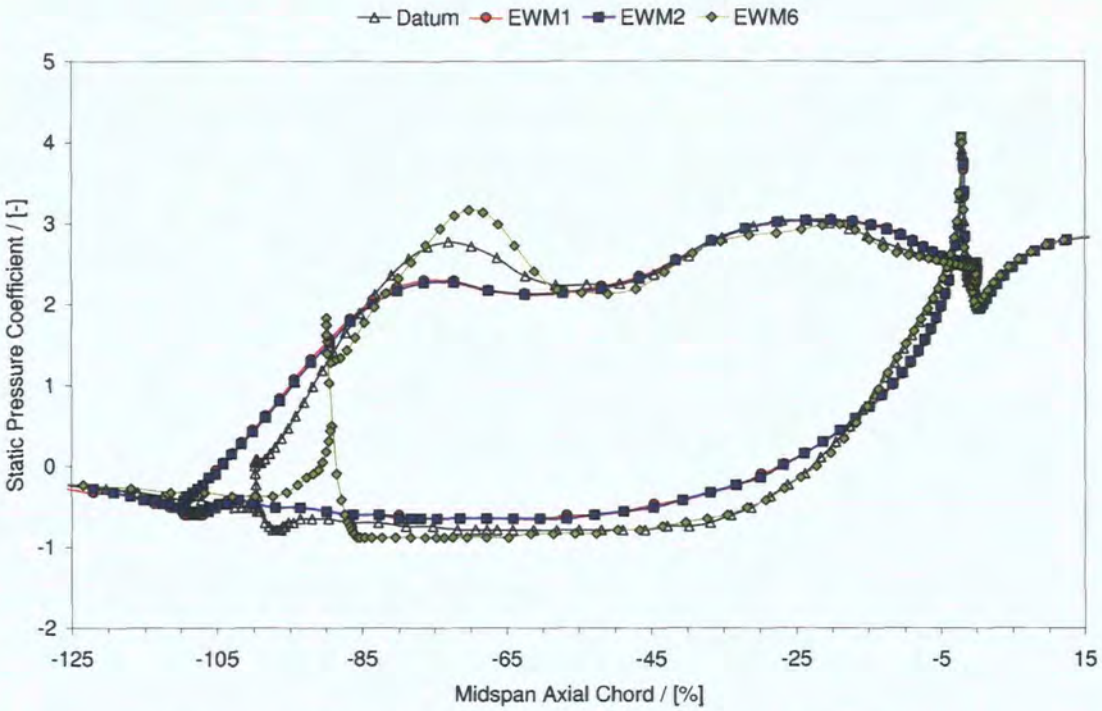

Figure 7.20: Surface Static Pressure Coefficient - 0% Span

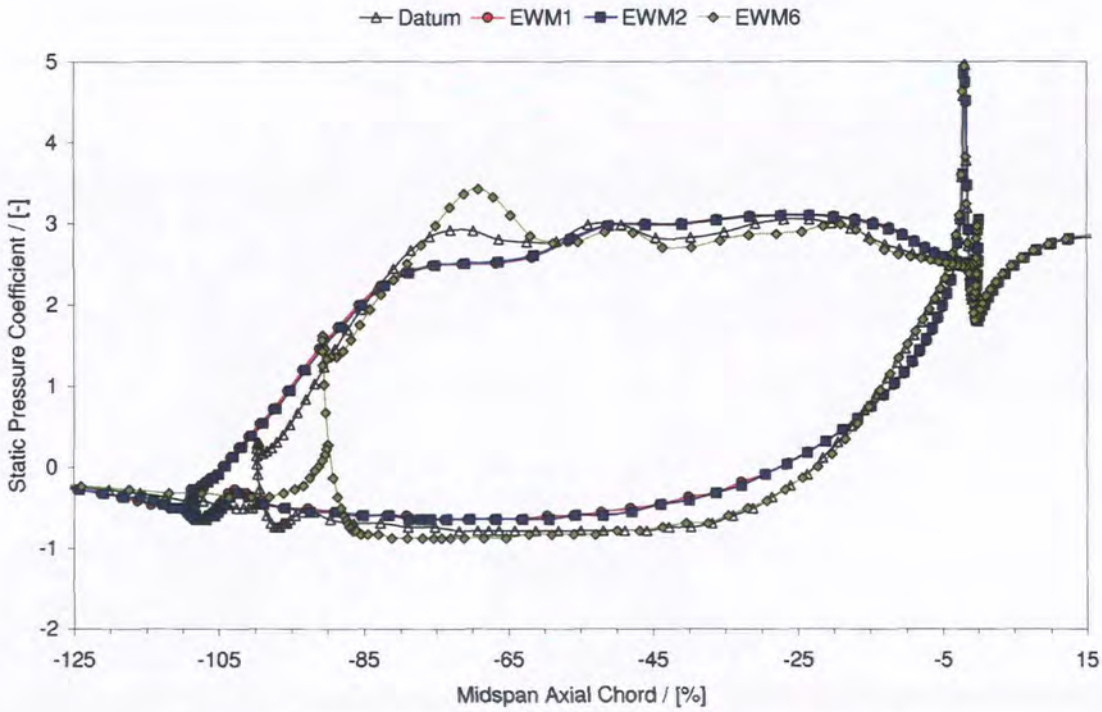

Figure 7.21: Surface Static Pressure Coefficient - 3% Span

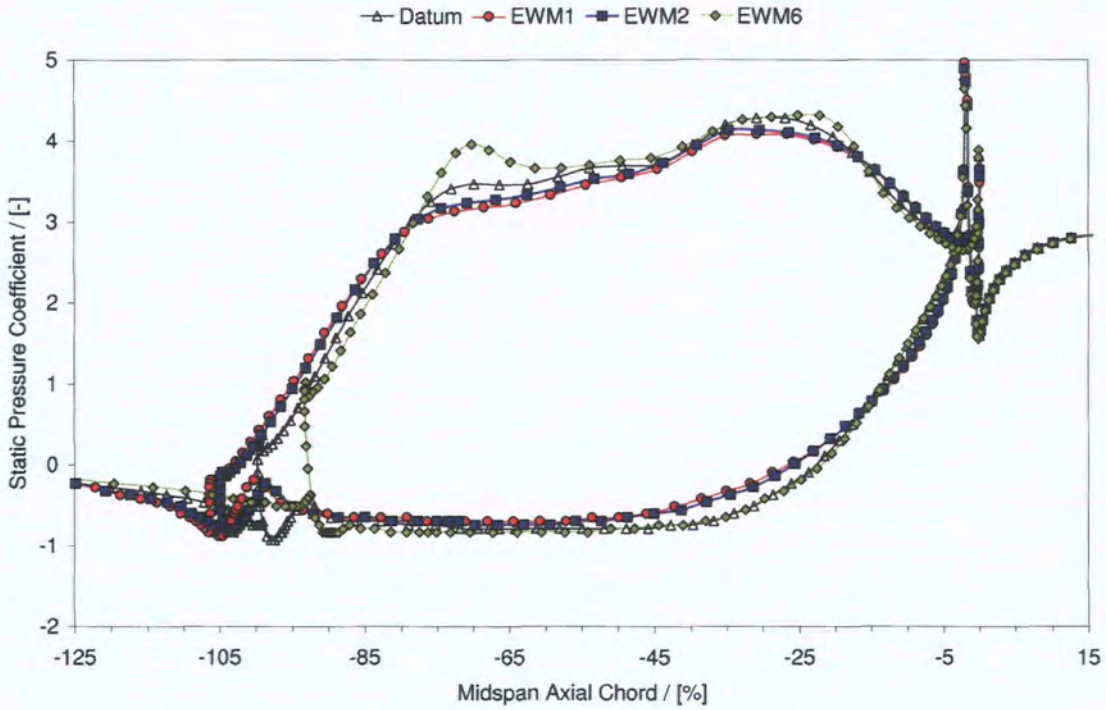

Figure 7.22: Surface Static Pressure Coefficient - 10% Span

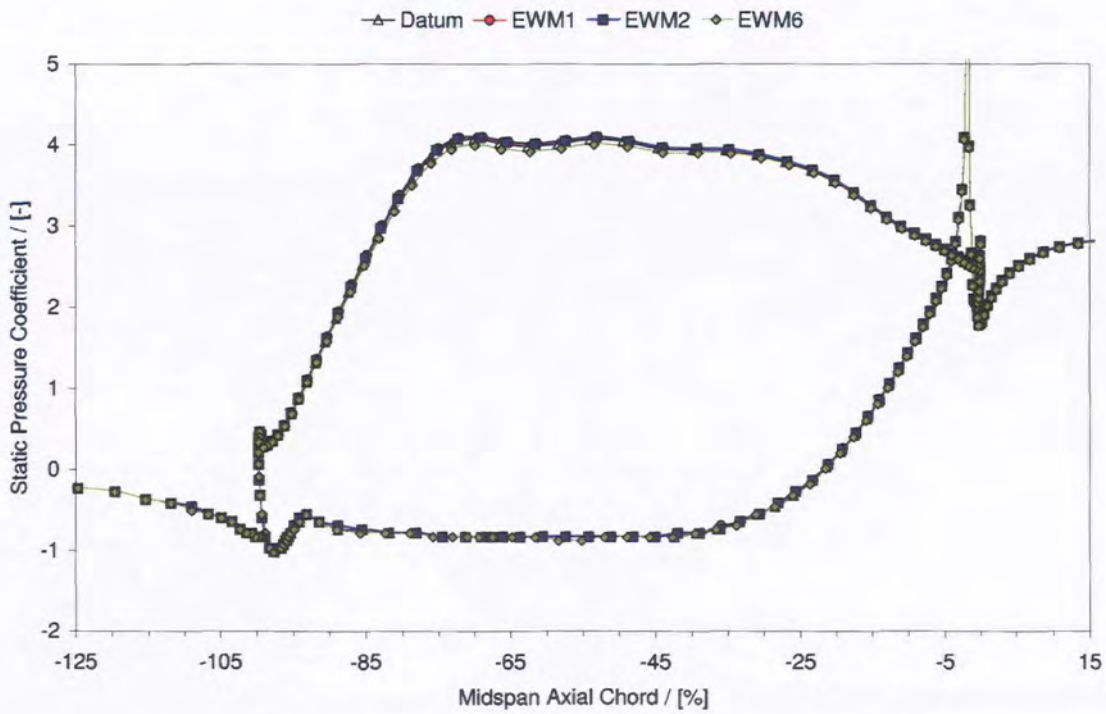

Figure 7.23: Surface Static Pressure Coefficient - 50% Span

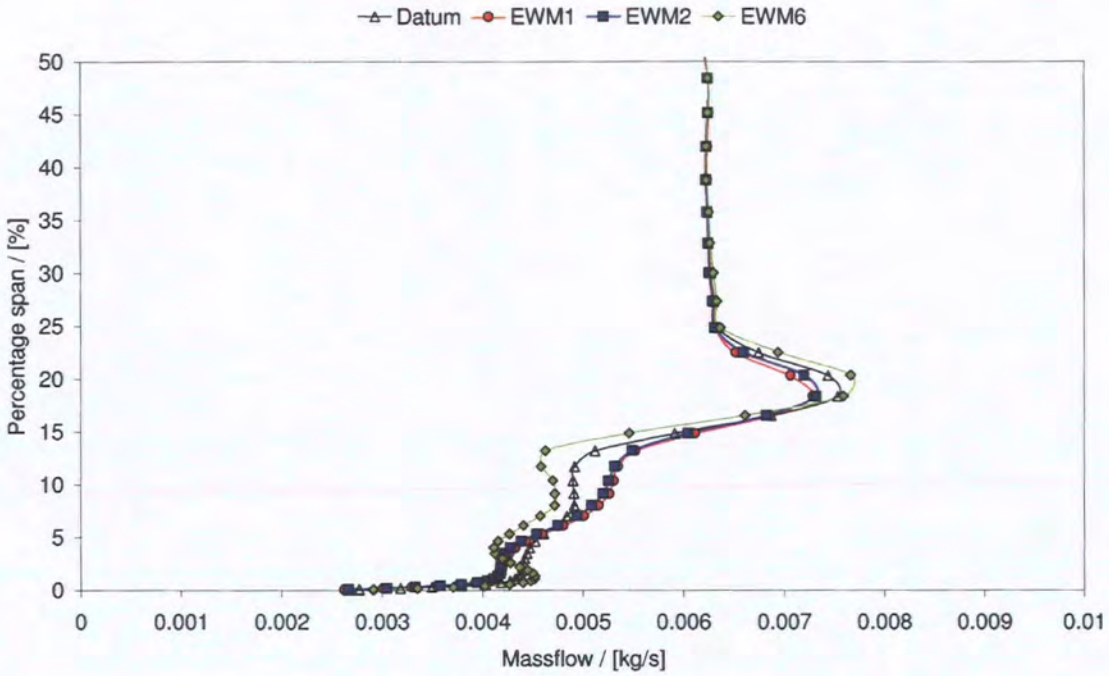

Figure 7.24: Pitchwise averaged Massflow at 128% C_{ax}

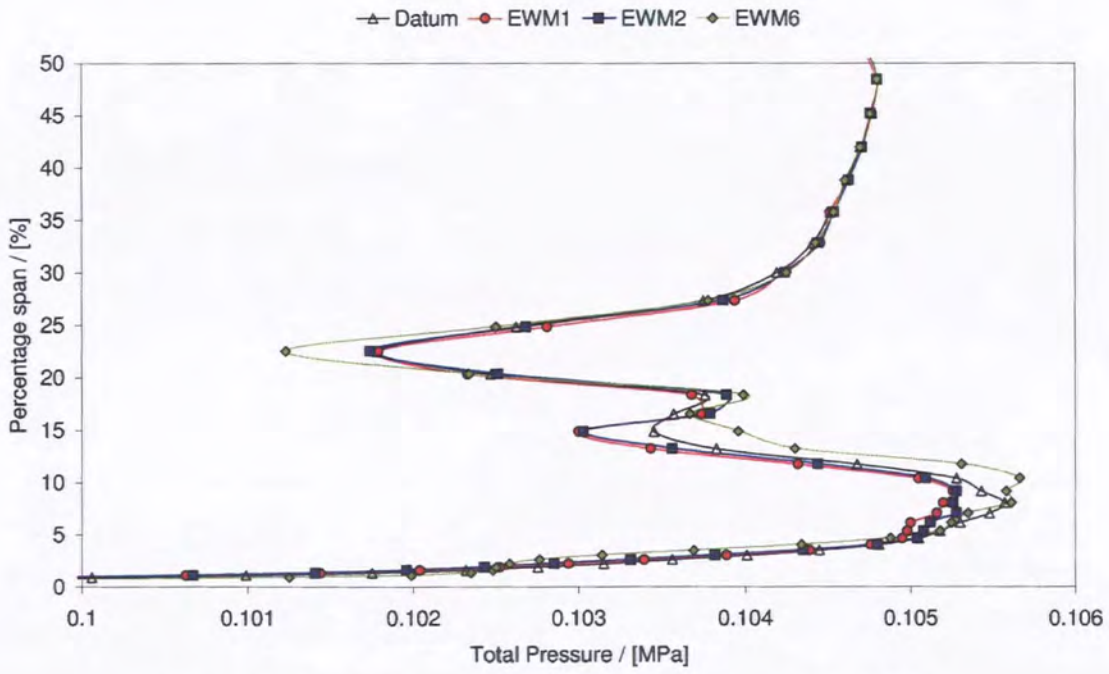

Figure 7.25: Pitchwise averaged Total Pressure at 128% C_{ax}

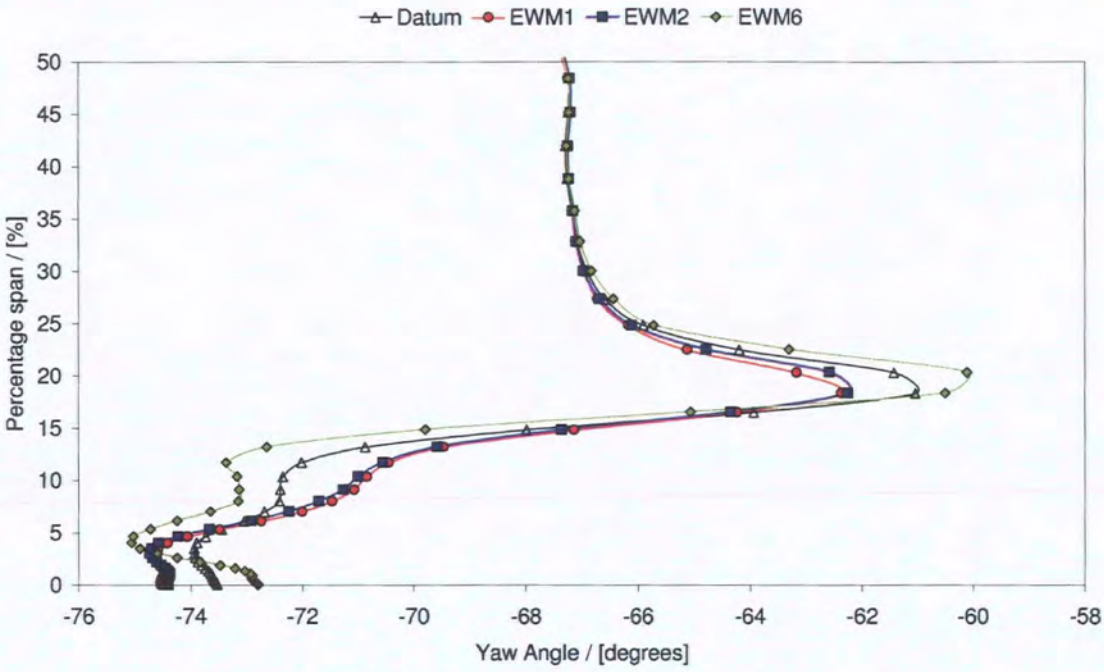

Figure 7.26: Pitchwise averaged Yaw Angle at 128% C_{ax}

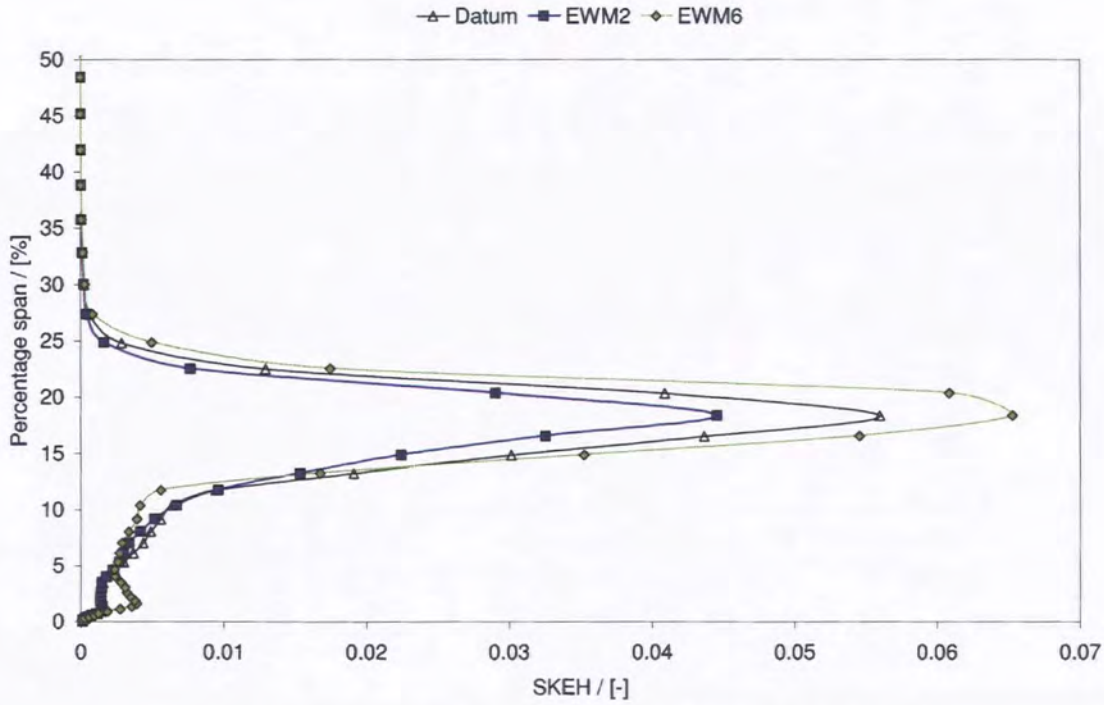

Figure 7.27: Pitchwise averaged SKEH at 128% C_{ax}

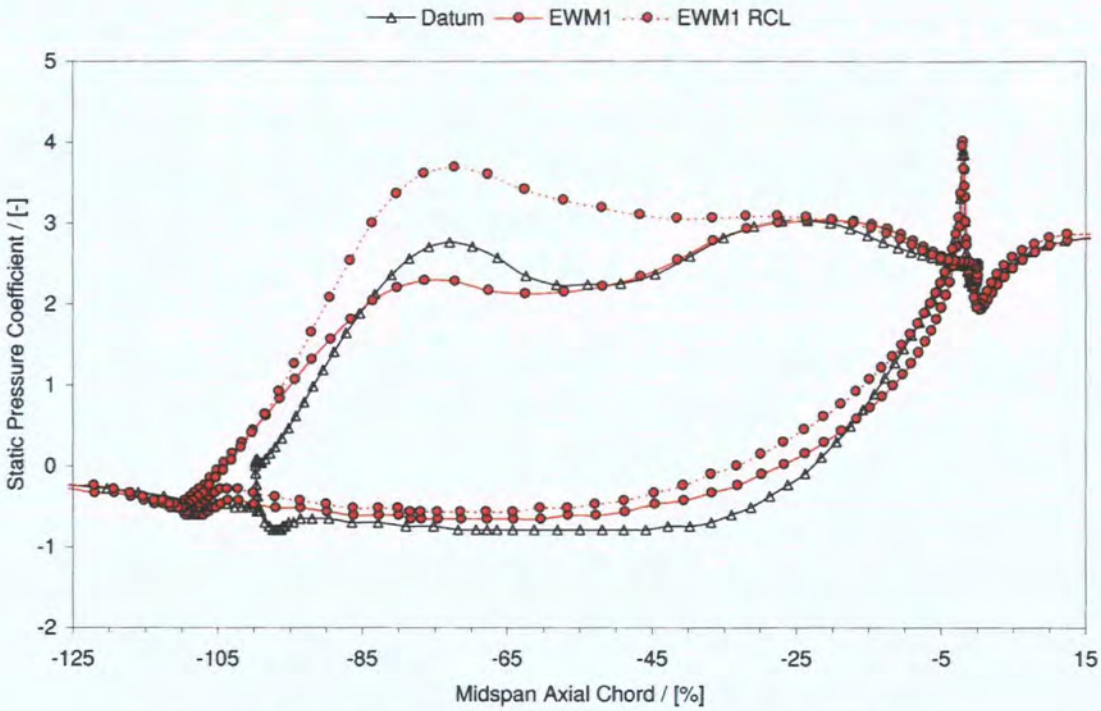

Figure 7.28: Surface Static Pressure Coefficient - 0% Span

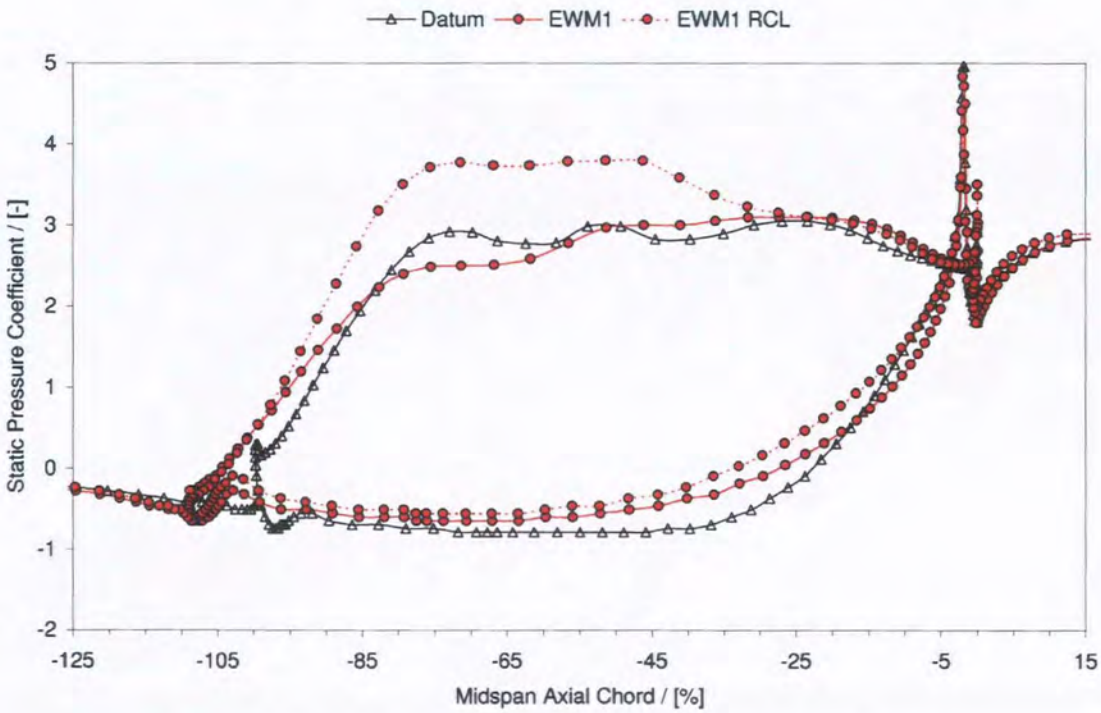

Figure 7.29: Surface Static Pressure Coefficient - 3% Span

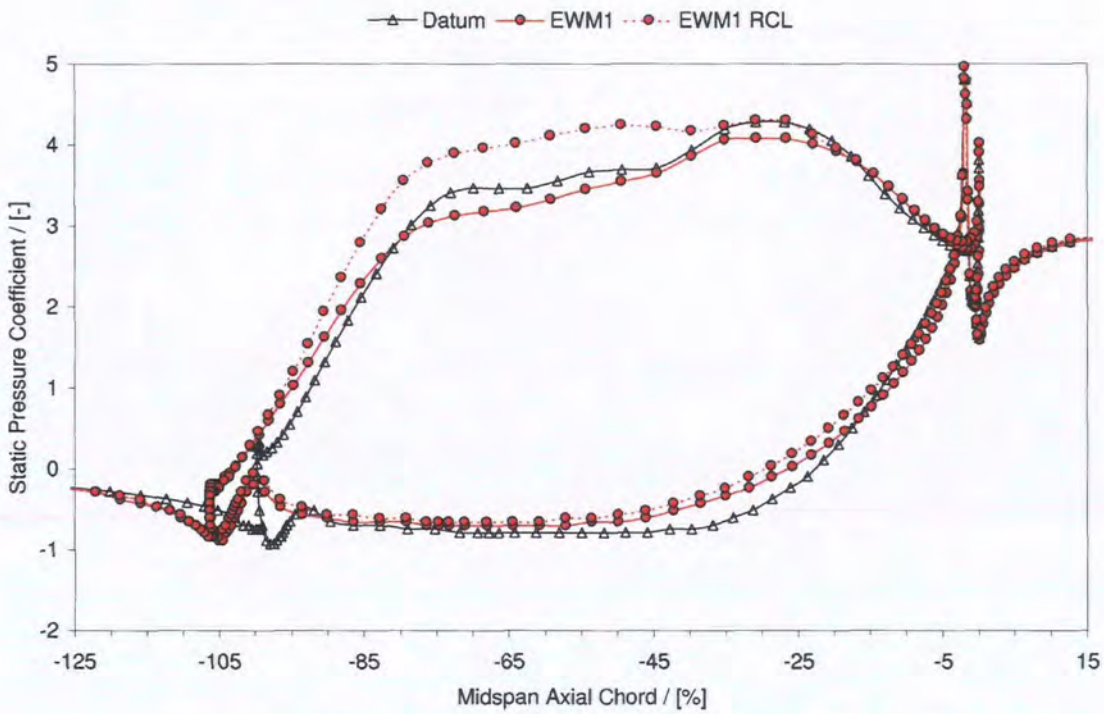

Figure 7.30: Surface Static Pressure Coefficient - 10% Span

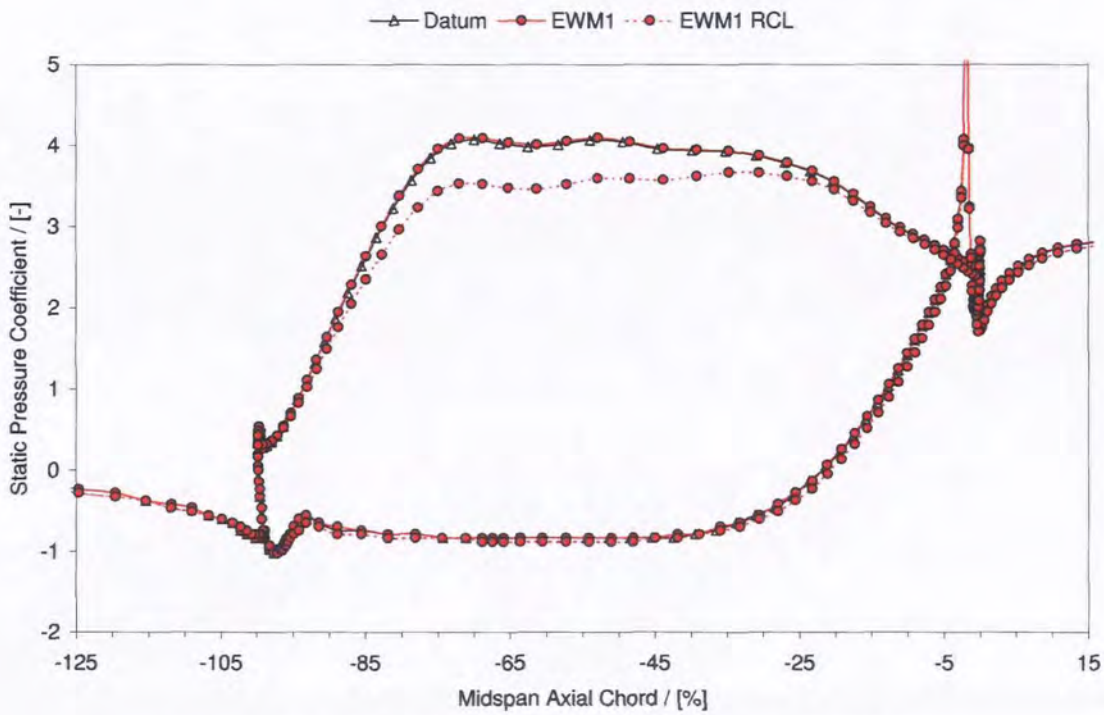

Figure 7.31: Surface Static Pressure Coefficient - 50% Span

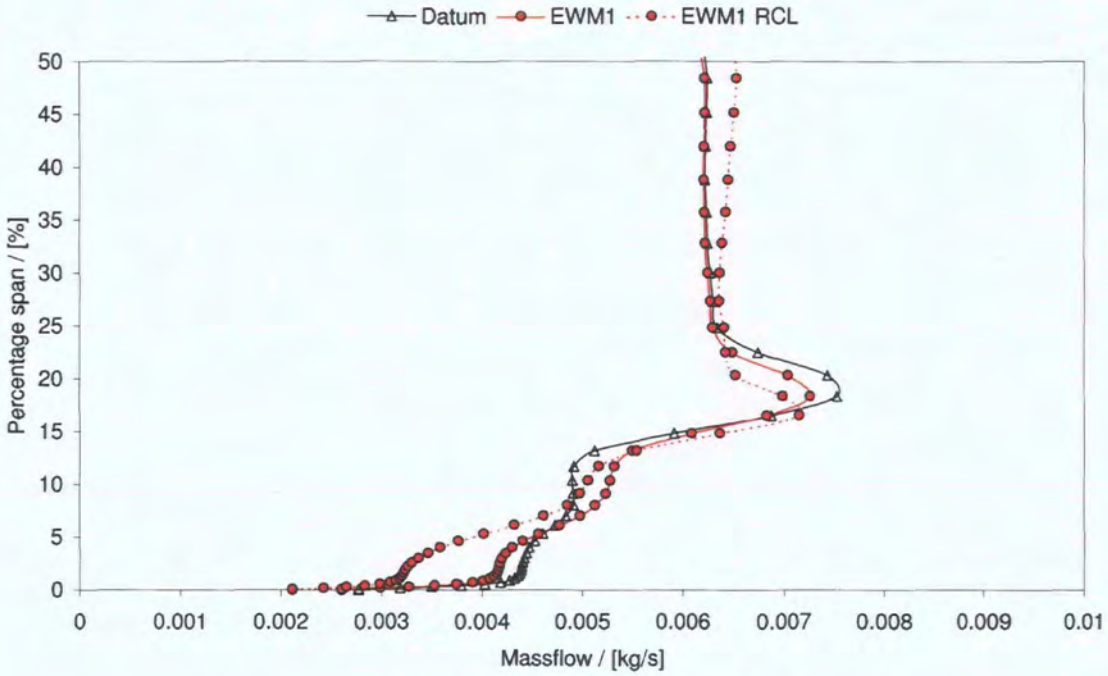

Figure 7.32: Pitchwise averaged Massflow at 128% C_{ax}

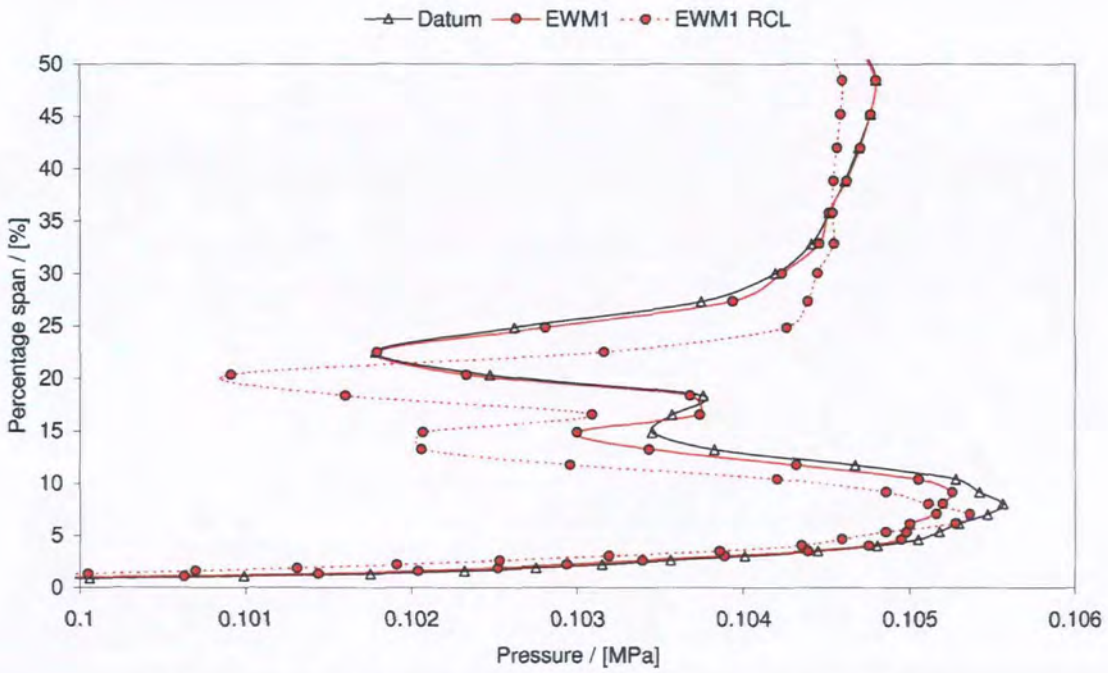

Figure 7.33: Pitchwise averaged Total Pressure at 128% C_{ax}

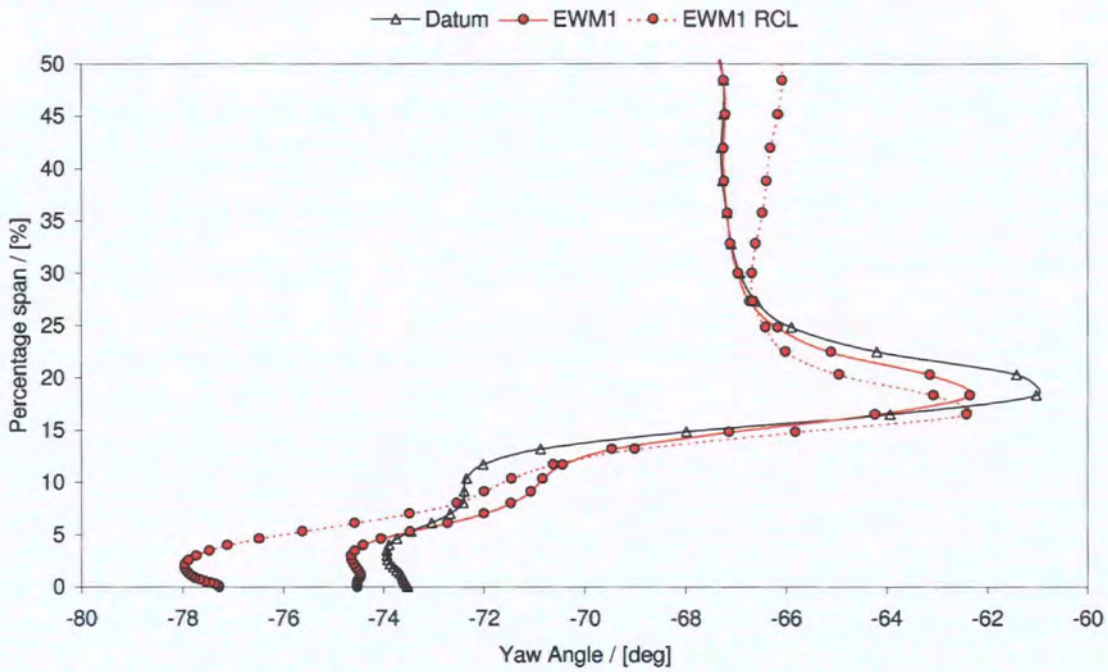

Figure 7.34: Pitchwise averaged Yaw Angle at 128% C_{ax}

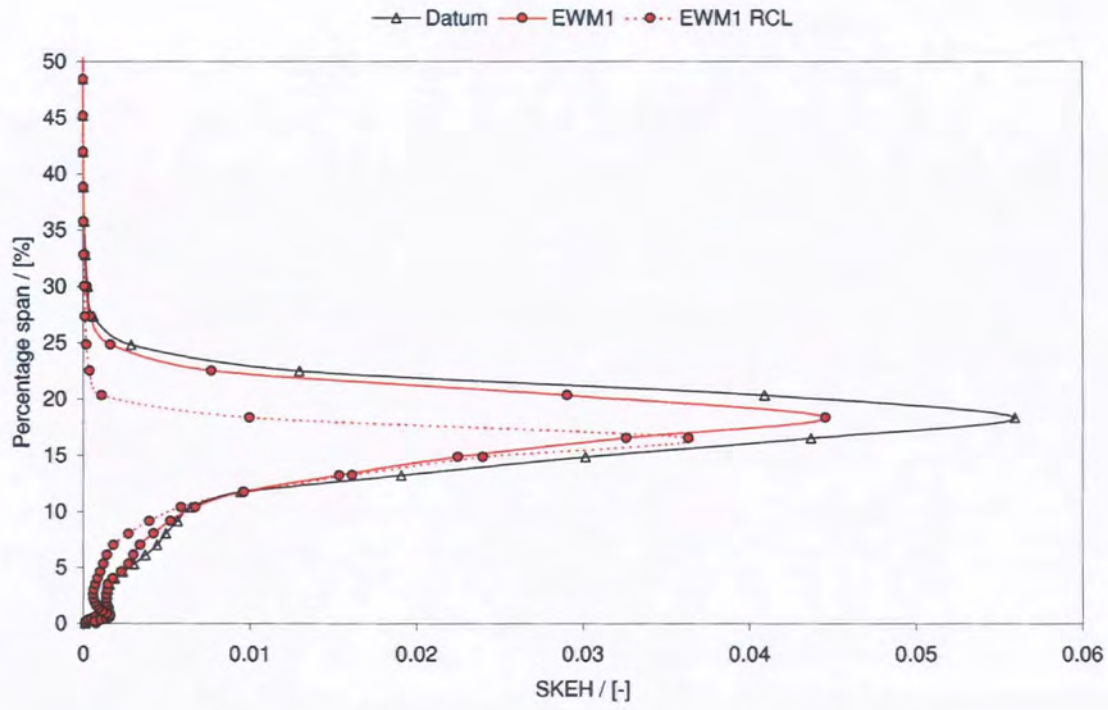

Figure 7.35: Pitchwise averaged SKEH at 128% C_{ax}

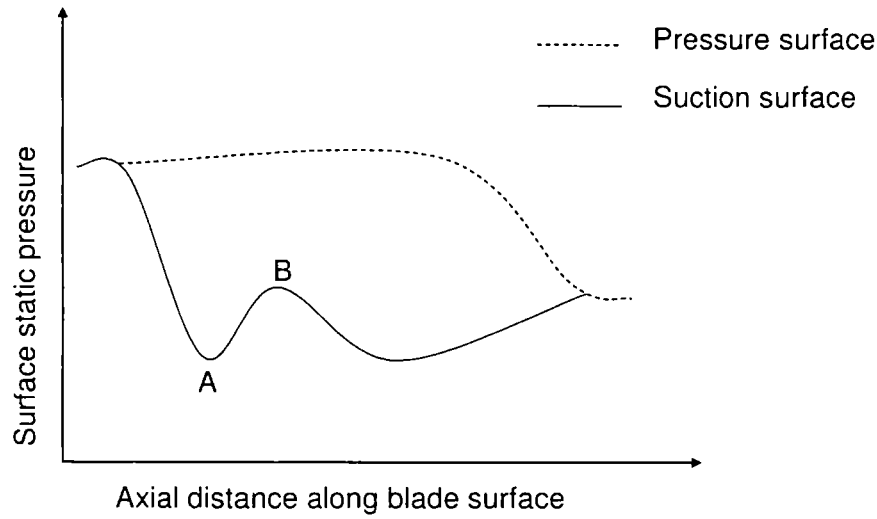

Figure 7.36: Typical diffusion near endwall due to PEW application

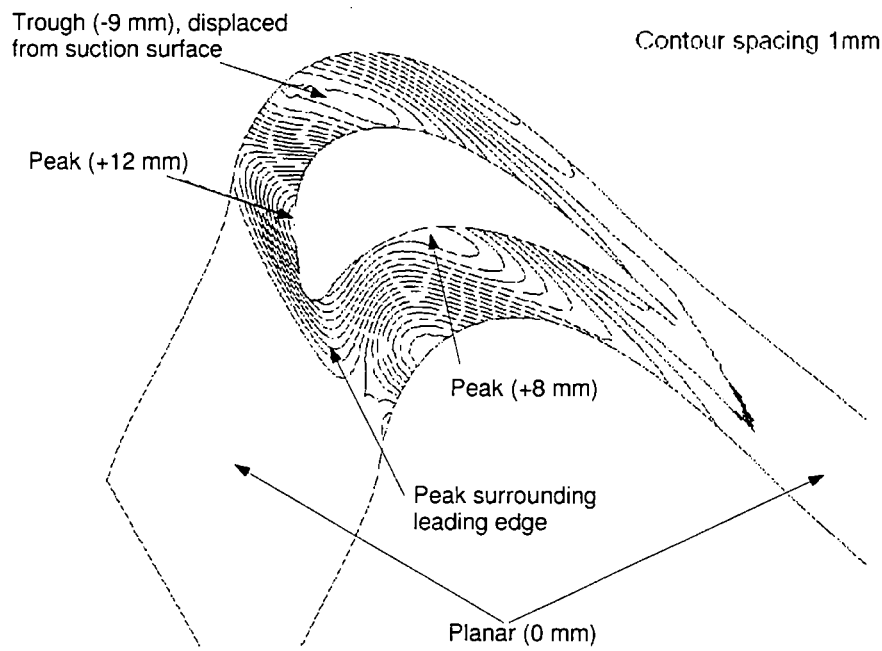

Figure 7.37: C2 - Aggressive (Lower) endwall heights

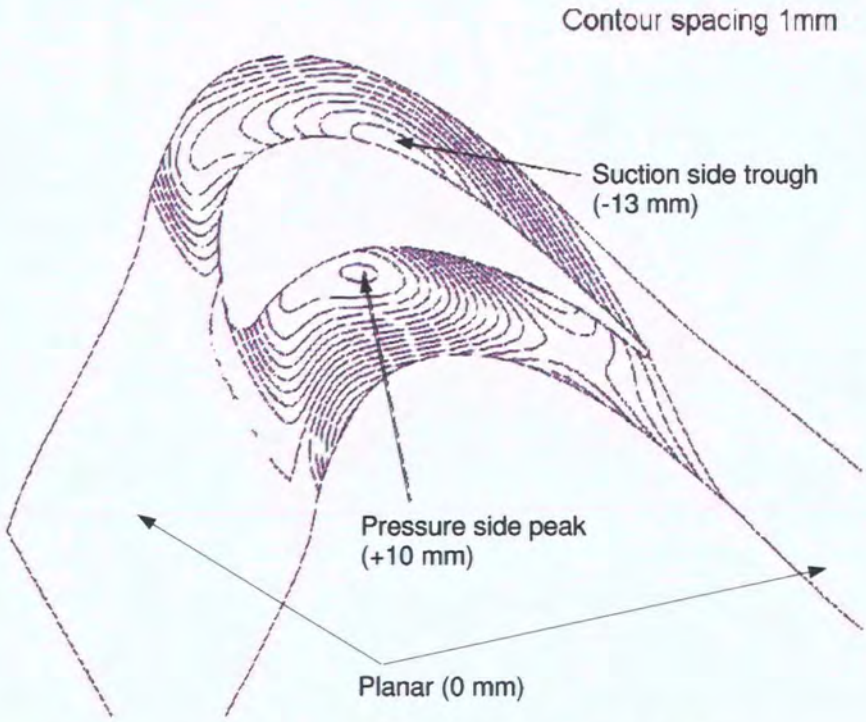

Figure 7.38: C2 - Mild (Upper) endwall heights

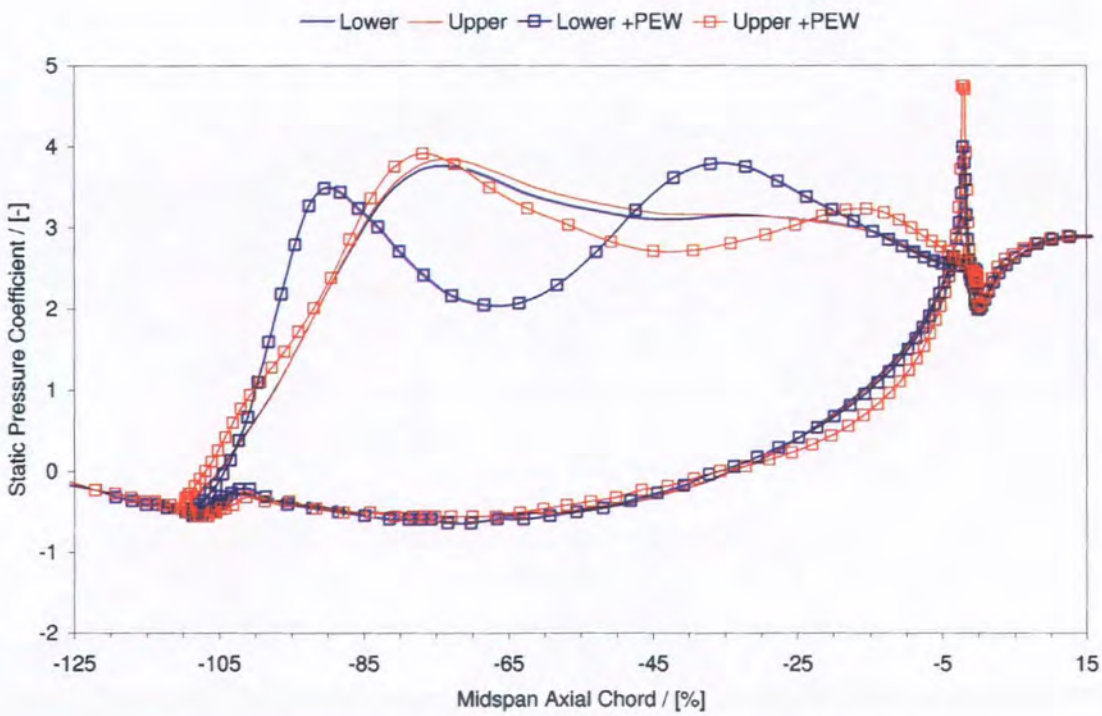

Figure 7.39: Surface Static Pressure Coefficient - 0% Span

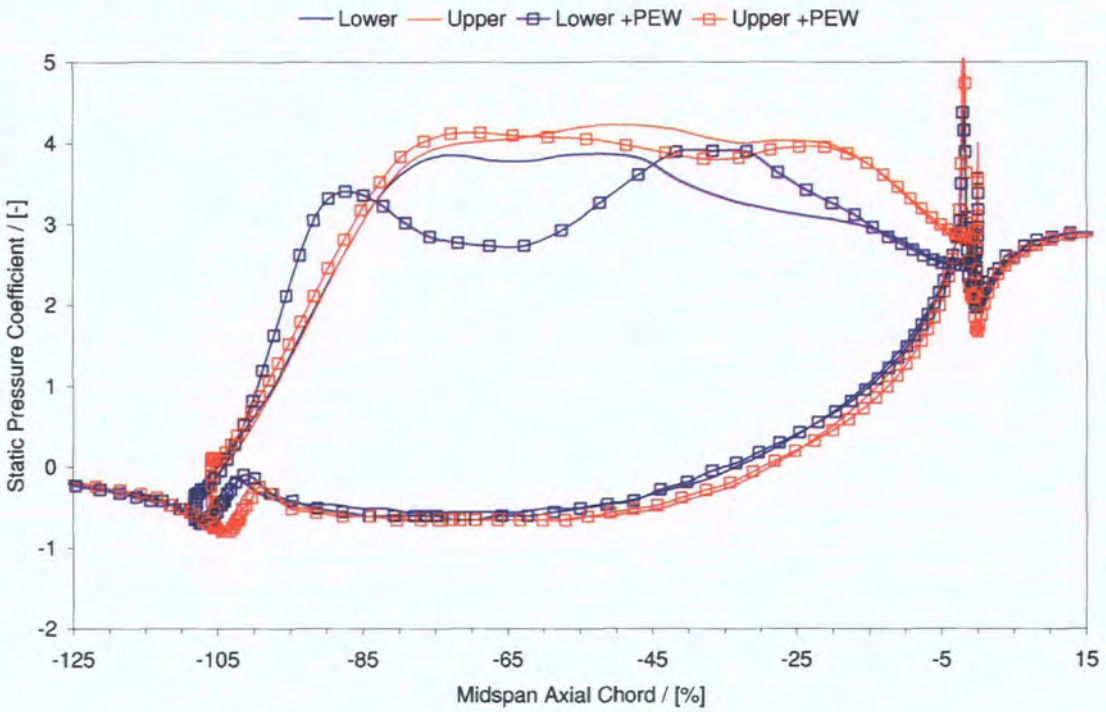

Figure 7.40: Surface Static Pressure Coefficient - 3% Span

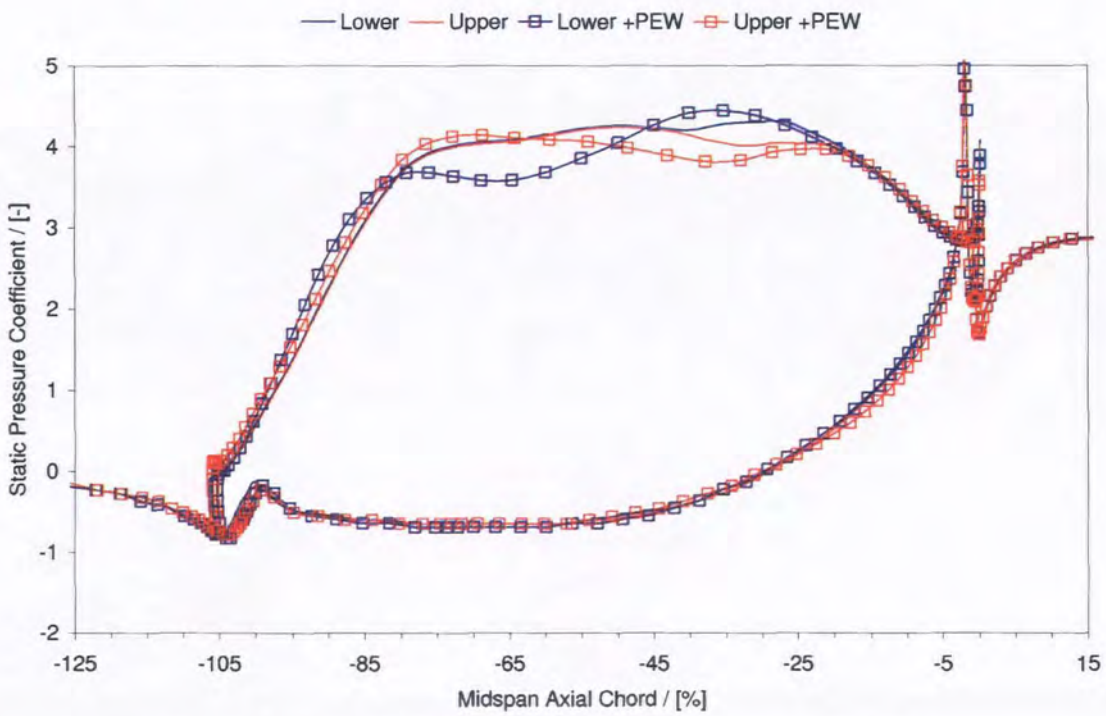

Figure 7.41: Surface Static Pressure Coefficient - 10% Span

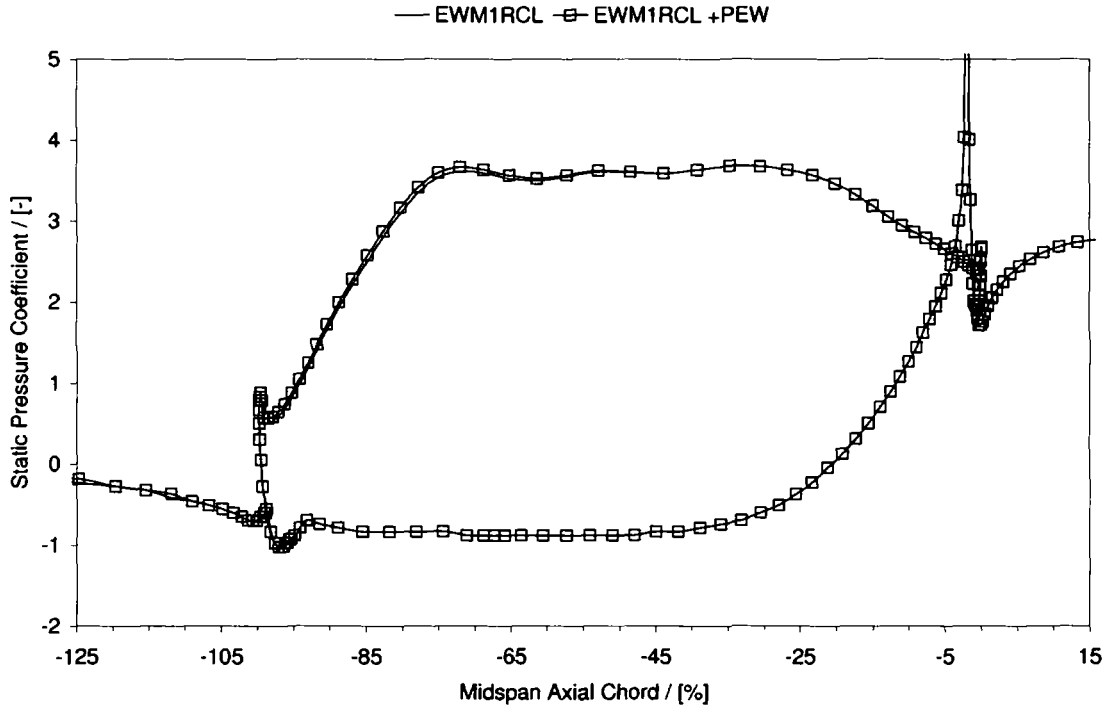

Figure 7.42: Surface Static Pressure Coefficient - 50% Span

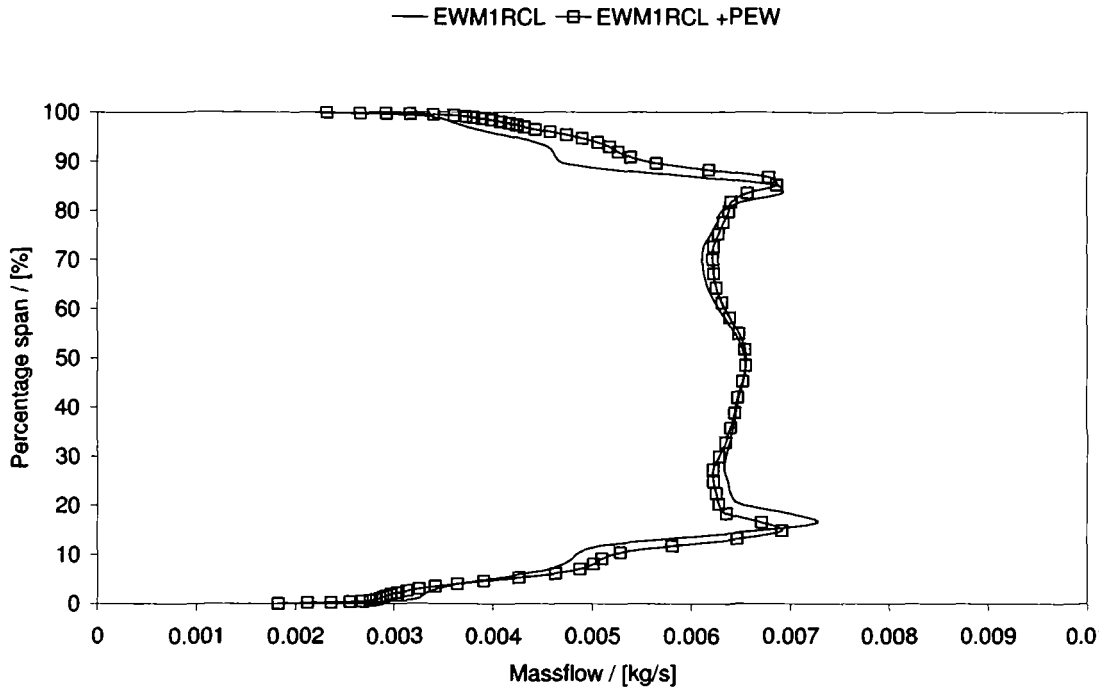

Figure 7.43: Pitchwise averaged Massflow at 128% C_{ax}

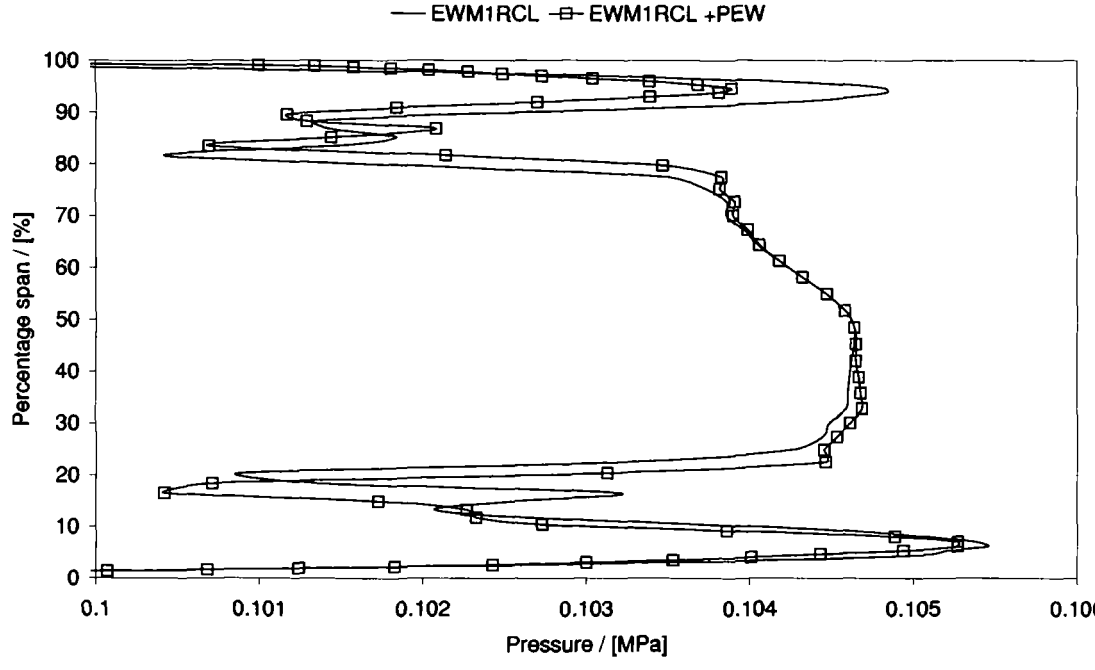

Figure 7.44: Pitchwise averaged Total Pressure at 128% C_{ax}

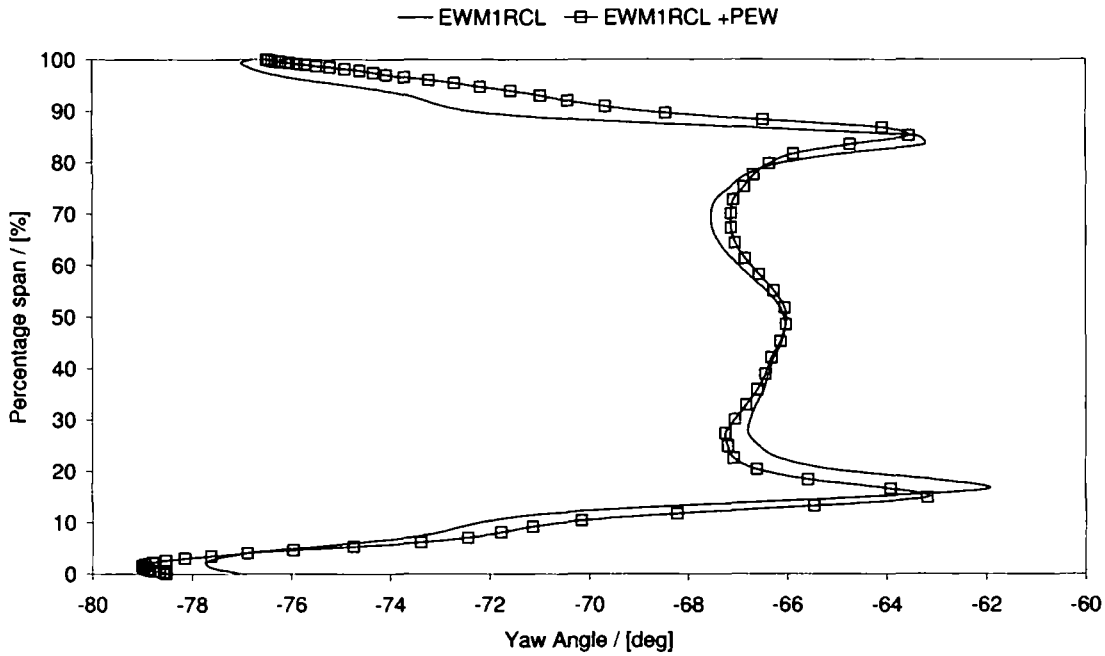

Figure 7.45: Pitchwise averaged Yaw at 128% C_{ax}

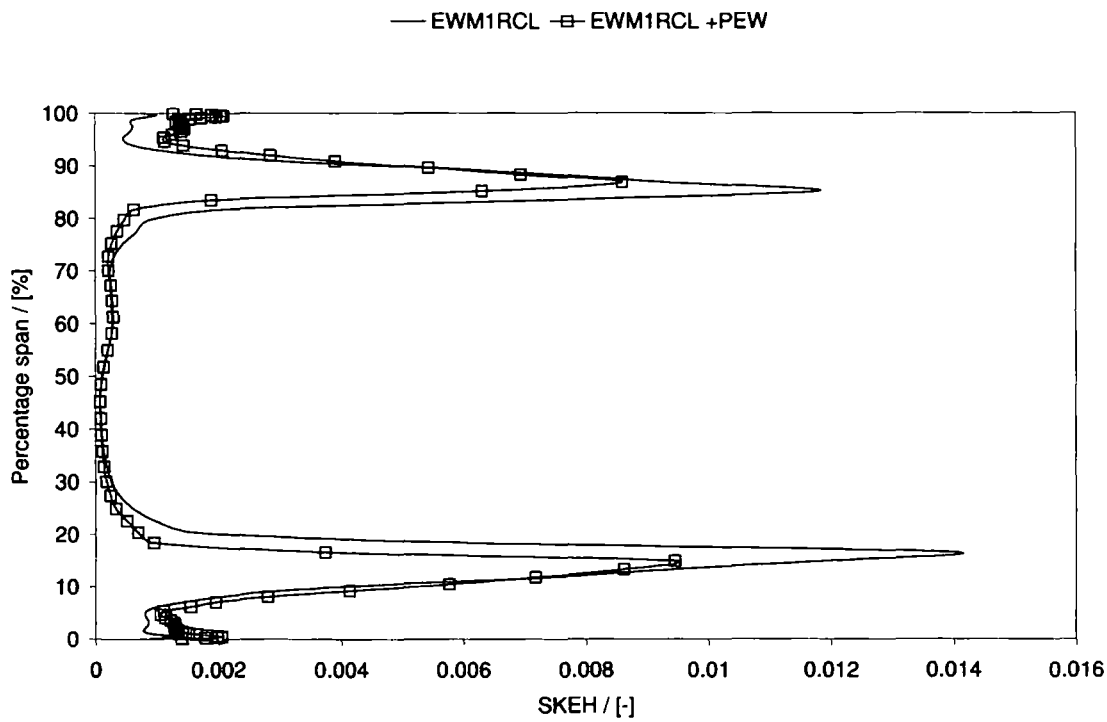

Figure 7.46: Pitchwise averaged SKEH at 128% C_{ax}

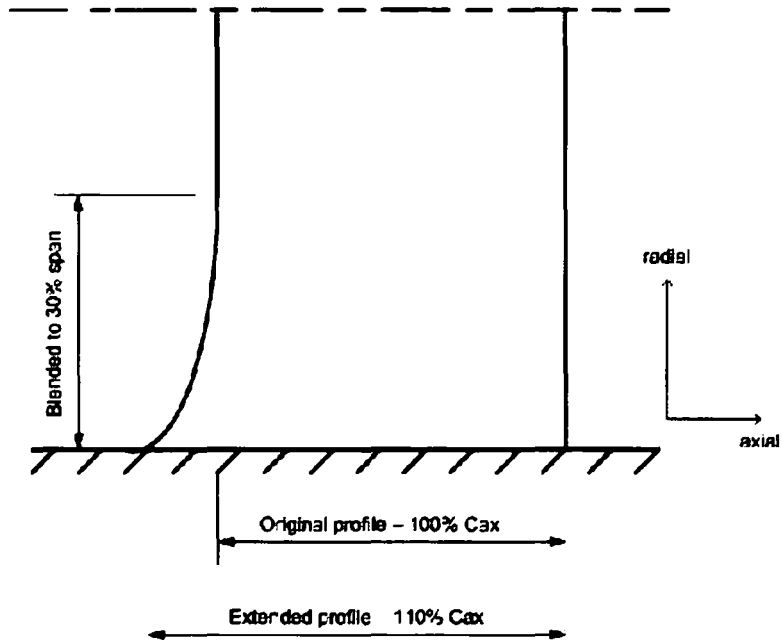

Figure 7.47: Axial Chord Extension - Definition

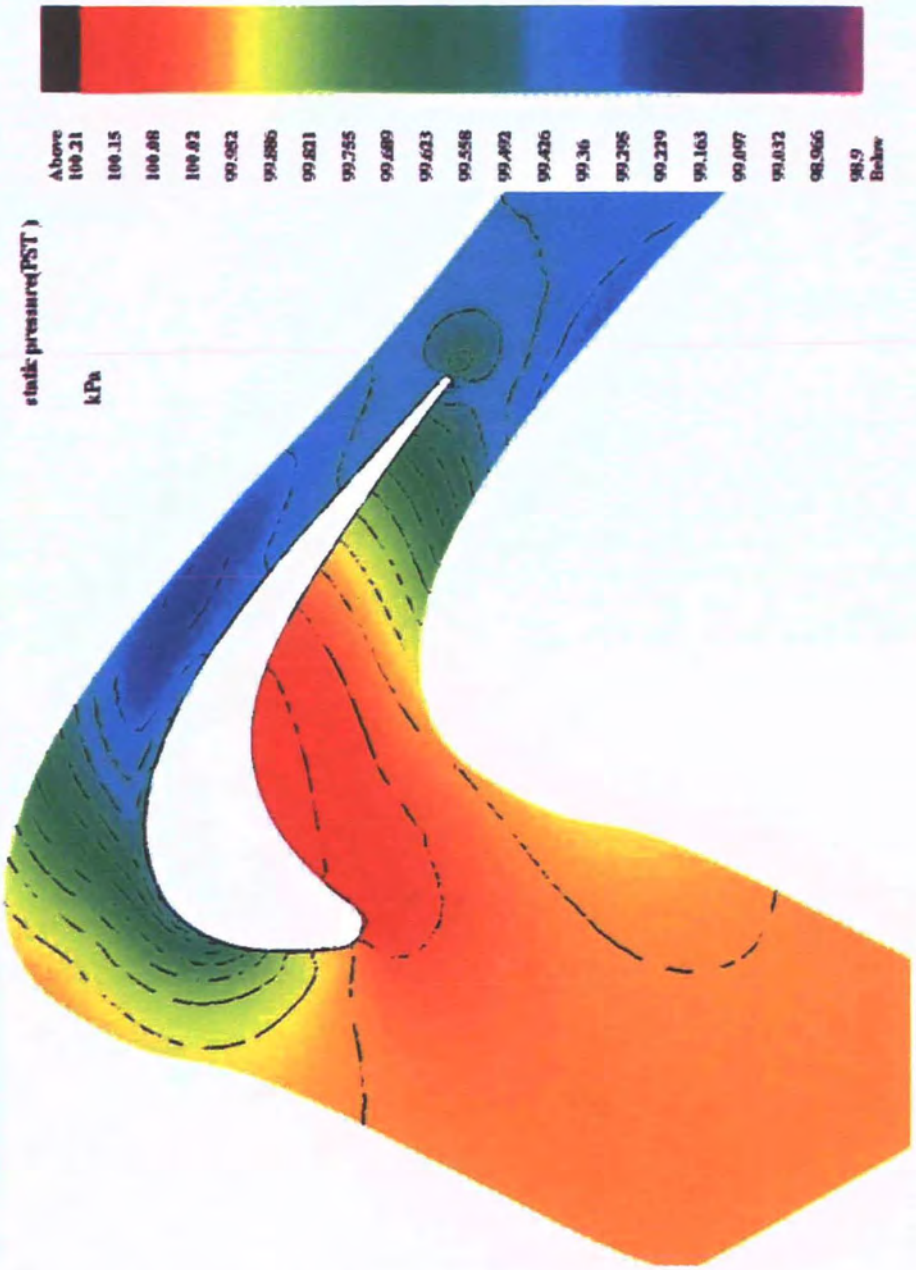

Figure 7.48: Endwall Static Pressure - C0a

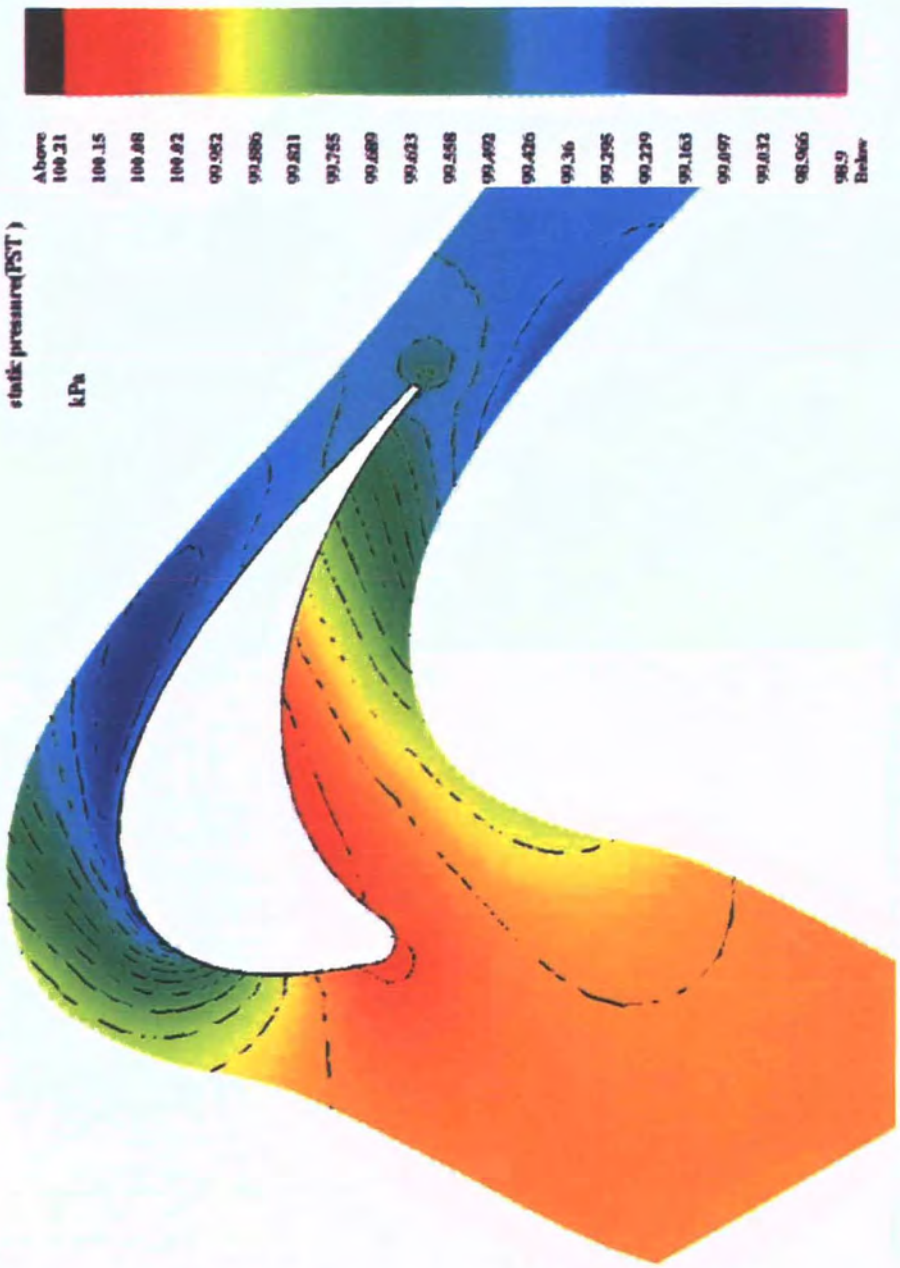

Figure 7.49: Endwall Static Pressure - C2 planar

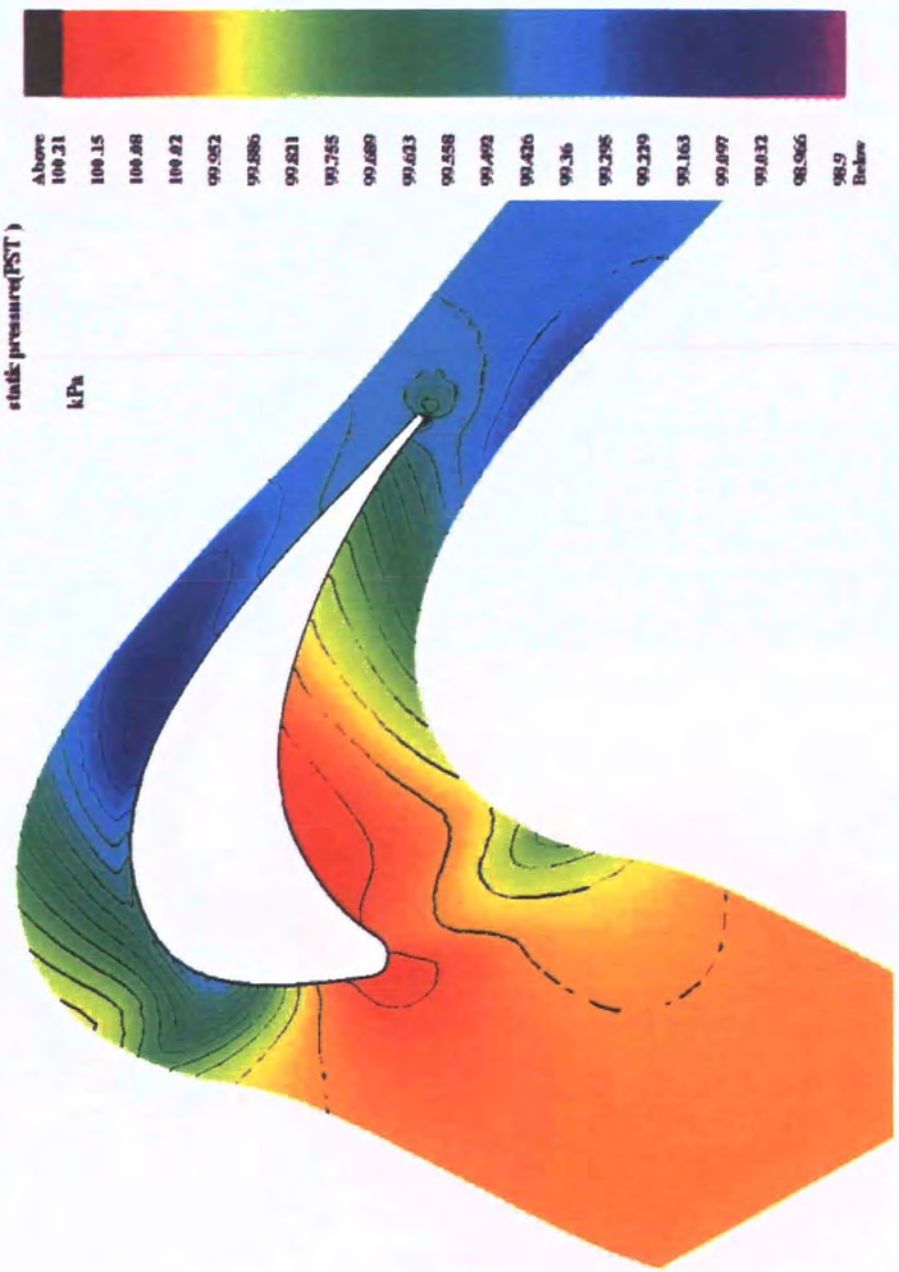

Figure 7.50: Endwall Static Pressure - C2 Aggr

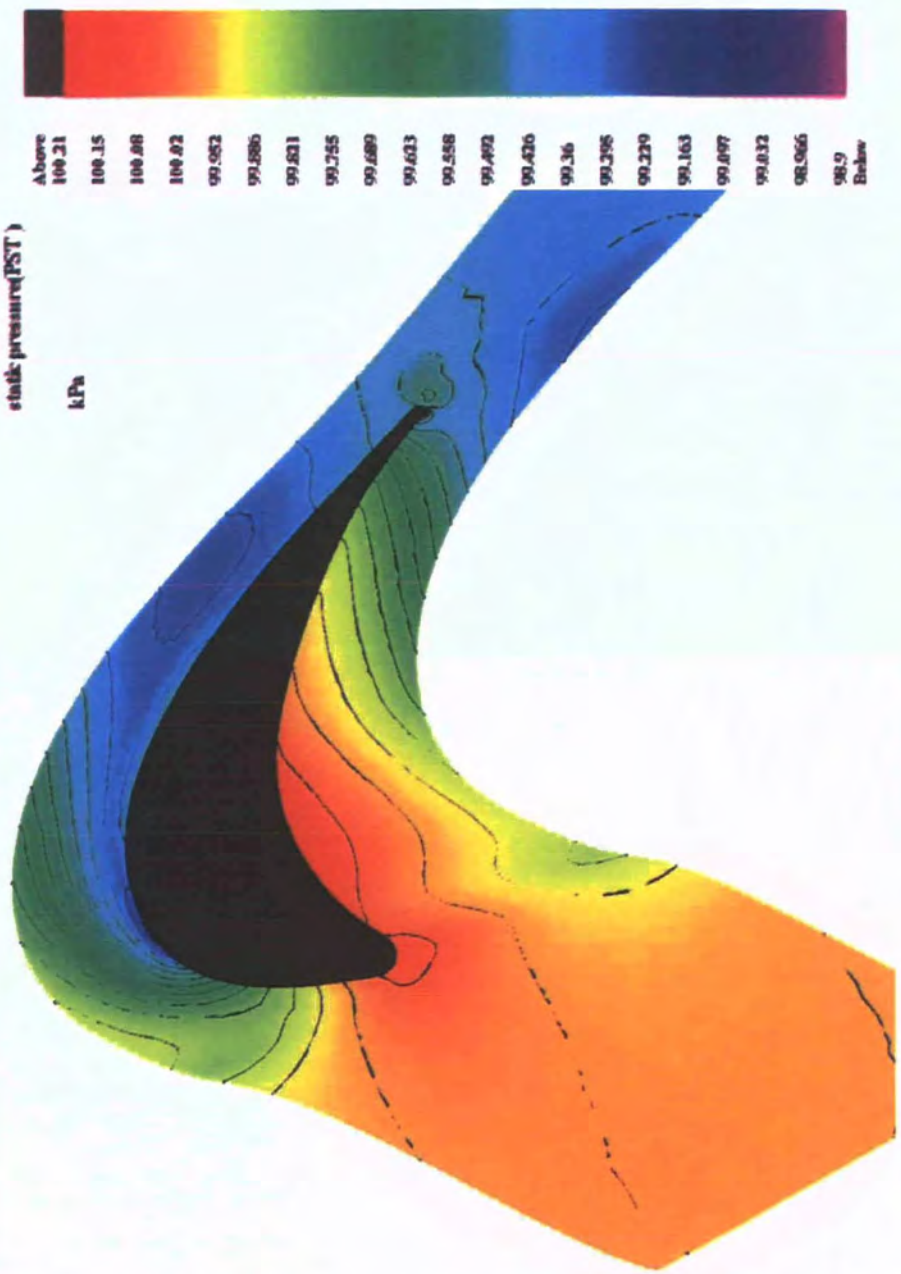

Figure 7.51: Endwall Static Pressure - C2 Mild

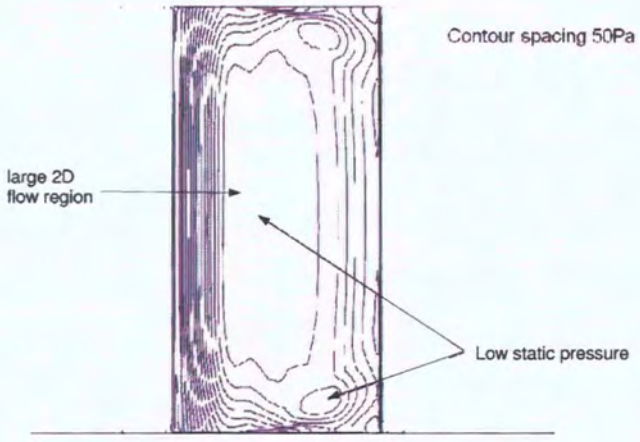

Figure 7.52: Suction Surface C_p - C0a

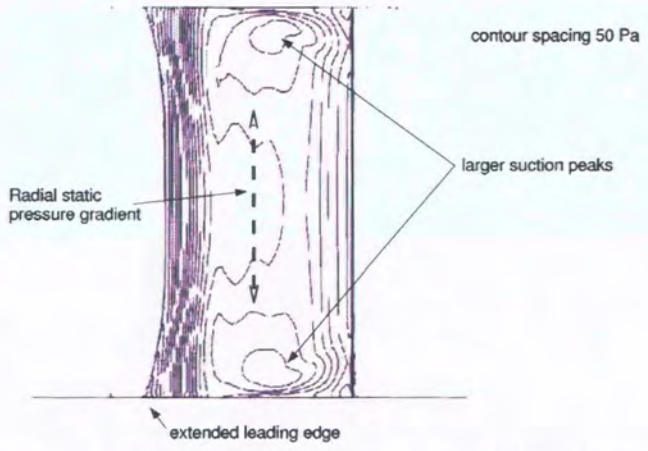

Figure 7.53: Suction Surface C_p - C2 Planar

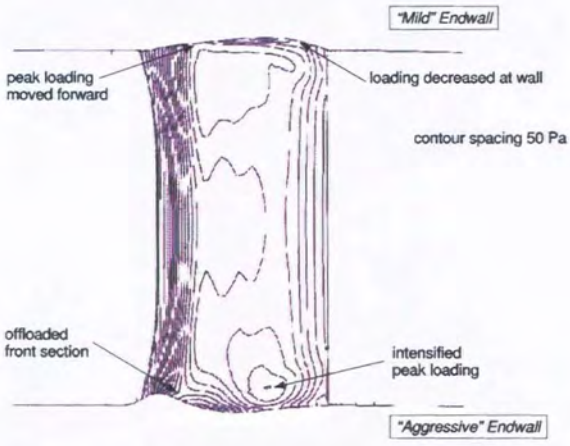

Figure 7.54: Suction Surface C_p - C2 PEW

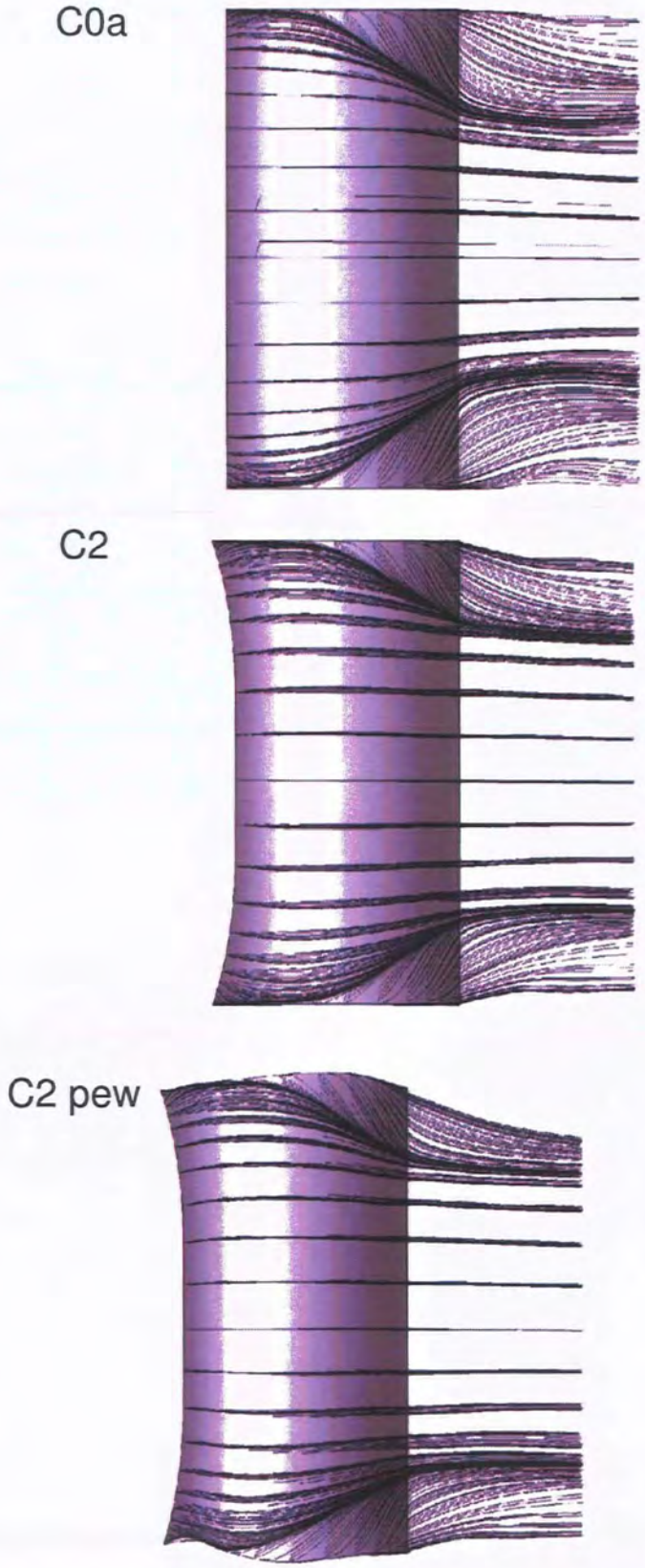

Figure 7.55: SS Flow Visualisation

Figure 7.56: Endwall Surface Flow Visualisation

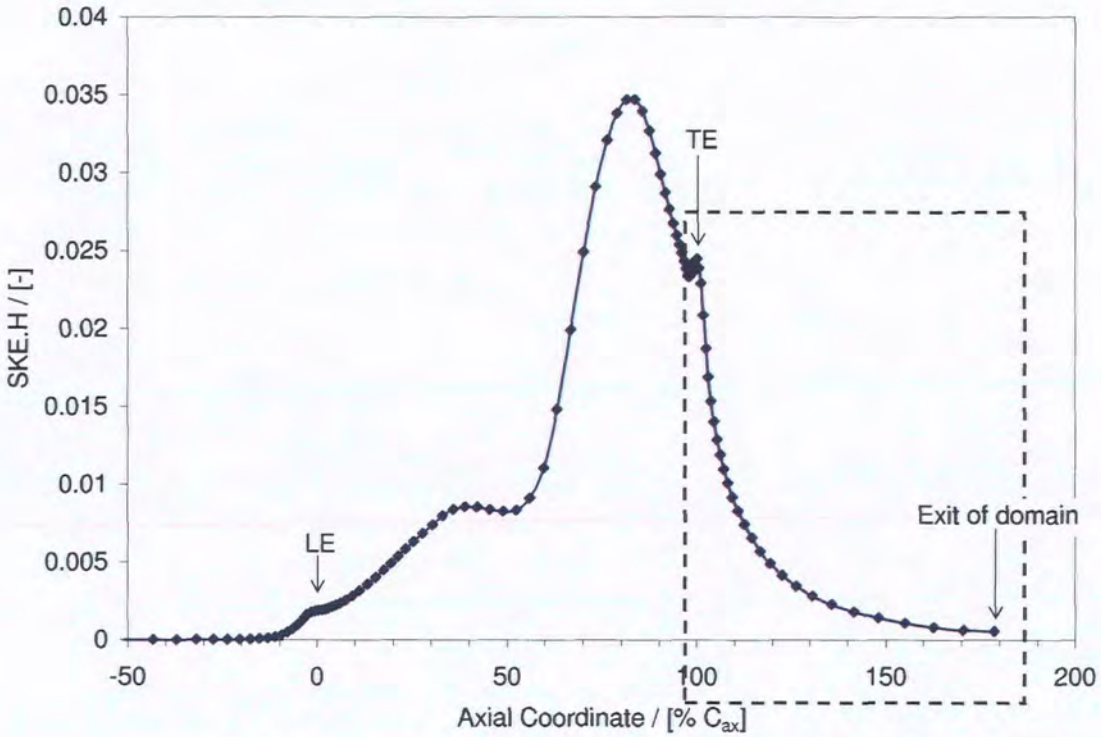

Figure 7.57: Sample AA SKE.H Distribution and area of interest

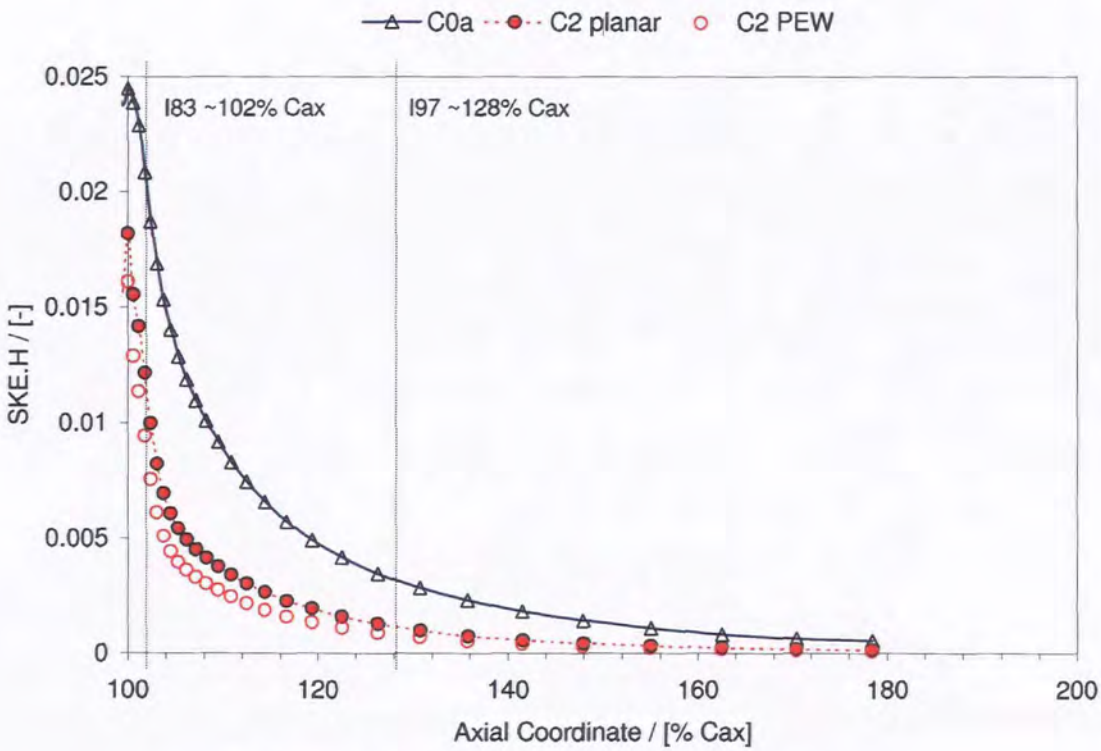

Figure 7.58: SKE.H Performance Comparison

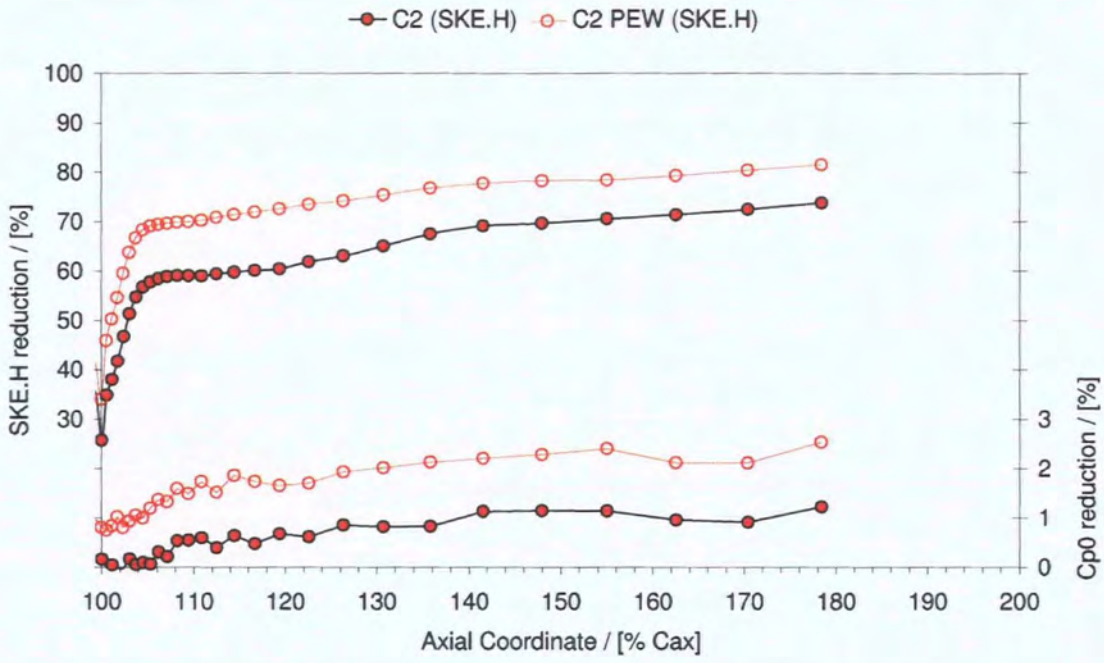

Figure 7.59: SKE.H and Loss Performance Comparisons

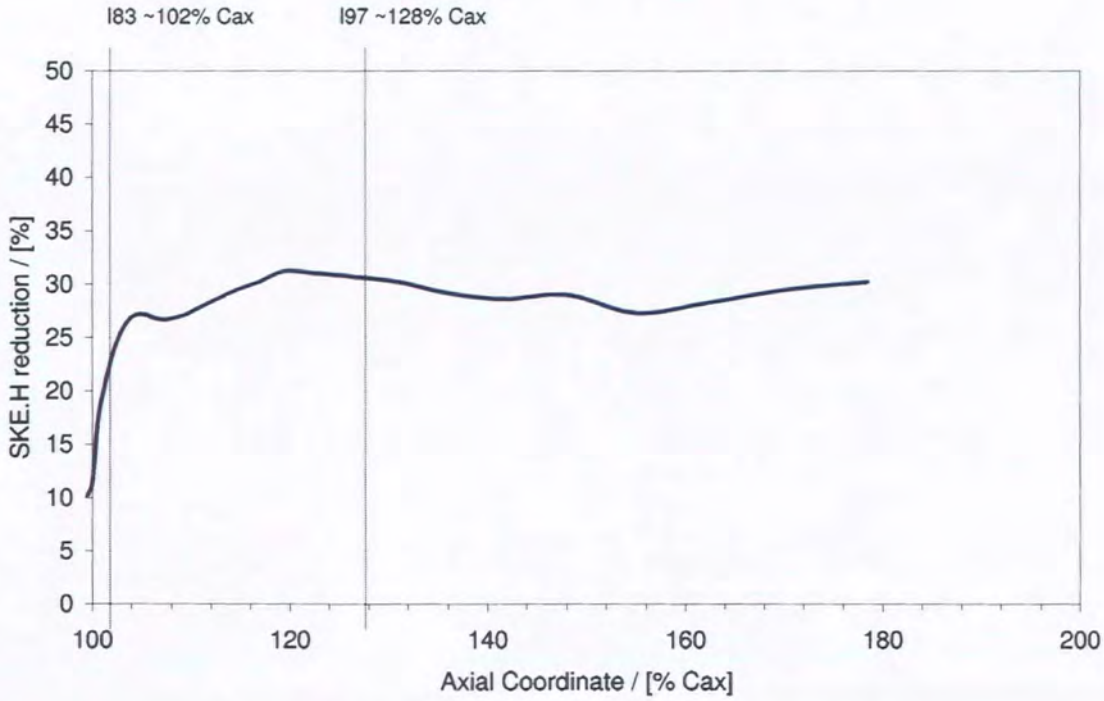

Figure 7.60: Effect of Application of PEWs on SKE.H

Chapter 8

Passage Shaped C2 - Experimental Results

THIS chapter details the results of experimental testing of the geometry defined in Chapter 7, undertaken on the Durham Cascade. The results include static pressure measurements, oil and dye surface flow visualisation images and a series of pressure probe traverses, at different axial locations. The experimental results are compared with the computational solution described in Chapter 7.

The pressure probe results comprise five hole probe readings from three traverse planes at 97%, 104% and 128% C_{ax} (Figure 3.15). Two geometries are discussed, these are the passage shaped C2 and the prismatic datum geometry C0a. It should be remembered that the flow fields at the two ends of the C2 geometry are a result of the same blade geometry, but of different PEW designs.

The five hole probe traverses give information on the total pressure loss, the secondary velocity vectors and the streamwise vorticity. The experiemtnal geometry was built with the endwalls at the opposite ends to those defined in the CFD study of the previous chapter. As such, the lower endwall now corresponds to the mild profiling, highlighted in Figure 8.1, and the upper endwall corresponds to the aggressive profiling, the detail of which can be found in Figure 8.2.

8.1 Five hole probe traverses

8.1.1 Area traverses at 97% C_{ax}

The traverse plane at 97% C_{ax} relates to Slot 8 of the old cascade and gives information on the flow field prior to the trailing edge mixing, therefore data on loss and vorticity not associated with the blade trailing edge and wake. Traversing was achieved using the new probe arrangement, described in Chapter 3.

It should be noted that the measurement data for geometry C2, at this plane, is the combination of two individual traverses that overlap at 50% span. The split of the traversing was required because of the leaned shape of the trailing edge.

The plots are bounded by the trailing edge geometry, shaded grey, and show the traversing region used for the geometries. The traverses are used to provide analysis

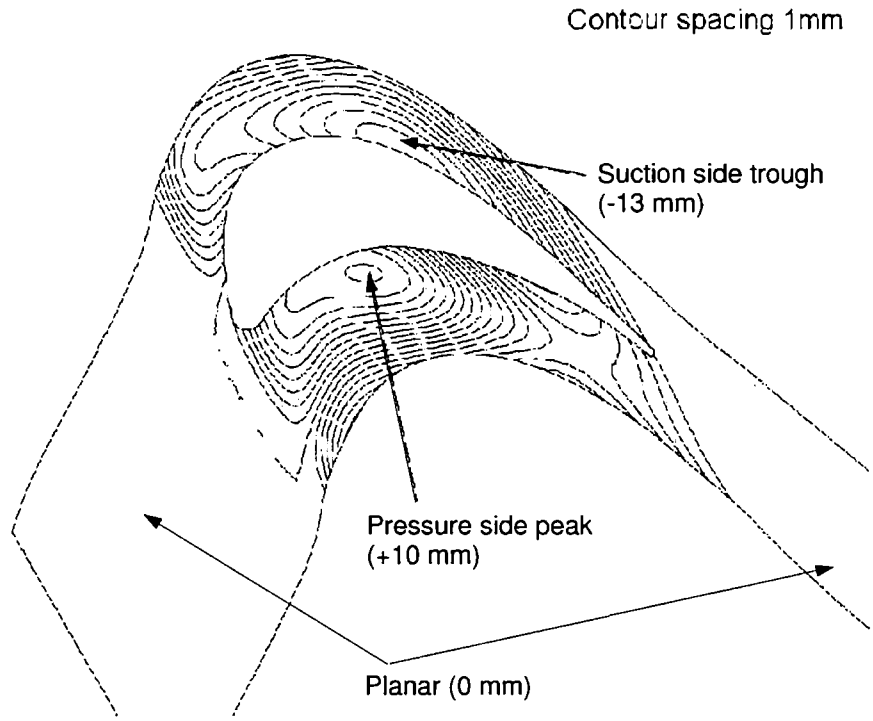

Figure 8.1: PEW Heights - Mild Endwall - 0% Span

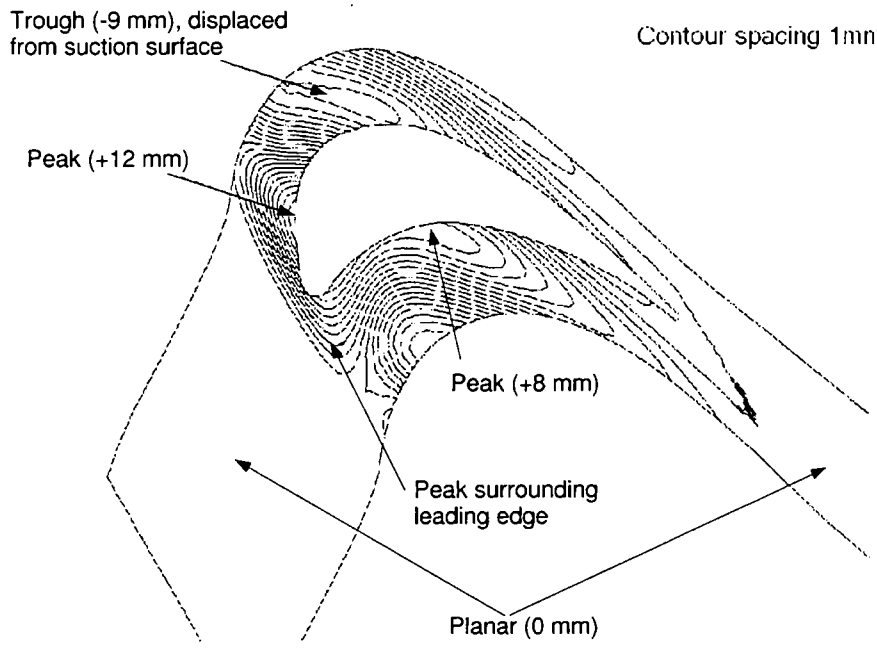

Figure 8.2: PEW Heights - Aggressive Endwall - 100% Span

of the development of the key structures. The traverses approach the suction surface to a different extent for the two cases. However, the key elements of the investigation were not considered to be located in this region close to the aerofoil surface.

Total pressure loss

Figures 8.3 and 8.4 show the total pressure loss contours for the C0a and C2 geometries at 97% C_{ax}. The traverses indicate a single loss feature for both geometries. This feature is the passage vortex loss core as it is drawn tangentially outwards from the blade.

The passage vortex loss feature for C2 is weaker than C0a and remains closer to the endwall. For geometry C2, there is a low magnitude loss region close to the endwall that covers 2/3 of the pitch, but this region has higher loss than C0a.

At this plane, the upper (aggressive) endwall has a more significant loss core that stretches further tangentially out into the passage. The two C0a endwalls have almost identical loss magnitudes.

Secondary velocity vectors

Figures 8.5 and 8.6 show the secondary velocity vectors for the C0a and C2 geometries at 97% C_{ax}. For both geometries the vectors resolve a single vortex structure only, the passage vortex. For C0a this passage vortex feature is predominantly on the left hand side (close to the SS), extends to 100 mm radially with its centre at location (-130,50).

For C2 the flow field is dominated by apparent strong velocities close to the SS, the 5h probe is close to the SS here and an interference with the SS may be causing unphysical reported velocities. The passage vortex for both endwalls of C2 is much smaller and closer to the endwall. Also evident is a diagonally outward flow that runs SS to PS, coming from the SS endwall corner. This may be a redistribution effect, as the lean induced static pressure field is reduced when the flow leaves the passage. At this traverse plane, the probe is well aligned with the mean flow and potential errors due to high probe incidence are low. At the lower endwall (where the PEW is less extreme) the PV is centred at (-80, 10) some 40 mm (11% span) nearer the endwall than C0a. The upper endwall PV is at a similar position to the lower endwall, again centred at mid pitch.

Overall, the radial extent of the secondary flow structures is reduced for the both ends of the C2 geometry.

Secondary kinetic energy coefficient

Figures 8.7 and 8.8 show the secondary kinetic energy coefficient contour plots for the C0a and C2 geometries at 97% C_{ax}. It should be noted that the peak C_{SKE} values are not aligned with the PV core. The C_{SKE} peaks for C0a sit between the PV and the blade itself; for the lower endwall it lies at location (-160,50). The C0a result indicates a slight asymmetry, with the upper endwall giving a higher peak value.

The peaks for C2 are much smaller and closer to the SS E/W corner at location (-175,20), aligned with the strong radial flow mentioned earlier.

Streamwise vorticity

Figures 8.9 and 8.10 show the streamwise vorticity contour plots for the C0a and C2 geometries at 97% C_{ax}.

For the C0a geometry the streamwise vorticity identifies three discrete features. These are, in order of magnitude, the passage vortex (PV), the suction side horseshoe vortex (SSHSV) and the corner vortex (CV). The PV is centred at (-140,50) and matches the secondary velocity vectors. The SSHSV lies above this and closer to the SS. The CV can be identified in the corner of the traverse region, with the same rotation direction as the SSHSV.

For the C2 geometry, the increased measurement range has picked up more of the features. The SSHSV is of similar size but at least 20 mm further in toward the endwall. At the upper (aggressive) endwall there is a vorticity peak below the SSHSV which would normally be associated with the PV. However, following the observations made of the secondary velocity vectors (where the PV was seen to lie along the endwall), it is likely that this vorticity is related to the strong radial flows instead.

8.1.2 Area traverses at 104% C_{ax}

The following analysis relates to a measurement plane 7mm downstream of the trailing edge, 104% C_{ax}. Comparison of this and the measurements taken at 97% C_{ax} gives greater understanding of the behaviour around the trailing edge.

Total pressure loss

Figures 8.11 and 8.12 show the total pressure loss contours for the C0a and C2 geometries at 104% C_{ax}. Both the C0a and C2 geometries have; a thin high loss wake, a high loss peak aligned with the wake, and an extended region of loss to the right of the wake, the suction side.

The high loss region aligned with the wake is a combination of the low momentum fluid of the inlet boundary layer, and the profile loss scraped by the passage vortex from between the feature itself and the endwall. The extended region to the right of the wake is also a result of the passage vortex, here the vortex is drawing the loss into the passage, spreading it tangentially outwards. This feature was also evident at 97% C_{ax}. Near the endwall there are no significant loss peaks, there is little evidence of the inlet boundary layer, and there is no observable core associated with the corner vortex.

The reverse compound lean of the C2 geometry reduces the profile loss. The high loss regions are higher and cover a larger area for geometry C2, but are also closer to the endwall. The extended region, to the right of the wake, covers a smaller area but it is of similar magnitude.

For the C2 upper endwall, the loss feature is drawn out from the blade to a greater degree, this ties in with the result at 97% C_{ax}.

Secondary velocity vectors

Figures 8.13 and 8.14 show the secondary velocity vector plots for the C0a and C2 geometries at 104% C_{ax}. At this location the C0a flow field is still dominated by the PV and its effect extends across the entire pitch. The core of the feature has moved and is now centred at (-170,50), a 30 mm tangential shift from 97% C_{ax}. The wake is visible as a radially aligned (vertical) gap in the vector field that the vectors are pointing away from. Across the wake a displacement of the vector directions indicates a sheared flow over the 30% span nearest the wall.

The C2 flow field does not contain the strong passage vortex feature present in C0a. There is a strong radial flow close to the wake at the endwall which, in combination with the strong overturning, presents a roll up similar to the passage vortex. The flow field at the wake position is dominated by a strong tangential mixing flow that decays toward the midspan. Due to this strong tangential flow it is not possible to observe the strength of any sheared flows across the wake. The diagonal flow (SS to PS, radially outward) observed at 97% C_{ax} is still present at 104% C_{ax} outside of the influence of the blade static pressure gradients. The C2 upper endwall velocities appear to have lower magnitudes than the lower endwall.

In both the C0a and C2 flow fields, the SSHSV and CV features are swamped by the strength of the other flows.

Secondary kinetic energy coefficient

Figures 8.15 and 8.16 show the secondary kinetic energy coefficient contour plots for the C0a and C2 geometries at 104% C_{ax}. By 104% C_{ax} the strong kinetic energy peak of C0a has moved to (-195,60), showing a 10mm radial and 35mm tangential shift. There is a marked difference in the magnitude of the C_{SKE} peak between the two geometries at this plane.

Comparing with the earlier vector plot, the C_{SKE} peaks of C2 are associated with wake mixing flows as much as the energy in vortical structures. There is an additional line that follows the wake to 140 mm (37% span), which accounts for the kinetic energy of the tangential flow in the wake mixing. There is also an energy peak at 10mm radius (3% span) that corresponds to the high overturning velocities seen here. Considering the sensitivity of the C_{SKE} parameter, there appears to be little difference between the upper and lower endwalls.

Whilst the relationship between the vortical flow and the energy seems to be less obvious in the C2 results, the significant reduction in the C_{SKE} peak is a clear benefit. The C0a peak is above 0.7 the C2 peak is at 0.35.

Streamwise vorticity

Figures 8.17 and 8.18 show the streamwise vorticity contour plots for the C0a and C2 geometries at 104% C_{ax}. There are clear similarities in the flow structures of the two geometries. For C0a the streamwise vorticity highlights the PV centred at (-170,50) and SSHSV centred at (-190,85), both seen at 97% C_{ax}. The vorticity plot also highlights a key feature aligned with the blade wake, this feature has higher vorticity than the SSHSV and follows the line of the wake, its vorticity increasing toward the endwall. The rotation of this wake feature is the same as the SSHSV.

For C2 the SSHSV has similar or slightly higher magnitude than the PV. The wake follows the curved path of the trailing edge, but has lower vorticity than the SSHSV, again with the same rotation as the SSHSV. An additional small region of vorticity is observed at 120mm radius (30% span).

The upper and lower endwalls of C2 have very similar vorticity magnitudes in the features, the upper endwall appears to have higher vorticity in the SSHSV and the lower endwall indicates a region of high vorticity next to the endwall.

SKE.H

Figures 8.19 and 8.20 show the SKE.H contour plots for the C0a and C2 geometries at 104% C_{ax}. For C0a the SKE.H plot has two distinct regions of opposite rotation, the larger higher magnitude region associated with the passage vortex and the thinner and lower magnitude region relating to the sheared flow in the wake.

For C2 the shapes and magnitudes of these regions have changed. The SKE.H of the passage vortex has reduced with similar magnitude for both endwalls. The linear SKE.H region, associated with the wake in C0a, has now redistributed and is concentrated in two regions, one close to the endwall, where the corner vortex is, the other directly above (radially outward) from the passage vortex, where the SSHSV is.

Overview

At 104% C_{ax} the detail of the effects of the wake can be observed as they develop and combine with pre-established features. The results have indicated:

- The significant impact of the C2 geometry on secondary flow magnitudes and loss
- The clear formation of the PV loss core from fluid drawn away the SS and the endwall boundary layer
- A high vorticity region in the wake that extends to a height equal to the inlet boundary layer

This region of high vorticity, extending to a height equal to the inlet boundary layer, is of interest as it appears to indicate the radial extent of the downstream trailing shed vorticity. This vorticity component, from classical secondary flow theory, is linked to changes in local blade loading caused by the reduced inlet momentum of the boundary layer fluid.

8.1.3 Area traverses at 128% C_{ax}

The results presented here use a non-uniform measurement grid that has higher density regions for the secondary flows and the near wall region. The traverse plane relates to Slot 10 of the old cascade, where the majority of the experimental analysis is performed. At this axial location the loss and vortical structures are well developed and an assessment of the comparative magnitudes is possible.

Total pressure loss

Figures 8.21 and 8.22 show the total pressure loss contours for the C0a and C2 geometries at 128% C_{ax}.

The datum C0a geometry exhibits good flow symmetry between the upper and lower endwalls. The overall flow features remain the same as those of C0, except slightly closer together due to the change in aspect ratio.

For C2, the reduced midspan (profile) loss coefficient is similar to the C1 blade, the bowed shape of which again follows that of C1.

In the lower half of the passage, with the mild endwall, the SSHSV and PV loss cores are evident as individual features, of similar peak magnitude. Both loss cores are closer to the endwall (15 mm and 20 mm for the PV and SSHSV respectively) but are of greater magnitude than in C0a. The corner vortex core has a tangential shift relative to C0a, indicating increased overturning at the wall.

In the upper half of the passage, with the aggressive endwall, the SSHSV and PV cores have merged into one strong core 65mm from the endwall (310mm span). The corner vortex core has a much larger tangential displacement (a further 50mm than the lower endwall) indicating high overturning here. Also note that the radial position of the corner vortex core is closer to the endwall.

The peak loss is greater in the upper endwall, but the PV feature is lesser at this end.

Additional 3h probe data

Combined five and three hole measurements for C0a and C2 are presented in Figures 8.23 and 8.24. The addition of the three hole probe data indicates the level of loss in the corner vortex loss core.

The C2 geometry indicates a significantly higher corner vortex loss core than C0a for both the upper and lower endwalls.

Secondary velocity vectors

Figures 8.25 and 8.26 show the secondary velocity vector plots for the C0a and C2 geometries at 128% C_{ax}. The symmetry of the flow is again apparent in the vectors of the C0a blade, with identically sized passage vortices at 65mm from the endwall (17% span). The lower half passage has a clearly visible corner vortex corresponding to the loss core in Figure 8.21 earlier.

The velocity vectors for the C2 blade can be seen in Figure 8.26. It should be noted that the magnitudes of the PV and SSHSV/ShV are significantly reduced. Furthermore, the spanwise locations of the vortices are much closer to the wall.

The upper and lower endwalls have similar secondary flow features, typical of the Durham cascade albeit compressed toward the endwall. The CV features are obscured by the higher overturning and the SSHSV is difficult to discern. Both endwalls exhibit increased levels of overturning at the endwall, as predicted by the design CFD.

Secondary Kinetic Energy Coefficient

Figures 8.27 and 8.28 show the contour plots of secondary kinetic energy coefficient for the C0a and C2 geometries at 128% C_{ax}. The C_{SKE} plot for geometry C0a (Figure 8.27) indicates a highly symmetrical flow field with C_{SKE} peaks located at the interaction of the PV and SSHSV features.

The C2 design has much reduced C_{SKE} values over the entire passage, this follows the evidence in the secondary velocity vectors. The C2 plot identifies the high overturning at the endwall. The magnitudes of the secondary kinetic energy in the upper (aggressive) half passage are smaller than in the lower (mild) half, this confirms the assessment of the secondary velocity vectors.

Streamwise vorticity

Figures 8.29 and 8.30 show the streamwise vorticity contour plots for the C0a and C2 geometries at 128% C_{ax}.

The three key vortical structures are seen in the plot for the datum C0a geometry. Again, the plot indicates the good symmetry of the features. The same three structures are visible for the C2 geometry, however their peak values are reduced and the radial extent is smaller. There is a clear tangential displacement and increase of the corner vortex for the C2 geometry as a result of the increased overturning. The lower (mild) endwall CV has higher vorticity than the upper.

Although there is a single loss core in the upper endwall, the vorticity plot shows the two distinct vortices of PV and SSHSV. C2 has a much larger area that is free of secondary flows.

SKE.H

Figures 8.31 and 8.32 illustrate the SKE.H for 128% C_{ax}. The SKEH indicates symmetry for C0a (Figure 8.31), with higher SKEH values for the PV. Two separate features can be observed rotating counter to the PV, these are the SSHSV and the CV.

The effect of C2 is a significant reduction in all of these features, except the CV on the lower endwall, which has increased in magnitude.

8.2 Pitchwise averaged results

The pitchwise averaged total pressure loss for axial locations at 104% and 128% C_{ax} are presented in Figures 8.33 and 8.34. The exit yaw angles are presented in Figures 8.35 and 8.36, the Secondary Kinetic Energy Coefficient at 128% C_{ax} is presented in Figure 8.37, and the SKE.H is presented in Figure 8.38.

The pitchwise averaged data provides a more quantitative assessment of the effect of the geometrical changes.

8.2.1 Total pressure loss

The pitchwise averaged total pressure loss coefficient has three distinct regions, these are; a 2D wake, a passage vortex loss core (which includes the ShV/SSHSV loss too) and a corner vortex loss core. At 128% C_{ax} the C2 geometry shows increased loss at both endwalls in the PV core and reduced loss over the middle of the blade. The region unaffected by secondary losses has grown significantly for the C2 geometry, Figure 8.34.

As shown in the contour plot, the upper endwall of C2 has a larger loss peak. This peak is not aligned with the passage vortex but with the ShV/SSHSV core and the wake. As the ShV component is unlikely to have changed, the likely reason is some low momentum fluid being drawn into the SSHSV. The surface flow visualisation results, in Section 8.4 give more information about this higher loss value.

In general, C0a has higher midspan loss, smaller loss peaks due to passage vortex loss core and a clear trough between the passage vortex loss core and the newly formed boundary layer loss. The results for C2 show overall a lower loss at midspan and an enlarged region unaffected by secondary flows. The passage vortex core has a larger peak but covers a reduced span.

Comparing the results at 104% C_{ax} and 128% C_{ax} in Figures 8.33 and 8.34, the difference in midspan loss is seen to grow slightly downstream. This may be an effect of the thin wake at 104% C_{ax}, which is not fully resolved by the measurement grid resolution.

8.2.2 Yaw Angle

The pitchwise averaged yaw angle results for the datum geometry, in Figures 8.35 and 8.36, show the classic over and under turning of the passage vortex. The effect of the corner vortex is seen as a reduction in overturning close to the endwall.

The C0a yaw angle plot at 128% C_{ax} is dominated by the strong passage vortex. This large over and under turning is typical of the Durham cascade geometry. The C2 result has much reduced underturning regions and no clear overturning region associated with the PV. The overturning of the boundary layer is greater at both endwalls, but greatest at the aggressive endwall.

Between 104% and 128% C_{ax} the features move radially outward, away from the endwall. The overturning at the wall increases, but the size of the secondary flow remains approximately the same. This is seen in the level of under and over turning.

8.2.3 Secondary Kinetic Energy Coefficient

The C_{SKE} at 128% C_{ax} is presented in Figure 8.37. The C0a blade has good symmetry with singular peaks for the interaction between the PV and SS HSV. The C2 blade has lower PV peaks but greater values at the overturned endwall. The upper (aggressive) endwall has the lowest C_{SKE} in the peak.

8.2.4 SKE.H

Figure 8.38 shows the similar nature of the effect of the C2 geometry on SKEH. The plot reiterates the ability of SKEH to resolve individual features. The two peaks are associated with the two key features in Figures 8.31 and 8.32.

The pitchwise averaged SKE.H results show that the greatest reduction is found on the lower endwall, which is consistent with the trends in loss production. This result is however contrary to that of the computational SKE.H benefit, where a larger reduction was predicted for the upper endwall.

8.3 Surface static pressures

Suction surface static pressures for C0a and C2 are illustrated using contour plots in Figures 8.39 and 8.40.

The measurements were taken at a series of discrete spanwise locations. The spanwise resolution was limited in the near-wall region, making a detailed investigation of the behaviour of the PEWs difficult. The plots present C_p in 0.1 contours. For C0a the leading edge is at 0mm, for C2 the leading edge is at 200mm. The profiled endwall shapes of the C2 geometry are not represented in the contour plot.

The datum geometry represented in Figure 8.39 matches the result of the computation (Figure 7.52) closely, with the positions of peak loading associated with the passage vortex being the same, and the symmetry of the two secondary flows being good.

The C2 geometry matches the computational result at the midspan, with the offloading observed in Figure 7.54 in Chapter 7. The endwall regions indicate the same effects as the CFD, but with lower resolution. There is a peak towards the front of the lower endwall which matches the CFD. There is also a clear offloading in a similar position on the upper endwall, this is associated with a diffusion behind a PEW hump and is discussed later.

Despite these localised features, the lower endwall can be described in general as fore loaded, the upper endwall as aft loaded.

8.4 Surface flow visualisation

As with previous work, an oil and dye mixture was spread on the blade and endwall surfaces, the blades were placed in the cascade and run with design inlet conditions for a number of minutes. The resulting patterns aid the location of vortical structures and other 3D features. The photographs in Figures 8.41 to 8.43 show comparative images of the C2 and C0a geometries for both endwalls. The images are annotated and relate to the following results.

1. A midspan flow with no separation bubble

2. A clear passage vortex radial migration (labelled A), the extent of which was measured at the TE (r_{TE}). Seen in Figure 8.41

3. A SSHSV migration (B) seen above the PV line on the SS of C0a, Figure 8.41, this feature is much less pronounced on C2

4. The effect of the RCL in C2, causing a noticeable radial shift of the SS surface flow near the point of maximum blade loading, (C). This results in a larger region of clean 2D flow

5. A PV endwall lift off line (D), also showing the corner vortex interaction, Figure 8.42

6. The smooth endwall flow (E) around the LE towards the point of SS migration. The axial distance to which is measured (x_{SS-A}), in Figure 8.43

7. A separation feature (F) close to the SS LE of geometry C2 Upper, indicated by the rapid change in endwall flow direction

8. Early SS attachment point of HSV (G), due to the separation feature, this is in contrast to the lower endwall which has a delayed radial migration of the PV

This 3D feature, in Figure 8.43, is most likely to be a small 3D separation. The location is similar to those found on the P3 and P4 geometries. The effect of the feature differs however, as the overall loss associated with the upper half of the blade passage is still 11% lower than the datum. It is likely that the low momentum fluid from this 3D feature is drawn into the SSHSV, as indicated in the contour plot of loss in Figure 8.22, and does not directly affect the passage vortex loss core.

8.4.1 Loss feature - 3h probe measurement

A number of additional traverses were undertaken to detect the level of loss near the observed separation feature on the upper endwall of C2. To enable the measurement of the flow close to the endwall surface, a special cranked three hole probe was manufactured. Figure 8.44 shows the new probe on the left hand side, next to the standard 3 and 5 hole probes. A compact measurement grid was used, covering the 35mm adjacent to each endwall, with 1mm radial x 8mm tangential spacing. The radial refinement was necessary to resolve the expected localised loss feature.

Figure 8.45 shows the total pressure loss for the upper endwall at 31% C_{ax}, just downstream of the highlighted separation feature. Figure 8.46 shows the equivalent loss plot for the lower endwall, where no separation feature was observed. The plots show little difference in the level of total pressure loss between the upper and lower endwalls. The upper endwall does have slightly higher loss in the region close to the SS, but the difference is not significant. The regions traversed relate to the endwall boundary layer loss that is rolled up into the PV loss core.

These results indicate that the separation feature does not affect this loss significantly. However, the oil flow patterns suggest this feature may be transported into the SSHSV feature.

8.5 Mass averaged results

Figure 8.47 contains the mass averaged results for C2 based on the five hole probe traversing and compares them to the datum geometry C0a. The figure indicates a 13% decrease in the total pressure loss, a 3-4% increase in the massflow and a 0.4° increase in the level of turning overall. This data is also split into the mild and aggressive (lower and upper) endwalls and the following can be seen. The mild endwall reduces the loss by 15%, the aggressive by 11%. The C_{SKE} is reduced by 59% at the mild and 69% at the aggressive end. The SKE.H reduction is of a similar order for both ends, with a 57% and 55% reduction at the mild and aggressive ends respectively. The mild endwall reduces the energy of the secondary flow and the total pressure loss to a greater degree.

Figure 8.48 contains the mass averaged results for the combined 5 hole and 3 hole probe traverses for C2. The combined dataset provides additional information on the impact of the near endwall measurement on the total pressure loss and yaw angle. The C_{SKE} and SKE.H results both require a full 5 hole probe and are thus not included in this analysis. Comparing this with the earlier information from Figure 8.47 for the 5h data alone indicates a change in the loss benefit. The addition of the 3 hole data decreases the loss reduction benefit by 0.6% But the mild endwall actually improves its performance by 0.3%. The near endwall flow, picked up by the 3h probe at the aggressive endwall, appears to lose 2% of the benefit previously stated. The turning increase, above C0a, is 0.6° overall, split between 0.9° at the mild endwall and 0.3° at the aggressive endwall.

The lower endwall appears to increase overall turning, reduce the secondary kinetic energies whilst also significantly reducing loss.

8.6 Axial development

8.6.1 Loss

Looking at the three contour plots of total pressure loss for C0a in Figures 8.3, 8.11 and 8.21, the development of the features is interesting. At 97% C_{ax} the loss associated with the passage vortex is only just picked up, by 104% C_{ax} the full pitch is available and the straight wake is clearly visible. By 128% C_{ax} the local velocities have worked on these low momentum regions, resulting in a redistribution of the previously tight loss peaks between three distinct features at each endwall.

At 104% C_{ax} there is a peak of loss at 80mm (21% span), this gathering of low momentum fluid is a combination of the loss associated with the SSHSV and that of the blade wake and endwall boundary layer forced radially outward by the action of the PV. Between 104% and 128% C_{ax} this peak loss is drawn into the PV feature, causing a mixing of this low energy fluid, and a reduction in its peak value.

Between 104% and 128% C_{ax}, the loss feature on the endwall due to the corner vortex, is shifted tangentially to a greater degree than the mean flow. This over-turning close to the wall is a result of the cross passage pressure gradient and is seen more clearly in the secondary vector plots. The radial position of the passage vortex loss core increases between these three axial locations.

For C2, in Figures 8.4, 8.12 and 8.22 the PV loss core remains the same magnitude between 97% and 104% C_{ax}. The blade wake is very thin and noticeably bowed at 104% C_{ax} with two large peak loss regions in the wake at the PV core. Again these cores relate to the roll up of the inlet and blade boundary layer low momentum fluids. By 128% C_{ax} the bow of the wake is less noticeable, the corner vortex cores are translated tangentially by the overturning and the high magnitudes have been distributed into wider cores and wake.

8.6.2 Secondary Velocity Vectors

The axial development of secondary flows for a geometry almost identical to C0a was investigated by Graves (1985) and Gregory-Smith and Graves (1983) and will not be reassessed here. Figures 8.6, 8.14 and 8.26 show the secondary velocity vectors for the geometry C2 at the same three axial planes.

At 97% C_{ax}, the capture of the vortex structure of the passage vortex is significantly better than that of the related loss core. Here there is one single feature at each end. Due to the strength of the PV, there is no evidence of the SSHSV which only appears at 128% C_{ax}.

The velocity vectors show the outward radial shift of the PV as the flow moves downstream. The PV also decays between these axial planes, due to a combination of viscous mixing and the removal of any pitch wise pressure gradients. At 97% C_{ax} the PV appears to be weak, very close to the endwall and spread over the entire measurement region (not a full pitch). There is no sign of the SSHSV or CV structures. By 104% C_{ax} the PV structure has moved outward but is not as well defined as that of the prismatic geometry. The lower endwall appears to have a greater intensity of PV but a reduced level of overturning at the endwall. At both 97% and 104% C_{ax} there is a clear radial velocity component to the whole pitch from 0% to approximately 25% span, this is a redistribution effect of the RCL. Between 104% and 128% C_{ax} the PV becomes more defined and the SSHSV structure is visible, but the radial position of the feature remains the same. The CV is not visible at 128% C_{ax}.

8.6.3 C_{SKE}

Figures 8.7, 8.15 and 8.27 show the secondary kinetic energy for C0a for the three axial measurement planes at 97%, 104% and 128% C_{ax}.

The secondary kinetic energy peak is of similar size at 97% and 104% C_{ax}. The magnitude decreases by 128% C_{ax}. The C_{SKE} magnitude relates to the kinetic energy of the secondary flow, a combination of the local radial and tangential velocity disturbance. The position of the C_{SKE} peak does not coincide with a vortex core, but where the velocities are greatest. For these results the C_{SKE} peak shifts around the PV core, it starts (at 97% C_{ax}) on the SS side of the PV core and moves above of the PV by 128% C_{ax}.

8.6.4 Vorticity

Figures 8.9, 8.17 and 8.29 show the streamwise vorticity for C2 for the three axial measurement planes at 97, 104 and 128% C_{ax}. The slight difference in conditions between the two traverses introduces the artificial vorticity on the SS of C2 (Figure 8.10) at midspan where the two flow fields are combined. At 97% C_{ax} the vorticity plot indicates two distinct features that were not visible in the secondary velocity vectors. The PV is slightly stronger than the SSHSV and they are both close to the SS. The PV appears to extend almost the entire tangential measurement range. There is no evidence of shed vorticity at this plane upstream of the TE. Between 104% C_{ax} and 128% C_{ax} the line of trailing vorticity combines with the two features of the same rotation, increasing their magnitudes.

8.6.5 Overall

The development of secondary flow structures is very interesting. At 97% C_{ax} the structure of both the PV and SSHSV are evident and a small corner vortex structure may be seen at 100% span, the SSHSV sits on top of the PV but closer to the SS. By 104% C_{ax} a line of vorticity is evident which follows the blade wake. This line extends to 30% span with intensity increasing toward the endwall. Interestingly, the high vorticity in the wake region reaches from the endwall to approximately 60mm or 15% span, this corresponds with the radial extent of the inlet boundary layer. The rotation direction of this vorticity is the same as the corner and SSHSV structures noted at 97% C_{ax}. The magnitude of this line is greater than the individual vorticity of either the CV or the SSHSV features.

8.7 Computational Results at 128% C_{ax}

The following section details the contour and velocity vector plots for the computational data. The data is extracted, using the point probe feature of CFD post-processing tool Fieldview, for each of the experimental measurement locations. This method enables a direct comparison with the experimental result.

The measurements are taken for a plane at 128% C_{ax} and compare the relative behaviours of the computational and experimental results at this plane, in addition to observing the effect of the C2 geometry. To compare with the experimental results, the dataset was flipped about midspan to ensure the endwall designs aligned.

8.7.1 Loss

Figures 8.49 and 8.50 present the computational total pressure loss coefficients of the C0a and C2 geometries. Comparing these with the experimental results presented in Figures 8.21 and 8.22, the computational results show significantly more midspan loss (0.7 compared with 0.5) and the wake region is spread out over a larger tangential range.

The computational result of C0a indicates a single loss peak, close to the wake associated with the SSHSV feature. The loss peak, previously observed to be aligned

with the PV feature, is not present in the computational result. The location of the SSHSV feature and the wake match the experiment well, both tangentially and radially. The CV feature is shifted tangentially relative to the experiment.

The C2 result, in Figure 8.50, indicates a slight reduction in the midspan loss associated with the offloading, but this is less significant than the experimental reduction. Again, the computational result does not resolve the two discrete loss features of the experiment at the lower endwall. The positions of the C2 loss features and wake are similar, but the level of overturning is again over predicted and the CV feature is translated further than in reality. However, the higher level of overturning at the upper endwall is resolved and follows the trend of the experiment.

The radially inward shift of the high loss regions is well predicted, with the upper endwall being shifted to a greater extent.

8.7.2 Secondary Velocity Vectors

Figures 8.51 and 8.52 present the computational secondary velocity vectors of the C0a and C2 geometries. The computational result matches the experimental location of the PV feature in both the C0a and C2 results. This contrasts with the prediction of the loss features, but is an encouraging result. The computational result over predicts the overturning at the endwall and under predicts the velocity in the PV and SSHSV features.

8.7.3 C_{SKE}

Figures 8.53 and 8.54 present the computational secondary kinetic energy of the C0a and C2 geometries. The C_{SKE} results reiterate the previous comment that, the computation under predicts the velocities and therefore energy in the secondary flow features. The reduction in secondary flow for C2 is evident in Figure 8.54, and the increased overturning is resolved as C_{SKE} at the endwall.

8.7.4 Vorticity

Figures 8.55 and 8.56 present the computational streamwise vorticity of the C0a and C2 geometries. The computational result indicates a higher (than experimental) magnitude region for the CV and a lower magnitude and more distributed region of vorticity for the PV feature. This lower magnitude again relates to the previously observed secondary velocity vectors. The approximate locations of the vorticity peaks are the same.

The C2 computational vorticity matches the experimental vorticity well, in relative magnitudes and locations.

8.7.5 Pitchwise averaged

Figure 8.57 shows the pitchwise averaged total pressure loss of the C0a and C2 geometries for CFD, compared with the previously presented experimental result. The computational result has higher loss in the 2D wakes and the change in loss

due to the C2 design is not fully accounted for here. The peaks associated with the C2 PV loss cores are overpredicted, but the C0a matches the experimental values.

Figure 8.58 shows the pitchwise averaged yaw angle result for C0a and C2, for both CFD and experiment. The high level of mixing has smeared the secondary flows, this is evident in the reduced underturning peak and lack of overturning associated with the PV for C0a. The midspan yaw matches well for C0a, but not for C2. The endwall overturning trends for the two C2 endwalls are picked up in the CFD.

Figure 8.59 shows the pitchwise averaged SKEH result for C0a and C2, for both CFD and experiment. The computational SKEH values for geometry C0a are not radially aligned with the experiment. The C2 results are much better and indicate a similar behaviour for the both ends.

8.8 Summary

The C2 geometry offloads the midspan region and reduces the midspan loss. The lean drives the secondary flows to the endwall, providing a larger region of clean flow. The secondary flow magnitudes are reduced by the LE extension and the application of PEWs. This is evident in the SKEH and vorticity plots. The total pressure loss indicates an increase in the peak losses but an overall mass averaged reduction.

The C1 geometry (Chapter 7) actually increased the secondary flow intensities and would be expected to do so in this geometry. The additional components of the LE extension and the PEWs provide a significant benefit. The resulting downstream flow is low in secondary kinetic energy, low in loss and the exit angles indicate a simpler yaw distribution, affected by a strong overturned region and weak disturbance due to the passage vortex.

The C2 geometry reduces the total pressure loss by 13%, reduces SKE.H by 56% whilst maintaining the massflow and slightly increasing the yaw angle.

The design provided different endwall profiling concepts, with both fore and aft focussed designs. The more traditionally shaped, yet aft focussed, mild endwall reduced SKE.H by 57% and loss by 15%. The aggressive endwall design produces an unusual hump region encircling the leading edge. The diffusion off the back of this hump appears to have resulted in a separation similar to those seen in P3 and P4. A traverse immediately downstream of the feature did not resolve any significant increase in endwall loss. It is thought that the low momentum fluid is instead drawn into the SSHSV. Despite the separation feature, the aggressive endwall reduced the loss by 11%.

8.9 Figures

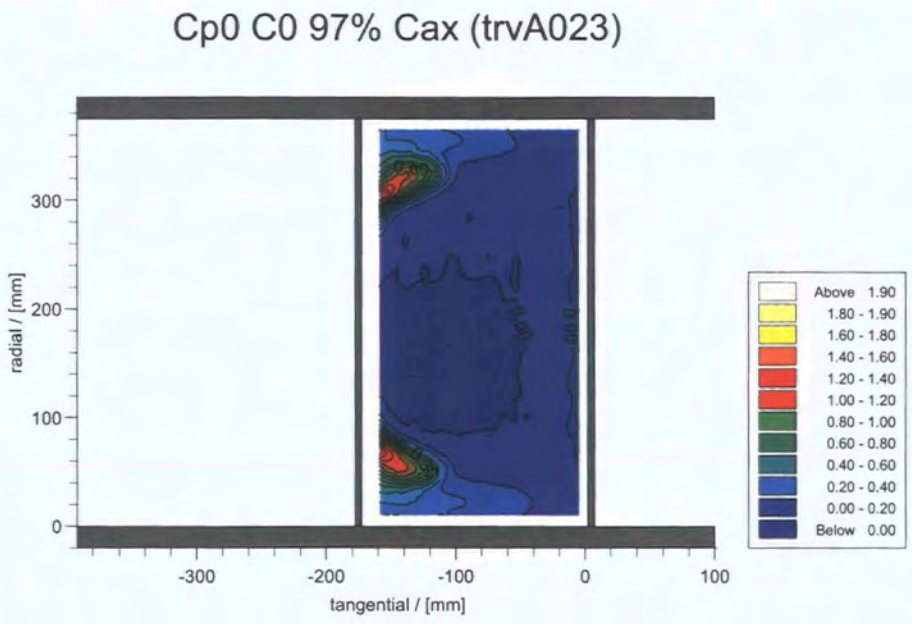

Figure 8.3: Loss C0a at 97% C_{ax}

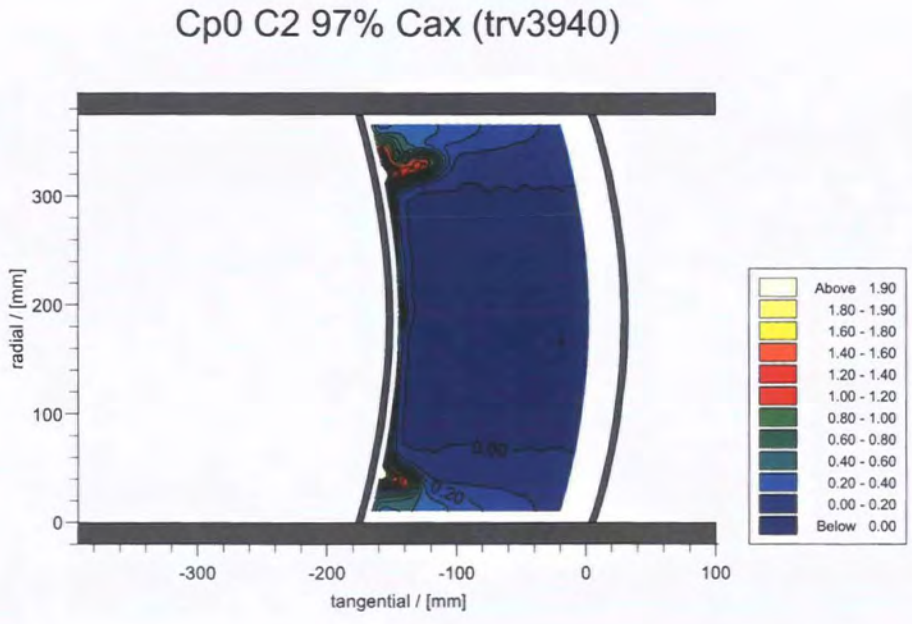

Figure 8.4: Loss C2 at 97% C_{ax}

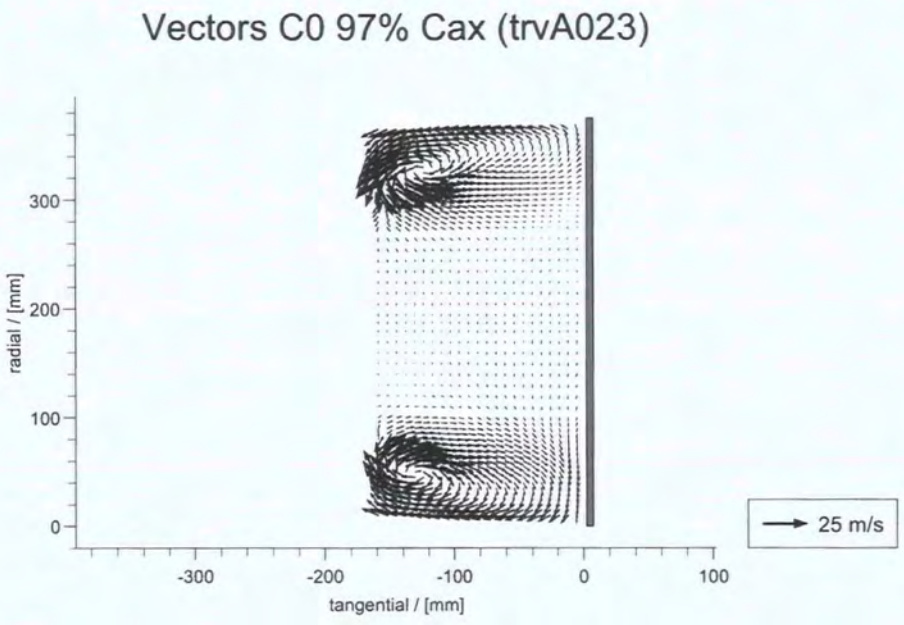

Figure 8.5: Secondary Velocity Vectors C0a at 97% C_{ax}

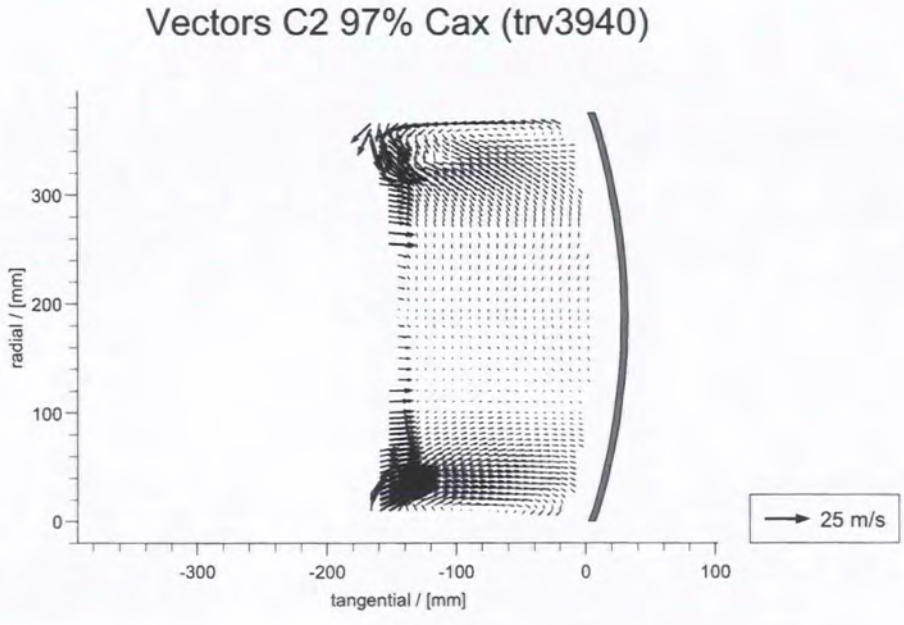

Figure 8.6: Secondary Velocity Vectors C2 at 97% C_{ax}

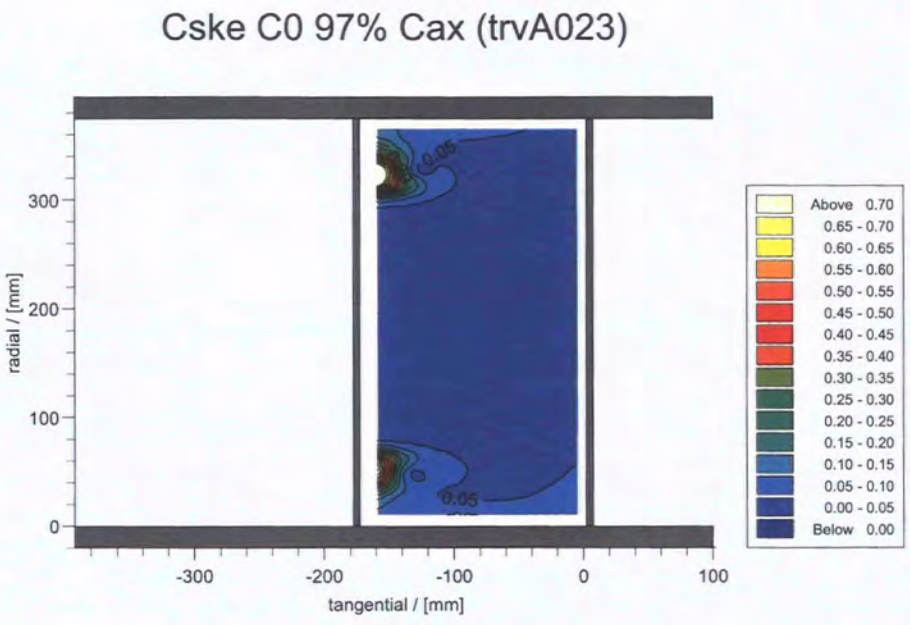

Figure 8.7: C_{SKE} C0a at 97% C_{ax}

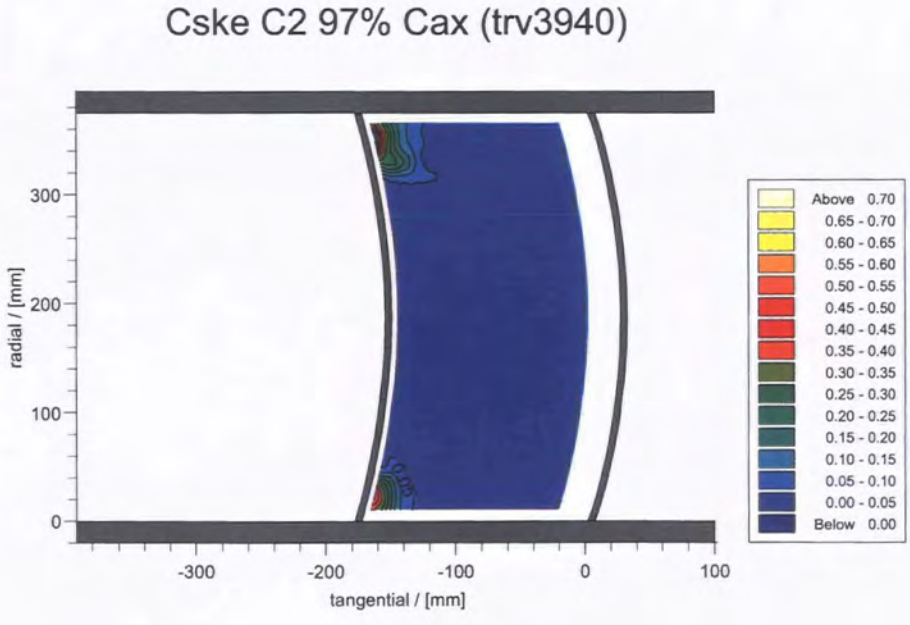

Figure 8.8: C_{SKE} C2 at 97% C_{ax}

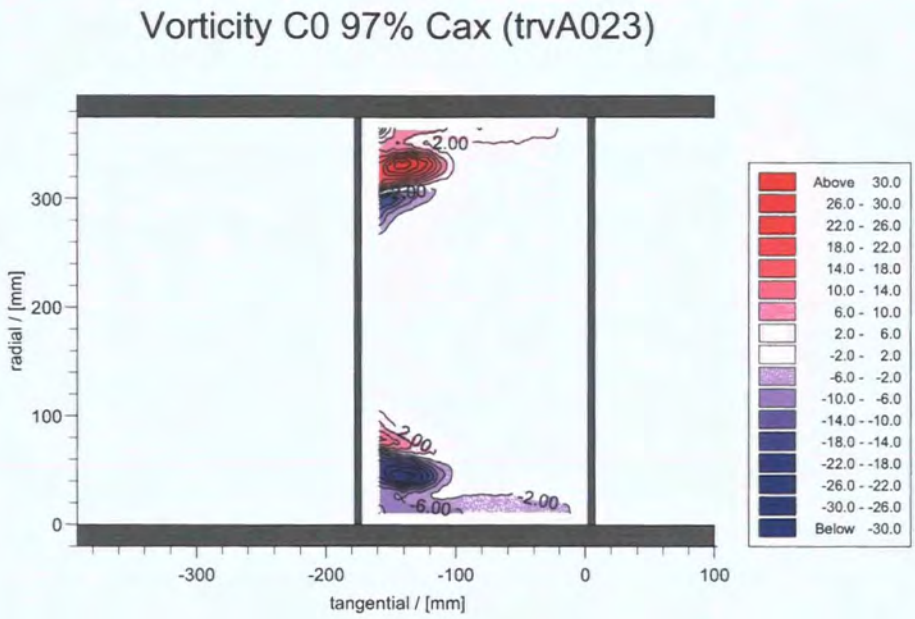

Figure 8.9: Vorticity C0a at 97% C_{ax}

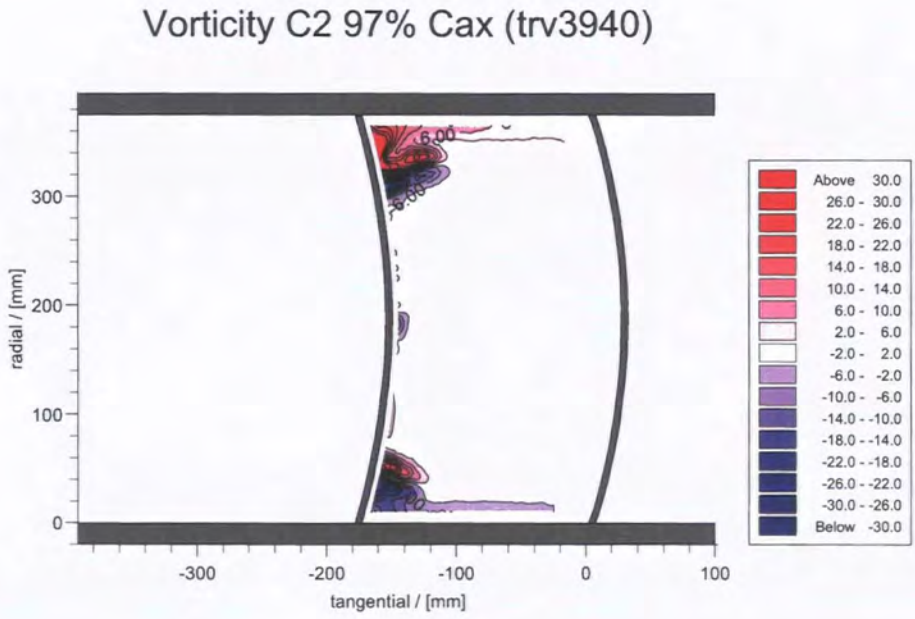

Figure 8.10: Vorticity C2 at 97% C_{ax}

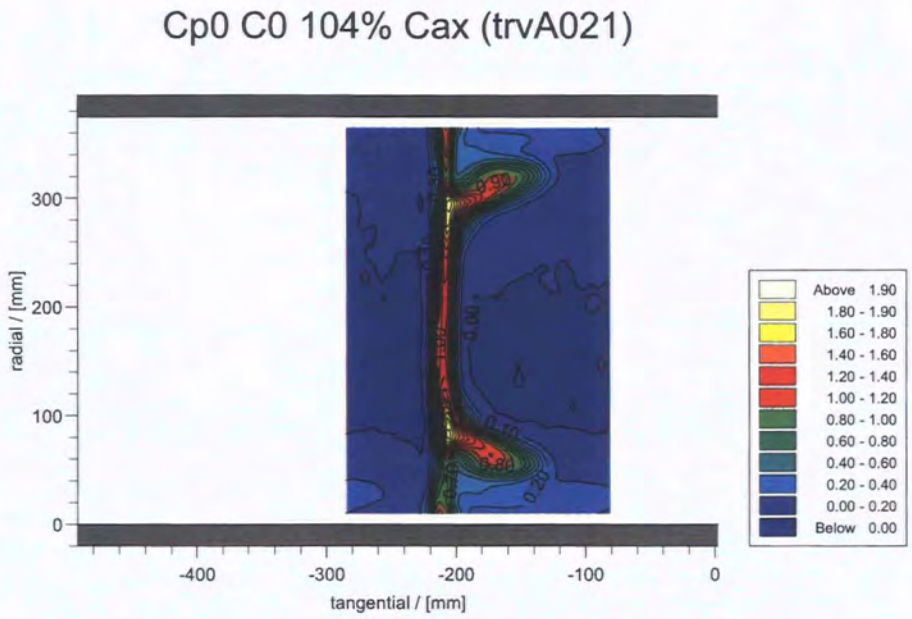

Figure 8.11: Loss C0a at 104% C_{ax}

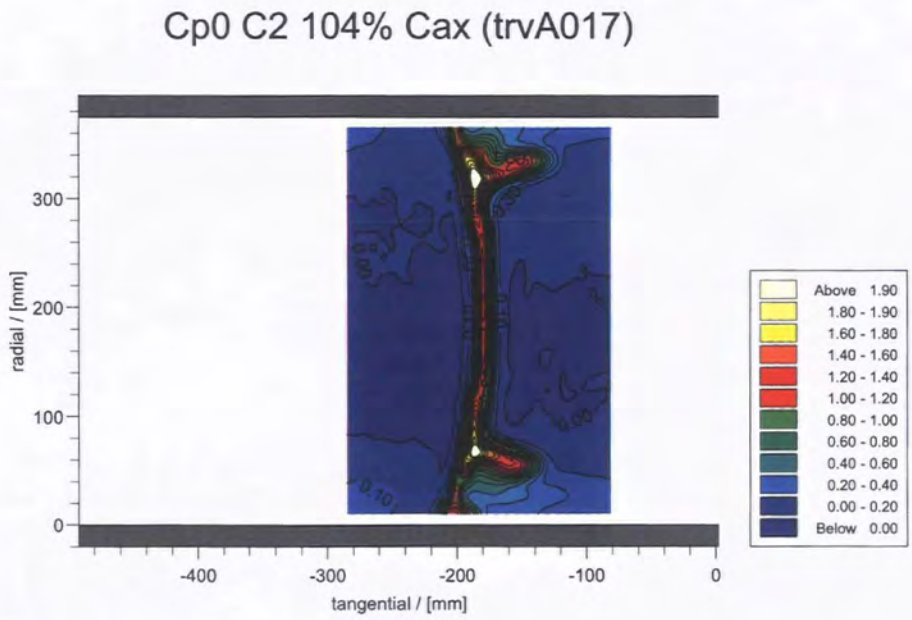

Figure 8.12: Loss C2 at 104% C_{ax}

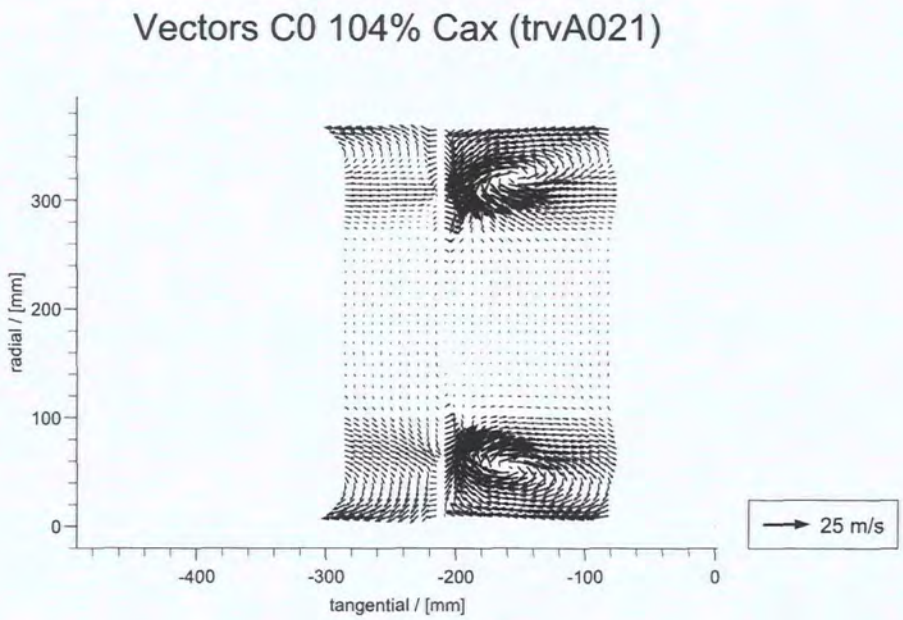

Figure 8.13: Secondary Velocity Vectors C0a at 104% C_{ax}

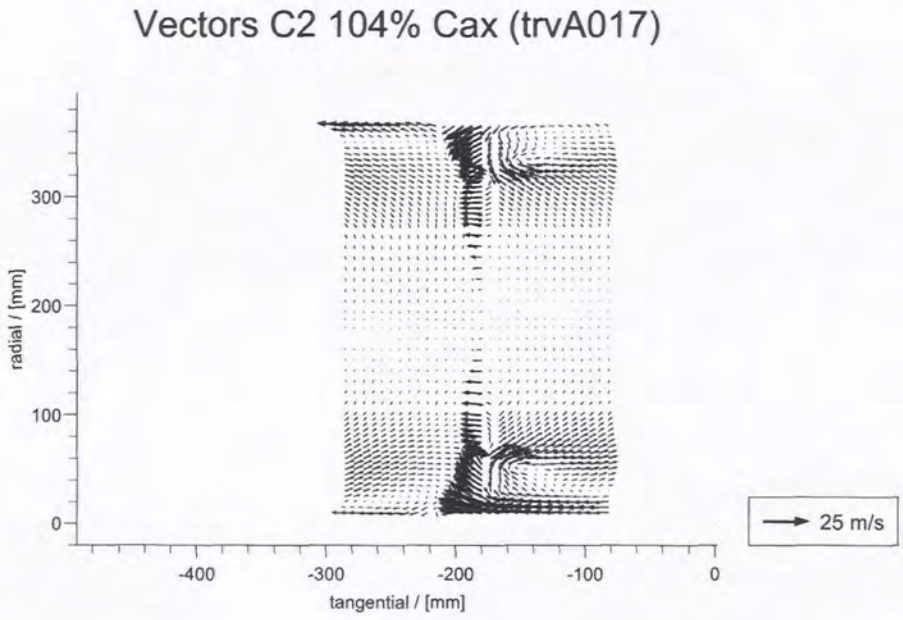

Figure 8.14: Secondary Velocity Vectors C2 at 104% C_{ax}

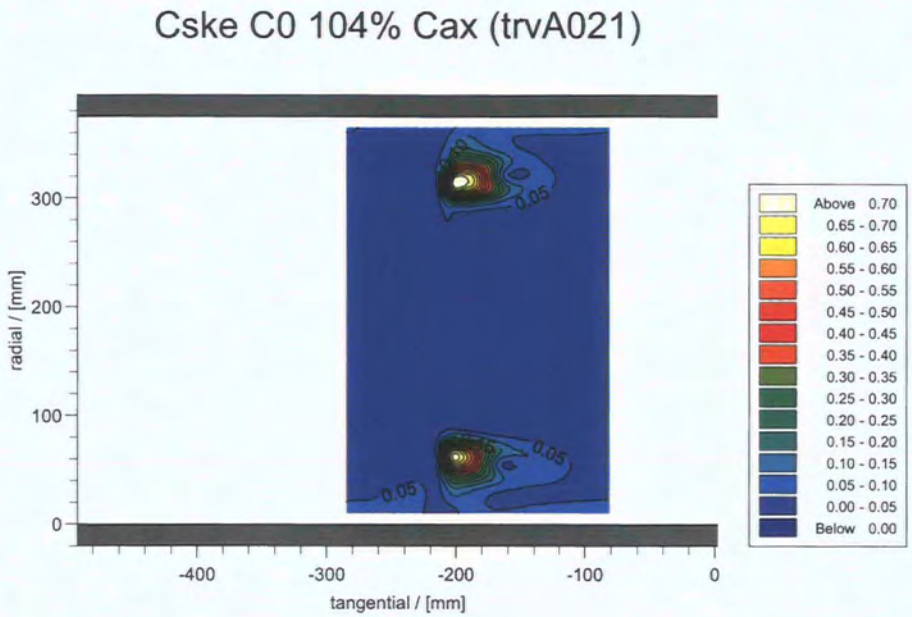

Figure 8.15: C_{SKE} C0a at 104% C_{ax}

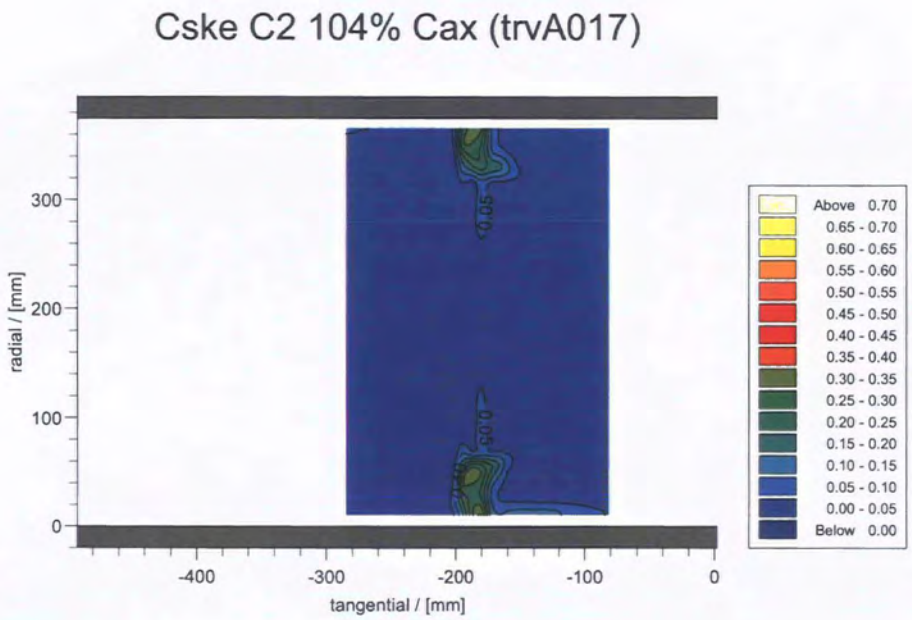

Figure 8.16: C_{SKE} C2 at 104% C_{ax}

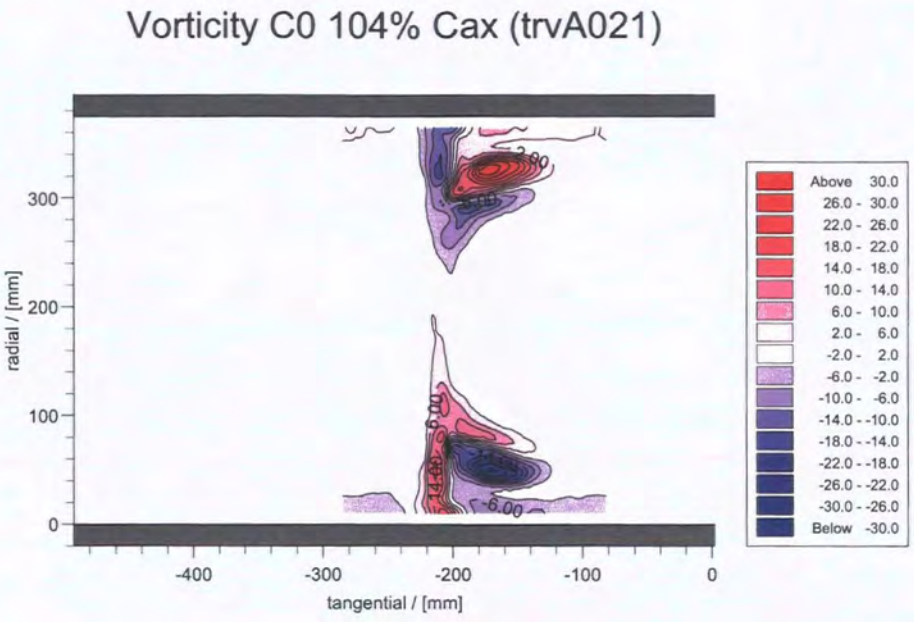

Figure 8.17: Vorticity C0a at 104% C_{ax}

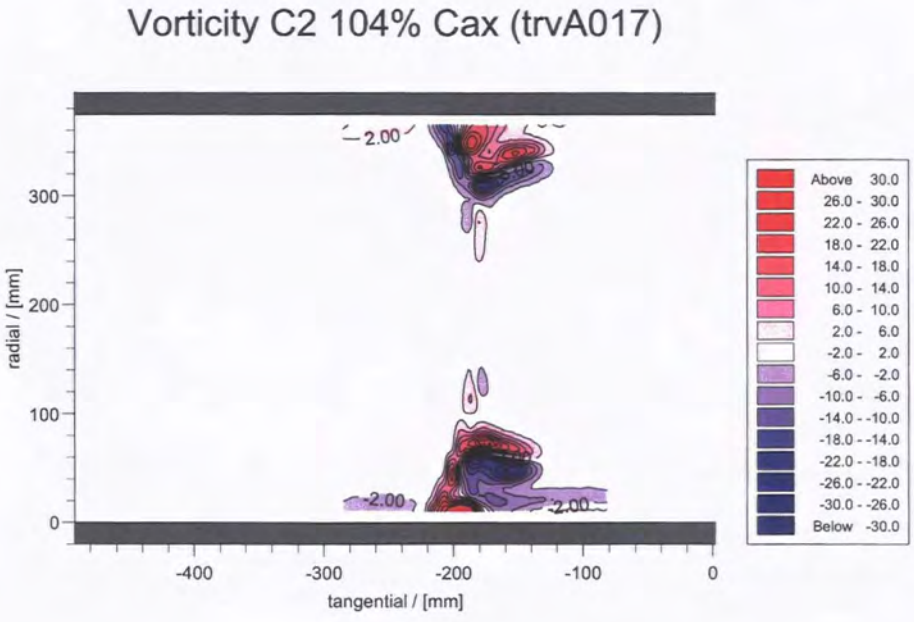

Figure 8.18: Vorticity C2 at 104% C_{ax}

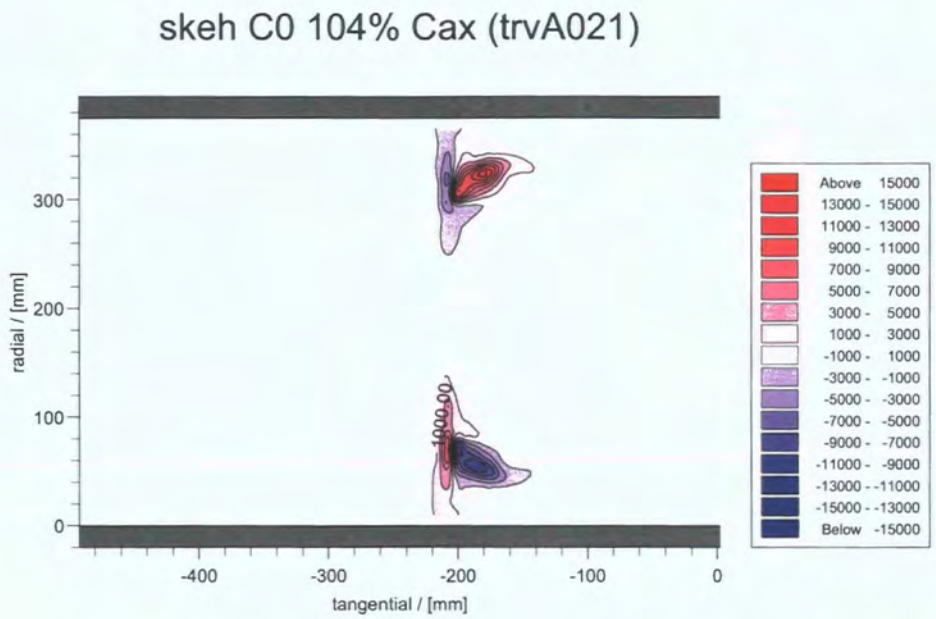

Figure 8.19: SKE.H C0a at 104% C_{ax}

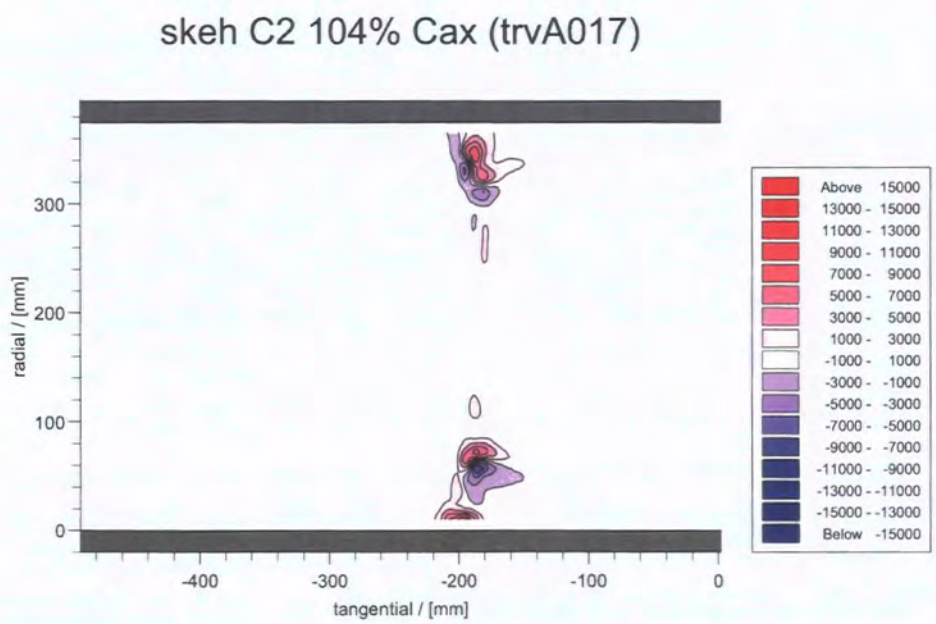

Figure 8.20: SKE.H C2 at 104% C_{ax}

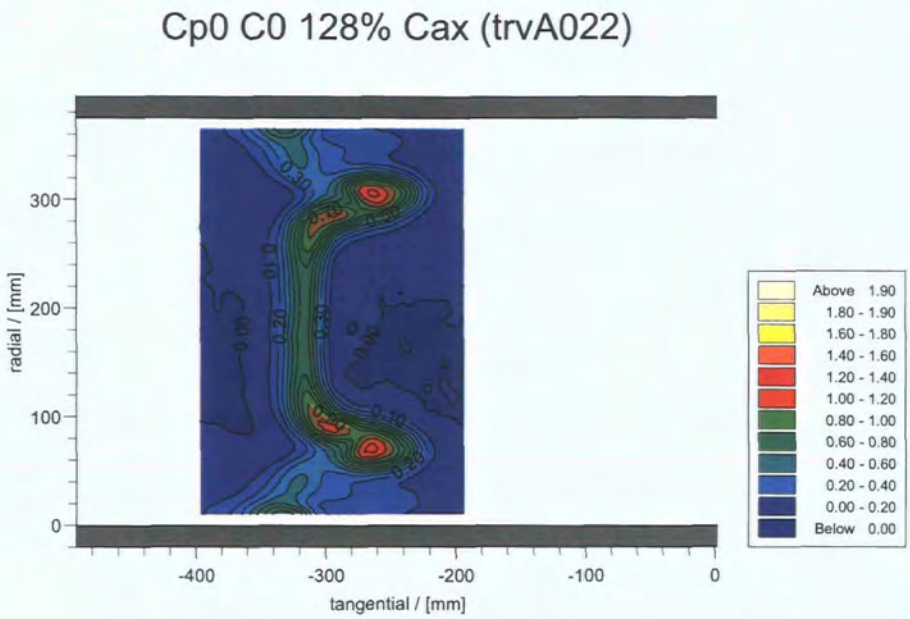

Figure 8.21: Loss C0a at 128% C_{ax}

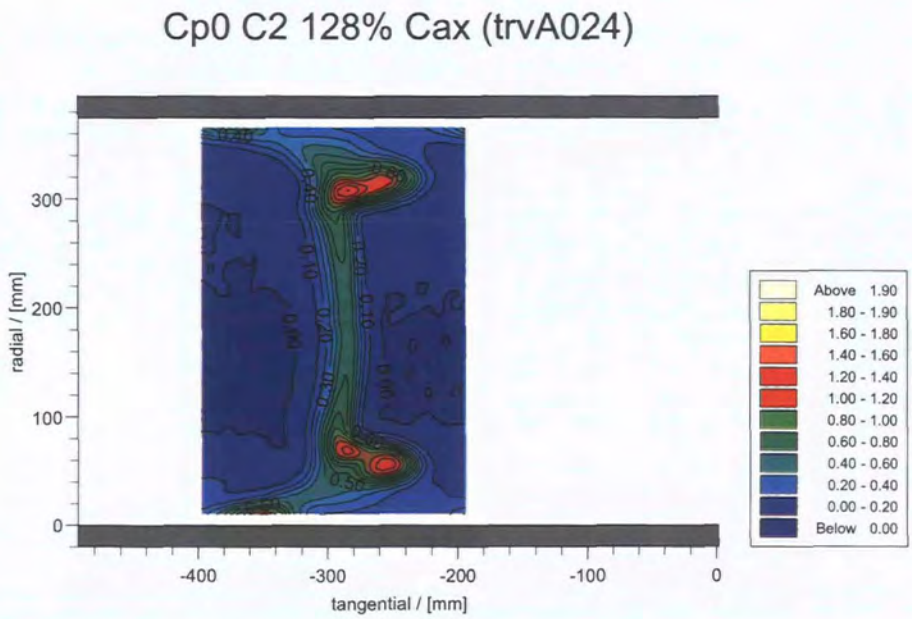

Figure 8.22: Loss C2 at 128% C_{ax}

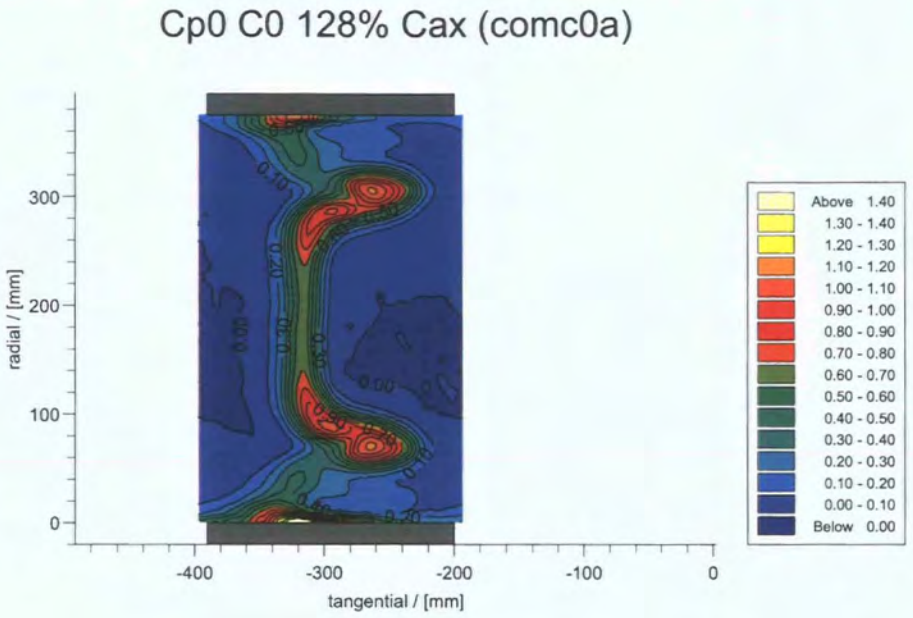

Figure 8.23: Combined 5h & 3h - Loss C0a at 128% C_{ax}

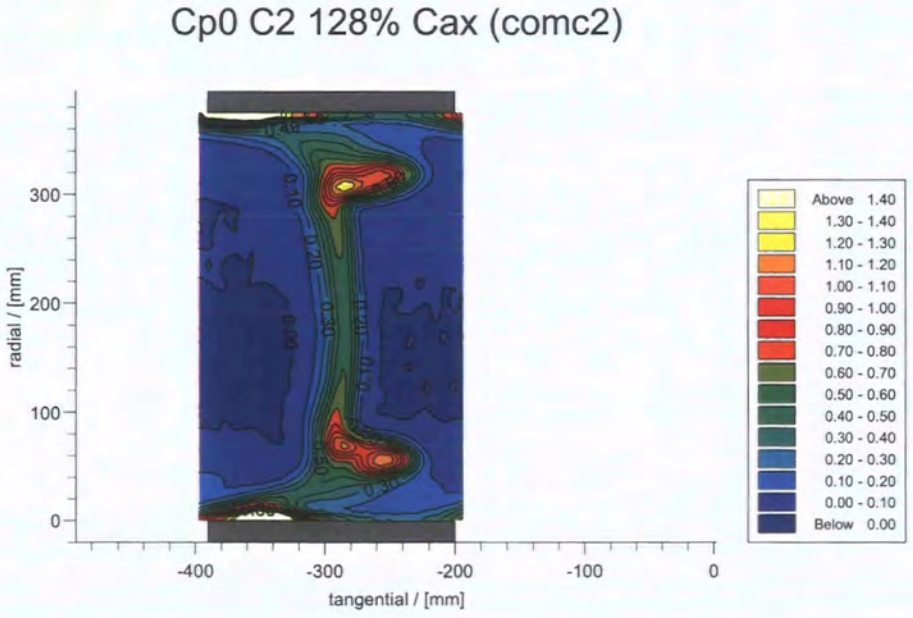

Figure 8.24: Combined 5h & 3h - Loss C2 at 128% C_{ax}

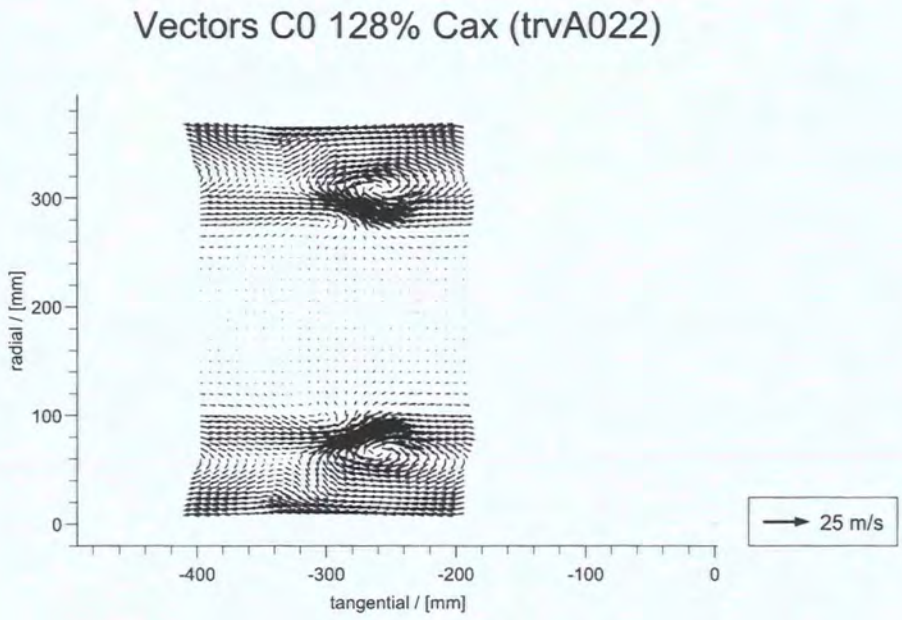

Figure 8.25: Secondary Velocity Vectors C0a at 128% C_{ax}

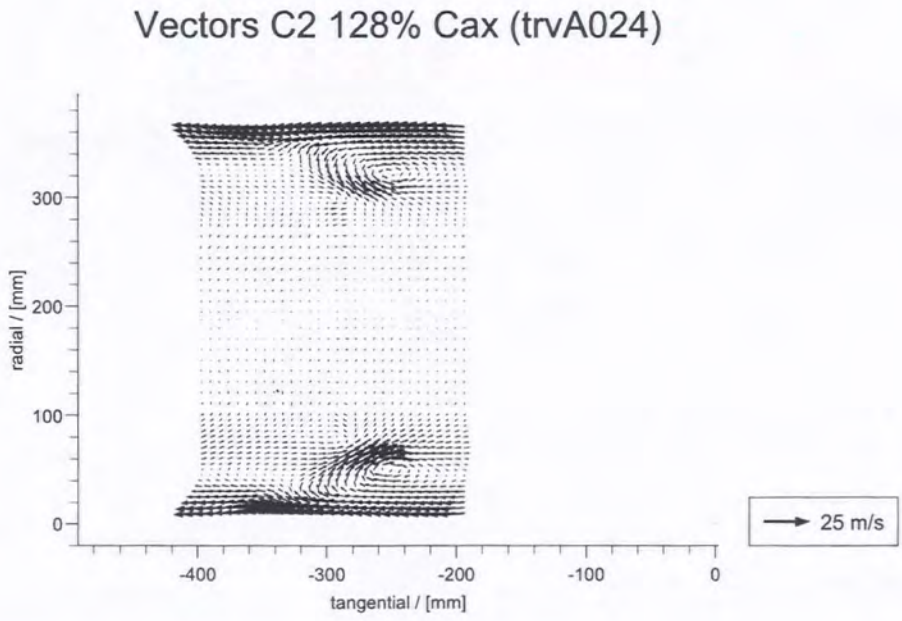

Figure 8.26: Secondary Velocity Vectors C2 at 128% C_{ax}

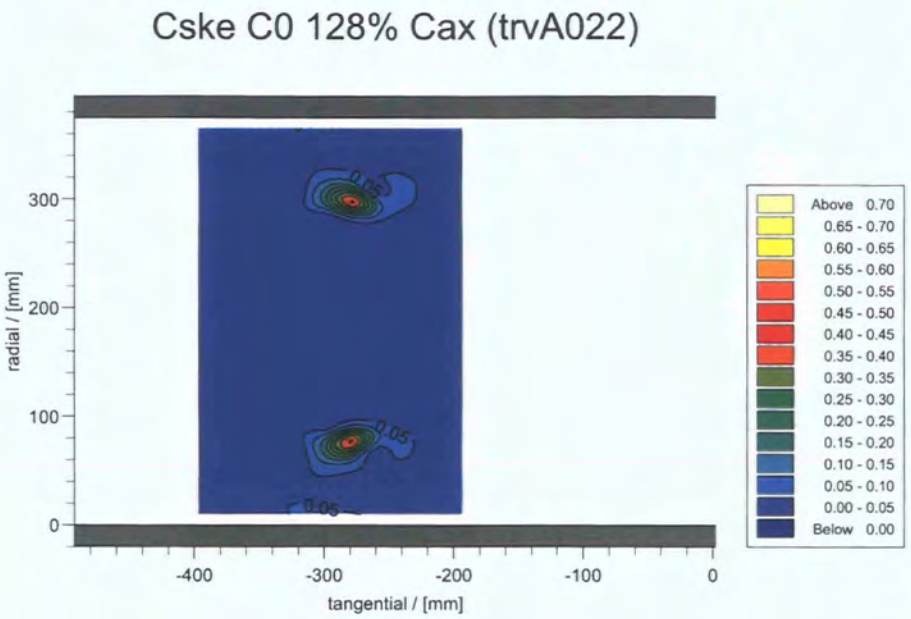

Figure 8.27: C_{SKE} C0a at 128% C_{ax}

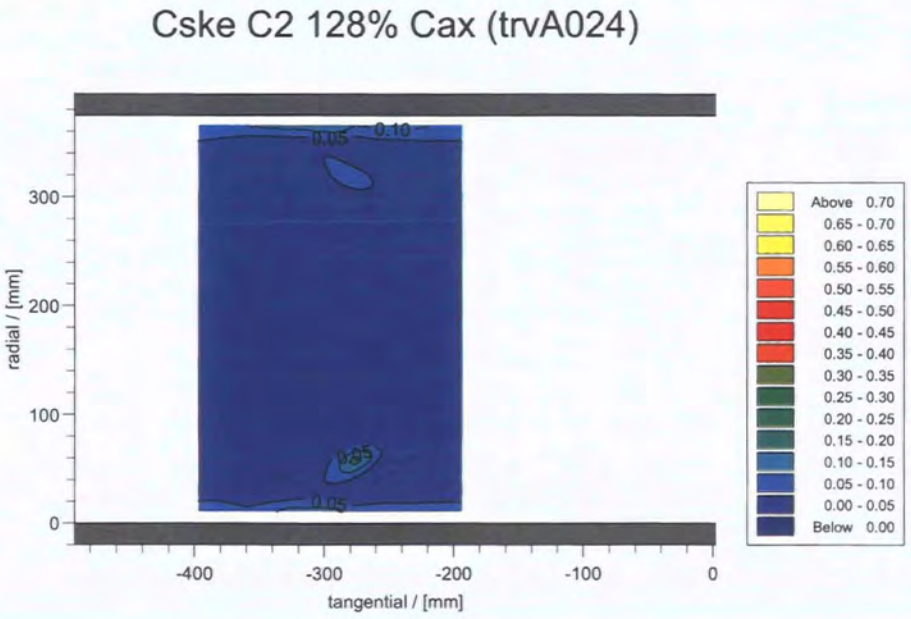

Figure 8.28: C_{SKE} C2 at 128% C_{ax}

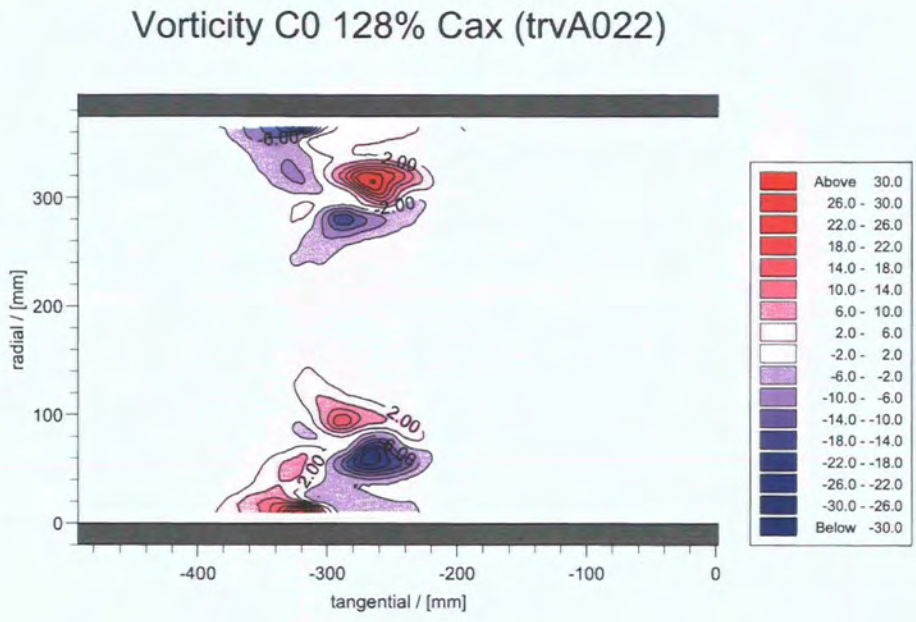

Figure 8.29: Vorticity C0a at 128% C_{ax}

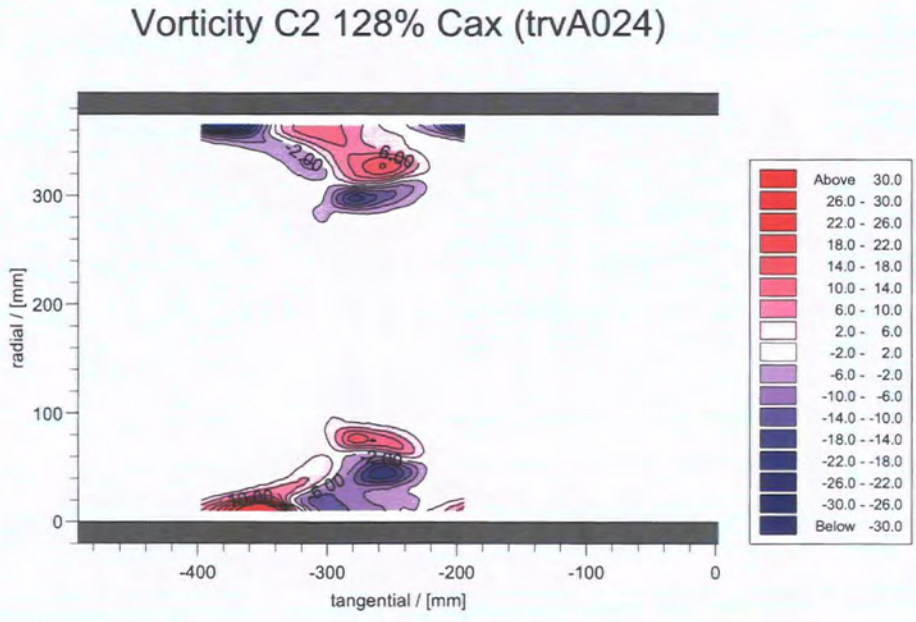

Figure 8.30: Vorticity C2 at 128% C_{ax}

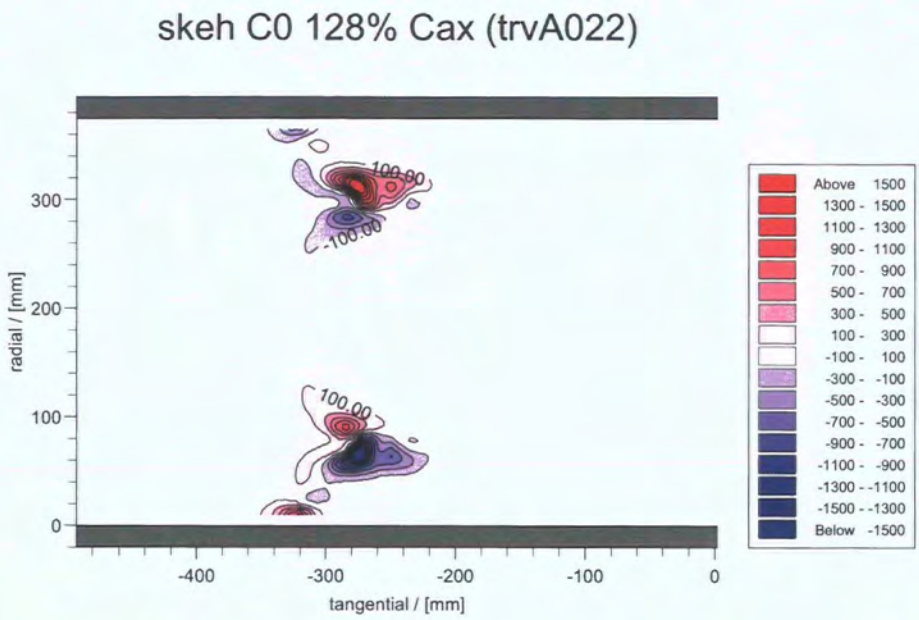

Figure 8.31: SKE.H C0a at 128% C_{ax}

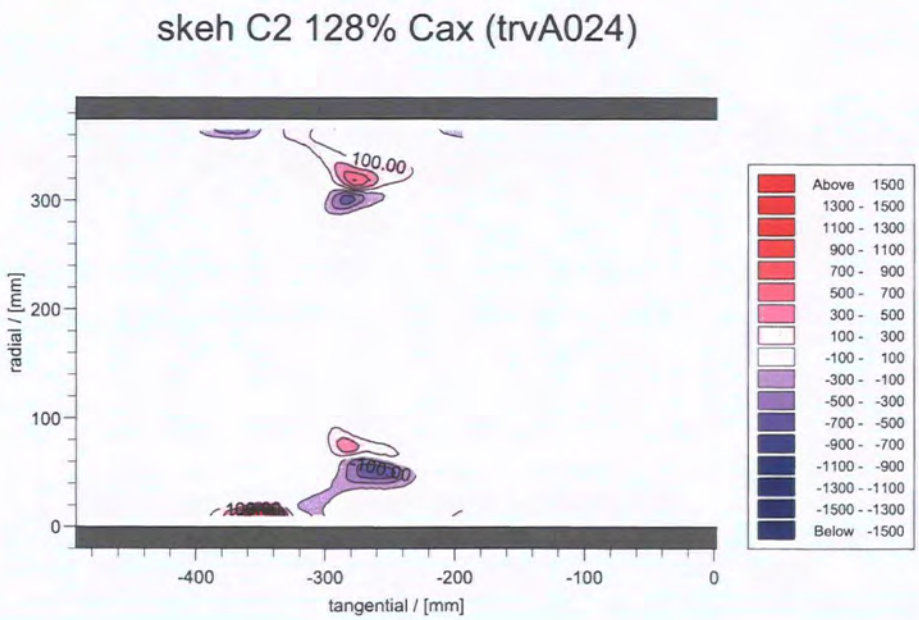

Figure 8.32: SKE.H C2 at 128% C_{ax}

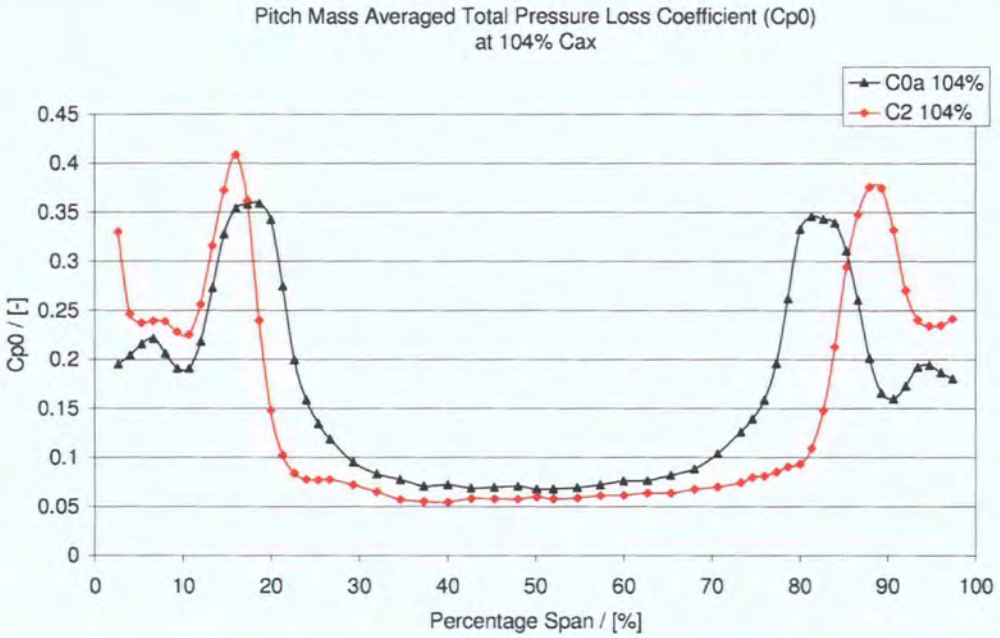

Figure 8.33: Pitchwise Averaged Loss Coefficient at 104%C_{ax}

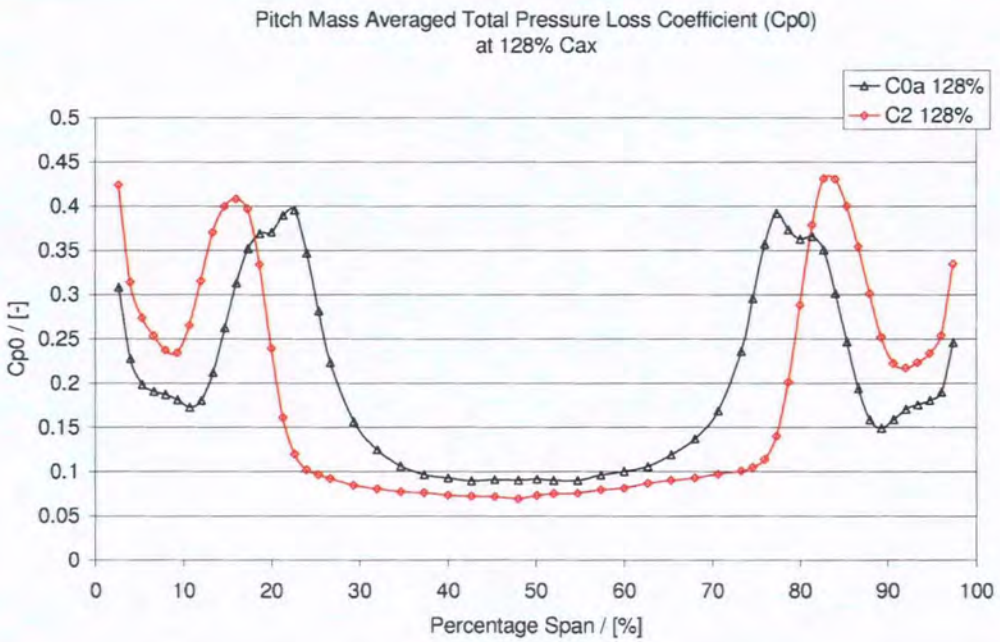

Figure 8.34: Pitchwise Averaged Loss Coefficient at 128%C_{ax}

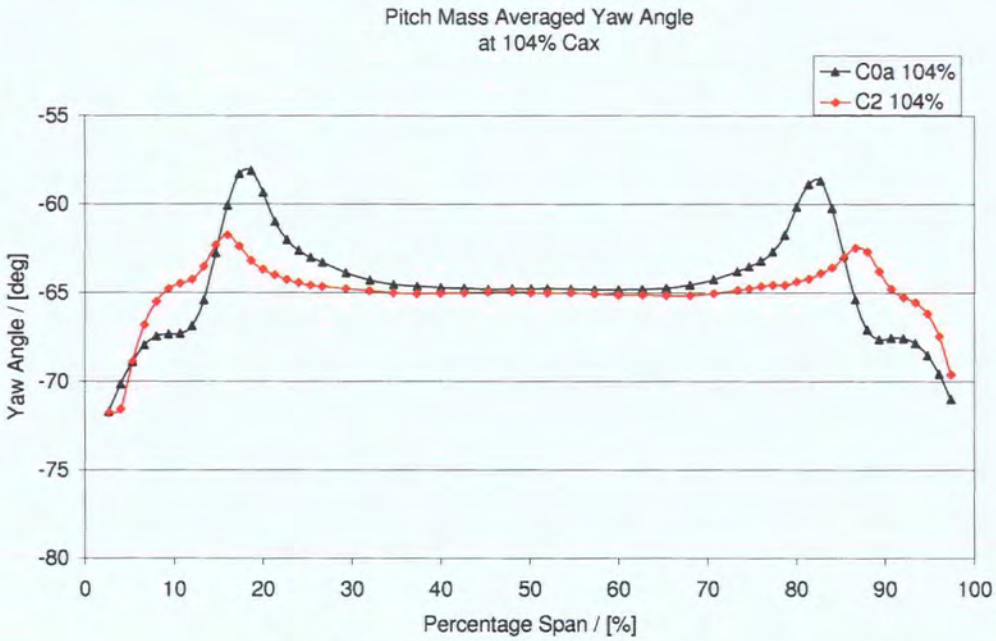

Figure 8.35: Pitchwise Averaged Yaw Angle at 104%C_{ax}

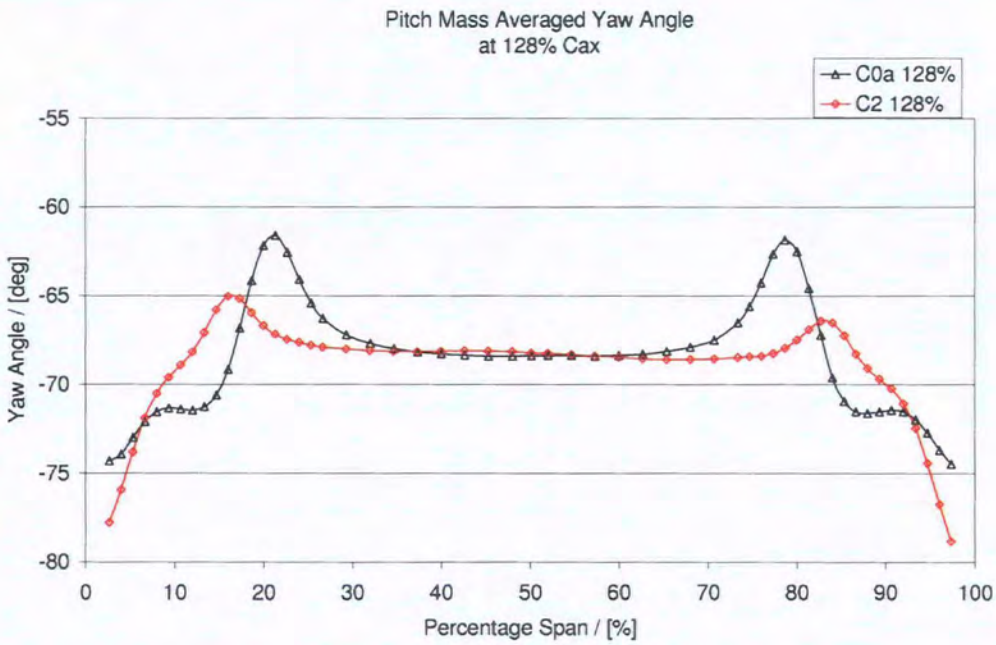

Figure 8.36: Pitchwise Averaged Yaw Angle at 128%C_{ax}

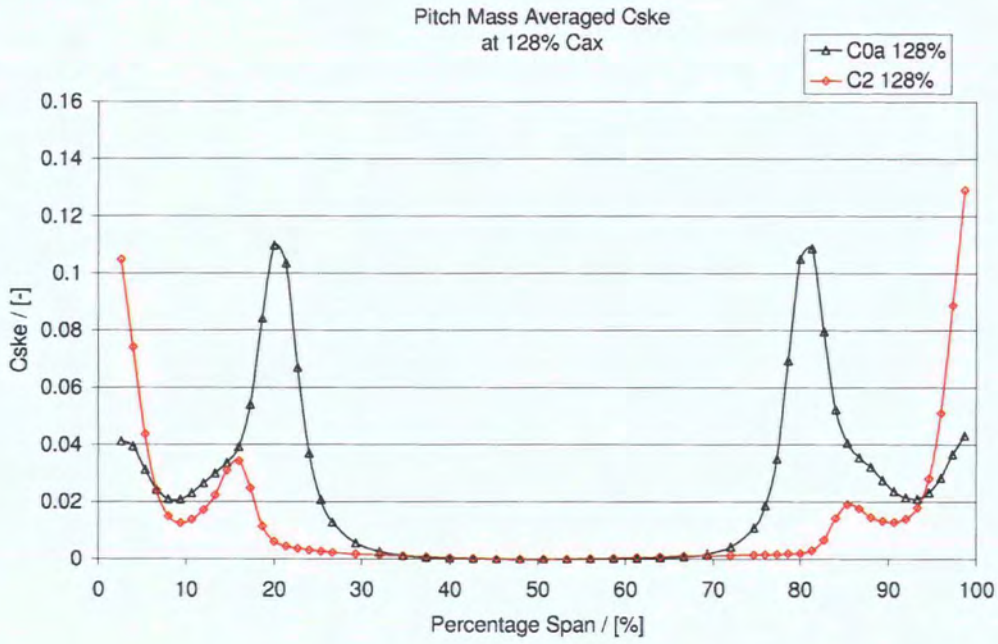

Figure 8.37: Pitchwise Averaged C_{SKE} at 128%C_{ax}

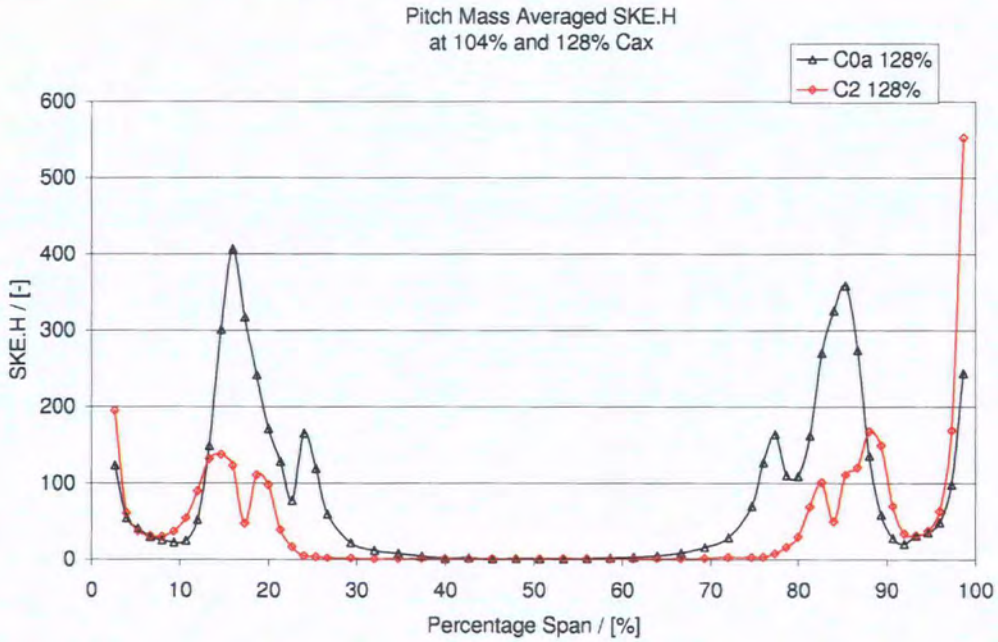

Figure 8.38: Pitchwise Averaged SKE.H at 128%C_{ax}

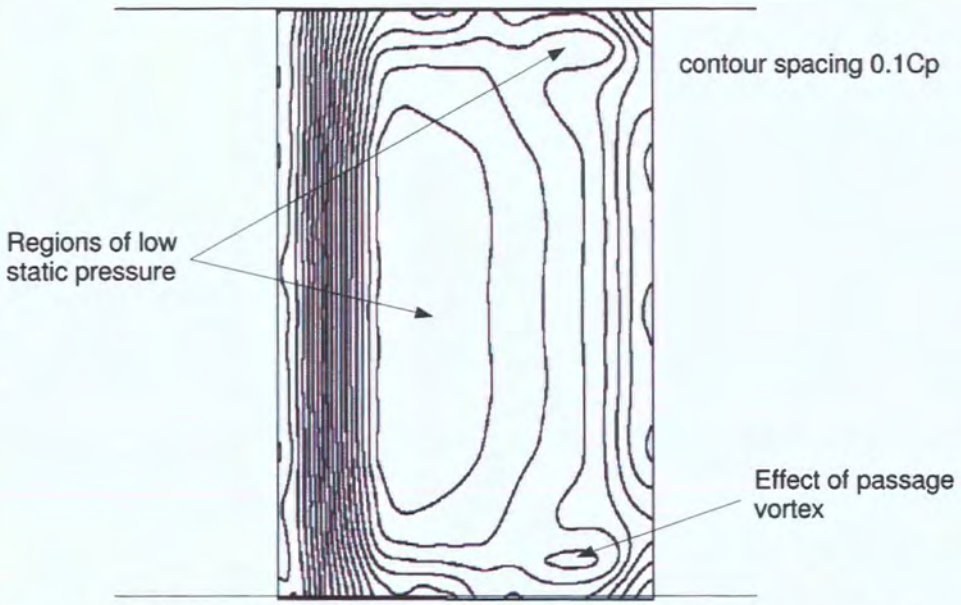

Figure 8.39: Suction surface static pressure distribution - Datum C0a

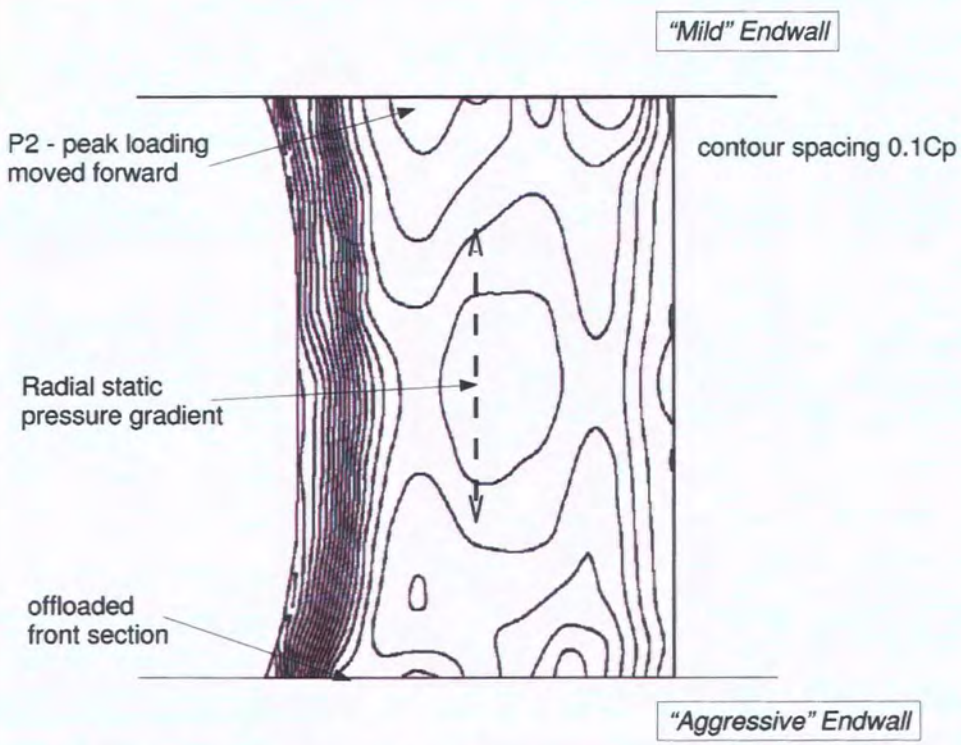

Figure 8.40: Suction surface static pressure distribution - C2

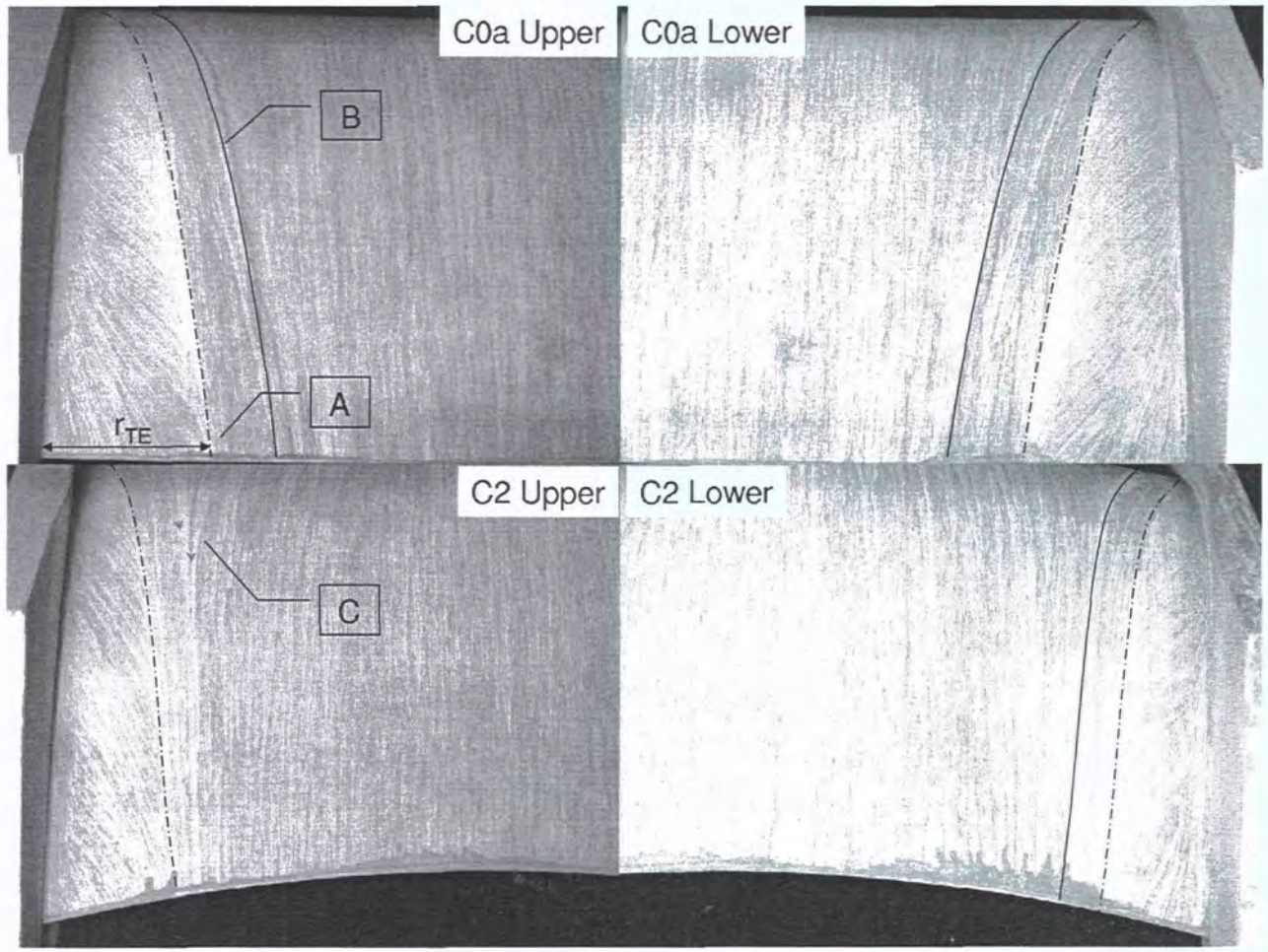

Figure 8.41: Flow visualisation - C0a C2 Aft Suction Surface

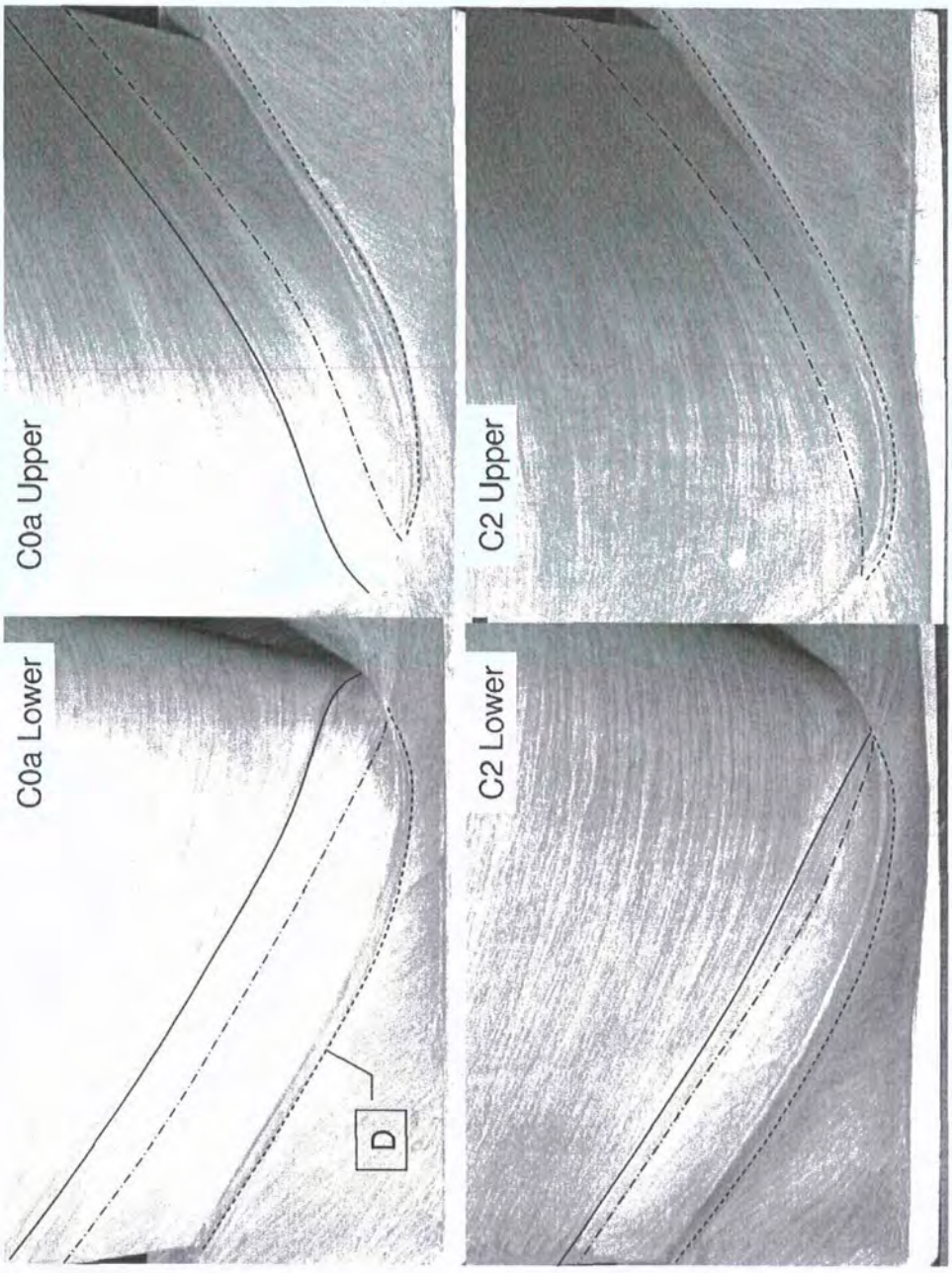

Figure 8.42: Flow visualisation - C0a C2 Suction Surface Endwall Corner

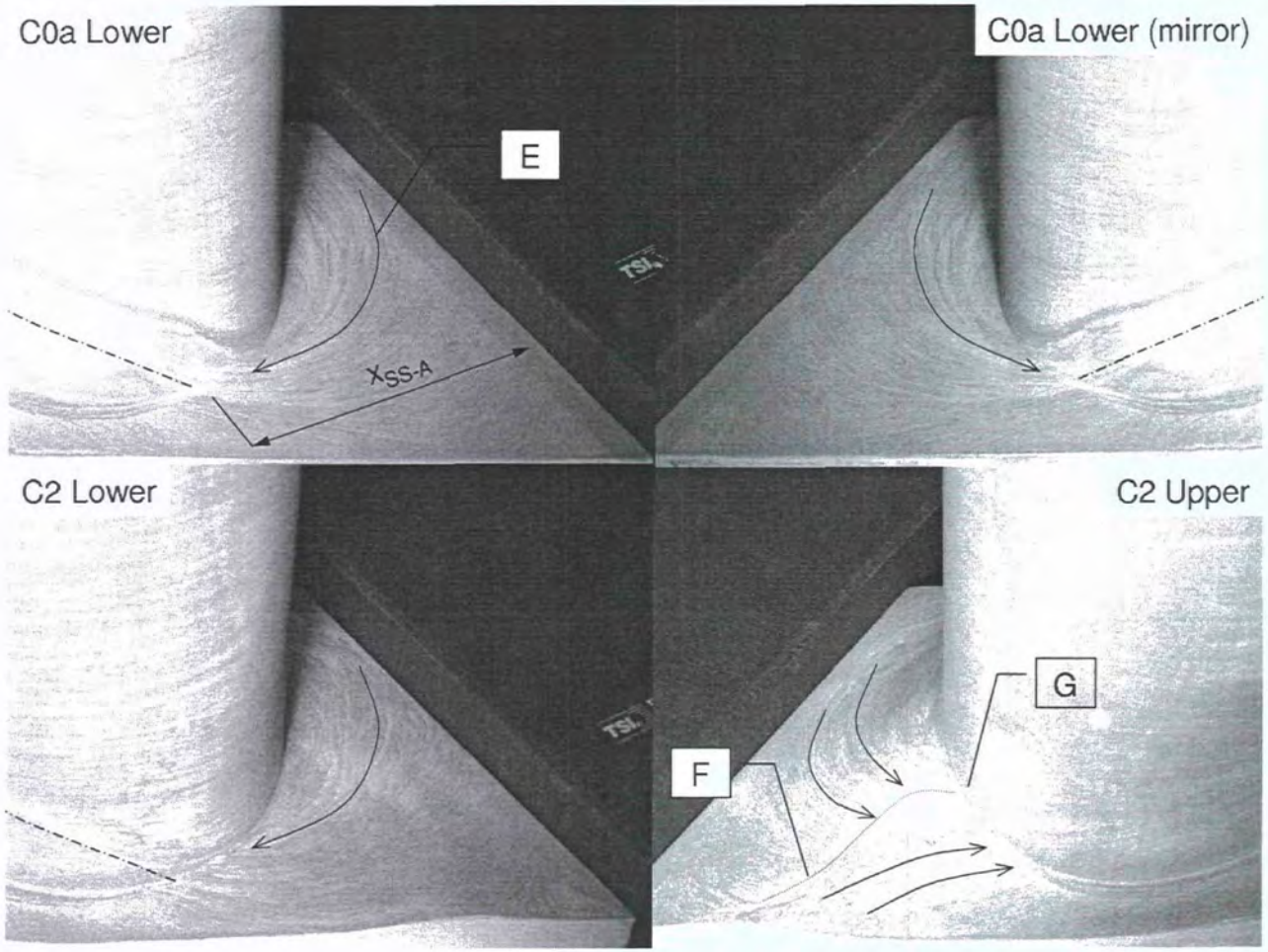

Figure 8.43: Flow visualisation - C0a C2 SSHSV Endwall Trace

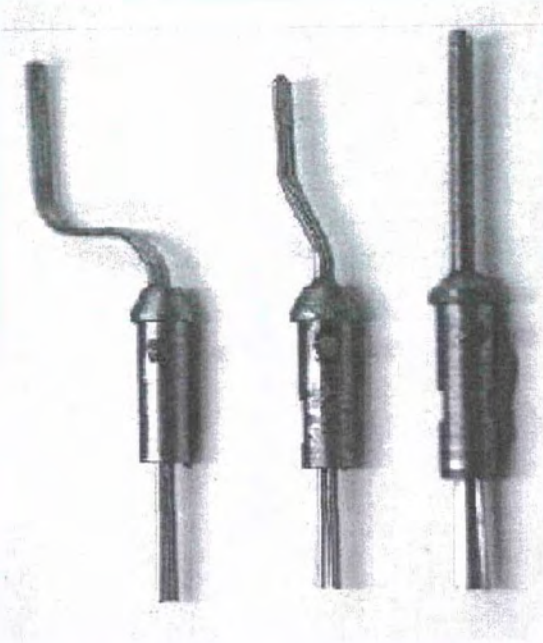

Figure 8.44: Pressure Probes 5h 3h and cranked

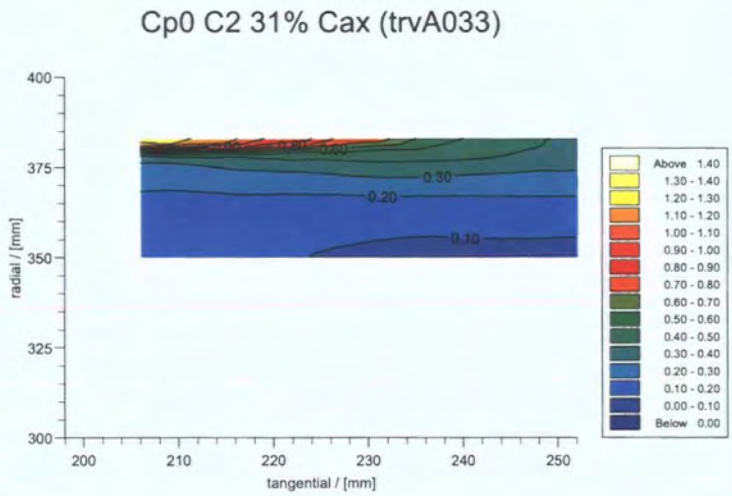

Figure 8.45: Loss for C2 Upper Endwall at 31% C_{ax}

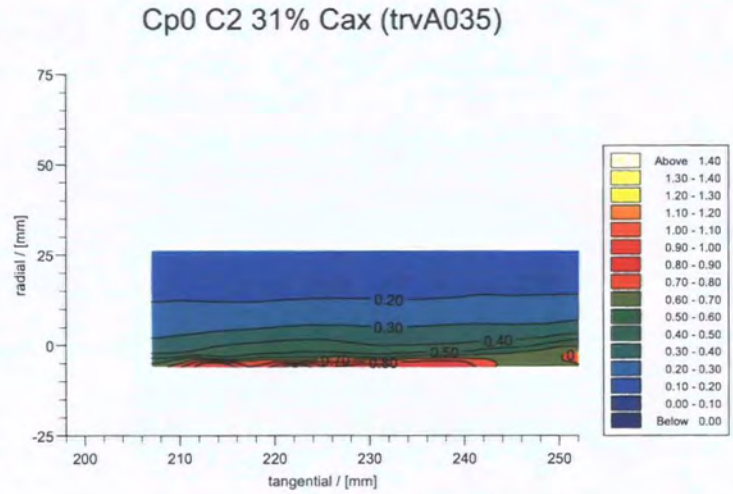

Figure 8.46: Loss for C2 Lower Endwall at 31% C_{ax}

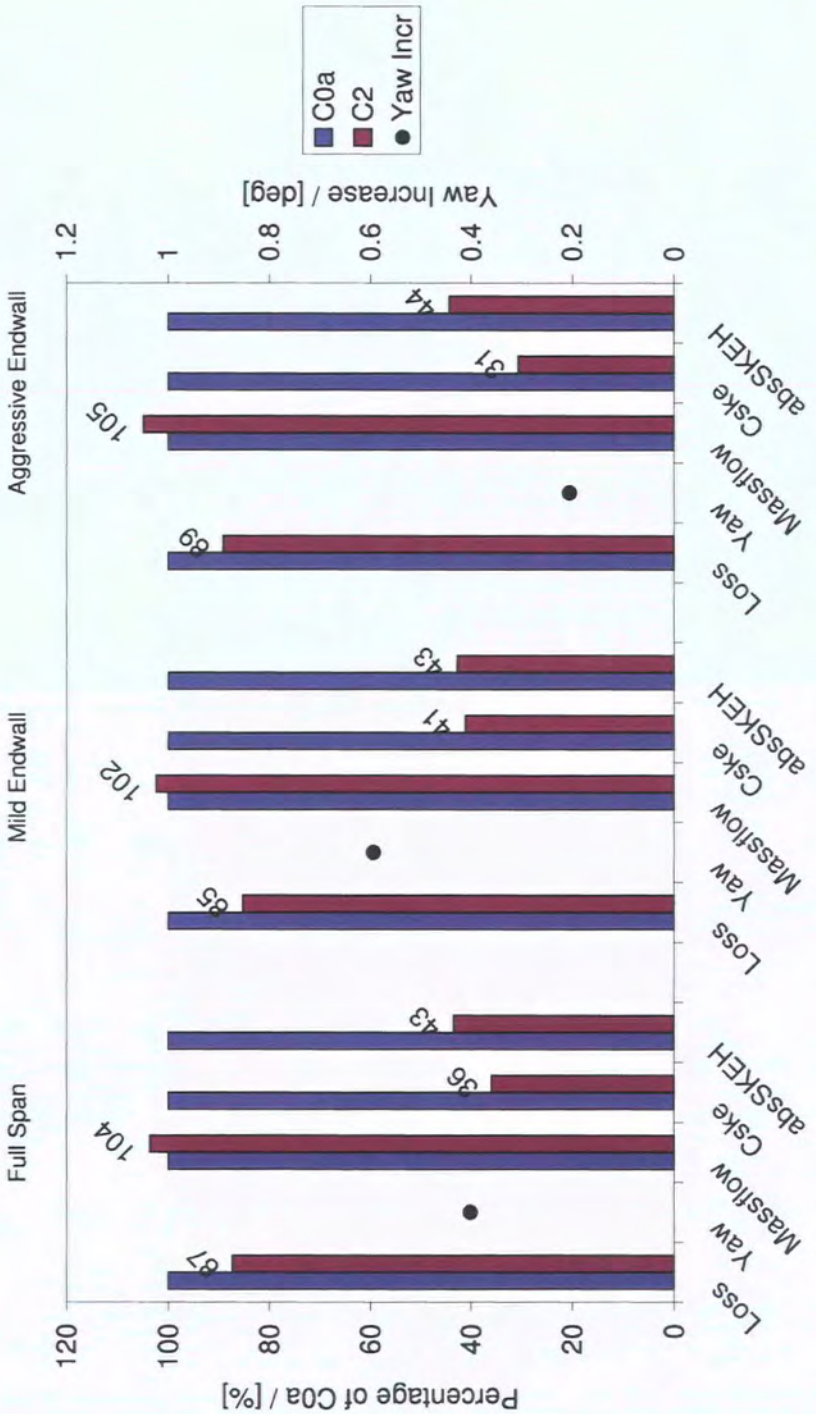

Figure 8.47: Mass averaged result of 5h probe traverse

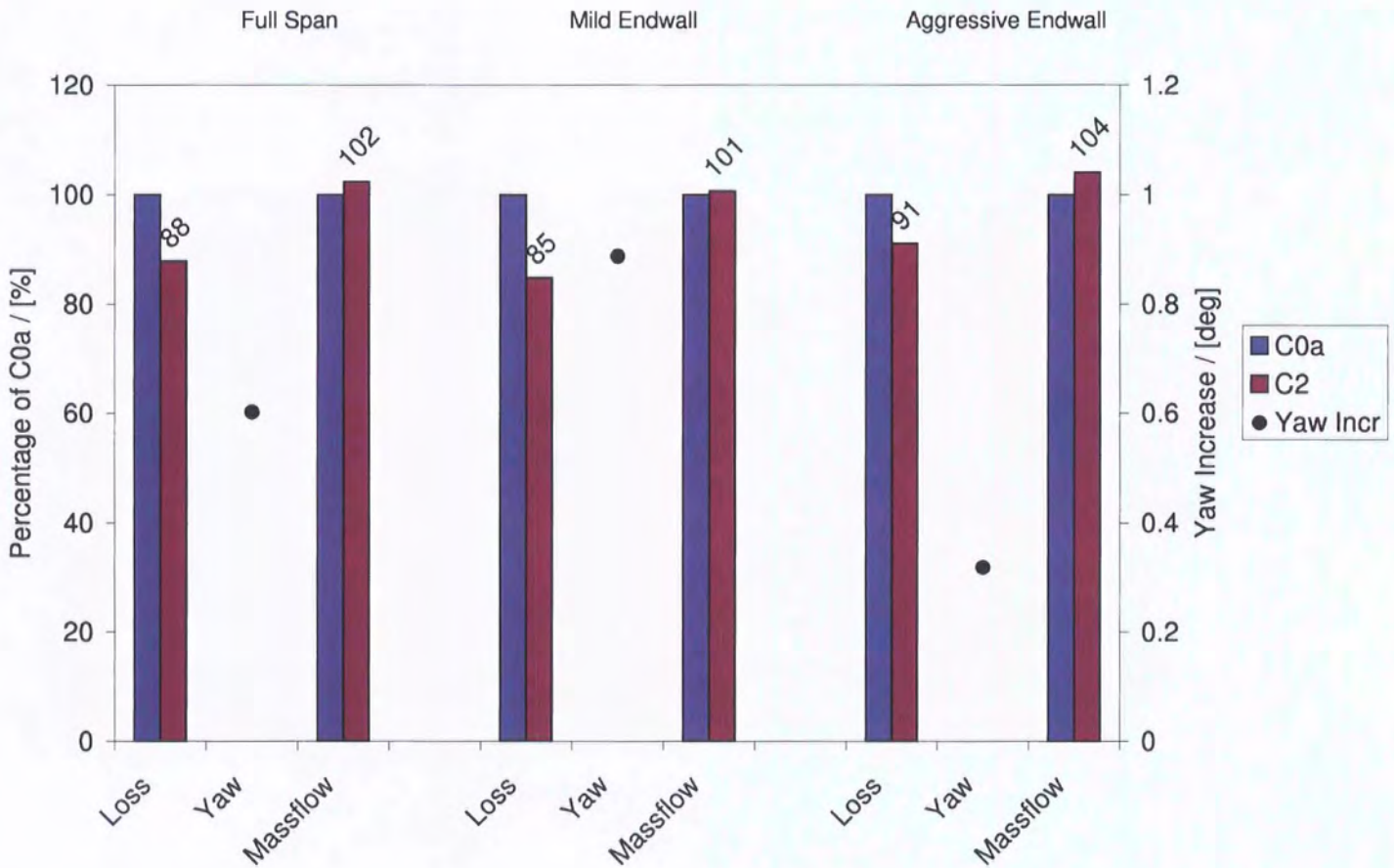

Figure 8.48: Mass averaged result of combined 3h and 5h probe traverses

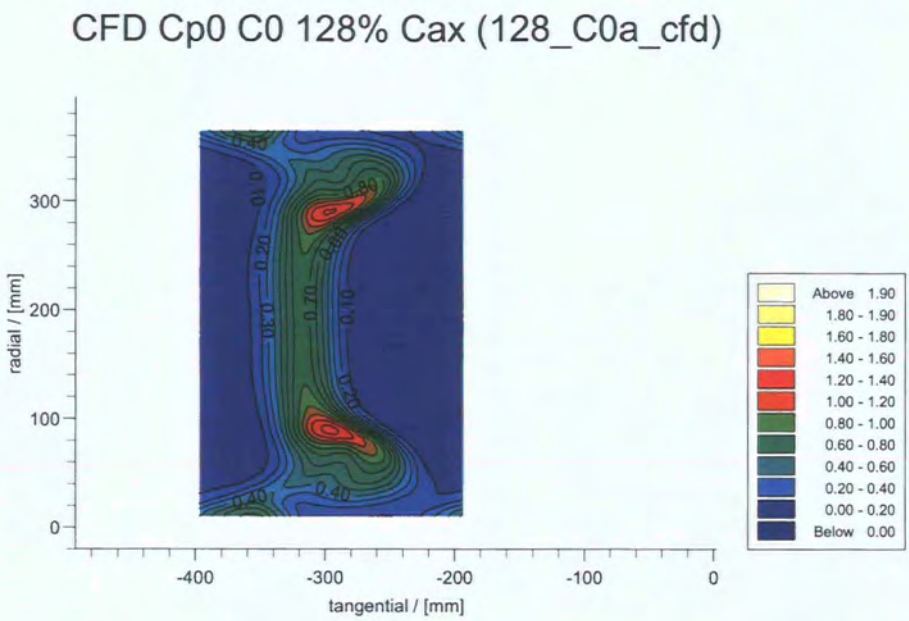

Figure 8.49: Loss C0a at 128% C_{ax} - CFD

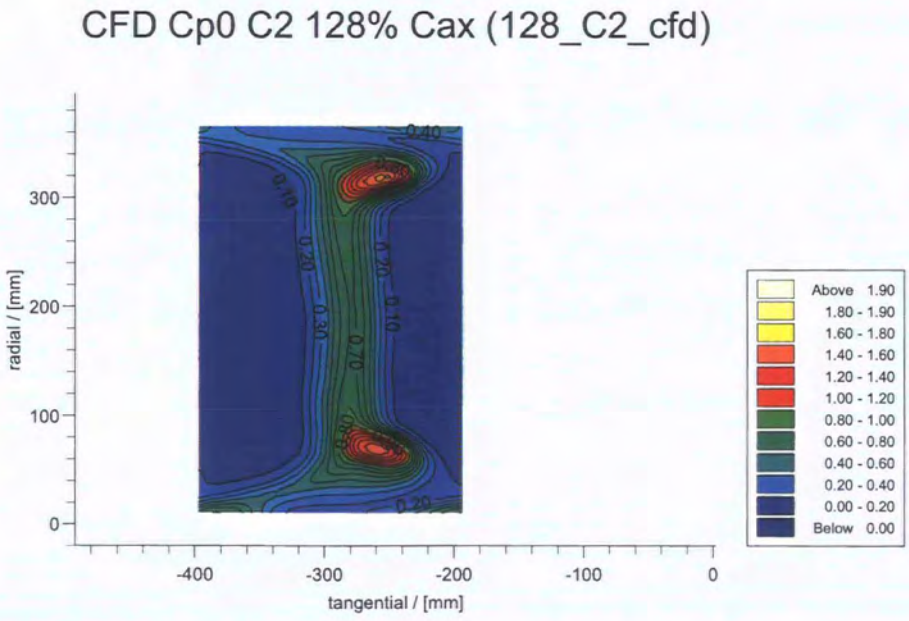

Figure 8.50: Loss C2 at 128% C_{ax} - CFD

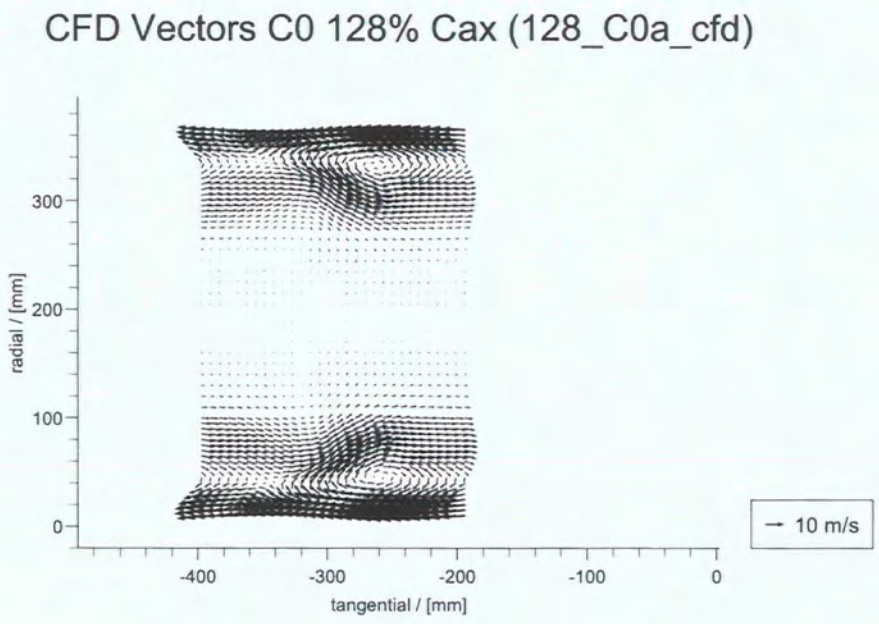

Figure 8.51: Secondary Velocity Vectors C0a at 128% C_{ax} - CFD

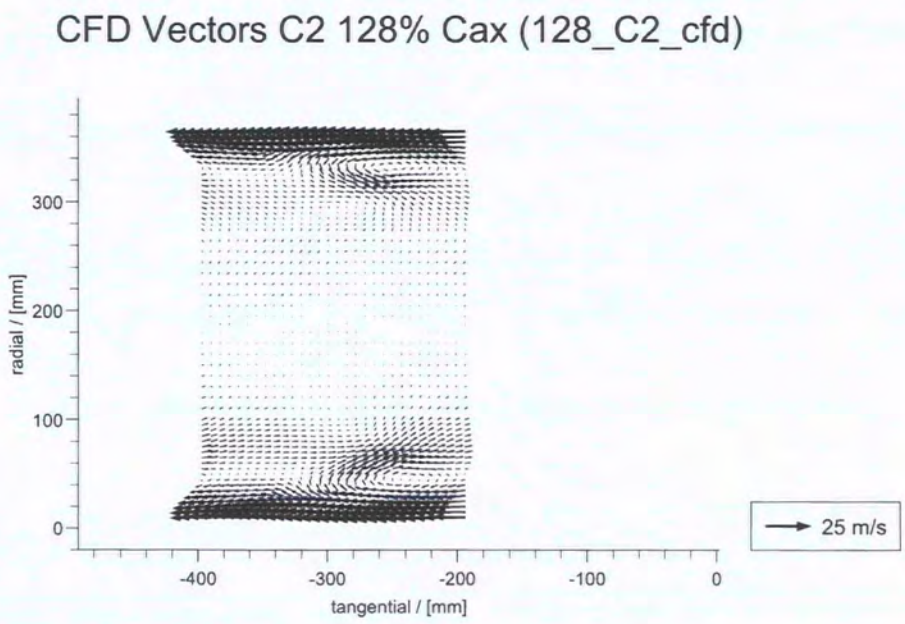

Figure 8.52: Secondary Velocity Vectors C2 at 128% C_{ax} - CFD

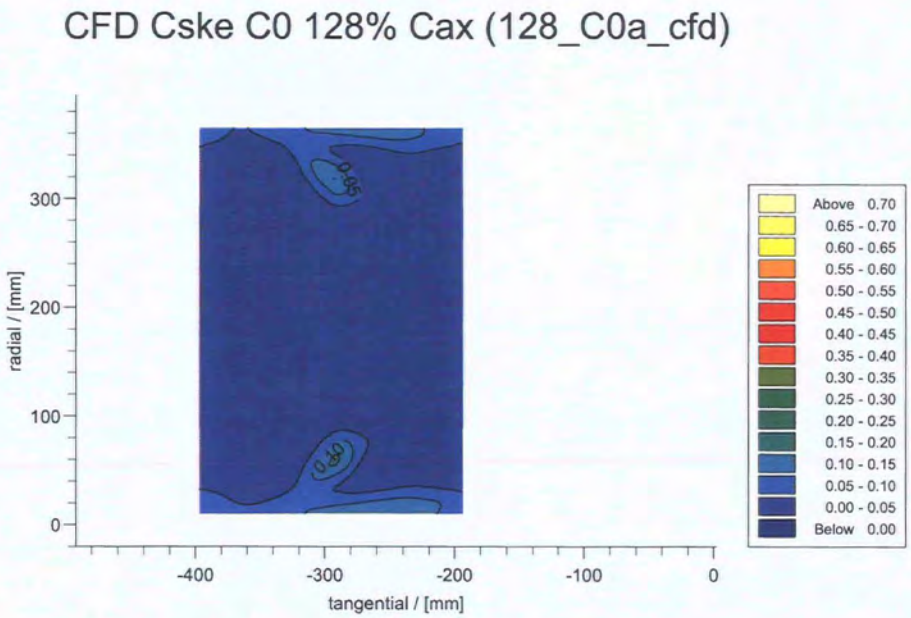

Figure 8.53: C_{SKE} C0a at 128% C_{ax} - CFD

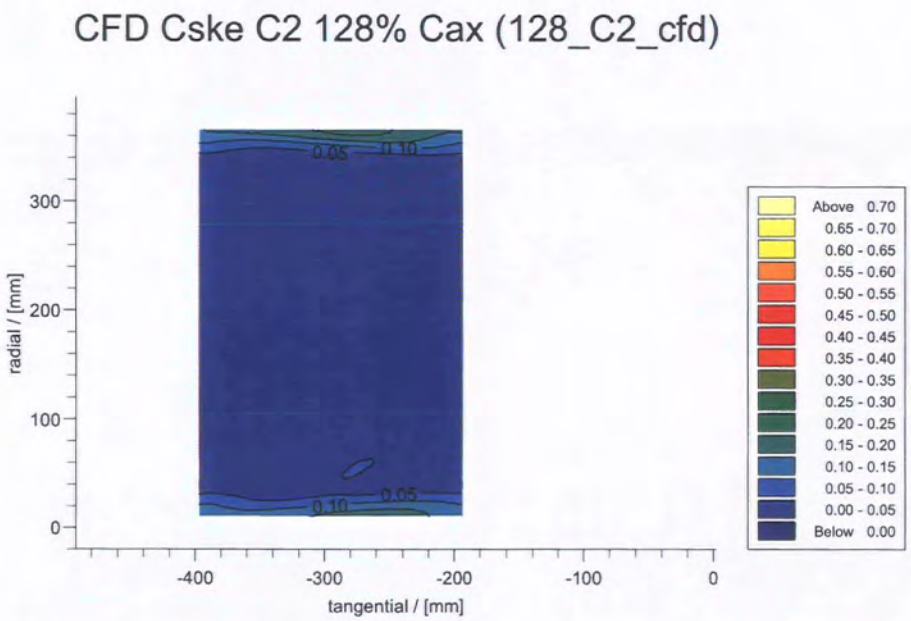

Figure 8.54: C_{SKE} C2 at 128% C_{ax} - CFD

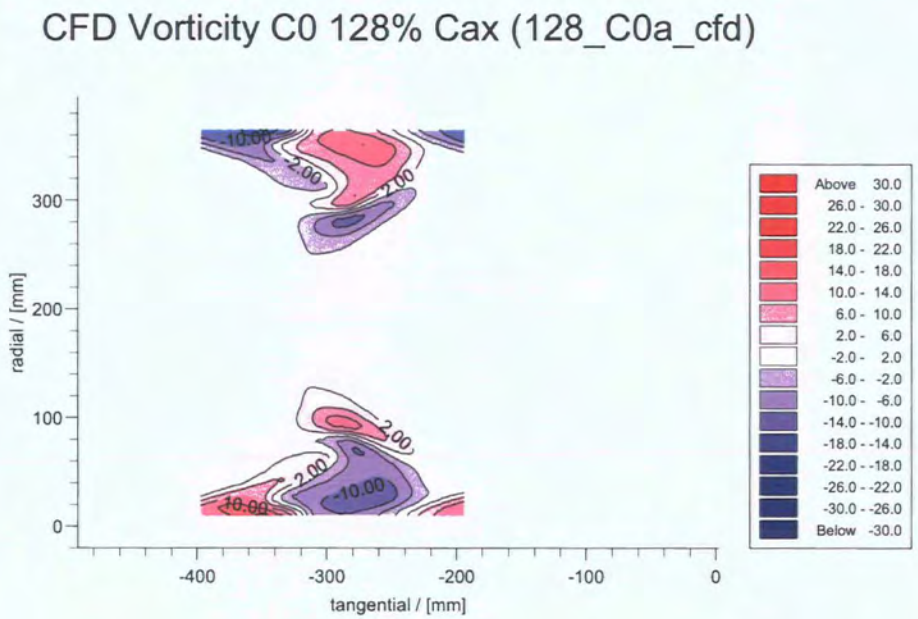

Figure 8.55: Vorticity C0a at 128% C_{ax} - CFD

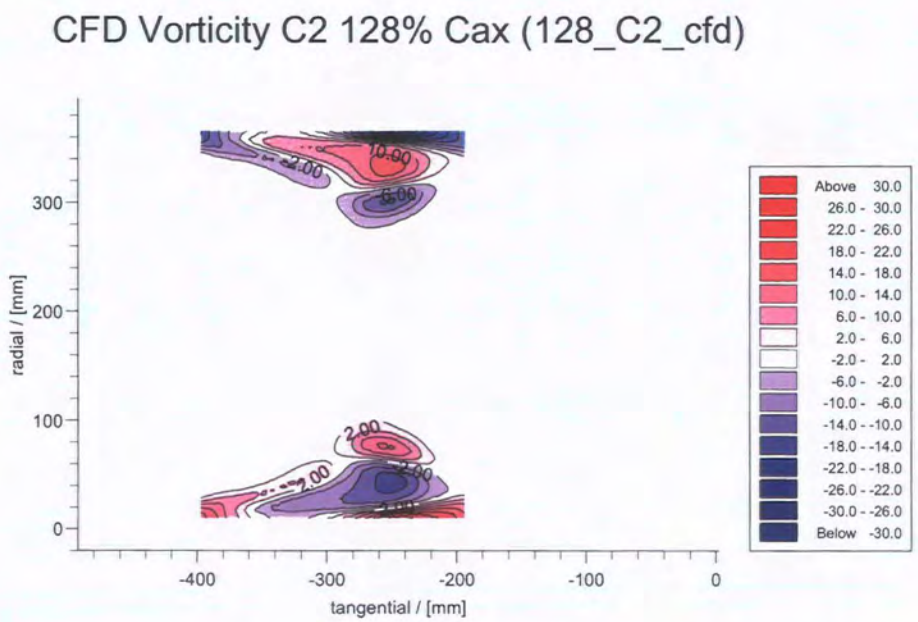

Figure 8.56: Vorticity C2 at 128% C_{ax} - CFD

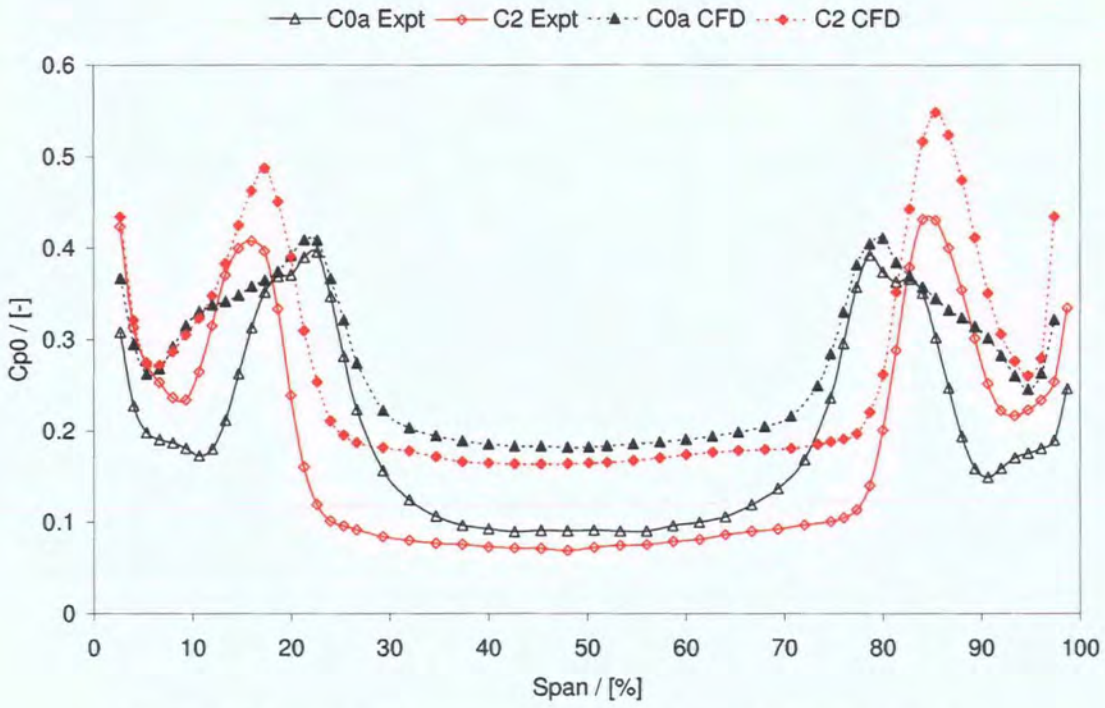

Figure 8.57: Pitchwise averaged Loss CFD and Expt at 128% C_{ax}

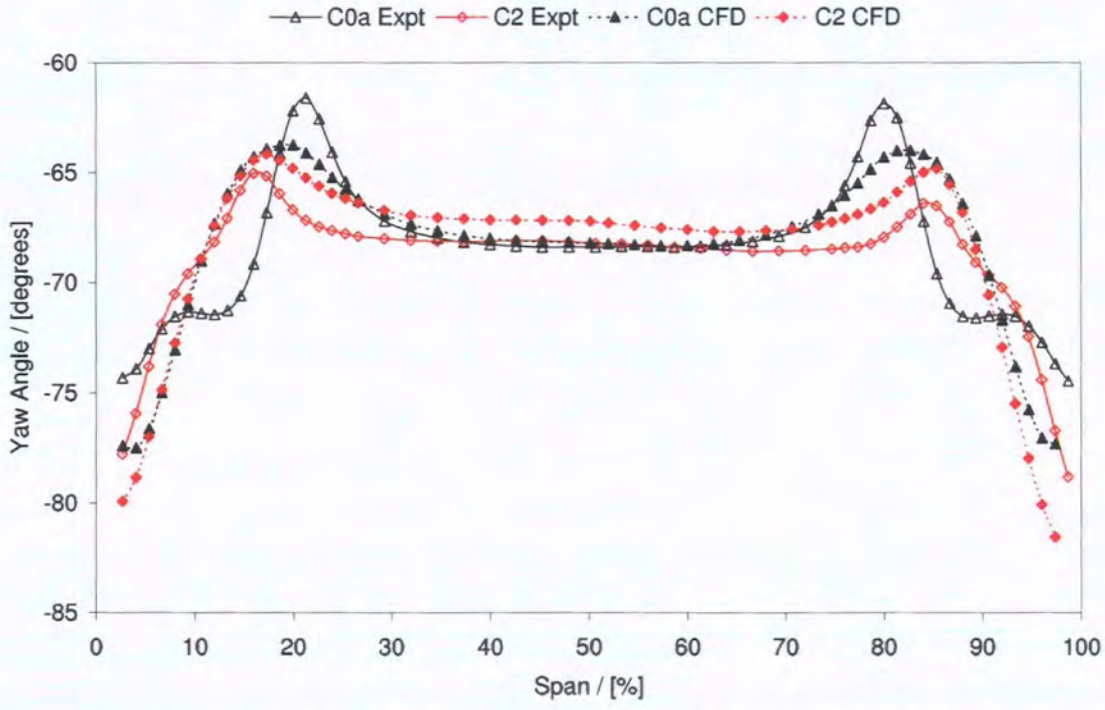

Figure 8.58: Pitchwise averaged Yaw Angle CFD and Expt at 128% C_{ax}

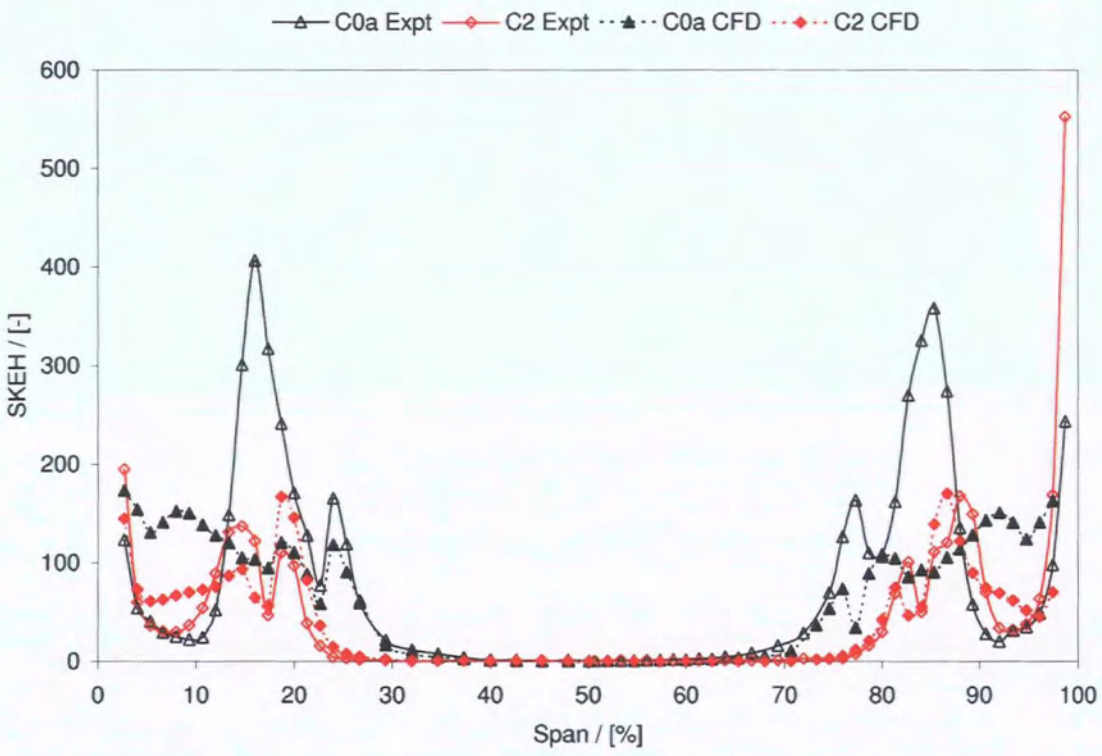

Figure 8.59: Pitchwise averaged SKEH CFD and Expt at 128% C_{ax}

Chapter 9

Passage Shaped C3

THIS chapter describes the work involved in the design, construction and testing of the C3 passage shaped geometry. The design is a progression of the C2 geometry and was developed from a desire to improve upon the passage shaping concept. The chapter is split into sections describing; the design decisions for C3, the computational and optimiser setup, and the resultant designs. This is followed by the results of experimental measurement at 128% C_{ax} and the equivalent CFD results.

9.1 Introduction

To enable continuity of design and provide a greater understanding of the passage shaping concepts, the existing aerofoil geometry was retained and two new endwalls were applied. Once again, the highly symmetrical cascade inflow enables the analysis of two endwall shapes within one series of tests.

For C3, one endwall was retained planar. In doing so, the summation of the effects of passage shaping can be better observed. The other endwall was profiled using the same design system as for C2.

The C2 geometry was designed to offer the maximum possible benefit from a passage shaped geometry. The geometry used two very different PEW designs. One endwall design was found to be too aggressive and resulted in a 3D separation similar to the P3 design. The other endwall design was less aggressive, did not separate and presented a significant reduction in loss over the base geometry.

9.2 Computational setup

The design computations for C3 did not require such an in-depth series of calculations as C2, and instead focussed on the 3D Navier-Stokes modelling using the MEFP based code.

The computational mesh resolutions, inlet conditions and boundary conditions used for C2 and C3 designs are essentially the same. However, changes were made to the optimiser settings for the new PEW design; these were:

- A greater restriction on diffusion (D). The endwall diffusion is measured by the

criterion defined in Equation 7.4 in Chapter 7. Here the diffusion on the blade surface close to the endwall is used as a proxy for endwall diffusion. Direct assessment of endwall diffusion is not currently possible within the design system. The diffusion criterion was reduced from 0.4 for C2, to 0.38 for C3.

- A reduction in the maximum perturbation amplitude - The lower 'aggressive' endwall of the C2 design had large endwall heights close to the leading edge. The 3D separation feature found in this region can be attributed to these large endwall perturbations. By restricting the maximum perturbation, it was expected that a more even distribution of PEW heights would result, and the probability of another separation would be reduced. The following are the maximum values for the zero and first order perturbations; the total amplitude is potentially twice this amount. For C2 the maximum value was 12.5 mm, for C3 it was 10 mm.

9.3 Design

9.3.1 Perturbation stations

It was decided that the axial extent of the endwall profiling for passage shaped geometries should be investigated. As noted in Chapter 5, the success of the endwall designs were not directly linked to the axial range available, but the reduction of passage vortex strength in the P1 geometry was observed to be greater than the P2 geometry with its restricted range.

An investigation was undertaken to ascertain the effect of the perturbation station positions. Three different arrangements of endwall were considered. The three designs were run using the same phase optimisation script, calculating the numerous geometries on a Linux cluster. Each trial geometry used identical base (aerofoil) geometry and identical inlet and boundary conditions, but used different axial position of the perturbation stations.

The stations were arranged with the same proportional spacing, but with altered upstream and downstream limits. The locations of the perturbation stations of the three arrangements are shown in Figure 9.1. The grouping of the stations towards the leading edge, was chosen so that the optimiser might have a greater design freedom in the early part of the passage, with the aim of reducing the cross passage gradient as early as possible.

A detailed systematic investigation of the effect of the station locations was not possible, due to time and computational constraints. Some interesting observations can be made however.

9.3.2 Optimiser Results

For each of the three endwall designs, the progression of the optimisation script is observed by its impact on SKE.H, aerofoil diffusion and capacity and the chosen endwall shape, by the resulting perturbation magnitudes. These are included in the plots in Figures 9.2 to 9.4, for the Datum, Compacted and Elongated designs. The bar graph illustrates the perturbation magnitudes for the zero and first order

harmonics. The line graph indicates the changes in the target function (SKE.H) and the limits of diffusion and capacity.

The different perturbation magnitudes and combinations used, indicate the flexibility of the optimisation. All plots show a general reduction in the SKE.H magnitude as the optimiser progresses. The level of diffusion also increases throughout the process, with a noticeable jump in the diffusion level at Station 4 for all designs. The level of capacity is maintained by all three designs, this is evident in the very small 'dcapacity' magnitudes.

The endwall height contours of the three key geometries are provided in Figures 9.5 to 9.7, with humps (positive amplitude) shown in yellow and red and dips (negative amplitude) shown in blues. The contour line spacing is set at 1mm.

The Datum spacing, with result in Figure 9.5, used the same station arrangement as the C2 design. The starting station is located at -211 mm, the finishing station is located at 10 mm. The design is different to the C2 aggressive endwall (Figure 7.38), because of the new restrictions on the maximum permissible diffusion level and maximum amplitude of perturbation.

The Elongated spacing, with result in Figure 9.6, was extended beyond that of the Datum, with a start station further upstream at -233 mm. Station 6 and the finish station were left relatively unchanged, but stations 1 to 5 were scaled with the same spacing ratios as the Datum. This elongated arrangement has resulted in a greater freedom of PEW design upstream of the blade leading edge.

The Compacted spacing, with result in Figure 9.7, was restricted to within the blade passage. The start and finish stations are defined at the blade leading and trailing edges, -199 mm and 0 mm respectively. The six perturbation stations have again been scaled in between these two limits by the same ratio as Datum.

9.3.3 Analysis

The following observations can be made about the three geometries:

- The datum and elongated arrangements have similar geometries for the first half of the passage (0 - 50% C_{ax}). There is a clear hump close to the leading edge on the pressure side and a corresponding dip close to the suction side.
- The datum and elongated arrangements differ in the second half of the passage, where the elongated arrangement shows a resurgent hump close to the pressure surface which does not exist on the datum arrangement.
- The PEW extends further upstream for the elongated arrangement.
- The compacted arrangement is almost entirely different, with a zero-order harmonic (axi-symmetric) dip near the leading edge and no hump dip arrangement. Further downstream the compacted arrangement has a ridge that is similar to the elongated arrangement.

A secondary hump close to the late PS was observed on the C3 elongated design. The reason for this hump is not likely to be the axial station location. There is a relatively minor change of axial position between these two designs. It is more likely

Criterion	Units	C2	-	C3	-	C3ElonEd	-
		Target	Weight	Target	Weight	Target	Weight
Capacity	**MFP**	**0.061**	**3300**	**0.07**	**1000**	**0.07**	**3500**
Loss	-	0.000188	1000	0.000187	3300	0.000187	200
Turning	^{o}	110.9	1000	109.7	1000	109.7	1000
Peak Mn	-	0.16	200	0.16	200	0.16	200
Diffusion	-	0.4	80	0.38	80	0.38	80

Table 9.1: Optimiser controls for C2 and C3 endwall geometries

that this difference (to C2) is due to the impact of the upstream profiling on the local flow.

It is clear, from the SKEH parameter, that the restrictive "compacted" design is less successful than either the datum or elongated ones. This result may be due to the station axial locations, as much as their overall range.

Further information on these two effects would require a systematic study of the endwall design process.

9.3.4 Capacity restriction

Analysis of the optimiser summary for this design (Figure 9.3), indicates a change in the capacity of +0.36%. This capacity change is outside of the permitted range for engine component design.

Concern over capacity changes, seen in the analysis of the C2 design, Chapter 8, has put more emphasis on maintaining the massflow parameter for the final design. As such a further PEW design was run through the phase optimisation script. The geometry is based on the elongated design, but with edited values for the weighting of Loss and Capacity. Table 9.1 summarises the weightings for all C3 designs and includes the C2 weightings. A much greater restriction is placed on the capacity, seen in bold font in the table.

The resultant design, generated by the script, is shown in Figure 9.9. The design has a similar hump/dip distribution to the Elongated design, the perturbations do not run as far upstream as the original Elongated design and the maximum positive perturbation is reduced by 1mm.

The optimiser summary chart, Figure 9.8 shows the effect of the tighter capacity control, with a capacity change of 0.06% from the planar endwall geometry. Interestingly, the diffusion magnitude is also much smaller than before.

9.3.5 Endwalls Compared

The results in Figure 9.10 show the development of the SKE.H reduction as the PEWs are built by the optimiser. All SKE.H values are obtained at the same axial plane, downstream of the geometry. The Elongated PEW design is shown to give the greatest benefit in raw SKE.H of the three geometries tested.

Table 9.2 compares the final SKE.H reductions of the four geometries. The table shows that the compacted arrangement reduced the SKE.H magnitude relative to the planar, but only by 19%. The original arrangement of stations gave an improved

Arrangement	SKE.H reduction [%]
Datum	24.95
Compacted	18.91
Elongated	27.29
Elongated(edit)	26.53

Table 9.2: Percentage change in target function

25% reduction. The elongated arrangement has the greatest potential in SKE.H reduction for this aerofoil geometry with 27% reduction.

The tighter control of the Elongated - Edit design slightly reduced the benefit, resulting in only a 26.5% reduction in SKE.H.

9.3.6 Chosen Endwall Design

It was ultimately decided that the capacity difference was less important than the SKE.H reduction, and the Elongated design was chosen for one end of the blade.

At the opposite end a planar endwall was applied. This combination of planar and profiled endwalls within one geometry, is applied to allow both the maximum benefit and the split of benefit (between aerofoil and endwall) to be determined, as discussed in the Section 9.1.

9.4 Results

9.4.1 Flow visualisation

The interaction of the secondary flows with the aerofoil and endwall surfaces is highlighted using the oil and dye surface flow visualisation technique, described earlier.

Figures 9.11, 9.12 and 9.13 contain the flow visualisation photographs of both ends of the C0a and C3 geometries. The photographs are illustrated in the same way as the C2 results and a description of the effects is given below. Initial observations of the flow visualisation indicated no SS separation and no 3D separation feature, unlike previous geometries. Since a key aim of the C3 PEW design was to avoid any separation features, this initial result was encouraging.

Figure 9.11 shows the full span on the suction surface and highlights the differences in the radial extent of the PV at the TE. The feature labelled:

A is the passage vortex lift off line which shows the path of the PV as it develops axially

B shows the maximum extent of the entrained boundary layer fluid, drawn off the endwall by the HSV SS leg.

The radial height r_{TE}, was measured for each of the designs, a comparison was made with the earlier results for C2 and is presented in Figure 9.14. Visually it is clear that both ends of C0a are the same and that the impact of the C3 planar

geometry is to reduce this height, with the additional PEW reducing it further. The values in Figure 9.14 indicate that the C3 planar gives the smallest radial change and that the C3 PEW and C2 Mild have similar reductions in this variable. The HSV is also affected by the C3 geometry and remains nearer to the endwall as it travels along the SS.

The impact of the reverse compound lean on the aerofoil flow visualisation, is the clear radial inward movement of the streaks near the SS maximum loading, at the top of the picture in Figure 9.11.

Figure 9.12 shows the endwall suction surface corner and highlights the corner vortex trace as well as the PV migration. The corner vortex trace, marked D for the C0a, is not visible for C3 with PEWs. The existence and position of the corner vortex trace does not appear to alter between the C0a and C3 Planar geometries.

Figure 9.13 shows the early platform features including; the attachment of PV to the SS and any potential separations at the point of peak loading. The axial distance, from the endwall platform leading edge, to the point of PV SS migration, is indicated by x_{SS-A} and is compared in Figure 9.14. The behaviour of the geometries with respect to the axial distance is less obvious. Here the C2 Mild has the largest distance and therefore greatest delay, C3 PEW has a shorter distance than C0a indicating an earlier SS attachment. C2 Aggr has the shortest axial distance, linked to the separation observed here.

In general the C3 PEW has brought forward the SS migration of secondary flows. There appears to be a strong radial migration of flow, associated with HSV migration. The addition of the PEW on C3, has reduced the radial extent of the PV interaction at the trailing edge, from 56mm to 48mm. The endwall appears to reduce the intensity of PV. There is a large corner vortex/passage vortex detachment line on the planar endwall, which runs from 50% C_{ax} to the TE. There is no obvious equivalent line at the PEW.

9.4.2 Traverses - 5 hole probe data

All traverses are taken at 128% C_{ax}, downstream of the trailing edge on a non uniform measurement grid. Contour plots covering more than one pitch of the cascade for the geometries C0a and C3 were taken using a five hole probe.

Figures 9.15 and 9.16 describe the total pressure loss for C0a and C3 respectively, Figures 9.19 and 9.20 the streamwise vorticity, Figures 9.21 and 9.22 the secondary kinetic energy and Figures 9.23 and 9.24 the SKE.H. Secondary velocity vectors are described in Figures 9.17 and 9.18.

The C0a geometry is symmetrical and analysis of only one end will be included. The analysis of the C3 geometry is split between the benefit of the aerofoil modifications (upper endwall) and the additional PEW modifications.

Total pressure loss

The first plot of total pressure loss (Figure 9.15) shows the well known features for this prismatic cascade geometry. The C3 geometry (Figure 9.16) has the characteristically curved wake, following that of both the C1 and C2 geometries. The

reduction in loading at midspan on the C3 blade and resulting reduction in total pressure loss are observed here too.

The radial pressure gradient, induced by the RCL, pushes the PV and other loss cores toward the endwall at both ends of the C3 geometry. There is a difference in magnitude of the cores for either end of C3. The PEW end (0% span) has greater loss in the SSHSV/ShV than the PV core, however at the planar end (100%) the loss is greater in the PV. Overall, the loss peaks are higher at the PEW end.

There are differences between the CV core for the planar and PEW ends; the PEW end has a larger core with greater tangential shift, but both have more shift than C0a, which is a result of the greater overturning on the endwall.

Secondary velocity vectors

The plot in Figure 9.17 shows a typical secondary velocity vector plot for the prismatic geometry, with three distinct vortical features at each end. The vectors plot for C3, in Figure 9.18, highlights the significant effect of the C3 geometry on the vortical structures.

The aerofoil effects, seen in the upper half of the passage, are as follows:

- A significant shift in the PV and SSHSV/ShV structures toward the endwall.
- An increase in overturning at the endwall
- A decrease in the magnitude of the PV and SSHSV/ShV

The additional effects of the PEW are as follows:

- A further significant decrease in the PV strength
- An additional increase in the level of overturning
- No change in the positions of the two features discussed, either radially or tangentially

The CV was not visible at either end, and is most likely swamped by the high level of overturning.

Streamwise vorticity

The streamwise vorticity for C0a is presented in Figure 9.19, the corresponding plot for C3 is presented in Figure 9.20. The vorticity plots indicate both the magnitude and rotation of the vortex structures. The plots reiterate the result of the secondary velocity vectors. However, the vorticity plot is able to resolve the small CV feature close to the endwall.

The C0a result shows the PV to have highest streamwise vorticity. The CV is the next highest and the SSHSV/ShV is smallest. There is also an area of counter clockwise rotation extending between the SSHSV/ShV and CV features - this relates to shed vorticity.

The C3 result shows a marked change in the position of the structures. The aerofoil effects are:

- As noted previously, the PV and SSHSV/ShV are pushed to the endwall, leaving a much greater area of clean 'primary' flow
- The SSHSV/ShV is slightly weaker
- The CV has shifted tangentially and is larger

The PEW effects are:

- A weaker PV
- A significant increase in vorticity near the endwall
- The CV is translated tangentially almost underneath the adjacent PV
- No change in the strength of SSHSV/ShV

Secondary kinetic energy coefficient (C_{SKE})

The secondary kinetic energy coefficient (C_{SKE}) is presented in Figures 9.21 and 9.22 and indicates individual peaks of energy relating to the secondary velocities. The C_{SKE} is sensitive to changes in secondary velocities, as it is based on the square of their components.

The result in Figure 9.21 for C0a has a single feature at each end. This feature corresponds to the interaction of the PV and SSHSV/ShV. The result in Figure 9.22 for C3 again indicates the dramatic effect of the C3 geometry on these flows.

The changes due to the aerofoil are as follows:

- An increase in the level of C_{SKE} close to the endwall, due to the higher overturning
- A reduction and radial shift of the main feature

The changes due to the application of PEWs are:

- A further reduction of the main feature to almost zero magnitude
- A further increase of the endwall overturning feature

Secondary kinetic energy and Helicity (SKE.H)

The SKE.H plots resemble the vorticity more than C_{SKE}. The SKE.H plot for C0a is presented in Figure 9.23, it picks up individual features and PV, CV, SSHSV/ShV are clearly defined. The SKE.H plot for C3 is presented in Figure 9.24.

The effects due to aerofoil changes are:

- A significant drop in SKE.H of the PV
- No change in SSHSV/ShV
- A radial shift of both features

The effects due to the additional PEW are:

- A further reduction in the PV feature
- A clear increase in the CV

9.4.3 Pitchwise averaged results

Pitch averaged total pressure loss

Figure 9.25 shows the pitchwise averaged total pressure loss coefficient for the three geometries:

- C0a - prismatic
- C3 - latest passage shaped geometry
- C2 - previously designed passage shaped geometry

As was seen with all reverse compound lean based geometries, the midspan loss reduces and the region of primary flow expands radially. For the C3 geometry the planar endwall (at 100% span) has a lower loss peak than the profiled endwall. The magnitude of the total pressure loss between the passage vortex core and the endwall is also lower for the planar endwall. The symmetry of the flows and the loss magnitudes of the C0a geometry, indicate that this is not related to poor inlet conditions and is a genuine geometrical effect.

The mass averaged data, covered in a later section, aims to resolve the quantitative difference of the two endwalls. The pitchwise averaged plot also contains the data for the C2 geometry. The two results are similar overall with differences at either end that relate to the endwall design.

- At the upper endwall (100% span) the C3 has a planar shape and C2 has the more aggressive PEW shape with known separation feature. The planar geometry appears to have lower loss than the C2 PEW shape, which most likely relates to the separation.
- At the lower endwall (0% span) both the C3 and C2 geometries have a profiled endwall. Interestingly, the latest PEW shape has higher peak loss than the earlier C2 shape. The latest design has a more restrictive optimisation criteria, including a limit on the maximum perturbation size, which limits the potential benefit.
- The radial location of the loss cores for the C2 upper (aggressive) PEW is further in toward the endwall than the planar (C3) geometry at the same location. This radial shift is similar for both C2 lower (less aggressive) and C3 PEW at the lower endwall and indicates that the PEW is the cause of this additional shift.
- The application of the PEW can be seen to increase the loss in the region between the PV and endwall for all three PEW shapes.
- The level of profile loss (indicated by the C_{p0} magnitude at midspan) is identical for C3 and the earlier C2 design.

Pitchwise averaged yaw angle

The pitchwise averaged yaw angle at 128% C_{ax} is presented in Figure 9.26. Here the same three geometries are compared at the same axial traverse plane. As predicted and seen previously with the C1 geometry, the yaw angle at midspan is reduced for C3 relative to the prismatic C0a case. This difference in yaw angle was discussed in Chapter 6 as an effect of the downstream redistribution of massflow.

At the planar endwall (100% span) both the under and over turning, associated with the passage vortex, have been reduced by the altered aerofoil shape. The overturning at the wall has however increased slightly, compared to C0a (C2 is higher still).

At the PEW (0% span) the under and over turning associated with the PV have been further reduced by the application of the PEW shape. The peak underturning at this end is within 1^o of the midspan yaw, this compares with $3-4^o$ for the planar end and 7^o for the C0a geometry. This additional fall in the underturning angle is wholly attributable to the application of the PEW, and the effect was previously noted for the both the upper and lower C2 endwalls.

The near wall overturning is further increased by the PEW on C3. Comparing with C2, the midspan turning is almost exactly the same. The radial migration of the vortical structures appears to vary depending on the benefit created by the PEW.

Pitchwise averaged C_{SKE}

The pitchwise averaged secondary kinetic energy, C_{SKE}, is presented in Figure 9.27. The C_{SKE} is a measure of the energy and not directly related to individual vortical structures. The typical (C0a) plot contains a large peak relating to the interaction of the PV and SSHSV/ShV. There are also high magnitudes associated with the endwall overturning, but these are small in the C0a plot. The classical definition of C_{SKE}, is such that deviation from the midspan yaw will give C_{SKE} magnitudes, i.e. a radial velocity component is not required to generate C_{SKE}. Therefore the overturning at the endwall is picked up.

The upper (planar) endwall of C3 indicates a reduction in C_{SKE} that relates to the aerofoil component. The peak C_{SKE} relating to PV and SSHSV/ShV interaction is reduced by around 60%. The peak is also radially shifted toward the endwall (by 2% span) as seen in the loss and yaw results previously. However, the peak associated with endwall overturning increases.

The lower endwall of C3 indicates the additional reduction relating to the PEW component. Now the peak is reduced overall by 90% and moved further radially inward (by 6% span). The two endwall designs of C2 exhibit similar behaviour, to a lesser extent.

Pitchwise averaged SKE.H

The pitchwise averaged SKE.H, is presented in Figure 9.28. The SKE.H indicates a reduction in line with that seen in the C_{SKE} and secondary velocity vector plots.

The aerofoil effect is seen as:

187 - 365 mm	C0a	C3	C3CFD
Loss	100%	91.5%	95.1%
C_{SKE}	100%	74.3%	87.3%
SKE.H	100%	49.9%	41.8%
Exit Yaw	-69.2(68.1)	-69.6	(67.3)

Table 9.3: Key parameters - Planar

10 - 187 mm	C0a	C3	C3CFD
Loss	100%	91.1%	97.8%
C_{SKE}	100%	43.1%	73.8%
SKE.H	100%	34.1%	29.5%
Exit Yaw	-69.0(68.1)	-69.5	(67.3)

Table 9.4: Key parameters - PEW

- A 50% reduction in the peak SKE.H
- A small radial shift of the peak

The effects due to the additional PEW are:

- A reduction in the peak values on top of the aerofoil effect
- A large radial shift of the peaks

The SKE.H shows an asymmetry in the peak magnitudes for the C0a result. This asymmetry was not observed in the C_{SKE} peaks. This may be the sensitivity of the helicity to the differentiation on the relatively coarse measurement grid. The vorticity and hence helicity is derived from the differentiation of the velocity.

9.4.4 Mass averaged results

Tables 9.3 and 9.4 include the area averaged results, comparing the C0a and C3 geometries at 128% C_{ax}. The results are presented as percentage reductions, relative to the base geometry C0a. The results are split into planar (aerofoil effects) and PEW (additional endwall profiling effects). The area averaged computational results are also presented. The values in parentheses are the CFD yaw angles.

Loss

The net reduction in loss for the entire passage is 9%. This reduction compares unfavourably with the 14% reduction for the RCL geometry C1 and 11-15% reduction for the C2 endwalls. The profiled endwall reduces the loss by half a percentage point over the planar endwall.

The computational results do not predict the same level of loss reduction, due to the specification of fully turbulent boundary layers.

Turning

As the geometry has a fixed inlet angle, the exit yaw angle indicates the level of turning in the cascade. The mass averaged data indicates a 0.4^o - 0.5^o increase in turning for the C3 geometry. The C2 geometry indicated a 0.6^o increase in the overall turning. The C1 geometry indicated a 0.4^o decrease in the overall turning.

The computational results are offset from the experimental values by around 0.9^o, this offset was described in the computational results of C1. The computational results indicate a 0.4^o decrease in yaw for C3 at both ends. This contrasts the increase seen experimentally and can be explained by the poor resolution of the secondary flows computationally.

Secondary flows

The aerofoil geometry (planar endwall) reduces C_{SKE} by 26%, the PEW addition increases this to 57%. The computational C_{SKE} reductions are much less significant than the experimental reductions. Whilst the computations predict a reduction the scale of the effect of the PEW is not seen.

The SKE.H reduction for the aerofoil alone is 50%, the PEW further reduces the SKE.H magnitude, with an overall reduction of 66%. The computational SKE.H values appear to follow the same trend as the experimental values, but tend to overpredict the actual gain. C2 results gave the less aggressive profiled endwall a 57% reduction and the separating (aggressive) endwall design a 56% reduction.

9.5 Computational Results

The following describes the behaviour of the computational results for both the C0a and the C3 geometries on the experimental measurement grid at 128% C_{ax}.

The results presented here include contour and velocity vector plots of the C0a and C3 geometries, using the same contour scales and ranges. The results were extracted for the same experimental measurement grid, as described in Chapter 4.

9.5.1 Total Pressure Loss

The loss contour plots for C0a and C3 are presented in Figures 9.29 and 9.30. The plots both indicate the typical over prediction of profile loss due to the boundary layer specification. Unlike the experimental result, there are no separate loss peaks for the PV and SSHSV/ShV features. The general shape of the loss peaks is the same, but the peak value is more closely aligned with the blade wake and the SSHSV/ShV region. This contrasts with the experimental result, where the peak loss is aligned with the PV feature. The CV loss is seen to be translated further tangentially in the computational result, but is of similar magnitude to the experiment.

The level of profile loss reduction between the C0a and C3 geometries appears, from the contour plots, to be less significant than the experimental.

9.5.2 Secondary Velocity Vectors

The secondary velocity vectors in Figures 9.31 and 9.32 show the significant under prediction of both the passage vortex feature and the endwall overturning. For both geometries, the PV appears to be tangentially aligned with the experimental result. The differing PV sizes between the planar and PEW ends are not well resolved in the secondary velocity vectors.

9.5.3 Streamwise Vorticity

The streamwise vorticity plots, in Figures 9.33 and 9.34, indicate the same behaviour as the experimental results, with discrete regions associated with the PV and SSHSV/ShV. The computational results differ in the lack of resolution of the CV feature, possibly because it is only partially observed in the measurement region.

The C3 PEW restricts the radial extent and magnitude of the PV and SSHSV features. The reduction of the vorticity in the SSHSV feature is counter to the experimental result, where a slight increase may be observed.

9.5.4 C_{SKE}

The secondary kinetic energy plots for C0a and C3 are presented in Figures 9.35 and 9.36. The plots highlight the energy in the secondary flows, but also the energy in the endwall overturning.

For C0a the CFD result indicates a higher energy near the endwall than the experiment. This ties in with the secondary velocity vectors, which show high velocities associated with the PV in this region.

For C3 a similar high energy region is observed at the endwall, here it is related to the overturned endwall boundary layer and is similar in shape to the experimental result.

A reduction in energy associated with the PV can be seen for C3 planar. A further reduction for the C3 PEW can be observed, however the contour range does not enable the magnitudes to be ascertained.

9.5.5 SKE.H

The SKEH results are contained within Figures 9.37 and 9.38. The corner vortex is again not resolved in the SKE.H result. The size and location of the PV and SSHSV/ShV features are similar to the experiment, but the magnitude of the PV is underpredicted. The C3 result shows two remaining regions that relate to the SSHSV/ShV feature. There is no evidence of the PV feature in the SKE.H contour plot.

9.5.6 Pitchwise averaged

The pitchwise averaged results summarise the differences described in the contour and vector plots. The loss prediction, in Figure 9.39, is seen to be poor, with a uniform over prediction of the profile loss. The overproduction of loss leads to a

reduced secondary flow intensity (Figure 9.40). The peak and endwall loss values and location match the experiment. The blockage associated with the higher profile loss results in reduced midspan turning for both C0a and C3 cases. The mixed out state of the secondary flows is evident in the magnitudes of over and under turning of the PV feature.

Figure 9.40 shows the pitchwise averaged yaw angle. The midspan yaw angle of C0a is well matched, as is the yaw angle in the endwall overturned region. The computational SKE.H results, shown in Figure 9.41, behave similarly to the experiment, but with considerably reduced magnitude.

9.6 Conclusions

A second generation of passage shaped geometry has been designed, built and tested. The design used the same aerofoil geometry as the earlier passage shaped design. The design has one planar endwall and one profiled endwall.

Oil and dye surface flow visualisation of the design, has highlighted a constrained radial extent of vortical structures. Additionally, some features no longer appear to interact with the wetted surfaces. Importantly, the flow visualisation does not indicate any boundary layer separation, either on the suction surface or as a 3D feature on the endwall.

Pneumatic probe measurements have been taken at the standard analysis plane, 128% C_{ax}, using a five hole probe. The results presented analyse the behaviour of the latest design, by splitting the effects into those associated with the aerofoil and those relating to the PEW geometry.

The aerofoil effects are:

- A reduced profile loss and a radial shift of and slight increase in PV loss core, both resulting in a 9% reduction in C_{p0}
- A 1^o reduction in the midspan yaw angle, combined with a 2^o reduction in the underturning peak and a 3^o increase in the overturning at the endwall. The overall yaw angle is 0.4^o greater
- A significant drop in the coefficients SKE.H and C_{SKE}, indicating a reduction in the strength of the secondary flows and the energy of their interaction

The PEW effects are:

- An increase in the peak loss of the passage vortex, combined with a further significant radial shift of the peak.
- An additional increase of loss in the region between the PV and the endwall.
- No additional loss benefit in the application of the PEW in this case at 128% C_{ax}
- A further reduction in the underturning, bringing the peak within 1^o of the midspan value. A 3^o increase in the overturning at the endwall giving a further 0.1^o to the overall yaw angle

- A further drop in the SKE.H and C_{SKE} coefficients, bringing the C_{SKE} peak to 1/10th its original size

The results show that the PEWs do not significantly effect the loss at this axial location. The PEWs work by reducing the level of secondary flows. This is seen in the pitchwise averaged yaw angle, C_{SKE} and SKE.H results.

The computational results indicate the same trends as the experiment, with similar changes in midspan turning and similar overturning at the endwall. The computational model does not predict the secondary flow strength well, seen in the underprediction of PV over and under turning. The midspan loss prediction is also too high, resulting in an underpredicted change in loss for the offloading effect of the lean.

9.7 Figures

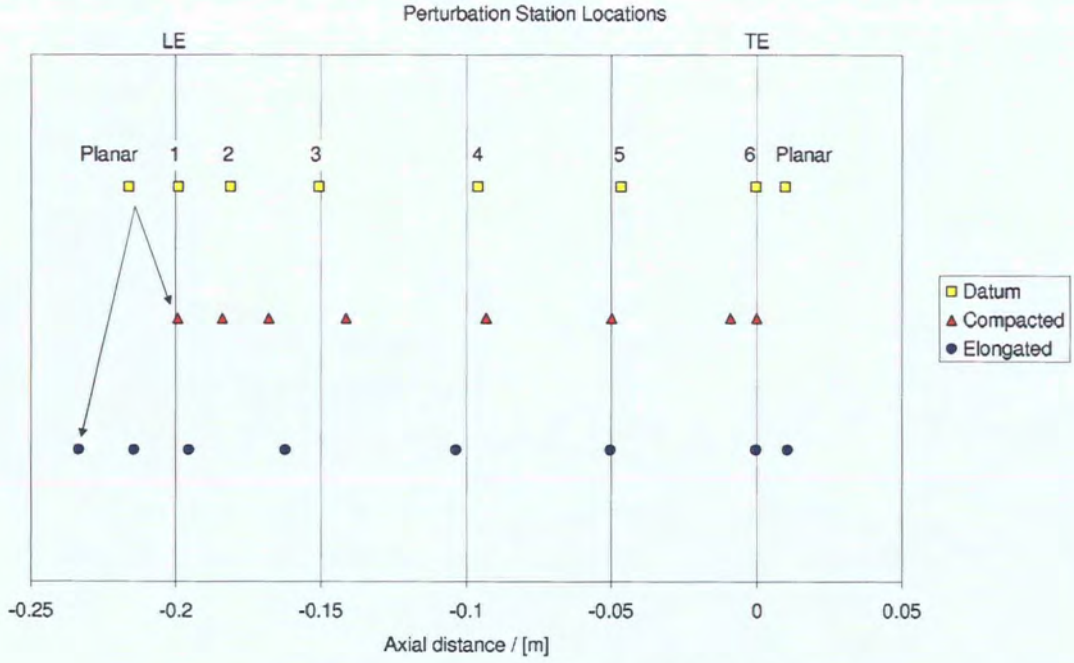

Figure 9.1: PEW Station Locations

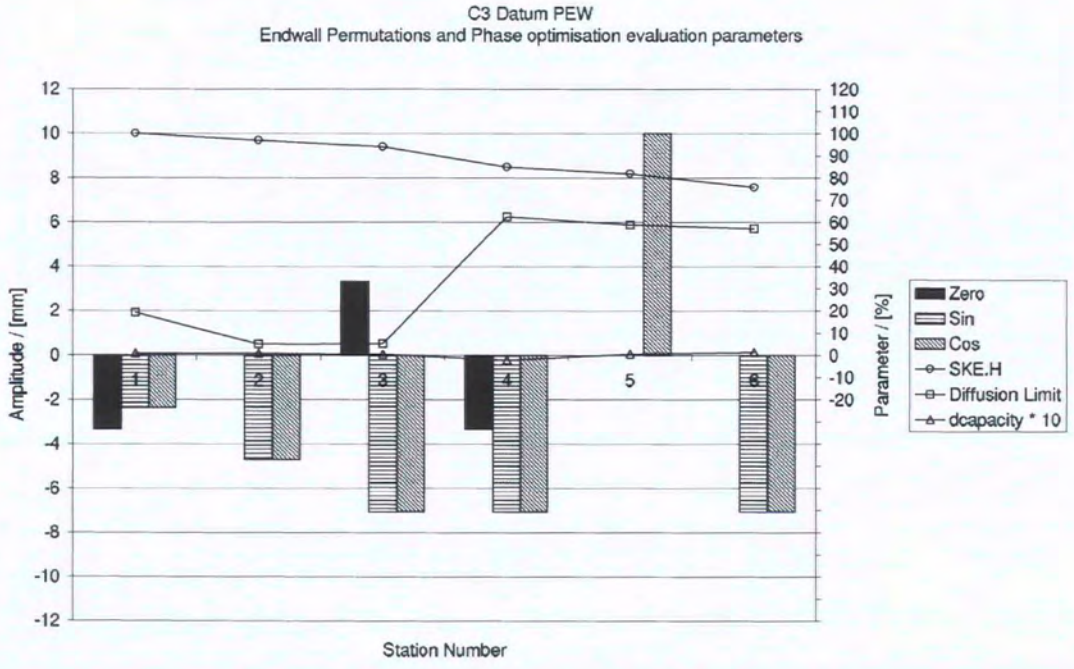

Figure 9.2: Optimiser Summary Chart - Datum

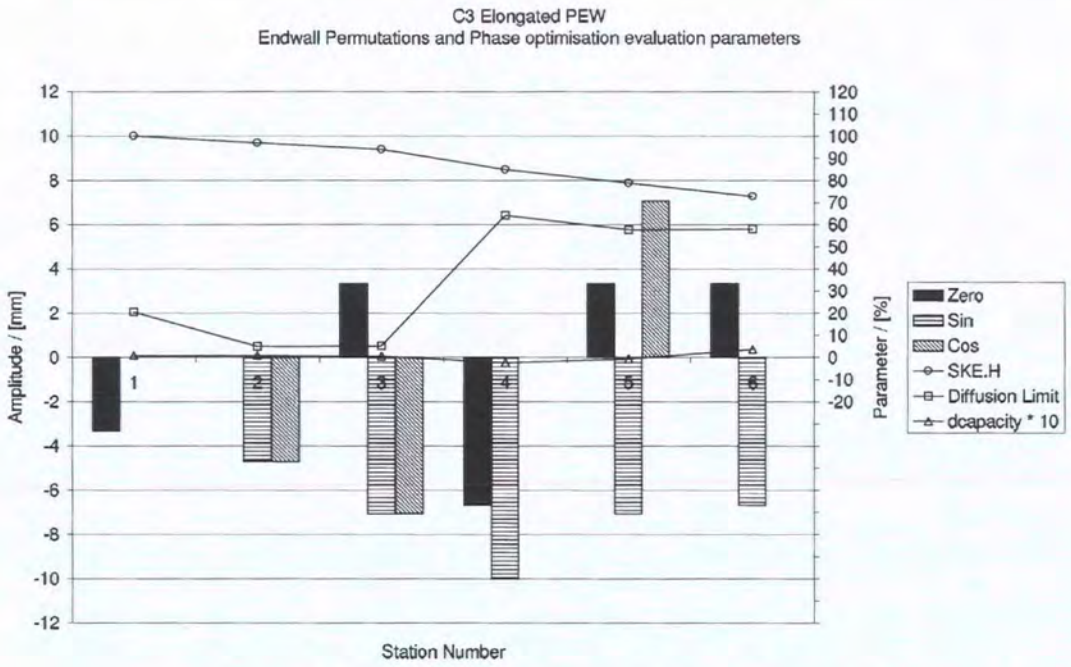

Figure 9.3: Optimiser Summary Chart - Elongated

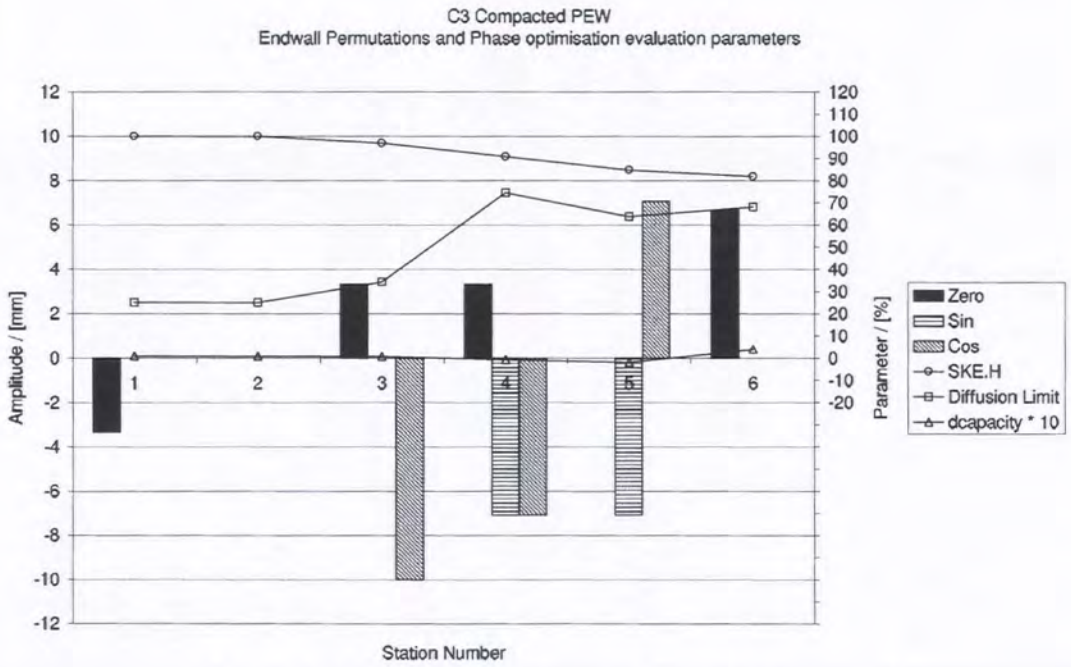

Figure 9.4: Optimiser Summary Chart - Compacted

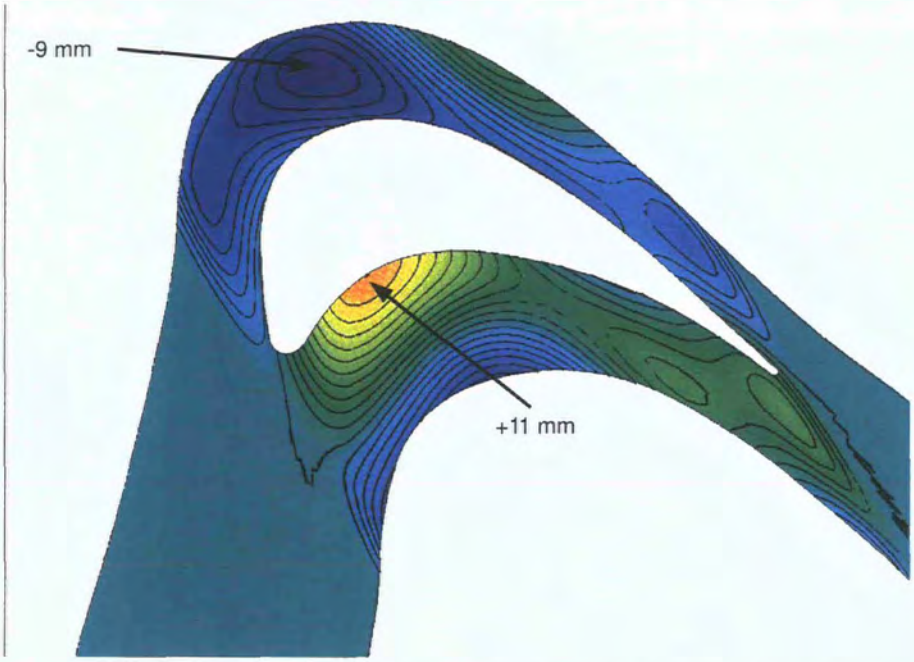

Figure 9.5: Endwall Height Contours - C3 Datum

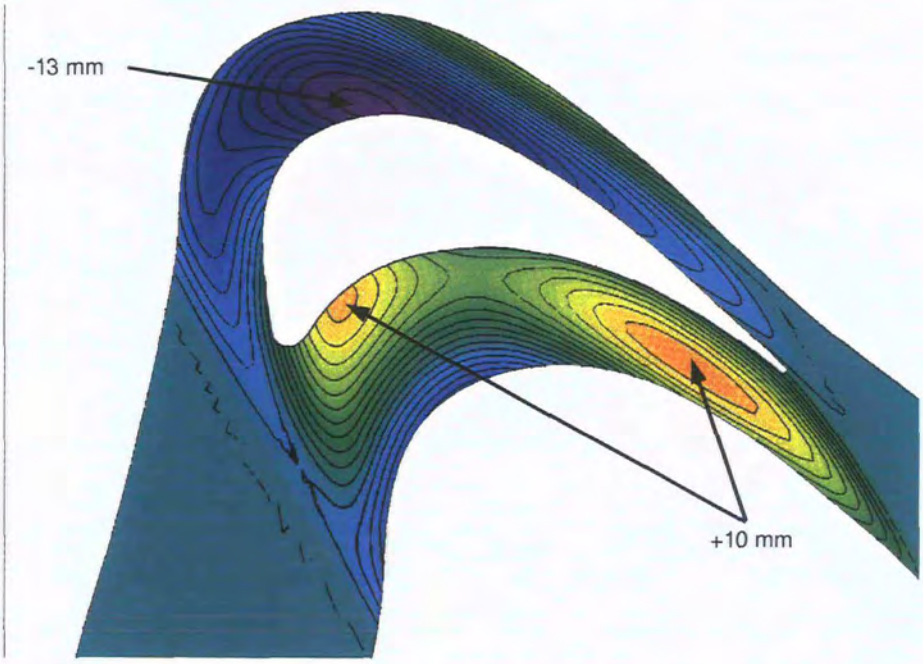

Figure 9.6: Endwall Height Contours - C3 Elongated

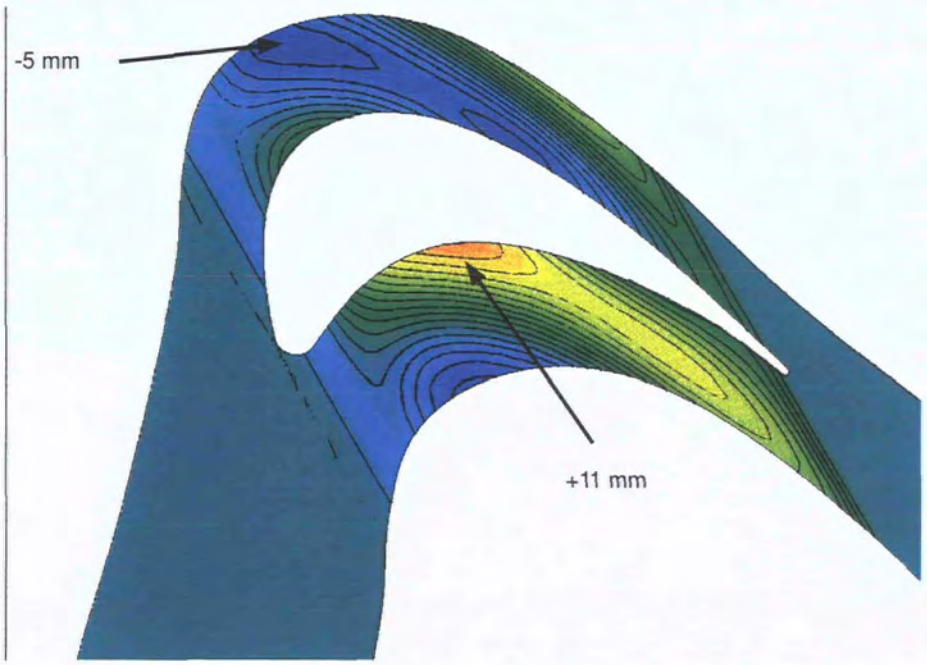

Figure 9.7: Endwall Height Contours - C3 Compacted

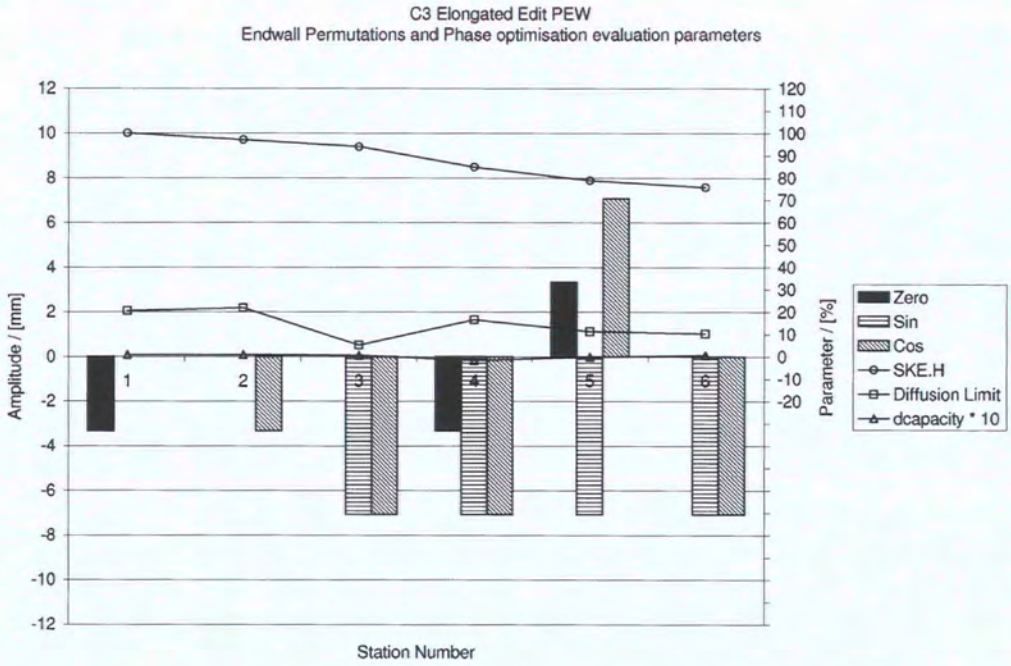

Figure 9.8: Optimiser Summary Chart - Elongated Edit

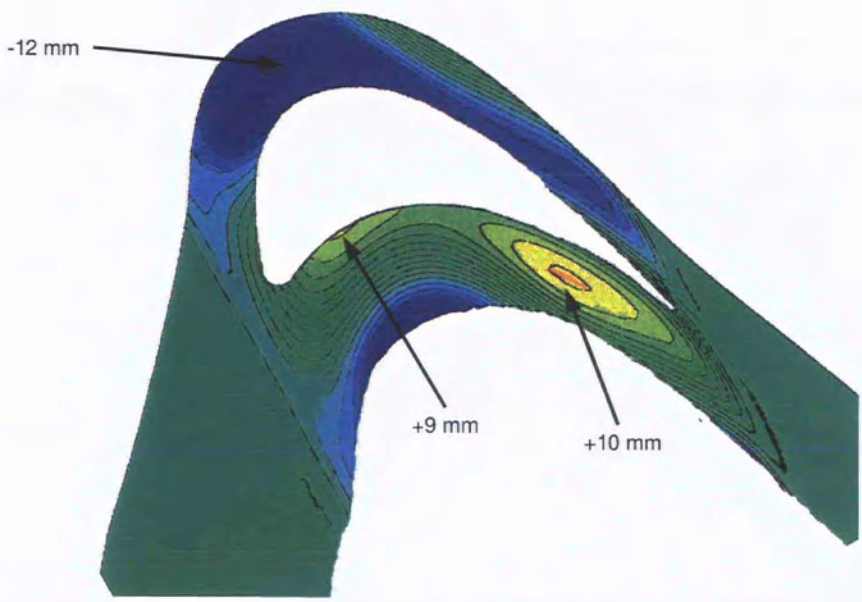

Figure 9.9: Endwall Height Contours - C3 Elongated Edit

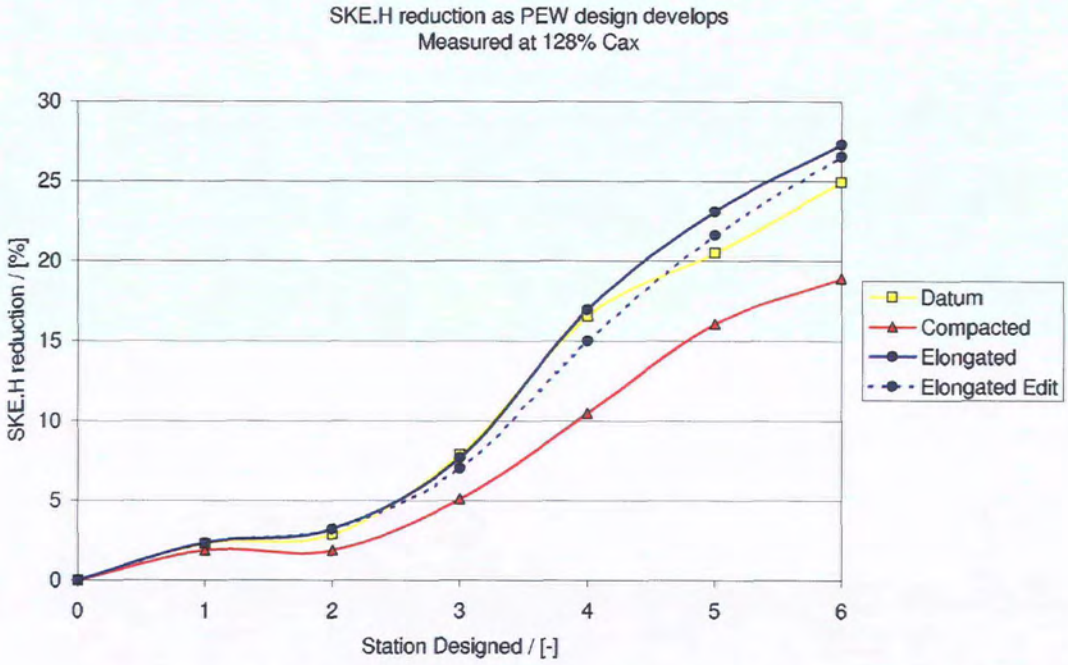

Figure 9.10: Optimisation Parameter SKE.H - C3 Endwall Designs

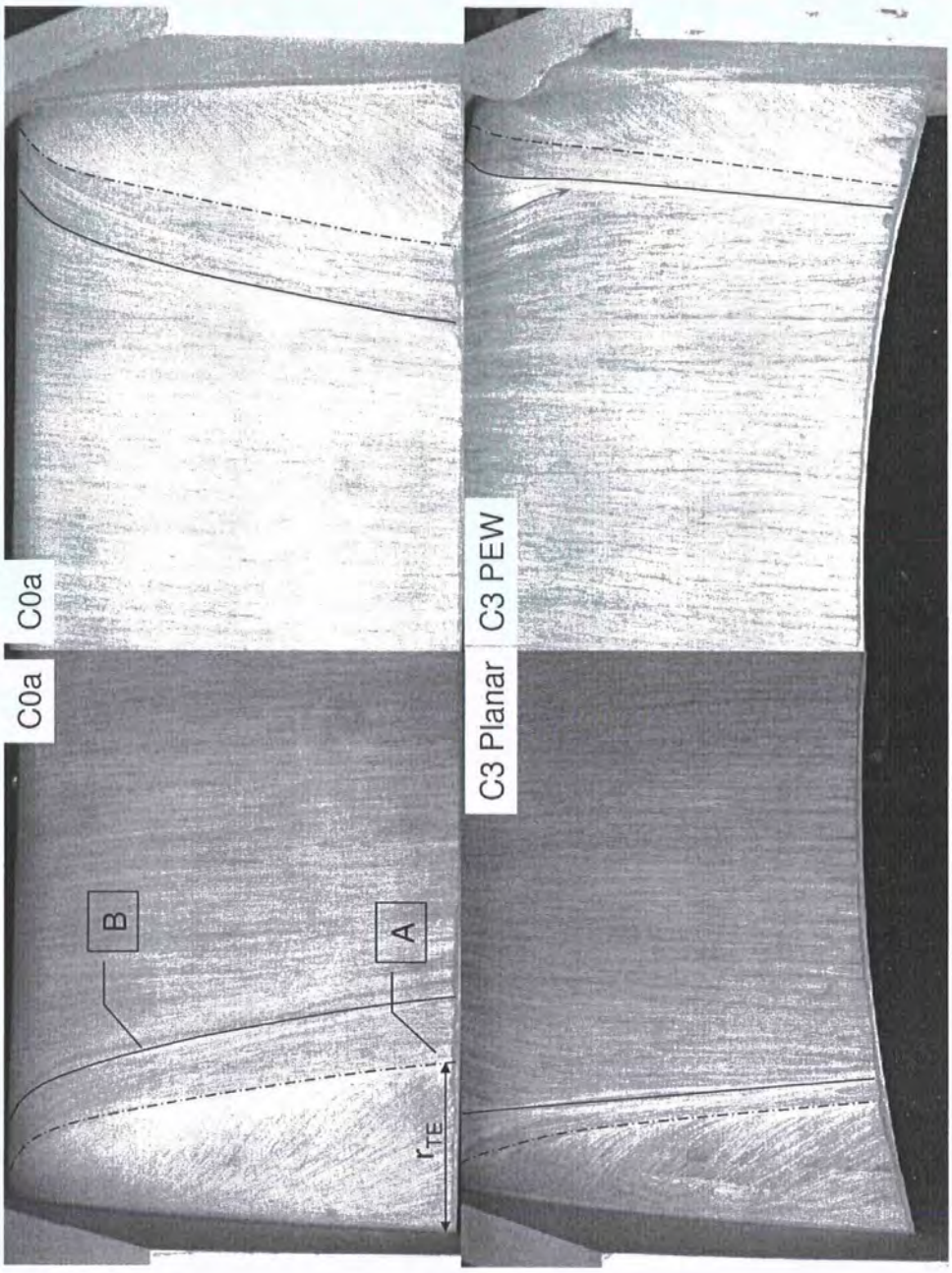

Figure 9.11: Flow Visualisation - C0a C3

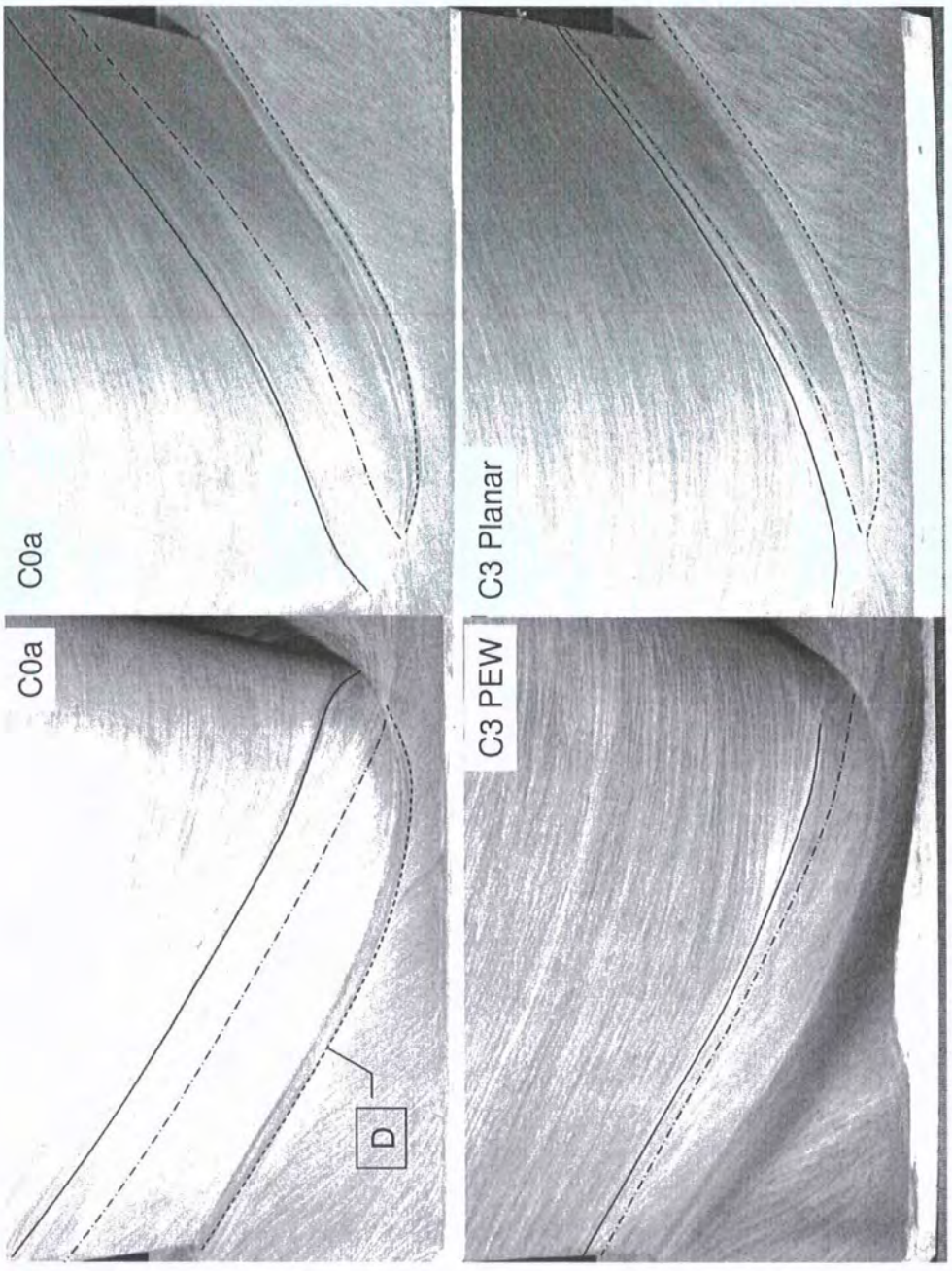

Figure 9.12: Flow Visualisation - C0a C3

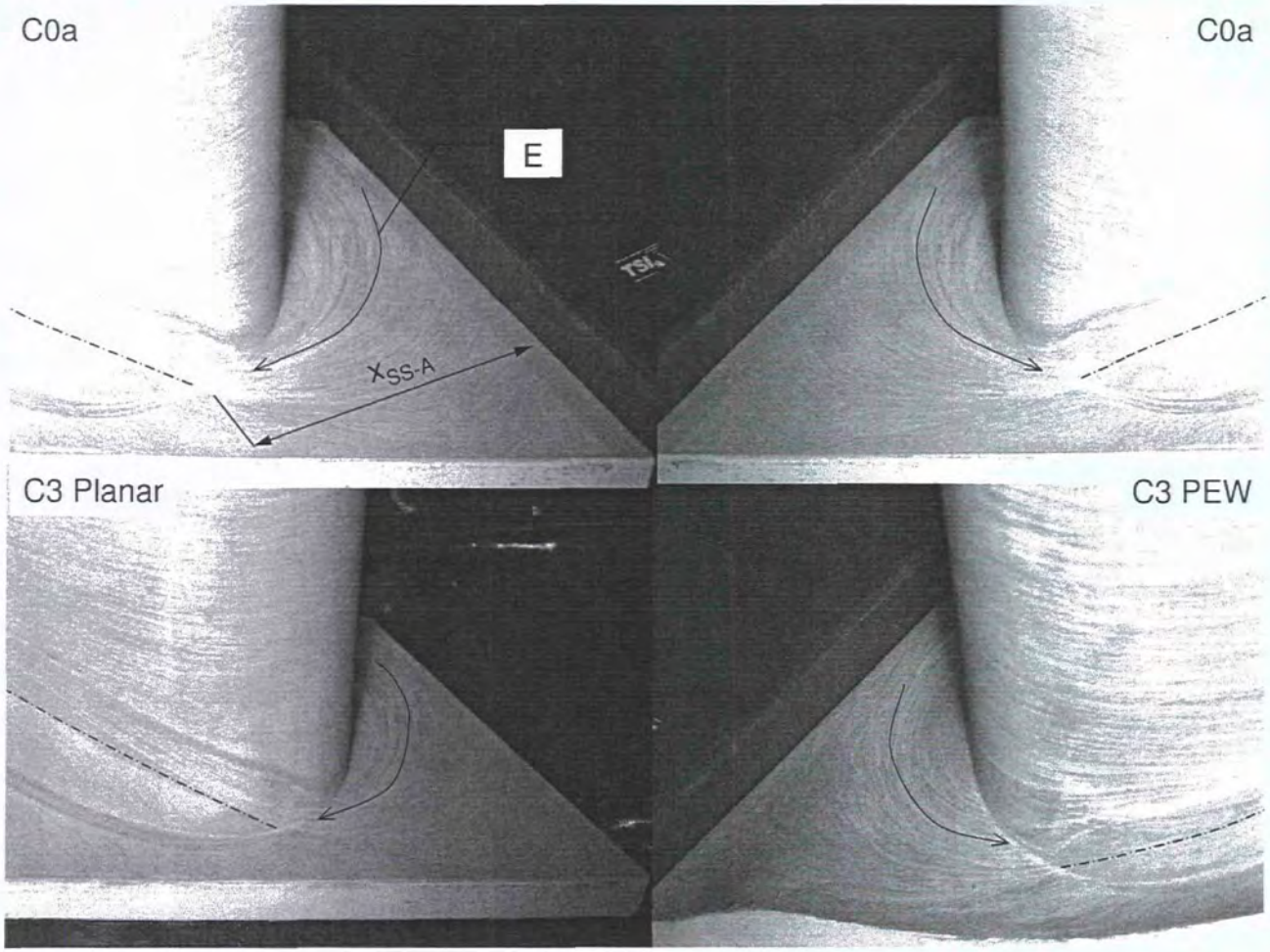

Figure 9.13: Flow Visualisation - C0a C3

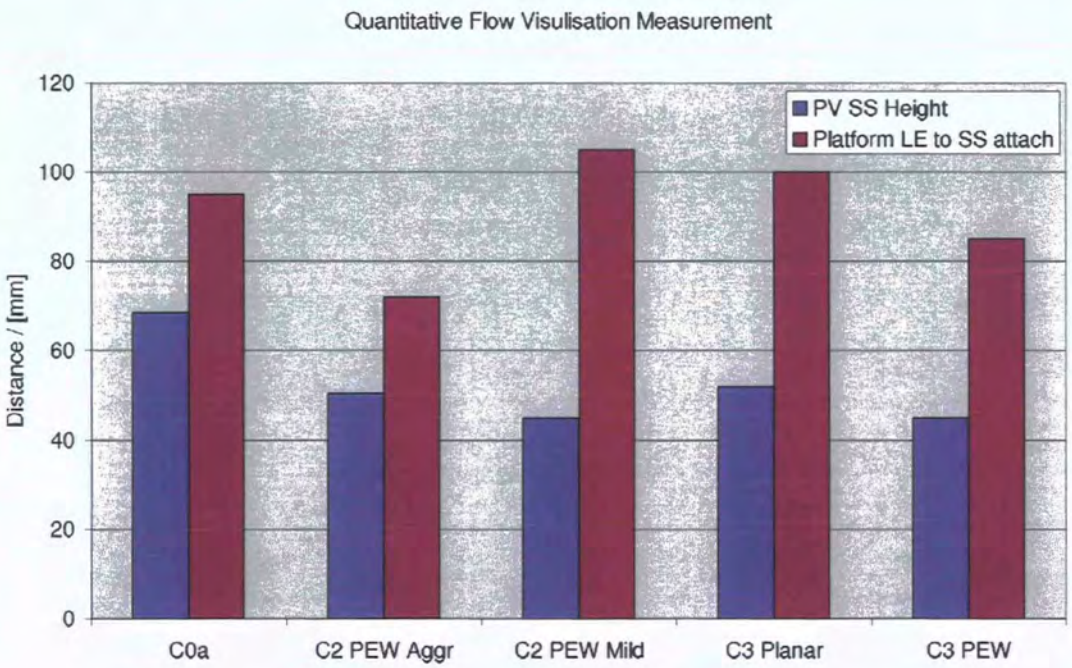

Figure 9.14: Flow Visualisation Quantitative Measurement - C0a C3

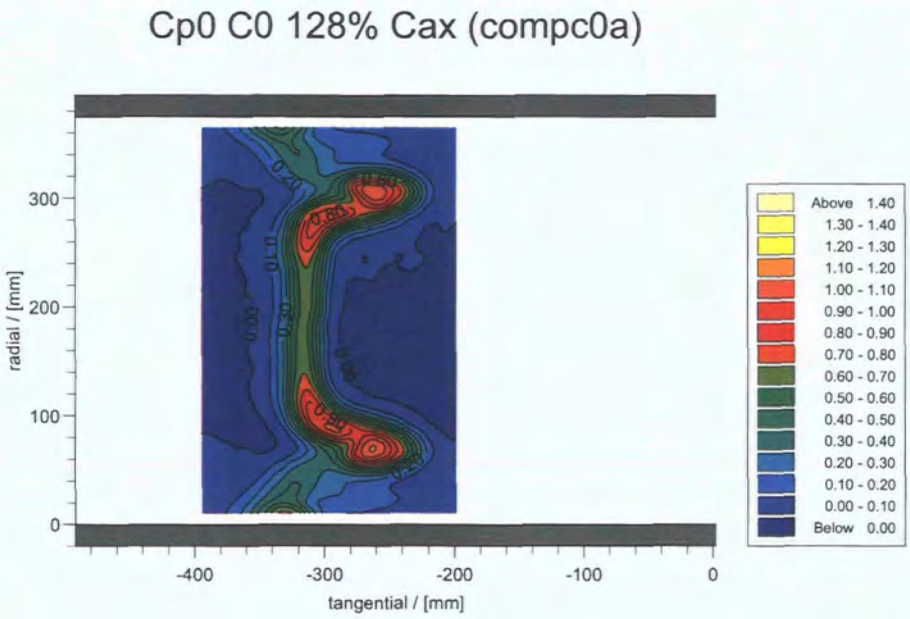

Figure 9.15: Expt Loss C0a at 128% C_{ax}

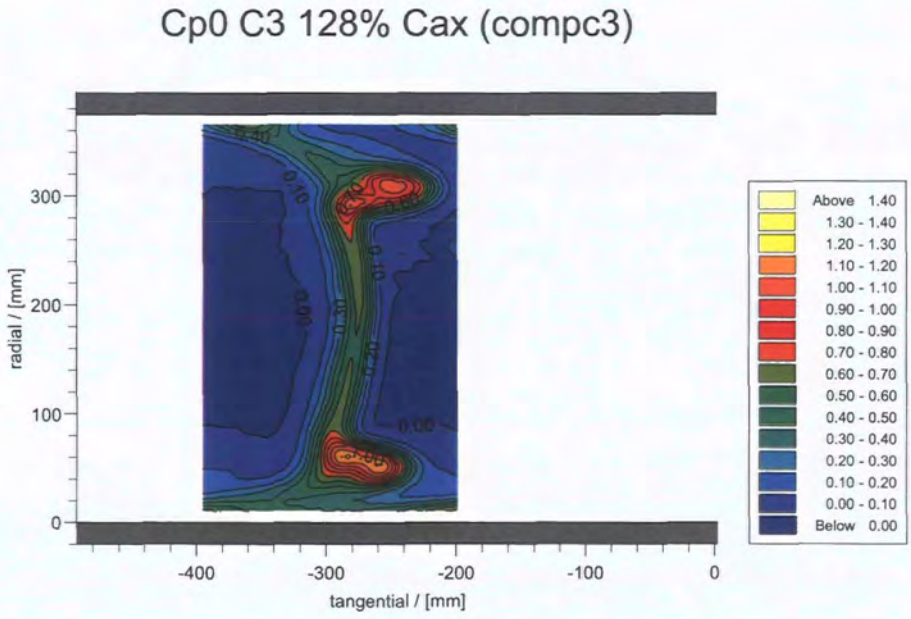

Figure 9.16: Expt Loss C3 at 128% C_{ax}

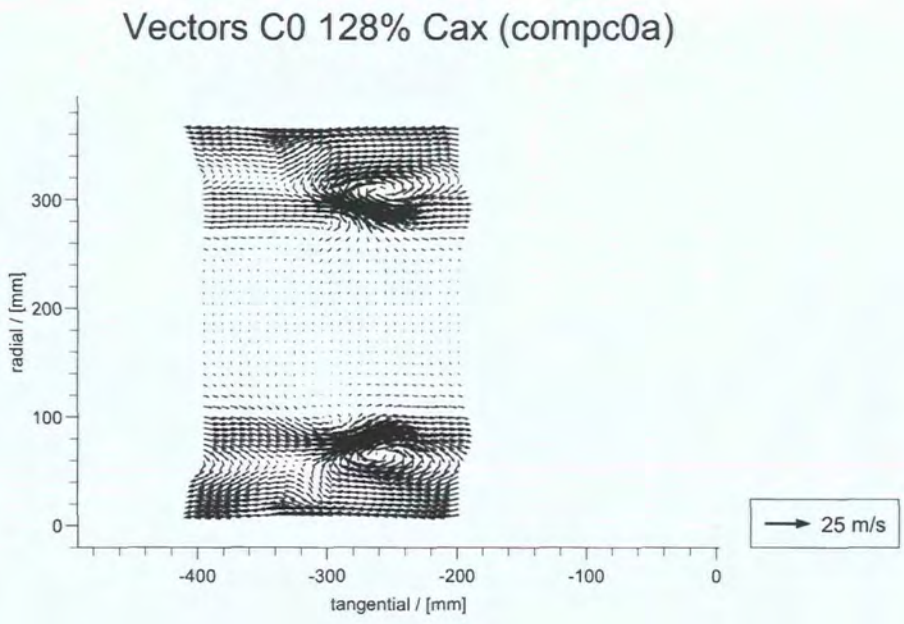

Figure 9.17: Expt Secondary Velocity Vectors C0a at 128% C_{ax}

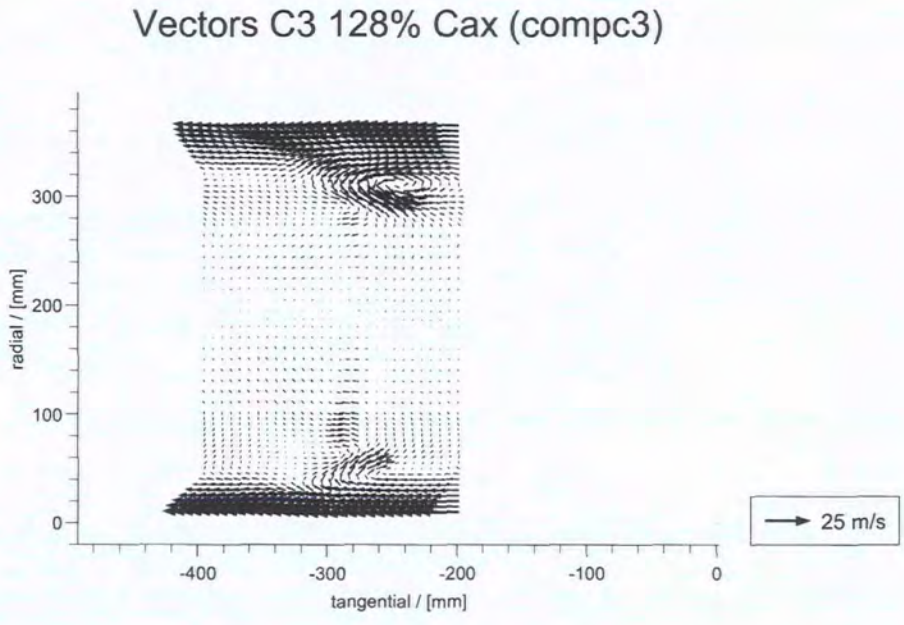

Figure 9.18: Expt Secondary Velocity Vectors C3 at 128% C_{ax}

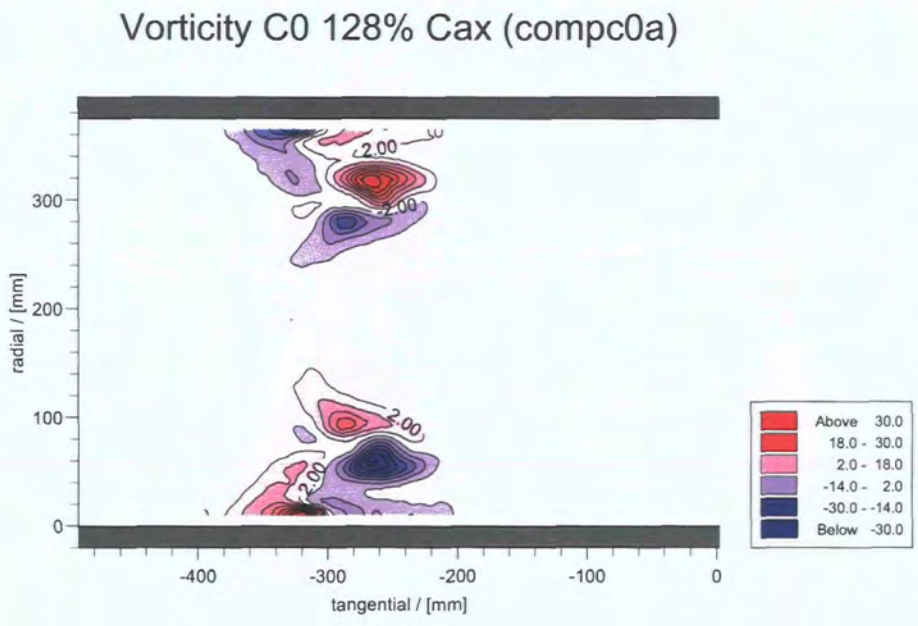

Figure 9.19: Expt Vorticity C0a at 128% C_{ax}

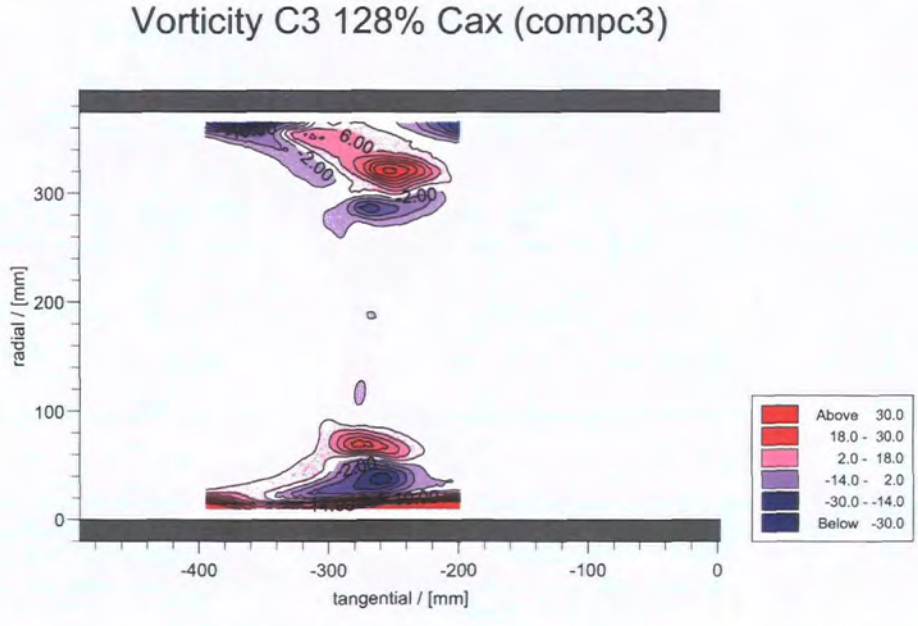

Figure 9.20: Expt Vorticity C3 at 128% C_{ax}

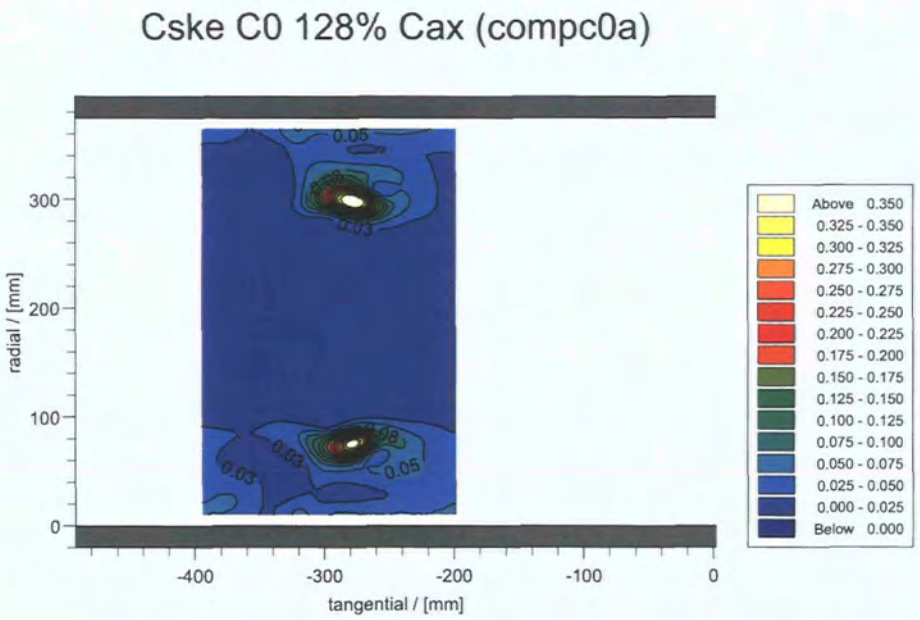

Figure 9.21: Expt C_{SKE} C0a at 128% C_{ax}

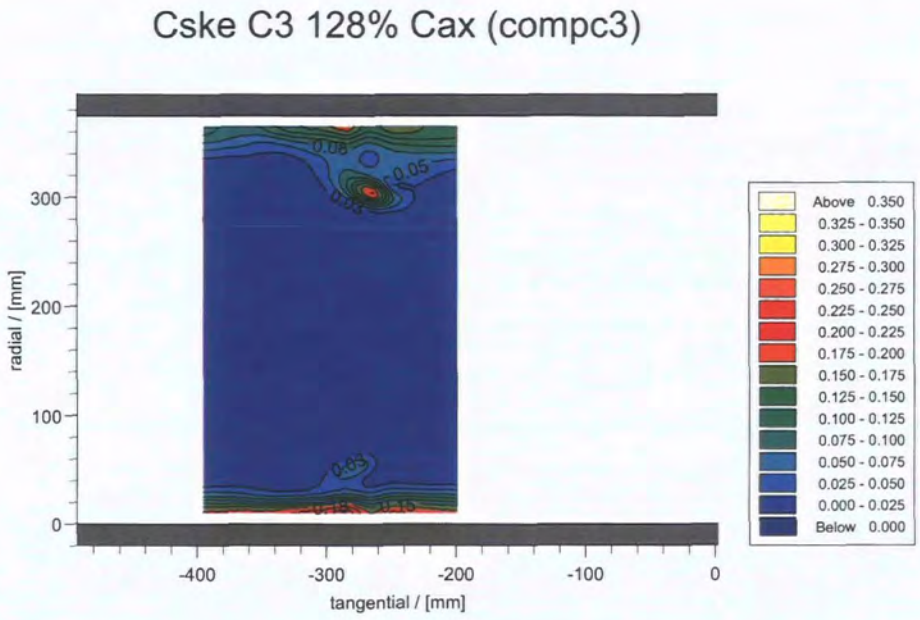

Figure 9.22: Expt C_{SKE} C3 at 128% C_{ax}

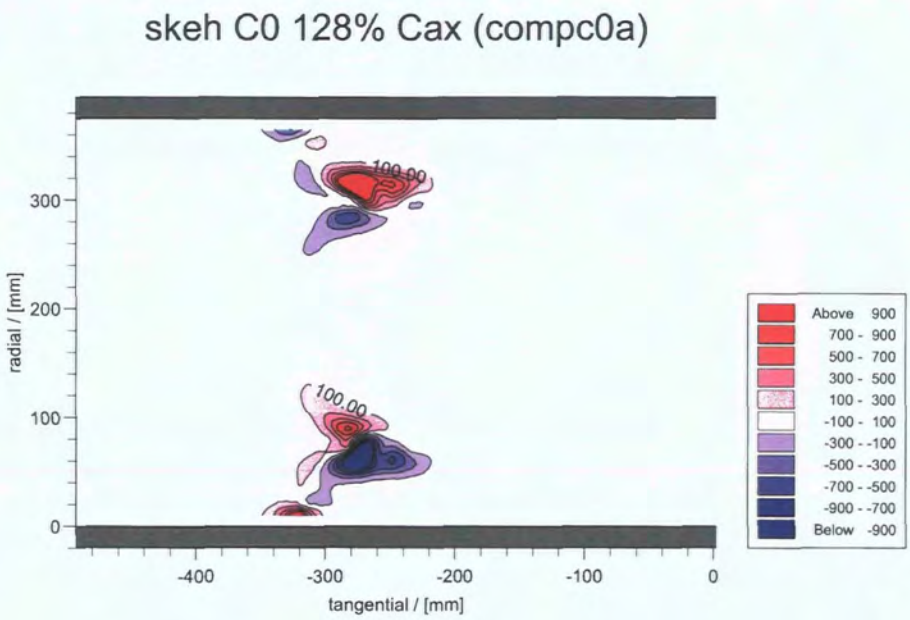

Figure 9.23: Expt SKE.H C0a at 128% C_{ax}

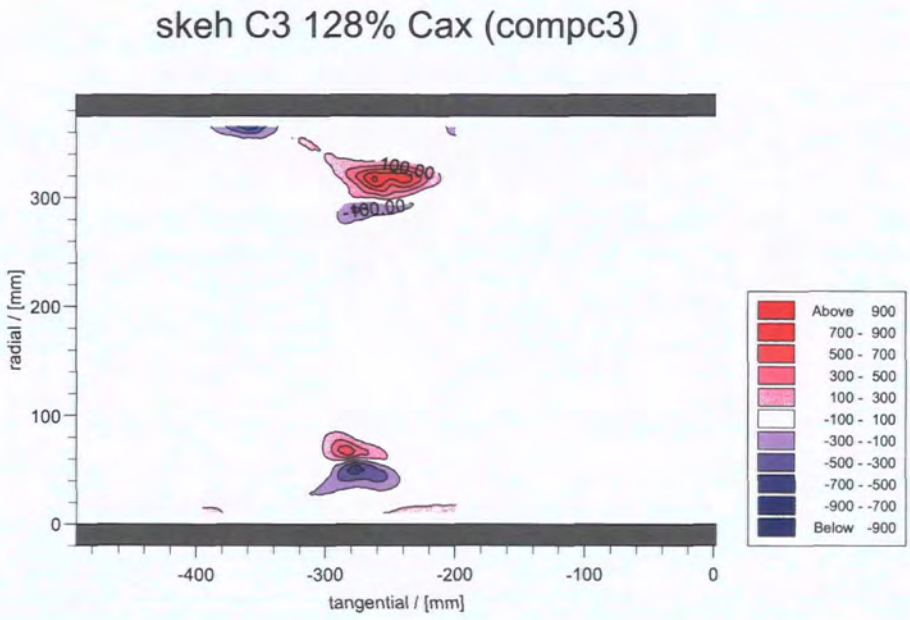

Figure 9.24: Expt SKE.H C3 at 128% C_{ax}

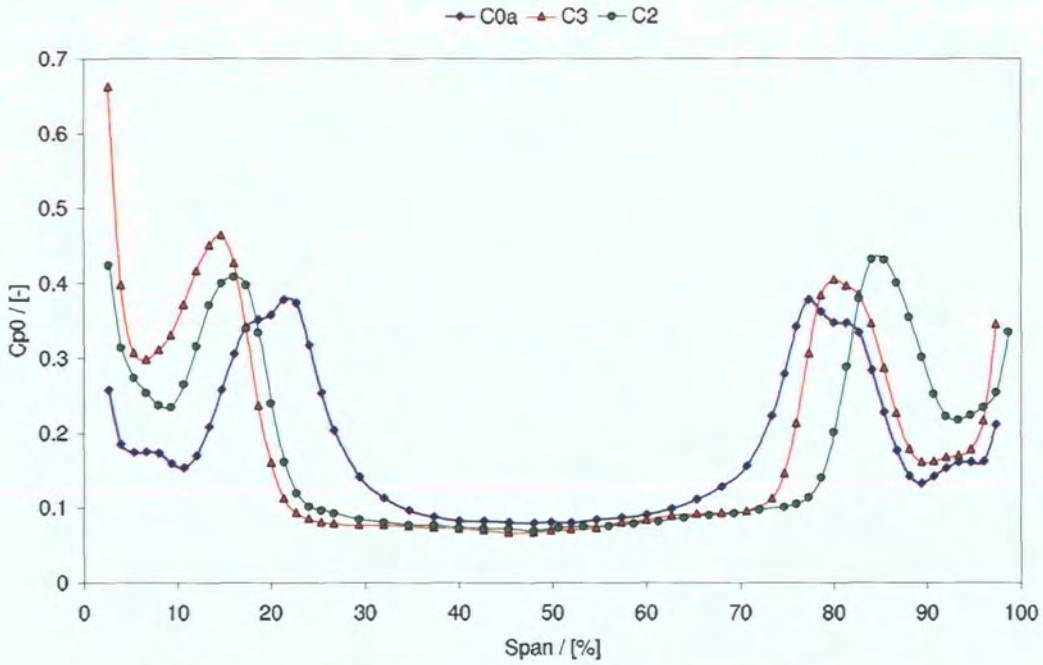

Figure 9.25: Pitchwise averaged Total Pressure Loss - C0a C3

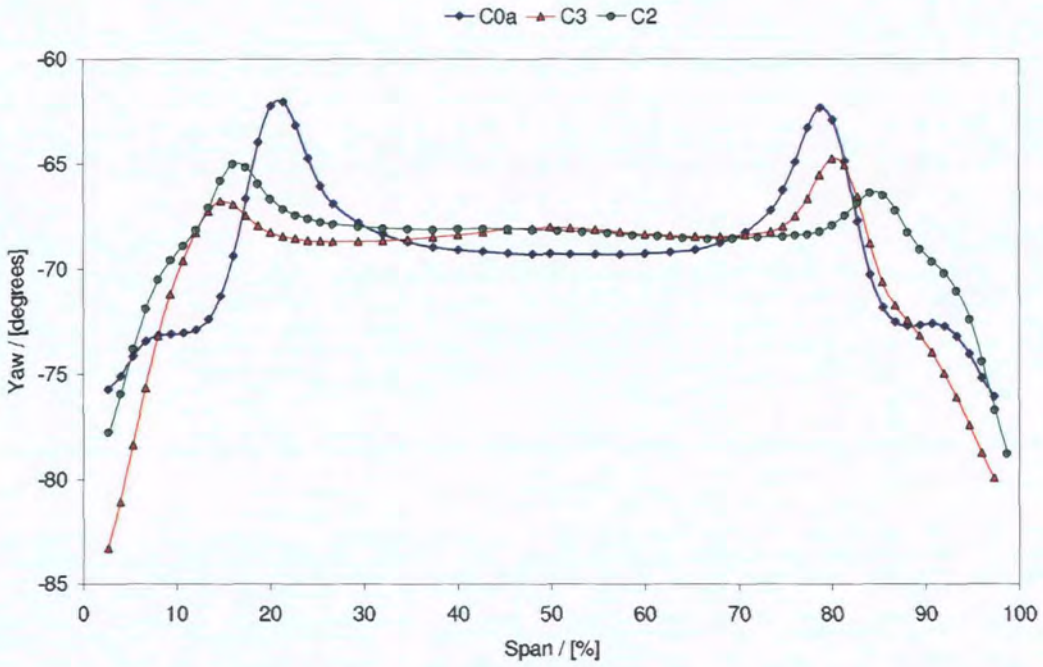

Figure 9.26: Pitchwise averaged Yaw - C0a C3

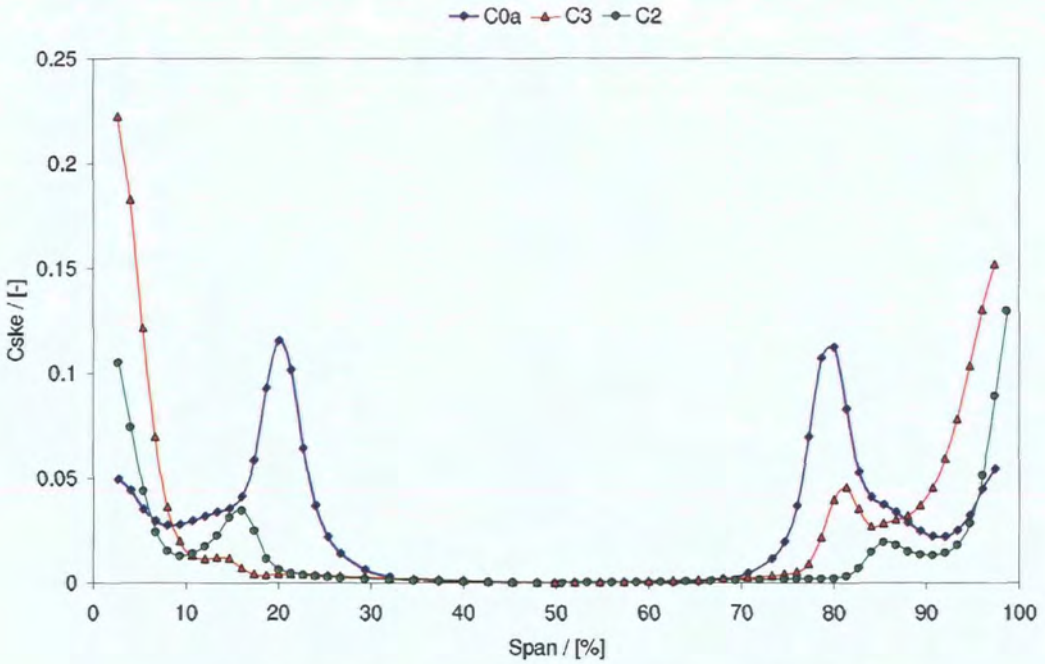

Figure 9.27: Pitchwise averaged C_{SKE} - C0a C3

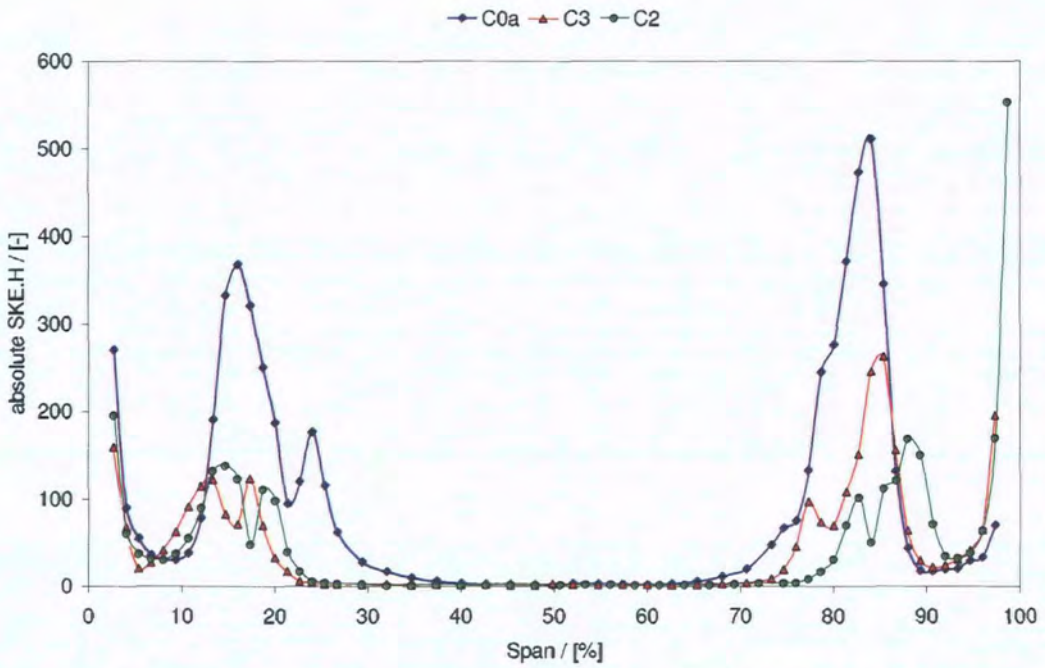

Figure 9.28: Pitchwise averaged SKE.H - C0a C3

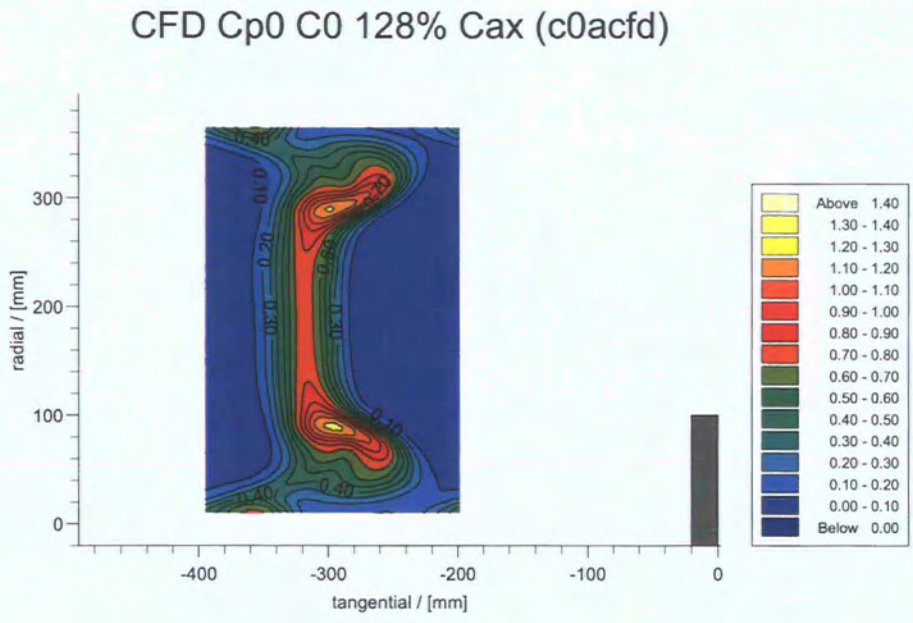

Figure 9.29: CFD Loss C0a at 128% C_{ax}

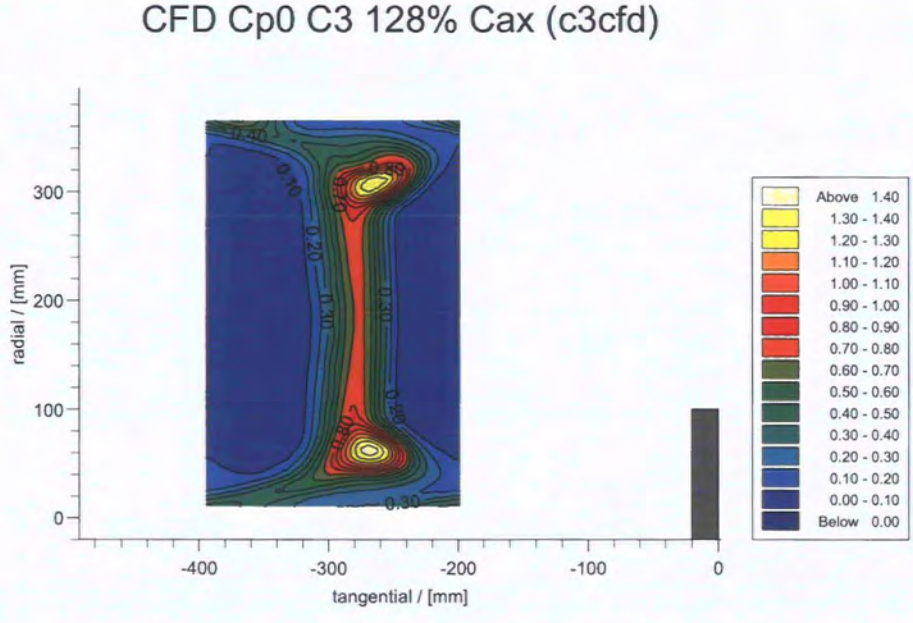

Figure 9.30: CFD Loss C3 at 128% C_{ax}

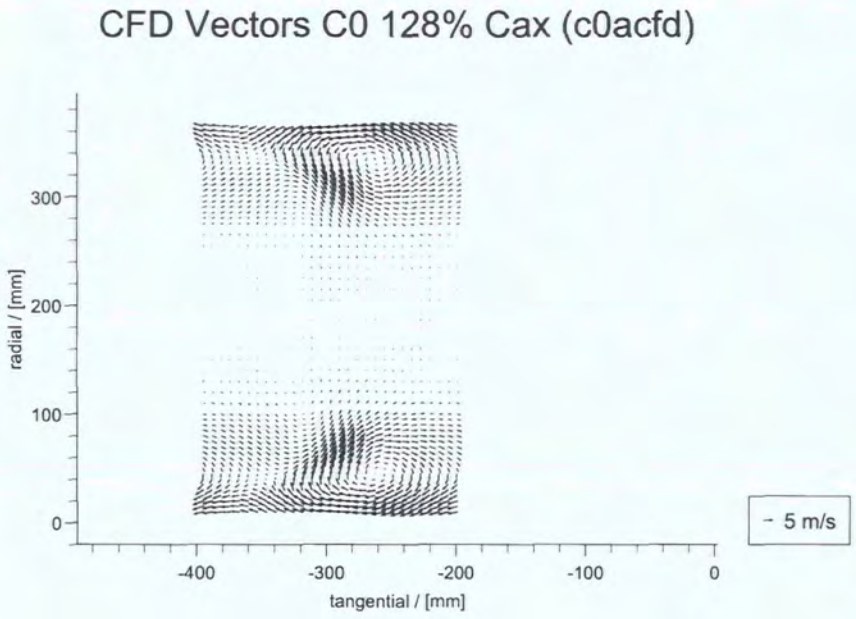

Figure 9.31: CFD Secondary Velocity Vectors C0a at 128% C_{ax}

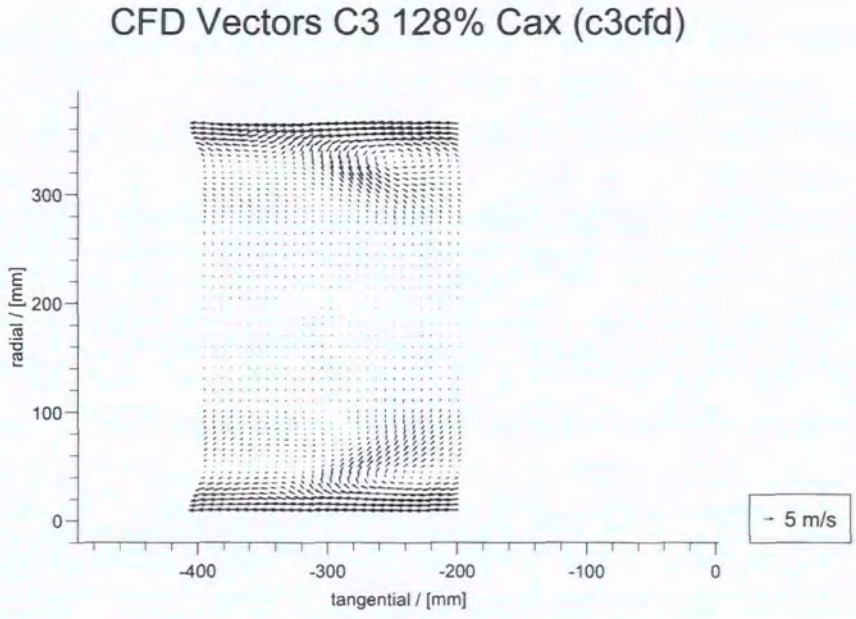

Figure 9.32: CFD Secondary Velocity Vectors C3 at 128% C_{ax}

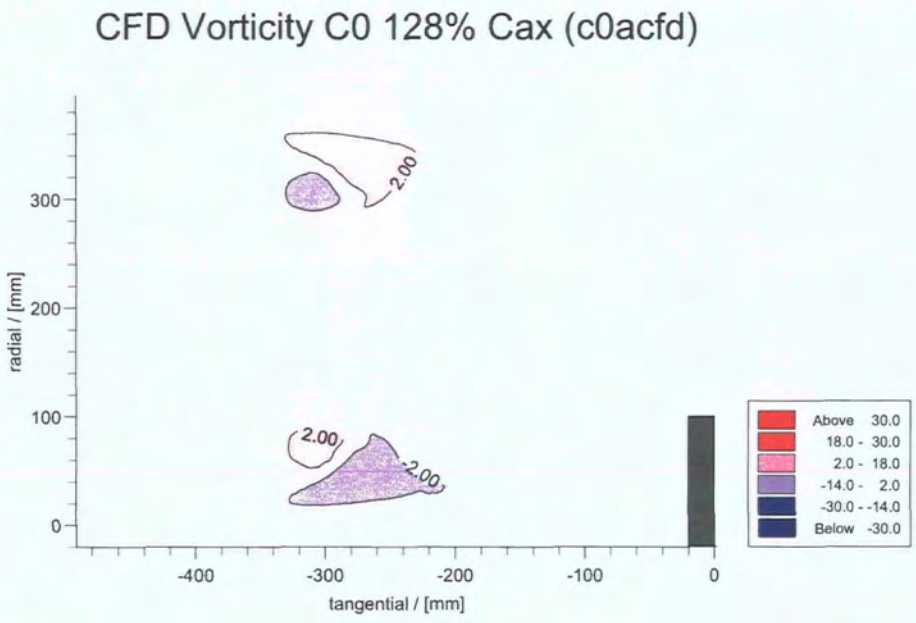

Figure 9.33: CFD Vorticity C0a at 128% C_{ax}

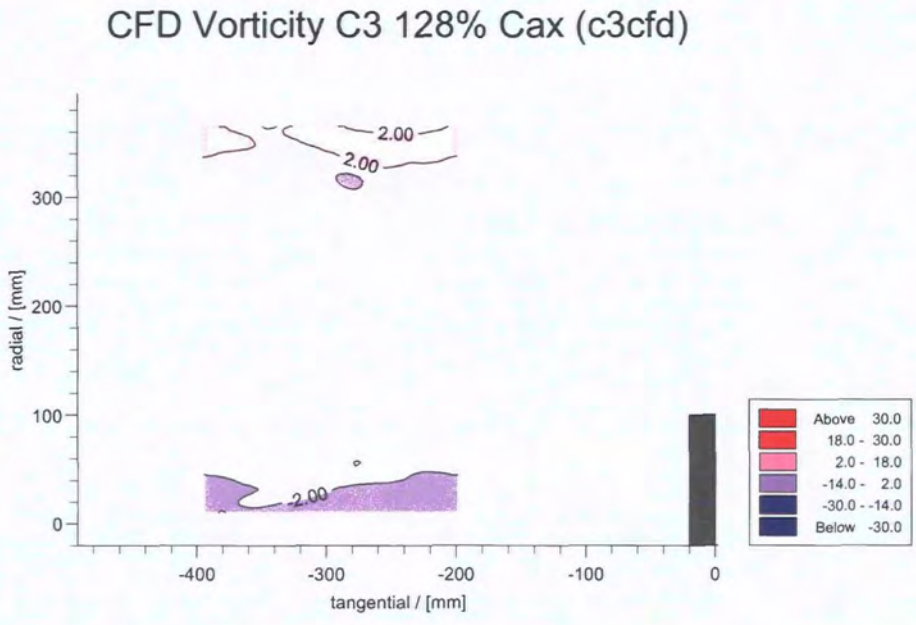

Figure 9.34: CFD Vorticity C3 at 128% C_{ax}

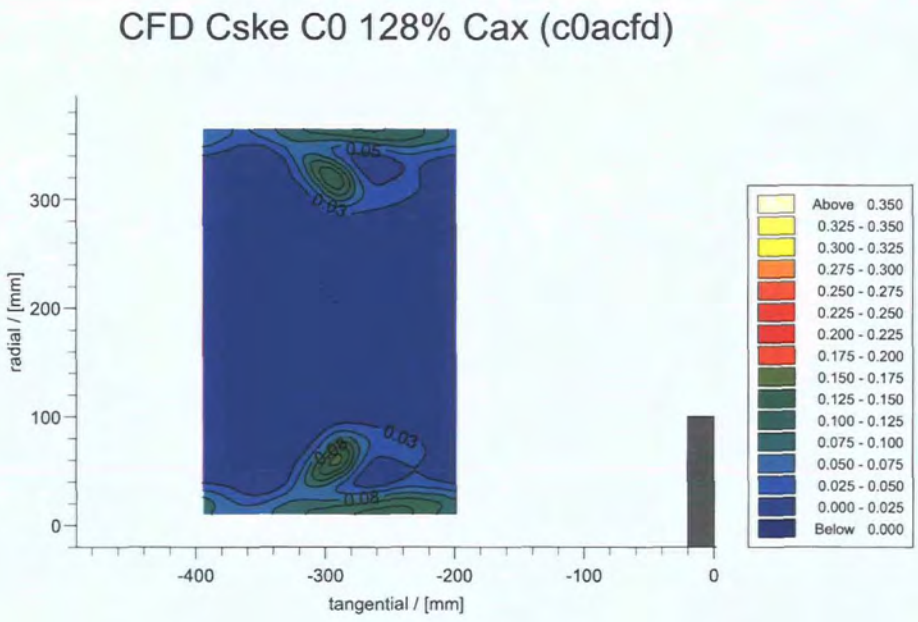

Figure 9.35: CFD C_{SKE} C0a at 128% C_{ax}

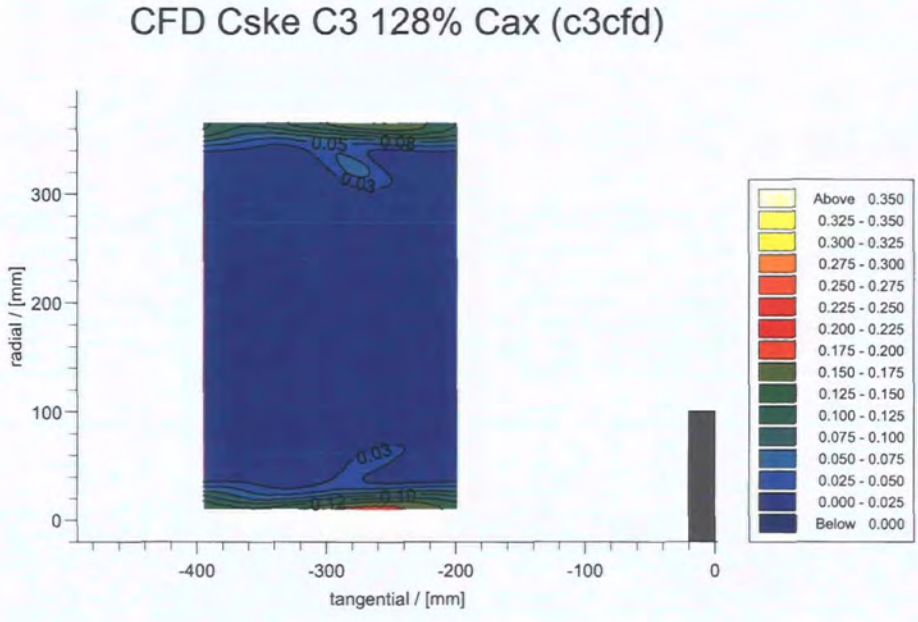

Figure 9.36: CFD C_{SKE} C3 at 128% C_{ax}

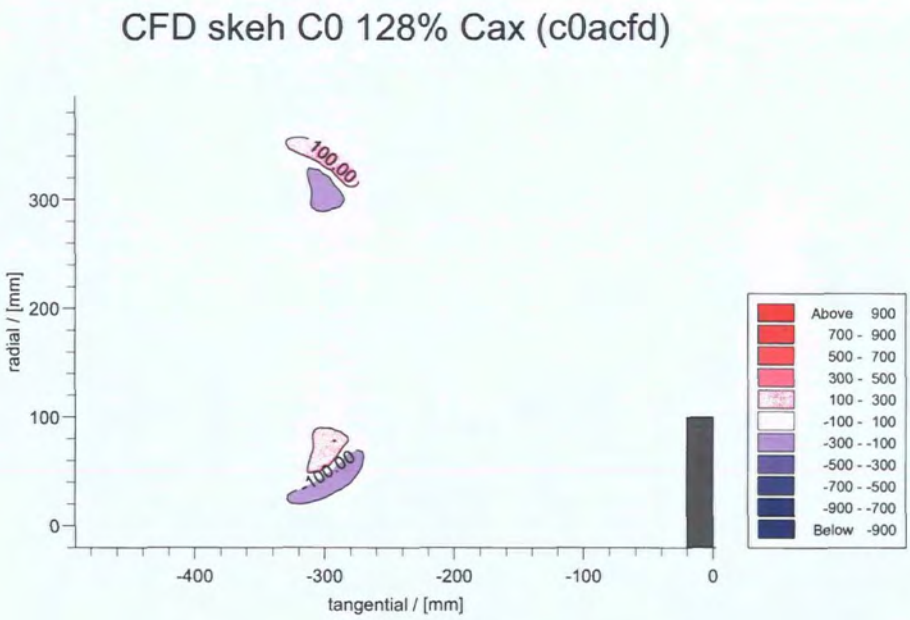

Figure 9.37: CFD SKE.H C0a at 128% C_{ax}

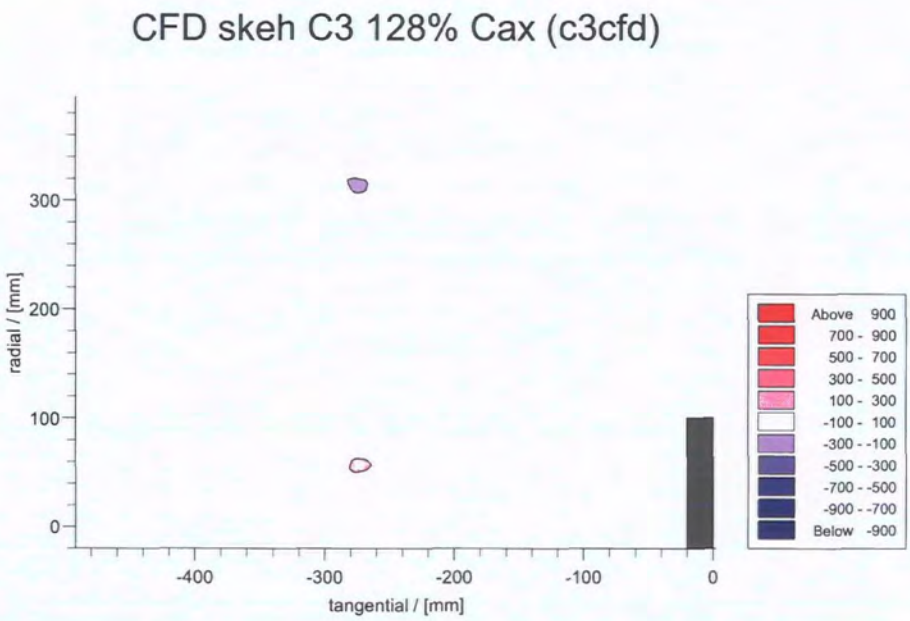

Figure 9.38: CFD SKE.H C3 at 128% C_{ax}

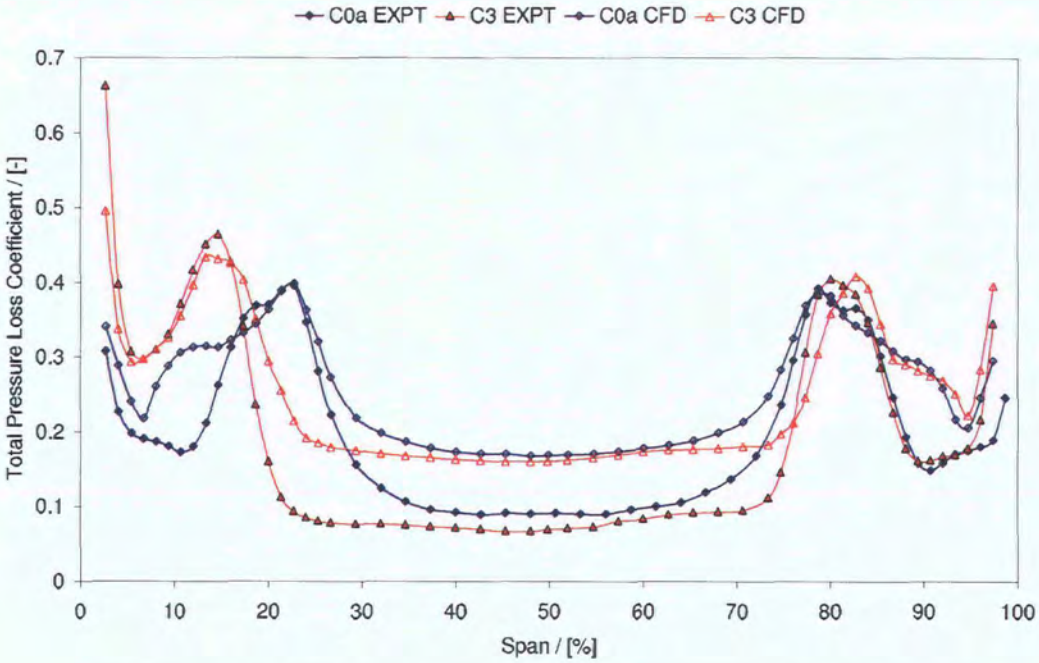

Figure 9.39: Pitchwise averaged Total Pressure Loss Expt vs. CFD

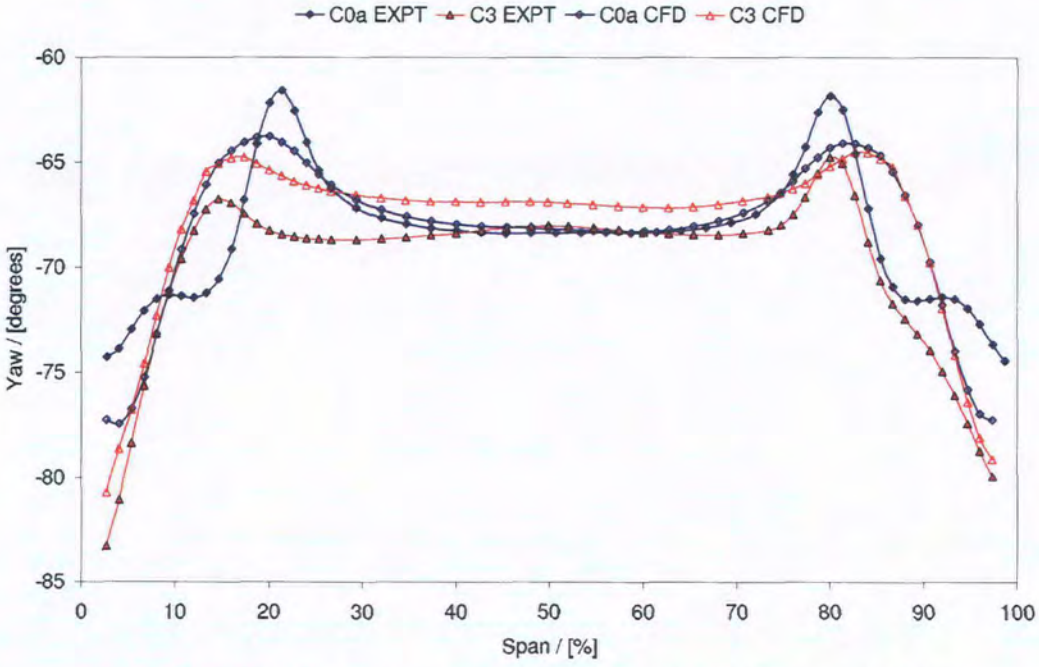

Figure 9.40: Pitchwise averaged Yaw Angle Expt vs. CFD

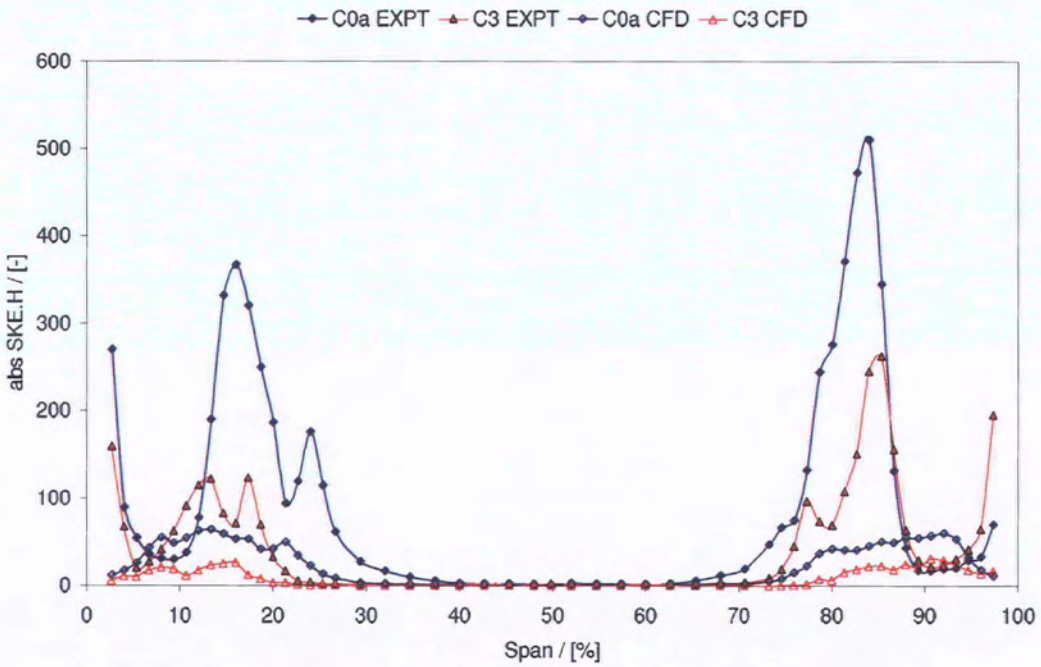

Figure 9.41: Pitchwise averaged SKE.H Expt vs. CFD

Chapter 10

Analysis

THIS chapter summarises the effects of the various geometrical modifications on total pressure loss and yaw angle. The chapter shows both the success of the combined concepts and the limitations observed in some of the designs.

10.1 Computations

The computations presented within this work have used the best available techniques, whilst retaining a desire for rapid computation, on a time scale equivalent to that required in a typical component design.

The relevance of the software choice has been emphasised and its limitations described (Chapter 4). The difficulty in the prediction of performance through total pressure loss remains and the use of proxy analysis variables has been shown to have reasonable success. The prediction falls down in its ability to detect localised separation on the endwall surfaces.

The comparisons of experimental and computational pitchwise averaged results (Chapters 6, 8 and 9) indicate the limitation in the calculation of the blade boundary layer state. The definition of fully turbulent boundary layers results in the over-prediction of profile loss, the under-prediction of secondary flow strength and the incorrect positioning of the key PV features. The use of a reliable transition model may improve this. The manual transition modelling by previous authors has shown good results in this area, but these techniques were not possible throughout the design cycles described in this work.

The impact of the choice of computational analysis plane was presented in Chapter 7 and attention should be paid to the behaviour of the key analysis parameters downstream of the trailing edge. This may be alleviated by the use of multiple analysis planes in the short term.

10.2 Experiments

The experimental techniques remain similar to those used by previous authors (Chapter 3). The measurement system has been updated to give more flexibility. The measurement range has been increased, with the full span now available

and symmetrical inlet conditions present. These alterations have enabled geometries with differing endwall design to be tested simultaneously, saving time and money.

Direct comparison with the results obtained prior to the modifications is not possible, and the performance benefits observed previously can only be used as a guide to the key effects observed here.

10.3 Geometrical effects

10.3.1 PEWs

Non-axisymmetric profiled endwalls in successful operation provide a drop in the strength of the cross passage pressure gradient, controlled by a primary hump/dip arrangement. This leads to a passage vortex reduction as evident in the yaw angles, C_{SKE} and SKE.H results. Where the profiled endwall magnitudes are pushed to a limit, separation of the endwall boundary layer can occur. It has been shown that this separation is not restricted to the endwall itself and loss can be drawn radially outward by the existing secondary flow features.

The review of PEWs in Chapter 5 described the work of previous authors and indicated a relationship between SKE.H and loss reductions in successful endwall design. The chapter set out key criteria for successful PEW design and highlighted the design limits that result in poor performance, not typically predicted computationally.

All the PEW designs affected the loss coefficient and yaw angle from 35% span inwards. The most successful PEW geometry (P2) (from the results of Ingram (2003)) is shown again here as an example of the successful use of PEWs. Figures 10.2 and 10.3 show the effect of PEWs on total pressure loss and exit yaw angle. The PEW decreases the PV loss peak, shifts it radially inward and does not alter the loss at the endwall or on the aerofoil boundary layer.

The yaw angle result indicates the significant reduction in secondary flow and associated radial shift of the secondary flow structure due to the application of PEWs. As the secondary flow reduces, the peak underturning decreases, whilst the overturning peak becomes mixed with the endwall overturned region. The endwall overturning increases above the prismatic value. All PEW designs maintained the same mass averaged exit yaw angle.

10.3.2 RCL

Reverse compound lean reduces the blade loading for the majority of the span. This results in significantly reduced profile loss for the region. The loading is redistributed to the near endwall region, increasing the passage vortex strength, seen in the PV vorticity magnitude and its associated loss, the PV loss core. The ShV/SSHSV is reduced, thus the interaction with the PV and the associated secondary kinetic energy magnitudes have reduced. The geometry induces additional (radially oriented) body forces, which restrain the radial movement of the secondary flows, providing a larger region of primary flow downstream.

The reverse compound lean, as presented in Chapter 6, works on the passage flows through different mechanisms to PEWs. The key effects of RCL on the Durham Cascade geometry are represented in Figures 10.4 and 10.5, and were found to be:

- An offloading of the midspan section, leading to a reduced profile loss, observed in C1 as 0.04 C_{p0}
- Increased secondary losses (0.04 C_{p0} on the PV peak), due to higher velocities in the near endwall region

The spanwise loading forces the PV to remain closer to the endwall. This is seen as a shift of 3-4% span between C0 and C1, leaving a larger region of primary flow. The massflow is redistributed downstream and this impacts the midspan yaw angle.

Whilst the exit metal angle is the same for the RCL geometry, the downstream redistribution of massflow accelerates the midspan flow, this impacts the axial component of the velocity here and the yaw angle is reduced. This value is approximately 1.8^o between geometries C0 and C1.

The use of RCL does not appear to significantly alter the magnitude of the secondary flows, as evident in the yaw angle distribution between C0 and C1. Both the peak underturning and peak overturning are within 0.2^o of C0.

Whilst the RCL has produced a loss reduction in this case, other authors have not had such success, and the balance of lean extent, level of turning and aspect ratio must be taken into account. For lower aspect ratios, the proportions of profile and secondary loss will be altered and the primary benefit of RCL will be reduced.

10.3.3 Passage Shaping

By combining the reverse compound lean with localised chord extension and pressure surface infill, the near endwall loading is reduced and the turning is maintained. These additional modifications do not reduce the magnitude of the passage vortex loss, despite reducing its intensity (seen in C_{SKE} and SKEH). This may be an increase in scrubbing loss because of the increased wetted surface area in the near endwall region.

The final passage shaped aerofoil design was presented in Chapter 7. The aerofoil was combined with a series of different PEW designs and a planar endwall for reference. The key features of the passage shaped geometry are; a RCL stack with extended leading edge and filled in pressure surface at the endwall. The reverse compound lean uses the same stacking profile as C1, but due to its reduced span the absolute midspan displacement is lower. As noted in Chapter 6, the impact of RCL is thought to be most significantly affected by the midspan displacement. As such, reduced effects were expected for the passage shaped component.

The leading edge extension design was significantly analysed and altered in Chapter 7 to obtain a successful offloading of the near endwall region. The design provides an additional 10% axial chord at the endwall, blended to 30% span. The leading edge extension design is quite different to earlier fillet and bulb geometries in both its size and design intent. The additional chord, associated weight and increased platform length must be accommodated in the real turbine and thus its final use may be influenced by this.

The pressure surface infill, associated with this extension, is important in geometries where the variation in inlet angle and thus incidence angle, can result in pressure surface separations. An additional benefit of the PS infill is the acceleration of the near PS flows, and the associated reduction in cross passage pressure gradient as a result. In this sense, the PS infill acts similarly to PEWs. Again, the use of PS infill may increase the mass of the aerofoil component and impact any decision for its use in a rotating environment.

The passage shaped aerofoil (C3 planar) works by the RCL mechanism driving the secondary flows toward the endwall, where the offloaded LE design and PS infill combine and decrease the secondary flow magnitudes.

The effects of passage shaping with planar endwalls, on loss and yaw angle, are presented in Figures 10.6 and 10.7. The C3 design reduces the midspan loss by approximately 0.025 C_{p0}. This is less than the 0.04 C_{p0} change of the C1 geometry. The loss in the PV core is the same as the prismatic whilst the loss between the PV core and the endwall is reduced slightly. The RCL shifts the PV further radially in, as evident in the yaw angles.

The peak underturning has dropped by more than 3^o. This reduction in the underturning peak contrasts the RCL behaviour and must therefore be the impact of the LE extension and PS infill. The midspan offloading and change in midspan loss, are less significant for all passage shaped geometries. This indicates the effect of the smaller midspan displacement. Due to the lessened midspan loss benefit, the C3 planar can be seen as less successful than C1 in Figure 10.10.

10.3.4 Passage Shaping + PEWs

The application of profiled endwalls to the newly shaped geometry, works in a similar manner to before. The profiled endwall reduces the cross passage pressure gradient and thus the strength of the passage vortex. The under turning and over turning peaks associated with the vortex are diminished, with successful geometries reducing the underturning to within 1^o of the midspan level. The overturning at the endwall is however significantly increased due to the higher loading there.

The impact of the profiled endwall on loss varies with the individual designs, indicating the continued difficulty in determining the optimum design. Where the profiling is focussed at the rear of the passage, as in the design of C2 mild, the loss reduction was found to be most significant. Where the profiling magnitudes are larger, an increase in loss is seen in the near wall region. The separations observed in the C2 aggressive design go some way to explaining this. It was observed during computational design, that the larger axial extent provides more freedom and greater potential for SKEH and loss reduction.

The C3 PEW was found to be the most successful design in terms of secondary flow reduction, with an SKEH reduction equal to the P2 endwall. In addition, the yaw angle distribution indicates a much smoother exit flow. The design of C3 PEW has significantly reduced the yaw angle variation and changed the downstream distribution. A two component yaw distribution (comprising a constant yaw section covering the middle 60% of the span and an overturned section covering the 20% span nearest the endwalls) replaces the over and under turning of the PV feature.

Geometry	Loss Reduction [%]	SKEH Reduction[%]	Yaw Increase (°)
P2	14.9	67	-
C1	14	22	-0.5
C3 Planar	8.5	50	+0.4
C2 Mild	17.8	57	+0.9
C2 Aggressive	11	55	+0.3
C3 PEW	8.9	66	+0.5

Table 10.1: Loss and SKEH reduction and Yaw increase at 128% C_{ax}, 5h probe

In doing so, the C3 PEW design presents the downstream blade row with a yaw distribution that may be more easily designed for.

The development of the PEWs was observed using a summary chart, with the parameters of interest indicated for each stage (perturbation station) of the PEW design.

10.4 Mass Averaged Results

The mass averaged experimental results of all geometries were analysed using five hole probe data covering the region 10mm - 187.5mm. Table 10.1 provides the loss and SKEH reductions and yaw angle increases, for the geometries tested in this study. These results are compared to the successful PEW design (P2). The results indicate that:

- All passage shaped geometries reduce SKEH by 50% and above
- All passage shaped geometries increase the yaw angle (between 0.3° and 0.9°)
- The loss benefit for passage shaping is more variable, with up to 17.8% reduction
- The best SKEH reductions match those obtained for P2
- The best loss reduction has an additional 2.9% reduction above P2

The mass averaged loss and SKEH values from these datasets are presented in Figure 10.10. The data for the P-series geometries, and the C0/C1 geometries, were truncated to correct for the change in span between the different cascade designs. Note should be taken of this and of the different endwall boundary layers present at the different design stages. The chart may be used as a guide to the relative ranking of these designs. The differences between designs C0a/C2/C3 is, however, more straightforward, as all the geometries have the same span and inlet conditions.

The figure expands upon Figure 5.15 of Chapter 5 to include all the C-series geometries. The previously discussed relationship between the SKEH reduction and loss reduction (indicated in the earlier figure by the dashed line) does not hold for geometries that affect loss by other means than through secondary flow. The dashed line is not included to emphasise this. Geometry C1 shows a significant loss reduction due to profile loss effects, but affects SKEH moderately. Geometries

C2 and C3 follow a general trend of reduced SKEH and loss, but different endwall shapes appear to have different results.

As observed in Chapter 8, the C2 Mild endwall design reduces total pressure loss by nearly 18%. This endwall design provided the greatest reduction in total pressure loss seen on the cascade. The endwall design is quite different to the P-series geometries, with the profiling focussed toward the rear of the passage and little profiling at the front.

As seen in Chapter 9, the C3 PEW design reduces the SKEH by 66%. This is almost as large as the reduction seen for the P2 endwall geometry, but the different inlet boundary layers for these two geometries prohibits direct comparison.

10.5 Design Development

The development of the passage shaping design and its impact on the blade static pressures and blade loading distributions is simplified in the sketches of Figure 10.1. The figure shows the design progression of the passage shaping work, comparing a prismatic aerofoil with planar endwalls, to reverse compound lean and the other intermediate developments toward a final passage shaped geometry.

The effects are split into those associated with general blade loading (seen at the top of the figure), and the impact on the static pressure either side of the aerofoil (in the lower half of the figure).

In the upper half, the positive symbols represent increases in loading, for example near the endwall on the RCL geometry and near the accelerations associated with the PEW humps. The negative symbols indicate an offloading, like the general effect at midspan for RCL and the effect of the leading edge extension for "midroot".

For the lower half, the development of the design is shown as a build up of effects on the static pressure. The figure shows the opposing effects of reverse compound lean and leading edge extension geometries. Their combined impact is seen in the C3 planar geometry, which enables the modification of the endwall shape for C2/C3PEW.

10.6 Flow Visualisation

The oil and dye method has proved to be an indispensable method of detecting the 3D separation features on the less successful designs. The technique also gives good approximation of the level of secondary flow by the interaction of the PV with the SS. This was measured for the C0a, C2 and C3 designs and presented in Figure 10.11, alongside the distence to suction surface interaction (x_{SS-A}).

The results indicate that:

- successful designs reduce the radial extent of the PV SS interaction at the TE
- the distance to the HSV SS interaction point can be measured as an indication of the design's success

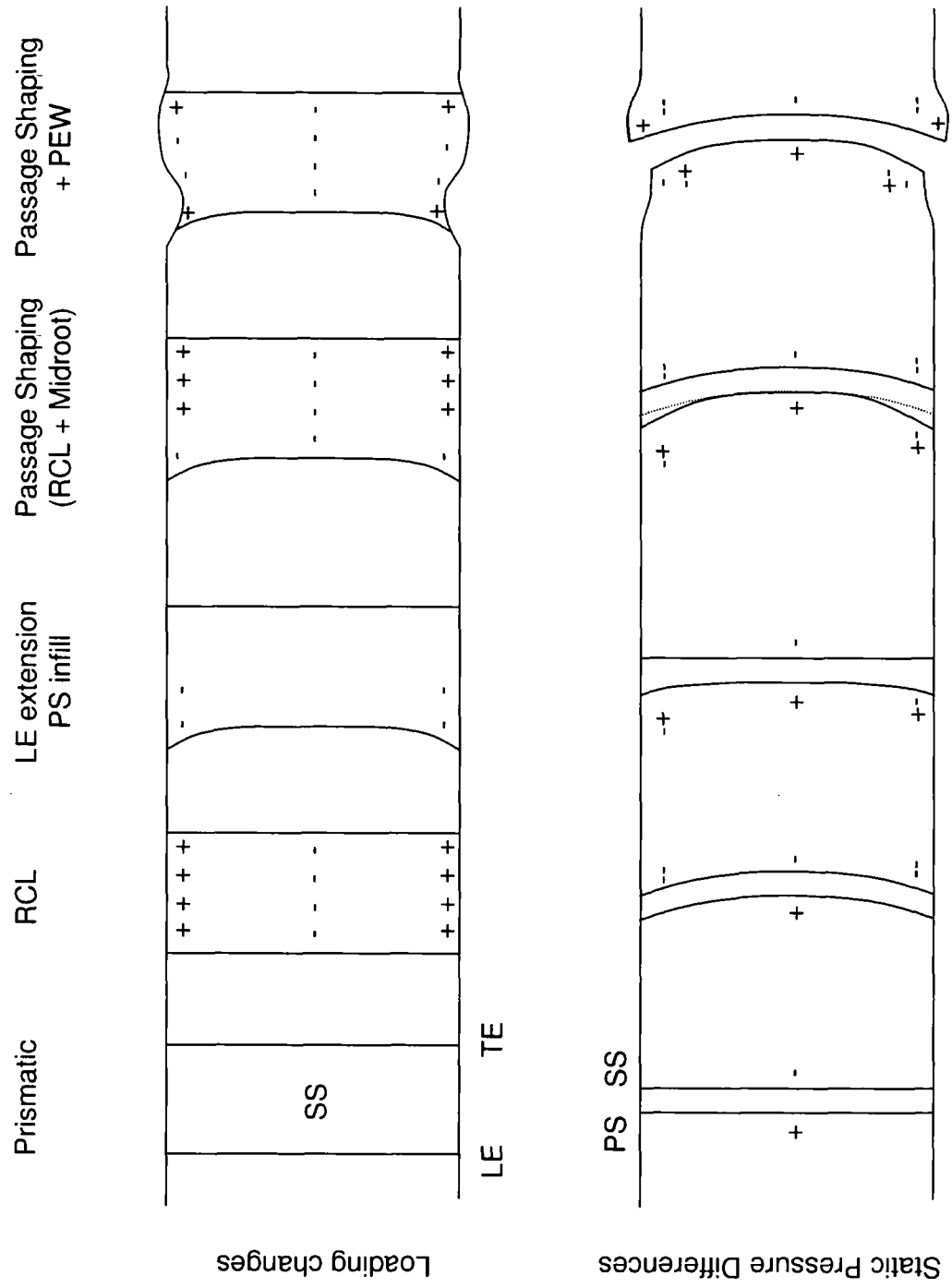

Figure 10.1: Sketch of geometries investigated and effects

10.7 Figures

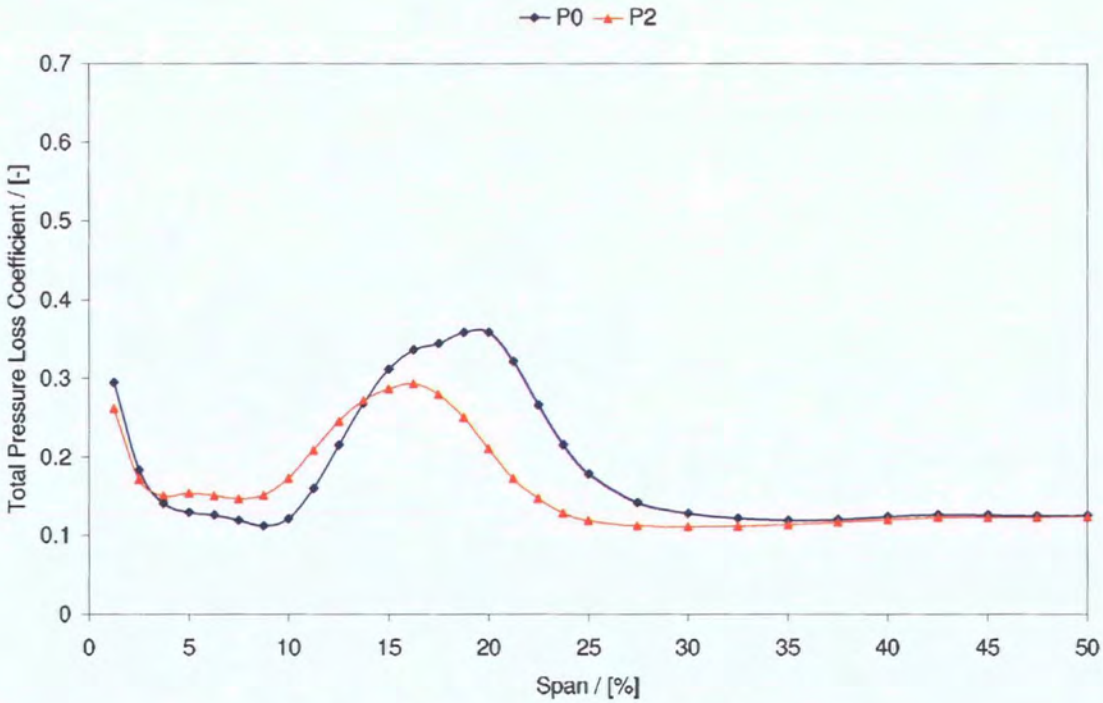

Figure 10.2: Profiled Endwalls - Loss

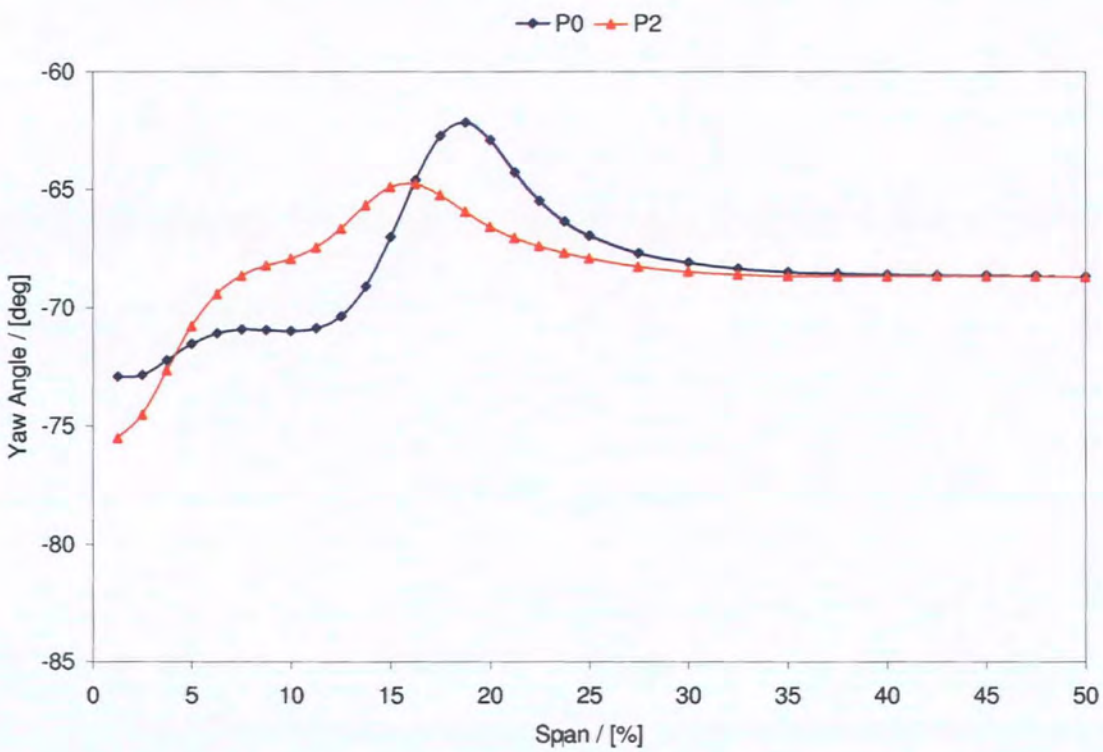

Figure 10.3: Profiled Endwalls - Yaw

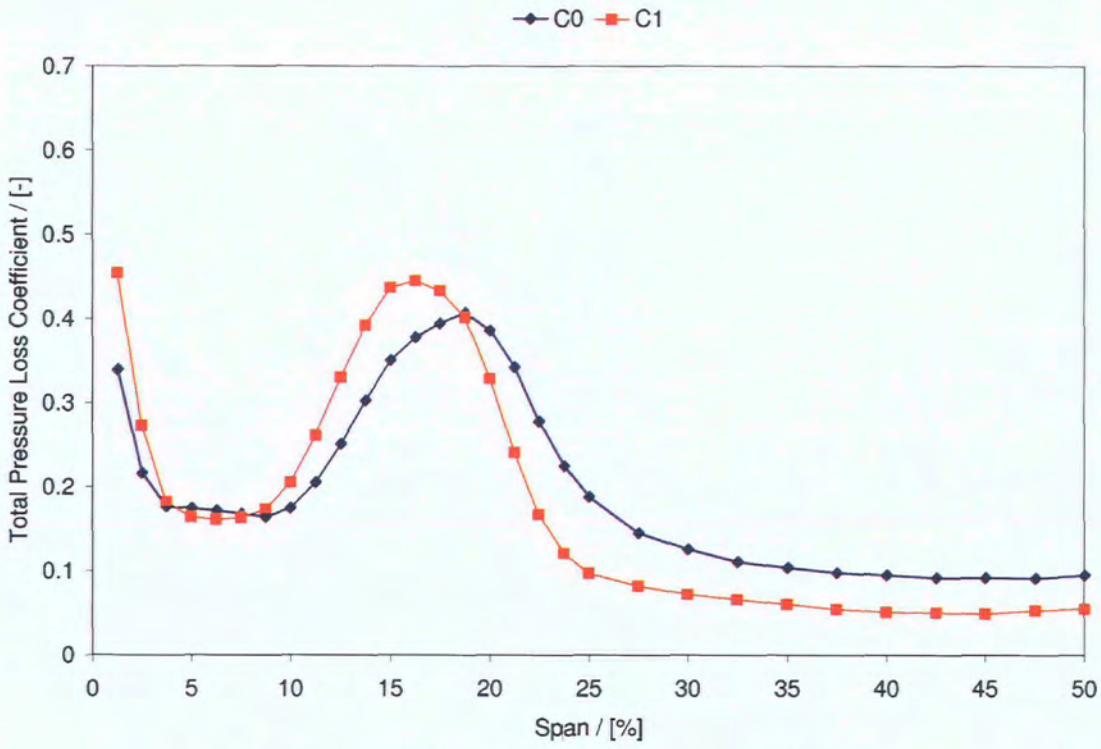

Figure 10.4: Reverse Compound Lean - Loss

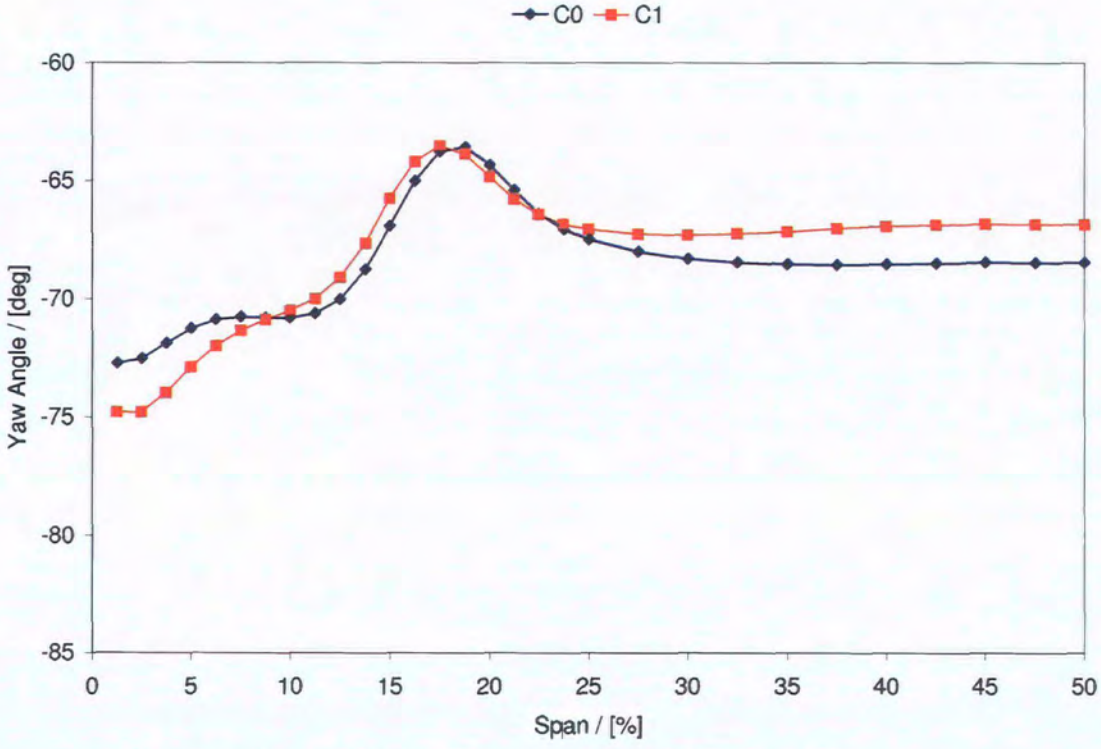

Figure 10.5: Reverse Compound Lean - Yaw

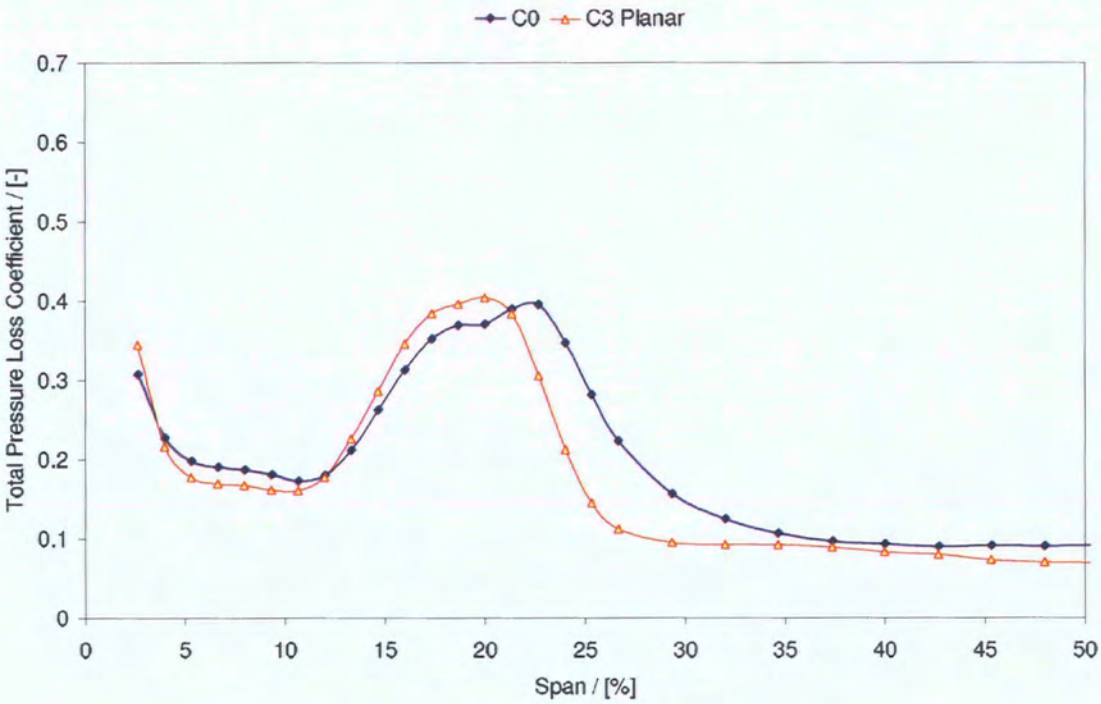

Figure 10.6: Passage Shaping - Loss

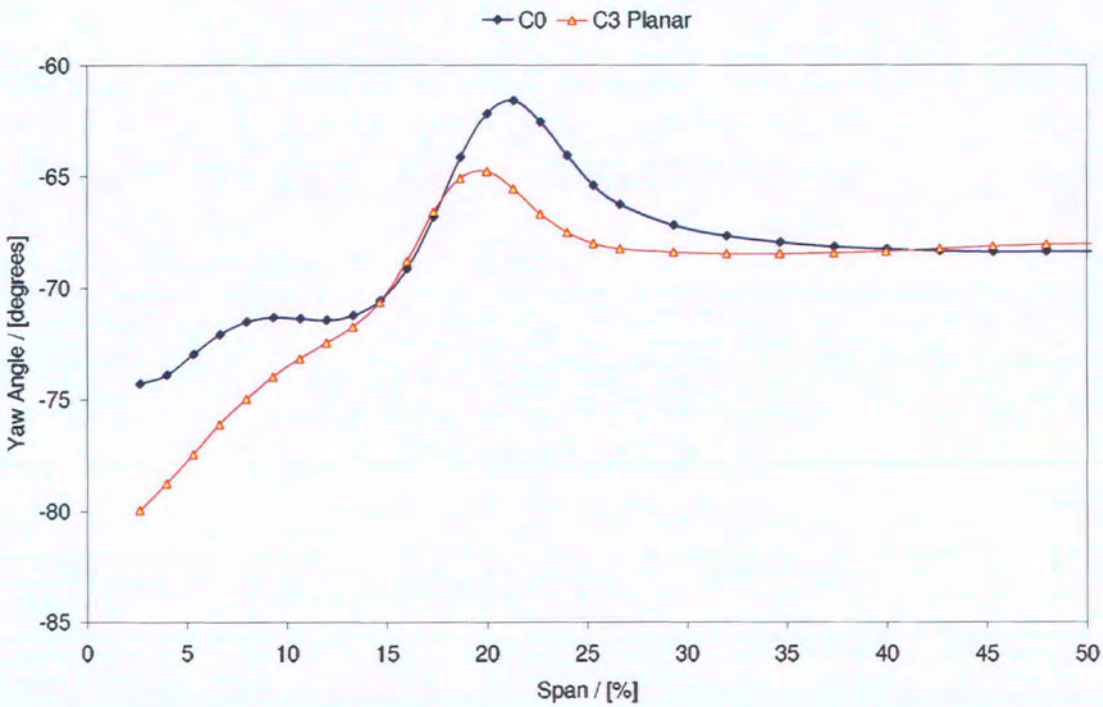

Figure 10.7: Passage Shaping - Yaw

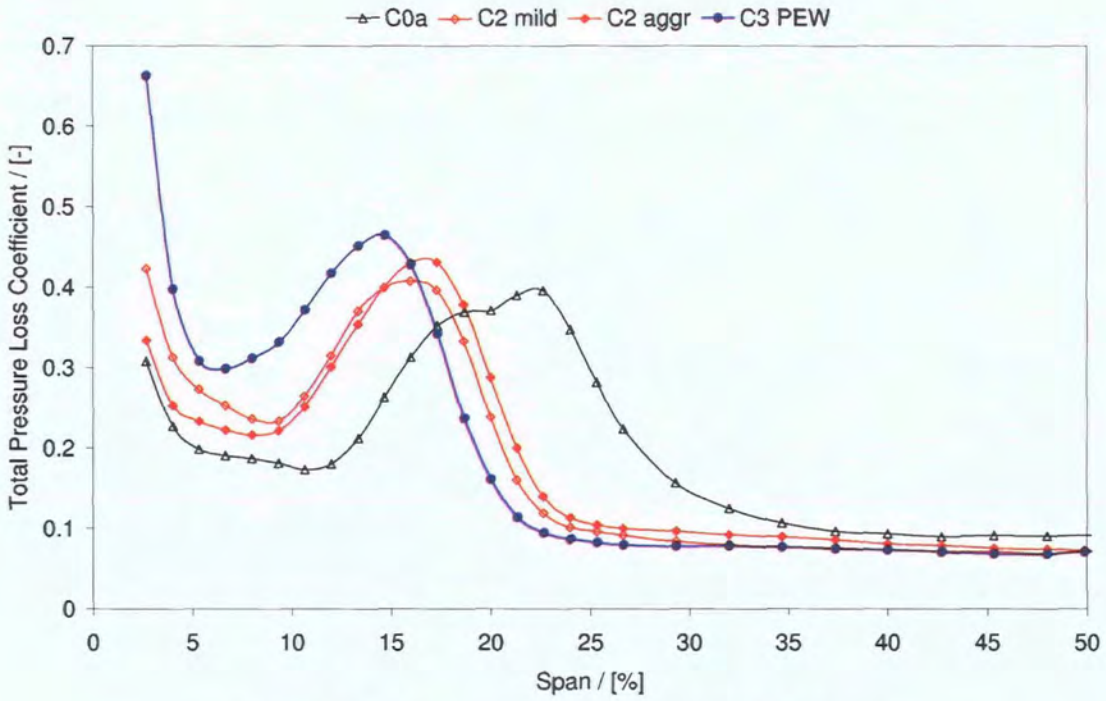

Figure 10.8: Passage Shaping with PEWs - Loss

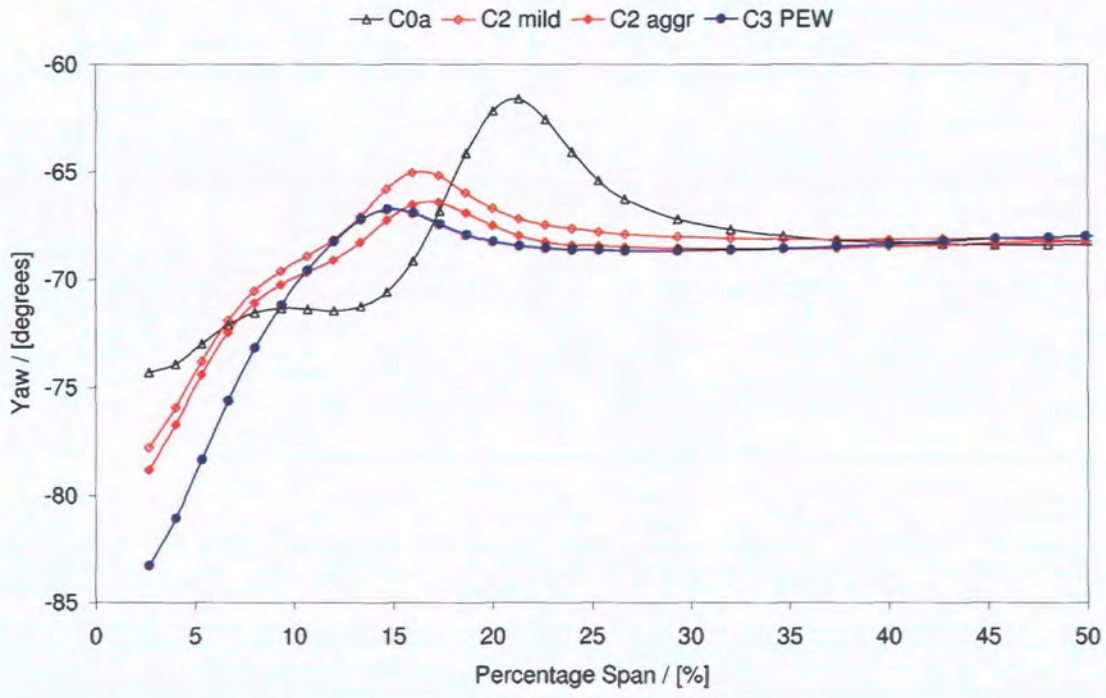

Figure 10.9: Passage Shaping with PEWs - Yaw

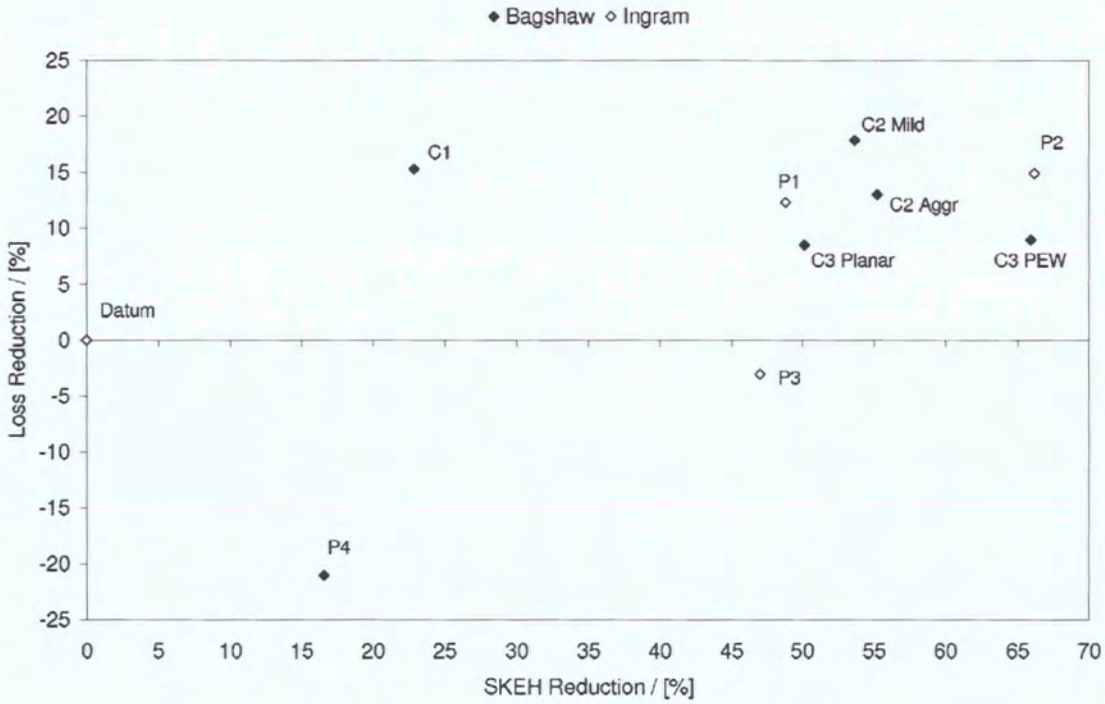

Figure 10.10: Loss and SKEH Comparison

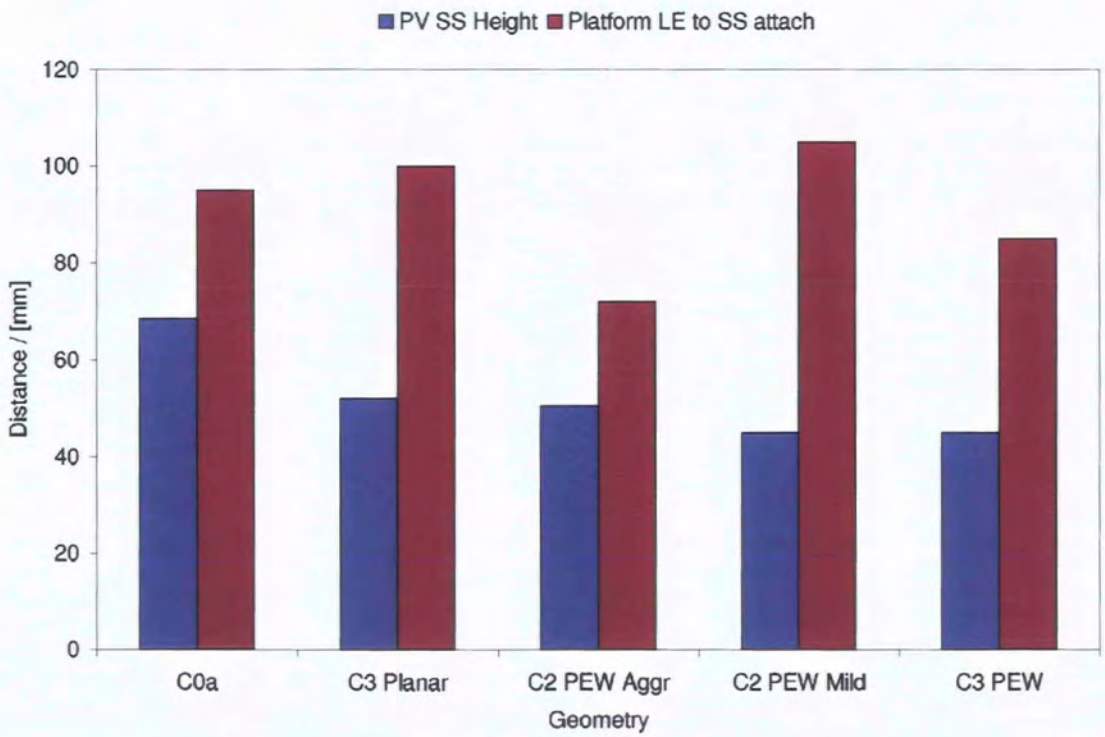

Figure 10.11: Flow Visualisation - Quantative Results

Chapter 11

Conclusions and Recommendations

THIS chapter brings out the key findings of the thesis. The chapter makes recommendations on a number of issues that arose throughout the work including; improvements to the Rolls-Royce design system and changes to cascade aerofoil manufacturing techniques.

11.1 Conclusions

The work has built on the experience and thorough experimental studies on endwall profiling undertaken on the Durham Cascade. The work has provided both highly successful loss and secondary flow reducing designs, alongside some designs with more moderate benefits. A greater understanding of reverse compound lean in highly loaded turbines has been achieved, with the resulting application of lean into a full three dimensional aerofoil shape. The use of a novel combination of aerofoil shaping features has enabled the combination of the endwall profiling designs with reverse compound lean in a successful manner.

The passage shaping geometries resulting from this work have increased the aerofoil length and thickness. These dimensions impact the component mass and length for the same level of turning. As such, it is likely that the implementation of these concepts will focus on stationary vane components. Some combination of these effects, with reduced magnitude, may also be utilised in rotating components.

Passage shaping, whilst not as successful as the P2 endwall geometry, has consistently reduced total pressure loss and SKEH for all designs tested here. The resulting downstream flow patterns are more uniform than those using profiled endwalls alone. This uniformity will produce gains in the stage efficiency beyond those found by applying PEWs alone.

11.1.1 Applicability

The applicability of the design concepts to other environments is dependant upon:

- The aspect ratio - which determines the split of profile and secondary loss

- The design freedom - the lean angles and axial extent at the endwall are key dimensions and restriction of these modifications will limit the benefit of passage shaping
- The boundary layer state - turbulent aerofoil boundary layers will reduce some of the passage shaping benefit

11.1.2 Successful Geometries

The following list describes the geometric designs that were found to be successful:

- Geometry C1 reduced the total pressure loss by 14% for reverse compound lean, a simple geometric change
- Geometry C3 planar combined the reverse compound lean with axial lean aerofoil modifications that resulted in a 50% SKEH reduction
- Geometry C2 Mild successfully combined profiled endwalls with C3 planar and provided a 15% reduction in total pressure loss. This is the highest loss reduction seen in the Durham Cascade
- Geometry C3 PEW, used the same aerofoil shape but a less aggressive endwall design. The geometry had a smaller loss benefit, but resulted in a significantly improved yaw angle distribution at exit. The design resulted in a 66% reduction in SKEH

11.1.3 Unsuccessful Geometries

The following list describes the geometric designs that were less successful:

- Geometry P4 provided a highly profiled design of endwall, resulting in a large endwall separation feature and a loss increase of more than 20%
- Geometry C2 Aggressive also had an endwall separation, despite considerable effort to check the computational model beforehand

11.1.4 Key Learning Points

- Reverse compound lean can be used to reduce loss and SKEH on the Durham Cascade geometry
- Leading edge extension and pressure surface infill combine well with reverse compound lean and further reduce SKEH
- Stacking of the aerofoil sections that results in a localised suction surface concavity, draws out the endwall boundary layer fluid and has a negative impact on performance. Even where the overall shape has reverse compound lean
- Aft focussed profiled endwall designs, provide an alternative concept where the endwall diffusion limits have already been reached

11.1.5 Inlet Boundary Layer

The inlet boundary layers were modified during the work to improve their symmetry and shape. This modification involved extra experimental work and construction. However, it is considered a worthwhile investment, as the boundary layers now present in the cascade are highly symmetrical. The extensive modifications have enabled the cascade to be used for investigations of two endwall geometries at once. This has reduced the manufacturing costs and, importantly, has reduced the experimental time or increased the number of potential geometries that can be examined in a measurement programme.

11.1.6 Traversing Equipment

The upgrade of the probe traversing equipment has provided a greater degree of flexibility to the measurement system. Traverses covering different passages and axial locations may be achieved without the need to manually move the equipment.

The new system provides additional axial traversing. This has not been used extensively in this work. This additional movement enables the automated measurement of multiple traversing planes in one run. This would provide a further advantage to any future testing programme.

11.2 Recommendations

The following recommendations are given from the viewpoint of an experimental researcher with limited experience of the true engine design constraints.

11.2.1 Separation Modelling

The separations observed in endwalls defined in this work, and in earlier work, were all located on the endwall surface. The continued measurement of endwall diffusion by assessment of the nearest aerofoil section does not appear to work. Whilst the reduction in diffusion limits (and endwall heights) appear to have worked for the C3 PEW, the methods involved are somewhat labour intensive.

The implementation of a robust endwall diffusion check would help in this respect. This could possibly be achieved by measurement of the static pressures along pathlines. The check would need to be automated, to ensure its use in the endwall design system.

11.2.2 Design

The arbitrary modification of the profiled endwall, without consideration of the mechanical fillet and the near-endwall aerofoil stacking, may result in poor performance. Designing the endwalls upon completion of an aerofoil design, will limit the potential range of passage designs. Ideally, the modifications would combine PEW and aerofoil surface changes as one.

The redefinition of the problem in terms of the hole through which the fluid passes, would enable the optimisation of the these surfaces in tandem.

11.2.3 Performance Assessment

The measurement of performance parameters during the automated endwall design could be improved upon. The use of multiple axial planes, or some decay rate of the performance parameter, may provide a more reliable performance measure.

11.3 Further Work

The understanding of the trade-offs in endwall profiling design is somewhat basic and requires further, more systematic, work; both experimental and computational. From this it is hoped that 3D separations associated with localised endwall static pressure gradients can be avoided and the full benefit of PEWs can be obtained.

The use of lean and its effects on loss are well researched, but the optimum lean angles and, in particular, lean direction for specific situations (relating to chosen aspect ratio, turning and stage efficiency benefits) remains open. Again, a more thorough breakdown of the behaviour of lean in different environments, will enable its more efficient use.

Bibliography

Barlow, Rae, and Pope (1999). *Low Speed Wind Tunnel Testing.* Number ISBN: 0-471-55774-9. Wiley & Sons, 3rd edition edition.

Barrigozzi, G., Franchini, G., and Perdichizzi, A. (2007). Inlet turbulence intensity effects on secondary flows and adiabatic effectiveness of a film cooled endwall. *Proceedings of the 7th European Conference on Turbomachinery.*

Becz, S. and Majewski, M. (2003). Leading edge modification effects on turbine cascade endwall loss. *ASME Paper 2003-GT-38898.*

Biesinger, T. (1993). *Secondary Flow Reduction Techniques in Linear Turbine Cascades.* PhD thesis, School of Engineering, University of Durham.

Brennan, G., Harvey, N., Rose, M., Formison, N., and Taylor, M. (2001). Improving the efficiency of the trent 500 hp turbine using non-axisymmetric end walls: Part 1 turbine design. *ASME Paper 2001-GT-0444.*

Came, P. and Marsh, H. (1974). Secondary flow in cascades: Two simple derivations for the components of vorticity. *Journal of Mechanical Engineering Science*, 16:391–401.

Cleak, J. (1989). *Validation of Viscous, Three-Dimensional Flow Calculations in an Axial Turbine Cascade.* PhD thesis, School of Engineering, University of Durham.

Corral, R. and Gisbert, F. (2006). Profiled endwall design using an adjoint navier-stokes solver. *ASME Paper GT2006-90650.*

Corriveau, D. and Sjolander, S. (2004). Influence of loading distribution on the performance of transonic high pressure turbine blades. *Journal of Turbomachinery, Transactions of the ASME*, 126:288–296.

Denton, J. (1993). Loss mechanisms in turbomachines. *ASME Paper 93-GT-435.*

Denton, J. and Xu, L. (1999). The explotation of three-dimensional flow in turbomachinery design. *Proceedings of the Institution of Mechanial Engineers*, 213(Part C):125–137.

D'Ippolito, G., Dossena, V., and Mora, A. (2007). A parametrical analysis of the effects produced by leaning and bowing techniques on turbine cascades flow field. *Proceedings of the 7th European Conference on Turbomachinery.*

Dominy, R. and Hodson, H. (1992). An investigation of factors influencing the calibration of 5-hole probes for 3-d flow measurements. *ASME 92-GT-216.*

Duden, A., Raab, I., and Fottner, L. (1999). Controlling the secondary flow in a turbine cascade by three dimensional airfoil design and endwall contouring. *Transactions of the ASME, Journal of Turbomachinery*, 121:191–199.

Eckerle, W. and Langston, L. (1987). Horseshoe vortex formation around a cylinder. *Transaction of the ASME, Journal of Turbomachinery*, 109:278–285.

Feiler, C., Berg, H., Haselbach, F., and Benton, R. (2005). Some aspects of flow and heat transfer measurements of a non-axisymmetrically contoured turbine endwall. *AIAA ISABE Conference Paper ISABE-2005-1117.*

Fischer, A., Riess, W., and Seume, J. (2004). Performance of strongly bowed stators in a four-stage high-speed compressor. *Transactions of the ASME, Journal of Turbomachinery*, 126:333–338.

Gier, J., Ardey, S., Eymann, S., Reinmller, U., and Niehuis, R. (2002). Improving 3d flow characteristics in a multistage lp turbine by means of endwall contouring and airfoil design modification - part 2: Numerical simulation and analysis. *ASME Paper GT-2002-30353.*

Goldstein, R. and Spores, R. (1988). Turbulent transport on the endwall in the region between adjacent turbine blades. *Transactions of the ASME, Journal of Heat Transfer*, 110:862–869.

Granovskiy, A., Kostege, M., Krupa, V., and Rudenko, S. (2007). Numerical and experimental investigation of two stage gas turbine with bowed vanes. *European Turbomachinery Conference - Athens.*

Graves, C. (1985). *Secondary flows and losses in gas turbines.* PhD thesis, School of Engineering, University of Durham.

Gregory-Smith, D. (1983). Secondary flows and losses in axial flow turbines. *ASME Paper 82-GT-19.*

Gregory-Smith, D. (1993). The ercoftac seminar and workshop on 3d turbomachinery flow predictions, december 1992. *ASME Paper 93-GT-423.*

Gregory-Smith, D. (1995a). 3d flow simulation in turbomachinery - the ercoftac seminar and workshop ii, january 1994. *Proceedings of the 1st European Conference on Turbomachinery.*

Gregory-Smith, D. (1995b). Calculations of the secondary flow in a turbine cascade. *AD-Vol 49, Computational Fluid Dynamics in Aeropropulsion*, (ISBN: 0-7918-1730-X):77–87. Presented at the 1995 ASME International Mechanical Engineering Congress and Exposition.

Gregory-Smith, D. (1997). Lectures on secondary flow. *von Karman Institute for Fluid Dynamics.* Secondary and Tip Clearance Flows in Axial Turbines.

Gregory-Smith, D. and Graves, C. (1983). Secondary flows and losses in a turbine cascade. *AGARD-CP-351, AGARD Conference Proceedings No. 351: Viscous Effects in Turbomachines.*

Gregory-Smith, D., Graves, C., and Walsh, J. (1987). Growth of secondary losses and vorticity in an axial turbine cascade. *ASME Paper 87-GT-114.*

Haller, B. (1997). Full 3d turbine blade design. *von Karman Institute for Fluid Dynamics.* Secondary and Tip Clearance Flows in Axial Turbines.

Harrison, S. (1990). The influence of blade lean on turbine losses. *ASME 90-GT-55.*

Hartland, J. (2001). *Secondary Loss Reduction in Rotor Blades by Non-axisymmetric end-wall profiling.* PhD thesis, University of Durham.

Hartland, J., Gregory-Smith, D., , Harvey, N., and Rose, M. (1999). Non-axisymmetric turbine end wall design: Part 2 experimental validation. *ASME Paper 99-GT-338.*

Hartland, J., Gregory-Smith, D., and Rose, M. (1998). Non-axisymmetric endwall profiling in a turbine rotor blade. *ASME Paper 98-GT-525.*

Harvey, N. and Ramsden, K. (2000). A computational study of a novel turbine rotor partial shroud. *ASME Paper 2000-GT-668.*

Harvey, N., Rose, M., Shahpar, S., Taylor, M., Hartland, J., and Gregory-Smith, D. (2000). Non-axisymmetric turbine end wall design: Part i: Three dimensional linear design system. *Transactions of the ASME, Journal of Turbomachinery,* 122:278–285.

Harvey, N., Rose, M., Taylor, M., Shahpar, S., Hartland, J., and Gregory-Smith, D. (1999). Non-axisymmetric turbine end wall design: Part i: Three dimensional linear design system. *ASME Paper 99-GT-337,* 1:1.

Hawthorne, W. R. and Armstrong (1955). Rotational flow through cascades part 1. the components of vorticity. *The Quarterly Journal of Mechanics and Applied Mathematics 1955 280-292,* Vol 8(3):pp280–292.

Hill, J. and Lewis, R. (1974). Experimental investigations of strongly swept turbine cascades with low speed flow. *Journal of Mechanical Engineering Science,* 16(1).

Hoeger, M., Schmidt-Eisenlohr, U., Gomez, S., Mller, R., and Sauer, H. (2002). Numerical simulation of the influence of a bulb and a fillet on the secondary flow in a compressor cascade. *Transactions of TASK Quarterly,* 6:25–57.

Holley, B. and Langston, L. (2006). Surface shear stress and pressure measurements in a turbine cascade. *ASME Paper GT2006-90580.*

Horton, G. (2004). *Forecasts of C02 emissions from civil aircraft for IPCC.* Qinetiq.

Houghton, E. and Carpenter, P. (2004). *Aerodynamics for Engineering Students.* Butterworth Heinemann, fifth edition edition.

Hourmouziadis, J. and Huebner, N. (1985). 3-d design of turbine airfoils. *ASME Paper 85-GT-188.*

Ingram, G. (2003). *Endwall profiling for the reduction of secondary flow in turbines.* PhD thesis, University of Durham.

Ingram, G. and Gregory-Smith, D. (2006). An automated instrumentation system for flow and loss measurements in a cascade. *Journal of Flow Measurement and Instrumentation.*

Ingram, G., Gregory-Smith, D., and Harvey, N. (2005). Investigation of a novel secondary flow feature in a turbine cascade with end wall profiling. *Transactions of the ASME, Journal of Turbomachinery*, 127:209–214.

Ingram, G., Gregory-Smith, D., Rose, M., Harvey, N., and Brennan, G. (2002). The effect of end-wall profiling on secondary flow and loss development in a turbine cascade. *ASME Paper GT-2002-30339.*

Jayaraman, P. (2000). An investigation of secondary flow in a turbine blade with end wall profiling. Master's thesis, School of Engineering, University of Durham.

Kawagishi, H. and Kawasaki, S. (1991). The effect of nozzle lean on turbine efficiency. *ASME PWR. Design, Repair, and Refurbishment of Steam Turbines*, 13.

Langston, L. (2001). Secondary flows in axial turbines - a review. *Annals of the New York Academy of Sciences: Heat Transfer in Gas Turbine Systems.*

Langston, L., Nice, M., and Hooper, R. (1977). Three-dimensional flow within a turbine cascade passage. *Transactions of the ASME, Journal of Engineering for Power.*

Lewis, R. and Hill, J. (1971). The influence of sweep and dihedral in turbomachinery blade rows. *Journal of Mechanical Engineering Science*, 13(4).

Mahmood, G., Gustafson, R., and Acharya, S. (2005). Experimental investigation of flow structure and nusselt number in a low-speed linear blade passage with and without leading-edge fillets. *Transactions of the ASME, Journal of Heat Transfer.*

Merzkirch (1974). *Flow Visualisation.* Number ISBN: 0-12-491350-4. Academic Press Inc, 1st edition edition.

Moore, H. (1995). *Experiments in a Turbine Cascade for the Validation of Turbulence and Transition Models.* PhD thesis, University of Durham.

Moore, J. G. (1985). Calculation of 3d flow without numerical mixing. *AGARD-LS-140 on 3D Computation Techniques applied ot Internal Flows in Propulsion Systems*, pages 8.1–8.15.

Nicholson, J. (1981). Experimental and theoretical studies of the aerodynamic and thermal performance of modern gas turbine blades. *D. Phil. Thesis, University of Oxford.*

Northall, J. (2006). The influence of variable gas properties on turbomachinery computational fluid dynamics. *Journal of Turbomachinery*, 128:632–638.

Northall, J., Moore, J., and Moore, J. (1987). Three-dimensional viscous flow calculations for loss prediction in turbine blade rows. *Paper No. C267, I. Mech. E. Conf. On Turbomachinery Efficiency Prediction and Improvement.*

Palafox, P., LaGraff, J., Oldfield, M., and Jones, T. (2005). Piv maps of tip leakage and secondary flow fields on a low speed turbine blade cascade. *ASME Paper GT2005-68189.*

Pankhurst, R. and Holder, D. (1968). *Wind Tunnel Technique - An account of experimental methods in low and high speed wind tunnels.* Sir Issac Pitman and Sons Ltd.

Pieringer, P. and Sanz, W. (2000). Influence of the fillet between blade and casing on the aerodynamic performance of a transonic turbine vane. *ASME Paper GT2004-53119.*

Pullan, G. and Harvey, N. (2006). The influence of sweep on axial flow turbine aerodyanmics at midspan. *ASME Paper GT-2006-91070.*

Pullan, G. and Harvey, N. (2007). The influence of sweep on axial flow turbine aerodynamics in the endwall region. *ASME Paper GT2007-27750.*

Rehder, H.-J. and Dannhauer, A. (2006). Experimental invstigation of turbine leakage flows on the 3d flow field and endwall heat transfer. *ASME Paper GT-2006-90173.*

Reid, K., Denton, J., Pullan, G., Curtis, E., and Longley, J. (2006a). The effect of stator-rotor hub sealing flow on the mainstream aerodynamics of a turbine. *ASME Paper GT-2006-90838.*

Reid, K., Denton, J., Pullan, G., Curtis, E., and Longley, J. (2006b). Reducing the performance penalty due to turbine inter-platform gaps. *ASME Paper GT-2006-90838.*

Roach, P. (1987). The generation of nearly isotropic turbulence by means of grids. *International Journal of Heat and Fluid Flow*, 8(2):82–92.

Rose, M. (1994). Non-axisymmetric endwall profiling in the hp ngvs of and axial flow gas turbine. *ASME Paper 94-GT-249.*

Saha, A. and Acharya, S. (2006). Computations of turbulent flow and heat transfer through a three-dimensional non-axisymmetric blade passage. *ASME Paper GT-2006-90390.*

Saha, A., Mahmood, G., and Acharya, S. (2006). The role of leading-edge contouring on endwall flow and heat transfer: Computations and experiments. *ASME Paper GT-2006-91318.*

Saravanamuttoo, H., Rogers, G., and Cohen, H. (2001). *Gas Turbine Theory.* Pearson Education, fifth edition edition.

Sauer, H. and Wolf, H. (1997). Influencing the secondary flow in turbine cascades by the modification of the blade leading edge. *Proceedings of the 2nd European Conference on Turbomachinery.*

Shahpar, S. (2001). Three-dimensional design and optimisation of turbomachinery blades using the navier-stokes equations. *ISABE 2001 Paper 1053.*

Shahpar, S. and Lapworth, B. (1998). A forward and inverse three-dimensional linear design system for turbomachinery applications. *Proceedings of 4th ECCOMASS Computational Fluid Dynamics Conference, Athens.*

Sharma, O., Kopper, F., Stetson, G., Magge, S., Price, F., and Ni, R. (2003). A perspective on the use of physical and numerical experiments in the advancement of design technology for axial flow turbines. *ISABE 2003, Cleveland Ohio.*

Sieverding, C. (1985). Recent progress in the understanding of basic aspects of secondary flows in turbine blades passages. *Transactions of the ASME, Journal of Engineering for Gas Turbines and Power*, 107:248.

Sieverding, C. and Bosche, V. D. (1983). The use of coloured smoke to visualize secondary flows in a turbine-blade cascade. *Journal of Fluid Mechanics, Cambridge University Press*, 134:85–89.

Smith, L. H. and Yeh, H. (1963). Sweep and dihedral effects in axial-flow turbomachinery. *Transaction of the ASME, Journal of Basic Engineering*, page pp401 to 416.

Squire, H. and Winter, K. (1951). The secondary flow in a cascade of airfoils in a nonuniform stream. *Journal of Aerodynamic Science.*

Stieger, R. and Hodson, H. (2004). The transition mechanism of highly loaded low-pressure turbine blades. *Transactions of the ASME, Journal of Turbomachinery.*

Stokes, M. (2003). Discussions on tangential lean - undocumented. *Rolls-Royce.*

Takeshi, K., Matsuura, M., Aoki, S., and Sato, T. (1989). An experimental study of heat transfer and film cooling on low aspect ratio turbine nozzles. *ASME 89-GT-187.*

Torre, D., Vazquez, R., de la Rosa Blanco, E., and Hodson, H. (2006). A new alternative for reduction of secondary flows in low pressure turbines. *ASME Paper 2006GT-91002.*

Treaster, A. and Yocum, A. (1979). The calibration and application of five hole probes. *ISA Transactions*, 18(2):23.

Vand, M. and Songtao, W. (2005). Numerical study of the effects of bowed blades on aerodynamic characteristics in a high pressure turbine blade. *ASME Paper GT2005-68214.*

Walker, P. and Hesketh, J. (1999). Design of low-reaction steam turbine blades. *Proceedings of the Institution of Mechanial Engineers*, 213(Part C):157–174.

Wallis, A., Denton, J., and Demargne, A. (2000). The control of shroud leakage flows to reduce aerodynamic losses in a low aspect ratio, shrouded axial flow turbine. *ASME Paper 2000-GT-475.*

Walsh, J. (1987). *Secondary Flows and Inlet Skew in Axial Flow Turbine Cascades.* PhD thesis, School of Engineering, University of Durham.

Wang, H., Olson, S., Goldstein, R., and Eckert, E. (1997). Flow visualization in a linear turbine cascade of high performance turbine blades. *Transactions of the ASME, Journal of Turbomachinery*, 119:1–8.

Wang, Z. (1999). Three dimensional theory and design method of bowed-twisted blade and its application to turbomachines. *von Karman Institute for Fluid Dynamics.* Turbomachinery Blade Design Systems.

Weiss, A. and Fottner, L. (1993). The influence of load distribution on secondary flow in straight turbine cascades. *ASME Paper 93-GT-86.*

Zess, G. and Thole, K. (2002). Computational design and experimental evaluation of using a leading edge fillet on a gas turbine vane. *Transactions of the ASME, Journal of Turbomachinery.*

Appendix A

Manufacturing of C-Series Geometries

A.1 Manufacturing Techniques

The following provides a brief description of the manufacturing techniques used in this work.

Stereolithography

Stereolithography (STL) uses a ultraviolet curable resin, over which a laser traces out the cross-sectional pattern of the part. This process solidifies the resin and combines it with the layer below. The solid level is dropped beneath the resin and the process is repeated.

Selective Laser Sintering

Selective Laser Sintering (SLS) also uses a laser, here it is used to fuse powders of plastic, metal or ceramic into the desired shape. Similarly the object is built up in layers, with each pass lowering the object and new powder being scraped across.

Polycarbonate Casting

For this process, a die is required to form the original mould. The relative casting cooling rates are affected by the material volume/surface-area ratio. Due to this, the leading and trailing edges cool at different rates and particular attention was needed to control this process.

A.2 Geometry C1

The C1 geometry, a reverse compound leaned aerofoil, was designed for the 400mm span cascade. The fixing method required the integration of a threaded bar at one end and a locating stub at the other.

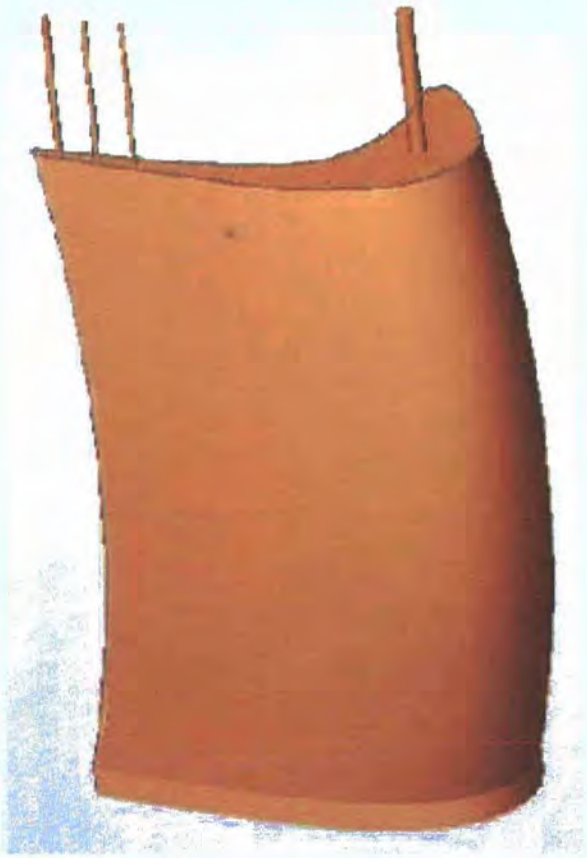

Figure A.1: C1 Aerofoil Geometry

An initial model was manufactured, using the STL technique, and used as a die to cast the six regular polycarbonate blades that make up the cascade. The new blades were designed to fit into the cascade with minimal modification.

A separate single piece blade was manufactured, using the STL technique, for the static pressure measurements. This enabled the integration of internal pneumatic channels of complex shape as seen in Figure A.2.

Figure A.1 presents the solid model of the C1 geometry, giving an indication of the blade shape involved. The datum, C0, geometry was made by modification of the existing P0 geometry.

A.3 Geometry C0a

The new cascade mounting design locates the cartridge units by their endwall edges. The cartridges are themselves separated by a defined split line, similar in orientation to that of an HP blade platform.

The tapped blade component was manufactured from high density model board, using CNC machining processes. The component has 50 tappings at 11 separate radial positions, covering the full span of the new 375mm height blades. One endwall was also drilled; here the 135 equally spaced tappings allow investigation of endwall

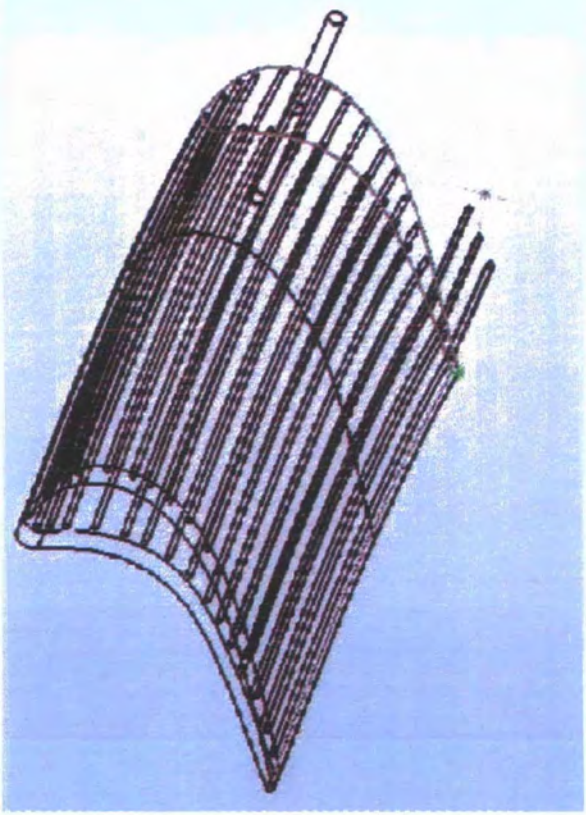

Figure A.2: Pressure Tapped C1 Aerofoil Geometry

Figure A.3: C0a and C2 Pressure Tapped Cartridges

surface pressure distributions.

The simple geometry of the regular blades enabled manufacture by polycarbonate resin casting. A mould was formed from a pre-existing aluminium die, the die was checked for geometric similarity on a coordinate measuring machine.

The pressure tapped cartridges for the C0a and C2 geometries are presented in Figure A.3

A.4 Geometry C2

The C2 geometry is considerably more complex and as such casting was not considered due to the high moulding costs involved. Instead, the six cartridge units were manufactured in three parts, consisting the two endwalls and aerofoil. Each part was machined from high density model board, the individual components were then glued together as they are assembled. The aerofoil component of the pressure tapped cartridge was again made using stereolithography. The endwalls were made from model board and subsequently tapped, assembled and glued. The final C2 geometry is presented in Figure A.4.

A.5 Geometry C3

For the C3 geometry an alternative method was used. A split was defined on the aerofoil away from the aerofoil-endwall intersection, allowing new endwall designs to be interchanged at a reduced cost. The cartridge geometry was constructed from three components, an upper and lower endwall each with a 50mm stub of aerofoil section and the an aerofoil midsection. SLS enabled this by combining a section of the aerofoil and endwall as a single unit. The three parts were combined and pneumatically sealed using a silicon based sealant.

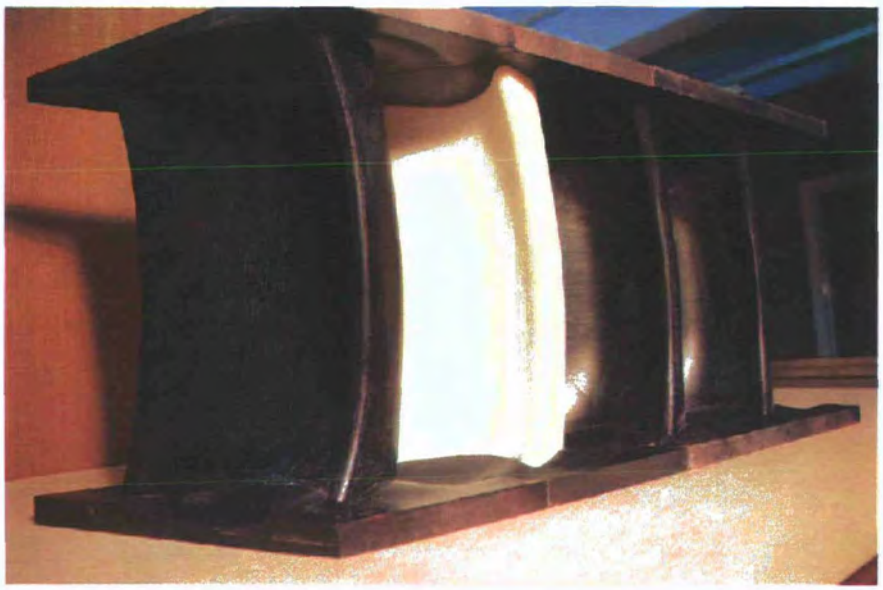

Figure A.4: C2 Cartridge Geometry

All geometries were painted black or white to contrast flow visualisation dyes and were sealed with a chemically resistant melamine lacquer.